Discrete Riemannian Calculus and A Posteriori Error Control on Shape Spaces

Dissertation
zur
Erlangung des Doktorgrades (Dr. rer. nat.)
der
Mathematisch-Naturwissenschaftlichen Fakultät
der
Rheinischen Friedrich-Wilhelms-Universität Bonn

vorgelegt von
Alexander Effland
aus
Oldenburg (Oldb)

Bonn, 2017

Angefertigt mit Genehmigung der Mathematisch-Naturwissenschaftlichen Fakultät der
Rheinischen Friedrich-Wilhelms-Universität Bonn

1. Gutachter: Prof. Dr. Martin Rumpf
2. Gutachter: Prof. Dr. Gabriele Steidl

Tag der Promotion: 13.12.2017
Erscheinungsjahr: 2018

Abstract

In this thesis, a novel discrete approximation of the curvature tensor on Riemannian manifolds is derived, efficient methods to interpolate and extrapolate images in the context of the time discrete metamorphosis model are analyzed, and an a posteriori error estimator for the binary Mumford–Shah model is examined.

Departing from the variational time discretization on (possibly infinite-dimensional) Riemannian manifolds originally proposed by Rumpf and Wirth, in which a consistent time discrete approximation of geodesic curves, the logarithm, the exponential map and parallel transport is analyzed, we construct the discrete curvature tensor and prove its convergence under certain smoothness assumptions. To this end, several time discrete parallel transports are applied to suitably rescaled tangent vectors, where each parallel transport is computed using Schild's ladder. The associated convergence proof essentially relies on multiple Taylor expansions incorporating symmetry and scaling relations. In several numerical examples we validate this approach for surfaces.

The by now classical flow of diffeomorphism approach allows the transport of image intensities along paths in time, which are characterized by diffeomorphisms, and the brightness of each image particle is assumed to be constant along each trajectory. As an extension, the metamorphosis model proposed by Trouvé, Younes and coworkers allows for intensity variations of the image particles along the paths, which is reflected by an additional penalization term appearing in the energy functional that quantifies the squared weak material derivative. Taking into account the aforementioned time discretization, we propose a time discrete metamorphosis model in which the associated time discrete path energy consists of the sum of squared L^2-mismatch functionals of successive square-integrable image intensity functions and a regularization functional for pairwise deformations. Our main contributions are the existence proof of time discrete geodesic curves in the context of this model, which are defined as minimizers of the time discrete path energy, and the proof of the Mosco-convergence of a suitable interpolation of the time discrete to the time continuous path energy with respect to the L^2-topology. Using an alternating update scheme as well as a multilinear finite element respectively cubic spline discretization for the images and deformations allows to efficiently compute time discrete geodesic curves. In several numerical examples we demonstrate that time discrete geodesics can be robustly computed for gray-scale and color images.

Taking into account the time discretization of the metamorphosis model we define the discrete exponential map in the space of images, which allows image extrapolation of arbitrary length for given weakly differentiable initial images and variations. To this end, starting from a suitable reformulation of the Euler–Lagrange equations characterizing the one-step extrapolation a fixed point iteration is employed to establish the existence of critical points of the Euler–Lagrange equations provided that the initial variation is small in L^2. In combination with an implicit function type argument requiring H^1-closeness of the initial variation one can prove the local existence as well as the local uniqueness of the discrete exponential map. The numerical algorithm for the one-step extrapolation is based on a slightly modified fixed point iteration using a spatial Galerkin scheme to obtain the optimal deformation associated with the unknown image, from which the unknown image itself can be recovered. To prove the applicability of the proposed method we compute the extrapolated image path for real image data.

A common tool to segment images and shapes into multiple regions was developed by Mumford and Shah. The starting point to derive a posteriori error estimates for the binary Mumford–Shah model, which is obtained by restricting the original model to two regions, is a uniformly convex and non-constrained relaxation of the binary model following the work by Chambolle and Berkels. In particular, minimizers of the binary model can be exactly recovered from minimizers of the relaxed model via thresholding. Then, applying duality techniques proposed by Repin and Bartels allows deriving a consistent functional a posteriori error estimate for the relaxed model. Afterwards, an a posteriori error estimate for the original binary model can be computed incorporating a suitable cut-out argument in combination with the functional error estimate. To calculate minimizers of the relaxed model on an adaptive mesh described by a quadtree structure, we employ a primal-dual as well as a purely dual algorithm. The quality of the error estimator is analyzed for different gray-scale input images.

Contents

List of Figures

List of Tables

Acknowledgements

FIRST and foremost I would like to express my deep gratitude to my advisor Prof. Dr. Martin Rumpf, who introduced me to many interesting topics in numerical mathematics like image processing and discrete geodesic calculus. Furthermore, I would like to thank him for his excellent guidance and his constant support throughout the past years.

I highly appreciate the willingness of Prof. Dr. Gabriele Steidl for co-reviewing this thesis and for giving me the opportunity to present parts of this thesis at the conferences "Advances in Mathematical Image Processing" and "Manifold-valued Image Processing".

I am also very indebted to Prof. Dr. Stefan Müller for his excellent training in the theory of partial differential equations, functional analysis as well as general applied analysis and for his great support.

Furthermore, I would like to express my gratitude to Prof. Dr. Alois Kneip for being part of the committee. I deeply appreciate the mentoring by Prof. Dr. Anton Bovier during my PhD studies. My thank also goes to my former office mate Prof. Dr. Benjamin Berkels for many discussions and collaborations during the past years.

I furthermore thank (in alphabetical order) Michael Buchner, Dr. Martina Franken, Benedict Geihe, Dr. Janusz Ginster, Dr. Behrend Heeren, Dr. Stefanie Heyden, Pascal Huber, Dr. Martin Lenz, Èric Lluch, Dr. Ricardo Perl, Florian Schäfer, Dr. Christian Seis, Stefan Simon, Gabriele Sodoge–Stork, Kirsten Stahn, Sascha Tölkes, Dr. Orestis Vantzos and Prof. Dr. Benedikt Wirth for numerous discussions and support.

I also gratefully acknowledge financial support from the Bonn International Graduate School of Mathematics and the CRC 1060 at the University of Bonn.

Finally, I am very grateful to my family for their love and support.

Chapter 1

Introduction

In this thesis, we develop a novel time discrete approximation of the curvature tensor for Hilbert manifolds and prove its convergence. Furthermore, a time discrete analog of the metamorphosis model is introduced, which allows the interpolation and extrapolation in the space of images endowed with a Riemannian structure. Finally, an efficient a posteriori error estimator for the binary Mumford–Shah model is proposed.

The structure of this thesis is as follows:

In Chapter 2, the foundations of Riemannian geometry on (possibly infinite-dimensional) Riemannian manifolds – with a special focus on geodesic curves, the logarithm, the exponential map and the parallel transport – are briefly presented, and we give a short survey of different approaches to model shape spaces. Afterwards, we review the variational time discretization of these concepts for certain Hilbert manifolds and state the corresponding convergence theorems following the work by Rumpf and Wirth [RW13, RW15]. The variational time discretization forms the basis of a novel discretization approach for the Riemann curvature tensor on Hilbert manifolds, whose proof is the core of this chapter. In detail, starting from the very definition of the Riemann curvature tensor via covariant derivatives, we approximate the iterated covariant derivative $\nabla_w \nabla_v \eta$ via discrete parallel transports along three sides of a geodesic parallelogram, where two sides scale quadratically and one linearly in the time step size τ. As an outcome, the discrete curvature tensor converges to its continuous counterpart w.r.t. the topology of the ambient space with a convergence rate of order τ. The associated convergence proof essentially relies on Taylor expansions of the optimality conditions by exploiting symmetry as well as scaling properties of the paths involved. Several numerical examples demonstrate the efficiency of this approach.

In Chapter 3, the metamorphosis model developed in [MY01, TY05a, TY05b] is introduced, in which the space of images is endowed with a Riemannian structure extending the flow of diffeomorphism approach. In detail, given two square-integrable image functions one aims at minimizing the path energy depending on the flow joining these images, which measures the contribution due to the transport of each image particle as well as the image intensity variation along the flow. In this context, energy minimizing flows determine (continuous) geodesics representing minimizers of the path energy. Picking up the ideas of the aforementioned time discretization, we propose a novel time discretization for the metamorphosis model and prove the existence of discrete geodesic curves defined as minimizers of the discrete path energy. Furthermore, we establish the Mosco-convergence of a suitable time interpolated discrete path energy to the continuous path energy of the metamorphosis model w.r.t. the L^2-topology, which in particular proves the existence of minimizers of the continuous model. Finally, discrete geodesic curves for two different discretization approaches – a nonconforming finite element as well as a conforming finite element respectively cubic spline approach – are computed for gray-scale and color images. This chapter is an extended version of [BER15] (joint work with Benjamin Berkels and Martin Rumpf).

Taking into account the time discrete metamorphosis model, we develop and prove the existence of a discrete exponential map in the space of images in Chapter 4, which in particular allows the image extrapolation for a given weakly differentiable input image and a weakly differentiable initial image variation, which is assumed to be sufficiently small in L^2. To this end, departing from the Euler–Lagrange equations of the one-step extrapolation, the existence of critical points of the Euler–Lagrange equations is established via a fixed point argument. By combining this result with an implicit function type argument, which additionally requires the smallness of the

initial variation in H^1, one can rigorously establish local uniqueness and existence of the discrete exponential map. A slightly modified version of the aforementioned fixed point iteration is employed for the actual computation of the discrete exponential map. In several applications to real image data we demonstrate the stability of the proposed methods. This chapter is an extended version of [ERS17a] and [ERS17b] (joint work with Martin Rumpf and Florian Schäfer).

In Chapter 5, we briefly recall the prominent Mumford–Shah model for image segmentation [MS85, MS89], its basic properties and numerical strategies to compute minimizers. Afterwards, we concentrate on the binary model, which can be deduced from the full model by restricting to only two regions. The main goal in this chapter is the derivation of a reliable a posteriori error estimator for the binary model. To this end, we exploit the fact that a minimizer of the binary model can be exactly retrieved from a minimizer of the convex relaxed model via thresholding (*cf*. [Cha05, Ber09]), and derive a functional a posteriori error estimator for the relaxed model using duality techniques and the uniform convexity of the data term following the work by Repin and Bartels (*cf*. [Rep00, Rep12, Bar15]). Then, the a posteriori error estimator for the original binary model relies on a cut-out argument for the non-properly identified phases (*i.e*. the neighborhood of the interfaces) combined with the functional error estimator. We propose a finite difference and two finite element discretizations, and the minimizer of the convex relaxed model is computed using a step size controlled primal-dual as well as a purely dual algorithm. Both error estimators are investigated in several numerical examples. Many results in this chapter have been published in [BER17] (joint work with Benjamin Berkels and Martin Rumpf).

Besides the aforementioned publications I also contributed to the publications [ERS$^+$15] and [BBE$^+$17] that are briefly summarized on page 87.

1.1 Preliminaries

In this section, we recall some general definitions, function spaces and their basic properties used throughout this thesis. An overview of the notation is given in Appendix B and an index can be found at the end of this thesis. Let us begin with some general remarks:

- The symbol C frequently indicates a generic finite positive constant.
- Depending on the context, $\mathbb{1}$ denotes either the identity mapping or the identity matrix.
- The Einstein summation convention is employed at some places.
- The symbol ":" denotes the sum over all pairwise products of two tensors, *e.g*. $A : B = \operatorname{tr}(A^T B)$ for two matrices $A, B \in \mathbb{R}^{n,n}$.
- We denote the variational derivative of a functional J at a point A in a direction B by $\partial_A J[A](B)$, *i.e*.

$$\partial_A J[A](B) = \frac{\mathrm{d}}{\mathrm{d}\varepsilon} J[A + \varepsilon B]\big|_{\varepsilon=0} .$$

- In this thesis, the gradient ∇, the divergence div and all higher order derivatives D^m are always evaluated w.r.t. the spatial variables if not otherwise specified.

Before introducing some function spaces, we briefly recall different regularity properties of domains:

Definition 1.1.1 (Geometric properties of domains (*cf*. [AF03]))**.** Let $\Omega \subset \mathbb{R}^n$ be any bounded, non-empty and open set with boundary $\partial\Omega$.

(i.) The domain Ω has a *Lipschitz boundary* if for each $x \in \partial\Omega$ there exists a neighborhood $U = U(x)$ of x and a Lipschitz function $f : \mathbb{R}^{n-1} \to \mathbb{R}$ such that

$$\Omega \cap U(x) = \{\, y = (y_1, \dots, y_n) \in U(x) \,:\, y_n > f(y_1, \dots, y_{n-1}) \,\} .$$

(ii.) Let $\sphericalangle(x,y)$ denote the angle between $x, y \in \mathbb{R}^n$. A *finite cone* associated with the triple $(v,\rho,\kappa) \in \mathbb{R}^n \times \mathbb{R}^+ \times (0, \frac{\pi}{2}]$ is the set

$$C(v,\rho,\kappa) = \{\, x \in \mathbb{R}^n \,:\, x = 0 \text{ or } 0 < |x| < \rho\,, \sphericalangle(x,v) \le \kappa \,\}\,.$$

The domain Ω satisfies the *cone condition* if there exists a finite cone $C(v,\rho,\kappa)$ such that each $x \in \partial\Omega$ is the vertex of a cone which is contained in Ω and congruent to $C(v,\rho,\kappa)$.

(iii.) The domain is *strongly Lipschitz* if Ω is a Lipschitz domain that satisfies the cone condition.

We set $\partial^\beta f = \partial_{x_1}^{\beta_1} \cdots \partial_{x_n}^{\beta_n} f$ and $|\beta| = \sum_{i=1}^n \beta_i$ for a multi-index $\beta = (\beta_1, \ldots, \beta_n) \in \mathbb{N}^n$. For $k \in \mathbb{N}$ we use standard notation for *the Banach space of continuous or continuously differentiable functions* $C^k(\overline{\Omega})$ on a compact set $\overline{\Omega} \subset \mathbb{R}^n$, which is endowed with the norm $\|\cdot\|_{C^k(\overline{\Omega})}$ and the seminorm $|\cdot|_{C^k(\overline{\Omega})}$ given by

$$\|f\|_{C^0(\overline{\Omega})} = \sup_{x\in\overline{\Omega}} |f(x)|\,, \qquad \|f\|_{C^k(\overline{\Omega})} = \sum_{|\beta|\le k} \|\partial^\beta f\|_{C^0(\overline{\Omega})}\,, \qquad |f|_{C^k(\overline{\Omega})} = \sum_{|\beta|=k} \|\partial^\beta f\|_{C^0(\overline{\Omega})}\,.$$

The space $C^k(\Omega)$ endowed with the metric $d(f,g) = \sum_{i\in\mathbb{N}} 2^{-i} \frac{\|f-g\|_{C^k(K_i)}}{1+\|f-g\|_{C^k(K_i)}}$ for a domain $\Omega \subset \mathbb{R}^n$ is a complete metric space, where $K_i \subset \Omega$ are compact sets such that $K_i \subset K_{i+1}$, $\Omega = \bigcup_{i\in\mathbb{N}} K_i$ and for all $x \in \Omega$ there exists $i \in \mathbb{N}$ and $r > 0$ such that $B_r(x) \cap \Omega \subset K_i$. Moreover, we set $C^\infty(\Omega) = \bigcap_{k\ge 0} C^k(\Omega)$. In addition, for $k \in \mathbb{N}$ and $\alpha \in (0,1]$ *the space of Hölder continuously differentiable functions* $C^{k,\alpha}(\overline{\Omega})$ is a Banach space when equipped with the norm $\|\cdot\|_{C^{k,\alpha}(\overline{\Omega})}$, and we denote by $|\cdot|_{C^{k,\alpha}(\overline{\Omega})}$ the associated seminorm, *i.e.*

$$|f|_{C^{k,\alpha}(\overline{\Omega})} = \sum_{|\beta|=k} \sup\left\{ \tfrac{|\partial^\beta f(x) - \partial^\beta f(y)|}{|x-y|^\alpha} \,:\, x, y \in \overline{\Omega}\,, x \ne y \right\}, \qquad \|f\|_{C^{k,\alpha}(\overline{\Omega})} = \|f\|_{C^k(\overline{\Omega})} + |f|_{C^{k,\alpha}(\overline{\Omega})}\,.$$

Let us agree to set $C^{k,0}(\overline{\Omega}) = C^k(\overline{\Omega})$ for any $k \in \mathbb{N}$. Finally, the subscript c always indicates compactly supported continuous or differentiable functions.

We use standard notation for *Lebesgue* and *Sobolev spaces* on a Lipschitz domain Ω (see [AF03] for details), *i.e.* $L^p(\Omega)$ and $W^{m,p}(\Omega)$ for $m \in \mathbb{N}$ and $p \in [1,\infty]$. In particular, we set $H^m(\Omega) = W^{m,2}(\Omega)$. For any $f, g \in H^m(\Omega)$, $m \ge 1$, we define

$$D^m f \cdot D^m g = \sum_{i_1,\ldots,i_m=1}^n \frac{\partial^m f}{\partial_{x_{i_1}} \cdots \partial_{x_{i_m}}} \cdot \frac{\partial^m g}{\partial_{x_{i_1}} \cdots \partial_{x_{i_m}}}\,, \qquad |D^m f| = (D^m f \cdot D^m f)^{\frac{1}{2}}\,.$$

The associated norms are denoted by $\|\cdot\|_{L^p(\Omega)}$, $\|\cdot\|_{W^{m,p}(\Omega)}$ and $\|\cdot\|_{H^m(\Omega)} = \|\cdot\|_{W^{m,2}(\Omega)}$, respectively, and the seminorms in $W^{m,p}(\Omega)$ and $H^m(\Omega)$ are referred to as $|\cdot|_{W^{m,p}(\Omega)}$ and $|\cdot|_{H^m(\Omega)}$. In detail, the definitions of the (semi-)norms read as

$$\|f\|_{L^p(\Omega)} = \left(\int_\Omega |f|^p \,\mathrm{d}x\right)^{\frac{1}{p}} \quad \text{for } 1 \le p < \infty\,, \qquad \|f\|_{L^\infty(\Omega)} = \inf_{N\subset\Omega:|N|=0} \sup_{x\in\Omega\setminus N} |f(x)|\,,$$

$$|f|_{W^{m,p}(\Omega)} = \|D^m f\|_{L^p(\Omega)}\,, \qquad \|f\|_{W^{m,p}(\Omega)} = \left(\sum_{j=0}^m |f|^p_{W^{j,p}(\Omega)}\right)^{\frac{1}{p}} \quad \text{for } 1 \le p < \infty\,,$$

$$\|f\|_{W^{m,\infty}(\Omega)} = \max_{0\le l\le m} \|D^l f\|_{L^\infty(\Omega)}\,.$$

Furthermore, $H_0^m(\Omega)$ is the closure of $C_c^\infty(\Omega)$ w.r.t. the norm $\|\cdot\|_{H^m(\Omega)}$, and we set $W^{0,p}(\Omega) = L^p(\Omega)$. Finally, we denote the dual space of $H_0^m(\Omega)$ by $H^{-m}(\Omega)$.

The space $H(\mathrm{div},\Omega)$ is defined as (the operator div is understood in the weak sense)

$$H(\mathrm{div},\Omega) = \left\{\, q \in L^2(\Omega,\mathbb{R}^n) \,:\, \mathrm{div} q \in L^2(\Omega) \,\right\}$$

and is endowed with the norm $\|q\|^2_{H(\mathrm{div},\Omega)} = \|q\|^2_{L^2(\Omega)} + \|\mathrm{div} q\|^2_{L^2(\Omega)}$. Moreover, we set $H_N(\mathrm{div},\Omega) = H(\mathrm{div},\Omega) \cap \{q \cdot \mathrm{n} = 0 \text{ on } \partial\Omega\}$, where n denotes the outer normal on $\partial\Omega$ and $q \cdot \mathrm{n}$ has to be understood in the sense of traces of Sobolev functions.

The subsequent two fundamental inequalities are of vital importance throughout this thesis.

Theorem 1.1.2 (Gagliardo–Nirenberg interpolation inequality)**.** *Let $\Omega \subset \mathbb{R}^n$ be a bounded domain satisfying the cone condition. If $f \in L^2(\Omega)$ and $D^m f \in L^2(\Omega)$, then there exist constants $C_{GN,1} = C_{GN,1}(\Omega, m, n) > 0$ and $C_{GN,2} = C_{GN,2}(\Omega, m, n) > 0$ such that for every $j \in \{1, \dots, m-1\}$*

$$|f|_{H^j(\Omega)} \leq C_{GN,1} |f|^{\frac{j}{m}}_{H^m(\Omega)} \|f\|^{1-\frac{j}{m}}_{L^2(\Omega)} + C_{GN,2} \|f\|_{L^2(\Omega)} \leq C_{GN,1} |f|_{H^m(\Omega)} + (C_{GN,1} + C_{GN,2}) \|f\|_{L^2(\Omega)} .$$

Proof. See [Nir66]. □

Theorem 1.1.3 (Korn's inequality)**.** *Let $\Omega \subset \mathbb{R}^n$ be a bounded domain with Lipschitz boundary. For $f \in H^1_0(\Omega)$ there exists a constant $C_{Korn} = C_{Korn}(\Omega, n) > 0$ satisfying*

$$C^{-1}_{Korn} \|f\|_{H^1(\Omega)} \leq \|(Df)^{\mathrm{sym}}\|_{L^2(\Omega)} \leq C_{Korn} \|f\|_{H^1(\Omega)} .$$

Proof. See [Cia88, Section 6.3] and the references therein. □

Let us conclude this section with the central embedding theorem for Sobolev and Hölder functions that we will frequently refer to:

Theorem 1.1.4 (Embedding theorem for Sobolev and Hölder functions)**.** *Let $\Omega \subset \mathbb{R}^n$ be a nonempty, open and bounded Lipschitz domain.*

(i.) If $m_1, m_2 \in \mathbb{N}$ and $p_1, p_2 \in [1, \infty)$ satisfy

$$m_1 - \frac{n}{p_1} \geq m_2 - \frac{n}{p_2} , \qquad m_1 \geq m_2 , \tag{1.1}$$

then a continuous embedding $W^{m_1,p_1}(\Omega) \hookrightarrow W^{m_2,p_2}(\Omega)$ exists and for all $f \in W^{m_1,p_1}(\Omega)$ one obtains

$$\|f\|_{W^{m_2,p_2}(\Omega)} \leq C(\Omega, n, m_1, m_2, p_1, p_2) \|f\|_{W^{m_1,p_1}(\Omega)} .$$

If both inequalities in (1.1) *are strict, then the embedding is compact.*

(ii.) If $m \in \mathbb{N}^+$ and $p \in [1, \infty)$ are given such that

$$m - \frac{n}{p} \geq k + \alpha \quad \text{for any } \alpha \in (0,1) , k \in \mathbb{N} \tag{1.2}$$

holds true, then a continuous embedding $W^{m,p}(\Omega) \hookrightarrow C^{k,\alpha}(\overline{\Omega})$ exists such that for all $f \in W^{m,p}(\Omega)$ a representative $\tilde{f}$ of f exists with $\tilde{f}(x) = f(x)$ for a.e. $x \in \Omega$ and

$$\|\tilde{f}\|_{C^{k,\alpha}(\overline{\Omega})} \leq C(\Omega, n, m, p, k, \alpha) \|\tilde{f}\|_{W^{m,p}(\Omega)} .$$

If the inequality (1.2) *is strict, then the embedding $W^{m,p}(\Omega) \hookrightarrow C^{k,\alpha}(\overline{\Omega})$ is additionally compact.*

Proof. See [AF03, Alt06]. □

Chapter 2

Foundations of the Variational Time Discretization and the Discrete Curvature Tensor

THIS chapter is divided into four parts: in Section 2.1, we present a short survey of concepts from Riemannian geometry, to which we will frequently refer to in later sections. Here, we assume that the Riemannian manifolds are modeled on general (possibly infinite-dimensional) Banach or Hilbert spaces. This generalization poses no conceptual difficulties, but many definitions and results in the finite-dimensional case cease to be true in the infinite-dimensional setting. In Section 2.2, the variational time discretization of geodesic calculus developed by Rumpf and Wirth is briefly introduced and related to the concept of shape spaces. Furthermore, the time discrete equivalents of the geodesic curve, the logarithm, the exponential map, and the parallel transport in the Riemannian sense are presented along with the corresponding consistency statements. We will pick up the concepts of the geodesic curve, the exponential map and the parallel transport in the time discrete setting in the context of the time discrete metamorphosis model in Chapter 3 and Chapter 4. Afterwards, in Section 2.3 we propose a novel discrete equivalent of the (Riemann) curvature tensor, which relies on multiple applications of the time discrete parallel transport to suitably rescaled vector fields, and prove the convergence to its continuous counterpart. Finally, we will comment on the applicability of the discrete curvature tensor to general shape spaces in Section 2.4.

2.1 Differentiable and Riemannian Manifolds on Hilbert Spaces

In this section, we briefly introduce the concept of a topological/differentiable/Riemannian manifold modeled on a (possibly infinite-dimensional) Banach or Hilbert space. Many definitions and theorems in the case of finite-dimensional manifolds (in particular those involving a finite basis of the tangent space) cease to be true for general Banach and Hilbert manifolds, that is why we present this survey of some general concepts in Riemannian geometry for general (possibly infinite-dimensional) manifolds. All definitions and results in this section are based on [Lan95, Kli95, Sak96, War83].

Differentiable and Riemannian manifolds, tangent spaces and the covariant derivative. Before discussing differentiable manifolds, we recall the concept of a topological manifold:[1]

Definition 2.1.1 (Topological manifold)**.** Let $\mathbf{E}$ be a (possibly infinite-dimensional) Banach or Hilbert space and $\mathcal{M}$ be a topological space.

(i.) $\mathcal{M}$ is *metrizable* if a metric on $\mathcal{M}$ exists that induces the topology of $\mathcal{M}$.

(ii.) If a countable base for the open sets of $\mathcal{M}$ exists, then $\mathcal{M}$ is *separable*.

[1] There are several different definitions of (topological) manifolds in the literature, which differ in terms of the properties of the manifold.

(iii.) If every point in $\mathcal{M}$ admits an open neighborhood which is homeomorphic to $\mathbf{E}$, then $\mathcal{M}$ is said to be *locally homeomorphic to* $\mathbf{E}$.

(iv.) A *topological manifold* with the model space $\mathbf{E}$ is a separable and metrizable space that is locally homeomorphic to $\mathbf{E}$.

If $\mathbf{E}$ is a Banach space, Hilbert space or $\mathbf{E} = \mathbb{R}^n$, respectively, then we refer to $\mathcal{M}$ as a Banach, Hilbert or n-dimensional manifold, respectively. If the transition mappings, *i.e.* the overlap mappings of arbitrary charts, are diffeomorphic, then one obtains a differentiable manifold:

Definition 2.1.2 (Differentiable manifold)**.** Let $\mathcal{M}$ be a topological manifold.

(i.) Let $(\mathcal{M}_i)_{i\in I}$ be an open covering of $\mathcal{M}$. If for each $\mathcal{M}_i$, $i \in I$, a homeomorphism $\phi_i : \mathcal{M}_i \to U_i$ onto an open set $U_i \subset \mathbf{E}$ exists, then $(\mathcal{M}_i, \phi_i)_{i\in I}$ is a family of *charts*.

(ii.) A C^k*-differentiable atlas* ($k \geq 1$) is a family of charts $(\mathcal{M}_i, \phi_i)_{i\in I}$ such that

$$\phi_j \circ \phi_i^{-1} : \phi_i(\mathcal{M}_i \cap \mathcal{M}_j) \to \phi_j(\mathcal{M}_i \cap \mathcal{M}_j)$$

is a C^k-diffeomorphism for each pair of indices $i, j \in I$. Two differentiable atlases are *equivalent* if the union of theses atlases is a differentiable atlas.

(iii.) A C^k*-differentiable structure* is an equivalence class of C^k-differentiable atlases. A C^k*-differentiable manifold* is a topological manifold endowed with a C^k-differentiable structure.

Notation 2.1.3. For the rest of this thesis, if not otherwise stated, we always assume that k is sufficiently large (possibly $k = \infty$) and omit the order of smoothness.

Having introduced the concept of a differentiable manifold, we now define the tangent space, the tangent bundle and the tangential for differentiable manifolds. Our starting point are open sets in a generic Banach space:

Definition 2.1.4. Let $\mathbf{E}, \mathbf{F}$ be Banach spaces, $U \subset \mathbf{E}$, $V \subset \mathbf{F}$ open and $u \in U$. Furthermore, we denote the canonical projections onto the corresponding components by $\mathrm{pr}_1 : U \times \mathbf{E} \to U$ and by $\mathrm{pr}_2 : U \times \mathbf{E} \to \mathbf{E}$.

(i.) The *tangent space* T_uU *of* U *at* u is given by $T_uU = \{(u, X) \,:\, X \in \mathbf{E}\}$ with a vector space structure induced by pr_2.

(ii.) Let $TU = \bigcup_{u\in U} T_uU$. Then $\tau_U = \mathrm{pr}_1 : TU \to U$ is the *tangent bundle* of U, TU is the *total tangent space* of U and τ_U its *projection*.

(iii.) Let $F : U \to V$ be differentiable. The *tangential* TF of F is given by

$$TF : TU \to TV\,, \quad (u, X) \to (F(u), DF(u)X)\,.$$

Next, we extend the definitions of the tangent space and the tangent bundle to general differentiable manifolds:

Definition 2.1.5. Let $\mathcal{M}$ be a differentiable manifold modeled on a Hilbert space $\mathbf{E}$, $y \in \mathcal{M}$, and let $(\mathcal{M}_1, \phi_1)$ and $(\mathcal{M}_2, \phi_2)$ be two charts covering y with $\phi_i(\mathcal{M}_i) = U_i \subset \mathbf{E}$ for $i = 1, 2$.

(i.) The space $T_{\phi_1(y)}U_1$ is a *representative of the tangent space of* $\mathcal{M}$ *at* y w.r.t. the chart $(\mathcal{M}_1, \phi_1)$. We call $X_{\phi_1(y)}$ the *principal part* of $(\phi_1(y), X_{\phi_1(y)}) \in T_{\phi_1(y)}U_1$. Furthermore, $\omega_1 = (\phi_1(y), X_{\phi_1(y)}) \in T_{\phi_1(y)}U_1$ and $\omega_2 = (\phi_2(y), X_{\phi_2(y)}) \in T_{\phi_2(y)}U_2$ represent the same tangent vector of the manifold $\mathcal{M}$ at y if $T_{\phi_1(y)}(\phi_2 \circ \phi_1^{-1})\omega_1 = \omega_2$, where $T_{\phi_1(y)}(\phi_2 \circ \phi_1^{-1})$ is the linear isomorphism

$$T_{\phi_1(y)}(\phi_2 \circ \phi_1^{-1}) : T_{\phi_1(y)}U_1 \to T_{\phi_2(y)}U_2\,.$$

Then, a *tangent vector of* $\mathcal{M}$ *at* y is defined as the equivalence class of all its representatives (given by all charts covering y) and the *tangent space* $T_y\mathcal{M}$ is the vector space of all tangent vectors at y, which is isomorphic to $\mathbf{E}$ with isomorphism given by $T_y\phi_1 : T_y\mathcal{M} \to T_{\phi_1(y)}U_1$.

(ii.) Let $T\mathcal{M} = \bigcup_{y\in\mathcal{M}} T_y\mathcal{M}$. The map $\tau_{\mathcal{M}} : T\mathcal{M} \to \mathcal{M}$, which assigns to any $\omega \in T_y\mathcal{M}$ the base point y, is called the *tangent bundle of* $\mathcal{M}$.

(iii.) The *differential* $D\phi_1$ *of* ϕ_1 *at* y is the map $\mathrm{pr}_2 \circ T_y\phi_1$.

(iv.) A *bundle* is a projection $\tau : Z \to \mathcal{M}$ from a set Z (representing the *total space of the bundle*) to $\mathcal{M}$ (frequently referred to as *the base space of the bundle*), and a *section of this bundle* is a differentiable map $\tilde{\tau} : \mathcal{M} \to Z$ such that $\tau \circ \tilde{\tau} = \mathbb{1}_{\mathcal{M}}$.

(v.) A *vector field* X is a section of the tangent bundle $\tau_{\mathcal{M}} : T\mathcal{M} \to \mathcal{M}$, *i.e.*

$$\begin{array}{ccc} & & T\mathcal{M} \\ & \overset{X}{\nearrow} & \big\downarrow{\scriptstyle \tau_{\mathcal{M}}} \\ \mathcal{M} & \xrightarrow{\mathbb{1}_{\mathcal{M}}} & \mathcal{M} \end{array}$$

commutes. We denote by $\mathfrak{X}(\mathcal{M})$ the set of all smooth vector fields and by $\mathcal{F}(\mathcal{M})$ the set of all smooth scalar-valued functions on $\mathcal{M}$. For $X \in \mathfrak{X}(\mathcal{M})$ and $f \in \mathcal{F}(\mathcal{M})$ we set $X(f) = \{\mathcal{M} \ni p \mapsto Df(p)X(p)\}$.

Proposition 2.1.6 (Tangential of a mapping between manifolds)**.** *Let $\mathcal{M}$ and $\mathcal{M}'$ be differentiable manifolds with atlases $(\mathcal{M}_i, \phi_i)_{i\in I}$ and $(\mathcal{M}'_j, \phi'_j)_{j\in J}$, respectively. A mapping $F : \mathcal{M} \to \mathcal{M}'$ is* differentiable *if*

$$\phi'_j \circ F \circ \left(\phi_i\big|_{\mathcal{M}_i \cap F^{-1}(\mathcal{M}'_j)}\right)^{-1} : \phi_i(\mathcal{M}_i \cap F^{-1}(\mathcal{M}'_j)) \to \phi'_j(\mathcal{M}'_j)$$

is differentiable for all $(i, j) \in I \times J$. In this case, the tangential $T_yF : T_y\mathcal{M} \to T_{F(y)}\mathcal{M}'$ of F at $y \in \mathcal{M}$ is given by

$$T_{\phi_i(y)}(\phi'_j \circ F \circ \phi_i^{-1}) : T_{\phi_i(y)}\mathcal{M}_i \to T_{\phi'_j(F(y))}\mathcal{M}'_j$$

for $(i, j) \in I \times J$, which is independent of the choice of the local charts. Then, the tangential $TF : T\mathcal{M} \to T\mathcal{M}'$ of F *is the differentiable mapping that commutes with the projections,* i.e.

$$\begin{array}{ccc} T\mathcal{M} & \xrightarrow{TF} & T\mathcal{M}' \\ \big\downarrow{\scriptstyle \tau_{\mathcal{M}}} & & \big\downarrow{\scriptstyle \tau_{\mathcal{M}'}} \\ \mathcal{M} & \xrightarrow{F} & \mathcal{M}' \end{array}$$

is commutative.

Proof. See [Kli95, Section 1.1-1.4]. □

Definition 2.1.7. Let $\mathcal{M}$ and $\widetilde{\mathcal{M}}$ be differentiable manifolds and $F : \mathcal{M} \to \widetilde{\mathcal{M}}$ be a differentiable mapping.

(i.) F is an *immersion at* $y \in \mathcal{M}$ if T_yF is injective and a closed mapping (*i.e.* closed sets are mapped to closed sets). If this holds true for all points $y \in \mathcal{M}$, then F is said to be an *immersion*.

(ii.) F is an *embedding* if F is an immersion and $F : \mathcal{M} \to F(\mathcal{M})$ is homeomorphic, where $F(\mathcal{M})$ is endowed with the induced topology.

(iii.) A subset $N \subset \mathcal{M}$ is called a *submanifold* of $\mathcal{M}$ if N admits the structure of a differentiable manifold such that the inclusion map is an embedding.

Let us conclude this section with the formal definition of a Riemannian manifold and some basic concepts. To define a Riemannian metric, we first introduce the concept of a tensor bundle:

Definition 2.1.8. Let $\mathbf{E}_1, \dots, \mathbf{E}_s, \mathbf{F}$ be Banach spaces. We denote by $L(\mathbf{E}_1, \dots, \mathbf{E}_s; \mathbf{F})$ the set of all s-linear mappings

$$\mathbf{E}_1 \times \mathbf{E}_2 \times \cdots \times \mathbf{E}_s \to \mathbf{F}$$

for $s \geq 1$. The *bundle of s-fold covariant tensors over a differentiable manifold* $\mathcal{M}$ is defined by

$$\tau_s : T_s^0\mathcal{M} = L(\underbrace{T\mathcal{M}, \dots, T\mathcal{M}}_{s}; \mathbb{R} \times \mathcal{M}) \to \mathcal{M}\,.$$

The space of *s-fold covariant and symmetric tensors* consists of all $T \in T_s^0\mathcal{M}$ such that

$$T(\omega_{\sigma(1)}, \omega_{\sigma(2)}, \dots, \omega_{\sigma(s)}) = T(\omega_1, \omega_2, \dots, \omega_s) \quad \forall \omega_1, \omega_2, \dots, \omega_s \in T\mathcal{M}$$

for all permutations $\sigma : \{1, \dots, s\} \to \{1, \dots, s\}$. By restricting τ_s to the space of all s-fold covariant and symmetric tensors one obtains the bundle $\sigma_s : S_s\mathcal{M} \to \mathcal{M}$ of s-fold covariant symmetric tensors.

A Riemannian manifold is a differentiable manifold with a distinct metric, this metric is a section of the bundle $\sigma_2 : S_2\mathcal{M} \to \mathcal{M}$ and is positive definite:

Definition 2.1.9 (Riemannian manifold)**.** Let $\mathcal{M}$ be a differentiable manifold modeled on a Hilbert space $\mathbf{E}$ with inner product $(\,\cdot\,,\,\cdot\,)_{\mathbf{E}}$. A *Riemannian metric* $g : \mathcal{M} \to S_2\mathcal{M}$ *on* $\mathcal{M}$ is a section of the bundle $\sigma_2 : S_2\mathcal{M} \to \mathcal{M}$ such that $g_y(X, X) \geq C(X, X)_{\mathbf{E}}$ for a positive constant C depending on g, all $y \in \mathcal{M}$ and all $X \in T_y\mathcal{M}$. The pair $(\mathcal{M}, g)$ is called a *Riemannian manifold*.

Every differentiable manifold can be given the structure of a Riemannian manifold:

Theorem 2.1.10. *On every differentiable manifold there exists a Riemannian metric.*

Proof. See [Kli95, Theorem 1.8.5]. □

Most of the subsequent concepts in Riemannian geometry can be characterized in terms of the covariant derivative. Moreover, the proof of the consistency of the discrete Riemann curvature tensor is based on a convergence analysis of the iterated discrete covariant derivative. Below, we provide a common definition for the covariant derivative, although the starting point of this convergence analysis for the Riemann curvature tensor emerges from an equivalent characterization:[2]

Definition 2.1.11. A *(linear) connection* on a differentiable manifold $\mathcal{M}$ is a mapping

$$\nabla : \mathfrak{X}(\mathcal{M}) \times \mathfrak{X}(\mathcal{M}) \to \mathfrak{X}(\mathcal{M})\,, \quad (X, Y) \mapsto \nabla_X Y$$

such that

$$\begin{aligned} \nabla_{f_1X_1 + f_2X_2} Y &= f_1 \nabla_{X_1} Y + f_2 \nabla_{X_2} Y\,, \\ \nabla_X (f_1Y_1 + f_2Y_2) &= f_1 \nabla_X Y_1 + X(f_1)Y_1 + f_2 \nabla_X Y_2 + X(f_2)Y_2\,, \end{aligned}$$

for all $X, X_1, X_2, Y, Y_1, Y_2 \in \mathfrak{X}(\mathcal{M})$ and $f_1, f_2 \in \mathcal{F}(\mathcal{M})$. We refer to $\nabla_X Y$ as the *covariant derivative* of Y w.r.t. X.

On every Riemannian manifold there is one distinct covariant derivative – called the Levi–Civita derivative – which is of vital importance for further applications. As a preparation, we recall the definitions of the Lie bracket, the torsion-freeness and the Riemannian property of a covariant derivative:

Definition 2.1.12. Let $(\mathcal{M}, g)$ be a Riemannian manifold with a covariant derivative ∇.

(i.) The *Lie bracket* is given by

$$[\,\cdot\,,\,\cdot\,] : \mathfrak{X}(\mathcal{M}) \times \mathfrak{X}(\mathcal{M}) \to \mathfrak{X}(\mathcal{M})\,, \quad [X, Y](f) = X(Y(f)) - Y(X(f))$$

for two vector fields $X, Y \in \mathfrak{X}(\mathcal{M})$ and all $f \in \mathcal{F}(\mathcal{M})$. Note that the Lie bracket is $\mathbb{R}$-bilinear, antisymmetric and satisfies the *Jacobi identity*

$$[[X, Y], Z] + [[Z, X], Y] + [[Y, Z], X] = 0 \qquad \forall X, Y, Z \in \mathfrak{X}(\mathcal{M})\,.$$

[2] Note that Definition 2.1.11 does not cover the most general case.

(ii.) The connection ∇ on $\mathcal{M}$ is *torsion-free* if

$$\nabla_X Y - \nabla_Y X = [X, Y] \qquad \forall X, Y \in \mathfrak{X}(\mathcal{M}) .$$

(iii.) The covariant derivative ∇ is *Riemannian* if

$$Xg(Y, Z) = g(\nabla_X Y, Z) + g(Y, \nabla_X Z) \qquad \forall X, Y, Z \in \mathfrak{X}(\mathcal{M}) .$$

Theorem 2.1.13. *Let $(\mathcal{M}, g)$ be a Riemannian manifold. Then there exists a unique covariant derivative which is Riemannian and torsion-free. This covariant derivative is called* Levi–Civita derivative*.*

Proof. See [Kli95, Theorem 1.8.11] and [Lan95, Theorem 4.1 in VIII, §4]. □

Notation 2.1.14. For the rest of this chapter, $\nabla_X Y$ always refers to the Levi–Civita derivative.

Geodesic curves, logarithm, exponential map and parallel transport. In what follows, we will successively introduce the concepts of geodesic curves, the Riemannian logarithm, the Riemannian exponential map and parallel transport for Riemannian manifolds modeled on Hilbert spaces. Again, all subsequent definitions and theorems are rigorously stated for general Hilbert manifolds, and we remark that some finite-dimensional relations cease to hold in the general setting. Hereinafter, we tacitly assume that $(\mathcal{M}, g)$ is a sufficiently smooth Riemannian manifold.

Definition 2.1.15. A smooth curve $y : [0, 1] \to \mathcal{M}$ is a *geodesic path or a geodesic* if $\nabla_{\dot{y}(t)} \dot{y}(t) = 0$ for all $t \in [0, 1]$.

In what follows, we list some fundamental properties of geodesic curves:

Proposition 2.1.16 (Properties of geodesic curves)**.** *Let $(\mathcal{M}, g)$ be a Riemannian manifold.*

(i.) For every $X \in T\mathcal{M}$ there exists a (maximal) open interval $I(X) \ni 0$ such that $y_X : I(X) \to \mathcal{M}$ is the unique geodesic curve satisfying $y_X(0) = \tau_{\mathcal{M}} X$ and $\dot{y}_X(0) = X$. Moreover, for $c > 0$ one can show $y_{cX}(t) = y_X(ct)$ and $I(cX) = c^{-1} I(X)$.

(ii.) There exists an open neighborhood $\widetilde{T\mathcal{M}} \subset T\mathcal{M}$ of $\mathcal{M}$, which is considered as a submanifold of $T\mathcal{M}$, such that for every $X \in \widetilde{T\mathcal{M}}$ the geodesic curve $y_X(t)$ is uniquely defined for all $|t| < 2$.

Proof. See [Kli95, Section 1.6] and [Lan95, Chapter VIII]. □

Taking into account Proposition 2.1.16 (ii.) one can infer that the map $X \mapsto y_X(1)$ is locally well-defined on $\widetilde{T\mathcal{M}}$, which we refer to as the *exponential map*:

Definition 2.1.17. With the notation of Proposition 2.1.16, the *exponential map* is defined as

$$\exp : \widetilde{T\mathcal{M}} \to \mathcal{M}, \quad X \mapsto y_X(1) . \tag{2.1}$$

The restriction $\exp\big|_{\widetilde{T\mathcal{M}} \cap T_y\mathcal{M}}$ for $y \in \mathcal{M}$ is denoted by $\exp_y$, and the corresponding inverse function

$$\log_y = (\exp_y)^{-1} : \mathcal{M} \to T_y\mathcal{M}$$

is called *logarithm*. The set $\widetilde{T\mathcal{M}} \cap T_y\mathcal{M}$ is often referred to as the *domain of definition of* $\exp_y$.

Definition 2.1.18. Let $(y(t))_{t\in[0,1]} \subset \mathcal{M}$ be a smooth path in $\mathcal{M}$. The *path length* and the *path energy* are given by

$$\mathcal{L}[(y(t))_{t\in[0,1]}] = \int_0^1 \sqrt{g_{y(t)}(\dot{y}(t), \dot{y}(t))}\, \mathrm{d}t , \tag{2.2}$$

$$\mathcal{E}[(y(t))_{t\in[0,1]}] = \int_0^1 g_{y(t)}(\dot{y}(t), \dot{y}(t))\, \mathrm{d}t , \tag{2.3}$$

respectively. Moreover, for $y_A, y_B \in \mathcal{M}$ the *(Riemannian) distance* $\mathrm{dist} : \mathcal{M} \times \mathcal{M} \to \mathbb{R}$ w.r.t. y_A and y_B is given by

$$\mathrm{dist}(y_A, y_B) = \inf \{\, \mathcal{L}(y(t)) \,:\, y : [0, 1] \to \mathcal{M} \text{ piecewise smooth}, y(0) = y_A, y(1) = y_B \,\} .$$

Remark 2.1.19. (i.) By using the Cauchy–Schwarz inequality we can infer $(\mathcal{L}[(y(t))_{t\in[0,1]}])^2 \leq \mathcal{E}[(y(t))_{t\in[0,1]}]$ with equality if and only if $g_{y(t)}(\dot{y}(t), \dot{y}(t))$ is constant.

(ii.) Note that dist defines a metric on $\mathcal{M}$ and the topology on $\mathcal{M}$ coincides with the topology induced from dist (see [Kli95, Theorem 1.9.5]).

A crucial question concerns the size of the set $\widetilde{T\mathcal{M}}$, which turns out to be related to the completeness of the manifold considered as a metric space provided that the manifold is finite-dimensional.

Theorem 2.1.20 (Hopf–Rinow)**.** *A manifold $\mathcal{M}$ is said to be* geodesically complete at a point $y \in \mathcal{M}$ *if the exponential map is defined on the entire tangent space $T_y\mathcal{M}$, and* geodesically complete *if this holds true for all points in the manifold. Moreover, the manifold $\mathcal{M}$ is* metrically complete *if the metric space $(\mathcal{M}, \mathrm{dist})$ is complete. If the model space of $\mathcal{M}$ is finite-dimensional, then $\mathcal{M}$ is metrically complete if and only if $\mathcal{M}$ is geodesically complete.*

Proof. See [Kli95, Theorem 2.1.3] and [Lan95, Chapter VIII]. □

One of the most fundamental tasks in Riemannian geometry is the calculation of the shortest path in a Riemannian manifold $\mathcal{M}$ joining two points $y_A, y_B \in \mathcal{M}$. It turns out that any shortest path locally coincides with a geodesic curve and is therefore often called *minimizing or shortest geodesic curve*.

Theorem 2.1.21. *With the notation of Proposition 2.1.16 and Definition 2.1.17, the exponential map* (2.1) *is differentiable and for every $y \in \mathcal{M}$ there exists $\eta = \eta(y) > 0$ such that for all $\varepsilon \in (0, \eta)$*

$$\exp_y \big|_{B_\varepsilon(0)} : B_\varepsilon(0) \to \exp_y(B_\varepsilon(0))$$

is a diffeomorphism. Moreover, for any $y_A, y_B \in \exp_y(B_\varepsilon(0))$ this diffeomorphism has the following properties:

(i.) There exists a unique geodesic curve y_{y_A,y_B} joining y_A and y_B such that $\mathcal{L}[(y_{y_A,y_B}(t))_{t\in[0,1]}] < 2\eta$.

(ii.) The mapping

$$y_{\cdot,\cdot} : \exp_y(B_\varepsilon(0)) \times \exp_y(B_\varepsilon(0)) \to \mathcal{M}\,, \quad (y_A, y_B) \mapsto y_{y_A,y_B}$$

is continuous.

(iii.) Any geodesic curve $\tilde{y} : [0,1] \to \mathcal{M}$ such that $\tilde{y}(0) = y_A$, $\tilde{y}(1) = y_B$ and $\mathcal{L}[(\tilde{y}(t))_{t\in[0,1]}] < 2\eta$ satisfies $\mathcal{L}[(\tilde{y}(t))_{t\in[0,1]}] = \mathrm{dist}(y_A, y_B)$ and is a shortest geodesic.

Proof. See [Kli95, Sections 1.8-1.9]. □

Finally, the *parallel transport* along a (not necessarily geodesic) path in the manifold is a concept of transferring tangent vectors along the path and ensuring that they "stay parallel w.r.t. the metric", which later enables the transfer of geometric data along a specified path. The precise statements read as follows:

Definition 2.1.22. A smooth vector field $X \in \mathfrak{X}(\mathcal{M})$ is called *parallel w.r.t. a smooth curve $y : I \to \mathcal{M}$, $I \subset \mathbb{R}$* open interval, if $\nabla_{\dot{y}(t)} X = 0$ for all $t \in I$.

Proposition 2.1.23. *Let $I \subset \mathbb{R}$ be an open interval, $t_0, t_1 \in I$, and $y : I \to \mathcal{M}$ be a smooth curve. Then for every $X_0 \in T_{y(t_0)}\mathcal{M}$ there exists a unique parallel vector field $X \in \mathfrak{X}(\mathcal{M})$ along y such that $X(t_0) = X_0$ and $X(t) \in T_{y(t)}\mathcal{M}$ for $t \in I$, and the mapping*

$$\mathrm{P}_{y(t_0)\to y(t_1)} : T_{y(t_0)}\mathcal{M} \to T_{y(t_1)}\mathcal{M}\,, \quad X_0 \mapsto X(t_1)$$

is a linear and isometric isomorphism, which is called parallel transport.

Proof. See [Kli95, Sections 1.6-1.8]. □

2.2 Time Discrete Geodesic Calculus

In this section, following [RW13, RW15] a variational time discretization of geodesic calculus is introduced, which works for finite- and infinite-dimensional manifolds under certain conditions to be presented below. In particular, this approach allows to rigorously define discrete analogs of geodesics, the logarithm, the exponential map and the parallel transport. The convergence of each object to its continuous counterpart was proven in [RW15]. We will pick up these concepts to define the discrete Riemann curvature tensor in the time discrete setting (see Section 2.3) as well as discrete geodesic curves, the discrete exponential map and the discrete parallel transport in the space of images in the context of the metamorphosis model (see Chapter 3 and Chapter 4).

2.2.1 Shape Spaces and Related Work

One central object of investigation in this thesis is the *shape space*, which lacks an all-encompassing definition. Intuitively, a shape can be seen as the structure of a geometric object (*cf*. [DZ11]) or – loosely speaking –

> "[...] what is left when the differences which can be attributed to translations, rotations, and dilatations have been quotiented out." (see [Ken84, p. 82])

Kendall [Ken84] defined the shape space of size l in $\mathbb{R}^n$ as the quotient space $(((\mathbb{R}^n)^{l-1})\backslash\{0\})/\sim$, $l \geq 2$, with $\sim$ referring to the equivalence class in the group generated by rotations and dilatations, where $\{0\}$ is excluded to avoid collapsed shapes. One can think of this space as the equivalence class of a set of vertices $x_1, \dots, x_l$ of a polygon in $\mathbb{R}^n$ undergoing rotations and dilatations. The prevailing definition of a shape space in this thesis is due to Rumpf and Wirth [RW11], who consider a shape as the boundary of a domain in a Euclidean space. This shape admits the physical interpretation as a deformable object (*cf*. Section 3.3 for more details on the physical background). In the context of the metamorphosis model (*cf*. Chapter 3 and Chapter 4) and the binary Mumford–Shah model (*cf*. Chapter 5) we additionally consider both gray-value and color images as shapes. For other common definitions we refer to the books [DZ11, You10] and the references therein.

During the past decades tools from Riemannian geometry had an increasing influence on shape analysis and imaging. In what follows, we briefly discuss some publications in which methods from Riemannian geometry enter into the analysis of certain shape spaces.

Younes *et al*. [YMSM08] introduced a novel Riemannian metric on the space of closed curves as a shape space in the complex plane, which is defined as the space of $C^\infty(\mathbb{S}^1, \mathbb{C})$-immersions with a fixed rotation number. In particular, this construction allows the explicit computation of geodesic curves. Such an explicit formula to compute geodesics is also implied by a geometric-type Sobolev metric in the space of planar curves proposed by Sundaramoorthi *et al*. [SMSY11], which intrinsically favors smooth transitions along the geodesic path. Unfortunately, these explicit formulas are only available for limited geometric settings.

Younes [You98] viewed each shape in the space of planar curves as an elastic object and defined a Riemannian metric on this space using the group action of an infinite-dimensional Lie group. It turns out that computing minimizing geodesic paths on this shape space amounts to calculating paths with minimal length in the associated group. Klassen *et al*. [KSMJ04] established an ODE-time discretization scheme to compute geodesic curves on a (pre-)shape space of closed immersed planar curves, which is prone to get stuck in local minima and lacks a symmetry property of the resulting distance. Schmidt *et al*. [SCC06] improved the aforementioned ansatz in terms of stability and computation time using variational methods to minimize the length functional, which is capable of properly interpolating curves with kinks or rough interfaces along the geodesic path and induces a symmetric distance. On a similar shape space, Michor and Mumford [MM06] elaborately studied the seemingly natural metric $g_{A,c}(h,k) = \int_{\mathbb{S}^1}(1 + A\kappa_c^2)\langle h, k\rangle |c'| \,\mathrm{d}x$ for a planar curve c with non-vanishing curvature κ_c, a constant $A > 0$ and normal vector fields h, k. Interestingly, in the case $A = 0$ the induced Riemannian distance always vanishes. In a subsequent paper [MM07], Michor and Mumford characterized the geodesic equation as the Hamiltonian flow w.r.t. the first fundamental form. Furthermore, they examined several Sobolev-type metrics in the space of immersions which guarantee the conservation of distinct quantities such as the momentum. Fuchs *et al*. [FJSY09] introduced an elastic energy evaluated at velocity fields on the shape space of smooth embeddings $\mathbb{S}^l \to \mathbb{R}^l$ modulo diffeomorphic reparameterizations, $l \in \{1, 2\}$, which coincides with the spatial integral of (3.26) to be motivated in the next chapter and – as opposed to the previous approaches – incorporates the entire object and not only its boundary.

In this and the two subsequent chapters, we will study the variational time discretization for geodesic calculus from the viewpoint of shape spaces, which in particular allows geodesic interpolation and extrapolation of shapes and proved to be stable as well as efficient in several numerical applications to be discussed below. The Γ-convergence as well as the convergence of stationary points for a certain class of time discrete functionals was rigorously proven by Müller and Ortiz [MO04] under the viewpoint of discrete dynamics. In particular, the discrete Lagrangian appearing in this context can be approximated using numerical quadrature schemes in such a way that the convergence properties remain valid, which nicely fits into the framework of variational integrators [LMOW04]. In the same spirit, Ober-Blöbaum *et al*. [OBJM11] examined dynamical systems underlying the (discrete) Lagrange–d'Alembert principle from an optimal control point of view, and exploited a time discretization to numerically solve the resulting ODEs. Wirth *et al*. [WBRS11] incorporated a viscous flow perspective on shape spaces to compute minimizing geodesics joining two- as well as three-dimensional shapes, in which each shape is characterized by a level set representation. From the viewpoint of elasticity theory, Rumpf and Wirth performed a shape averaging [RW09b] and a covariance analysis [RW09a] in the space of shapes considered as the contours of domains in $\mathbb{R}^n$. In a series of papers, Heeren *et al*. applied the time discrete geodesic calculus to the space of shells in the context of geodesic interpolation [HRWW12], geodesic extrapolation and parallel transport [HRS$^+$14], and Riemannian splines [HRS$^+$16].

2.2.2 Foundations of the Variational Time Discretization

In all applications involving the variational time discretization on Hilbert manifolds, we restrict to the subsequent functional analytic setting:

Assumption 2.2.1. The manifold $\mathcal{M}$ is path-connected and the closure of an open subset of a separable and reflexive Banach space $\mathbf{V}$, where $\mathbf{V}$ is compactly embedded into a Banach space $\mathbf{Y}$, *i.e.* $\mathcal{M} \subset \mathbf{V} \xhookrightarrow{\text{cmpct.}} \mathbf{Y}$. If $\partial\mathcal{M} \neq \emptyset$, then $\partial\mathcal{M}$ is assumed to be sufficiently smooth.

Henceforth, we tacitly assume that all manifolds satisfy the Assumption 2.2.1 and we identify the tangent space $T_y\mathcal{M}$, $y \in \mathcal{M}$, with the Banach space $\mathbf{V}$. Furthermore, we endow $\mathcal{M}$ with the metric $g : \mathcal{M} \times \mathbf{V} \times \mathbf{V} \to \mathbb{R}$, which turns $\mathcal{M}$ into a Riemannian manifold $(\mathcal{M}, g)$, and assume

(H1) g is uniformly bounded and $\mathbf{V}$-coercive, *i.e.*

$$c^* \|v\|_{\mathbf{V}}^2 \leq g_y(v,v) \leq C^* \|v\|_{\mathbf{V}}^2 \qquad \forall v \in \mathbf{V}\,, y \in \mathcal{M}\,,$$

for fixed constants $0 < c^* < C^* < \infty$. In addition, g is continuous in the sense

$$|g_y(v,v) - g_{\tilde{y}}(v,v)| \leq \beta(\|y - \tilde{y}\|_{\mathbf{Y}}) \|v\|_{\mathbf{V}}^2 \qquad \forall v \in \mathbf{V}\,, y, \tilde{y} \in \mathcal{M}\,,$$

where β is a strictly increasing, continuous function with $\beta(0) = 0$.

Although these assumptions exclude several classes of Riemannian manifolds, we emphasize that smooth n-dimensional manifolds ($n < \infty$) satisfy the Assumption 2.2.1 and Hypothesis (H1) by choosing $\mathbf{V} = \mathbf{Y} = \mathbb{R}^n$ and $g_y(v,w) = v^T D\mathrm{X}(y)^T D\mathrm{X}(y) w$ for a parametrization X. As a further application, Rumpf and Wirth discussed the space of viscous rods in the context of this framework (*cf*. [RW15, Section 7.2] based on [LDR95, FJMM03]).

Hypothesis (H1) already suffices to guarantee the existence and local uniqueness of minimizing geodesic paths in the manifold $\mathcal{M}$, which additionally exhibit certain regularity properties.

Theorem 2.2.2 (Existence and uniqueness of continuous geodesics)**.** *For a Riemannian manifold $(\mathcal{M}, g)$ satisfying the Assumption (H1) and $g \in C^2(\mathcal{M}; \mathbf{V}' \otimes \mathbf{V}')$, the energy* (2.3) *is lower semicontinuous w.r.t. the weak convergence in $W^{1,2}((0,1), \mathcal{M})$. Furthermore, for $y_A, y_B \in \mathcal{M}$ there exists a classical geodesic connecting y_A and y_B,* i.e. *a minimizer of $\mathcal{E}$ in the space of all paths $(y(t))_{t\in[0,1]} \in W^{1,2}((0,1), \mathcal{M})$ with $y(0) = y_A$ and $y(1) = y_B$. In particular, y is Hölder continuous w.r.t. the $\mathbf{V}$-norm. Finally, geodesics are locally unique,* i.e. *given $y_A \in \mathring{\mathcal{M}}$ there is a small constant $\delta > 0$ depending on y_A such that for all $y_B \in \mathcal{M}$ with $\|y_A - y_B\|_{\mathbf{V}} < \delta$ the shortest classical geodesic between y_A and y_B is unique.*

Proof. See [RW15, Theorem 4.1 and 4.2]. □

To formulate the time discretization, we first have to ensure the existence of a functional $\mathcal{W} : \mathcal{M} \times \mathcal{M} \to \mathbb{R}$ that locally approximates the squared Riemannian distance up to higher order terms.

(H2) There exists a weakly lower semicontinuous functional $\mathcal{W} : \mathcal{M} \times \mathcal{M} \to \mathbb{R}$ and constants $\varepsilon, C > 0$ such that if $\mathrm{dist}(y, \tilde{y}) \leq \varepsilon$, then

$$|\mathcal{W}[y, \tilde{y}] - \mathrm{dist}^2(y, \tilde{y})| \leq C\mathrm{dist}^3(y, \tilde{y})$$

for all $y, \tilde{y} \in \mathcal{M}$. $\mathcal{W}$ is coercive in the sense $\mathcal{W}[y, \tilde{y}] \geq \gamma(\mathrm{dist}(y, \tilde{y}))$ for a strictly increasing, continuous function γ with $\gamma(0) = 0$ and $\lim_{t\to\infty} \gamma(t) = \infty$.

Note that we did neither assume symmetry nor any regularity of $\mathcal{W}$. However, for some theorems (especially for the consistency results) the subsequent regularity properties are additionally required:

(H3) The metric g is $C^2(\mathbf{Y}, \mathbf{V}' \otimes \mathbf{V}')$-smooth.

(H4) The energy $\mathcal{W}$ is $C^4(\mathcal{M} \times \mathcal{M}, \mathbb{R})$-smooth with bounded derivatives.

Let $y : [0, 1] \to \mathcal{M}$ be a smooth path on the manifold, $K \geq 1$ and $(y_0, \ldots, y_K) \in \mathcal{M}^{K+1}$ be points on the manifold obtained by sampling the path y at the times $t_k = \frac{k}{K}$, $k = 0, \ldots, K$, *i.e.* $y_k = y(t_k)$. Taking into account Hypothesis (H2), we can approximate lower bounds for the path length and path energy of $(y(t))_{t\in[0,1]}$ as follows:

$$\mathcal{L}[(y(t))_{t\in[0,1]}] \geq \sum_{k=1}^{K} \mathrm{dist}(y_{k-1}, y_k) \approx \sum_{k=1}^{K} \sqrt{\mathcal{W}(y_{k-1}, y_k)}\,, \tag{2.4}$$

$$\mathcal{E}[(y(t))_{t\in[0,1]}] \geq K \sum_{k=1}^{K} \mathrm{dist}^2(y_{k-1}, y_k) \approx K \sum_{k=1}^{K} \mathcal{W}(y_{k-1}, y_k)\,. \tag{2.5}$$

To deduce the inequality appearing in (2.5) one can employ Jensen's inequality. The lower bounds (2.4) and (2.5) motivate the definition of the discrete path length and discrete path energy:

Definition 2.2.3 (Discrete length and energy)**.** Let $(\mathcal{M}, g)$ be a Riemannian manifold. A *discrete* $(K+1)$*-path for* $K \geq 1$ is a $(K+1)$-tuple $(y_0, \ldots, y_K) \in \mathcal{M}^{K+1}$. The *discrete path length* and the *discrete path energy* associated with this path are defined as

$$\mathbf{L}_K[(y_0, \ldots, y_K)] = \sum_{k=1}^{K} \sqrt{\mathcal{W}[y_{k-1}, y_k]}\,, \tag{2.6}$$

$$\mathbf{E}_K[(y_0, \ldots, y_K)] = K \sum_{k=1}^{K} \mathcal{W}[y_{k-1}, y_k]\,. \tag{2.7}$$

The definition of the discrete geodesic curve and all derived concepts rely on the minimization of (2.7) rather than on the minimization of (2.6), we will comment on this below.

2.2.3 Geodesic Curves, Logarithm, Exponential Map and Parallel Transport in the Time Discrete Setting

In the forthcoming paragraphs, we will successively introduce geodesics, the logarithm, the exponential map and the parallel transport in the time discrete case and present related results.

Notation 2.2.4. We will frequently use the notation

$$\mathcal{W}_{,\alpha_1\cdots\alpha_r}[x, y] = \partial_{\alpha_1} \cdots \partial_{\alpha_r} \mathcal{W}[x, y]\,,$$

for $\alpha_l \in \{1, 2\}$, $l \in \{1, \ldots, r\}$ and $r \geq 1$. For instance, the first order variational derivatives w.r.t. the direction $\psi \in \mathbf{V}$ are given by

$$\mathcal{W}_{,1}[x, y](\psi) = \tfrac{\mathrm{d}}{\mathrm{d}t}\mathcal{W}[x + t\psi, y]\big|_{t=0}\,, \qquad \mathcal{W}_{,2}[x, y](\psi) = \tfrac{\mathrm{d}}{\mathrm{d}t}\mathcal{W}[x, y + t\psi]\big|_{t=0}\,,$$

the generalization to higher order derivatives is obvious.

Let us recall some consistency conditions and symmetry relations of $\mathcal{W}$, which are of vital importance in several convergence proofs shown below.

Lemma 2.2.5. *Let $\zeta, \eta, \theta \in \mathbf{V}$ and $y \in \mathring{\mathcal{M}}$. Under the Assumptions (H1)-(H4), the following identities hold true:*

$$\mathcal{W}[y, y] = 0\,, \tag{2.8}$$

$$\mathcal{W}_{,1}[y, y](\zeta) = \mathcal{W}_{,2}[y, y](\zeta) = 0\,, \tag{2.9}$$

$$\mathcal{W}_{,22}[y, y](\zeta, \eta) = 2g_y(\zeta, \eta)\,. \tag{2.10}$$

Furthermore, one obtains the subsequent symmetry relations

$$\mathcal{W}_{,11}[y, y](\zeta, \eta) = -\mathcal{W}_{,12}[y, y](\zeta, \eta) = -\mathcal{W}_{,21}[y, y](\zeta, \eta) = \mathcal{W}_{,22}[y, y](\zeta, \eta)\,, \tag{2.11}$$

$$\begin{aligned}&\mathcal{W}_{,221}[y, y](\zeta, \eta, \theta) + \mathcal{W}_{,222}[y, y](\zeta, \eta, \theta) = \mathcal{W}_{,111}[y, y](\zeta, \eta, \theta) + \mathcal{W}_{,112}[y, y](\zeta, \eta, \theta)\\ =& -\mathcal{W}_{,121}[y, y](\zeta, \eta, \theta) - \mathcal{W}_{,122}[y, y](\zeta, \eta, \theta) = -\mathcal{W}_{,211}[y, y](\zeta, \eta, \theta) - \mathcal{W}_{,212}[y, y](\zeta, \eta, \theta)\,.\end{aligned} \tag{2.12}$$

Proof. Apart from (2.12), all assertions are presented in [RW15, Lemma 4.6]. By differentiating (2.11) one can straightforwardly show (2.12). □

Discrete geodesic curves. Time discrete geodesic curves are defined as minimizing $(K + 1)$-paths w.r.t. the discrete path energy for fixed end points:

Definition 2.2.6. A *(time) discrete geodesic of length $K+1$* is a discrete $(K+1)$-path $(y_0, \dots, y_K)$ that minimizes the discrete path energy (2.7) for fixed end points $y_0, y_K \in \mathcal{M}$.

The counterpart of Theorem 2.2.2 for discrete geodesic curves is the following:

Theorem 2.2.7 (Existence and local uniqueness of discrete geodesics)**.** *Let $y_A, y_B \in \mathcal{M}$ and $K \geq 2$ be fixed. Under the Assumption (H1) there exists a discrete geodesic path $(y_0, \dots, y_K) \in \mathcal{M}^{K+1}$ which minimizes the discrete path energy $\mathbf{E}_K$ w.r.t. all discrete $(K+1)$-paths $(\tilde{y}_0, \dots, \tilde{y}_K) \in \mathcal{M}^{K+1}$ with boundary conditions $\tilde{y}_0 = y_A$ and $\tilde{y}_K = y_B$. If in addition (H2) holds true and $\mathcal{W}$ is twice Fréchet differentiable on $\mathcal{M} \times \mathcal{M}$, then there exists $\varepsilon > 0$ such that there exists a unique discrete geodesic $(y_0, \dots, y_K) \in \mathcal{M}^{K+1}$ with $y_0 = y_A$ and $y_K = \tilde{y}$ for all $\tilde{y} \in \mathcal{M}$ with $\|y_A - \tilde{y}\|_{\mathbf{V}} < \varepsilon$.*

Proof. See [RW15, Theorem 4.3 and Theorem 4.7]. □

The points of a discrete geodesic curve of length $K + 1$ are approximately equidistributed, *i.e.* the maximum of the Riemannian distance of two adjacent points is roughly proportional to the length $\tau = \frac{1}{K}$ of the time interval and the Riemannian distance of the endpoints.

Theorem 2.2.8. *Assuming (H1) and (H2), there exists $\varepsilon > 0$ such that if $\operatorname{dist}(y_A, y_B) < \sqrt{K}\varepsilon$ for all K, then discrete geodesics satisfy*

$$\operatorname{dist}(y_{k-1}, y_k) \leq C\frac{\operatorname{dist}(y_A, y_B)}{K}$$

for all $k = 1, \dots, K$ and a constant C solely depending on $\operatorname{dist}(y_A, y_B)$.

Proof. See [RW15, Theorem 4.5]. □

Remark 2.2.9. A well-known result in the time continuous setting states that minimizing the path length (2.2) is equivalent to minimizing the path energy (2.3) (*cf*. Section 2.1). However, in the time discrete setting minimizers of the discrete path length (2.6) are in general not related to discrete geodesics, *i.e*. minimizers of the discrete path energy (2.7). As an example, consider a manifold $\mathcal{M} \subset \mathbf{V}$ and two points $y_A, y_B \in \mathcal{M}$, which are close w.r.t. the norm induced by $\mathbf{V}$, but relatively far apart w.r.t. the Riemannian distance on $\mathcal{M}$. In this case, a minimizer of the path length is likely to "jump" through the ambient space $\mathbf{V}$ and is therefore not expected to approximate time continuous geodesics properly. However, when minimizing the path energy for K sufficiently large the approximate equidistribution of the sample points guarantees the Γ-convergence of $\mathbf{E}_K$ to $\mathcal{E}$ (see Subsection 3.5.1 for a definition of Γ-convergence) and the uniform convergence of a subsequence of discrete geodesics to the time continuous geodesic curve, the precise statement is given in the subsequent theorem.

Theorem 2.2.10. *Under the Assumptions (H1) and (H2),* $\mathbf{E}_K$ *Γ-converges w.r.t. the* $L^2((0,1),\mathbf{Y})$*-topology to* $\mathcal{E}$*. Moreover, any sequence of minimizers of* $\mathbf{E}_K$ *has a subsequence which converges to a minimizer of the path energy* $\mathcal{E}$ *in* $C^0([0,1],\mathbf{Y})$*.*

Proof. See [RW15, Theorem 4.8 and Corollary 4.9]. □

Discrete logarithm. In the preceding section, we have defined the Riemannian logarithm as the initial variation of a geodesic y joining two points $y_A, y_B \in \mathcal{M}$. The observation $\log_{y_A} y_B = \dot{y}(0) \approx K(y(\frac{1}{K}) - y(0))$, $K \geq 1$, motivates the definition of the discrete logarithm as the difference of the first sample points of a time discrete geodesic curve with end points y_A and y_B:

Definition 2.2.11. Let $K \geq 1$ and let $(y_0, \dots, y_K)$ be the unique discrete geodesic of length $K+1$ such that $y_0 = y_A$ and $y_K = y_B$. Then the *discrete logarithm* is defined as

$$\mathrm{LOG}^K_{y_A}(y_B) = y_1 - y_0\,.$$

The convergence of the discrete logarithm is established in the next theorem.

Theorem 2.2.12 (Convergence of the discrete logarithm, local uniqueness of LOG^2)**.** *Assume that (H1)-(H4) hold true. Let* $y_A, y_B \in \mathring{\mathcal{M}}$ *be points in the manifold such that both the continuous and the discrete geodesic curve joining* y_A *and* y_B *are unique and the continuous geodesic is contained in* $\mathring{\mathcal{M}}$*. Then*

$$K(\mathrm{LOG}^K_{y_A}(y_B)) \to \log_{y_A} y_B$$

w.r.t. the weak topology in $\mathbf{V}$ *and the strong topology in* $\mathbf{Y}$ *as* $K \to \infty$*. Moreover, there exists* $\varepsilon > 0$ *such that for all* $0 < \delta \leq \varepsilon$*,* $y_0 \in \mathring{\mathcal{M}}$ *and*

$$y_2 \in B_\delta(y_0) = \{\, y \in \mathbf{V} \,:\, \|y - y_0\|_{\mathbf{V}} < \delta \,\} \subset \mathcal{M}$$

the functional $B_\delta(y_0) \ni \tilde{y} \mapsto \mathbf{E}_2[(y_0, \tilde{y}, y_2)]$ *is strictly convex with a bounded coercive Hessian on* $B_\delta(y_0)$ *and* $\mathrm{LOG}^2_{y_0}(y_2)$ *is unique.*

Proof. See [RW15, Theorem 5.1 and Lemma 5.3]. □

Discrete exponential map. Before defining the discrete exponential map, let us consider two points $y_A, y_B \in \mathring{\mathcal{M}}$ with $y : [0,1] \to \mathring{\mathcal{M}}$ being the unique geodesic such that $y(0) = y_A$ and $y(1) = y_B$. The definition of the (continuous) exponential map readily implies

$$\exp_{y_A}(\tfrac{k}{K} v) = y(\tfrac{k}{K}) \tag{2.13}$$

for $v = \dot{y}(0) \in T_{y_A}\mathcal{M}$ and for all $0 \leq k \leq K$, and the subsequent recursive definition can be immediately derived from (2.13)

$$y(\tfrac{k}{K}) = \exp_{y_A}(\tfrac{k}{K} v) = \exp_{y((k-2)/K)}(2 v_{k-1}) \quad \text{for } v_{k-1} = \log_{y((k-2)/K)} y(\tfrac{k-1}{K}) \text{ and } k \in \{2, \dots, K\}\,.$$

Incorporating the variational time discretization and replacing continuous objects by their discrete counterparts, we arrive at the following definition of the discrete exponential map:

Definition 2.2.13. Let $y_0 \in \mathring{\mathcal{M}}$ and let $\xi \in \mathbf{V}$ be sufficiently small such that $y_0 + \xi \in \mathring{\mathcal{M}}$. The *discrete exponential map* $y_k = \mathrm{EXP}^k_{y_0}(\xi)$ is recursively defined as follows:

$$\begin{aligned} &y_1 = (\mathrm{LOG}^1_{y_0})^{-1}(\xi) = y_0 + \xi\,, \qquad y_2 = (\mathrm{LOG}^2_{y_0})^{-1}(\xi)\,, \\ &y_k = \mathrm{EXP}^2_{y_{k-2}}(\xi_{k-1}) \quad \text{with } \xi_{k-1} = \mathrm{LOG}^1_{y_{k-2}} y_{k-1} = y_{k-1} - y_{k-2} \quad \text{for } k \geq 2\,. \end{aligned} \tag{2.14}$$

Here, $y_k = \mathrm{EXP}^2_{y_{k-2}}(\xi_{k-1})$, $k \geq 2$, if the triple $(y_{k-2}, y_{k-1}, y_k) \in \mathcal{M}^3$ satisfies

$$y_{k-1} = \operatorname*{argmin}_{\tilde{y} \in \mathcal{M}} (\mathcal{W}[y_{k-2}, \tilde{y}] + \mathcal{W}[\tilde{y}, y_k])\,. \tag{2.15}$$

Remark 2.2.14. (i.) The smallness assumption for $\xi \in \mathbf{V}$ is required to guarantee the invertibility of the discrete logarithm (see Theorem 2.2.12).

(ii.) The discrete exponential map can recover a discrete geodesic curve provided that the initial point as well as the initial variation are known and the geodesic is unique. To be precise, if for $K \geq 2$ the path $(y_0, \dots, y_K)$ is the unique discrete geodesic curve joining y_0 and y_K, then $\mathrm{EXP}^k_{y_0}(y_1 - y_0) = y_k$ for $0 \leq k \leq K$. In other words, the definition of the exponential map does not depend on the number of time steps K since if $(y_0, \dots, y_K)$ is a discrete geodesic, then $(y_0, \dots, y_k)$ with $k \leq K$ is also a discrete geodesic.

(iii.) Definition 2.2.13 demonstrates that the discrete exponential map can be computed of arbitrary length via an iterative application of the one-step extrapolation map EXP^2. The local existence of a unique minimizer in (2.15) follows from Theorem 2.2.15 below (*cf*. Figure 2.1).

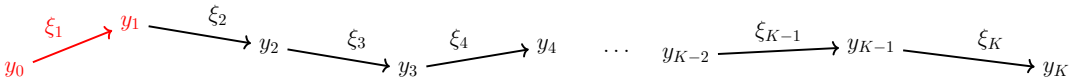

Figure 2.1: Schematic drawing of $\mathrm{EXP}^k_{y_0}(\xi_1)$, $k = 1, \dots, K$, input data is highlighted in red.

As in the case of the discrete logarithm, the rescaled discrete exponential map converges to its continuous counterpart, which is the content of the next theorem.

Theorem 2.2.15 ((Local) existence and convergence of EXP^K)**.** *We assume that (H1)-(H4) hold true.*

(i.) Then there exists $\varepsilon > 0$ such that for all $0 < \delta \leq \varepsilon$ and all $y_0 \in \mathring{\mathcal{M}}$ such that $B_{3\delta}(y_0) \subset \mathcal{M}$ the discrete exponential map $\mathrm{EXP}^2_{y_0}(v)$ exists for any $v \in \mathbf{V}$ with $\|v\|_{\mathbf{V}} < \delta$.

(ii.) Let $y : [0,1] \to \mathring{\mathcal{M}}$ be a smooth geodesic. For K sufficiently large $\mathrm{EXP}^K_{y(0)}(\frac{\dot{y}(0)}{K})$ exists and for $\tau = \frac{1}{K}$ one obtains

$$\left\| y(1) - \mathrm{EXP}^K_{y(0)}\left(\frac{\dot{y}(0)}{K}\right) \right\|_{\mathbf{V}} = \mathcal{O}(\tau)\,.$$

Proof. See [RW15, Lemma 5.6 and Theorem 5.10]. □

Discrete parallel transport. Let us conclude this section with the definition of the discrete parallel transport along a (not necessarily geodesic) discrete $(K+1)$-path $(y_0, \dots, y_K) \in \mathring{\mathcal{M}}^{K+1}$, $K \geq 2$, which is, for instance, obtained by sampling from a smooth path $y : [0,1] \to \mathcal{M}$, *i.e.* $y_k = y(\frac{k}{K})$. The definition of the discrete parallel transport relies on a discrete parallelogram construction called Schild's ladder (*cf*. [KMN00]) and is used to transport a tangent vector $\xi_{k-1} \in \mathbf{V}$ attached at the point y_{k-1} to a tangent vector $\xi_k \in \mathbf{V}$ attached at the point y_k, the precise definition reads as follows:

Definition 2.2.16. Let $K \geq 2$, $\mathbf{y} = (y_0, \dots, y_K) \in \mathring{\mathcal{M}}^{K+1}$ such that $y_k - y_{k-1}$ is sufficiently small for $k = 1, \dots, K$. Then the *discrete parallel transport* of a sufficiently small tangent vector $\xi_0 \in \mathbf{V}$ along the $(K+1)$-path $\mathbf{y}$ is defined for $k = 1, \dots, K$ via the iteration

$$\begin{aligned} y^p_{k-1} &= y_{k-1} + \xi_{k-1}\,, \\ y^c_k &= y^p_{k-1} + \mathrm{LOG}^2_{y^p_{k-1}}(y_k)\,, \\ y^p_k &= \mathrm{EXP}^2_{y_{k-1}}(y^c_k - y_{k-1})\,, \\ \xi_k &= y^p_k - y_k\,. \end{aligned} \tag{2.16}$$

In this case, $\xi_k = \mathbf{P}_{y_k,\dots,y_0}\xi_0$ is the transported vector attached to y_k.

Remark 2.2.17. We highlight the subsequent observations w.r.t. the discrete parallel transport.

(i.) The smallness assumptions in Definition 2.2.16 are required for the well-posedness of the discrete logarithm and the exponential map as in the preceding paragraphs.

(ii.) It is clear from the definition that

$$\mathbf{P}_{y_K,\dots,y_0}\mathbf{P}_{\tilde{y}_L,\dots,\tilde{y}_0} = \mathbf{P}_{y_K,\dots,y_1,\tilde{y}_L,\dots,\tilde{y}_0}$$

for two discrete paths $(y_0,\dots,y_K) \in \mathring{\mathcal{M}}^{K+1}$ and $(\tilde{y}_0,\dots,\tilde{y}_L) \in \mathring{\mathcal{M}}^{L+1}$ such that $y_0 = \tilde{y}_L$. Furthermore, if $\mathcal{W}$ is in addition symmetric, we have $\mathbf{P}^{-1}_{y_K,\dots,y_0} = \mathbf{P}_{y_0,\dots,y_K}$.

(iii.) Figure 2.2 depicts two steps of the discrete parallel transport via Schild's ladder along the discrete $(K+1)$-path $(y_0,\dots,y_K)$. Starting from the tangent vector ξ_{k-1} attached at the point y_{k-1}, the projected point y^p_{k-1} is obtained via vector addition. Afterwards, the midpoint y^c_k of the discrete geodesic parallelogram is retrieved using a 3-point geodesic interpolation of y^p_{k-1} and y_k (dotted gray line). In the third step, the end point y^p_k of the transported vector ξ_k is computed using the one-step extrapolation EXP^2 with y_{k-1} as base point and $y^c_k - y_{k-1}$ as initial variation (gray solid line), and the transported vector is given as the difference of y^p_k and y_k. This procedure can be iterated to obtain a parallel transport of arbitrary length provided that the smallness assumptions are kept.

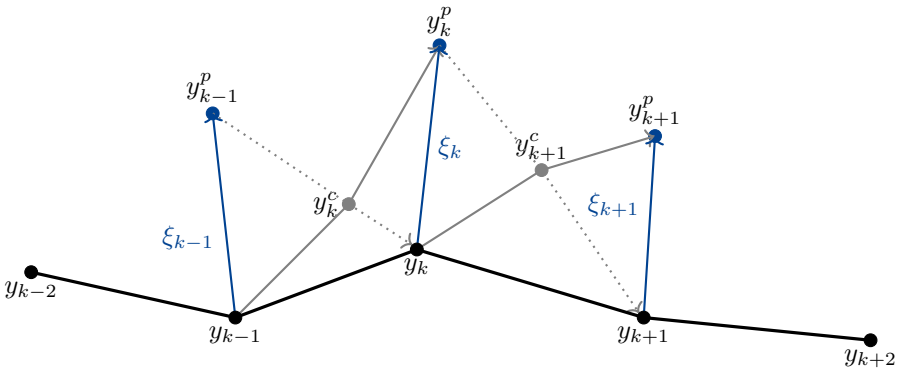

Figure 2.2: Parallel transport along $(y_0,\dots,y_K)$ of a tangent vector ξ_k attached to y_k using Schild's ladder.

(iv.) The starting point of the convergence proofs of the discrete parallel transport and the curvature tensor (to be shown in the forthcoming section) are the Euler–Lagrange equations for the discrete parallel transport in the k^{th} step:

$$\begin{aligned} \mathcal{W}_{,2}[y_{k-1}+\xi_{k-1}, y^c_k] + \mathcal{W}_{,1}[y^c_k, y_k] &= 0\,, \\ \mathcal{W}_{,2}[y_{k-1}, y^c_k] + \mathcal{W}_{,1}[y^c_k, y_k+\xi_k] &= 0\,. \end{aligned} \tag{2.17}$$

These equations coincide with the Euler–Lagrange equations for the inverse discrete parallel transport $\mathbf{P}^{-1}$ applied to a 2-path.

The discrete parallel transport converges to the continuous parallel transport if we divide the initial vector by K, transport this modified vector along $\{y_k = y(\frac{k}{K})\}_{0\le k\le K}$, and multiply the transported vector in the final step by K.

Theorem 2.2.18 (Existence and convergence of $\mathbf{P}_{y_K,\dots,y_0}$)**.** *Assume that (H1)-(H4) hold true, let $K \in \mathbb{N}$, $\tau = \frac{1}{K}$, $y : [0,1] \to \mathring{\mathcal{M}}$ be a smooth path and $\xi : [0,1] \to \mathbf{V}$ be a parallel vector field along y.*

(i.) If $y_k = y(k\tau)$, then the discrete parallel transport satisfies

$$\left\| K\mathbf{P}_{y_K,\dots,y_0}(\tfrac{\xi(0)}{K}) - \xi(1) \right\|_{\mathbf{V}} = \mathcal{O}(\tau)\,.$$

(ii.) If for $\varepsilon > 0$ all $y_k \in \mathring{\mathcal{M}}$ satisfy $\|y_k - y(k\tau)\|_{\mathbf{V}} \le \varepsilon$, $k = 0,\dots,K$, then

$$\left\| K\mathbf{P}_{y_K,\dots,y_0}(\tfrac{\xi(0)}{K}) - \xi(1) \right\|_{\mathbf{V}} = \mathcal{O}(\tau+\varepsilon)\,.$$

Proof. See [RW15, Theorem 5.11 and Corollary 5.12]. □

The assertion in (i.) ensures the convergence of the discrete parallel transport along a $(K+1)$-path consisting of sampled points. If these sample points are slightly perturbed, the additional error directly enters into the total error of the discrete parallel transport as an additional summand (*cf*. (ii.)). One central idea in the convergence proof of the discrete curvature tensor is that the choice $\varepsilon = \mathcal{O}(\tau)$ does not result in any additional error of lower order.

2.3 Discrete Approximation of the Riemann Curvature Tensor

In this section, we will propose a novel discrete version of the Riemann curvature tensor based on multiple applications of the time discrete parallel transport. The consistency of this approach is proven under the hypotheses of the preceding section as well as additional smoothness assumptions.

2.3.1 Related Work

In what follows, we will briefly present some pioneering numerical approximation schemes for several different notions of curvature. We remark that due to the various different approaches to be found in the literature this survey is by far not exhaustive.

One of the earliest approaches to numerically estimate the curvature tensor at the vertices of a polyhedral approximation of a surface was proposed by Taubin [Tau95]. In detail, this ansatz exclusively works for embedded two-dimensional manifolds in $\mathbb{R}^3$ and relies on the observation that the directional curvature function corresponds to a quadratic form, which can be estimated with linear complexity and from which the curvature tensor can be retrieved.

Starting from the triangulation of a two-dimensional manifold embedded in $\mathbb{R}^3$, Meyer *et al*. [MDSB02] defined discrete operators representing, for instance, the mean and the Gaussian curvature by spatial averaging of suitably rescaled geometric quantities. Using a mixed finite element/finite volume discretization of the mesh as well as a Voronoi decomposition principal curvatures can be robustly estimated.

Cohen–Steiner and Morvan [CSM03] proposed an integral approximation of the curvature tensor on smooth or polyhedral surfaces taking into account normal cycles, and proved its linear convergence if the polyhedral triangulation is Delaunay.

Hildebrandt *et al*. [HPW06] showed that if a sequence of polyhedral surfaces isometrically embedded in $\mathbb{R}^3$ converges to a differentiable manifold $\mathcal{M}$ w.r.t. the Hausdorff distance, then the convergence of the normal field is equivalent to the convergence of the metric tensor, which itself is equivalent to the convergence of the surface area. In addition, under suitable assumptions they established the convergence of geodesic curves and the mean curvature functionals on discrete surfaces to their limiting counterparts on $\mathcal{M}$.

In [KSNS07], Kalogerakis *et al*. approximated the second fundamental form of a possibly noisy surface using M-estimation, which amounts to an efficient data fitting approach using the method of iteratively reweighted least square. Here, the surface is either represented by polygon meshes or by point clouds.

Hildebrandt and Polthier [HP11] introduced generalized shape operators for smooth and polyhedral surfaces as linear operators on Sobolev spaces and provided error estimates to approximate the generalized shape operator on smooth surfaces by polyhedral surfaces, from which several geometric quantities can be recovered.

Starting from a weak formulation of the Ricci curvature, Fritz [Fri13] employed a surface finite element method to approximate the Ricci curvature on isometrically embedded hypersurfaces $\mathcal{M}$ and proved that the rate of convergence is $\frac{2}{3}$ and $\frac{1}{3}$ w.r.t. the $L^2(\mathcal{M})$- and $H^1(\mathcal{M})$-norm, respectively.

In earlier approaches to compute the discrete curvature tensor, we also tried a curvature approximation originating from the work of Wald [Wal35], where the Gaussian curvature of a surface is locally approximated using properly scaled quadruples. This approach proved to be numerically unstable and no obvious extension to more general manifolds exists. A further attempt to consistently define the discrete curvature tensor has been based on the well-known Ambrose–Singer Theorem [AS53] and its extension to the infinite-dimensional setting (*cf*. for instance [Mag04]). However, this approach turned out not to be numerically feasible since the time discrete parallel transport along a closed loop as required by the Ambrose–Singer Theorem relies on a very accurate approximation of the parallel transport resulting in large computation time and is very prone to numerical errors.

2.3.2 Discrete Riemann Curvature Tensor

This subsection is devoted to the construction of the discrete curvature tensor via the discrete parallel transport, and the central convergence theorem for the discrete curvature tensor is presented.

We begin with the definition of the curvature tensor:[3]

Definition 2.3.1. Let $(\mathcal{M}, g)$ be a Riemannian manifold modeled on a Hilbert space. The *Riemann curvature tensor* is defined as

$$\mathrm{R} : \mathfrak{X}(\mathcal{M}) \times \mathfrak{X}(\mathcal{M}) \times \mathfrak{X}(\mathcal{M}) \to \mathfrak{X}(\mathcal{M}) , \quad \mathrm{R}(\zeta, \eta)\theta = \nabla_\zeta \nabla_\eta \theta - \nabla_\eta \nabla_\zeta \theta - \nabla_{[\zeta,\eta]}\theta \quad \forall \zeta, \eta, \theta \in \mathfrak{X}(\mathcal{M}) . \tag{2.18}$$

We refer to the literature at the beginning of this chapter for properties and further results of the curvature tensor.

For the rest of this chapter, we tacitly assume that the functional analytic setting presented in Assumption 2.2.1 holds true. The starting point of the discrete curvature tensor is the definition of the discrete connection:

Definition 2.3.2. Let $y \in \mathring{\mathcal{M}}$ and let $\xi \in \mathbf{V}$ be sufficiently small. The *discrete connection* associated with the discrete vector field determined by the vectors $\eta_0, \eta_1 \in \mathbf{V}$, which are attached to y respectively $y + \xi$, is defined as

$$\boldsymbol{\nabla}_\xi(\eta_0, \eta_1) = \mathbf{P}^{-1}_{y+\xi,y}\eta_1 - \eta_0 .$$

The subsequent result states that the discrete connection approximates the covariant derivative with first order.

Theorem 2.3.3. *Let $\tau > 0$, $y \in \mathring{\mathcal{M}}$, $\xi \in \mathbf{V}$ and $\eta : \mathring{\mathcal{M}} \to \mathbf{V}$ be a smooth vector field. We define*

$$\boldsymbol{\nabla}^\tau_\xi \eta(y) = \frac{1}{\tau^2}\boldsymbol{\nabla}_{\tau\xi}(\tau\eta(y), \tau\eta(y + \tau\xi)) = \frac{1}{\tau^2}\left(\mathbf{P}^{-1}_{y+\tau\xi,y}\tau\eta(y + \tau\xi) - \tau\eta(y)\right) . \tag{2.19}$$

Then under the Hypotheses (H1)-(H4) we have for any $y \in \mathring{\mathcal{M}}$

$$\left\|\boldsymbol{\nabla}^\tau_\xi \eta(y) - \nabla_\xi \eta(y)\right\|_{\mathbf{V}} = \mathcal{O}(\tau) .$$

Proof. See [RW15, Theorem 5.13]. □

Interestingly, the proof of this theorem is mainly based on the corresponding convergence proof of the discrete parallel transport and the identity

$$\nabla_\xi \eta(y) = \frac{\mathrm{P}_{\theta(\tau)\to y}\eta(\theta(\tau)) - \eta(y)}{\tau} + \mathcal{O}(\tau \left\|\xi\right\|_{\mathbf{V}}) , \tag{2.20}$$

where θ is a geodesic with $\theta(0) = y$ and $\dot\theta(0) = \xi$. We will exploit this identity several times in the subsequent convergence proof.

Let $(\mathcal{M}, g)$ be a Riemannian manifold satisfying Assumption 2.2.1 and $\eta : \mathring{\mathcal{M}} \to \mathbf{V}$ be smooth vector field. For a fixed element $y \in \mathring{\mathcal{M}}$ and fixed tangent vectors $v, w \in \mathbf{V}$ we set

$$h : B_{2\tau_0{}^2}(0) \times B_{2\tau_0}(0) \to \mathring{\mathcal{M}} , \quad (s, t) \mapsto \exp_y(sv + tw) ,$$

where we assume that $\tau_0 > 0$ is chosen sufficiently small. In particular, $sv + tw$ for $(s, t) \in B_{2\tau_0{}^2}(0) \times B_{2\tau_0}(0)$ is supposed to lie in the domain of definition of $\exp_y$. For the rest of this chapter we always assume that the time step $\tau > 0$ is smaller than τ_0. Finally, we define

$$\widetilde{h}^\tau : B_{2\tau_0{}^2}(0) \to \mathring{\mathcal{M}} , \quad s \mapsto \exp_{h(0,\tau)}(sv) .$$

Note that $h(0, \tau) = \widetilde{h}^\tau(0)$. Below, we will use h and $\widetilde{h}^\tau$ to characterize the continuous paths along which the tangent vectors are transported.

In what follows, we will derive the discrete curvature tensor $\mathbf{R}^\tau(v, w)\eta$ associated with $\mathrm{R}(v, w)\eta$ by approximating each summand in (2.18) separately. To this end, we first employ the characterization (2.20) to approximate

[3] There is a minor subtlety regarding this definition, for details we refer to [Kli95, Proposition 1.4.14 and Proposition 1.5.4].

the iterated covariant derivative $\nabla_w \nabla_v \eta$ and use a quadratic as well as a linear scaling for the inner and outer covariant derivative, respectively, which yields

$$\begin{aligned}\nabla_v \eta(y) &= \frac{\mathrm{P}_{h(\tau^2,0)\to y}\eta(h(\tau^2,0)) - \eta(y)}{\tau^2} + \mathcal{O}(\tau^2)\,,\\ \nabla_w \nabla_v \eta(y) &= \frac{\mathrm{P}_{h(0,\tau)\to y}\left(\mathrm{P}_{\widetilde{h}^\tau(\tau^2)\to\widetilde{h}^\tau(0)}\eta(\widetilde{h}^\tau(\tau^2)) - \eta(\widetilde{h}^\tau(0))\right)}{\tau^3}\\ &\quad - \frac{\mathrm{P}_{h(\tau^2,0)\to y}\eta(h(\tau^2,0)) - \eta(y)}{\tau^3} + \mathcal{O}(\tau)\,,\end{aligned} \tag{2.21}$$

where we omit the dependency on the tangent vectors in the remainder term. One can verify that in general a smaller scaling factor w.r.t. the inner covariant derivative is necessary to ensure the convergence in (2.21). These different scaling factors are incorporated in the following discrete approximation of the iterated covariant derivative $\nabla_w \nabla_v \eta$

$$\boldsymbol{\nabla}_w^\tau \boldsymbol{\nabla}_v^{\tau^2} \eta(y) = \frac{1}{\tau^2}\left(\mathbf{P}^{-1}_{y_w^\tau,y}\frac{1}{\tau^3}\left(\mathbf{P}^{-1}_{y_{v,w}^\tau,y_w^\tau}\tau^2\eta(y_{v,w}^\tau) - \tau^2\eta(y_w^\tau)\right)\right) - \frac{1}{\tau^5}\left(\mathbf{P}^{-1}_{y_v^\tau,y}\tau^2\eta(y_v^\tau) - \tau^2\eta(y)\right)\,, \tag{2.22}$$

which readily follows from (*cf*. (2.19))

$$\begin{aligned}\boldsymbol{\nabla}_v^{\tau^2}\eta(y) &= \frac{1}{\tau^4}\left(\mathbf{P}^{-1}_{y+\tau^2 v,y}\tau^2\eta(y+\tau^2 v) - \tau^2\eta(y)\right)\,,\\ \boldsymbol{\nabla}_w^\tau \boldsymbol{\nabla}_v^{\tau^2}\eta(y) &= \frac{1}{\tau^2}\left(\mathbf{P}^{-1}_{y+\tau w,y}\tau\boldsymbol{\nabla}_v^{\tau^2}\eta(y+\tau w) - \tau\boldsymbol{\nabla}_v^{\tau^2}\eta(y)\right)\,,\end{aligned}$$

where we use the notation

$$y_v^\tau = y + \tau^2 v\,,\quad y_w^\tau = y + \tau w\,,\quad y_{v,w}^\tau = y_w^\tau + \tau^2 v\,.$$

Note that for the proposed approximation in (2.22) only three inverse discrete parallel transport steps – each along a 2-path – are required, which implies that the computation time is roughly independent of the choice of τ. Figure 2.3 depicts the continuous (red) and discrete (blue) paths associated with all parallel transports involved.

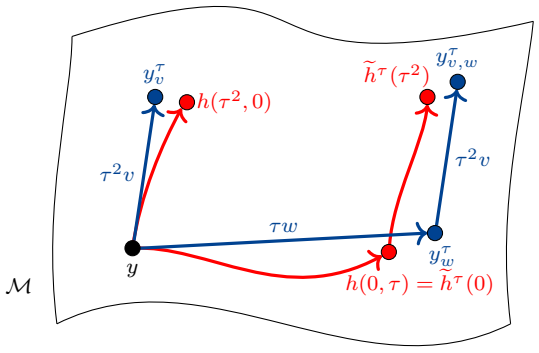

Figure 2.3: Scheme of the continuous and discrete paths involved in the continuous (red) and discrete (blue) approximations of the iterated covariant derivatives.

To prove the convergence of the curvature tensor, the following additional smoothness assumptions w.r.t. the metric and the energy are required:

(H3') The metric g is $C^3(\mathbf{Y}, \mathbf{V}' \otimes \mathbf{V}')$-smooth.

(H4') The energy $\mathcal{W}$ is $C^5(\mathcal{M}\times\mathcal{M},\mathbb{R})$-smooth with bounded derivatives.

The central convergence theorem reads as follows.

Theorem 2.3.4. *Assume that (H1), (H2), (H3') and (H4') are valid. Let $v,w\in\mathbf{V}$, $y\in\mathring{\mathcal{M}}$ and $\eta:\mathring{\mathcal{M}}\to\mathbf{V}$ be a smooth vector field. Then there exists $\tau_0>0$ such that for all $\tau\in(0,\tau_0)$*

$$\left\|\boldsymbol{\nabla}^\tau_w\boldsymbol{\nabla}^{\tau^2}_v\eta(y)-\nabla_w\nabla_v\eta(y)\right\|_{\mathbf{V}}=\mathcal{O}(\tau)\,. \tag{2.23}$$

Taking into account the previous steps, we finally arrive at the following definition and convergence result.

Theorem 2.3.5. *Under the assumptions of Theorem 2.3.4, the* discrete curvature tensor *is defined as*

$$(\mathbf{R}^\tau(v,w)\eta)(y)=\boldsymbol{\nabla}^\tau_v\boldsymbol{\nabla}^{\tau^2}_w\eta(y)-\boldsymbol{\nabla}^\tau_w\boldsymbol{\nabla}^{\tau^2}_v\eta(y)\,,$$

and this approximation converges with first order to $(\mathrm{R}(v,w)\eta)(y)$, i.e.

$$\|(\mathbf{R}^\tau(v,w)\eta)(y)-(\mathrm{R}(v,w)\eta)(y)\|_{\mathbf{V}}=\mathcal{O}(\tau)\,.$$

Proof. This proof follows immediately from Theorem 2.3.4 by noting that the Lie bracket vanishes on constant vector fields. □

The remainder of this section is devoted to the convergence analysis of the iterated discrete covariant derivatives.

Proof of Theorem 2.3.4. Let us recall the representations of the continuous and discrete second order covariant derivatives (*cf*. (2.21) and (2.22)):

$$\begin{aligned}
\nabla_w\nabla_v\eta(y)&=\frac{\mathrm{P}_{h(0,\tau)\to y}\left(\mathrm{P}_{\widetilde{h}^\tau(\tau^2)\to\widetilde{h}^\tau(0)}\eta(\widetilde{h}^\tau(\tau^2))-\eta(\widetilde{h}^\tau(0))\right)}{\tau^3}\\
&\quad-\frac{\mathrm{P}_{h(\tau^2,0)\to y}\eta(h(\tau^2,0))-\eta(y)}{\tau^3}+\mathcal{O}(\tau)\,,\\
\boldsymbol{\nabla}^\tau_w\boldsymbol{\nabla}^{\tau^2}_v\eta(y)&=\tfrac{1}{\tau^2}\left(\mathbf{P}^{-1}_{y^\tau_w,y}\tfrac{1}{\tau^3}\left(\mathbf{P}^{-1}_{y^\tau_{v,w},y^\tau_w}\tau^2\eta(y^\tau_{v,w})-\tau^2\eta(y^\tau_w)\right)-\tfrac{1}{\tau^3}\left(\mathbf{P}^{-1}_{y^\tau_v,y}\tau^2\eta(y^\tau_v)-\tau^2\eta(y)\right)\right)\,.
\end{aligned}$$

To facilitate the subsequent presentation, we introduce the following auxiliary variables:

$$\begin{aligned}
\zeta^\tau_{\mathrm{I}}&=\mathrm{P}_{\widetilde{h}^\tau(\tau^2)\to\widetilde{h}^\tau(0)}\tau^2\eta(\widetilde{h}^\tau(\tau^2))\,,&\xi^\tau_{\mathrm{I}}&=\mathbf{P}^{-1}_{y^\tau_{v,w},y^\tau_w}\tau^2\eta(y^\tau_{v,w})\,,\\
\zeta^\tau_{\mathrm{II}}&=\tfrac{1}{\tau^3}(\zeta^\tau_{\mathrm{I}}-\tau^2\eta(h(0,\tau)))\,,&\xi^\tau_{\mathrm{II}}&=\tfrac{1}{\tau^3}\left(\mathbf{P}^{-1}_{y^\tau_{v,w},y^\tau_w}\tau^2\eta(y^\tau_{v,w})-\tau^2\eta(y^\tau_w)\right)=\tfrac{1}{\tau^3}\left(\xi^\tau_{\mathrm{I}}-\tau^2\eta(y^\tau_w)\right)\,,\\
\zeta^\tau_{\mathrm{III}}&=\mathrm{P}_{h(0,\tau)\to y}\zeta^\tau_{\mathrm{II}}\,,&\xi^\tau_{\mathrm{III}}&=\mathbf{P}^{-1}_{y^\tau_w,y}\xi^\tau_{\mathrm{II}}\,,\\
\zeta^\tau_{\mathrm{IV}}&=\mathrm{P}_{h(\tau^2,0)\to y}\tau^2\eta(h(\tau^2,0))\,,&\xi^\tau_{\mathrm{IV}}&=\mathbf{P}^{-1}_{y^\tau_v,y}\tau^2\eta(y^\tau_v)\,,\\
\zeta^\tau_{\mathrm{V}}&=\tfrac{1}{\tau^3}(\zeta^\tau_{\mathrm{IV}}-\tau^2\eta(y))\,,&\xi^\tau_{\mathrm{V}}&=\tfrac{1}{\tau^3}\left(\mathbf{P}^{-1}_{y^\tau_v,y}\tau^2\eta(y^\tau_v)-\tau^2\eta(y)\right)=\tfrac{1}{\tau^3}\left(\xi^\tau_{\mathrm{IV}}-\tau^2\eta(y)\right)\,.
\end{aligned}$$

We denote by $\mathbf{A}^{\mathrm{disc}}_\tau$, $\mathbf{B}^{\mathrm{disc}}_\tau$ and $\mathbf{C}^{\mathrm{disc}}_\tau$ the discrete paths from $y^\tau_{v,w}$ to y^τ_w, from y^τ_w to y, and from y^τ_v to y, respectively (*cf*. Figure 2.3). The centers of the geodesic parallelograms in Schild's ladder associated with these discrete paths are referred to as y^c_A, y^c_B and y^c_C, respectively. We will see that the relations $\zeta^\tau_i\approx\xi^\tau_i$ for $i\in\{\mathrm{I},\mathrm{II},\mathrm{III},\mathrm{IV},\mathrm{V}\}$ hold true, which will be examined in detail below. With these definitions at hand, the continuous and discrete iterated covariant derivatives have the form

$$\nabla_w\nabla_v\eta(y)=\tfrac{1}{\tau^2}\left(\zeta^\tau_{\mathrm{III}}-\zeta^\tau_{\mathrm{V}}\right)+\mathcal{O}(\tau)\,,\qquad\boldsymbol{\nabla}^\tau_w\boldsymbol{\nabla}^{\tau^2}_v\eta(y)=\tfrac{1}{\tau^2}\left(\xi^\tau_{\mathrm{III}}-\xi^\tau_{\mathrm{V}}\right)\,. \tag{2.24}$$

The proof consists of three steps:

(i.) *Derivation of the optimality conditions emerging from Schild's ladder for each discrete parallel transport.*

Starting from the Euler–Lagrange equations (2.17) for the discrete parallel transport, we use a Taylor expansion to derive optimality conditions for each of the three parallel transports involved in the construction of the iterated covariant derivatives. Furthermore, we show that the remainder terms are of lower order and are therefore negligible. As already pointed out in Remark 2.2.17 (iv.), the Euler–Lagrange equations for the one-step discrete parallel transport and the corresponding discrete inverse transport coincide, which will tacitly be employed in this step.

(ii.) *Derivation of the continuous optimality conditions.*

Taking into account the definition of the parallel transport via the covariant derivative and Christoffel operators, we compute optimality conditions that relate distinct ζ_i^τ for $i \in \{\mathrm{I}, \mathrm{II}, \mathrm{III}, \mathrm{IV}, \mathrm{V}\}$. A key ingredient in this step is the smoothness of the (continuous) paths and the vector field.

(iii.) *Convergence of the iterated covariant derivatives.*

In this step, we compare relevant distinct expressions appearing in the preceding steps and show that all quantities involved are of higher order w.r.t. τ, which implies that

$$\mathcal{W}_{,22}[y_w^\tau, y_w^\tau](\zeta_{\mathrm{III}}^\tau - \xi_{\mathrm{III}}^\tau, \psi) + \mathcal{W}_{,22}[y, y](\xi_{\mathrm{V}}^\tau - \zeta_{\mathrm{V}}^\tau, \psi) = \mathcal{O}(\tau^3) \tag{2.25}$$

and thus implies the convergence statement (2.23) in combination with (2.24). Besides scaling relations we make use of the symmetry relations (2.12).

We highlight that in the first and second step the current proof shares some similarities with the convergence proof for the discrete parallel transport shown in [RW15, Theorem 5.11]. However, we emphasize that the convergence for the curvature tensor is not implied by the convergence result of the discrete parallel transport. Instead, in the forthcoming proof a more involved estimation of the resulting remainder terms is required.

ad (i.): *Derivation of the optimality conditions emerging from Schild's ladder for each discrete parallel transport.*

The optimality conditions for a one-step discrete parallel transport of the vector $\tilde{\xi}_1 \in \mathbf{V}$ attached to $\tilde{y}_1 \in \mathring{\mathcal{M}}$ to a vector $\tilde{\xi}_2 \in \mathbf{V}$ attached to $\tilde{y}_2 \in \mathring{\mathcal{M}}$ with $\tilde{y}^c \in \mathring{\mathcal{M}}$ denoting the midpoint of the geodesic parallelogram read as (*cf*. Remark 2.2.17 (iv.))

$$\mathcal{W}_{,2}[\tilde{y}_1 + \tilde{\xi}_1, \tilde{y}^c](\psi) + \mathcal{W}_{,1}[\tilde{y}^c, \tilde{y}_2](\psi) = 0\,, \tag{2.26}$$

$$\mathcal{W}_{,2}[\tilde{y}_1, \tilde{y}^c](\psi) + \mathcal{W}_{,1}[\tilde{y}^c, \tilde{y}_2 + \tilde{\xi}_2](\psi) = 0 \tag{2.27}$$

for any $\psi \in \mathbf{V}$. Again, we assume $\tilde{y}_1 - \tilde{y}_2$, $\tilde{\xi}_1$ and $\tilde{\xi}_2$ to be sufficiently small in $\mathbf{V}$. A Taylor expansion of $\mathcal{W}[\tilde{y}_1 + \tilde{\xi}_1, \tilde{y}^c]$ w.r.t. the base point $\tilde{y} \in \mathring{\mathcal{M}}$ yields

$$\begin{aligned}
\mathcal{W}[\tilde{y}_1 + \tilde{\xi}_1, \tilde{y}^c] = {} & \mathcal{W}[\tilde{y}, \tilde{y}] + \mathcal{W}_{,1}[\tilde{y}, \tilde{y}](\tilde{y}_1 + \tilde{\xi}_1 - \tilde{y}) + \mathcal{W}_{,2}[\tilde{y}, \tilde{y}](\tilde{y}^c - \tilde{y}) \\
& + \int_0^1 (1-s)\Big(\underline{\mathcal{W}_{,11}[\tilde{y} + s(\tilde{y}_1 + \tilde{\xi}_1 - \tilde{y}), \tilde{y} + s(\tilde{y}^c - \tilde{y})](\tilde{y}_1 + \tilde{\xi}_1 - \tilde{y}, \tilde{y}_1 + \tilde{\xi}_1 - \tilde{y})} \\
& + \uwave{2\mathcal{W}_{,12}[\tilde{y} + s(\tilde{y}_1 + \tilde{\xi}_1 - \tilde{y}), \tilde{y} + s(\tilde{y}^c - \tilde{y})](\tilde{y}_1 + \tilde{\xi}_1 - \tilde{y}, \tilde{y}^c - \tilde{y})} \\
& + \dashuline{\mathcal{W}_{,22}[\tilde{y} + s(\tilde{y}_1 + \tilde{\xi}_1 - \tilde{y}), \tilde{y} + s(\tilde{y}^c - \tilde{y})](\tilde{y}^c - \tilde{y}, \tilde{y}^c - \tilde{y})}\Big)\,\mathrm{d}s\,.
\end{aligned}$$

Note that (2.8) and (2.9) imply that $\mathcal{W}[\tilde{y}, \tilde{y}] = \mathcal{W}_{,1}[\tilde{y}, \tilde{y}](\tilde{y}_1 + \tilde{\xi}_1 - \tilde{y}) = \mathcal{W}_{,2}[\tilde{y}, \tilde{y}](\tilde{y}^c - \tilde{y}) = 0$. To keep

track of each term, we underline related expressions with the same line style. Thus,

$$
\begin{aligned}
&\mathcal{W}_{,2}[\tilde{y}_1+\tilde{\xi}_1,\tilde{y}^c](\psi)\\
&=\int_0^1(1-s)\Big(\underline{\mathcal{W}_{,112}[\tilde{y}+s(\tilde{y}_1+\tilde{\xi}_1-\tilde{y}),\tilde{y}+s(\tilde{y}^c-\tilde{y})](\tilde{y}_1+\tilde{\xi}_1-\tilde{y},\tilde{y}_1+\tilde{\xi}_1-\tilde{y},s\psi)}\\
&\quad+\underline{2\mathcal{W}_{,12}[\tilde{y}+s(\tilde{y}_1+\tilde{\xi}_1-\tilde{y}),\tilde{y}+s(\tilde{y}^c-\tilde{y})](\tilde{y}_1+\tilde{\xi}_1-\tilde{y},\psi)}\\
&\quad+\underline{2\mathcal{W}_{,122}[\tilde{y}+s(\tilde{y}_1+\tilde{\xi}_1-\tilde{y}),\tilde{y}+s(\tilde{y}^c-\tilde{y})](\tilde{y}_1+\tilde{\xi}_1-\tilde{y},\tilde{y}^c-\tilde{y},s\psi)}\\
&\quad+\underline{2\mathcal{W}_{,22}[\tilde{y}+s(\tilde{y}_1+\tilde{\xi}_1-\tilde{y}),\tilde{y}+s(\tilde{y}^c-\tilde{y})](\tilde{y}^c-\tilde{y},\psi)}\\
&\quad+\underline{\mathcal{W}_{,222}[\tilde{y}+s(\tilde{y}_1+\tilde{\xi}_1-\tilde{y}),\tilde{y}+s(\tilde{y}^c-\tilde{y})](\tilde{y}^c-\tilde{y},\tilde{y}^c-\tilde{y},s\psi)}\Big)\,\mathrm{d}s\\
&=-\underline{\mathcal{W}_{,22}[\tilde{y},\tilde{y}](\tilde{y}_1+\tilde{\xi}_1-\tilde{y},\psi)}+\underline{\mathcal{W}_{,22}[\tilde{y},\tilde{y}](\tilde{y}^c-\tilde{y},\psi)}\\
&\quad+\int_0^1\int_0^1 s(1-s)\Big(\underline{\mathcal{W}_{,112}[\tilde{y}+s(\tilde{y}_1+\tilde{\xi}_1-\tilde{y}),\tilde{y}+s(\tilde{y}^c-\tilde{y})](\tilde{y}_1+\tilde{\xi}_1-\tilde{y},\tilde{y}_1+\tilde{\xi}_1-\tilde{y},\psi)}\\
&\quad+\underline{2\mathcal{W}_{,112}[\tilde{y}+rs(\tilde{y}_1+\tilde{\xi}_1-\tilde{y}),\tilde{y}+rs(\tilde{y}^c-\tilde{y})](\tilde{y}_1+\tilde{\xi}_1-\tilde{y},\tilde{y}_1+\tilde{\xi}_1-\tilde{y},\psi)}\\
&\quad+\underline{2\mathcal{W}_{,122}[\tilde{y}+rs(\tilde{y}_1+\tilde{\xi}_1-\tilde{y}),\tilde{y}+rs(\tilde{y}^c-\tilde{y})](\tilde{y}_1+\tilde{\xi}_1-\tilde{y},\tilde{y}^c-\tilde{y},\psi)}\\
&\quad+\underline{2\mathcal{W}_{,122}[\tilde{y}+s(\tilde{y}_1+\tilde{\xi}_1-\tilde{y}),\tilde{y}+s(\tilde{y}^c-\tilde{y})](\tilde{y}_1+\tilde{\xi}_1-\tilde{y},\tilde{y}^c-\tilde{y},\psi)}\\
&\quad+\underline{2\mathcal{W}_{,122}[\tilde{y}+rs(\tilde{y}_1+\tilde{\xi}_1-\tilde{y}),\tilde{y}+rs(\tilde{y}^c-\tilde{y})](\tilde{y}_1+\tilde{\xi}_1-\tilde{y},\tilde{y}^c-\tilde{y},\psi)}\\
&\quad+\underline{2\mathcal{W}_{,222}[\tilde{y}+rs(\tilde{y}_1+\tilde{\xi}_1-\tilde{y}),\tilde{y}+rs(\tilde{y}^c-\tilde{y})](\tilde{y}^c-\tilde{y},\tilde{y}^c-\tilde{y},\psi)}\\
&\quad+\underline{\mathcal{W}_{,222}[\tilde{y}+s(\tilde{y}_1+\tilde{\xi}_1-\tilde{y}),\tilde{y}+s(\tilde{y}^c-\tilde{y})](\tilde{y}^c-\tilde{y},\tilde{y}^c-\tilde{y},s\psi)}\Big)\,\mathrm{d}r\,\mathrm{d}s\,.
\end{aligned}
\tag{2.28}
$$

In detail, the first equality follows by a straightforward derivation. Moreover, to infer the second identity, we employ the fundamental theorem of calculus, (2.11) and the relation $\int_0^1(1-s)\,\mathrm{d}s=\frac{1}{2}$. For instance,

$$
\begin{aligned}
&\int_0^1(1-s)\underline{2\mathcal{W}_{,12}[\tilde{y}+s(\tilde{y}_1+\tilde{\xi}_1-\tilde{y}),\tilde{y}+s(\tilde{y}^c-\tilde{y})](\tilde{y}_1+\tilde{\xi}_1-\tilde{y},\psi)}\,\mathrm{d}s-\underline{\mathcal{W}_{,12}[\tilde{y},\tilde{y}](\tilde{y}_1+\tilde{\xi}_1-\tilde{y},\psi)}\\
&=\int_0^1\int_0^1 s(1-s)\Big(\underline{2\mathcal{W}_{,112}[\tilde{y}+rs(\tilde{y}_1+\tilde{\xi}_1-\tilde{y}),\tilde{y}+rs(\tilde{y}^c-\tilde{y})](\tilde{y}_1+\tilde{\xi}_1-\tilde{y},\tilde{y}_1+\tilde{\xi}_1-\tilde{y},\psi)}\\
&\qquad\qquad+\underline{2\mathcal{W}_{,122}[\tilde{y}+rs(\tilde{y}_1+\tilde{\xi}_1-\tilde{y}),\tilde{y}+rs(\tilde{y}^c-\tilde{y})](\tilde{y}_1+\tilde{\xi}_1-\tilde{y},\tilde{y}^c-\tilde{y},\psi)}\Big)\,\mathrm{d}r\,\mathrm{d}s\,.
\end{aligned}
$$

In exactly the same manner as above, we consider the following Taylor expansion of $\mathcal{W}[\tilde{y}^c,\tilde{y}_2]$ w.r.t. $\tilde{y}$

$$
\begin{aligned}
\mathcal{W}[\tilde{y}^c,\tilde{y}_2]=\int_0^1(1-s)\Big(&\mathcal{W}_{,11}[\tilde{y}+s(\tilde{y}^c-\tilde{y}),\tilde{y}+s(\tilde{y}_2-\tilde{y})](\tilde{y}^c-\tilde{y},\tilde{y}^c-\tilde{y})\\
&+2\mathcal{W}_{,12}[\tilde{y}+s(\tilde{y}^c-\tilde{y}),\tilde{y}+s(\tilde{y}_2-\tilde{y})](\tilde{y}^c-\tilde{y},\tilde{y}_2-\tilde{y})\\
&+\mathcal{W}_{,22}[\tilde{y}+s(\tilde{y}^c-\tilde{y}),\tilde{y}+s(\tilde{y}_2-\tilde{y})](\tilde{y}_2-\tilde{y},\tilde{y}_2-\tilde{y})\Big)\,\mathrm{d}s\,,
\end{aligned}
$$

and proceed as in (2.28) to reformulate $\mathcal{W}_{,1}[\tilde{y}^c,\tilde{y}_2](\psi)$. To sum up, (2.26) is equivalent to

$$
\begin{aligned}
0=&-\mathcal{W}_{,22}[\tilde{y},\tilde{y}](\tilde{y}_1+\tilde{\xi}_1-\tilde{y},\psi)+\mathcal{W}_{,22}[\tilde{y},\tilde{y}](\tilde{y}^c-\tilde{y},\psi)+\mathcal{W}_{22}[\tilde{y},\tilde{y}](\tilde{y}^c-\tilde{y},\psi)-\mathcal{W}_{,22}[\tilde{y},\tilde{y}](\tilde{y}_2-\tilde{y},\psi)\\
&+\int_0^1\int_0^1 s(1-s)\Big(\mathcal{W}_{,112}[\tilde{y}+s(\tilde{y}_1+\tilde{\xi}_1-\tilde{y}),\tilde{y}+s(\tilde{y}^c-\tilde{y})](\tilde{y}_1+\tilde{\xi}_1-\tilde{y},\tilde{y}_1+\tilde{\xi}_1-\tilde{y},\psi)\\
&+2\mathcal{W}_{,112}[\tilde{y}+rs(\tilde{y}_1+\tilde{\xi}_1-\tilde{y}),\tilde{y}+rs(\tilde{y}^c-\tilde{y})](\tilde{y}_1+\tilde{\xi}_1-\tilde{y},\tilde{y}_1+\tilde{\xi}_1-\tilde{y},\psi)
\end{aligned}
$$

$$
\begin{aligned}
&+ 2\mathcal{W}_{,122}[\tilde{y} + rs(\tilde{y}_1 + \tilde{\xi}_1 - \tilde{y}), \tilde{y} + rs(\tilde{y}^c - \tilde{y})](\tilde{y}_1 + \tilde{\xi}_1 - \tilde{y}, \tilde{y}^c - \tilde{y}, \psi)\\
&+ 2\mathcal{W}_{,122}[\tilde{y} + s(\tilde{y}_1 + \tilde{\xi}_1 - \tilde{y}), \tilde{y} + s(\tilde{y}^c - \tilde{y})](\tilde{y}_1 + \tilde{\xi}_1 - \tilde{y}, \tilde{y}^c - \tilde{y}, \psi)\\
&+ 2\mathcal{W}_{,122}[\tilde{y} + rs(\tilde{y}_1 + \tilde{\xi}_1 - \tilde{y}), \tilde{y} + rs(\tilde{y}^c - \tilde{y})](\tilde{y}_1 + \tilde{\xi}_1 - \tilde{y}, \tilde{y}^c - \tilde{y}, \psi)\\
&+ 2\mathcal{W}_{,222}[\tilde{y} + rs(\tilde{y}_1 + \tilde{\xi}_1 - \tilde{y}), \tilde{y} + rs(\tilde{y}^c - \tilde{y})](\tilde{y}^c - \tilde{y}, \tilde{y}^c - \tilde{y}, \psi)\\
&+ \mathcal{W}_{,222}[\tilde{y} + s(\tilde{y}_1 + \tilde{\xi}_1 - \tilde{y}), \tilde{y} + s(\tilde{y}^c - \tilde{y})](\tilde{y}^c - \tilde{y}, \tilde{y}^c - \tilde{y}, \psi)\\
&+ 2\mathcal{W}_{,111}[\tilde{y} + rs(\tilde{y}^c - \tilde{y}), \tilde{y} + rs(\tilde{y}_2 - \tilde{y})](\tilde{y}^c - \tilde{y}, \tilde{y}^c - \tilde{y}, \psi)\\
&+ 2\mathcal{W}_{,112}[\tilde{y} + rs(\tilde{y}^c - \tilde{y}), \tilde{y} + rs(\tilde{y}_2 - \tilde{y})](\tilde{y}^c - \tilde{y}, \psi, \tilde{y}_2 - \tilde{y})\\
&+ \mathcal{W}_{,111}[\tilde{y} + s(\tilde{y}^c - \tilde{y}), \tilde{y} + s(\tilde{y}_2 - \tilde{y})](\tilde{y}^c - \tilde{y}, \tilde{y}^c - \tilde{y}, \psi)\\
&+ 2\mathcal{W}_{,112}[\tilde{y} + rs(\tilde{y}^c - \tilde{y}), \tilde{y} + rs(\tilde{y}_2 - \tilde{y})](\tilde{y}^c - \tilde{y}, \psi, \tilde{y}_2 - \tilde{y})\\
&+ 2\mathcal{W}_{,122}[\tilde{y} + rs(\tilde{y}^c - \tilde{y}), \tilde{y} + rs(\tilde{y}_2 - \tilde{y})](\psi, \tilde{y}_2 - \tilde{y}, \tilde{y}_2 - \tilde{y})\\
&+ 2\mathcal{W}_{,112}[\tilde{y} + s(\tilde{y}^c - \tilde{y}), \tilde{y} + s(\tilde{y}_2 - \tilde{y})](\tilde{y}^c - \tilde{y}, \psi, \tilde{y}_2 - \tilde{y})\\
&+ \mathcal{W}_{,122}[\tilde{y} + s(\tilde{y}^c - \tilde{y}), \tilde{y} + s(\tilde{y}_2 - \tilde{y})](\psi, \tilde{y}_2 - \tilde{y}, \tilde{y}_2 - \tilde{y})\Big)\,\mathrm{d}r\,\mathrm{d}s\,. \qquad (2.29)
\end{aligned}
$$

Likewise, we expand (2.27) in the same way as (2.26) (by replacing $\tilde{y}_1 + \tilde{\xi}_1$ and $\tilde{y}_2$ by $\tilde{y}_1$ and $\tilde{y}_2 + \tilde{\xi}_2$, respectively), and subtract the resulting equation from (2.29), which yields

$$
\begin{aligned}
0 =&\mathcal{W}_{,22}[\tilde{y}, \tilde{y}](\tilde{\xi}_2 - \tilde{\xi}_1, \psi)\\
&+ \int_0^1 \int_0^1 s(1-s)\Big(\mathcal{W}_{,112}[\tilde{y} + s(\tilde{y}_1 + \tilde{\xi}_1 - \tilde{y}), \tilde{y} + s(\tilde{y}^c - \tilde{y})](\tilde{y}_1 + \tilde{\xi}_1 - \tilde{y}, \tilde{y}_1 + \tilde{\xi}_1 - \tilde{y}, \psi)\\
&+ 2\mathcal{W}_{,112}[\tilde{y} + rs(\tilde{y}_1 + \tilde{\xi}_1 - \tilde{y}), \tilde{y} + rs(\tilde{y}^c - \tilde{y})](\tilde{y}_1 + \tilde{\xi}_1 - \tilde{y}, \tilde{y}_1 + \tilde{\xi}_1 - \tilde{y}, \psi)\\
&+ 4\mathcal{W}_{,122}[\tilde{y} + rs(\tilde{y}_1 + \tilde{\xi}_1 - \tilde{y}), \tilde{y} + rs(\tilde{y}^c - \tilde{y})](\tilde{y}_1 + \tilde{\xi}_1 - \tilde{y}, \tilde{y}^c - \tilde{y}, \psi)\\
&+ 2\mathcal{W}_{,122}[\tilde{y} + s(\tilde{y}_1 + \tilde{\xi}_1 - \tilde{y}), \tilde{y} + s(\tilde{y}^c - \tilde{y})](\tilde{y}_1 + \tilde{\xi}_1 - \tilde{y}, \tilde{y}^c - \tilde{y}, \psi)\\
&+ 2\mathcal{W}_{,222}[\tilde{y} + rs(\tilde{y}_1 + \tilde{\xi}_1 - \tilde{y}), \tilde{y} + rs(\tilde{y}^c - \tilde{y})](\tilde{y}^c - \tilde{y}, \tilde{y}^c - \tilde{y}, \psi)\\
&+ \mathcal{W}_{,222}[\tilde{y} + s(\tilde{y}_1 + \tilde{\xi}_1 - \tilde{y}), \tilde{y} + s(\tilde{y}^c - \tilde{y})](\tilde{y}^c - \tilde{y}, \tilde{y}^c - \tilde{y}, \psi)\\
&+ 2\mathcal{W}_{,111}[\tilde{y} + rs(\tilde{y}^c - \tilde{y}), \tilde{y} + rs(\tilde{y}_2 - \tilde{y})](\tilde{y}^c - \tilde{y}, \tilde{y}^c - \tilde{y}, \psi)\\
&+ 4\mathcal{W}_{,112}[\tilde{y} + rs(\tilde{y}^c - \tilde{y}), \tilde{y} + rs(\tilde{y}_2 - \tilde{y})](\tilde{y}^c - \tilde{y}, \psi, \tilde{y}_2 - \tilde{y})\\
&+ \mathcal{W}_{,111}[\tilde{y} + s(\tilde{y}^c - \tilde{y}), \tilde{y} + s(\tilde{y}_2 - \tilde{y})](\tilde{y}^c - \tilde{y}, \tilde{y}^c - \tilde{y}, \psi)\\
&+ 2\mathcal{W}_{,122}[\tilde{y} + rs(\tilde{y}^c - \tilde{y}), \tilde{y} + rs(\tilde{y}_2 - \tilde{y})](\psi, \tilde{y}_2 - \tilde{y}, \tilde{y}_2 - \tilde{y})\\
&+ 2\mathcal{W}_{,112}[\tilde{y} + s(\tilde{y}^c - \tilde{y}), \tilde{y} + s(\tilde{y}_2 - \tilde{y})](\tilde{y}^c - \tilde{y}, \psi, \tilde{y}_2 - \tilde{y})\\
&+ \mathcal{W}_{,122}[\tilde{y} + s(\tilde{y}^c - \tilde{y}), \tilde{y} + s(\tilde{y}_2 - \tilde{y})](\psi, \tilde{y}_2 - \tilde{y}, \tilde{y}_2 - \tilde{y})\\
&- \mathcal{W}_{,112}[\tilde{y} + s(\tilde{y}_1 - \tilde{y}), \tilde{y} + s(\tilde{y}^c - \tilde{y})](\tilde{y}_1 - \tilde{y}, \tilde{y}_1 - \tilde{y}, \psi)\\
&- 2\mathcal{W}_{,112}[\tilde{y} + rs(\tilde{y}_1 - \tilde{y}), \tilde{y} + rs(\tilde{y}^c - \tilde{y})](\tilde{y}_1 - \tilde{y}, \tilde{y}_1 - \tilde{y}, \psi)\\
&- 4\mathcal{W}_{,122}[\tilde{y} + rs(\tilde{y}_1 - \tilde{y}), \tilde{y} + rs(\tilde{y}^c - \tilde{y})](\tilde{y}_1 - \tilde{y}, \tilde{y}^c - \tilde{y}, \psi)\\
&- 2\mathcal{W}_{,122}[\tilde{y} + s(\tilde{y}_1 - \tilde{y}), \tilde{y} + s(\tilde{y}^c - \tilde{y})](\tilde{y}_1 - \tilde{y}, \tilde{y}^c - \tilde{y}, \psi)\\
&- 2\mathcal{W}_{,222}[\tilde{y} + rs(\tilde{y}_1 - \tilde{y}), \tilde{y} + rs(\tilde{y}^c - \tilde{y})](\tilde{y}^c - \tilde{y}, \tilde{y}^c - \tilde{y}, \psi)\\
&- \mathcal{W}_{,222}[\tilde{y} + s(\tilde{y}_1 - \tilde{y}), \tilde{y} + s(\tilde{y}^c - \tilde{y})](\tilde{y}^c - \tilde{y}, \tilde{y}^c - \tilde{y}, \psi)\\
&- 2\mathcal{W}_{,111}[\tilde{y} + rs(\tilde{y}^c - \tilde{y}), \tilde{y} + rs(\tilde{y}_2 + \tilde{\xi}_2 - \tilde{y})](\tilde{y}^c - \tilde{y}, \tilde{y}^c - \tilde{y}, \psi)\\
&- 4\mathcal{W}_{,112}[\tilde{y} + rs(\tilde{y}^c - \tilde{y}), \tilde{y} + rs(\tilde{y}_2 + \tilde{\xi}_2 - \tilde{y})](\tilde{y}^c - \tilde{y}, \psi, \tilde{y}_2 + \tilde{\xi}_2 - \tilde{y})\\
&- \mathcal{W}_{,111}[\tilde{y} + s(\tilde{y}^c - \tilde{y}), \tilde{y} + s(\tilde{y}_2 + \tilde{\xi}_2 - \tilde{y})](\tilde{y}^c - \tilde{y}, \tilde{y}^c - \tilde{y}, \psi)\\
&- 2\mathcal{W}_{,122}[\tilde{y} + rs(\tilde{y}^c - \tilde{y}), \tilde{y} + rs(\tilde{y}_2 + \tilde{\xi}_2 - \tilde{y})](\psi, \tilde{y}_2 + \tilde{\xi}_2 - \tilde{y}, \tilde{y}_2 + \tilde{\xi}_2 - \tilde{y})\\
&- 2\mathcal{W}_{,112}[\tilde{y} + s(\tilde{y}^c - \tilde{y}), \tilde{y} + s(\tilde{y}_2 + \tilde{\xi}_2 - \tilde{y})](\tilde{y}^c - \tilde{y}, \psi, \tilde{y}_2 + \tilde{\xi}_2 - \tilde{y})\\
&- \mathcal{W}_{,122}[\tilde{y} + s(\tilde{y}^c - \tilde{y}), \tilde{y} + s(\tilde{y}_2 + \tilde{\xi}_2 - \tilde{y})](\psi, \tilde{y}_2 + \tilde{\xi}_2 - \tilde{y}, \tilde{y}_2 + \tilde{\xi}_2 - \tilde{y})\Big)\,\mathrm{d}r\,\mathrm{d}s\,. \qquad (2.30)
\end{aligned}
$$

In what follows, we will apply (2.30) three times to describe the inverse parallel transports appearing in the definitions of ξ_{I}^τ, ξ_{III}^τ and ξ_{IV}^τ along the discrete paths $\mathbf{A}_\tau^{\mathrm{disc}}$, $\mathbf{B}_\tau^{\mathrm{disc}}$ and $\mathbf{C}_\tau^{\mathrm{disc}}$, respectively (*cf*. Figure 2.3). To this end, we choose $\tilde{y}$, $\tilde{y}^c$, $\tilde{y}_1$, $\tilde{\xi}_1$, $\tilde{y}_2$ and $\tilde{\xi}_2$ for each of the paths as follows:

	$\tilde{y}$	$\tilde{y}^c$	$\tilde{y}_1$	$\tilde{\xi}_1$	$\tilde{y}_2$	$\tilde{\xi}_2$
$\mathbf{A}_\tau^{\mathrm{disc}}$	y_w^τ	y_A^c	y_w^τ	ξ_{I}^τ	$y_{v,w}^\tau$	$\tau^2\eta(y_{v,w}^\tau)$
$\mathbf{B}_\tau^{\mathrm{disc}}$	y_w^τ	y_B^c	y	ξ_{III}^τ	y_w^τ	ξ_{II}^τ
$\mathbf{C}_\tau^{\mathrm{disc}}$	y	y_C^c	y	ξ_{IV}^τ	y_v^τ	$\tau^2\eta(y_v^\tau)$

Table 2.1: Particular choice of the variables for the discrete paths.

We highlight the particular choice of the base points $\tilde{y}$ of the Taylor expansion, all other variables are already determined by the construction of the iterated discrete covariant derivative.

Below, we will derive simplified expressions of (2.30) incorporating the choices in Table 2.1. All details are solely presented for the discrete path $\mathbf{A}_\tau^{\mathrm{disc}}$ since the line of arguments for the remaining paths is analogous. By inserting the particular choice for path $\mathbf{A}_\tau^{\mathrm{disc}}$ one obtains after some straightforward transformations

$$
\begin{aligned}
0 =&\mathcal{W}_{,22}[y_w^\tau, y_w^\tau](\tau^2\eta(y_{v,w}^\tau) - \xi_{\mathrm{I}}^\tau, \psi)\\
&+ \int_0^1\int_0^1 s(1-s)\Big(\mathcal{W}_{,112}[y_w^\tau + s\xi_{\mathrm{I}}^\tau, y_w^\tau + s(y_A^c - y_w^\tau)](\xi_{\mathrm{I}}^\tau, \xi_{\mathrm{I}}^\tau, \psi)\\
&+ 2\mathcal{W}_{,112}[y_w^\tau + rs\xi_{\mathrm{I}}^\tau, y_w^\tau + rs(y_A^c - y_w^\tau)](\xi_{\mathrm{I}}^\tau, \xi_{\mathrm{I}}^\tau, \psi)\\
&+ 4\mathcal{W}_{,122}[y_w^\tau + rs\xi_{\mathrm{I}}^\tau, y_w^\tau + rs(y_A^c - y_w^\tau)](\xi_{\mathrm{I}}^\tau, y_A^c - y_w^\tau, \psi)\\
&+ 2\mathcal{W}_{,122}[y_w^\tau + s\xi_{\mathrm{I}}^\tau, y_w^\tau + s(y_A^c - y_w^\tau)](\xi_{\mathrm{I}}^\tau, y_A^c - y_w^\tau, \psi)\\
&+ 2\mathcal{W}_{,222}[y_w^\tau + rs\xi_{\mathrm{I}}^\tau, y_w^\tau + rs(y_A^c - y_w^\tau)](y_A^c - y_w^\tau, y_A^c - y_w^\tau, \psi)\\
&+ \mathcal{W}_{,222}[y_w^\tau + s\xi_{\mathrm{I}}^\tau, y_w^\tau + s(y_A^c - y_w^\tau)](y_A^c - y_w^\tau, y_A^c - y_w^\tau, \psi)\\
&+ 2\mathcal{W}_{,111}[y_w^\tau + rs(y_A^c - y_w^\tau), y_w^\tau + rs\tau^2 v](y_A^c - y_w^\tau, y_A^c - y_w^\tau, \psi)\\
&+ 4\mathcal{W}_{,112}[y_w^\tau + rs(y_A^c - y_w^\tau), y_w^\tau + rs\tau^2 v](y_A^c - y_w^\tau, \psi, \tau^2 v)\\
&+ \mathcal{W}_{,111}[y_w^\tau + s(y_A^c - y_w^\tau), y_w^\tau + s\tau^2 v](y_A^c - y_w^\tau, y_A^c - y_w^\tau, \psi)\\
&+ 2\mathcal{W}_{,122}[y_w^\tau + rs(y_A^c - y_w^\tau), y_w^\tau + rs\tau^2 v](\psi, \tau^2 v, \tau^2 v)\\
&+ 2\mathcal{W}_{,112}[y_w^\tau + s(y_A^c - y_w^\tau), y_w^\tau + s\tau^2 v](y_A^c - y_w^\tau, \psi, \tau^2 v)\\
&+ \mathcal{W}_{,122}[y_w^\tau + s(y_A^c - y_w^\tau), y_w^\tau + s\tau^2 v](\psi, \tau^2 v, \tau^2 v)\\
&- 2\mathcal{W}_{,222}[y_w^\tau, y_w^\tau + rs(y_A^c - y_w^\tau)](y_A^c - y_w^\tau, y_A^c - y_w^\tau, \psi)\\
&- \mathcal{W}_{,222}[y_w^\tau, y_w^\tau + s(y_A^c - y_w^\tau)](y_A^c - y_w^\tau, y_A^c - y_w^\tau, \psi)\\
&- 2\mathcal{W}_{,111}[y_w^\tau + rs(y_A^c - y_w^\tau), y_w^\tau + rs(\tau^2 v + \tau^2\eta(y_{v,w}^\tau))](y_A^c - y_w^\tau, y_A^c - y_w^\tau, \psi)\\
&- 4\mathcal{W}_{,112}[y_w^\tau + rs(y_A^c - y_w^\tau), y_w^\tau + rs(\tau^2 v + \tau^2\eta(y_{v,w}^\tau))](y_A^c - y_w^\tau, \psi, \tau^2 v + \tau^2\eta(y_{v,w}^\tau))\\
&- \mathcal{W}_{,111}[y_w^\tau + s(y_A^c - y_w^\tau), y_w^\tau + s(\tau^2 v + \tau^2\eta(y_{v,w}^\tau))](y_A^c - y_w^\tau, y_A^c - y_w^\tau, \psi)\\
&- 2\mathcal{W}_{,122}[y_w^\tau + rs(y_A^c - y_w^\tau), y_w^\tau + rs(\tau^2 v + \tau^2\eta(y_{v,w}^\tau))](\psi, \tau^2 v + \tau^2\eta(y_{v,w}^\tau), \tau^2 v + \tau^2\eta(y_{v,w}^\tau))\\
&- 2\mathcal{W}_{,112}[y_w^\tau + s(y_A^c - y_w^\tau), y_w^\tau + s(\tau^2 v + \tau^2\eta(y_{v,w}^\tau))](y_A^c - y_w^\tau, \psi, \tau^2 v + \tau^2\eta(y_{v,w}^\tau))\\
&- \mathcal{W}_{,122}[y_w^\tau + s(y_A^c - y_w^\tau), y_w^\tau + s(\tau^2 v + \tau^2\eta(y_{v,w}^\tau))](\psi, \tau^2 v + \tau^2\eta(y_{v,w}^\tau), \tau^2 v + \tau^2\eta(y_{v,w}^\tau))\Big)\,\mathrm{d}r\,\mathrm{d}s\,.
\end{aligned}
\tag{2.31}
$$

Let us for the moment assume that all energies appearing in (2.31) can be evaluated at (y_w^τ, y_w^τ) resulting in

an error of order τ^6, which follows from the estimates (to be verified below)

$$\left\|\tau^2\eta(y^\tau_{v,w})\right\|_{\mathbf{V}} = \mathcal{O}(\tau^2)\,, \tag{2.32}$$

$$\|y^c_A - y^\tau_w\|_{\mathbf{V}} = \mathcal{O}(\tau^2)\,, \tag{2.33}$$

$$\|\xi^\tau_{\mathrm{I}}\|_{\mathbf{V}} = \mathcal{O}(\tau^2)\,. \tag{2.34}$$

For instance, one obtains the following estimate for the first integrand appearing in (2.31)

$$\begin{aligned}&\left|\int_0^1\int_0^1 s(1-s)\left(\mathcal{W}_{,112}[y^\tau_w + s\xi^\tau_{\mathrm{I}}, y^\tau_w + s(y^c_A - y^\tau_w)](\xi^\tau_{\mathrm{I}},\xi^\tau_{\mathrm{I}},\psi) - \mathcal{W}_{,112}[y^\tau_w, y^\tau_w](\xi^\tau_{\mathrm{I}},\xi^\tau_{\mathrm{I}},\psi)\right)\,\mathrm{d}r\,\mathrm{d}s\right| \\ &= \mathcal{O}\left(\left(\|\xi^\tau_{\mathrm{I}}\|_{\mathbf{V}} + \|y^c_A - y^\tau_w\|_{\mathbf{V}}\right)\|\xi^\tau_{\mathrm{I}}\|^2_{\mathbf{V}}\,\|\psi\|_{\mathbf{V}}\right) = \mathcal{O}(\tau^6)\,.\end{aligned}$$

Here and in all further equations, to increase readability we solely state the order of convergence in the remainder (using the $\mathcal{O}$-notation) and omit the explicit dependency on the variables involved.

Then, by using $\int_0^1 s(1-s)\,\mathrm{d}s = \frac{1}{6}$ we deduce from (2.31) the relation

$$\begin{aligned}\mathcal{O}(\tau^6) = {}& \mathcal{W}_{,22}[y^\tau_w, y^\tau_w](\tau^2\eta(y^\tau_{v,w}) - \xi^\tau_{\mathrm{I}},\psi) + \tfrac{1}{2}\mathcal{W}_{,112}[y^\tau_w, y^\tau_w](\xi^\tau_{\mathrm{I}},\xi^\tau_{\mathrm{I}},\psi) \\ &+ \mathcal{W}_{,122}[y^\tau_w, y^\tau_w](\xi^\tau_{\mathrm{I}}, y^c_A - y^\tau_w,\psi) - \mathcal{W}_{,112}[y^\tau_w, y^\tau_w](y^c_A - y^\tau_w,\psi,\tau^2\eta(y^\tau_{v,w})) \\ &- \mathcal{W}_{,122}[y^\tau_w, y^\tau_w](\psi,\tau^2 v,\tau^2\eta(y^\tau_{v,w})) - \tfrac{1}{2}\mathcal{W}_{,122}[y^\tau_w, y^\tau_w](\psi,\tau^2\eta(y^\tau_{v,w}),\tau^2\eta(y^\tau_{v,w}))\,.\end{aligned} \tag{2.35}$$

Due to the smoothness of the vector field η we can immediately infer (2.32). The estimate (2.33) is a consequence of

$$\|y^c_A - y^\tau_w\|_{\mathbf{V}} = \mathcal{O}\left(\left\|y^\tau_{v,w} + \tau^2\eta(y^\tau_{v,w}) - y^\tau_w\right\|_{\mathbf{V}}\right) = \mathcal{O}\left(\left\|\tau^2 v + \tau^2\eta(y^\tau_{v,w})\right\|_{\mathbf{V}}\right) = \mathcal{O}(\tau^2)\,.$$

Finally, the proof of (2.34) is based on an error propagation formula derived in the convergence proof of the discrete parallel transport (*cf*. [RW15]) tailored to our specific construction. At first, we remark that the relation $y^\tau_{v,w} = y^\tau_w + \tau^2 v$, the smoothness of h as well as Taylor expansions imply

$$\left\|y^\tau_{v,w} - \widetilde{h}^\tau(\tau^2)\right\|_{\mathbf{V}} \le \|y^\tau_w - h(0,\tau)\|_{\mathbf{V}} + \left\|h(0,\tau) + \tau^2 v - \widetilde{h}^\tau(\tau^2)\right\|_{\mathbf{V}} = \mathcal{O}(\tau^2)\,,$$

and $\|e_0\|_{\mathbf{V}} = \mathcal{O}(\tau^2)$ with $e_0 := \eta(y^\tau_{v,w}) - \eta(\widetilde{h}^\tau(\tau^2))$. By setting $e_1 := \frac{1}{\tau^2}(\xi^\tau_{\mathrm{I}} - \zeta^\tau_{\mathrm{I}})$ we can deduce by taking into account [RW15, (6.22)] and the subsequent reasoning that $\|e_1\|_{\mathbf{V}} = \mathcal{O}(1)$. Since the parallel transport associated with a Riemannian covariant derivative is an isometry (*cf*. [Sak96, Chapter II]), one obtains $\|\zeta^\tau_{\mathrm{I}}\|_{\mathbf{V}} = \mathcal{O}(\tau^2)$, which readily implies (2.34). Alternatively, one can infer (2.34) using (2.29) with the variables given in Table 2.1.

Likewise, starting from (2.30), choosing the variables associated with the discrete path $\mathbf{B}^{\mathrm{disc}}_\tau$ according to Table 2.1 and following the same line of arguments as above taking into account the estimates

$$\|\xi^\tau_{\mathrm{II}}\|_{\mathbf{V}} = \mathcal{O}(\tau)\,, \tag{2.36}$$

$$\|y^c_B - y^\tau_w\|_{\mathbf{V}} = \mathcal{O}(\tau)\,, \tag{2.37}$$

$$\|\xi^\tau_{\mathrm{III}}\|_{\mathbf{V}} = \mathcal{O}(\tau)\,, \tag{2.38}$$

we finally obtain

$$\begin{aligned}\mathcal{O}(\tau^3) = {}& \mathcal{W}_{,22}[y^\tau_w, y^\tau_w](\xi^\tau_{\mathrm{II}} - \xi^\tau_{\mathrm{III}},\psi) + \tfrac{1}{2}\mathcal{W}_{,112}[y^\tau_w, y^\tau_w](\xi^\tau_{\mathrm{III}},\xi^\tau_{\mathrm{III}},\psi) \\ &- \mathcal{W}_{,112}[y^\tau_w, y^\tau_w](\tau w,\xi^\tau_{\mathrm{III}},\psi) + \mathcal{W}_{,122}[y^\tau_w, y^\tau_w](\xi^\tau_{\mathrm{III}}, y^c_B - y^\tau_w,\psi) \\ &- \mathcal{W}_{,112}[y^\tau_w, y^\tau_w](y^c_B - y^\tau_w,\psi,\xi^\tau_{\mathrm{II}}) - \tfrac{1}{2}\mathcal{W}_{,122}[y^\tau_w, y^\tau_w](\psi,\xi^\tau_{\mathrm{II}},\xi^\tau_{\mathrm{II}})\,.\end{aligned} \tag{2.39}$$

Next, we solely prove (2.36) since the proofs of (2.37) and (2.38) are similar to (2.33) and (2.34), respectively. To this end, we first note that all summands involving third derivatives of $\mathcal{W}$ on the right-hand side of (2.35) are of order τ^4 due to (2.32)-(2.34), which implies

$$\mathcal{W}_{,22}[y^\tau_w, y^\tau_w](\tau^2\eta(y^\tau_{v,w}) - \xi^\tau_{\mathrm{I}},\psi) = \mathcal{O}(\tau^4)\,.$$

Thus, incorporating the Hypotheses (H1) and (H4') shows that $\left\|\tau^2\eta(y^\tau_{v,w}) - \xi^\tau_{\mathrm{I}}\right\|_{\mathbf{V}} = \mathcal{O}(\tau^4)$ due to

$$c^* \left\|v\right\|_{\mathbf{V}} \leq g_{\tilde{y}}\left(v, \tfrac{v}{\|v\|_{\mathbf{V}}}\right) \leq \sup_{\psi\in\mathbf{V},\|\psi\|_{\mathbf{V}}=1} g_{\tilde{y}}(v,\psi) = \sup_{\psi\in\mathbf{V},\|\psi\|_{\mathbf{V}}=1} \tfrac{1}{2}\mathcal{W}_{,22}[\tilde{y},\tilde{y}](v,\psi) \tag{2.40}$$

for arbitrary $v \in \mathbf{V}$ and $\tilde{y} \in \mathring{\mathcal{M}}$. We will frequently employ (2.40) below. Hence,

$$\|\xi^\tau_{\mathrm{II}}\|_{\mathbf{V}} \leq \tfrac{1}{\tau^3}(\left\|\xi^\tau_{\mathrm{I}} - \tau^2\eta(y^\tau_{v,w})\right\|_{\mathbf{V}} + \left\|\tau^2\eta(y^\tau_{v,w}) - \tau^2\eta(y^\tau_w)\right\|_{\mathbf{V}}) = \mathcal{O}(\tau)\,.$$

By adding $\frac{1}{\tau^3}$(2.35) and (2.39) and recalling the definitions of ξ^τ_{I} and ξ^τ_{II} we conclude (only the second derivatives of the energy are modified)

$$\begin{aligned}
\mathcal{O}(\tau^3) = {}& \mathcal{W}_{,22}[y^\tau_w, y^\tau_w](-\xi^\tau_{\mathrm{III}}, \psi) + \tfrac{1}{2}\mathcal{W}_{,112}[y^\tau_w, y^\tau_w](\xi^\tau_{\mathrm{III}}, \xi^\tau_{\mathrm{III}}, \psi)\\
& - \mathcal{W}_{,112}[y^\tau_w, y^\tau_w](\tau w, \xi^\tau_{\mathrm{III}}, \psi) + \mathcal{W}_{,122}[y^\tau_w, y^\tau_w](\xi^\tau_{\mathrm{III}}, y^c_B - y^\tau_w, \psi)\\
& - \mathcal{W}_{,112}[y^\tau_w, y^\tau_w](y^c_B - y^\tau_w, \psi, \xi^\tau_{\mathrm{II}}) - \tfrac{1}{2}\mathcal{W}_{,122}[y^\tau_w, y^\tau_w](\psi, \xi^\tau_{\mathrm{II}}, \xi^\tau_{\mathrm{II}})\\
& + \frac{1}{\tau^3}\Big(\mathcal{W}_{,22}[y^\tau_w, y^\tau_w](\tau^2\eta(y^\tau_{v,w}) - \tau^2\eta(y^\tau_w)) + \tfrac{1}{2}\mathcal{W}_{,112}[y^\tau_w, y^\tau_w](\xi^\tau_{\mathrm{I}}, \xi^\tau_{\mathrm{I}}, \psi)\\
& \qquad + \mathcal{W}_{,122}[y^\tau_w, y^\tau_w](\xi^\tau_{\mathrm{I}}, y^c_A - y^\tau_w, \psi) - \mathcal{W}_{,112}[y^\tau_w, y^\tau_w](y^c_A - y^\tau_w, \psi, \tau^2\eta(y^\tau_{v,w}))\\
& \qquad - \mathcal{W}_{,122}[y^\tau_w, y^\tau_w](\psi, \tau^2 v, \tau^2\eta(y^\tau_{v,w})) - \tfrac{1}{2}\mathcal{W}_{,122}[y^\tau_w, y^\tau_w](\psi, \tau^2\eta(y^\tau_{v,w}), \tau^2\eta(y^\tau_{v,w}))\Big)\,.
\end{aligned} \tag{2.41}$$

Finally, the analogous equation to (2.35) and (2.39) for the discrete path $\mathbf{C}^{\mathrm{disc}}_\tau$ with variables chosen in accordance with Table 2.1 reads as

$$\begin{aligned}
\mathcal{O}(\tau^6) = {}& \mathcal{W}_{,22}[y, y](\tau^2\eta(y^\tau_v) - \xi^\tau_{\mathrm{IV}}, \psi) + \tfrac{1}{2}\mathcal{W}_{,112}[y, y](\xi^\tau_{\mathrm{IV}}, \xi^\tau_{\mathrm{IV}}, \psi)\\
& + \mathcal{W}_{,122}[y, y](\xi^\tau_{\mathrm{IV}}, y^c_C - y, \psi) - \mathcal{W}_{,112}[y, y](y^c_C - y, \psi, \tau^2\eta(y^\tau_v))\\
& - \mathcal{W}_{,122}[y, y](\psi, \tau^2 v, \tau^2\eta(y^\tau_v)) - \tfrac{1}{2}\mathcal{W}_{,122}[y, y](\psi, \tau^2\eta(y^\tau_v), \tau^2\eta(y^\tau_v))\,.
\end{aligned} \tag{2.42}$$

This equation immediately follows from the estimates

$$\left\|\tau^2\eta(y^\tau_v)\right\|_{\mathbf{V}} = \mathcal{O}(\tau^2)\,, \qquad \|y^c_C - y\|_{\mathbf{V}} = \mathcal{O}(\tau^2)\,, \qquad \|\xi^\tau_{\mathrm{IV}}\|_{\mathbf{V}} = \mathcal{O}(\tau^2)\,, \tag{2.43}$$

which can be proven in the same manner as (2.32)-(2.34).

ad (ii.): *Derivation of the continuous optimality conditions.*

Let $z : [0,1] \to \mathring{\mathcal{M}}$ be a smooth path and $\zeta : \mathring{\mathcal{M}} \to \mathbf{V}$ be a smooth parallel vector field along z. We recall that ζ is parallel along z if

$$0 = g_{z(t)}(\nabla_{z(t)}\zeta(t), \psi) = g_{z(t)}(\dot{\zeta}(t), \psi) + g_{z(t)}(\Gamma(\dot{z}(t), \zeta(t)), \psi) \tag{2.44}$$

for all $\psi \in \mathbf{V}$ and all $t \in [0,1]$. Here, the *Christoffel operator* $\Gamma : \mathbf{V} \times \mathbf{V} \to \mathbf{V}$ is implicitly defined as

$$g_{z(t)}(\Gamma(\phi,\chi),\psi) = \tfrac{1}{2}\big((D_z g_{z(t)})(\chi)(\psi,\phi) + (D_z g_{z(t)})(\phi)(\psi,\chi) - (D_z g_{z(t)})(\psi)(\phi,\chi)\big) \tag{2.45}$$

for all $\phi, \chi, \psi \in \mathbf{V}$. By combining (2.44) and (2.45) and using (2.10) we obtain

$$\begin{aligned}
0 = {}& \mathcal{W}_{,22}[z(t), z(t)](\dot{\zeta}(t), \psi) + \frac{1}{2}\Big((\mathcal{W}_{,221}[z(t), z(t)] + \mathcal{W}_{,222}[z(t), z(t)])(\psi, \dot{z}(t), \zeta(t))\\
& \qquad + (\mathcal{W}_{,221}[z(t), z(t)] + \mathcal{W}_{,222}[z(t), z(t)])(\psi, \zeta(t), \dot{z}(t))\\
& \qquad - ((\mathcal{W}_{,221}[z(t), z(t)] + \mathcal{W}_{,222}[z(t), z(t)])(\dot{z}(t), \zeta(t), \psi))\Big)\\
= {}& \mathcal{W}_{,22}[z(t), z(t)](\dot{\zeta}(t), \psi) + \frac{1}{2}\Big(\mathcal{W}_{,222}[z(t), z(t)](\zeta(t), \dot{z}(t), \psi) + \mathcal{W}_{,122}[z(t), z(t)](\zeta(t), \dot{z}(t), \psi)\\
& \qquad + \mathcal{W}_{,122}[z(t), z(t)](\dot{z}(t), \zeta(t), \psi) - \mathcal{W}_{,122}[z(t), z(t)](\psi, \zeta(t), \dot{z}(t))\Big)\,.
\end{aligned} \tag{2.46}$$

Hence, by evaluating (2.46) at $t = 0$ and $t = 1$ and adding both equations one obtains

$$\begin{aligned}
0 = \frac{1}{2}\Big(&\mathcal{W}_{,22}[z(0), z(0)](\dot\zeta(0), \psi) + \mathcal{W}_{,22}[z(1), z(1)](\dot\zeta(1), \psi)\Big)\\
&+ \frac{1}{4}\Big(\mathcal{W}_{,222}[z(0), z(0)](\zeta(0), \dot z(0), \psi) + \mathcal{W}_{,222}[z(1), z(1)](\zeta(1), \dot z(1), \psi)\\
&\quad + \mathcal{W}_{,122}[z(0), z(0)](\zeta(0), \dot z(0), \psi) + \mathcal{W}_{,122}[z(1), z(1)](\zeta(1), \dot z(1), \psi)\\
&\quad + \mathcal{W}_{,122}[z(0), z(0)](\dot z(0), \zeta(0), \psi) + \mathcal{W}_{,122}[z(1), z(1)](\dot z(1), \zeta(1), \psi)\\
&\quad - \mathcal{W}_{,122}[z(0), z(0)](\psi, \zeta(0), \dot z(0)) - \mathcal{W}_{,122}[z(1), z(1)](\psi, \zeta(1), \dot z(1))\Big)\,.
\end{aligned} \tag{2.47}$$

In what follows, we will apply (2.47) to each of the three paths

$$\begin{aligned}
z_A^\tau(s) &= \widetilde{h}^\tau(s\tau^2)\,,\\
z_B^\tau(s) &= h(0, s\tau)\,,\\
z_C^\tau(s) &= h(s\tau^2, 0)
\end{aligned}$$

for $s \in [0, 1]$, which can be regarded as the continuous counterparts of the discrete paths $\mathbf{A}_\tau^{\mathrm{disc}}$, $\mathbf{B}_\tau^{\mathrm{disc}}$ and $\mathbf{C}_\tau^{\mathrm{disc}}$, respectively (*cf*. Figure 2.3). As in the previous step, we will focus on the derivation of optimality conditions for the path z_A^τ since the remaining optimality conditions can be inferred in exactly the same manner.

Let $\rho_A^\tau \in C^2(B_{2\tau^2}(0), \mathbf{V})$ be the parallel vector field along $B_{2\tau^2}(0) \ni s \mapsto \widetilde{h}^\tau(s)$ such that $\rho_A^\tau(\tau^2) = \eta(\widetilde{h}^\tau(\tau^2))$. Clearly, $\zeta_A^\tau(s) = \tau^2 \rho_A^\tau(s\tau^2)$ is a parallel vector field along z_A^τ, and the subsequent relations immediately follow from the definitions and Taylor expansions

$$\begin{aligned}
\dot z_A^\tau(0) &= \tau^2 v\,, & \sup_{s\in[0,1]} \|\dot z_A^\tau(s)\|_{\mathbf{V}} &= \mathcal{O}(\tau^2)\,,\\
\|z_A^\tau(1) - z_A^\tau(0)\|_{\mathbf{V}} &= \mathcal{O}(\tau^2)\,, & \|\dot z_A^\tau(1) - \dot z_A^\tau(0)\|_{\mathbf{V}} &= \mathcal{O}(\tau^4)\,.
\end{aligned} \tag{2.48}$$

Here, we used $g \in C^3(\mathbf{Y}, \mathbf{V}' \otimes \mathbf{V}')$ (*cf*. (H3')), which implies $h \in C^2(B_{2\tau_0{}^2}(0) \times B_{2\tau_0}(0))$ and $\{(t, \tau) \mapsto \widetilde{h}^\tau(t)\} \in C^2(B_{2\tau_0{}^2}(0) \times B_{2\tau_0}(0))$ (*cf*. [Lan95, Chapter IV]). To derive the first estimate in (2.48) we additionally employ the fact that the derivative of the exponential map at the origin is the identity, *i.e*. $D\exp(0) = \mathbb{1}$. Moreover, the smoothness of the vector field combined with the regularity of h as well as $\widetilde{h}^\tau$ and Taylor expansions leads to the estimates (*cf*. [Lan95, Chapter VIII] and [Kli95, Section 1.6 and 1.7])

$$\begin{aligned}
\sup_{s\in[0,1]} \|\zeta_A^\tau(s)\|_{\mathbf{V}} &= \mathcal{O}(\tau^2)\,, & \sup_{s\in[0,1]} \left\|\dot\zeta_A^\tau(s)\right\|_{\mathbf{V}} &= \mathcal{O}(\tau^4)\,,\\
\sup_{s\in[0,1]} \left\|\ddot\zeta_A^\tau(s)\right\|_{\mathbf{V}} &= \mathcal{O}(\tau^6)\,, & \|\zeta_A^\tau(1) - \zeta_A^\tau(0)\|_{\mathbf{V}} &= \mathcal{O}(\tau^4)\,.
\end{aligned} \tag{2.49}$$

Hence, applying (2.47) to $\zeta = \zeta_A^\tau$ and $z = z_A^\tau$ and taking into account (2.48) and (2.49) yields

$$\begin{aligned}
0 = \frac{1}{2}\Big(&\mathcal{W}_{,22}[z_A^\tau(0), z_A^\tau(0)](\dot\zeta_A^\tau(0), \psi) + \mathcal{W}_{,22}[z_A^\tau(1), z_A^\tau(1)](\dot\zeta_A^\tau(1), \psi)\Big)\\
&+ \frac{1}{4}\Big(\mathcal{W}_{,222}[z_A^\tau(0), z_A^\tau(0)](\zeta_A^\tau(0), \dot z_A^\tau(0), \psi) + \mathcal{W}_{,222}[z_A^\tau(1), z_A^\tau(1)](\zeta_A^\tau(1), \dot z_A^\tau(1), \psi)\\
&\quad + \mathcal{W}_{,122}[z_A^\tau(0), z_A^\tau(0)](\zeta_A^\tau(0), \dot z_A^\tau(0), \psi) + \mathcal{W}_{,122}[z_A^\tau(1), z_A^\tau(1)](\zeta_A^\tau(1), \dot z_A^\tau(1), \psi)\\
&\quad + \mathcal{W}_{,122}[z_A^\tau(0), z_A^\tau(0)](, \zeta_A^\tau(0), \psi) + \mathcal{W}_{,122}[z_A^\tau(1), z_A^\tau(1)](\dot z_A^\tau(1), \zeta_A^\tau(1), \psi)\\
&\quad - \mathcal{W}_{,122}[z_A^\tau(0), z_A^\tau(0)](\psi, \zeta_A^\tau(0), \dot z_A^\tau(0)) - \mathcal{W}_{,122}[z_A^\tau(1), z_A^\tau(1)](\psi, \zeta_A^\tau(1), \dot z_A^\tau(1))\Big)\\
= \mathcal{W}_{,22}&[z_A^\tau(0), z_A^\tau(0)](\tau^2\eta(z_A^\tau(1)) - \zeta_{\mathrm{I}}^\tau, \psi)\\
&+ \frac{1}{2}\Big(\mathcal{W}_{,222}[z_A^\tau(0), z_A^\tau(0)](\tau^2\eta(z_A^\tau(1)), \tau^2 v, \psi) + \mathcal{W}_{,122}[z_A^\tau(0), z_A^\tau(0)](\tau^2\eta(z_A^\tau(1)), \tau^2 v, \psi)\\
&+ \mathcal{W}_{,122}[z_A^\tau(0), z_A^\tau(0)](\tau^2 v, \tau^2\eta(z_A^\tau(1)), \psi) - \mathcal{W}_{,122}[z_A^\tau(0), z_A^\tau(0)](\psi, \tau^2\eta(z_A^\tau(1)), \tau^2 v)\Big) + \mathcal{O}(\tau^6)\,.
\end{aligned} \tag{2.50}$$

In detail, the transformation of the first line follows from

$$\begin{aligned}
&\frac{1}{2}\Big(\mathcal{W}_{,22}[z_A^\tau(0),z_A^\tau(0)](\dot\zeta_A^\tau(0),\psi)+\mathcal{W}_{,22}[z_A^\tau(1),z_A^\tau(1)](\dot\zeta_A^\tau(1),\psi)\Big)\\
&=\frac{1}{2}\Big(\mathcal{W}_{,22}[z_A^\tau(0),z_A^\tau(0)](\dot\zeta_A^\tau(0),\psi)+\mathcal{W}_{,22}[z_A^\tau(0),z_A^\tau(0)](\dot\zeta_A^\tau(1),\psi)\Big)+\mathcal{O}(\tau^6)\\
&=\frac{1}{2}\mathcal{W}_{,22}[z_A^\tau(0),z_A^\tau(0)](\dot\zeta_A^\tau(0)+\dot\zeta_A^\tau(1),\psi)+\mathcal{O}(\tau^6)=\mathcal{W}_{,22}[z_A^\tau(0),z_A^\tau(0)](\zeta_A^\tau(0)-\zeta_A^\tau(1),\psi)+\mathcal{O}(\tau^6)\,,
\end{aligned}$$

where we have used the estimate $\zeta_A^\tau(0)-\zeta_A^\tau(1)=\frac{1}{2}(\dot\zeta_A^\tau(0)+\dot\zeta_A^\tau(1))+\mathcal{O}(\tau^6)$, which can be proven by adding two Taylor expansions w.r.t. 0 and 1, respectively. The remaining transformations can be deduced from multiple Taylor expansions using (2.48) and (2.49).

Likewise, we define $\rho_B^\tau\in C^2(B_{2\tau}(0),\mathbf{V})$ as the parallel vector field along $B_{2\tau}(0)\ni s\mapsto h(0,s)$ satisfying $\rho_B^\tau(\tau)=\rho_A^\tau(0)$ and set $\zeta_B^\tau(s)=\tau\rho_B^\tau(s)$, which is a parallel vector field along z_B^τ. The analogous estimate of (2.50) for z_B^τ is given by

$$\begin{aligned}
\mathcal{O}(\tau^3)&=\mathcal{W}_{,22}[z_B^\tau(1),z_B^\tau(1)](\zeta_{\mathrm{II}}^\tau-\zeta_{\mathrm{III}}^\tau,\psi)\\
&\quad+\frac{1}{2}\Big(\mathcal{W}_{,222}[z_B^\tau(1),z_B^\tau(1)](\zeta_B^\tau(0),\tau w,\psi)+\mathcal{W}_{,122}[z_B^\tau(1),z_B^\tau(1)](\zeta_B^\tau(0),\tau w,\psi)\\
&\qquad+\mathcal{W}_{,122}[z_B^\tau(1),z_B^\tau(1)](\tau w,\zeta_B^\tau(0),\psi)-\mathcal{W}_{,122}[z_B^\tau(1),z_B^\tau(1)](\psi,\zeta_B^\tau(0),\tau w)\Big)\,,
\end{aligned}\tag{2.51}$$

where the subsequent estimates were employed:

$$\begin{aligned}
&\dot z_B^\tau(0)=\tau w\,,\qquad \sup_{s\in[0,1]}\|\dot z_B^\tau(s)\|_{\mathbf{V}}=\mathcal{O}(\tau)\,,\qquad \|z_B^\tau(1)-z_B^\tau(0)\|_{\mathbf{V}}=\mathcal{O}(\tau)\,,\\
&\|\dot z_B^\tau(1)-\dot z_B^\tau(0)\|_{\mathbf{V}}=\mathcal{O}(\tau^2)\,,\qquad \sup_{s\in[0,1]}\|\zeta_B^\tau(s)\|_{\mathbf{V}}=\mathcal{O}(\tau)\,,\qquad \sup_{s\in[0,1]}\Big\|\dot\zeta_B^\tau(s)\Big\|_{\mathbf{V}}=\mathcal{O}(\tau^2)\,,\\
&\sup_{s\in[0,1]}\Big\|\ddot\zeta_B^\tau(s)\Big\|_{\mathbf{V}}=\mathcal{O}(\tau^3)\,,\qquad \|\zeta_B^\tau(1)-\zeta_B^\tau(0)\|_{\mathbf{V}}=\mathcal{O}(\tau^2)\,.
\end{aligned}$$

We merely remark that ζ_B^τ smoothly depends on the initial data $\rho_B^\tau(\tau)=\rho_A^\tau(0)$, which itself smoothly depends on the vector field and h and thus already justifies the aforementioned estimates involving ζ_B^τ.

Hence, by adding $\frac{1}{\tau^3}$(2.50) and (2.51) one gets by taking into account the definitions of ζ_{I}^τ, ζ_{II}^τ, z_A^τ and z_B^τ

$$\begin{aligned}
\mathcal{O}(\tau^3)&=\mathcal{W}_{,22}[z_B^\tau(1),z_B^\tau(1)](-\zeta_{\mathrm{III}}^\tau,\psi)\\
&\quad+\frac{1}{2}\Big(\mathcal{W}_{,222}[z_B^\tau(1),z_B^\tau(1)](\zeta_B^\tau(0),\tau w,\psi)+\mathcal{W}_{,122}[z_B^\tau(1),z_B^\tau(1)](\zeta_B^\tau(0),\tau w,\psi)\\
&\qquad+\mathcal{W}_{,122}[z_B^\tau(1),z_B^\tau(1)](\tau w,\zeta_B^\tau(0),\psi)-\mathcal{W}_{,122}[z_B^\tau(1),z_B^\tau(1)](\psi,\zeta_B^\tau(0),\tau w)\Big)\\
&\quad+\frac{1}{\tau^3}\Big(\mathcal{W}_{,22}[z_B^\tau(1),z_B^\tau(1)](\tau^2\eta(z_A^\tau(1))-\tau^2\eta(z_B^\tau(1)),\psi)\\
&\qquad+\frac{1}{2}\Big(\mathcal{W}_{,222}[z_B^\tau(1),z_B^\tau(1)](\tau^2\eta(z_A^\tau(1)),\tau^2v,\psi)+\mathcal{W}_{,122}[z_B^\tau(1),z_B^\tau(1)](\tau^2\eta(z_A^\tau(1)),\tau^2v,\psi)\\
&\qquad+\mathcal{W}_{,122}[z_B^\tau(1),z_B^\tau(1)](\tau^2v,\tau^2\eta(z_A^\tau(1)),\psi)-\mathcal{W}_{,122}[z_B^\tau(1),z_B^\tau(1)](\psi,\tau^2\eta(z_A^\tau(1)),\tau^2v)\Big)\Big)\,.
\end{aligned}\tag{2.52}$$

We will see below that by subtracting the discrete counterpart (2.41) all summands involving third derivatives of the energy are of order τ^3 and therefore negligible.

Finally, consider the parallel vector field $\rho_C^\tau\in C^2(B_{2\tau^2}(0),\mathbf{V})$ along $B_{2\tau^2}(0)\ni s\mapsto h(s,0)$ such that $\rho_C^\tau(\tau^2)=\eta(h(\tau^2,0))$. As before, $\zeta_C^\tau(s)=\tau^2\rho_C^\tau(s\tau^2)$ is parallel along z_C^τ, and (2.47) implies in this case

$$\begin{aligned}
\mathcal{O}(\tau^6)&=\mathcal{W}_{,22}[y,y](\tau^2\eta(z_C^\tau(1))-\zeta_{\mathrm{IV}}^\tau,\psi)\\
&\quad+\frac{1}{2}\Big(\mathcal{W}_{,222}[y,y](\tau^2\eta(z_C^\tau(1)),\tau^2v,\psi)+\mathcal{W}_{,122}[y,y](\tau^2\eta(z_C^\tau(1)),\tau^2v,\psi)\\
&\qquad+\mathcal{W}_{,122}[y,y](\tau^2v,\tau^2\eta(z_C^\tau(1)),\psi)-\mathcal{W}_{,122}[y,y](\psi,\tau^2\eta(z_C^\tau(1)),\tau^2v)\Big)\,.
\end{aligned}\tag{2.53}$$

The corresponding auxiliary relations that were used to infer (2.53) read as

$$\dot{z}_C^\tau(0) = \tau^2 v\,, \qquad \sup_{s\in[0,1]} \|\dot{z}_C^\tau(s)\|_{\mathbf{V}} = \mathcal{O}(\tau^2)\,, \qquad \|z_B^\tau(1) - z_B^\tau(0)\|_{\mathbf{V}} = \mathcal{O}(\tau^2)\,,$$
$$\|\dot{z}_C^\tau(1) - \dot{z}_C^\tau(0)\|_{\mathbf{V}} = \mathcal{O}(\tau^4)\,, \qquad \sup_{s\in[0,1]} \|\zeta_C^\tau(s)\|_{\mathbf{V}} = \mathcal{O}(\tau^2)\,, \qquad \sup_{s\in[0,1]} \left\|\dot{\zeta}_C^\tau(s)\right\|_{\mathbf{V}} = \mathcal{O}(\tau^4)\,,$$
$$\sup_{s\in[0,1]} \left\|\ddot{\zeta}_C^\tau(s)\right\|_{\mathbf{V}} = \mathcal{O}(\tau^6)\,, \qquad \|\zeta_C^\tau(1) - \zeta_C^\tau(0)\|_{\mathbf{V}} = \mathcal{O}(\tau^4)\,.$$

ad (iii.): *Convergence of the iterated covariant derivatives.*

In this step, we will relate the discrete optimality conditions to their continuous counterparts to prove the convergence of the discrete curvature tensor.

To estimate the second term in (2.25) and thus $\|\xi_{\mathrm{V}}^\tau - \zeta_{\mathrm{V}}^\tau\|_{\mathbf{V}}$, we subtract (2.53) from (2.42) and divide by τ^3, which results in

$$\begin{aligned}
\mathcal{O}(\tau^3) = \mathcal{W}_{,22}[y,y](\zeta_{\mathrm{V}}^\tau - \xi_{\mathrm{V}}^\tau, \psi) + \frac{1}{\tau^3}\Big(&\tfrac{1}{2}\mathcal{W}_{,112}[y,y](\xi_{\mathrm{IV}}^\tau, \xi_{\mathrm{IV}}^\tau, \psi)\\
&+ \mathcal{W}_{,122}[y,y](\xi_{\mathrm{IV}}^\tau, y_C^c - y, \psi) - \mathcal{W}_{,112}[y,y](y_C^c - y, \psi, \tau^2\eta(y_v^\tau))\\
&- \mathcal{W}_{,122}[y,y](\psi, \tau^2 v, \tau^2\eta(y_v^\tau)) - \tfrac{1}{2}\mathcal{W}_{,122}[y,y](\psi, \tau^2\eta(y_v^\tau), \tau^2\eta(y_v^\tau))\\
&+ \mathcal{W}_{,22}[y,y](\tau^2\eta(y_v^\tau) - \tau^2\eta(z_C^\tau(1)), \psi)\\
&- \tfrac{1}{2}\mathcal{W}_{,222}[y,y](\tau^2\eta(z_C^\tau(1)), \tau^2 v, \psi) - \tfrac{1}{2}\mathcal{W}_{,122}[y,y](\tau^2\eta(z_C^\tau(1)), \tau^2 v, \psi)\\
&- \tfrac{1}{2}\mathcal{W}_{,122}[y,y](\tau^2 v, \tau^2\eta(z_C^\tau(1)), \psi) + \tfrac{1}{2}\mathcal{W}_{,122}[y,y](\psi, \tau^2\eta(z_C^\tau(1)), \tau^2 v)\Big)\,.
\end{aligned}$$

To simplify this expression, we will use the subsequent relations

$$\left\|\tau^2\eta(z_C^\tau(1)) - \tau^2\eta(y_v^\tau)\right\|_{\mathbf{V}} = \mathcal{O}(\tau^6)\,, \tag{2.54}$$
$$\left\|\xi_{\mathrm{IV}}^\tau - \tau^2\eta(y_v^\tau)\right\|_{\mathbf{V}} = \mathcal{O}(\tau^4)\,. \tag{2.55}$$

The estimate (2.54) can be shown via a Taylor expansion, and (2.42) in combination with (2.43) implies (2.55). Thus, taking into account (2.54) and (2.55) as well as Young's Theorem yields[4]

$$\begin{aligned}
\mathcal{O}(\tau^3) &= \underline{\mathcal{W}_{,22}[y,y](\zeta_{\mathrm{V}}^\tau - \xi_{\mathrm{V}}^\tau, \psi)} + \frac{1}{\tau^3}\Big(\underbrace{\tfrac{1}{2}\mathcal{W}_{,211}[y,y](\psi, \tau^2\eta(y_v^\tau), \tau^2\eta(y_v^\tau))}\\
&\quad + \underbrace{\mathcal{W}_{,212}[y,y](\psi, \tau^2\eta(y_v^\tau), y_C^c - y)} - \underbrace{\mathcal{W}_{,121}[y,y](\psi, \tau^2\eta(y_v^\tau), y_C^c - y)}\\
&\quad - \underbrace{\tfrac{1}{2}\mathcal{W}_{,122}[y,y](\psi, \tau^2\eta(y_v^\tau), \tau^2\eta(y_v^\tau))} - \underline{\tfrac{1}{2}\mathcal{W}_{,122}[y,y](\psi, \tau^2\eta(y_v^\tau), \tau^2 v)}\\
&\quad - \underline{\tfrac{1}{2}\mathcal{W}_{,222}[y,y](\psi, \tau^2\eta(y_v^\tau), \tau^2 v)} - \underline{\tfrac{1}{2}\mathcal{W}_{,212}[y,y](\psi, \tau^2\eta(y_v^\tau), \tau^2 v)}\\
&\quad - \underline{\tfrac{1}{2}\mathcal{W}_{,221}[y,y](\psi, \tau^2\eta(y_v^\tau), \tau^2 v)}\Big)\\
&= \underline{\mathcal{W}_{,22}[y,y](\zeta_{\mathrm{V}}^\tau - \xi_{\mathrm{V}}^\tau, \psi)}\\
&\quad + \frac{1}{\tau^3}\Big(\underbrace{\big(\mathcal{W}_{,121}[y,y] - \mathcal{W}_{,212}[y,y]\big)(\psi, \tau^2\eta(y_v^\tau), \tfrac{1}{2}\tau^2\eta(y_v^\tau) - (y_C^c - y))}\\
&\quad + \underline{\big(\mathcal{W}_{,121}[y,y] - \mathcal{W}_{,212}[y,y]\big)(\psi, \tau^2\eta(y_v^\tau), \tfrac{1}{2}\tau^2 v)}\Big)\,.
\end{aligned} \tag{2.56}$$

For the second equality we employed the identities $\mathcal{W}_{,211}[y,y] - \mathcal{W}_{,122}[y,y] = \mathcal{W}_{,121}[y,y] - \mathcal{W}_{,212}[y,y]$ (waved terms) and $-\mathcal{W}_{,221}[y,y] - \mathcal{W}_{,222}[y,y] = \mathcal{W}_{,121}[y,y] + \mathcal{W}_{,122}[y,y]$ (dashed terms) (*cf*. (2.12)). Now, the central insight to estimate the equation above stems from the relation

$$\left\|\tfrac{1}{2}\tau^2\eta(y_v^\tau) - (y_C^c - (y + \tfrac{1}{2}\tau^2 v))\right\|_{\mathbf{V}} = \mathcal{O}(\tau^4) \tag{2.57}$$

[4] As before, we underline related terms in the same line style.

to be verified below. Intuitively, (2.57) states that the vector $y_C^c-(y+\frac{1}{2}\tau^2 v)$ attached at the midpoint $y+\frac{1}{2}\tau^2 v$ of the discrete path $\mathbf{C}_\tau^{\mathrm{disc}}$ allows an approximation of the scaled vector $\frac{1}{2}\tau^2\eta(y_v^\tau)$ of fourth order. Combining the trivial estimate $\big\|\tau^2\eta(y_v^\tau)\big\|_{\mathbf{V}}=\mathcal{O}(\tau^2)$ with (2.56) one can immediately deduce $\mathcal{W}_{,22}[y,y](\zeta_{\mathrm{V}}^\tau-\xi_{\mathrm{V}}^\tau,\psi)=\mathcal{O}(\tau^3)$ and thus $\|\zeta_{\mathrm{V}}^\tau-\xi_{\mathrm{V}}^\tau\|_{\mathbf{V}}=\mathcal{O}(\tau^3)$.

To prove (2.57), we expand (2.27) in an analogous manner to (2.29) with the variables taken from Table 2.1 for the discrete path $\mathbf{C}_\tau^{\mathrm{disc}}$, which results after some straightforward transformations in

$$\begin{aligned}\mathcal{O}(\tau^4)&=\mathcal{W}_{,22}[y,y](y_C^c-y,\psi)+\mathcal{W}_{22}[y,y](y_C^c-y,\psi)-\mathcal{W}_{,22}[y,y](y_v^\tau+\tau^2\eta(y_v^\tau)-y,\psi)\\&=-2\mathcal{W}_{,22}[y,y](\tfrac{1}{2}\tau^2\eta(y_v^\tau)-(y_C^c-(y+\tfrac{1}{2}\tau^2 v)),\psi)\,.\end{aligned}$$

We still have to show that the first summand in (2.25) is of order τ^3, which readily implies $\|\xi_{\mathrm{III}}^\tau-\zeta_{\mathrm{III}}^\tau\|_{\mathbf{V}}=\mathcal{O}(\tau^3)$. To this end, we subtract (2.52) from (2.41) and evaluate all energies at the point (y_w^τ,y_w^τ) causing an error of order τ^3, the result is as follows

$$\begin{aligned}\mathcal{O}(\tau^3)&=\mathcal{W}_{,22}[y_w^\tau,y_w^\tau](\zeta_{\mathrm{III}}^\tau-\xi_{\mathrm{III}}^\tau,\psi)+\tfrac{1}{2}\mathcal{W}_{,112}[y_w^\tau,y_w^\tau](\xi_{\mathrm{III}}^\tau,\xi_{\mathrm{III}}^\tau,\psi)\\&\quad-\mathcal{W}_{,112}[y_w^\tau,y_w^\tau](\tau w,\xi_{\mathrm{III}}^\tau,\psi)+\mathcal{W}_{,122}[y_w^\tau,y_w^\tau](\xi_{\mathrm{III}}^\tau,y_B^c-y_w^\tau,\psi)\\&\quad-\mathcal{W}_{,112}[y_w^\tau,y_w^\tau](y_B^c-y_w^\tau,\psi,\xi_{\mathrm{II}}^\tau)-\tfrac{1}{2}\mathcal{W}_{,122}[y_w^\tau,y_w^\tau](\psi,\xi_{\mathrm{II}}^\tau,\xi_{\mathrm{II}}^\tau)\\&\quad+\frac{1}{\tau^3}\Big(\mathcal{W}_{,22}[y_w^\tau,y_w^\tau](\tau^2\eta(y_{v,w}^\tau)-\tau^2\eta(y_w^\tau))+\tfrac{1}{2}\mathcal{W}_{,112}[y_w^\tau,y_w^\tau](\xi_{\mathrm{I}}^\tau,\xi_{\mathrm{I}}^\tau,\psi)\\&\qquad+\mathcal{W}_{,122}[y_w^\tau,y_w^\tau](\xi_{\mathrm{I}}^\tau,y_A^c-y_w^\tau,\psi)-\mathcal{W}_{,112}[y_w^\tau,y_w^\tau](y_A^c-y_w^\tau,\psi,\tau^2\eta(y_{v,w}^\tau))\\&\qquad-\mathcal{W}_{,122}[y_w^\tau,y_w^\tau](\psi,\tau^2 v,\tau^2\eta(y_{v,w}^\tau))-\tfrac{1}{2}\mathcal{W}_{,122}[y_w^\tau,y_w^\tau](\psi,\tau^2\eta(y_{v,w}^\tau),\tau^2\eta(y_{v,w}^\tau))\Big)\\&\quad+\frac{1}{2}\Big(-\mathcal{W}_{,222}[y_w^\tau,y_w^\tau](\zeta_B^\tau(0),\tau w,\psi)-\mathcal{W}_{,122}[y_w^\tau,y_w^\tau](\zeta_B^\tau(0),\tau w,\psi)\\&\qquad-\mathcal{W}_{,122}[y_w^\tau,y_w^\tau](\tau w,\zeta_B^\tau(0),\psi)+\mathcal{W}_{,122}[y_w^\tau,y_w^\tau](\psi,\zeta_B^\tau(0),\tau w)\Big)\\&\quad+\frac{1}{\tau^3}\Big(-\mathcal{W}_{,22}[y_w^\tau,y_w^\tau](\tau^2\eta(z_A^\tau(1))-\tau^2\eta(z_B^\tau(1)),\psi)\\&\qquad+\frac{1}{2}\Big(-\mathcal{W}_{,222}[y_w^\tau,y_w^\tau](\tau^2\eta(z_A^\tau(1)),\tau^2 v,\psi)-\mathcal{W}_{,122}[y_w^\tau,y_w^\tau](\tau^2\eta(z_A^\tau(1)),\tau^2 v,\psi)\\&\qquad-\mathcal{W}_{,122}[y_w^\tau,y_w^\tau](\tau^2 v,\tau^2\eta(z_A^\tau(1)),\psi)+\mathcal{W}_{,122}[y_w^\tau,y_w^\tau](\psi,\tau^2\eta(z_A^\tau(1)),\tau^2 v)\Big)\Big)\,.\end{aligned}\tag{2.58}$$

Following the same line of arguments as above, one can infer that all summands in (2.58) apart from the first are of order τ^3, which proves that $\mathcal{W}_{,22}[y_w^\tau,y_w^\tau](\zeta_{\mathrm{III}}^\tau-\xi_{\mathrm{III}}^\tau,\psi)=\mathcal{O}(\tau^3)$ and thus $\|\zeta_{\mathrm{III}}^\tau-\xi_{\mathrm{III}}^\tau\|_{\mathbf{V}}=\mathcal{O}(\tau^3)$. The theorem follows from (2.24) and (2.25).

This concludes the proof of the convergence of the discrete curvature tensor. □

2.3.3 Numerical Results

In this subsection, we will examine the approximation error of the discrete curvature tensor in the case of smooth two-dimensional manifolds embedded in $\mathbb{R}^3$, namely the sphere $\mathbb{S}^2$ and the torus $\mathbb{T}^2$.

Before discussing the discrete approximation, let us very briefly derive an explicit formula for the curvature tensor for a finite-dimensional Riemannian manifold $(\mathcal{M},g)$ (this exposition is based on [Sak96, Kli95]). For a fixed basis $(\frac{\partial}{\partial y_1},\dots,\frac{\partial}{\partial y_n})$ of the tangent space $T_y\mathcal{M}$, let $\xi,\eta,\nu\in\mathfrak{X}(\mathcal{M})$ be smooth vector fields with $\xi=\xi^i\frac{\partial}{\partial y_i}$, $\eta=\eta^i\frac{\partial}{\partial y_i}$ and $\nu=\nu^i\frac{\partial}{\partial y_i}$.[5] The *Christoffel symbols of the second kind* are defined as

$$\Gamma_{i,j}^k=\tfrac{1}{2}g^{kl}(g_{li,j}+g_{lj,i}-g_{ij,l})\,,$$

where $g_{ij}=g(\frac{\partial}{\partial y_i},\frac{\partial}{\partial y_j})$, $g_{ij,l}=\partial_l g_{ij}$, and g^{ij} denotes the (i,j)-component of the inverse of the matrix g_{ij}. In this case, the covariant derivative can be computed as follows

$$\nabla_\xi\eta=(\xi^i\eta^j\Gamma_{i,j}^k+\xi^i\partial_i\eta^k)\tfrac{\partial}{\partial y_k}\,.$$

[5] We will frequently use the Einstein summation convention.

By iterating this formula we obtain a representation for the second order covariant derivative, *i.e.*

$$\nabla_\nu \nabla_\xi \eta = (\nu^l(\xi^i \eta^j \Gamma^m_{i,j} + \xi^i \partial_i \eta^m)\Gamma^k_{l,m} + \nu^l \partial_l(\xi^i \eta^m \Gamma^k_{i,m} + \xi^i \partial_i \eta^k))\tfrac{\partial}{\partial y_k}\,.$$

Since $[\xi,\nu] = (\xi^i \partial_i \nu^j - \nu^i \partial_i \xi^j)\frac{\partial}{\partial y_j}$, one can easily derive a formula for the curvature tensor $\mathrm{R}(\xi,\nu)\eta = \nabla_\xi \nabla_\nu \eta - \nabla_\nu \nabla_\xi \eta - \nabla_{[\xi,\nu]}\eta$ in terms of the coefficients of the vector fields and the Christoffel symbols. We recall that the *sectional curvature* for a two-dimensional subspace σ of the tangent space $T_y\mathcal{M}$ with basis (ξ,η) is defined as

$$K_\sigma(\xi,\eta) = \frac{g(\mathrm{R}(\xi,\eta)\eta,\xi)}{g(\xi,\xi)g(\eta,\eta) - g(\xi,\eta)^2}\,,$$

which coincides with the Gaussian curvature for two-dimensional embedded manifolds.

The parameterizations of the sphere $\mathbb{S}^2$ and the torus $\mathbb{T}^2$ (with $0 < r < R$) that we will consider in all further computations are given in Table 2.2 along with the metric tensors and non-vanishing Christoffel symbols, where we assumed the parameterizations X to be injective (by possibly shrinking the domains if required). Throughout this subsection, we choose $r = 1$ and $R = 2$. Clearly, $\mathbf{V}$ and $\mathbf{Y}$ coincide with $\mathbb{R}^2$ and are endowed with the standard Euclidean norm.

	Sphere $\mathbb{S}^2$	Torus $\mathbb{T}^2$
parameterization $\mathrm{X}((y_1,y_2))$	$\begin{pmatrix} r\sin y_1 \cos y_2 \\ r \sin y_1 \sin y_2 \\ r\cos y_1 \end{pmatrix}$	$\begin{pmatrix} (R + r\cos y_2)\cos y_1 \\ (R + r\cos y_2)\sin y_1 \\ r \sin y_2 \end{pmatrix}$
metric tensor $g((y_1,y_2))$	$\begin{pmatrix} r^2 & 0 \\ 0 & (r\sin y_1)^2 \end{pmatrix}$	$\begin{pmatrix} (R+r\cos y_2)^2 & 0 \\ 0 & r^2 \end{pmatrix}$
non-vanishing Christoffel symbols $\Gamma^k_{i,j}$	$\Gamma^1_{2,2} = -\sin y_1 \cos y_1$, $\Gamma^2_{1,2} = \Gamma^2_{2,1} = \cot y_1$	$\Gamma^1_{1,2} = \Gamma^1_{2,1} = -\frac{r\sin y_2}{R + r\cos y_2}$, $\Gamma^2_{1,1} = \frac{(R+r\cos y_2)\sin y_2}{r}$

Table 2.2: Parameterizations, metric tensor and (non-vanishing) Christoffel symbols of the sphere and the torus.

The numerical approximation of the Riemann curvature tensor essentially amounts to computing parallel transports using Schild's ladder taking into account the energy $\mathcal{W}$ as an approximation of the corresponding metric (*cf*. (H2)). In all examples, we either consider the particular energy

$$\mathcal{W}[y,\tilde{y}] = |\mathrm{X}(\tilde{y}) - \mathrm{X}(y)|^2\,, \tag{2.59}$$

which quantifies the elastic energy in a spring joining the points y and $\tilde{y}$ measured in the topology of the space $\mathbb{R}^3$, or

$$\mathcal{W}[y,\tilde{y}] = g_y(\tilde{y} - y, \tilde{y} - y)\,, \tag{2.60}$$

which can be regarded as a non-symmetric approximation of the metric g. The relation (2.10) justifies that both energies are indeed suitable approximations of the metric g.

To compute the discrete geodesic of length 3 in order to retrieve the midpoint of the geodesic parallelogram, an unconstrained trust region solver (*cf*. [CGT00, Algorithm 6.1.1]) is employed to minimize

$$\mathring{\mathcal{M}} \ni \tilde{y} \mapsto \mathcal{W}[y^p_{k-1},\tilde{y}] + \mathcal{W}[\tilde{y},y_k]$$

in the second step of the construction (2.16). Furthermore, the calculation of the one-step extrapolation (third step in (2.16)) is based on an unconstrained Newton minimization with an Armijo step size control applied to the functional

$$\mathring{\mathcal{M}} \ni \tilde{y} \mapsto \mathcal{W}_{,2}[y_{k-1}, y^c_k] + \mathcal{W}_{,1}[y^c_k,\tilde{y}]\,.$$

Both optimizations are stopped if the $\mathbf{V}$-norm of two consecutive iterates is below 10^{-20}.

Figure 2.4 depicts four log-log-plots relating $\|\mathbf{R}^\tau(v,w)\eta(y) - \mathrm{R}(v,w)\eta(y)\|_{\mathbf{V}}$ to τ, where we use the smooth vector field $\eta((y_1,y_2)) = (-2\sin(y_1) + y_2, -4y_2)^T$. It turns out that in all settings the discrete curvature tensor is capable of approximating the curvature tensor with an error of order τ for sufficiently small τ. However, the

quantity of the error significantly depends on the setting. Moreover, it is revealed that the energy (2.59) outperforms the energy (2.60) in terms of the approximation error in all situations considered. We emphasize that the linear order of convergence cannot be observed for larger time steps τ since many convergence results involved in the numerical approximation of the curvature tensor are purely local. On the other hand, our method fails for very small time steps due to the insufficient precision of floats of type `long double` (with 18 significant decimal digits) resulting from the large scaling factors appearing in (2.22), which can be easily remedied using an arbitrary precision arithmetic at the expense of additional computation time.

The first drawing in Figure 2.5 depicts the exact sectional (or Gaussian) curvature of the torus. Furthermore, the second and third drawing show the local approximation error $|K_\sigma(\mathrm{e}_1, \mathrm{e}_2) - \mathbf{K}^\tau_\sigma(\mathrm{e}_1, \mathrm{e}_2)|$ for $\tau = 5 \cdot 10^{-2}$ and $\tau = 5 \cdot 10^{-3}$, respectively. Here, $\mathbf{K}^\tau_\sigma(\mathrm{e}_1, \mathrm{e}_2)$ denotes the discrete sectional curvature given by

$$\mathbf{K}^\tau_\sigma(\mathrm{e}_1, \mathrm{e}_2) = \frac{2\mathcal{W}_{,22}[y,y](\mathbf{R}^\tau(\mathrm{e}_1, \mathrm{e}_2)\mathrm{e}_2, \mathrm{e}_1)}{\mathcal{W}_{,22}[y,y](\mathrm{e}_1, \mathrm{e}_1)\mathcal{W}_{,22}[y,y](\mathrm{e}_2, \mathrm{e}_2) - \mathcal{W}_{,22}[y,y](\mathrm{e}_1, \mathrm{e}_2)^2}$$

and $\mathrm{e}_1, \mathrm{e}_2$ denote the unit vectors in $\mathbf{V}$. As a result, the maximum local error roughly decreases with a rate of order τ as expected (*cf*. Theorem 2.3.5) and the approximation error significantly varies depending on y_2.

2.4 Conclusion and Outlook

In this chapter, we have developed a novel discrete approximation of the Riemann curvature tensor incorporating constructions of the time discrete geodesic calculus and provided a rigorous convergence analysis. So far, we solely analyzed the convergence properties for smooth embedded hypersurfaces numerically, but we are aiming at extending this construction to more general manifolds, shape spaces or subdivision surfaces. A key prerequisite for the applicability to these more general settings is the existence of a sufficiently smooth metric and vector field.

One of the main advantages of the proposed construction of the discrete curvature tensor clearly arises from its versatility since we do neither restrict to n-dimensional manifolds for a fixed $n \in \mathbb{N}$ nor to the measurement of a specific notion of curvature like Gaussian or Ricci as required in many other approaches. Instead, our proposed method is capable of computing the curvature tensor on infinite-dimensional Hilbert manifolds provided that the functional analytic Assumption 2.2.1 holds true, which significantly enlarges the variety of possible applications. Furthermore, we highlight that the computation time for the discrete curvature tensor at a given point in the manifold is (approximately) independent of the time step τ and thus of the precision. For instance, the computation time for each of the examples shown in Figure 2.5 containing 12.500 data points was less than one second (CPU: 3.40 GHz, four parallel threads).

The major drawback of the entire construction stems from the smoothness assumptions w.r.t. the metric, the energy and the vector field (*cf*. (H3') and (H4')), which limit the scope of potential applications. However, some numerical examples indicate that these smoothness assumptions can be slightly weakened. A further drawback emerges from the strong requirements w.r.t. the precision of the floating point arithmetic, which can be easily remedied by passing to an arbitrary precision arithmetic at the expense of additional computation time.

Finally, let us remark that there are strong theoretical as well as numerical evidences that $\mathbf{R}^\tau(v, w)\eta$ is capable of approximating $\mathrm{R}(v, w)\eta$ even if v and w are smooth non-constant vector fields.

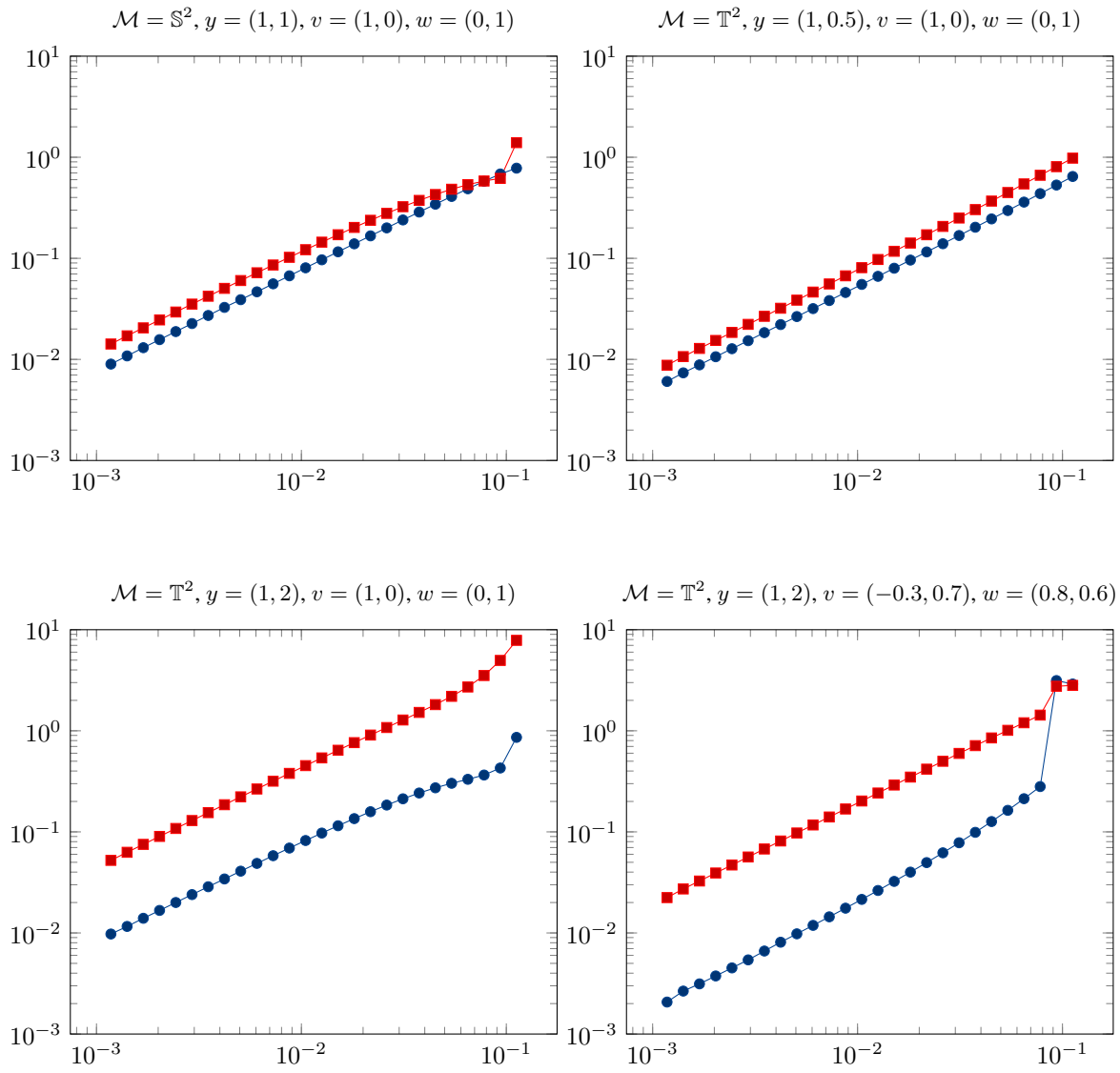

Figure 2.4: The values of $\|\mathbf{R}^\tau(v,w)\eta(y) - \mathrm{R}(v,w)\eta(y)\|_{\mathbf{V}}$ in relation to τ for four different settings using $\eta((y_1,y_2)) = (-2\sin(y_1) + y_2, -4y_2)^T$ and the energies (2.59) (blue, ●) and (2.60) (red, ■) are displayed.

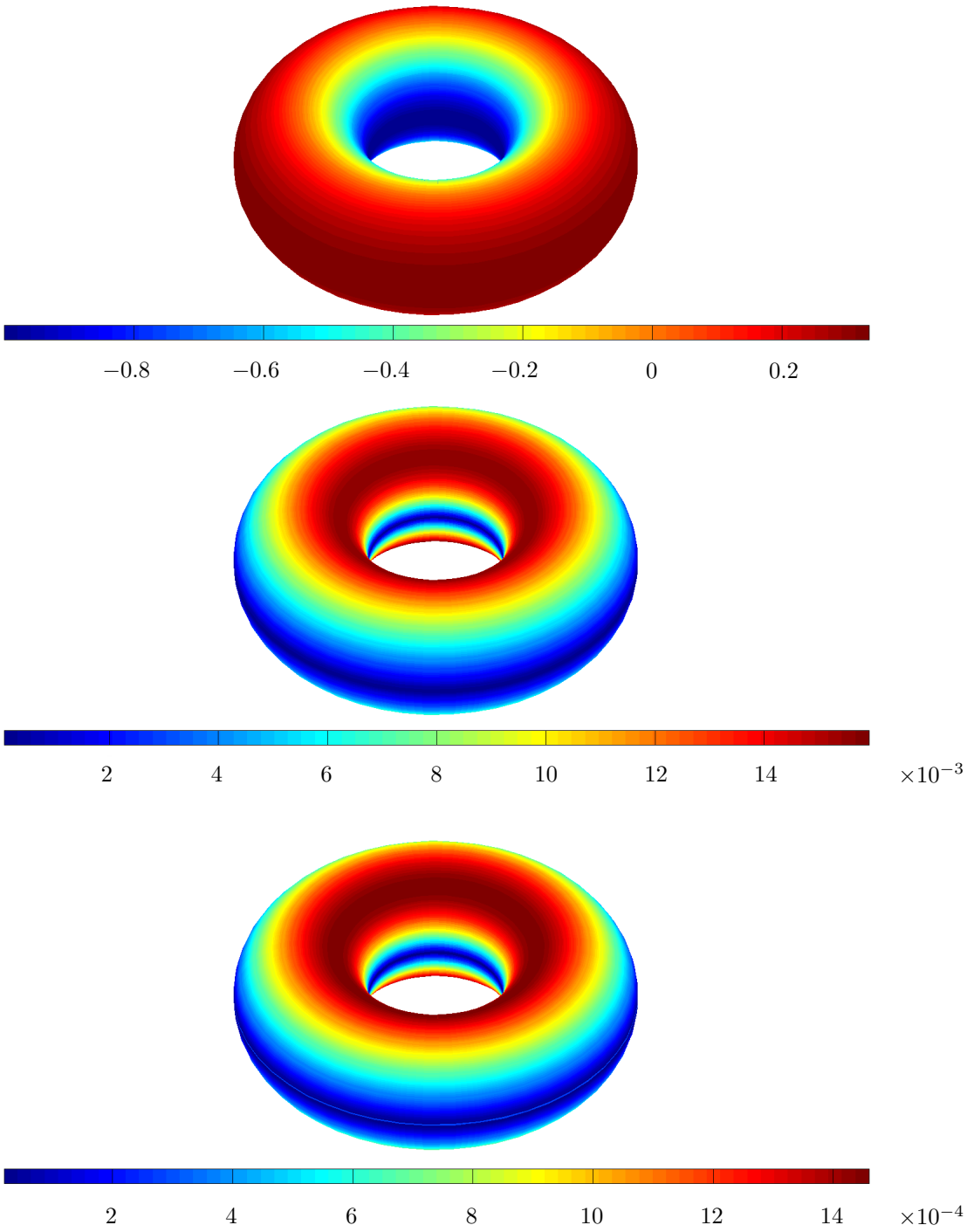

Figure 2.5: The color coded sectional curvature of the torus (first image) as well as the local approximation error $|K_\sigma(\mathrm{e}_1, \mathrm{e}_2) - \mathbf{K}_\sigma^\tau(\mathrm{e}_1, \mathrm{e}_2)|$ for $\tau = 5 \cdot 10^{-2}$ (second image) and $\tau = 5 \cdot 10^{-3}$ (third image) using the energy (2.59) are shown.

Chapter 3

Time Discrete Geodesic Curves in the Space of Images

In this chapter, the space of images is considered as a Riemannian manifold from the perspective of the metamorphosis approach originally proposed by Miller, Trouvé and Younes [MY01, TY05a, TY05b]. The metamorphosis model (as a special kind of image morphing) is an extension of the flow of diffeomorphism model, in which each image particle is transported along a flow determined by a diffeomorphism and the underlying metric solely measures the Eulerian velocity associated with the flow. As an extension, the metamorphosis model allows the variation of image intensities along trajectories of the flow, which is reflected by a squared material derivative in the energy functional.

The particular contribution of this chapter is the development of a variational time discretization of the path energy in the metamorphosis model and the study of its convergence behavior. Here, we focus on the analysis of time discrete geodesic paths defined as minimizers of the discrete path energy (2.7), in which each pairwise energy functional $\mathcal{W}$ is composed of regularization terms for the deformations resulting from registration problems and a squared L^2-penalization of the image variation of consecutive images. The existence of time discrete geodesic paths can be proven for bounded input images and a local existence result is established for square-integrable input images. The Mosco-convergence of a suitable time interpolation of the discrete path energy to the continuous metamorphosis energy functional is presented for square-integrable image paths, which in particular implies an alternative existence result for geodesics in the continuous case. Two different spatial discretization schemes – a nonconforming scheme based on finite elements as well as a conforming spatial discretization incorporating cubic splines respectively bilinear finite elements to model the discrete deformations and images – are introduced and an alternating algorithm is derived to approximate discrete geodesics numerically. In the final section, several computational results demonstrate the robustness and efficiency of the proposed discretization schemes to approximate time discrete geodesic curves. This chapter is a significantly extended version of the publication [BER15] (joint work with Benjamin Berkels and Martin Rumpf).

The structure of this chapter is as follows: A short survey of the flow of diffeomorphism approach and the time continuous metamorphosis model as well as an overview of related work are contained in Section 3.1. Picking up the ideas of the variational time discretization presented in Section 2.2, we define the time discrete metamorphosis model in Section 3.2. A physical motivation for the particular choice of the time continuous and time discrete path energies is contained in Section 3.3. The proof of the existence of time discrete geodesic curves as minimizers of the time discrete path energy is deferred to Section 3.4. In Section 3.5, the Mosco-convergence is proven for a suitable time interpolation of the time discrete path energy to its continuous counterpart. Two spatial discretization schemes and an alternating update algorithm for the computation of time discrete geodesic curves are proposed in Section 3.6. Qualitative and quantitative properties of this algorithm are analyzed in Section 3.7 for several applications to artificial and real test data. Finally, we briefly comment on three extensions of the time discrete metamorphosis model, namely Bézier curve in the space of images, applications to medical data using a GPU acceleration, and image extrapolation using the discrete exponential map in the space of images (*cf*. Section 3.8).

3.1 Review of the Metamorphosis Model and Related Work

3.1.1 Flow of Diffeomorphism Model

In this subsection, we will introduce the *flow of diffeomorphism model* (*cf*. [Arn66, AK98, DGM98, BMTY05, JM00, MTY02]) which can be viewed as a primary stage of the metamorphosis model to be introduced in Subsection 3.1.2. Heuristically, for two input images or shapes one tries to compute an energetically optimal family of diffeomorphisms that transports each particle smoothly from the start image at time $t = 0$ to the end image at time $t = 1$, where the energy solely depends on the velocity field associated with the family of diffeomorphisms. The resulting flow thus defines a one-to-one correspondence to the image intensity values for each sample point $t \in [0, 1]$, which is also known as image warping.

For the rest of this chapter, we assume $\Omega \subset \mathbb{R}^n$ for $n \in \{2, 3\}$ to be a bounded and strongly Lipschitz domain. In this setting, a *one-parameter group or family of diffeomorphisms* is a smooth map $\psi : [0, 1] \times \Omega \to \Omega$ such that for all $s, t \in [0, 1]$ with $s + t \in [0, 1]$ and $x \in \Omega$ the map $\psi(s, \cdot)$ is diffeomorphic and $\psi(s, \psi(t, x)) = \psi(s + t, x)$. Arnold [Arn66, AK98] combined this family of diffeomorphisms approach with Lie group methods to describe the temporal evolution of fluids. In what follows, we are aiming at applying analogous methods to two fixed image intensity functions $u_A, u_B \in L^2(\Omega)$. In particular, we will study the temporal change of the image intensities $u(t) = u_A \circ \psi^{-1}(t, \cdot)$ along the family of diffeomorphisms $\psi : [0, 1] \times \Omega \to \Omega$ that minimizes the *path energy*

$$\mathcal{E}[\psi] = \int_0^1 g_{\psi_t}(\dot{\psi}_t, \dot{\psi}_t) \, \mathrm{d}t \,,$$

where $\psi_t(x) = \psi(t, x)$ and $\dot{\psi}_t(x) = \partial_t \psi(t, x)$. Here, the associated *metric* g_{ψ_t} is given by

$$g_{\psi_t}(\dot{\psi}_t, \dot{\psi}_t) = \int_\Omega L[v(t, x), v(t, x)] \, \mathrm{d}x$$

with $v(t, x) = \dot{\psi}_t \circ \psi_t^{-1}(x)$ representing the *Eulerian velocity of the underlying flow* and L defining a quadratic form corresponding to a higher order elliptic operator to be specified below. Dupuis *et al*. [DGM98, Section 2] proved that any mapping $\psi : [0, 1] \times \Omega \to \Omega$ is a family of diffeomorphisms if $\psi(0) = \psi_A$ and $\psi(1) = \psi_B$ for fixed diffeomorphisms $\psi_A, \psi_B : \Omega \to \Omega$, the metric g_{ψ_t} is $H^3(\Omega)$-coercive and $\mathcal{E}[\psi] < \infty$. Moreover, any minimizing sequence of paths has a uniformly converging subsequence and the limiting minimizing path ψ and its associated velocity field v satisfy $\dot{\psi}_t(x) = v(t, \psi(t, x))$ for every $t \in [0, 1]$ and $x \in \Omega$ (*cf*. [DGM98, Theorem 3.1]).

For the rest of this chapter, we consider the following specific choice of L:

$$L[v(t, x), v(t, x)] = \frac{\lambda}{2}(\mathrm{tr}(\varepsilon[v(t, x)]))^2 + \mu \mathrm{tr}(\varepsilon[v(t, x)]^2) + \gamma |D^m v(t, x)|^2 \,, \tag{3.1}$$

where $\varepsilon[v] = (\nabla v)^{\mathrm{sym}} = \frac{1}{2}(\nabla v + \nabla v^T)$ denotes the symmetric part of the gradient, $m > 1 + \frac{n}{2}$ and $\lambda, \mu, \gamma > 0$. The fact that a rotational flow does not lead to any friction is reflected by the sole dependency on the symmetric part of the gradient $\varepsilon[v]$ in the lower order terms of L since velocity fields associated with infinitesimal rotations have skew-symmetric gradients. In other words, this model is invariant under rigid body motions which are generated by motion fields v with spatially constant, skew-symmetric gradient, for which $\varepsilon[v] = 0$ and $D^m v = 0$. The spatially integrated terms $\int_\Omega (\mathrm{tr}(\varepsilon[v(t, x)]))^2 \, \mathrm{d}x$ and $\int_\Omega \mathrm{tr}(\varepsilon[v(t, x)]^2) \, \mathrm{d}x$ roughly quantify the average change of volume and length induced by v, respectively (*cf*. [Cia88]). By combining Korn's inequality (*cf*. Theorem 1.1.3) applied to the lower order terms in L with the classical Gagliardo–Nirenberg inequality (*cf*. Theorem 1.1.2) one can immediately infer the H^3-coercivity of g_{ψ_t} for the elliptic operator (3.1), which implies that any mapping $\psi : [0, 1] \times \Omega \to \Omega$ with finite path energy such that $\psi(0, \cdot)$ and $\psi(1, \cdot)$ are diffeomorphic is actually a family of diffeomorphisms. For a physical motivation of the particular choice of L we refer to Section 3.3.

3.1.2 Time Continuous Metamorphosis Model

In the flow of diffeomorphism approach, it is assumed that each image particle moves along the motion paths induced by the family of diffeomorphisms without any change of the intensity. The metamorphosis approach proposed by Miller and Younes [MY01], Trouvé and Younes [TY05b, TY05a] allows in addition for image intensity variations along these motion paths. In this case, the *metric of the metamorphosis model* additionally incorporates

the material derivative $\frac{D}{\partial t}u = \dot{u} + \nabla u \cdot v$ of the image path u, which quantifies the temporal change of the intensity of the image particle, as a penalization term with penalization parameter $\delta > 0$. Intuitively, the metamorphosis model combines image warping with blending in an energetically optimal way.

Before discussing the metamorphosis model in its full generality, let us define *preliminary versions* of the metric and the induced path energy in the metamorphosis model as follows:

$$g_u(\dot{u}, \dot{u}) = \min_{v \in H^m(\Omega) \cap H_0^1(\Omega)} \int_\Omega L[v, v] + \frac{1}{\delta}(\dot{u} + \nabla u \cdot v)^2 \, \mathrm{d}x \,, \tag{3.2}$$

$$\mathcal{E}[u] = \int_0^1 g_u(\dot{u}(t), \dot{u}(t)) \, \mathrm{d}t \,. \tag{3.3}$$

The term $L[v, v]$ appearing in (3.2) (using the particular choice of the elliptic operator specified in (3.1)) quantifies the cost of the underlying transport, whereas the expression $\frac{1}{\delta}(\frac{D}{\partial t}u)^2$ penalizes the variation of the image intensity along the trajectories. However, these definitions are *not* appropriate for at least two reasons:

(P1) Due to $\dot{u} = \frac{D}{\partial t}u - \nabla u \cdot v$ it becomes apparent that the same temporal change $\dot{u}$ in the image intensity can be implied by different motion fields v and different associated material derivatives $\frac{D}{\partial t}u$.

(P2) The classical definition of the material derivative present in the metric (3.2) requires image paths that are differentiable in time and in space. Commonly, image paths do not exhibit any classical smoothness properties, that is why g is not well-defined.

To remedy these issues and to rigorously define the metric (3.2) as well as the path energy (3.3), we will employ a local construction proposed by Trouvé and Younes [TY05a], in which a nonlinear geometric structure on the space of images $L^2(\Omega) := L^2(\Omega, \mathbb{R})$ is developed. In detail, the starting point of this nonlinear geometric structure is the definition of the equivalence class $\sim$ of pairs $(v, \frac{D}{\partial t}u)$ as tangent vectors in the space of images. Here, two pairs $(v, \frac{D}{\partial t}u)$ and $(\tilde{v}, \widetilde{\frac{D}{\partial t}u})$ are equivalent if and only if they imply the same temporal change $\dot{u}$. Hence, to evaluate the metric on such tangent vectors one has to minimize over all elements of this equivalence class.

In what follows, we will present a simplified version of this approach by Trouvé and Younes tailored to our specific setting. Throughout this chapter, we assume that $\Omega \subset \mathbb{R}^n$, $n \in \{2, 3\}$, is a bounded and strongly Lipschitz domain, and $\gamma, \delta, \lambda, \mu > 0$ are fixed parameters. We denote by $\mathcal{B} = H^m(\Omega, \mathbb{R}^n) \cap H_0^1(\Omega, \mathbb{R}^n)$, $m > 1 + \frac{n}{2}$, the *space of motion fields* and refer to $L^2(\Omega, \mathbb{R})$ as the *space of weak material derivatives*. Furthermore, we endow the space $W = \mathcal{B} \times L^2(\Omega, \mathbb{R})$ with the norm $\|w\|_W = \|v\|_{H^m(\Omega)} + \|z\|_{L^2(\Omega)}$ for $w = (v, z) \in W$. By considering a suitable quotient space of W we can rigorously define the tangent space for any $u \in L^2(\Omega)$ and thus solve the issue addressed in (P1):

Definition 3.1.1 (Tangent space of an image)**.** For an image $u \in L^2(\Omega)$, we define the nonlinear structure

$$N_u = \left\{ w = (v, z) \in W \,:\, \int_\Omega z\eta + u\mathrm{div}(\eta v) \, \mathrm{d}x = 0 \quad \forall \eta \in C_c^\infty(\Omega) \right\} .$$

The *tangent space at* u is defined as $T_u L^2(\Omega) = \{u\} \times W/N_u$ and elements in this tangent space, which are in the same equivalence class, are denoted by $\gamma = (u, \overline{(v, z)})$. The space $T_u L^2(\Omega)$ is endowed with the norm $\|\gamma\| = \inf\{\|w\|_W \,:\, \gamma = (u, \overline{w})\}$. The associated *tangent bundle* is given by

$$TL^2(\Omega) = \bigcup_{u \in L^2(\Omega)} T_u L^2(\Omega) \,,$$

and the *canonical projection onto the image manifold* is defined as $\pi : TL^2(\Omega) \to L^2(\Omega), T_u L^2(\Omega) \ni (u, \overline{w}) \mapsto u$.

Next, we define the weak material derivative for an image path and introduce the concepts of differentiable and regular curves in the space of images (*cf*. [TY05a]):

Definition 3.1.2. Let $u \in L^2([0, 1], L^2(\Omega))$ be an image curve and $v \in L^2([0, 1], \mathcal{B})$ a velocity field.

(i.) A function $z \in L^2([0,1], L^2(\Omega))$ is the *weak material derivative* associated with the image path u and the velocity field v if

$$\int_0^1 \int_\Omega \eta z \,\mathrm{d}x \,\mathrm{d}t = -\int_0^1 \int_\Omega (\partial_t \eta + \mathrm{div}(v\eta)) u \,\mathrm{d}x \,\mathrm{d}t \tag{3.4}$$

for all $\eta \in C_c^\infty([0,1] \times \Omega)$.

(ii.) The image curve u is said to be *continuously differentiable* (denoted by $u \in C^1([0,1], L^2(\Omega))$) if $u \in C^0([0,1], L^2(\Omega))$ (using the standard $L^2(\Omega)$-topology), a curve $w = (v, z) \in C^0([0,1], W)$ exists such that for any $\eta \in C_c^\infty(\Omega)$ the mapping $t \mapsto \int_\Omega u(t)\eta \,\mathrm{d}x$ is continuously differentiable and

$$\frac{\mathrm{d}}{\mathrm{d}t}\left(\int_\Omega u(t)\eta \,\mathrm{d}x\right) = \int_\Omega z(t)\eta + u(t)\mathrm{div}(\eta v(t)) \,\mathrm{d}x\,. \tag{3.5}$$

The function z is the weak material derivative of the curve $\{t \mapsto \gamma(t) = (u(t), \overline{(v(t), z(t))})\} \in TL^2(\Omega)$ if (3.5) holds true for all $t \in [0,1]$.

(iii.) The image curve u is defined to be *regular* in the space of images (denoted by $u \in H^1([0,1], L^2(\Omega))$) if $u \in C^0([0,1], L^2(\Omega))$, a measurable path $\gamma : [0,1] \to TL^2(\Omega)$ with $\pi(\gamma(t)) = u(t)$, $t \in [0,1]$, exists such that $\int_0^1 \|\gamma_t\|^2 \,\mathrm{d}t < \infty$ and

$$-\int_0^1 \int_\Omega u\partial_t \eta \,\mathrm{d}x \,\mathrm{d}t = \int_0^1 \int_\Omega z\eta + u\mathrm{div}(\eta v) \,\mathrm{d}x \,\mathrm{d}t \tag{3.6}$$

for all $\eta \in C_c^\infty([0,1] \times \Omega)$.

It turns out that the continuous differentiability of an image curve implies its regularity.

Proposition 3.1.3. *Every continuously differentiable curve in the space of images is regular,* i.e.

$$C^1([0,1], L^2(\Omega)) \subset H^1([0,1], L^2(\Omega))\,.$$

Proof. See [TY05a, Proposition 4]. □

Based on these preliminaries we can now provide the rigorous definition of the *path energy for the metamorphosis model*, which does not suffer from the problems addressed in (P1) and (P2).

Definition 3.1.4 (Path energy for the (time continuous) metamorphosis model)**.** The *path energy for the metamorphosis model* evaluated at a regular image curve $u \in H^1([0,1], L^2(\Omega))$ is

$$\mathcal{E}[u] = \int_0^1 \inf_{\overline{(v,z)} \in T_{u(t)}L^2(\Omega)} \int_\Omega L[v,v] + \frac{1}{\delta} z^2 \,\mathrm{d}x \,\mathrm{d}t\,. \tag{3.7}$$

Here, L is the quadratic form defined in (3.1).

Note that the elliptic operator $L[v,v]$ is coercive on $\mathcal{B}$, which is a direct consequence of Korn's inequality 1.1.3, and the underlying manifold lacks a Hilbert structure.

Definition 3.1.5 (Geodesic curve in the space of images)**.** Let $u_A, u_B \in L^2(\Omega)$ be arbitrary input images. A regular curve $u \in H^1([0,1], L^2(\Omega))$ with $u(0) = u_A$ and $u(1) = u_B$ such that

$$\mathcal{E}[u] = \inf\left\{\, \mathcal{E}[\tilde{u}] \,:\, \tilde{u} \in H^1([0,1], L^2(\Omega)), \tilde{u}(0) = u_A, \tilde{u}(1) = u_B \,\right\} \tag{3.8}$$

is called a *geodesic curve in the space of images*.

A crucial property of the time continuous metamorphosis model is the existence of geodesic curves for arbitrary square-integrable input images u_A and u_B.

Theorem 3.1.6 (Existence of geodesic curves)**.** *For arbitrary images $u_A, u_B \in L^2(\Omega)$ there exists a minimizing regular curve for the path energy $\mathcal{E}$,* i.e. *a curve $u \in H^1([0,1], L^2(\Omega))$ satisfying* (3.8)*. Moreover, the infimum in* (3.7) *is attained for all $t \in [0,1]$,* i.e. *there exists a minimizing curve $(v(t), z(t)) \in T_{u(t)}L^2(\Omega)$.*

Proof. The existence of a geodesic path follows from [TY05a, Theorem 6] by noting that $\mathcal{B}$ compactly embeds into $C_c^{1,\alpha}(\Omega)$ for $\alpha < m - 1 - \frac{n}{2}$, and the addendum follows from Theorem 3.1.8. □

This embedding property of $\mathcal{B}$ also guarantees the existence of a global flow associated with each motion field:

Theorem 3.1.7. *Let $v \in L^2([0,1], \mathcal{B})$. Then there exists a* global flow *$\psi \in H^1([0,1], \mathcal{B})$ such that $\psi(0,x) = x$ and*

$$\psi(t,x) = \int_0^t v(s, \psi(s,x))\,\mathrm{d}s + x$$

for a.e. $x \in \Omega$ and all $t \in [0,1]$. In particular, $\psi(t, \cdot\,)$ is a homeomorphism for all $t \in [0,1]$.

Proof. See [DGM98, TY05a, Tro95]. □

In the proof of the Mosco-convergence, we will frequently use the subsequent equivalent formulation of regular curves that allows to express the image $u(t, \cdot\,)$ in terms of the deformed initial image $u(0, \psi_{t,0}(\cdot\,))$ and a contribution of the weak material derivative at deformed positions (*cf*. (3.9)):

Theorem 3.1.8. *An image curve u is regular (*i.e. *$u \in H^1([0,1], L^2(\Omega))$) if and only if there exists $w = (v,z) \in L^2([0,1], W)$ such that*

$$u(t,x) = u(0, \psi_{t,0}(x)) + \int_0^t z(s, \psi_{t,s}(x))\,\mathrm{d}s\,, \tag{3.9}$$

where ψ is the global flow associated with v (see Theorem 3.1.7) and $\psi_{t,s} = \psi(s, \psi^{-1}(t, \cdot\,))$ for $s,t \in [0,1]$.

Proof. See [TY05a, Theorem 2 and Lemma 6]. □

Notation 3.1.9. Let $k \in \mathbb{N}$ and $\alpha \in [0,1]$. The norms for $f \in C^0([0,1], C^{k,\alpha}(\overline{\Omega}))$ and $g \in L^\infty([0,1], C^{k,a}(\overline{\Omega}))$ are given by

$$\begin{aligned}
\|f\|_{C^0([0,1],C^{k,\alpha}(\overline{\Omega}))} &= \sup_{t\in[0,1]} \|f(t,\cdot\,)\|_{C^{k,\alpha}(\overline{\Omega})}\,,\\
\|g\|_{L^\infty([0,1],C^{k,\alpha}(\overline{\Omega}))} &= \inf_{N\subset[0,1]:|N|=0} \sup_{t\in[0,1]\setminus N} \|g(t,\cdot\,)\|_{C^{k,\alpha}(\overline{\Omega})}\,.
\end{aligned}$$

The next theorem provides a uniform bound for the global flow ψ in $C^{1,\alpha}(\overline{\Omega})$ with an upper bound solely depending on the norm of the associated motion field:

Theorem 3.1.10. *Let $v \in L^1([0,1], \mathcal{B})$ with global flow ψ and $\alpha \in [0, m-1-\frac{n}{2})$. Then*

$$\|\psi\|_{C^0([0,1],C^{1,\alpha}(\overline{\Omega}))} \le \widetilde{C} \exp\left(C \int_0^1 \|v(s,\cdot\,)\|_{C^{1,\alpha}(\overline{\Omega})}\,\mathrm{d}s\right), \tag{3.10}$$

$$\|\psi^{-1}\|_{C^0([0,1],C^{1,\alpha}(\overline{\Omega}))} \le \widetilde{C} \exp\left(C \int_0^1 \|v(s,\cdot\,)\|_{C^{1,\alpha}(\overline{\Omega})}\,\mathrm{d}s\right). \tag{3.11}$$

If $\alpha > 0$, the constant $\widetilde{C}$ additionally depends on $\int_0^1 \|\nabla v(s,\cdot\,)\|_{C^{0,\alpha}(\overline{\Omega})}\,\mathrm{d}s$.

Proof. The first inequality (3.10) follows from [TY05a, Lemma 7] and relies on Gronwall's inequality when considering the $C^0([0,1], C^1(\overline{\Omega}))$-norm on the left-hand side and the $H^m(\Omega)$-norm in the exponent on the right-hand side. We remark that the generalization to the $C^{1,\alpha}(\overline{\Omega})$-norm in the exponent only requires minor modifications. In what follows, we will only sketch the proof of (3.10) when employing the $C^0([0,1], C^{1,\alpha}(\overline{\Omega}))$-norm on the left-hand side.

Let $i \in \{1, \dots, n\}$, $t \in (0,1)$ and $x, y \in \Omega$. Taking into account the aforementioned result we can assume $\|\psi\|_{C^0([0,1],C^1(\overline{\Omega}))} \leq C(v) = C \exp\left(C \int_0^1 \|v(s,\,\cdot\,)\|_{C^{1,\alpha}(\overline{\Omega})}\,\mathrm{d}s\right)$. Then, a nonrigorous computation yields

$$
\begin{aligned}
&\left|\tfrac{\mathrm{d}}{\mathrm{d}t}|\partial_i\psi(t,x) - \partial_i\psi(t,y)|\right| \leq |\nabla v(t,\psi(t,x)) \cdot \partial_i\psi(t,x) - \nabla v(t,\psi(t,y)) \cdot \partial_i\psi(t,y)| \\
&\leq |\nabla v(t,\psi(t,x)) - \nabla v(t,\psi(t,y))|\,|\partial_i\psi(t,x)| + |\nabla v(t,\psi(t,y))|\,|\partial_i\psi(t,x) - \partial_i\psi(t,y)| \\
&\leq C\|\nabla v(t,\,\cdot\,)\|_{C^{0,\alpha}(\overline{\Omega})}\|\psi\|^{1+\alpha}_{C^0([0,1],C^1(\overline{\Omega}))}|x-y|^\alpha + \|\nabla v(t,\,\cdot\,)\|_{C^0(\overline{\Omega})}|\partial_i\psi(t,x) - \partial_i\psi(t,y)| \\
&\leq C(v)^{1+\alpha}\|\nabla v(t,\,\cdot\,)\|_{C^{0,\alpha}(\overline{\Omega})}|x-y|^\alpha + \|\nabla v(t,\,\cdot\,)\|_{C^0(\overline{\Omega})}|\partial_i\psi(t,x) - \partial_i\psi(t,y)|\,.
\end{aligned}
$$

Here, ∂_i refers to the i^{th} spatial partial derivative. Thus,

$$
\begin{aligned}
&\frac{\mathrm{d}}{\mathrm{d}t}\left(\exp\left(-\int_0^t \|\nabla v(s,\,\cdot\,)\|_{C^0(\overline{\Omega})}\,\mathrm{d}s\right)|\partial_i\psi(t,x) - \partial_i\psi(t,y)|\right) \\
&\leq C(v)^{1+\alpha}\|\nabla v(t,\,\cdot\,)\|_{C^{0,\alpha}(\overline{\Omega})}\exp\left(-\int_0^t \|\nabla v(s,\,\cdot\,)\|_{C^0(\overline{\Omega})}\,\mathrm{d}s\right)|x-y|^\alpha \\
&\leq C(v)^{1+\alpha}\|\nabla v(t,\,\cdot\,)\|_{C^{0,\alpha}(\overline{\Omega})}|x-y|^\alpha\,. \qquad (3.12)
\end{aligned}
$$

The integration of both sides of (3.12) w.r.t. t yields

$$
\begin{aligned}
&\exp\left(-\int_0^t \|\nabla v(s,\,\cdot\,)\|_{C^0(\overline{\Omega})}\,\mathrm{d}s\right)|\partial_i\psi(t,x) - \partial_i\psi(t,y)| \\
&\leq \underbrace{|\partial_i\psi(0,x) - \partial_i\psi(0,y)|}_{=0} + C(v)^{1+\alpha}\int_0^1 \|\nabla v(t,\,\cdot\,)\|_{C^{0,\alpha}(\overline{\Omega})}\,\mathrm{d}t|x-y|^\alpha\,,
\end{aligned}
$$

which readily implies (3.10). This proof can be further generalized to $C^0([0,1], C^{k,\alpha}(\overline{\Omega}))$-norms provided that m is sufficiently large. Moreover, the inequality (3.11) follows from (3.10) by noting that $\psi^{-1}(t,\,\cdot\,)$ is the flow associated with the (backward) motion field $-v(1-t,\,\cdot\,)$. □

The mapping that associates with each motion field the corresponding global flow is weakly continuous in the following sense:

Theorem 3.1.11. *The mapping $L^2([0,1],\mathcal{B}) \to C^1([0,1]\times\overline{\Omega},\mathbb{R}^n)$ that associates with each Eulerian motion field $v \in L^2([0,1],\mathcal{B})$ the corresponding global flow $\psi \in C^1([0,1]\times\overline{\Omega},\mathbb{R}^n)$ is continuous w.r.t. the weak topology in $L^2([0,1],\mathcal{B})$ and the $L^\infty([0,1],C^0(\overline{\Omega}))$-topology in $C^1([0,1]\times\overline{\Omega},\mathbb{R}^n)$.*

Proof. See [TY05a, Theorem 9]. □

3.1.3 Related Work

Let us conclude this section with an overview of the literature for the flow of diffeomorphism and the metamorphosis model. Moreover, we will present some related publications dealing with numerical methods for optimal transport that are to some extent related to the metamorphosis approach. A comprehensive overview of these topics is given in the excellent books by Younes [You10] and Santambrogio [San15] as well as in the review article by Miller, Trouvé and Younes [MTY15], for a historic account we additionally refer to [MTY02].

Flow of diffeomorphism. The flow of diffeomorphism approach alongside the *large deformation diffeomorphic metric mapping (LDDMM) framework* were initiated by Christensen *et al.* [CRM96], Dupuis *et al.* [DGM98] and Trouvé [Tro95, Tro98], and proved to be powerful tools to rigorously examine the diffeomorphic change of coordinates $\psi(1,\,\cdot\,)$ such that $u_A \circ \psi^{-1}(1,\,\cdot\,) = u_B$ for two images u_A, u_B. The associated variational problem leads to the prototype image matching functional

$$
\inf\left\{\int_0^1 \|v(t,\,\cdot\,)\|_{\mathcal{V}}\,\mathrm{d}x + \operatorname{dist}(u_A \circ \psi^{-1}(1,\,\cdot\,), u_B) \,:\, \partial_t\psi(t,\,\cdot\,) = v(t,\psi(t,\,\cdot\,))\ \forall t \in [0,1], \psi(0,\,\cdot\,) = \mathbb{1}\right\},
$$

where $\|\cdot\|_{\mathcal{V}}$ is a suitable norm in the space of velocity fields and dist is a distance in the space of images, which might coincide with the discrete metric (in the topological sense). Trouvé [Tro95, Tro98] constructed a distance in the space of deformations by exploiting Lie group methods, where deformations are viewed as actions of an infinitesimal transformation group on images. In [JM00], Joshi and Miller applied this framework to (inexact and exact) landmark matching, where landmarks are sets of labeled points in a Euclidean space. Beg *et al*. [BMTY05] studied Euler–Lagrange equations for minimizing vector fields in the LDDMM framework and proposed an efficient algorithm incorporating a gradient descent scheme and a semi-Lagrangian method to integrate the velocity fields. Miller *et al*. [MTY06] proved the conservation of the initial momentum in Lagrangian coordinates associated with a geodesic in the LDDMM framework, which allows for geodesic generation via shooting. Younes [You07] used Jacobi fields in the flow of diffeomorphism approach to derive gradient descent methods for the path energy. In [HZN09], Hart *et al*. examined an optimal control perspective of the LDDMM model which possesses a natural extension to image manifolds. Vialard and Santambrogio [VS09] investigated the flow of diffeomorphism approach for images in the space of functions of bounded variation. Vialard *et al*. [VRRC12, VRRH12] studied methods from optimal control theory to accurately estimate the initial momentum and established a relation to the Hamiltonian formulation of the geodesic flow. Furthermore, they used the associated Karcher mean to compute intrinsic means of medical images. One of the earliest applications of this approach to medical data was proposed in [BMTY02], where the diffeomorphisms represent deformations of anatomic reference structures.

Metamorphosis model. As already mentioned earlier, the metamorphosis model can be regarded as a generalization of the aforementioned flow of diffeomorphism model, in which deformable templates (in our case the images) are additionally allowed to vary in time. Miller and Younes [MY01] introduced a left-invariant distance on the set of registered objects defined as the product space of a transformation group and the family of images, which allows variations of the image intensities in addition to changes of the geometry. Trouvé and Younes [TY05b] rigorously introduced the metamorphosis metric in the space of images and analyzed the geodesic equation for this metric as well as the temporal evolution of the velocity field and the material derivative. In [TY05a], Trouvé and Younes examined the local geometry of the resulting Riemannian manifold and proved the existence of geodesic curves for square-integrable images and the (local) existence as well as the uniqueness of solutions to the initial value problem for the geodesic equation in the case of weakly differentiable images. Holm *et al*. [HTY09] studied a Lagrangian formulation for the metamorphosis model and proved existence for both the boundary value and the initial value problem in the case of measure-valued images. Based on the previous approach, Richardson and Younes [RY16] proposed a robust shooting method for images contained in a reproducing kernel Hilbert space. Charon *et al*. [CCT16] generalized the metamorphosis model to functional shapes representing scalar-valued signals such as curves or finite-dimensional submanifolds. Hong *et al*. [HJS$^+$12] proposed a metamorphosis regression model and developed a shooting method to reliably recover initial momenta. Richardson and Younes [RY13] extended the metamorphosis framework to discrete measures and provided a rigorous analysis of singularities that can be generated along the geodesic path.

Optimal transport. The metamorphosis model shares certain similarities with optimal transport, in which image intensity functions are frequently considered as probability measures. One of the most prominent approaches to tackle the optimal transport problem numerically is due to Benamou and Brenier [BB00], who proposed a flow reformulation of the Kantorovich problem using methods from continuum mechanics, where the mass preserving condition is encoded in the continuity equation. Based on these ideas, Papadakis *et al*. [PPO14] proposed a staggered grid discretization for the fluid mechanics formulation by Benamou and Brenier and employed proximal splitting algorithms to solve the resulting optimization problem numerically. Furthermore, they approximated an optimal transport problem on a Riemannian manifold using spatially varying weights. In [MRSS15], Maas *et al*. introduced a variational time discretization in the context of the Benamou–Brenier optimal transport formulation, which shares several similarities with the time discrete metamorphosis model to be presented below, in particular w.r.t. the rough structure of the time discrete energy functional, the spatial discretization and the numerical optimization method. Fitschen *et al*. [FLS16] proposed two variational models to numerically characterize the optimal transport of RGB images, where the first model relies on Papadakis' approach to treat the continuity equation as a constraint and the second problem penalizes the continuity equation following roughly the ansatz by Maas and coworkers. Peyré [Pey15] examined a novel scheme to approximate gradient flows associated with the Wasserstein metric numerically taking into account an entropy regularization, in which the resulting convex optimization

problem involves the Kullback–Leibler divergence. Zhang *et al*. [ZYHT07] minimize the Monge–Kantorovich functional over all mass preserving mappings using an improved gradient descent method, which allows, for instance, image morphing of color images.

3.2 Variational Time Discretization of the Metamorphosis Model

The aim of this section is the rigorous definition of the discrete analog of the (time continuous) path energy (3.7) in the metamorphosis model based on the variational time discretization approach presented in Section 2.2. Afterwards, we will discuss two distinct energy density functions that will also be employed in the numerical simulations.

3.2.1 Variational Time Discretization of the Path Energy

As in the (time) continuous metamorphosis model, we suppose that $\gamma, \delta > 0$, $m > 1 + \frac{n}{2}$, and $\Omega \subset \mathbb{R}^n$, $n \in \{2, 3\}$, is a bounded and strongly Lipschitz domain throughout the rest of this chapter. Then, the *(time) discrete pairwise energy* for two images $u, \tilde{u} \in \mathcal{I}$ is given by

$$\mathcal{W}[u, \tilde{u}] = \min_{\phi \in \mathcal{A}} \left\{ \mathcal{W}^D[u, \tilde{u}, \phi] = \int_\Omega \mathrm{W}(D\phi) + \gamma |D^m \phi|^2 + \frac{1}{\delta}(\tilde{u} \circ \phi - u)^2 \, \mathrm{d}x \right\} . \tag{3.13}$$

Here, $\mathcal{A}$ is the *set of admissible deformations* defined as

$$\mathcal{A} = \{ \, \phi \in H^m(\Omega, \Omega) \, : \, \det(D\phi) > 0 \text{ a.e. in } \Omega \, , \phi = \mathbb{1} \text{ on } \partial\Omega \, \} \, . \tag{3.14}$$

Furthermore, $\mathcal{I}$ is the space of images, which is either the space of square-integrable or essentially bounded functions (for details see Section 3.4), and W is an *energy density function*. We refer to the function $\phi - \mathbb{1}$ as the *displacement* associated with $\phi \in \mathcal{A}$. In the subsequent sections it will become apparent that the assumptions w.r.t. W to prove the existence of time discrete geodesic curves and the Mosco-convergence vary depending on the image space $\mathcal{I}$. We collect all potential assumptions in the following list:

(W1) $\mathrm{W} : \mathbb{R}^{n,n} \to \mathbb{R}_0^+$, $\mathrm{W} \in C^4(\mathrm{GL}^+(n))$ is polyconvex and

$$\mathrm{W}(\mathbb{1}) = 0 \, , \qquad D\mathrm{W}(\mathbb{1}) = 0 \, ,$$

(W2) $\mathrm{W}(A) \geq \beta_0 (\det(A))^{-s} - \beta_1$ for $\beta_0, \beta_1 > 0$, $s > n - 1$ and every invertible matrix A with $\det(A) > 0$, $\mathrm{W}(A) = \infty$ for $\det(A) \leq 0$,

(W3) the following consistency assumption with respect to the differential operator L holds true:

$$\frac{1}{2} D^2 \mathrm{W}(\mathbb{1})(A, A) = \frac{\lambda}{2} (\mathrm{tr} A)^2 + \mu \mathrm{tr}\left((A^{\mathrm{sym}})^2 \right) \quad \forall A \in \mathbb{R}^{n,n} \, , \tag{3.15}$$

(W4) $\mathrm{W}(A) \geq C_{\mathrm{W},1} |A^{\mathrm{sym}} - \mathbb{1}|^2$ if $|A - \mathbb{1}| < r_{\mathrm{W}}$, $\mathrm{W}(A) \geq C_{\mathrm{W},2}$ if $|A - \mathbb{1}| \geq r_{\mathrm{W}}$ for $C_{\mathrm{W},1}, C_{\mathrm{W},2}, r_{\mathrm{W}} > 0$ and all $A \in \mathrm{GL}^+(n)$.

Remark 3.2.1. (i.) The first condition in (W4) can be replaced by $\mathrm{W}(A) \geq C_{\mathrm{W},1} |A - \mathbb{1}|^2$ without any substantial effect on the theory to be presented below.

(ii.) For the definition of polyconvexity and for a motivation of the special structure (3.15) of the Hessian of the energy density we refer to Subsection 3.2.2 and Section 3.3. We merely note that the particular form of the Hessian is required to guarantee the consistency of W with the quadratic form L.

(iii.) The variational problem (3.13) is a special instance of an *elastic registration* (see [BK89, FM04]).

In Section 3.4, we will prove that the discrete energy $\mathcal{W}$ is well-defined in the sense that the minimum in (3.13) is actually attained for any images $u, \tilde{u} \in L^\infty(\Omega)$ provided that (W1) and (W2) are valid. In this case, the minimizing deformation $\phi \in \mathcal{A}$ is a homeomorphism, but not necessarily a diffeomorphism. On the other hand, if $u, \tilde{u} \in L^2(\Omega)$ are sufficiently close in $L^2(\Omega)$ and (W1) as well as (W4) are satisfied, then the existence of a minimizing deformation $\phi \in \mathcal{A}$ in (3.13) can be established and ϕ is a $C^1(\Omega)$-diffeomorphism. In other words, no interpenetration of matter can occur in a deformation field ϕ that belongs to $\mathcal{A}$.

Departing from the discrete pairwise energy functional $\mathcal{W}$, one can define for any discrete $(K+1)$-path $\mathbf{u} = (u_0, \dots, u_K) \in \mathcal{I}^{K+1}$, $K \geq 1$, the discrete path energy and discrete geodesics in the same way as in Definition 2.2.6 for general Hilbert manifolds:

Definition 3.2.2 (Discrete path energy and discrete geodesics in the metamorphosis model)**.** Let $u_0 = u_A, u_K = u_B \in \mathcal{I}$ and $K \geq 1$. The *discrete path energy* $\mathbf{E}_K$ for a discrete $(K+1)$-path $\mathbf{u} = (u_0, \dots, u_K) \in \mathcal{I}^{K+1}$ is defined as

$$\mathbf{E}_K[\mathbf{u}] := K \sum_{k=1}^{K} \mathcal{W}[u_{k-1}, u_k]\,. \tag{3.16}$$

A *discrete geodesic* for the images u_A and u_B is a discrete $(K+1)$-path that minimizes $\mathbf{E}_K$ over all discrete curves $\mathbf{u} = (u_A, \hat{\mathbf{u}}, u_B) \in \mathcal{I}^{K+1}$ with $\hat{\mathbf{u}} = (u_1, \dots, u_{K-1}) \in \mathcal{I}^{K-1}$. Furthermore, for $\mathbf{u} \in \mathcal{I}^{K+1}$ and $\mathbf{\Phi} = (\phi_1, \dots, \phi_K) \in \mathcal{A}^K$ we set

$$\mathbf{E}_K^D[\mathbf{u}, \mathbf{\Phi}] := K \sum_{k=1}^{K} \mathcal{W}^D[u_{k-1}, u_k, \phi_k]\,. \tag{3.17}$$

Remark 3.2.3. (i.) Due to (W1) and (W3), the Taylor expansion of the first summand in (3.13) has the form

$$\int_\Omega \mathrm{W}(D\phi)\,\mathrm{d}x = \int_\Omega \frac{\lambda}{2}(\mathrm{tr}(D\phi - \mathbb{1})^{\mathrm{sym}})^2 + \mu \mathrm{tr}\left(((D\phi - \mathbb{1})^{\mathrm{sym}})^2\right)\,\mathrm{d}x + \mathcal{O}\left(\|D\phi - \mathbb{1}\|^3_{L^3(\Omega)}\right)\,. \tag{3.18}$$

Thus, the first two summands of the energy on the right-hand side of (3.13) approximately scale quadratically for small displacements $\phi - \mathbb{1}$. This already motivates the coefficient K in front of the discrete path energy since we expect the displacements to scale linearly in the time step $\tau = \frac{1}{K}$. For a rigorous justification, we refer to the proof of Theorem 3.5.6.

(ii.) When minimizing the discrete path energy, two opposing effects can be observed: the first two terms approximately quantify the deviation of each minimizing deformation $\phi_1, \dots, \phi_K$ from the identity, whereas the last term measures the intensity variation of successive images u_{k-1} and u_k contained in the minimizing discrete path $\mathbf{u} = (u_0, u_1, \dots, u_K)$ along the discrete transport path

$$(x, \phi_1(x), (\phi_2 \circ \phi_1)(x), \dots, (\phi_K \circ \dots \circ \phi_1)(x))$$

and thereby forces each deformation to properly transport image features resulting in non-constant displacements.

(iii.) The reverse path $(u_K, u_{K-1}, \dots, u_0)$ of a minimizing path $\mathbf{u} = (u_0, u_1, \dots, u_K)$ is in general no minimizer of $\mathbf{E}_K$ with boundary data $u_0 = u_B$ and $u_K = u_A$.

Let us briefly recall the notions of polyconvexity and quasiconvexity as well as their relation to the weak lower semicontinuity of functionals tailored to our specific functional for $n = 3$, from which the case $n = 2$ easily follows. This exposition is based on [Dac08].

Definition 3.2.4. (i.) A function $f : \mathbb{R}^{3,3} \to \overline{\mathbb{R}}$ is *polyconvex* if there exists a convex function $F : \mathbb{R}^{3,3} \times \mathbb{R}^{3,3} \times \mathbb{R} \to \mathbb{R}$ such that $f(A) = F(A, \mathrm{cof}(A), \det(A))$ for every $A \in \mathbb{R}^{3,3}$.

(ii.) A Borel measurable and locally bounded function $f : \mathbb{R}^{3,3} \to \mathbb{R}$ is *quasiconvex* if for all bounded and open sets $\Omega' \subset \mathbb{R}^3$, all $A \in \mathbb{R}^{3,3}$ and all $g \in W_0^{1,\infty}(\Omega', \mathbb{R}^3)$ the following inequality holds true:

$$f(A) \leq \fint_{\Omega'} f(A + Dg)\,\mathrm{d}x\,.$$

Proposition 3.2.5. *Let $f : \mathbb{R}^{3,3} \to \mathbb{R}$. Then*

$$f \text{ convex} \quad \Rightarrow \quad f \text{ polyconvex} \quad \Rightarrow \quad f \text{ quasiconvex}.$$

Proof. See [Dac08, Theorem 5.3]. □

The most important reason to introduce these notions of convexity originates from the weak lower semicontinuity of quasiconvex functionals. We highlight that under suitable assumptions the weak lower semicontinuity of a functional is actually equivalent to the quasiconvexity of the integrand.

Proposition 3.2.6. *Let $\Omega \subset \mathbb{R}^3$ be a bounded domain with Lipschitz boundary, $1 \leq p < \infty$ and $f : \mathbb{R}^{3,3} \to \mathbb{R}$ be a quasiconvex and $\mathcal{L}^3$-a.e. continuous function. Set $I(g) = \int_\Omega f(Dg)\,\mathrm{d}x$ for $g \in W^{1,p}(\Omega, \mathbb{R}^3)$. Then I is (sequentially) lower semicontinuous in $W^{1,p}(\Omega, \mathbb{R}^3)$,* i.e. *for every sequence $\{g_k\}_{k\in\mathbb{N}} \subset W^{1,p}(\Omega, \mathbb{R}^3)$ such that $g_k \rightharpoonup g$ in $W^{1,p}(\Omega, \mathbb{R}^3)$ the inequality*

$$\liminf_{k\to\infty} I(g_k) \geq I(g)$$

holds true.

Proof. See [Dac08, Theorem 8.11]. □

3.2.2 Two Examples of Energy Density Functions

In this subsection, we introduce two particular energy density functions that will be used in the numerical applications (*cf*. Section 3.6): an energy density representing an *Ogden-type material* as well as a *simplified energy density*, which is numerically beneficial but does neither comply with (W2) nor with (W3).

The Ogden-type material. In this paragraph, we briefly introduce an Ogden-type material which is compatible with the Assumptions (W1)-(W4).

One can show (*cf*. [Cia88, Theorem 4.8-1]) that no *convex* function $\widehat{\mathrm{W}} : \mathrm{GL}^+(n) \to \mathbb{R}$ exists such that $\widehat{\mathrm{W}}(A) \to \infty$ as $\det(A) \searrow 0$ (sometimes referred to as *compression response*), which in particular implies that there is no convex energy density function satisfying (W2). Clearly, polyconvex functions can satisfy the axiom of compression response, *e.g.* $\widehat{\mathrm{W}}(A) = \det(A)^{-s}$ for $s > 0$.

A class of energy density functions which is particularly well suited for our applications are *Ogden-type materials*, which are hyperelastic materials with a stored energy function of the form (*cf*. [Cia88, Section 4.9/4.10])

$$\widehat{\mathrm{W}}(A) = \sum_{i=1}^{M} a_i \mathrm{tr}(A^T A)^{\frac{\alpha_i}{2}} + \sum_{j=1}^{N} \mathrm{tr}(\mathrm{cof}(A^T A))^{\frac{\beta_j}{2}} + \Gamma(\det(A))$$

for $n = 3$ with $a_i > 0$, $\alpha_i, \beta_j \geq 1$ ($1 \leq i \leq M$, $1 \leq j \leq N$) and $\Gamma : \mathbb{R}^+ \to \mathbb{R}$ a convex function such that $\lim_{x\searrow 0} \Gamma(x) = \infty$. In the case $n = 2$, we consider in the numerical examples to be shown in Section 3.7 the following particular choice of an energy density representing an Ogden-type material:

$$\mathrm{W}(A) = a_1 \left(\mathrm{tr}(A^T A)\right)^q + a_2(\det(A))^r + a_3(\det(A))^{-s} + a_4 \tag{3.19}$$

for $A \in \mathbb{R}^{2,2}$, parameters $q, r \geq 1$ and $s > n - 1$, and coefficients

$$a_1 = \frac{2^{-q}\mu}{q}, \qquad a_2 = \frac{\lambda + \mu - \mu q - \mu s}{r^2 + rs},$$
$$a_3 = \frac{\lambda + \mu - \mu q + \mu r}{rs + s^2}, \qquad a_4 = \frac{\mu\left(q^2 - rs - q(1 + r - s)\right) - \lambda q}{qrs}.$$

It is possible to choose for given $\lambda, \mu > 0$ the parameters q, r, s such that the coefficients a_1, a_2 and a_3 are positive, which ensures the polyconvexity of W. We highlight that this particular W is isotropic, homogeneous, polyconvex and frame indifferent (*cf*. Subsection 3.3.1). In particular, for such a choice of parameters the Assumptions (W1)-(W4) are satisfied and the third term appearing in (3.19) ensures the required response of the energy on strong compression.

The simplified energy density. As a second choice of an energy density function W, we consider a quadratic penalization of the displacements, *i.e*.

$$\mathrm{W}(A) = |A - \mathbb{1}|^2 \,, \tag{3.20}$$

which is associated with the quadratic form $L[v, v] = Dv : Dv + \gamma \Delta v \cdot \Delta v$. This energy density is termed *simplified energy density* since it does neither comply with (W2) nor with (W3). Nevertheless, an optimal deformation for the pairwise energy induced by the energy density (3.20) exists (see Theorem 3.4.11 below with minor modifications). This very basic model represents a simple thin plate spline regularization (see [MF03]).

3.3 Review of the Physical Background

This section is devoted to the elucidation of the physical background of the energies involved in the time continuous as well as the time discrete metamorphosis model. We recall that the energy in the flow of diffeomorphism approach, which coincides with the contribution of the regularization terms in the (time continuous) metamorphosis model, is given by

$$\psi \mapsto \int_0^1 \int_\Omega \frac{\lambda}{2} (\mathrm{tr}(\varepsilon[v(t,x)]))^2 + \mu \mathrm{tr}(\varepsilon[v(t,x)]^2) + \gamma |D^m v(t,x)|^2 \,\mathrm{d}x \,\mathrm{d}t \tag{3.21}$$

for $v(t,x) = \dot{\psi}_t \circ \psi_t^{-1}(x)$ and $\varepsilon[v] = (\nabla v)^{\mathrm{sym}}$. Likewise, by taking into account (3.18) and neglecting the remainder one can express the regularization terms for the pairwise deformations contributing to the path energy of the time discrete metamorphosis model as follows

$$\widetilde{\mathbf{E}}_K[\mathbf{\Phi}] = K \sum_{k=1}^K \int_\Omega \frac{\lambda}{2} (\mathrm{tr}(D\phi_k - \mathbb{1})^{\mathrm{sym}})^2 + \mu \mathrm{tr}\left(((D\phi_k - \mathbb{1})^{\mathrm{sym}})^2 \right) + \gamma |D^m \phi_k|^2 \,\mathrm{d}x \tag{3.22}$$

for $\mathbf{\Phi} \in \mathcal{A}^K$. Despite the seemingly similar shape of both energies there exist various fundamental conceptual differences from a physical perspective that we will focus on below. To this end, recall that in this thesis shapes are viewed as boundaries of geometric objects (represented by domains) in the ambient (Euclidean) space (*cf*. Subsection 2.2.1). Following [RW11], the shape space inherent in the flow of diffeomorphism or the time continuous metamorphosis model is *path-based*, in which each shape represents a *viscous fluid object*, and the energy (3.21) quantifies the *dissipation in a multipolar viscous fluid*. Vice versa, each shape in the time discrete metamorphosis model can be interpreted as an *elastic object* of a *state-based* shape space, where the path energy (3.22) is the *stored energy function of a hyperelastic material*. Heuristically, both perspectives, that we will elaborate on in the next subsections, are connected by *Rayleigh's paradigm* [Ray45], which states that to derive an energy penalizing viscous dissipation from an elastic energy one has to exchange strains of the elastic material by strain rates of the viscous fluid. Moreover, in the special case of the metamorphosis energy, both perspectives are consistent in the limit $K \to \infty$ due to the Mosco-convergence to be presented in Section 3.5. The structure of this section is as follows: in Subsection 3.3.1 and Subsection 3.3.2 we will briefly review fundamental facts of elasticity theory and fluid mechanics to an extent required for the comparison of both perspectives (see Subsection 3.3.3).

3.3.1 Foundations of Elasticity Theory

In this subsection, we briefly recall some fundamental concepts from elasticity theory to motivate the shape of the energy (3.22), the references for this subsection are [Cia88, MH83]. The following exposition is tailored to $n = 3$ with small modifications for $n = 2$.

Let $D \subset \mathbb{R}^3$ be a bounded domain with smooth boundary, which we refer to as the *reference configuration* since it is assumed not to be subjected to any form of deformation. A *deformation in the sense of elasticity theory* is a smooth and injective (apart from the boundary) orientation-preserving vector field $\phi : \overline{D} \to \mathbb{R}^3$. By deforming the reference configuration D with the deformation ϕ we obtain the *deformed configuration* $D^\phi = \phi(D)$. One of the most fundamental results in continuum mechanics is the *Euler–Cauchy stress principle*, which asserts that if the reference configuration is subjected to *applied body forces* $f^\phi \in L^2(\overline{D^\phi}, \mathbb{R}^n)$ or *applied surface forces*

$g^\phi \in L^2(\partial D^\phi, \mathbb{R}^n)$, then a vector field $t^\phi : \overline{D^\phi} \times \mathbb{S}^{n-1} \to \mathbb{R}^n$ (known as *Cauchy stress vector*) exists such that for any open subdomain $\widetilde{D} \subset \overline{D^\phi}$ with smooth boundary the following equations hold true:

$$t^\phi(x^\phi, \mathrm{n}^\phi) = g^\phi(x^\phi) \quad \text{for all } x^\phi \in \partial\widetilde{D} \cap \partial D^\phi\,,$$

$$\int_{\widetilde{D}} f^\phi \,\mathrm{d}x^\phi + \int_{\partial\widetilde{D}} t^\phi(x^\phi, \widetilde{\mathrm{n}}^\phi)\,\mathrm{d}a^\phi = 0\,, \tag{3.23}$$

$$\int_{\widetilde{D}} x^\phi \times f^\phi \,\mathrm{d}x^\phi + \int_{\partial\widetilde{D}} x^\phi \times t^\phi(x^\phi, \widetilde{\mathrm{n}}^\phi)\,\mathrm{d}a^\phi = 0\,, \tag{3.24}$$

where $\mathrm{d}x^\phi = \det(\nabla\phi)\,\mathrm{d}x$ and $\mathrm{d}a^\phi = |\mathrm{cof}(\nabla\phi)\mathrm{n}|\,\mathrm{d}\mathcal{H}^{n-1}$ denote the volume and area element in the deformed configuration, respectively. Furthermore, n^ϕ respectively $\widetilde{\mathrm{n}}^\phi$ are the outer normals of $\partial\widetilde{D} \cap \partial D^\phi$ and $\partial\widetilde{D}$. The equations (3.23) and (3.24) are the axioms of *force balance* and *momentum balance*, respectively. Now, a fundamental theorem by Cauchy guarantees the existence of a symmetric tensor field $\mathrm{T}^\phi : \overline{D^\phi} \to \mathbb{R}^{n,n}$ (called *Cauchy stress tensor*) such that

$$t^\phi(x^\phi, a) = \mathrm{T}^\phi(x^\phi)a\,, \qquad -\mathrm{div}(\mathrm{T}^\phi(\hat{x}^\phi)) = f^\phi(\hat{x}^\phi)\,, \qquad \mathrm{T}^\phi(\tilde{x}^\phi)\mathrm{n}^\phi = g^\phi(\tilde{x}^\phi)$$

for all $x^\phi \in \overline{D^\phi}$, $\hat{x}^\phi \in D^\phi$, $\tilde{x}^\phi \in \partial D^\phi$ and $a \in \mathbb{S}^2$, where n^ϕ denotes the unit outer normal of ∂D^ϕ. The associated tensor in the reference configuration is the *first Piola–Kirchhoff stress tensor* defined as $\mathrm{T}(x) = \mathrm{T}^\phi(\phi(x))\mathrm{cof}(\nabla\phi(x))$ for all $x \in \overline{D}$.

The constitutive equation of an *elastic material* states that there exist *response functions* $\widehat{\mathrm{T}}$ *and* $\widehat{\mathrm{T}}^D$ associated with T and T^ϕ such that one of the equivalent relations

$$\mathrm{T}(x) = \widehat{\mathrm{T}}(x, \nabla\phi(x))\,, \qquad \mathrm{T}^\phi(\phi(x)) = \widehat{\mathrm{T}}^D(x, \nabla\phi(x))$$

holds true for any $x \in \overline{D}$ and for any deformation ϕ, which means that the deformations only affect the stress tensors via their gradients. The elastic material satisfies the *axiom of frame-invariance* if the equality $\widehat{\mathrm{T}}^D(x, OA) = O\widehat{\mathrm{T}}^D(x, A)O^T$ is valid, and the elastic material is said to be *isotropic* if $\widehat{\mathrm{T}}^D(x, AO) = \widehat{\mathrm{T}}^D(x, A)$ for all $x \in \overline{D}$, $A \in \mathrm{GL}^+(n)$ and $O \in \mathrm{SO}(n)$. Furthermore, the material is *homogeneous* if the response function is independent of the position in the reference configuration, *i.e.* $\mathrm{T}^\phi(\phi(x)) = \widehat{\mathrm{T}}^D(\nabla\phi(x))$, and the reference configuration of a material is referred to as a *natural state* if the response function vanishes in undeformed regimes, *i.e.* $\widehat{\mathrm{T}}(x, \mathbb{1}) = \widehat{\mathrm{T}}^D(x, \mathbb{1}) = 0$ for all $x \in \overline{D}$. Likewise, these properties can be equivalently expressed in terms of the *second Piola–Kirchhoff stress tensor* $\Sigma(x) = \nabla\phi^{-1}(x)\mathrm{T}(x)$ with corresponding elastic response function $\widehat{\Sigma}$, *i.e.* $\Sigma(x) = \widehat{\Sigma}(x, \nabla\phi(x))$ for all $x \in \overline{D}$.

According to the *Rivlin–Ericksen representation theorem* (*cf*. [RE55]) the response function of an isotropic material with frame-invariance of the observer admits the particular representation

$$\widehat{\Sigma}(x, \nabla\phi(x)) = c_0(x, \iota_C)\mathbb{1} + c_1(x, \iota_C)C + c_2(x, \iota_C)C^2\,,$$

where $C = \nabla\phi^T\nabla\phi$ is the associated *right Cauchy–Green strain tensor*, c_0, c_1 and c_2 are scalar-valued functions depending on the principal invariants $\iota_C = (\mathrm{tr}(C), \mathrm{cof}(C), \det(C))$ of C. As a direct consequence of this representation theorem, the response function of the second Piola–Kirchhoff stress tensor for a frame-invariant, homogeneous and isotropic material, whose reference configuration is a natural state, has the particular form

$$\widehat{\Sigma}(A) = \widetilde{\Sigma}(E) = \lambda\mathrm{tr}(E)\mathbb{1} + 2\mu E + \mathrm{o}(E) \tag{3.25}$$

for all $A \in \mathrm{GL}^+(n)$ and $E \in \mathbb{R}^{n,n}$ such that $A^TA = \mathbb{1} + 2E$, where λ and μ are called *Lamé constants*. An elastic material is a *Saint Venant–Kirchhoff material* if the remainder in (3.25) vanishes for all E.

Furthermore, *hyperelastic materials* are elastic materials for which there exists a sufficiently smooth function $\widehat{\mathrm{W}} : \overline{D} \times \mathrm{GL}^+(n) \to \mathbb{R}$ (*stored energy function*) such that $\widehat{\mathrm{T}}(x, A) = \frac{\partial\widehat{\mathrm{W}}(x,A)}{\partial A}$ for all $x \in D$ and all $A \in \mathrm{GL}^+(n)$. One can show that the Saint Venant–Kirchhoff material is hyperelastic with stored energy density function given by

$$\widehat{\mathrm{W}}(A) = \widetilde{\mathrm{W}}(E) = \frac{\lambda}{2}\mathrm{tr}(E)^2 + \mu\mathrm{tr}(E^2)$$

for all $A \in \mathrm{GL}^+(n)$ and $E \in \mathbb{R}^{n,n}$ such that $A^TA = \mathbb{1} + 2E$, which already motivates the particular expression for the Hypothesis (W3) and thus the lower order terms in (3.22).

3.3.2 Some Fundamental Concepts in Fluid Mechanics

In this subsection, we very briefly clarify some notions in fluid mechanics in order to motivate the shape of the energy (3.21) (see [Bat99, MOHR13, CM90, MWS06, RW11] and the references therein for further details).

The *dissipation* is a measure of the rate at which any form of internal energy (in most cases kinetic energy and potential energy due to gravitational body forces) is (irreversibly) converted into thermal energy. Moreover, the *viscosity of a fluid* quantifies the resistance of the fluid to shear if the fluid is subjected to external motion. In detail, assume that a fluid is enclosed between a stationary and a uniformly moving plate of infinite size such that the velocities of the fluid and the plates coincide at the interfaces (see Figure 3.1). We denote by $\tau(x)$ the tangential shear stress of any infinitesimally small volume element of the fluid as depicted by the magnifying lens. Then the viscosity $\eta(x)$ of a homogeneous fluid is defined as the ratio of the shear stress and the tangential velocity gradient $\frac{\partial}{\partial x_2} v^{\mathrm{tangent}}(x)$, *i.e.* $\eta(x) = \tau(x)(\frac{\partial}{\partial x_2} v^{\mathrm{tangent}}(x))^{-1}$ for $x = (x_1, x_2)$.

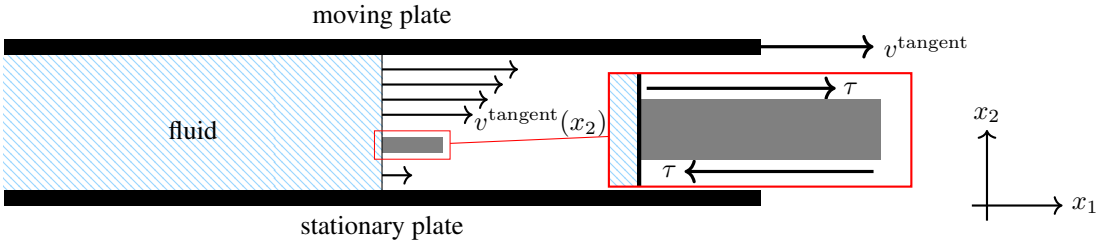

Figure 3.1: Flow between parallel plates to illustrate viscosity, figure adapted from [HB67].

A *Newtonian fluid* is a fluid with a viscosity that is spatially constant and thus results in a stress tensor that linearly depends on the velocity gradient. One can verify that the stress tensor of an isotropic Newtonian fluid is $\lambda \mathrm{tr}(\varepsilon[v])\mathbb{1} + 2\mu\varepsilon[v]$ with v denoting the velocity, $\varepsilon[v] = (\nabla v)^{\mathrm{sym}}$ and λ, μ are Lamé constants as before. Here, only the symmetric components of the velocity gradient affect the stress tensor because the antisymmetric parts generate infinitesimal rotations and are therefore ruled out. Moreover, in the case of an *incompressible fluid* the first summand vanishes due to $\mathrm{tr}(\varepsilon[v]) = \mathrm{div} v = 0$. Since the stress tensor coincides with the first variation of *the local rate of (viscous) dissipation*, this rate is given by

$$\mathrm{diss}[v] = \tfrac{\lambda}{2}(\mathrm{tr}(\varepsilon[v]))^2 + \mu \mathrm{tr}((\varepsilon[v])^2) \tag{3.26}$$

for isotropic Newtonian fluids, and the associated *path-dependent total dissipation along the velocity field* is characterized as

$$\mathrm{Diss}[v] = \int_0^1 \int_\Omega \mathrm{diss}[v(t,x)] \,\mathrm{d}x \,\mathrm{d}t \,.$$

Heuristically, the dissipation can be viewed as an infinitesimal indicator for (internal) energy since infinitesimal displacements inside the fluid result in stresses caused by friction, which are instantaneously absorbed by dissipation. Nečas and Šilhavý [NŠ91] (based on earlier work by Green and Rivlin [GR64b, GR64a]) observed that in many fluid dynamic applications it is more appropriate to model the stress of a fluid as a function additionally involving higher order derivatives of the velocity field, that is why they derived constitutive equations for *multipolar viscous fluids*, in which higher order derivatives of the velocity field are added to the usual second order stress tensor. In our case, the multipolarity is mathematically reflected by the additional integrand $\gamma |D^m v(t,x)|^2$ appearing in the energy (3.21). We observe that the associated induced metric reads as

$$g(v,\tilde{v}) = \int_\Omega \tfrac{\lambda}{2}(\mathrm{tr}(\varepsilon[v]))(\mathrm{tr}(\varepsilon[\tilde{v}])) + \mu \mathrm{tr}(\varepsilon[v]\varepsilon[\tilde{v}]) + \gamma D^m v : D^m \tilde{v} \,\mathrm{d}x \,. \tag{3.27}$$

To sum up, the energy (3.21) admits the physical interpretation as a dissipation density in a multipolar viscous fluid.

3.3.3 Path- and State-Based Shape Spaces

In the previous subsections we derived the particular energies (3.21) and (3.22) from a physical point of view. In this subsection, we will contrast path- with state-based shape spaces in more detail, the main reference for this subsection is [RW11].

As we have already defined at the beginning of this section, shapes in the path-based shape space should be considered as viscous fluid objects occupying a certain subdomain of Ω, where one can assume void outside this subdomain without restriction. Any path in this shape space determines the shape at any time $t \in [0,1]$, and the path energy corresponding to two shapes at different time points is clearly path-dependent. Moreover, the metric (3.27) induces a Riemannian distance which is actually a metric. Indeed, if v is a minimizing velocity field associated with the Riemannian distance of two shapes (*e.g.* images) u_A and u_B, then a minimizing velocity field associated with the Riemannian distance of u_B and u_A is obtained by the inversion $v(t) \curvearrowright -v(1-t)$.

In contrast, in state-based shape spaces one regards shapes as elastic objects – potentially encompassed by a relatively soft material for theoretical reasons – subjected to elastic deformations, and a discrete path in such a shape space (*cf*. Definition 2.2.3) solely determines each shape at the discrete time points $\frac{k}{K}$, $k \in \{0,\dots,K\}$. This in particular implies that the induced path energy (3.22) only incorporates the shape structures at these discrete time points and ignores all other points. Furthermore, this energy is in general not symmetric (*i.e.* $\widetilde{\mathbf{E}}_K[(\phi_1,\dots,\phi_K)] \neq \widetilde{\mathbf{E}}_K[(\phi_K,\dots,\phi_1)]$), albeit one could pass to the symmetrized energy $\frac{1}{2}(\widetilde{\mathbf{E}}_K[(\phi_1,\dots,\phi_K)] + \widetilde{\mathbf{E}}_K[(\phi_K,\dots,\phi_1)])$. Finally, by restricting, for instance, to the case $K=1$ one can define the following dissimilarity measure in the flow of diffeomorphism approach $\operatorname{dist}(u_A,u_B) = \min_{\phi\in\mathcal{A}:\phi(u_A)=u_B} \widetilde{\mathbf{E}}_1[\phi]$, where we tacitly assume that the minimizer is actually attained and finite. Unfortunately, this dissimilarity measure is in general *not* expected to satisfy a triangle inequality and thus does not induce a canonical Riemannian distance.

Interestingly, both energies (3.21) and (3.22) solely depend on derivatives of the velocity field and the deformations, respectively, which is immediate from the very definitions of viscous dissipation and elasticity.

3.4 Existence of Time Discrete Geodesics

In what follows, we will prove the existence of discrete geodesic curves $\mathbf{u} = (u_0,u_1,\dots,u_K) \in \mathcal{I}^{K+1}$ for fixed $K \geq 2$ and fixed end points $u_0 = u_A \in \mathcal{I}$ and $u_K = u_B \in \mathcal{I}$ (see Theorem 3.4.11). To this end, we will first verify in Proposition 3.4.2 the well-posedness of $\mathcal{W}$, *i.e.* for two images $u,\tilde{u} \in \mathcal{I}$ a minimizing deformation $\phi \in \mathcal{A}$ of the variational problem (3.13) exists. Then, we will show in Proposition 3.4.8 that there exists a unique vector $\hat{\mathbf{u}} \in \mathcal{I}^{K-1}$ minimizing

$$\mathcal{I}^{K-1} \ni \tilde{\mathbf{u}} \mapsto \mathbf{E}_K^D[(u_A,\tilde{\mathbf{u}},u_B),\mathbf{\Phi}]$$

for given end points $u_A,u_B \in \mathcal{I}$ and a given vector of deformations $\mathbf{\Phi} \in \mathcal{A}^K$. Finally, the combination of both propositions yields the existence theorem for time discrete geodesics.

Throughout this subsection, there are two different settings present to ensure the existence of minimizing images or deformations:

(i.) If the image space $\mathcal{I}$ coincides with the space of essentially bounded functions $L^\infty(\Omega)$, then the input images need not satisfy any additional assumptions, but the minimizing deformations are in general only homeomorphic and not necessarily diffeomorphic.

(ii.) In the case $\mathcal{I} = L^2(\Omega)$, we either have to impose the $L^2(\Omega)$-closeness of the input images or the strict positivity of the determinants of all deformation gradients, which immediately implies that all minimizing deformations are indeed $C^1(\Omega)$-diffeomorphisms.

The homeomorphism and diffeomorphism properties are consequences of the following theorem:

Theorem 3.4.1 (Global invertibility of smooth and Sobolev functions)**.** *Let $\Omega \subset \mathbb{R}^n$ be strongly Lipschitz and bounded.*

(i.) Let $\hat{f} \in C^0(\overline{\Omega},\mathbb{R}^n)$ be injective. If $f \in C^0(\overline{\Omega},\mathbb{R}^n) \cap C^1(\Omega,\mathbb{R}^n)$ satisfies

$$\det(Df(x)) > 0\,, \qquad f(y) = \hat{f}(y)$$

for all $x \in \Omega$ and all $y \in \partial\Omega$, then $f : \overline{\Omega} \to f(\overline{\Omega})$ is a homeomorphism, $f : \Omega \to f(\Omega)$ is a diffeomorphism and $\hat{f}(\Omega) = f(\Omega)$ as well as $\hat{f}(\overline{\Omega}) = f(\overline{\Omega})$ hold true.

(ii.) Let $\hat{f} \in C^0(\overline{\Omega}, \mathbb{R}^n)$ be injective in Ω and $f \in W^{1,q}(\Omega, \mathbb{R}^n)$, $q > n$, be a function such that $f\big|_{\partial\Omega} = \hat{f}\big|_{\partial\Omega}$ and $\det(Df(x)) > 0$ for a.e. $x \in \Omega$. Then $\hat{f}(\overline{\Omega}) = f(\overline{\Omega})$ and $|\{x \in f(\overline{\Omega}) \,:\, \#(f^{-1}(x)) > 1\}| = 0$. Moreover, if $\hat{f}(\Omega)$ is strongly Lipschitz and

$$\int_\Omega |(Df)^{-1}|^q \det(Df)\,\mathrm{d}x < \infty$$

holds true, then $f : \overline{\Omega} \to f(\overline{\Omega})$ is a homeomorphism, $f^{-1} \in W^{1,q}(f(\Omega))$ and

$$\int_{f(\Omega)} \left|\partial_i (f^{-1})_j\right|^q \,\mathrm{d}y \le \int_\Omega |\mathrm{cof}(Df)_{j,i}|^q (\det(Df))^{1-q}\,\mathrm{d}x \quad \text{for all } 1 \le i,j \le n\,.$$

Finally, the change of variables formula

$$\int_{\Omega'} g \circ f \det(Df)\,\mathrm{d}x = \int_{f(\Omega')} g\,\mathrm{d}y \tag{3.28}$$

is valid for any measurable set $\Omega' \subset \overline{\Omega}$ and any measurable function $g : \mathbb{R}^n \to \mathbb{R}$ provided that one of the integrals in (3.28) *exists.*

Proof. (i.) is due to [Cia88, Theorem 5.5-2] and (ii.) was shown in [Bal81, Theorem 1 and Theorem 2]. □

Let us begin with the proof of the well-posedness of $\mathcal{W}$.

Proposition 3.4.2 (Well-posedness of $\mathcal{W}$)**.** *Let $\Omega \subset \mathbb{R}^n$, $n \in \{2,3\}$, be a bounded and strongly Lipschitz domain.*

(i.) Let $u, \tilde{u} \in \mathcal{I} := L^\infty(\Omega)$. Under the assumptions (W1) and (W2), there exists a minimizing deformation $\phi \in \mathcal{A}$ of the variational problem (3.13)*,* i.e. *$\mathcal{W}[u,\tilde{u}] = \mathcal{W}^D[u,\tilde{u},\phi]$, and $\phi : \overline{\Omega} \to \overline{\Omega}$ is a* homeomorphism.

(ii.) Let $u \in \mathcal{I} := L^2(\Omega)$. Under the assumptions (W1) and (W4), there exists a constant $C_{\mathcal{W}} > 0$ depending on Ω, m, n, γ, δ, $C_{\mathrm{W},1}$, $C_{\mathrm{W},2}$ and r_{W} such that for every

$$\tilde{u} \in \left\{\, v \in L^2(\Omega) \,:\, \|v - u\|_{L^2(\Omega)} < C_{\mathcal{W}} \,\right\}$$

there exists a minimizing deformation $\phi \in \mathcal{A}$ of (3.13) *and ϕ is a $C^1(\Omega,\Omega)$-*diffeomorphism.

Proof. The proof employs the direct method in the calculus of variations (see [Dac08]).

ad (i.): For fixed $u, \tilde{u} \in L^\infty(\Omega)$, let $\{\phi^j\}_{j\in\mathbb{N}} \subset \mathcal{A}$ be a minimizing sequence for $\phi \mapsto \mathcal{W}^D[u,\tilde{u},\phi]$ that converges to $\underline{\mathbf{W}} = \inf_{\phi\in\mathcal{A}} \mathcal{W}^D[u,\tilde{u},\phi]$. Using (W1) and $\mathbb{1} \in \mathcal{A}$ we can assume without restriction

$$0 \le \underline{\mathbf{W}} \le \mathcal{W}^D[u,\tilde{u},\phi^j] \le \overline{\mathbf{W}} := \mathcal{W}^D[u,\tilde{u},\mathbb{1}] = \tfrac{1}{\delta}\|\tilde{u}-u\|^2_{L^2(\Omega)} < \infty \qquad \forall j \in \mathbb{N}\,. \tag{3.29}$$

Thus, taking into account the boundedness of Ω we can deduce that $\{\phi^j\}_{j\in\mathbb{N}}$ is uniformly bounded in $L^2(\Omega)$, and due to $|\phi^j|^2_{H^m(\Omega)} \le \frac{\overline{\mathbf{W}}}{\gamma}$ we can infer the uniform boundedness of the minimizing sequence w.r.t. the $H^m(\Omega)$-seminorm. Then, the Gagliardo–Nirenberg inequality for bounded domains (see Theorem 1.1.2) implies the uniform boundedness of this minimizing sequence in $H^m(\Omega)$. Since $H^m(\Omega,\Omega)$ is reflexive, there exists a weakly convergent subsequence (again denoted by ϕ^j) such that $\phi^j \rightharpoonup \phi$ in $H^m(\Omega)$, and by using the Sobolev Embedding Theorem 1.1.4 as well as the Arzelà–Ascoli Theorem we can additionally infer that for a subsequence (labeled in the same way) $\phi^j \to \phi$ in $C^{1,\alpha}(\overline{\Omega})$ for $\alpha \in (0, m-1-\frac{n}{2})$ holds true.

Claim: All deformations ϕ^j as well as the limiting deformation ϕ belong to $\mathcal{A}$ and are homeomorphisms.

For sufficiently small $\varepsilon > 0$ set $S_\varepsilon = \{x \in \Omega \,:\, \det(D\phi) \le \varepsilon\}$. Then,

$$\begin{aligned}
&\beta_0 \varepsilon^{-s} |S_\varepsilon| \le \beta_0 \int_{S_\varepsilon} (\det(D\phi))^{-s}\,\mathrm{d}x \\
&\le \int_{S_\varepsilon} \mathrm{W}(D\phi)\,\mathrm{d}x + \beta_1|\Omega| \le \liminf_{j\to\infty} \int_{S_\varepsilon} \mathrm{W}(D\phi^j)\,\mathrm{d}x + \beta_1|\Omega| \le \overline{\mathbf{W}} + \beta_1|\Omega|\,.
\end{aligned}$$

For the first inequality we used the definition of the set S_ε, the second inequality follows from (W2), the third inequality can be deduced from (W1) in combination with Proposition 3.2.6, and the final inequality is a direct consequence of the estimate (3.29). Hence,

$$|S_\varepsilon| \leq \frac{(\overline{\mathbf{W}} + \beta_1|\Omega|)\varepsilon^s}{\beta_0}\,, \tag{3.30}$$

which shows $|S_0| = 0$ and thus $\det(D\phi) > 0$ $\mathcal{L}^n$-a.e. in Ω as well as $\phi \in \mathcal{A}$. Due to (W2) and $A^{-1} = \frac{\operatorname{cof}(A)^T}{\det(A)}$ for $A \in \mathrm{GL}(n)$ we can additionally infer for $q = s + 1 > n$ that

$$\begin{aligned}\int_\Omega |(D\phi)^{-1}|^q \det(D\phi)\,\mathrm{d}x &= \int_\Omega |\operatorname{cof}(D\phi)^T|^q \det(D\phi)^{-s}\,\mathrm{d}x \\ \leq C\|\phi\|^{q(n-1)}_{C^1(\overline{\Omega})} \int_\Omega \frac{W(D\phi)+\beta_1}{\beta_0}\,\mathrm{d}x &< \infty\,.\end{aligned} \tag{3.31}$$

Here, we used the uniform boundedness of $D\phi$ and therefore $\operatorname{cof}(D\phi)$ in $C^0(\overline{\Omega})$ due to Theorem 1.1.4. By taking into account $\phi \in H^m(\Omega)$ as well as $\phi \in W^{1,q}(\Omega)$, which again follows from Theorem 1.1.4, Theorem 3.4.1 (ii.) implies that the deformation ϕ is actually homeomorphic and the $W^{1,q}(\Omega)$-seminorm of the inverse deformation ϕ^{-1} is bounded from above by the q^{th} root of the last expression in (3.31). Likewise, by an analogous reasoning taking into account $\sup_{j\in\mathbb{N}} \|\phi^j\|^{q(n-1)}_{C^1(\overline{\Omega})} \leq C$ we can infer that $\{\phi^j\}_{j\in\mathbb{N}}$ are also homeomorphisms and $|(\phi^j)^{-1}|^q_{W^{1,q}(\Omega)}$ can be uniformly controlled using the corresponding version of the right-hand side of (3.31) as an upper bound. This proves the claim.

Claim: The mismatch functional $\|\tilde{u}\circ\phi^j - u\|_{L^2(\Omega)}$ converges to $\|\tilde{u}\circ\phi - u\|_{L^2(\Omega)}$ as $j \to \infty$.

By using the uniform boundedness of the mismatch functionals we estimate

$$\begin{aligned}&\left|\int_\Omega (\tilde{u}\circ\phi^j - u)^2 - (\tilde{u}\circ\phi - u)^2\,\mathrm{d}x\right| \\ &\leq \int_\Omega (|\tilde{u}\circ\phi^j - u| + |\tilde{u}\circ\phi - u|)|\tilde{u}\circ\phi^j - \tilde{u}\circ\phi|\,\mathrm{d}x \\ &\leq \left(\|\tilde{u}\circ\phi^j - u\|_{L^2(\Omega)} + \|\tilde{u}\circ\phi - u\|_{L^2(\Omega)}\right)\|\tilde{u}\circ\phi^j - \tilde{u}\circ\phi\|_{L^2(\Omega)} \\ &\leq 2\sqrt{\delta\overline{\mathbf{W}}}\|\tilde{u}\circ\phi^j - \tilde{u}\circ\phi\|_{L^2(\Omega)}\,.\end{aligned}$$

To estimate the last expression on the right-hand side, we approximate $\tilde{u}$ in $L^2(\Omega)$ by a sequence of smooth functions $\{\tilde{u}_i\}_{i\in\mathbb{N}} \subset C^\infty(\Omega)$ such that $\|\tilde{u}-\tilde{u}_i\|_{L^2(\Omega)} \leq 2^{-i}$ and $\|\tilde{u}_i\|_{L^\infty(\Omega)} \leq C\|\tilde{u}\|_{L^\infty(\Omega)}$, and by passing to a subsequence (also denoted by $\tilde{u}_i$) we can assume that $\tilde{u}_i$ converges to $\tilde{u}$ for a.e. $x \in \Omega$. Then,

$$\|\tilde{u}\circ\phi^j - \tilde{u}\circ\phi\|_{L^2(\Omega)} \leq \|\tilde{u}\circ\phi^j - \tilde{u}_i\circ\phi^j\|_{L^2(\Omega)} + \|\tilde{u}_i\circ\phi^j - \tilde{u}_i\circ\phi\|_{L^2(\Omega)} + \|\tilde{u}_i\circ\phi - \tilde{u}\circ\phi\|_{L^2(\Omega)}\,. \tag{3.32}$$

Let $\varepsilon > 0$ be sufficiently small and set $S_{\varepsilon,j} = \{x \in \Omega : \det(D\phi^j) < \varepsilon\}$. Using the same line of arguments as in the derivation of (3.30) we deduce that a continuous function $\omega : \mathbb{R}^+_0 \to \mathbb{R}^+_0$ exists such that $\omega(0) = 0$ and $|S_{\varepsilon,j}| \leq \omega(\varepsilon)$ for all $j \in \mathbb{N}$. Next, we will derive an upper bound for the first summand on the right-hand side of (3.32). To this end, we employ the transformation formula, the homeomorphism property of ϕ^j as well as the Cauchy–Schwarz inequality in the following way:

$$\begin{aligned}\|\tilde{u}\circ\phi^j - \tilde{u}_i\circ\phi^j\|^2_{L^2(\Omega)} &= \int_\Omega (\tilde{u}-\tilde{u}_i)^2 \det(D(\phi^j)^{-1})\,\mathrm{d}x = \int_\Omega (\tilde{u}-\tilde{u}_i)^2 \frac{1}{\det((D\phi^j)\circ(\phi^j)^{-1})}\,\mathrm{d}x \\ \leq \|\tilde{u}-\tilde{u}_i\|^2_{L^\infty(\Omega)} \int_{\phi^j(S_{\varepsilon,j})} \frac{1}{\det((D\phi^j)\circ(\phi^j)^{-1})}\,\mathrm{d}x &+ \frac{1}{\varepsilon}\int_{\Omega\setminus\phi^j(S_{\varepsilon,j})} (\tilde{u}-\tilde{u}_i)^2\,\mathrm{d}x \\ \leq \|\tilde{u}-\tilde{u}_i\|^2_{L^\infty(\Omega)}|\phi^j(S_{\varepsilon,j})|^{\frac{1}{2}}\|(\det((D\phi^j)\circ(\phi^j)^{-1}))^{-1}\|_{L^2(\Omega)} &+ \frac{1}{\varepsilon}\int_\Omega (\tilde{u}-\tilde{u}_i)^2\,\mathrm{d}x\,.\end{aligned} \tag{3.33}$$

Below, we will estimate the Lebesgue measure of $\phi^j(S_{\varepsilon,j})$. To this end, we apply the Besicovitch Covering Theorem (see [Bog07, Corollary 5.8.3]) to cover the open set $S_{\varepsilon,j}$ by an at most countable collection of

nonempty and open balls $\{B_k\}_{k\in\mathbb{N}} \subset S_{\varepsilon,j}$ with radii $\{r_k\}_{k\in\mathbb{N}}$ such that $\overline{B_k} \cap \overline{B_l} = \emptyset$ for $k \neq l$ and $|S_{\varepsilon,j}\backslash\mathcal{B}_{\varepsilon,j}| = 0$ for $\mathcal{B}_{\varepsilon,j} = \bigcup_{k\in\mathbb{N}} B_k$. The following result is due to [HK14]: let $f \in W^{1,p}(\Omega)$ with $p > n$ and $B \subset \Omega$ a ball with radius r_B. Then $|f(B)| \leq C r_B^{n(1-\frac{n}{p})} |f|^n_{H^p(B)}$. Hence, since $\{\phi^j\}_{j\in\mathbb{N}} \subset W^{1,q}(\Omega)$ we can deduce

$$|\phi^j(S_{\varepsilon,j})| = |\phi^j(\mathcal{B}_{\varepsilon,j})| = \sum_{k\in\mathbb{N}} |\phi^j(B_k)| \leq \sum_{k\in\mathbb{N}} C r_k^{n(1-\frac{n}{q})} |\phi^j|^n_{H^q(B_k)}$$

$$\leq C \left(\sum_{k\in\mathbb{N}} r_k^n\right)^{1-\frac{n}{q}} \left(\sum_{k\in\mathbb{N}} |\phi^j|^q_{H^q(B_k)}\right)^{\frac{n}{q}} \leq C \left(\sum_{k\in\mathbb{N}} r_k^n\right)^{1-\frac{n}{q}} |\phi^j|^n_{H^q(\Omega)} \tag{3.34}$$

$$\leq C\omega(\varepsilon)^{1-\frac{n}{q}}\,. \tag{3.35}$$

The first inequality in (3.34) is due to Hölder's inequality with parameters $(1-\frac{n}{q})^{-1}$ and $\frac{q}{n}$. Since all deformations are uniformly bounded w.r.t. the $W^{1,q}(\Omega)$-seminorm one can readily obtain (3.35). Alternatively, an upper bound for the Lebesgue measure of the set $\phi^j(S_{\varepsilon,j})$ could have been derived by exploiting the $C^{1,\alpha}(\Omega)$-regularity of the deformations using standard techniques. However, in the proof of Proposition 3.4.8 one additionally requires an upper bound of the Lebesgue measure of the preimage set $\phi^{-1}(S)$ for a measurable set $S \in \Omega$, which readily follows from (3.35). Since the inverse deformations in general only exhibit a $W^{1,p}(\Omega)$-regularity for $p > n$, the standard result is not applicable.

Finally, to estimate the L^2-norm of the determinant of the inverse deformations appearing in (3.33) we proceed as follows:

$$\|(\det((D\phi^j)\circ(\phi^j)^{-1}))^{-1}\|^2_{L^2(\Omega)} = \int_\Omega \frac{1}{\det(D\phi^j)}\,\mathrm{d}x \tag{3.36}$$

$$\leq \int_\Omega (\det(D\phi^j))^{-s} + 1\,\mathrm{d}x \leq \int_\Omega \frac{\mathrm{W}(D\phi^j)+\beta_1}{\beta_0} + 1\,\mathrm{d}x \leq \frac{\overline{\mathbf{W}}+\beta_1|\Omega|}{\beta_0} + |\Omega| =: C(\Omega,\overline{\mathbf{W}})\,. \tag{3.37}$$

To derive (3.36) we employ the transformation formula, and the estimates in (3.37) rely on (W2) noting that $s > n-1$ (recall that we always assume $n \geq 2$). By combining (3.33), (3.35) and (3.37) we finally achieve

$$\|\tilde{u}\circ\phi^j - \tilde{u}_i\circ\phi^j\|^2_{L^2(\Omega)} \leq C\sqrt{C(\Omega,\overline{\mathbf{W}})}\|\tilde{u}-\tilde{u}_i\|^2_{L^\infty(\Omega)}\omega(\varepsilon)^{\frac{1}{2}(1-\frac{n}{p})} + \frac{1}{\varepsilon}\int_\Omega (\tilde{u}-\tilde{u}_i)^2\,\mathrm{d}x\,.$$

Thus, by first choosing $\varepsilon > 0$ sufficiently small and then passing to the limit $i \to \infty$ we have proven that the first summand on the right-hand side of (3.32) converges to 0 independently of j. Likewise, by an analogous reasoning we can immediately infer that the last term also converges to 0. Finally, for fixed i and ε the middle term in (3.32) vanishes for $j \to \infty$ due to the smoothness of $\tilde{u}_i$ and the convergence of ϕ^j to ϕ in $C^{1,\alpha}(\Omega)$. This proves the claim.

Let us conclude the proof of the lower semicontinuity of the discrete energy along the sequence ϕ^j. To this end, for $\varepsilon > 0$ we choose $j_0 \in \mathbb{N}$ such that

$$\mathcal{W}^D[u,\tilde{u},\phi^j] \leq \mathcal{W}^D[u,\tilde{u},\phi^{j_0}] \leq \underline{\mathbf{W}} + \varepsilon\,,$$
$$\left|\int_\Omega (\tilde{u}\circ\phi^j - u)^2 - (\tilde{u}\circ\phi - u)^2\,\mathrm{d}x\right| \leq \varepsilon$$

for all $j \geq j_0$. By using (W1), Proposition 3.2.6 and Fatou's lemma, we can infer

$$\underline{\mathbf{W}} = \mathcal{W}^D[u,\tilde{u},\phi] = \int_\Omega \mathrm{W}(D\phi) + \gamma|D^m\phi|^2 + \frac{1}{\delta}(\tilde{u}\circ\phi - u)^2\,\mathrm{d}x$$
$$\leq \liminf_{j\to\infty} \int_\Omega \mathrm{W}(D\phi^j) + \gamma|D^m\phi^j|^2 + \frac{1}{\delta}(\tilde{u}\circ\phi^j - u)^2\,\mathrm{d}x + \frac{\varepsilon}{\delta} \leq \underline{\mathbf{W}} + \varepsilon + \frac{\varepsilon}{\delta}\,,$$

which implies (i.).

ad (ii.): The proof of (ii.) is based on the following lemma:

Lemma 3.4.3. *Under the assumptions (W1) and (W4), there exists a continuous and monotonously increasing function $\theta : \mathbb{R}_0^+ \to \mathbb{R}_0^+$ with $\theta(0) = 0$ – solely depending on Ω, m, n, γ, $C_{\mathrm{W},1}$, $C_{\mathrm{W},2}$ and r_{W} – such that*

$$\|\phi - \mathbb{1}\|_{H^m(\Omega)} \leq \theta\big(\mathcal{W}^D[u, \tilde{u}, \phi]\big)$$

for all $u, \tilde{u} \in L^2(\Omega)$ and all $\phi \in \mathcal{A}$. Furthermore, $\theta(x) \leq C(x + x^2)^{\frac{1}{2}}$ for a constant $C > 0$.

Proof. Set $\overline{\mathcal{W}} = \mathcal{W}^D[u, \tilde{u}, \phi]$. The Gagliardo–Nirenberg interpolation inequality (*cf*. Theorem 1.1.2) implies

$$\|\phi - \mathbb{1}\|_{H^m(\Omega)} \leq C(\|\phi - \mathbb{1}\|_{L^2(\Omega)} + |\phi - \mathbb{1}|_{H^m(\Omega)}) \,. \tag{3.38}$$

The $H^m(\Omega)$-seminorm of the displacement can be controlled as follows:

$$|\phi - \mathbb{1}|_{H^m(\Omega)} \leq |\phi|_{H^m(\Omega)} \leq \sqrt{\frac{\overline{\mathcal{W}}}{\gamma}} \,, \tag{3.39}$$

which follows from the definition of $\mathcal{W}^D$. Since $\phi \in H^m(\Omega, \Omega)$, this already shows for $\alpha \in (0, m - 1 - \frac{n}{2})$

$$\|\phi - \mathbb{1}\|_{C^{1,\alpha}(\overline{\Omega})} \leq C\|\phi - \mathbb{1}\|_{H^m(\Omega)} \leq C + C\sqrt{\overline{\mathcal{W}}} \,. \tag{3.40}$$

To control the lower order term appearing on the right-hand side of the estimate (3.38), we first define the set $\Omega' = \{x \in \Omega \,:\, |D\phi(x) - \mathbb{1}| < r_{\mathcal{W}}\}$. Then, by using (W1) and (W4) we obtain

$$|\Omega \backslash \Omega'| C_{\mathrm{W},2} \leq \int_\Omega \mathrm{W}(D\phi) \,\mathrm{d}x \leq \overline{\mathcal{W}} \,,$$

which implies $|\Omega \backslash \Omega'| \leq \frac{\overline{\mathcal{W}}}{C_{\mathrm{W},2}}$. Hence, by taking into account the embedding $H^m(\Omega) \hookrightarrow C^1(\overline{\Omega})$ as well as (3.40) one can deduce

$$\begin{aligned} \int_\Omega |(D\phi)^{\mathrm{sym}} - \mathbb{1}|^2 \,\mathrm{d}x &= \int_{\Omega'} |(D\phi)^{\mathrm{sym}} - \mathbb{1}|^2 \,\mathrm{d}x + \int_{\Omega \backslash \Omega'} |(D\phi)^{\mathrm{sym}} - \mathbb{1}|^2 \,\mathrm{d}x \\ &\leq \int_\Omega \frac{\mathrm{W}(D\phi)}{C_{\mathrm{W},1}} \,\mathrm{d}x + |\Omega \backslash \Omega'| \left(C + C\sqrt{\overline{\mathcal{W}}}\right)^2 \leq \frac{\overline{\mathcal{W}}}{C_{\mathrm{W},1}} + \frac{\overline{\mathcal{W}}}{C_{\mathrm{W},2}} \left(C + C\overline{\mathcal{W}}\right) \,. \end{aligned} \tag{3.41}$$

By applying Korn's inequality 1.1.3 one can deduce that the left-hand side of (3.41) is an upper bound for $\|\phi - \mathbb{1}\|^2_{L^2(\Omega)}$. Thus, the lemma follows by combining (3.38), (3.39) and (3.41). □

In what follows, we solely highlight the differences to the proof of (i.). Let $\{\phi^j\}_{j \in \mathbb{N}} \subset H^m(\Omega)$ be a minimizing sequence such that $\phi^j \rightharpoonup \phi$ in $H^m(\Omega)$ and $\phi^j \to \phi$ in $C^{1,\alpha}(\overline{\Omega})$ for $\alpha \in (0, m - 1 - \frac{n}{2})$ (see (i.)). Then, Lemma 3.4.3, (3.29) and $H^m(\Omega) \hookrightarrow C^1(\overline{\Omega})$ imply

$$\|\phi^j - \mathbb{1}\|_{C^1(\overline{\Omega})} \leq C\|\phi^j - \mathbb{1}\|_{H^m(\Omega)} \leq C\theta(\mathcal{W}^D[u, \tilde{u}, \phi^j]) \leq C\theta(\overline{\mathbf{W}}) \,,$$

where $\overline{\mathbf{W}} = \frac{1}{\delta}\|\tilde{u} - u\|^2_{L^2(\Omega)} \leq \frac{C^2_{\mathcal{W}}}{\delta}$. Thus, by choosing $C_{\mathcal{W}}$ sufficiently small we can assume

$$\|\det(D\phi^j) - 1\|_{L^\infty(\Omega)} \leq C_{\mathrm{det}} \tag{3.42}$$

for a constant $C_{\mathrm{det}} \in (0, 1)$ and all j sufficiently large. By combining (3.42) and Theorem 3.4.1 (i.) one can immediately deduce that the limiting deformation ϕ belongs to $\mathcal{A}$ and is $C^1(\Omega)$-diffeomorphic.

Claim: The matching functional $\|\tilde{u} \circ \phi^j - u\|_{L^2(\Omega)}$ converges to $\|\tilde{u} \circ \phi - u\|_{L^2(\Omega)}$ as $j \to \infty$.

As in the proof of (i.), we approximate $\tilde{u}$ by smooth functions and use the decomposition (3.32). It essentially remains to verify the convergence of $\|\tilde{u} \circ \phi^j - \tilde{u}_i \circ \phi^j\|_{L^2(\Omega)}$ to 0 for $i \to \infty$ and all j. To this end, we apply

the transformation formula and by taking into account (3.42) and the diffeomorphism property of ϕ^j we can infer for any j sufficiently large

$$\|\tilde{u} \circ \phi^j - \tilde{u}_i \circ \phi^j\|^2_{L^2(\Omega)} \leq \|\det(D(\phi^j)^{-1})\|_{L^\infty(\Omega)} \|\tilde{u} - \tilde{u}_i\|^2_{L^2(\Omega)} \leq \frac{1}{1 - C_{\det}} \|\tilde{u} - \tilde{u}_i\|^2_{L^2(\Omega)} .$$

The convergence proof for $\|\tilde{u} \circ \phi - \tilde{u}_i \circ \phi\|_{L^2(\Omega)}$ is nearly identical, which proves this claim.

The proof of the lower semicontinuity of the discrete energy along the sequence ϕ^j proceeds in exactly the same way as the corresponding proof in (i.), which implies (ii.).

This proves the proposition. □

Remark 3.4.4. Proposition 3.4.2 guarantees the existence of an admissible vector of deformations $\mathbf{\Phi} \in \mathcal{A}^K$ such that $\mathbf{E}^D_K[\mathbf{u}, \mathbf{\Phi}] = \mathbf{E}_K[\mathbf{u}]$ provided that each pair of images (u_k, u_{k+1}) contained in $\mathbf{u} = (u_0, \dots, u_K) \in \mathcal{I}^{K+1}$ satisfies the assumptions of this proposition. If the images $u_0, \dots, u_K$ are additionally weakly differentiable, the corresponding system of Euler–Lagrange equations for ϕ_k is given by

$$\int_\Omega D\mathrm{W}(D\phi_k) : D\psi + 2\gamma D^m \phi_k : D^m \psi + \frac{2}{\delta}(u_k \circ \phi_k - u_{k-1})(\nabla u_k \circ \phi_k) \cdot \psi \, \mathrm{d}x = 0$$

for all $1 \leq k \leq K$ and all test deformations $\psi \in H^m(\Omega, \Omega)$, which is a system of nonlinear partial differential equations of order $2m$.

Before we discuss the existence of discrete geodesics, we first present a partial result, which can be regarded as a counterpart of Proposition 3.4.2 because it establishes the existence of an energy minimizing vector of images $\mathbf{u}$ for a given vector of deformations $\mathbf{\Phi}$. The proof of this partial existence result relies on some fundamental properties of irreducibly diagonally dominant matrices (see [HJ90, Chapter 6]) to be presented below.

Definition 3.4.5 (Irreducible matrix)**.** A matrix $A \in \mathbb{R}^{n,n}$, $n \geq 2$, is said to be *reducible* if a permutation matrix $P \in \mathbb{R}^{n,n}$ as well as an integer $r \in \{1, \dots, n-1\}$ exists such that

$$P^T A P = \begin{bmatrix} A_1 & A_2 \\ N & A_3 \end{bmatrix}$$

for matrices $A_1 \in \mathbb{R}^{r,r}$, $A_2 \in \mathbb{R}^{r,n-r}$, $A_3 \in \mathbb{R}^{n-r,n-r}$, and the null matrix $N \in \mathbb{R}^{n-r,r}$. A not reducible matrix is *irreducible*.

Definition 3.4.6 (Irreducibly diagonally dominant matrix)**.** A matrix $A = (A_{i,j})_{1 \leq i,j \leq n} \in \mathbb{R}^{n,n}$, $n \geq 2$, is *irreducibly diagonally dominant* if A is irreducible and

$$|A_{i,i}| \geq \sum_{j=1, j \neq i}^{n} |A_{i,j}| \quad \text{for all } 1 \leq i \leq n ,$$

where a strict inequality holds true for at least one row index.

Proposition 3.4.7. *Every irreducibly diagonally dominant matrix $A \in \mathbb{R}^{n,n}$ is invertible.*

Proof. See [HJ90, Corollary 6.2.27]. □

Proposition 3.4.8. *Let $K \geq 2$ and assume that (W1) is valid. Furthermore, we fix the vector of deformations $\mathbf{\Phi} = (\phi_1, \dots, \phi_K) \in \mathcal{A}^K$.*

(i.) Let $u_A, u_B \in \mathcal{I} := L^\infty(\Omega)$. Then, there exists a unique vector of images $\mathbf{u} = (u_0, \dots, u_K) \in (L^\infty(\Omega))^{K+1}$ with $u_0 = u_A$ and $u_K = u_B$ such that

$$\mathbf{E}^D_K[\mathbf{u}, \mathbf{\Phi}] = \inf \left\{ \mathbf{E}^D_K[(u_A, \hat{\mathbf{u}}, u_B), \mathbf{\Phi}] \, : \, \hat{\mathbf{u}} \in \mathcal{I}^{K-1} \right\} . \tag{3.43}$$

Moreover, each inner image u_k, $1 \leq k \leq K-1$, is uniformly bounded in $L^\infty(\Omega)$ by a constant solely depending on $\|u_A\|_{L^\infty(\Omega)}$ and $\|u_B\|_{L^\infty(\Omega)}$.

(ii.) Let $u_A, u_B \in \mathcal{I} := L^2(\Omega)$ *and*

$$\min_{k\in\{1,\dots,K\}} \inf_{x\in\overline{\Omega}} \det(D\phi_k(x)) \geq C_{\det} \tag{3.44}$$

for a constant $C_{\det} > 0$*. Then the unique minimizer* $\mathbf{u} = (u_0, \dots, u_K) \in (L^2(\Omega))^{K+1}$ *with* $u_0 = u_A$ *and* $u_K = u_B$ *of the variational problem* (3.43) *is attained.*

Proof. We define for $x \in \Omega$ the *discrete transport path* $X(x) = (X_0(x), \dots, X_K(x))^T \in \Omega^{K+1}$ via $X_0(x) = x$ and $X_k(x) = \phi_k(X_{k-1}(x))$ for $k \in \{1, \dots, K\}$, and note that the diffeomorphic discrete transport path describes the temporal evolution of the image particle x.

ad (i.): Consider the minimizing sequence $\hat{\mathbf{u}}^j = (u_1^j, \dots, u_{K-1}^j) \in (L^2(\Omega))^{K-1}$ for the energy

$$\mathcal{I}^{K-1} \ni \hat{\mathbf{v}} \mapsto \mathbf{E}_K^D[(u_A, \hat{\mathbf{v}}, u_B), \mathbf{\Phi}]$$

such that

$$\begin{aligned} 0 &\leq \inf_{\tilde{\mathbf{u}}\in(L^2(\Omega))^{K-1}} \mathbf{E}_K^D[(u_A, \tilde{\mathbf{u}}, u_B), \mathbf{\Phi}] \leq \mathbf{E}_K^D[(u_A, \hat{\mathbf{u}}^j, u_B), \mathbf{\Phi}] \\ &\leq \mathbf{E}_K^D[(u_A, (u_A, \dots, u_A), u_B), \mathbf{\Phi}] =: \overline{\mathbf{E}_K^D}\,. \end{aligned}$$

The upper bound $\overline{\mathbf{E}_K^D}$ is finite since

$$\begin{aligned} \overline{\mathbf{E}_K^D} &= K \sum_{k=1}^{K} \int_\Omega \mathrm{W}(D\phi_k) + \gamma |D^m \phi_k|^2 \,\mathrm{d}x \\ &\quad + \frac{K}{\delta} \left(\sum_{k=1}^{K-1} \|u_A \circ \phi_k - u_A\|_{L^2(\Omega)}^2 + \|u_B \circ \phi_K - u_A\|_{L^2(\Omega)}^2 \right) \\ &\leq CK \sum_{k=1}^{K} \left(\|\mathrm{W}(D\phi_k)\|_{L^\infty(\Omega)} + \|\phi_k\|_{H^m(\Omega)}^2 \right) + CK^2 (\|u_A\|_{L^\infty(\Omega)} + \|u_B\|_{L^\infty(\Omega)})^2 < \infty\,. \end{aligned}$$

Next, we prove that each image u_k is uniformly bounded in $L^\infty(\Omega)$. The definition of the set $\mathcal{A}$ as well as the proof of Proposition 3.4.2 imply that each deformation $\phi_k \in H^m(\Omega) \hookrightarrow C^1(\overline{\Omega})$ is a homeomorphism with $\phi_k, \phi_k^{-1} \in W^{1,q}(\Omega)$, $q > n$, and $|\phi_k(N)| = 0$ as well as $|\phi_k^{-1}(N)| = 0$ for all Lebesgue null sets $N \subset \Omega$ using an analogous reasoning as in (3.35). Hence, one can verify by comparison arguments that for the optimal images u_k the inequality

$$|u_k(x)| \leq g_k(x) = \max\{|u_A \circ \phi_1^{-1} \circ \cdots \circ \phi_k^{-1}(x)|, |u_B \circ \phi_K \circ \cdots \circ \phi_{k+1}(x)|\}$$

must hold true for a.e. $x \in \Omega$ and for all $k \in \{1, \dots, K-1\}$. Since $\|g_k\|_{L^\infty(\Omega)} < \infty$ for all k considered, we can replace each image u_k^j in the minimizing sequence by $\max\{\min\{u_k^j(x), g_k(x)\}, -g_k(x)\}$, which possibly reduces the energy, and infer the uniform boundedness of $\hat{\mathbf{u}}^j$ in $(L^\infty(\Omega))^{K-1}$. Thus, there exists a weakly convergent subsequence in $(L^2(\Omega))^{K-1}$ with weak limit $\hat{\mathbf{u}} \in (L^2(\Omega))^{K-1}$. Next, we derive the Euler–Lagrange equations for the inner images, which – as a byproduct – lead to an update formula for these inner images for fixed deformations that will later be employed in the optimization algorithm. By applying the transformation formula to the sum of consecutive matching functionals one can infer for $k \in \{1, \dots, K-1\}$

$$\int_\Omega (u_k \circ \phi_k - u_{k-1})^2 + (u_{k+1} \circ \phi_{k+1} - u_k)^2 \,\mathrm{d}x = \int_\Omega \frac{(u_k - u_{k-1} \circ \phi_k^{-1})^2}{\det(D\phi_k) \circ \phi_k^{-1}} + (u_{k+1} \circ \phi_{k+1} - u_k)^2 \,\mathrm{d}x\,.$$

Note that this functional is strictly convex in u_k. Thus, the Euler–Lagrange equation $\partial_{u_k} \mathbf{E}_K^D[\mathbf{u}, \mathbf{\Phi}](v) = 0$ for $\mathbf{u} = (u_A, \hat{\mathbf{u}}, u_B)$, $k \in \{1, \dots, K-1\}$ and any $v \in L^\infty(\Omega)$ results in the pointwise condition

$$\frac{u_k - u_{k-1} \circ \phi_k^{-1}}{(\det D\phi_k) \circ \phi_k^{-1}} + u_k - u_{k+1} \circ \phi_{k+1} = 0 \quad \text{a.e. in } \Omega\,,$$

which is equivalent to

$$u_k(x) = \frac{u_{k+1} \circ \phi_{k+1}(x) + (u_{k-1} \circ \phi_k^{-1}(x))((\det D\phi_k)^{-1} \circ \phi_k^{-1}(x))}{1 + (\det D\phi_k)^{-1} \circ \phi_k^{-1}(x)} \tag{3.45}$$

for a.e. $x \in \Omega$. All equations of the form (3.45) can be rewritten as the following block tridiagonal linear system of equations, in which evaluations of the images at deformed positions are combined with evaluations at non-deformed positions:

$$A[\mathbf{\Phi}](x)U(\hat{\mathbf{u}}, \mathbf{\Phi})(x) = R[\mathbf{\Phi}](x) \quad \text{for a.e. } x \in \Omega\,. \tag{3.46}$$

In this case, $U(\hat{\mathbf{u}}, \mathbf{\Phi})$ is the vector of intensity values

$$U(\hat{\mathbf{u}}, \mathbf{\Phi})(x) = (u_1(X_1(x)), u_2(X_2(x)), \dots, u_{K-1}(X_{K-1}(x)))^T \in \mathbb{R}^{K-1}\,, \tag{3.47}$$

$A[\mathbf{\Phi}](x) \in \mathbb{R}^{K-1,K-1}$ is a tridiagonal matrix with

$$(A[\mathbf{\Phi}](x))_{k,k+1} = -\frac{1}{1 + (\det D\phi_k)^{-1} \circ \phi_k^{-1}(X_k(x))} = -\frac{1}{1 + (\det D\phi_k)^{-1}(X_{k-1}(x))}\,,$$

$$(A[\mathbf{\Phi}](x))_{k,k} = 1\,,$$

$$(A[\mathbf{\Phi}](x))_{k,k-1} = -\frac{(\det D\phi_k)^{-1} \circ \phi_k^{-1}(X_k(x))}{1 + (\det D\phi_k)^{-1} \circ \phi_k^{-1}(X_k(x))} = -\frac{(\det D\phi_k)^{-1}(X_{k-1}(x))}{1 + (\det D\phi_k)^{-1}(X_{k-1}(x))}\,,$$

and $R[\mathbf{\Phi}](x) \in \mathbb{R}^{K-1}$ is given by

$$R[\mathbf{\Phi}](x) = \left(\frac{u_A(x)(\det D\phi_1)^{-1}(x)}{1 + (\det D\phi_1)^{-1}(x)}\,, 0\,, \dots\,, 0\,, \frac{u_B(X_K(x))}{1 + (\det D\phi_{K-1})^{-1}(X_{K-2}(x))}\right)^T.$$

Since $\det(D\phi_k(x)) > 0$ for $k = 1, \dots, K$ and a.e. $x \in \Omega$, we can infer that $A[\mathbf{\Phi}](x)$ is irreducibly diagonally dominant for a.e. $x \in \Omega$, which already proves the invertibility of this matrix using Proposition 3.4.7. To sum up, for a.e. $x \in \Omega$ there exists a unique solution $U(\hat{\mathbf{u}}, \mathbf{\Phi})(x)$ to (3.46).

ad (ii.): If $\mathcal{I} = L^2(\Omega)$, we only have to show $\overline{\mathbf{E}}_K = \mathbf{E}_K^D[(u_A, (u_A, \dots, u_A), u_B), \mathbf{\Phi}] < \infty$ and the uniform boundedness of the minimizing sequence in $(L^2(\Omega))^{K-1}$, the rest of the proof is analogous to the proof of (i.). The boundedness of $\overline{\mathbf{E}}_K$ follows from

$$\begin{aligned}\overline{\mathbf{E}_K^D} &= K\left(\sum_{k=1}^{K}\int_\Omega \mathrm{W}(D\phi_k) + \gamma|D^m\phi_k|^2\,\mathrm{d}x\right)\\ &\quad + \frac{K}{\delta}\left(\sum_{k=1}^{K-1}\|u_A \circ \phi_k - u_A\|_{L^2(\Omega)}^2 + \|u_B \circ \phi_K - u_A\|_{L^2(\Omega)}^2\right)\\ &\leq CK\sum_{k=1}^{K}\left(\|\mathrm{W}(D\phi_k)\|_{L^\infty(\Omega)} + \|\phi_k\|_{H^m(\Omega)}^2\right) + CK^2\left((1 + C_{\det}^{-\frac{1}{2}})\|u_A\|_{L^2(\Omega)} + C_{\det}^{-\frac{1}{2}}\|u_B\|_{L^2(\Omega)}\right)^2,\end{aligned}$$

where we used the transformation formula in combination with (3.44). Furthermore, by taking into account (3.44), we can infer

$$\|u_k^j\|_{L^2(\Omega)} \leq \|u_{k+1}^j \circ \phi_{k+1} - u_k^j\|_{L^2(\Omega)} + \|u_{k+1}^j \circ \phi_{k+1}\|_{L^2(\Omega)} \leq \sqrt{\tfrac{\delta\overline{\mathbf{E}}_K}{K}} + C_{\det}^{-\frac{1}{2}}\|u_{k+1}^j\|_{L^2(\Omega)}\,.$$

Thus, an induction argument (starting from $k = K-1$) shows that $\hat{\mathbf{u}}^j = (u_1^j, \dots, u_{K-1}^j)$ is uniformly bounded in $(L^2(\Omega))^{K-1}$ independently of j.

This proves the proposition. □

Remark 3.4.9 (Inherited regularity). If $u_A, u_B \in C^{0,\alpha}(\overline{\Omega})$ for $\alpha \in (0, m-1-\frac{n}{2})$, then the proof of Proposition 3.4.8 also shows that $\hat{\mathbf{u}} \in (C^{0,\alpha}(\overline{\Omega}))^{K-1}$.

Remark 3.4.10. The intensity values along the discrete transport path $X(x)$ depend in a unique way on the values at the two end points x and $X_K(x)$. Furthermore, each image intensity value $u_k(X_k(x))$ is a weighted average of the intensities $u_A(x)$ and $u_B(X_K(x))$, where the weights reflect the compression and expansion associated with the deformations along the discrete transport paths.

As announced above, the existence of discrete geodesics can be deduced by combining Proposition 3.4.2 and Proposition 3.4.8.

Theorem 3.4.11 (Existence of discrete geodesics)**.** *Let $K \geq 2$.*

(i.) Let $u_A, u_B \in \mathcal{I} := L^\infty(\Omega)$ and assume that (W1) and (W2) hold true. Then there exists $\hat{\mathbf{u}} \in (L^\infty(\Omega))^{K-1}$ such that

$$\mathbf{E}_K[(u_A, \hat{\mathbf{u}}, u_B)] = \inf_{\hat{\mathbf{v}} \in (L^\infty(\Omega))^{K-1}} \mathbf{E}_K[(u_A, \hat{\mathbf{v}}, u_B)]$$

and the associated minimizing deformations are homeomorphic.

(ii.) Let $u_A \in \mathcal{I} := L^2(\Omega)$. If (W1) and (W4) are valid, then a constant $C_{\mathbf{E}} > 0$ exists, which is independent of K, such that for every

$$u_B \in \left\{ v \in L^2(\Omega) \,:\, \|v - u_A\|_{L^2(\Omega)} < C_{\mathbf{E}} \sqrt{K} \right\} \tag{3.48}$$

a minimizer $\hat{\mathbf{u}} \in (L^2(\Omega))^{K-1}$ of

$$\mathbf{E}_K[(u_A, \hat{\mathbf{u}}, u_B)] = \inf_{\hat{\mathbf{v}} \in (L^2(\Omega))^{K-1}} \mathbf{E}_K[(u_A, \hat{\mathbf{v}}, u_B)]$$

exists and the minimizing deformations are diffeomorphic.

Proof. Let $\bar{u}_k = \frac{k}{K} u_B + (1 - \frac{k}{K}) u_A \in L^2(\Omega)$ be a convex combination of the input images for $k \in \{0, \dots, K\}$. We first note that

$$\overline{\mathbf{E}}_K := \mathbf{E}_K^D[(\bar{u}_0, \bar{u}_1, \dots, \bar{u}_K), (\mathbb{1}, \dots, \mathbb{1})] = \frac{1}{\delta} \|u_B - u_A\|^2_{L^2(\Omega)} \tag{3.49}$$

is a finite upper bound of the energy.

ad (i.): Let $\{(\hat{\mathbf{u}}^j, \mathbf{\Phi}^j) = ((u_1^j, \dots, u_{K-1}^j), (\phi_1^j, \dots, \phi_K^j))\}_{j \in \mathbb{N}} \subset (L^2(\Omega))^{K-1} \times \mathcal{A}^K$ be a minimizing sequence for the energy

$$(L^2(\Omega))^{K-1} \times \mathcal{A}^K \ni (\hat{\mathbf{v}}, \mathbf{\Phi}) \mapsto \mathbf{E}_K^D[(u_A, \hat{\mathbf{v}}, u_B), \mathbf{\Phi}]$$

with finite upper bound $\overline{\mathbf{E}}_K$. Since each deformation ϕ_k^j is contained in $H^m(\Omega, \Omega)$ and satisfies the coercivity estimate $|\phi_k^j|^2_{H^m(\Omega)} \leq \frac{\overline{\mathbf{E}}_K}{\gamma}$, the Gagliardo–Nirenberg inequality (see Theorem 1.1.2) implies that all deformations $\{\phi_k^j\}$ are uniformly bounded in $H^m(\Omega)$ for all $k = 1, \dots, K$ and all j. Moreover, by replacing $\hat{\mathbf{u}}^j$ with the (unique) minimizer of

$$(L^2(\Omega))^{K-1} \ni \hat{\mathbf{u}} \mapsto \mathbf{E}_K^D[(u_A, \hat{\mathbf{u}}, u_B), \mathbf{\Phi}^j]\,,$$

which possibly reduces the energy (see Proposition (3.4.8) (i.)), we can assume that $\hat{\mathbf{u}}^j$ is uniformly bounded in $(L^\infty(\Omega))^{K-1}$ independently of j. By passing to subsequences (labeled in the same way) we can additionally assume that $\hat{\mathbf{u}}^j \rightharpoonup \hat{\mathbf{u}} = (u_1, \dots, u_{K-1})$ weakly in $(L^2(\Omega))^{K-1}$, $\mathbf{\Phi}^j \rightharpoonup \mathbf{\Phi} = (\phi_1, \dots, \phi_K)$ weakly in $(H^m(\Omega))^K$ and $\mathbf{\Phi}^j \to \mathbf{\Phi}$ in $(C^{1,\alpha}(\overline{\Omega}))^K$ due to the embedding $H^m(\Omega) \hookrightarrow C^{1,\alpha}(\overline{\Omega})$ for $0 < \alpha < m - 1 - \frac{n}{2}$. By taking into account Proposition 3.4.2 it is clear that $\det(D\phi_k^j) > 0$ a.e. in Ω, $\phi_k^j \in \mathcal{A}$ and ϕ_k^j are homeomorphisms for $k = 1, \dots, K$ and all $j \in \mathbb{N}$, the same assertions apply to the limiting deformations $\{\phi_k\}_{1 \leq k \leq K}$.

Claim:

$$\sum_{k=1}^K \int_\Omega (u_k \circ \phi_k - u_{k-1})^2 \,\mathrm{d}x \leq \liminf_{j \to \infty} \sum_{k=1}^K \int_\Omega (u_k^j \circ \phi_k^j - u_{k-1}^j)^2 \,\mathrm{d}x\,.$$

To prove the claim, we define for $x \in \Omega$ the discrete transport paths (*cf*. the proof of Proposition 3.4.8) as follows:

$$X^j(x) = (X_0^j(x), \dots, X_K^j(x))^T \quad \text{s.t. } X_0^j(x) = x\,, X_k^j(x) = \phi_k^j(X_{k-1}^j(x)) \quad \text{for } k \in \{1, \dots, K\}\,,$$

the limiting transport path X is defined analogously. Taking into account the optimality of $\hat{\mathbf{u}}^j$ and (3.46) we can infer due to the uniqueness of this image vector

$$u_k^j(X_k^j(x)) = ((A[\mathbf{\Phi}^j]^{-1} R[\mathbf{\Phi}^j])(x))_k \quad \text{for a.e. } x \in \Omega\,. \tag{3.50}$$

Choose $\varepsilon > 0$. Let $S_\varepsilon \subset \Omega$ be an open set such that $|S_\varepsilon| < \varepsilon$ and for all j sufficiently large and $k \in \{1, \dots, K\}$

$$\det(D\phi_k^j(X_{k-1}^j(x))) > c_\varepsilon\,, \quad \det(A[\mathbf{\Phi}^j](x)) > c_\varepsilon \qquad \forall x \in \Omega \backslash S_\varepsilon \tag{3.51}$$

for a constant $c_\varepsilon > 0$ (depending on ε) holds true. Indeed, this is clearly possible due to the strong convergence of $\mathbf{\Phi}^j$ to $\mathbf{\Phi}$ in $(C^{1,\alpha}(\overline{\Omega}))^K$, (3.30) and the irreducible diagonal dominance of $A[\mathbf{\Phi}^j](x)$ for a.e. $x \in \Omega$. Hence, $(A[\mathbf{\Phi}^j])^{-1}$ converges uniformly to $(A[\mathbf{\Phi}])^{-1}$ in $\Omega \backslash S_\varepsilon$. Moreover, following the same line of arguments as in the proof of Proposition 3.4.2 (*cf*. (3.32)) one can deduce that $u_B(X_K^j)$ converges to $u_B(X_K)$ in $L^2(\Omega \backslash S_\varepsilon)$. By incorporating Proposition 3.4.8 and (3.50) this already implies the convergence of $R[\mathbf{\Phi}^j]$ to $R[\mathbf{\Phi}]$ in $(L^2(\Omega \backslash S_\varepsilon))^{K-1}$ and thus the convergence of $u_k^j(X_k^j)$ to $u_k(X_k)$ in $L^2(\Omega \backslash S_\varepsilon)$ for $k \in \{1, \dots, K-1\}$. Since the Lebesgue measure of the set S_ε can be chosen arbitrarily small and $\{\hat{\mathbf{u}}^j\}_{j \in \mathbb{N}} \subset (L^\infty(\Omega))^{K-1}$, we can even infer the L^2-convergence of $u_k^j(X_k^j)$ to $u_k(X_k)$ on the entire domain Ω. Hence,

$$\begin{aligned}
&\left| \int_\Omega (u_k^j)^2 - u_k^2 \,\mathrm{d}x \right| = \left| \int_\Omega (u_k^j(X_k^j))^2 \det(DX_k^j) - (u_k(X_k))^2 \det(DX_k)\,\mathrm{d}x \right| \\
&\leq \left| \int_\Omega \left((u_k^j(X_k^j))^2 - (u_k(X_k))^2 \right) \det(DX_k^j)\,\mathrm{d}x \right| + \left| \int_\Omega (u_k(X_k^j))^2 (\det(DX_k^j) - \det(DX_k))\,\mathrm{d}x \right|\,,
\end{aligned}$$

which vanishes for $j \to \infty$. We recall that the weak convergence in $L^2(\Omega)$ and the convergence of the $L^2(\Omega)$-norms already imply the (strong) $L^2(\Omega)$-convergence (see [AF03]), which shows $\hat{\mathbf{u}}^j \to \hat{\mathbf{u}}$ in $(L^2(\Omega))^{K-1}$. Now, the claim readily follows from the strong convergence of the deformations and the images in $C^{1,\alpha}(\overline{\Omega})$ and $L^2(\Omega)$, respectively, following an analogous line of arguments as above. We omit further details.

Finally, because $\phi \mapsto \int_\Omega \mathrm{W}(D\phi) + \gamma |D^m \phi|^2 \,\mathrm{d}x$ is weakly lower semicontinuous along the sequence ϕ_k^j for each k due to (W1) and Proposition 3.2.6, we obtain

$$\mathbf{E}_K[u_A, \hat{\mathbf{u}}, u_B] = \mathbf{E}_K^D[(u_A, \hat{\mathbf{u}}, u_B), \mathbf{\Phi}] \leq \liminf_{j \to \infty} \mathbf{E}_K^D[(u_A, \hat{\mathbf{u}}^j, u_B), \mathbf{\Phi}^j] = \liminf_{j \to \infty} \mathbf{E}_K[u_A, \hat{\mathbf{u}}^j, u_B]\,.$$

This proves (i.).

ad (ii.): As before, consider a minimizing sequence $\{(\hat{\mathbf{u}}^j, \mathbf{\Phi}^j)\}_{j \in \mathbb{N}} \subset (L^2(\Omega))^{K-1} \times \mathcal{A}^K$ for the discrete path energy $(\hat{\mathbf{u}}, \mathbf{\Phi}) \mapsto \mathbf{E}_K^D[(u_A, \hat{\mathbf{u}}, u_B), \mathbf{\Phi}]$ with finite upper bound $\overline{\mathbf{E}}_K = \frac{1}{\delta} \|u_B - u_A\|_{L^2(\Omega)}^2$ (see (3.49)). Then,

$$\sup_{j \in \mathbb{N}} \max_{k \in \{1, \dots, K\}} \mathcal{W}^D[u_{k-1}^j, u_k^j, \phi_k^j] \leq \sup_{j \in \mathbb{N}} \frac{1}{K} \mathbf{E}_K^D[(u_A, \hat{\mathbf{u}}^j, u_B), \mathbf{\Phi}^j] \leq \frac{1}{K\delta} \|u_B - u_A\|_{L^2(\Omega)}^2 \leq \frac{C_{\mathbf{E}}}{\delta}$$

for a constant $C_{\mathbf{E}} > 0$ to be specified below. By taking into account Lemma 3.4.3 as well as the embedding $H^m(\Omega) \hookrightarrow C^1(\overline{\Omega})$ we can conclude

$$\inf_{j \geq j_0} \min_{k \in \{1, \dots, K\}} \inf_{x \in \overline{\Omega}} \det(D\phi_k^j(x)) > C_{\det} \tag{3.52}$$

for a constant $C_{\det} > 0$ and $j_0 \in \mathbb{N}$ sufficiently large provided that u_B is sufficiently close to u_A, which is guaranteed by suitably adapting $C_{\mathbf{E}}$. Proposition 3.4.2 (ii.) guarantees the existence of an optimal deformation vector $\mathbf{\Phi}^j$ associated with $\hat{\mathbf{u}}^j$. Next, we replace the vector $\hat{\mathbf{u}}^j$ by the unique optimal inner vector

of images associated with $\mathbf{\Phi}^j$ (that we also denote by $\hat{\mathbf{u}}^j$), which possibly reduces the energy (see Proposition 3.4.8). In what follows, we solely comment on the lower semicontinuity of the matching functional along the minimizing sequence, the rest of the proof of (ii.) proceeds in nearly the same way as the proof of (i.).

Claim:

$$\sum_{k=1}^{K} \int_\Omega (u_k \circ \phi_k - u_{k-1})^2 \,\mathrm{d}x \leq \liminf_{j\to\infty} \sum_{k=1}^{K} \int_\Omega (u_k^j \circ \phi_k^j - u_{k-1}^j)^2 \,\mathrm{d}x\,.$$

The proof of the claim is nearly identical to the corresponding proof in (i.) since due to (3.52) we can conclude that (3.51) is satisfied for all $x \in \Omega$ and all j sufficiently large provided that $c_\varepsilon > 0$ is appropriately chosen. Furthermore, $u_B(X_K^j)$ converges to $u_B(X_K)$ in $L^2(\Omega)$, which follows by the same line of arguments as in the proof of Proposition 3.4.2 (ii.). We omit further details.

This proves the theorem. □

3.5 Convergence of Discrete Geodesic Paths

The main result of this section is the proof of the Mosco-convergence of a suitable interpolation of the time discrete metamorphosis functional (3.16) to the continuous functional (3.7).

To this end, the definition and some basic properties of Γ-convergence and Mosco-convergence are briefly presented (Subsection 3.5.1). Afterwards, we rigorously define the time interpolation $\mathcal{E}_K$ of the time discrete functional $\mathbf{E}_K$ and give the precise statement of the Mosco-convergence for the metamorphosis model, which suffices to establish the existence of a minimizer of the continuous metamorphosis model in an alternative way (Subsection 3.5.2). The proof of the Mosco-convergence is postponed to the final Subsection 3.5.3.

3.5.1 Foundations of Γ- and Mosco-convergence

Γ-convergence can be regarded as a notion of convergence for variational problems, which is particularly designed to establish the convergence of minimizers. In this subsection, we introduce the concepts of Γ- and Mosco-convergence in the case of metric spaces and present a few basic properties. The references for this short exposition are [DM93, Bra06, Mos69].

Definition 3.5.1 (Γ- and Mosco-convergence in metric spaces)**.** Let (X, d) be a metric space and let $\{J_k\}_{k\in\mathbb{N}}$ and J be functionals mapping from X to $\overline{\mathbb{R}}$. Then, the sequence J_k is said to Γ-*converge to* J *w.r.t. the topology induced by* d if the following conditions are satisfied:

(i.) for every $x \in X$ and for every sequence $\{x_k\}_{k\in\mathbb{N}} \subset X$, that converges to x in X, the $\liminf$-*inequality*

$$J[x] \leq \liminf_{k\to\infty} J_k[x_k]$$

holds true, and

(ii.) for every $x \in X$ there exists a sequence $\{x_k\}_{k\in\mathbb{N}} \subset X$ (*recovery sequence*) converging to x in X such that

$$J[x] = \lim_{k\to\infty} J_k[x_k]\,.$$

If instead of (i.) the weaker condition

(i.') for every $x \in X$ and for every sequence $\{x_k\}_{k\in\mathbb{N}} \subset X$, that *weakly* converges to x in X, one has

$$J[x] \leq \liminf_{k\to\infty} J_k[x_k]$$

holds true, then J_k is said to converge to J in the sense of *Mosco*.

Definition 3.5.2. A subset $K \subset X$ of a metric space (X, d) is *countably compact* if every sequence $\{x_k\}_{k\in\mathbb{N}} \subset K$ has at least one cluster point $x \in K$. A sequence of functionals $\{J_k\}_{k\in\mathbb{N}}$, $J_k : X \to \overline{\mathbb{R}}$, is *equi-coercive* on X if for every $t \in \mathbb{R}$ there exists a closed countably compact set $K \subset X$ such that for all $k \in \mathbb{N}$

$$\{\, x \in X \,:\, J_k[x] \leq t \,\} \subset K\,.$$

A more practical characterization of equi-coercivity is phrased in the following proposition:

Proposition 3.5.3. *Let (X, d) be a metric space. A sequence $\{J_k : X \to \overline{\mathbb{R}}\}_{k\in\mathbb{N}}$ is equi-coercive if and only if there exists a coercive and lower semicontinuous functional $\tilde{J} : X \to \overline{\mathbb{R}}$ such that $J_k \geq \tilde{J}$ for all $k \in \mathbb{N}$.*

Proof. See [DM93, Proposition 7.7]. □

The following theorem relates the infimum of the approximate functionals J_k to the minimum of the limiting functional J:

Theorem 3.5.4. *Let (X, d) be a metric space. Suppose that $\{J_k : X \to \overline{\mathbb{R}}\}_{k\in\mathbb{N}}$ is a sequence of equi-coercive functionals that Γ-converges to $J : X \to \overline{\mathbb{R}}$ in X. Then J is coercive and*

$$\min_{x\in X} J[x] = \lim_{k\to\infty} \inf_{x\in X} J_k[x]\,.$$

Proof. See [DM93, Theorem 7.8]. □

A nice characterization of Mosco-convergence exists if the sequence of functionals $\{J_k\}_{k\in\mathbb{N}}$ as well as the limiting functional J are proper, convex and lower-semicontinuous. In this case, the Mosco-convergence of J_k to J is equivalent to the pointwise convergence of the Moreau–Yosida envelopes of J_k to the Moreau–Yosida envelope of J, which was proven in the case of Hilbert spaces by Attouch [Att84] and in the case of Hadamard spaces by Bačák *et al*. [BMS17].

3.5.2 Mosco-convergence of the Time Discrete Metamorphosis Model

In what follows, we will introduce a natural temporal extension $\mathcal{E}_K$ of the discrete variational model $\mathbf{E}_K$ (see (3.16)) and prove the Mosco-convergence to the limiting functional $\mathcal{E}$ (*cf*. (3.7)). One key observation of the proof stems from the fact that the sum of the spatial integrals of $K(u_k \circ \phi_k - u_{k-1})$ corresponds to the time discrete material derivative along the discrete motion path and converges to the weak material derivative z. Furthermore, as a consequence of the Assumption (W3) we will see that the properly rescaled and spatially integrated energy density W converges to the integrated first two summands of L (see (3.1)) reflecting the dissipation density in a Newtonian fluid.

Before presenting the rigorous definition of the time interpolation of $\mathbf{E}_K$ (*cf*. (3.55)), we introduce some basic definitions in a preliminary step. For fixed $K \geq 2$ the *time step size* is defined as $\tau = \frac{1}{K}$ and the image u_k^K in the vector of images $\mathbf{u}^K = (u_0^K, \dots, u_K^K) \in (L^2(\Omega))^{K+1}$ is associated with each *time step* $t_k^K = k\tau$, $k \in \{0, \dots, K\}$. Let us for the time being assume that a vector $\mathbf{\Phi}^K = (\phi_1^K, \dots, \phi_K^K) \in \mathcal{A}^K$ of optimal deformations exists, *i.e.* $\mathbf{\Phi}^K \in \operatorname{argmin}_{\widetilde{\mathbf{\Phi}}\in\mathcal{A}^K} \mathbf{E}_K^D[\mathbf{u}^K, \widetilde{\mathbf{\Phi}}]$. The existence of such a deformation vector was verified in Theorem 3.4.11 provided that u_0^K and u_K^K are sufficiently close in $L^2(\Omega)$ and K is sufficiently large (*cf*. (3.48)). For $k = 1, \dots, K$ we define the *(discrete) transport map* as

$$y_k^K(t, x) = x + (t - t_{k-1}^K)K(\phi_k^K(x) - x) \quad \text{for } t \in [t_{k-1}^K, t_k^K] \text{ and all } x \in \Omega\,. \tag{3.53}$$

Note that $y_k^K(t_{k-1}^K, x) = x$ and $y_k^K(t_k^K, x) = \phi_k^K(x)$ at the end points of each time interval $[t_{k-1}^K, t_k^K]$. We denote by $v_k^K = K(\phi_k^K - \mathbb{1})$ the *discrete motion field* associated with y_k^K. If we assume

$$\max_{k\in\{1,\dots,K\}} \|D\phi_k^K - \mathbb{1}\|_{C^0(\overline{\Omega})} < 1\,,$$

then [Cia88, Theorem 5.5-1] guarantees $\det(Dy_k^K(t, x)) > 0$ for all $x \in \Omega$ and $t \in [t_{k-1}^K, t_k^K]$ (note that $Dy_k^K(t, x)$ denotes the spatial derivative). Hence, by employing Theorem 3.4.1 (i.) we can infer that $y_k^K(t, \cdot)$ is invertible

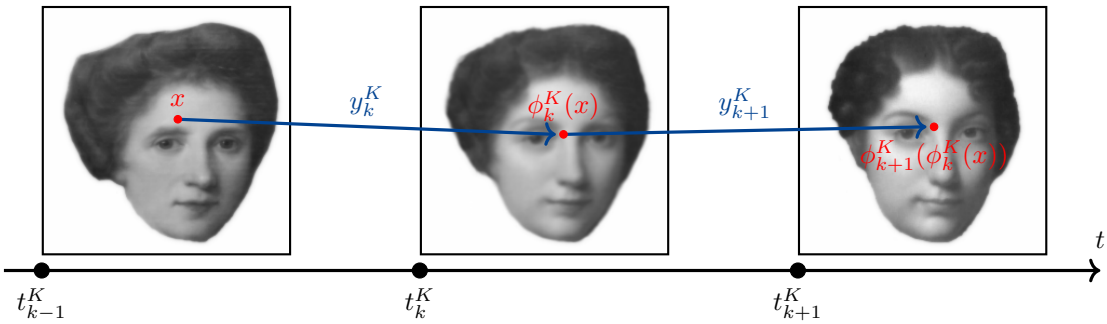

Figure 3.2: Schematic drawing of the trajectory of the point $x \in \Omega$ on the time interval t_{k-1}^K to t_{k+1}^K.

with inverse $x_k^K(t, \cdot)$. Intuitively, $x_k^K(t, \tilde{x})$ for $t \in [t_{k-1}^K, t_k^K]$ retraces the point $\tilde{x} \in \Omega$ at time t to the base point $x \in \Omega$ at time t_{k-1}^K along the corresponding trajectory of the discrete motion path (see Figure 3.2).

For fixed K, $\mathbf{u}^K$ and $\mathbf{\Phi}^K$ we define the *image interpolation* $\mathcal{U}_K[\mathbf{u}^K, \mathbf{\Phi}^K] \in L^2((0,1) \times \Omega)$ for $t \in [t_{k-1}^K, t_k^K]$ as follows:

$$\mathcal{U}_K[\mathbf{u}^K, \mathbf{\Phi}^K](t, x) = u_{k-1}^K(x_k^K(t, x)) + K(t - t_{k-1}^K)(u_k^K \circ \phi_k^K - u_{k-1}^K)(x_k^K(t, x)) \,. \tag{3.54}$$

To motivate this interpolation operator, we consider a point $x \in \Omega$ at time $t = t_{k-1}^K$. Then, $\mathcal{U}_K[\mathbf{u}^K, \mathbf{\Phi}^K]$ describes a linear blending between the images $u_{k-1}^K(x) = \mathcal{U}_K[\mathbf{u}^K, \mathbf{\Phi}^K](t_{k-1}^K, x)$ and $u_k^K(x) = \mathcal{U}_K[\mathbf{u}^K, \mathbf{\Phi}^K](t_k, x)$ along the affine transport path $\{(t, y_k^K(t, x)) \,:\, t \in [t_{k-1}^K, t_k^K]\}$ on the interval $[t_{k-1}^K, t_k^K]$.

Remark 3.5.5. We note that the invertibility of $y_k^K(t, \cdot)$ is guaranteed for K sufficiently large since it will become apparent during the proof of the Mosco-convergence that any deformation ϕ_k^K converges to the identity in $C^{1,\alpha}(\overline{\Omega})$, which already ensures the invertibility due to Theorem 3.4.1 (i.).

Based on this interpolation, a straightforward extension $\mathcal{E}_K : L^2((0,1) \times \Omega) \to [0, \infty]$ of the discrete path energy $\mathbf{E}_K^D$ is given by

$$\mathcal{E}_K[u] = \begin{cases} \mathbf{E}_K^D[\mathbf{u}^K, \mathbf{\Phi}^K] \,, & \text{if } u = \mathcal{U}_K[\mathbf{u}^K, \mathbf{\Phi}^K] \text{ with } \mathbf{u}^K \in (L^2(\Omega))^{K+1} \\ & \text{and } \mathbf{\Phi}^K \in \operatorname{argmin}_{\widetilde{\mathbf{\Phi}} \in \mathcal{A}^K} \mathbf{E}_K^D[\mathbf{u}^K, \widetilde{\mathbf{\Phi}}] \,, \\ +\infty \,, & \text{else} \,. \end{cases} \tag{3.55}$$

The next theorem is one of the main results of this chapter, the proof is postponed to Subsection 3.5.3.

Theorem 3.5.6 (Mosco-convergence in the metamorphosis model)**.** *Under the Assumptions (W1), (W3) and (W4), the time discrete path energy $\mathcal{E}_K$ converges to $\mathcal{E}$ in sense of Mosco w.r.t. the $L^2(\Omega)$-topology,* i.e.

(i.) for every sequence $\{u^K\}_{K \in \mathbb{N}} \subset L^2((0,1) \times \Omega)$ with $u^K \rightharpoonup u$ (weakly) in $L^2((0,1) \times \Omega)$ the estimate

$$\liminf_{K \to \infty} \mathcal{E}_K[u^K] \geq \mathcal{E}[u]$$

holds true,

(ii.) for every $u \in L^2((0,1) \times \Omega)$ there exists a recovery sequence $\{u^K\}_{K \in \mathbb{N}} \subset L^2((0,1) \times \Omega)$ with $u^K \to u$ (strongly) in $L^2((0,1) \times \Omega)$ such that the estimate

$$\limsup_{K \to \infty} \mathcal{E}_K[u^K] \leq \mathcal{E}[u]$$

is valid.

This theorem implies the convergence of discrete geodesic paths. In particular, a minimizer of the time continuous path energy exists:

Theorem 3.5.7 (Convergence of discrete geodesic paths)**.** *Let $u_A, u_B \in L^2(\Omega)$ and suppose that (W1), (W3) and (W4) hold true, and for every $K \in \mathbb{N}$ let u^K be a minimizer of $\mathcal{E}_K$ subject to $u^K(0) = u_A$ and $u^K(1) = u_B$. Then, a subsequence of $\{u^K\}_{K\in\mathbb{N}}$ converges weakly in $L^2((0,1)\times\Omega)$ to a minimizer of the continuous path energy $\mathcal{E}$ as $K \to \infty$, and the associated sequence of discrete energies converges to the minimal continuous path energy.*

Proof. See Subsection 3.5.3. □

Remark 3.5.8. In Remark 3.4.9 we have noted that for a fixed $K \in \mathbb{N}$ the regularity of the input images u_A and u_B transfers to all inner images u_k, $k = 1, \dots, K-1$, in the time discrete metamorphosis model. For the continuous model, the analogous statement is as follows: the Hölder-regularity of the input images u_A and u_B (up to the Hölder-exponent α) inherits to the continuous solution $u(t, \cdot)$ of the metamorphosis model for all $t \in (0,1)$. The proof is based on the observation that any minimizer $u \in L^2((0,1)\times\Omega)$ of the continuous path energy with $u_A = u(0, \cdot) \in L^2(\Omega)$ and $u_B = u(1, \cdot) \in L^2(\Omega)$ allows the representation

$$u(t, \cdot) = u(0, \psi^{-1}(t, \cdot)) + \left(z \int_0^t (\det(D\psi(s, \cdot)))^{-1} \, \mathrm{d}s \right) \circ \psi(t, \cdot)^{-1},$$

where $z \in L^2(\Omega)$ is the weak material derivative and ψ the underlying diffeomorphic flow (*cf*. Theorem 3.1.7). By evaluating this expression at $t = 1$ we obtain

$$z = (u(1, \psi(1, \cdot)) - u(0)) \left(\int_0^1 (\det(D\psi(s, \cdot)))^{-1} \, \mathrm{d}s \right)^{-1}.$$

Hence, z is as regular as u_A and u_B (up to the Hölder-exponent α) and the same holds true for $u(t, \cdot)$ for all $t \in [0,1]$.

3.5.3 Proof of the Mosco-convergence and of Related Theorems

Proof of Theorem 3.5.6. We will verify both inequalities required for the Mosco-convergence (see Definition 3.5.1) separately.

liminf-estimate. Let us at first briefly outline the structure of the proof of the $\liminf$-inequality to facilitate reading.

(i.) *Reconstruction of the flow and the weak material derivative.* Any sequence of images $u^K \in L^2((0,1)\times\Omega)$ with uniformly bounded path energy admits the representation $u^K = \mathcal{U}_K[\mathbf{u}^K, \mathbf{\Phi}^K]$ for a discrete $(K+1)$-path $\mathbf{u}^K = (u_0^K, \dots, u_K^K) \in (L^2(\Omega))^{K+1}$ and an associated vector of optimal matching deformations $\mathbf{\Phi}^K = (\phi_1^K, \dots, \phi_K^K) \in \mathcal{A}^K$ due to the definition of $\mathcal{E}_K$. For any such sequence of images, one can rigorously define a discrete weak material derivative as well as an induced motion field. Furthermore, we will prove that the mismatch energy term coincides with the weak material derivative in the limit.

(ii.) *Weak lower semicontinuity of the path energy.* Here, we will prove a weak lower semicontinuity result required for the $\liminf$-inequality, which essentially follows from the Taylor expansion of the energy density function W (*cf*. (W3)), and establish a priori bounds for the sequence of motion fields and material derivatives.

(iii.) *Identification of the limit of the material derivatives as the material derivative for the limiting image sequence.* In this step, we will demonstrate that each pair of weak limits of the velocity fields and the material derivatives is indeed an instance of a tangent vector of the limiting image. To this end, a certain flow formulation in Lagrangian coordinates of the image sequence is investigated. A crucial ingredient of this step is the weak convergence of $u^K(t, \cdot)$ to $u(t, \cdot)$ in $L^2(\Omega)$ for every $t \in [0,1]$, which results from a trace theorem type argument.

ad (i.): *Reconstruction of the flow and the weak material derivative.*

Let $\{u^K\}_{K\in\mathbb{N}} \subset L^2((0,1)\times\Omega)$ be any sequence of image paths that converges weakly in $L^2((0,1)\times\Omega)$ to an image curve $u \in L^2((0,1)\times\Omega)$. To exclude the trivial case $\liminf_{K\to\infty} \mathcal{E}_K[u^K] = \infty$, we may assume that

$$\mathcal{E}_K[u^K] \leq \overline{\mathcal{E}} < \infty \quad \text{for all } K \in \mathbb{N}\,. \tag{3.56}$$

Thus, due to the definition of $\mathcal{E}_K$ we can immediately infer that $u^K = \mathcal{U}_K[\mathbf{u}^K, \mathbf{\Phi}^K]$ for a vector of images $\mathbf{u}^K = (u_0^K, \dots, u_K^K) \in (L^2(\Omega))^{K+1}$ and an associated vector of deformations $\mathbf{\Phi}^K = (\phi_1^K, \dots, \phi_K^K) \in \mathcal{A}^K$. Each deformation ϕ_k^K solves the pairwise matching problem $\mathcal{W}^D[u_{k-1}^K, u_k^K, \cdot\,]$ (*cf.* (3.13)) and is not necessarily unique. Set $t_k^K = \frac{k}{K}$ for $k = 1, \dots, K$. As above, the transport map is given by $y_k^K(t,x) = x + (t - t_{k-1}^K)K(\phi_k^K(x) - x)$ for $t \in [t_{k-1}^K, t_k^K]$ and all $x \in \Omega$. Furthermore, we associate with each transport path y_k^K the discrete velocity field $v_k^K = K(\phi_k^K - \mathbb{1})$ as well as the map $x_k^K(t,\cdot\,)$ as the spatial inverse of $y_k^K(t,\cdot\,)$ representing a pullback, which will turn out to exist for any K sufficiently large (see below).

Due to the definition of $\mathbf{E}_K$ we can infer

$$\sum_{k=1}^{K} \mathcal{W}^D[u_{k-1}^K, u_k^K, \phi_k^K] \leq \frac{\overline{\mathcal{E}}}{K}\,, \tag{3.57}$$

and by combining this estimate with Lemma 3.4.3 and the usual embedding $H^m(\Omega) \hookrightarrow C^{1,\alpha}(\overline{\Omega})$, $0 < \alpha < m - 1 - \frac{n}{2}$, we obtain

$$\max_{k\in\{1,\dots,K\}} \|\phi_k^K - \mathbb{1}\|_{C^{1,\alpha}(\overline{\Omega})} \leq C \max_{k\in\{1,\dots,K\}} \|\phi_k^K - \mathbb{1}\|_{H^m(\Omega)} \leq C\theta(\overline{\mathcal{E}}K^{-1})\,. \tag{3.58}$$

Hence, by choosing K large enough we may assume that $\max_{k\in\{1,\dots,K\}} \|\det(D\phi_k^K) - 1\|_{C^0(\overline{\Omega})} \leq C_{\det}$ for a constant $C_{\det} \in (0,1)$, which guarantees that all deformations considered are indeed $C^1(\Omega)$-diffeomorphisms due to Theorem 3.4.1 (i.) and – as we pointed out in Subsection 3.5.2 – the inverse transport paths x_k^K are well-defined in this situation.

In what follows, we will examine affine transport paths which intersect the base point $x_k^K(t,y)$ at time $t = t_{k-1}^K$ and thus have the motion velocity

$$\tilde{v}_k^K(t,y) = K(\phi_k^K - \mathbb{1})(x_k^K(t,y)) \tag{3.59}$$

for all $t \in [t_{k-1}^K, t_k^K)$. Globally, we set $\tilde{v}^K(t,y) = \tilde{v}_k^K(t,y)$ for $t \in [t_{k-1}^K, t_k^K)$. Note that $\tilde{v}^K(t,x) = 0$ for all $x \in \partial\Omega$ and all $t \in (0,1)$, which is related to the assumption that the continuous velocity field v in the metamorphosis model has vanishing trace. Recall that $\mathcal{U}_K$ can be viewed as the piecewise affine reconstruction of u^K along straight line segments from x to $\phi_k^K(x)$. Hence, the classical material derivative of u^K evaluated along the transport path $y^K(t,x)$ coincides with the deformed mismatch term $K(u_k^K \circ \phi_k^K - u_{k-1}^K)(x_k^K(t,y))$ for all $t \in (t_{k-1}^K, t_k^K)$ and all $x \in \Omega$, *i.e.*

$$z^K(t,y) := \frac{\mathrm{d}}{\mathrm{d}s} u^K(t+s, y + s\tilde{v}_k^K(t,y))\big|_{s=0} = K(u_k^K \circ \phi_k^K - u_{k-1}^K)(x_k^K(t,y))\,, \tag{3.60}$$

which is clear since $s \mapsto x_k^K(t+s, y + s\tilde{v}_k^K(t,y))$ is constant for s sufficiently small. Since each deformation ϕ_k^K, $k \in \{1,\dots,K\}$, is a $C^1(\Omega)$-diffeomorphism, z^K fulfills the equation for the weak material derivative (3.4), *i.e.*

$$\int_\Omega \int_0^1 z^K \psi \,\mathrm{d}t\,\mathrm{d}x = -\int_\Omega \int_0^1 (\partial_t \psi + \operatorname{div}(\tilde{v}^K \psi)) u^K \,\mathrm{d}t\,\mathrm{d}x \tag{3.61}$$

for all $\psi \in H_0^1((0,1)\times\Omega)$.

Claim: The discrete weak material derivative coincides with the sum over all pairwise matching functionals in the limit $K \to \infty$, *i.e.*

$$\lim_{K\to\infty} \int_\Omega \int_0^1 (z^K)^2 \,\mathrm{d}t\,\mathrm{d}x = \lim_{K\to\infty} K \sum_{k=1}^{K} \int_\Omega (u_k^K \circ \phi_k^K - u_{k-1}^K)^2 \,\mathrm{d}x\,. \tag{3.62}$$

By combining the transformation formula with (3.60) we obtain

$$\int_\Omega \int_0^1 (z^K)^2 \,\mathrm{d}t\,\mathrm{d}x = \sum_{k=1}^K \int_\Omega \int_{t_{k-1}^K}^{t_k^K} K^2 \left(\left(u_k^K \circ \phi_k^K - u_{k-1}^K\right)(x_k^K(t,x))\right)^2 \,\mathrm{d}t\,\mathrm{d}x$$
$$= \sum_{k=1}^K \int_\Omega \int_{t_{k-1}^K}^{t_k^K} K^2 \left(\left(u_k^K \circ \phi_k - u_{k-1}^K\right)(x)\right)^2 \det(Dy_k^K(t,x)) \,\mathrm{d}t\,\mathrm{d}x\,. \tag{3.63}$$

Here, $Dy_k^K(t,x) = \mathbb{1} + K(t - t_{k-1}^K)(D\phi_k^K(x) - \mathbb{1})$. The uniform boundedness of the energy straightforwardly shows

$$\sum_{k=1}^K \int_\Omega K(u_k^K \circ \phi_k^K - u_{k-1}^K)^2 \,\mathrm{d}x \le \delta\overline{\mathcal{E}}\,. \tag{3.64}$$

Moreover, the embedding $H^m(\Omega) \hookrightarrow C^1(\overline{\Omega})$, the closeness of each deformation to the identity in $C^1(\overline{\Omega})$ (*cf.* (3.58)) as well as the Taylor expansion $\det(\mathbb{1} + A) = 1 + \mathrm{tr}(A) + \mathcal{O}(|A|^2)$ imply

$$\|\det\left(\mathbb{1} + K(\,\cdot\, - t_{k-1}^K)(D\phi_k^K - \mathbb{1})\right) - 1\|_{L^\infty((t_{k-1}^K, t_k^K)\times\Omega)} \le C\|\phi_k^K - \mathbb{1}\|_{C^1(\overline{\Omega})}\,. \tag{3.65}$$

Thus, taking into account (3.64) as well as (3.65) we can estimate the difference of the right-hand sides of (3.62) and (3.63) as follows:

$$\left|\sum_{k=1}^K K^2 \left(\int_\Omega \int_{t_{k-1}^K}^{t_k^K} \left(\left(u_k^K \circ \phi_k - u_{k-1}^K\right)(x)\right)^2 \det(Dy_k^K(t,x)) - \left(\left(u_k^K \circ \phi_k^K - u_{k-1}^K\right)(x)\right)^2 \,\mathrm{d}t\,\mathrm{d}x\right)\right|$$
$$\le C\delta\overline{\mathcal{E}} \max_{k\in\{1,\dots,K\}} \|\phi_k^K - \mathbb{1}\|_{C^1(\overline{\Omega})} \le C\delta\overline{\mathcal{E}}\theta(\overline{\mathcal{E}}K^{-1})\,.$$

For the last inequality we employed (3.58), from which the claim follows.

ad (ii.): *Weak lower semicontinuity of the path energy.*

In what follows, we will prove the weak lower semicontinuity of the path energy along the sequence $\{u^K\}_{K\in\mathbb{N}}$. The previous claim (3.62) and the uniform bound of the energy (3.64) directly show that the weak material derivatives $\{z^K\}_{K\in\mathbb{N}}$ are uniformly bounded in $L^2((0,1)\times\Omega)$ independently of K. Thus, there exists a subsequence (labeled in the same way) which converges weakly in $L^2((0,1)\times\Omega)$ to $z \in L^2((0,1)\times\Omega)$ as $K \to \infty$. By the lower semicontinuity of the $L^2(\Omega)$-norm w.r.t. weak convergence and the aforementioned claim one achieves

$$\int_\Omega \int_0^1 z^2 \,\mathrm{d}t\,\mathrm{d}x \le \liminf_{K\to\infty} \int_\Omega \int_0^1 (z^K)^2 \,\mathrm{d}t\,\mathrm{d}x = \liminf_{K\to\infty} K \sum_{k=1}^K \int_\Omega (u_k^K \circ \phi_k^K - u_{k-1}^K)^2 \,\mathrm{d}x\,. \tag{3.66}$$

It remains to verify that there exists a velocity field $v \in L^2((0,1),\mathcal{B})$ (recall $\mathcal{B} = H^m(\Omega,\mathbb{R}^n) \cap H_0^1(\Omega,\mathbb{R}^n)$) such that $\overline{(v,z)} \in T_u L^2$ and

$$\int_0^1 \int_\Omega L[v,v] \,\mathrm{d}x\,\mathrm{d}t \le \liminf_{K\to\infty} K \sum_{k=1}^K \int_\Omega \mathrm{W}(D\phi_k^K) + \gamma|D^m\phi_k^K|^2 \,\mathrm{d}x\,. \tag{3.67}$$

The second order Taylor expansion around t_{k-1}^K of the function $t \mapsto \mathrm{W}(\mathbb{1} + (t - t_{k-1}^K)Dv_k^K)$ evaluated at $t = t_k^K$ yields

$$\mathrm{W}(D\phi_k^K) = \mathrm{W}(\mathbb{1}) + \frac{1}{K}D\mathrm{W}(\mathbb{1})(Dv_k^K) + \frac{1}{2K^2}D^2\mathrm{W}(\mathbb{1})(Dv_k^K, Dv_k^K) + \mathcal{O}(K^{-3}|Dv_k^K|^3)$$
$$= \frac{1}{K^2}\left(\frac{\lambda}{2}\left(\mathrm{tr}(\varepsilon[v_k^K])\right)^2 + \mu\mathrm{tr}(\varepsilon[v_k^K]^2)\right) + \mathcal{O}(K^{-3}|Dv_k^K|^3)\,.$$

Here, the lower order terms vanish due to (W1) and the last equality follows from (W3). Recall that $\varepsilon[v_k^K]$ refers to the symmetric part of the gradient of the discrete velocity field $v_k^K = K(\phi_k^K - \mathbb{1})$. Then,

$$\begin{aligned} &K\sum_{k=1}^{K}\int_\Omega \mathrm{W}(D\phi_k^K) + \gamma|D^m\phi_k^K|^2\,\mathrm{d}x \\ &\leq \frac{1}{K}\sum_{k=1}^{K}\int_\Omega \frac{\lambda}{2}(\mathrm{tr}(\varepsilon[v_k^K]))^2 + \mu\mathrm{tr}(\varepsilon[v_k^K]^2) + \gamma|D^m v_k^K|^2\,\mathrm{d}x + C\sum_{k=1}^{K} K\int_\Omega K^{-3}|Dv_k^K|^3\,\mathrm{d}x\,, \end{aligned}$$

and the last term is of order $K^{-\frac{1}{2}}$. To see this, we apply Lemma 3.4.3, (3.57), (3.58) and the uniform bound of the energy to deduce

$$\begin{aligned} &K\sum_{k=1}^{K}\int_\Omega K^{-3}|Dv_k^K|^3\,\mathrm{d}x \leq CK\max_{k=1,\dots,K}\|\phi_k^K - \mathbb{1}\|_{C^1(\overline{\Omega})}\sum_{k=1}^{K}\|\phi_k^K - \mathbb{1}\|_{H^m(\Omega)}^2 \\ &\leq CK\theta(\overline{\mathcal{E}}K^{-1})\sum_{k=1}^{K}\theta(\mathcal{W}^D[u_{k-1}^K, u_k^K, \phi_k^K])^2 \leq CK^{\frac{1}{2}}\sum_{k=1}^{K}\mathcal{W}^D[u_{k-1}^K, u_k^K, \phi_k^K] \leq C\overline{\mathcal{E}}K^{-\frac{1}{2}}\,. \end{aligned}$$

To prove (3.67), we globally define $v^K \in L^2((0,1)\times\Omega)$ as $v^K(t,\,\cdot\,) = v_k^K$ for $t \in [t_{k-1}^K, t_k^K)$. Taking into account (3.58) we can assume for all K large enough that $\max_{k\in\{1,\dots,K\}}\|D\phi_k^K - \mathbb{1}\|_{C^0(\overline{\Omega})} < r_{\mathrm{W}}$ (see (W4)). Then, v^K is uniformly bounded in $L^2((0,1),\mathcal{B})$ due to the estimates

$$\begin{aligned} &\int_0^1\int_\Omega |v^K|^2\,\mathrm{d}x\,\mathrm{d}t \leq C\sum_{k=1}^{K}\int_{t_{k-1}^K}^{t_k^K}\int_\Omega K^2|(D\phi_k^K)^{\mathrm{sym}} - \mathbb{1}|^2\,\mathrm{d}x\,\mathrm{d}t \leq CK\sum_{k=1}^{K}\int_\Omega \frac{\mathrm{W}(D\phi_k^K)}{C_{\mathrm{W},1}}\,\mathrm{d}x \leq \frac{C\overline{\mathcal{E}}}{C_{\mathrm{W},1}}\,, \\ &\int_0^1\int_\Omega |D^m v^K|^2\,\mathrm{d}x\,\mathrm{d}t = \sum_{k=1}^{K}\int_{t_{k-1}^K}^{t_k^K}\int_\Omega K^2|D^m(\phi_k^K - \mathbb{1})|^2\,\mathrm{d}x\,\mathrm{d}t = \sum_{k=1}^{K} K\int_\Omega |D^m\phi_k^K|^2\,\mathrm{d}x \leq \frac{\overline{\mathcal{E}}}{\gamma} \end{aligned}$$

and the Gagliardo–Nirenberg inequality 1.1.2. For the estimates in the first line we incorporated the Poincaré inequality, Korn's inequality 1.1.3 and (W4). Thus, by passing to a subsequence (again labeled in the same way) we can deduce $v^K \rightharpoonup v \in L^2((0,1),\mathcal{B})$ for $K\to\infty$. Finally, a standard weak lower semicontinuity argument (*cf*. Proposition 3.2.6 and [Dac08]) implies

$$\begin{aligned} &\liminf_{K\to\infty} K\sum_{k=1}^{K}\int_\Omega \mathrm{W}(D\phi_k^K) + \gamma|D^m\phi_k^K|^2\,\mathrm{d}x \\ &= \liminf_{K\to\infty}\frac{1}{K}\sum_{k=1}^{K}\int_\Omega \frac{\lambda}{2}(\mathrm{tr}\varepsilon[v_k^K])^2 + \mu\mathrm{tr}(\varepsilon[v_k^K]^2) + \gamma|D^m v_k^K|^2\,\mathrm{d}x \\ &= \liminf_{K\to\infty}\int_0^1\int_\Omega \frac{\lambda}{2}(\mathrm{tr}\varepsilon[v^K])^2 + \mu\mathrm{tr}(\varepsilon[v^K]^2) + \gamma|D^m v^K|^2\,\mathrm{d}x\,\mathrm{d}t \\ &\geq \int_0^1\int_\Omega \frac{\lambda}{2}(\mathrm{tr}\varepsilon[v])^2 + \mu\mathrm{tr}(\varepsilon[v]^2) + \gamma|D^m v|^2\,\mathrm{d}x\,\mathrm{d}t\,, \end{aligned}$$

which proves the weak lower semicontinuity of the path energy along the sequence $\{u^K\}_{K\in\mathbb{N}}$.

ad (iii.): *Identification of the limit of the material derivatives as the material derivative for the limiting image sequence.*

In what follows, we will verify that we can pass to the limit in (3.61) for $K\to\infty$. In particular, we will prove that v is actually the weak limit of $\tilde{v}^K$ in $L^2((0,1)\times\Omega)$ and z is the weak material derivative associated with the image path u and the velocity field v, *i.e.* the tuple (u,v,z) fulfills (3.6) and $\overline{(v,z)} \in T_u L^2(\Omega)$. The main difficulty when passing to the limit in (3.61) arises from the proof of the weak continuity of the mapping $(u,v)\mapsto u\mathrm{div}(v\eta)$. To circumvent this problem, our starting point is the equivalent reformulation

of regular curves as stated in Theorem 3.1.8. To this end, let us denote by $\psi^K \in L^2([0,1], C^{1,\alpha}(\overline{\Omega}))$ the global flow induced by the motion field $\tilde{v}^K$ as characterized in Theorem 3.1.7, *i.e.*

$$\dot{\psi}^K(t,x) = \tilde{v}^K(t, \psi^K(t,x))\,. \tag{3.68}$$

Due to (3.60) we can deduce that $(u^K, \tilde{v}^K, z^K)$ obeys

$$u^K(t,x) = u^K(0, \psi^K_{t,0}(x)) + \int_0^t z^K(s, \psi^K_{t,s}(x))\,\mathrm{d}s \tag{3.69}$$

for $x \in \Omega$ and $t \in [0,1]$, where $\psi^K_{t,s} = \psi^K(s, (\psi^K)^{-1}(t,\,\cdot\,))$ represents the relative global flow from time t to time s. In detail, to justify (3.69) we observe that the intensity of an image particle at time $t = r \in [0,1]$ which is located at $x \in \Omega$ at time $t = 0$, can be recovered via

$$u^K(r, \psi(r,x)) = u^K(0,x) + \int_0^r z^K(s, \psi^K(s,x))\,\mathrm{d}s\,,$$

where we employed (3.68). Thus, the general assertion (3.69) follows by a change of variables.

It remains to verify the assertions in the following claim since (3.70) and Theorem 3.1.8 imply that u is a regular image curve that in particular satisfies (3.6) as was to be proven.

Claim: The representation formula

$$u(t,x) = u(0, \psi_{t,0}(x)) + \int_0^t z(s, \psi_{t,s}(x))\,\mathrm{d}s \tag{3.70}$$

for the limiting image curve u, the limiting motion field $v \in L^2((0,1), \mathcal{B})$ and the limiting weak material derivative $z \in L^2((0,1), L^2(\Omega))$ holds true. Here, ψ denotes the global flow associated with v, *i.e.*

$$\dot{\psi}(t,\,\cdot\,) = v(t, \psi(t,\,\cdot\,))\,, \tag{3.71}$$

and $\psi_{t,s} = \psi(s, \psi^{-1}(t,\,\cdot\,))$ for $s,t \in [0,1]$ is the relative global flow associated with ψ.

We will first prove the strong convergence of ψ^K to ψ, where the limiting global flow ψ satisfies (3.71). Clearly,

$$\|y^K_k(t,\,\cdot\,)\|_{C^{1,\alpha}(\overline{\Omega})} \leq C(1 + \|\phi^K_k - \mathbb{1}\|_{C^{1,\alpha}(\overline{\Omega})})$$

for $t \in [t^K_{k-1}, t^K_k)$. Recall that $\phi^K_k \in C^{1,\alpha}(\overline{\Omega})$, $0 < \alpha < m - 1 - \frac{n}{2}$, due to the embedding $H^m(\Omega) \hookrightarrow C^{1,\alpha}(\overline{\Omega})$. Furthermore, one can deduce for the spatial inverse $x^K_k(t,\,\cdot\,)$ of $y^K_k(t,\,\cdot\,)$ that $\|x^K_k(t,\,\cdot\,)\|_{C^{1,\alpha}(\overline{\Omega})} \leq C$ holds true for K sufficiently large. Indeed, this follows from (3.58) by noting that $Dy^K_k(t,x) = \mathbb{1} + K(t - t^K_{k-1})(D\phi^K_k(x) - \mathbb{1})$ is arbitrarily close to the identity in $C^{0,\alpha}(\overline{\Omega})$ for K sufficiently large. The following estimate for the $C^{1,\alpha^2}(\overline{\Omega})$-norm of the concatenation of two functions $f \in C^{1,\alpha}(\overline{\Omega})$ and $g \in C^{1,\alpha}(\overline{\Omega}, \overline{\Omega})$ can be shown by straightforward arguments:

$$\|f \circ g\|_{C^{1,\alpha^2}(\overline{\Omega})} \leq \|f\|_{C^0(\overline{\Omega})} + |f|_{C^1(\overline{\Omega})}|g|_{C^1(\overline{\Omega})} + |f|_{C^{1,\alpha}(\overline{\Omega})}|g|^{\alpha}_{C^{0,\alpha}(\overline{\Omega})}|g|_{C^1(\overline{\Omega})} + C|f|_{C^1(\overline{\Omega})}|g|_{C^{1,\alpha}(\overline{\Omega})}\,. \tag{3.72}$$

Hence, (3.58), (3.72) and the aforementioned estimates yield

$$\|\tilde{v}^K_k(t,\,\cdot\,)\|_{C^{1,\alpha^2}(\overline{\Omega})} \leq C\|v^K_k(t,\,\cdot\,)\|_{C^{1,\alpha}(\overline{\Omega})}\,. \tag{3.73}$$

Thus, the uniform boundedness of $\{v^K\}_{K\in\mathbb{N}}$ in $L^2((0,1), \mathcal{B})$ and the embedding $H^m(\Omega) \hookrightarrow C^{1,\alpha}(\overline{\Omega})$ imply that $\{\tilde{v}^K\}_{K\in\mathbb{N}}$ is uniformly bounded in $L^2((0,1), C^{1,\alpha^2}(\overline{\Omega}))$, and by using Theorem 3.1.10, we can infer that $\{\psi^K\}_{K\in\mathbb{N}}$ is uniformly bounded in $C^0((0,1), C^{1,\alpha^2}(\overline{\Omega}))$. Hence, for $s,t \in [0,1]$ we obtain

$$\begin{aligned}\|\psi^K(t,\,\cdot\,) - \psi^K(s,\,\cdot\,)\|_{C^{1,\alpha^2}(\overline{\Omega})} &\leq C\left|\int_s^t \|v^K(r,\,\cdot\,)\|_{C^{1,\alpha}(\overline{\Omega})}\,\mathrm{d}r\right| \\ &\leq C|t-s|^{\frac{1}{2}}\left|\int_0^1 \|v^K(r,\,\cdot\,)\|^2_{C^{1,\alpha}(\overline{\Omega})}\,\mathrm{d}r\right|^{\frac{1}{2}} \leq C|t-s|^{\frac{1}{2}}\,,\end{aligned} \tag{3.74}$$

where we employed (3.68) and (3.73). Thus, $\{\psi^K\}_{K\in\mathbb{N}}$ is uniformly bounded in $C^{0,\frac{1}{2}}([0,1],C^{1,\alpha^2}(\overline{\Omega}))$ and a subsequence of $\{\psi^K\}_{K\in\mathbb{N}}$ (as usual labeled in the same way) converges strongly in $C^{0,\beta}([0,1],C^{1,\beta}(\overline{\Omega}))$ to $\psi\in C^{0,\beta}([0,1],C^{1,\beta}(\overline{\Omega}))$ for some $\beta\in(0,\min\{\frac{1}{2},\alpha^2\})$ as $K\to\infty$. We claim that ψ is the global flow associated with v and satisfies (3.71) as well as $\psi\in C^{0,\frac{1}{2}}([0,1],C^{1,\alpha}(\overline{\Omega}))$. Indeed, taking into account Theorem 3.1.7 as well as Theorem 3.1.11 shows that ψ is actually the global flow induced by v, the additional regularity properties follow from Theorem 3.1.10 and an analogous reasoning as in (3.74). Moreover, $\{(\psi^K)^{-1}\}_{K\in\mathbb{N}}$ is uniformly bounded in $C^{0,\frac{1}{2}}([0,1],C^{1,\alpha}(\overline{\Omega}))$ due to Theorem 3.1.10.

Let $x\in\Omega$, $t\geq 0$ and $\tau>0$ such that $t+\tau\leq 1$. A direct application of (3.69) yields

$$\begin{aligned}
&u^K(t+\tau,\psi^K(t+\tau,x))-u^K(t,\psi^K(t,x))\\
&=u^K(0,\psi^K_{t+\tau,0}(\psi^K(t+\tau,x)))+\int_0^{t+\tau}z^K(s,\psi^K_{t+\tau,s}(\psi^K(t+\tau,x)))\,\mathrm{d}s\\
&\quad-u^K(0,\psi^K_{t,0}(\psi^K(t,x)))-\int_0^t z^K(s,\psi^K_{t,s}(\psi^K(t,x)))\,\mathrm{d}s\\
&=\int_t^{t+\tau}z^K(s,\psi^K(s,x))\,\mathrm{d}s
\end{aligned}$$

by taking into account $\psi^K_{t,s}(\psi^K(t,x))=\psi^K(s,x)$. Thus, by using Jensen's inequality, the uniform boundedness of $\{(\psi^K)^{-1}\}_{K\in\mathbb{N}}$ in $C^{0,\frac{1}{2}}([0,1],C^{1,\alpha}(\overline{\Omega}))$, and the uniform boundedness of the weak material derivatives $\{z^K\}_{K\in\mathbb{N}}$ in $L^2((0,1),L^2(\Omega))$, which is due to (3.56) and (3.66), we obtain

$$\begin{aligned}
&\int_\Omega\left(u^K(t+\tau,\psi^K(t+\tau,x))-u^K(t,\psi^K(t,x))\right)^2\,\mathrm{d}x\leq\int_\Omega\left(\int_t^{t+\tau}z^K(s,\psi^K(s,x))\,\mathrm{d}s\right)^2\,\mathrm{d}x\\
&\leq\tau\|\det(D((\psi^K)^{-1}))\|_{L^\infty((0,1)\times\Omega)}\int_\Omega\int_t^{t+\tau}(z^K)^2\,\mathrm{d}s\,\mathrm{d}x\leq C\tau\,,
\end{aligned}\tag{3.75}$$

which also holds true for (u,v,z).

By multiplying (3.69) with a test function $\eta\in C_c^\infty(\Omega)$ and integrating w.r.t. Ω we obtain for any $t\in[0,1]$

$$\begin{aligned}
0&=\int_\Omega u^K(t,x)\eta(x)\,\mathrm{d}x-\int_\Omega u^K(0,\psi^K_{t,0}(x))\eta(x)\,\mathrm{d}x-\int_0^t\int_\Omega z^K(s,\psi^K_{t,s}(x))\eta(x)\,\mathrm{d}x\,\mathrm{d}s\\
&=\int_\Omega u^K(t,x)\eta(x)\,\mathrm{d}x-\int_\Omega u^K(0,y)\eta((\psi^K_{t,0})^{-1}(y))\det(D(\psi^K_{t,0})^{-1})\,\mathrm{d}y\\
&\quad-\int_0^t\int_\Omega z^K(s,y)\eta((\psi^K_{t,s})^{-1}(y))\det(D(\psi^K_{t,s})^{-1})\,\mathrm{d}y\,\mathrm{d}s\,.
\end{aligned}\tag{3.76}$$

In the next claim we will show that for a subsequence of $\{u^K\}_{K\in\mathbb{N}}$ (again labeled in the same way) $u^K(t,\cdot)\rightharpoonup u(t,\cdot)$ weakly in $L^2(\Omega)$ for all $t\in[0,1]$. Hence, by additionally taking into account the strong convergence results for $(\psi^K)^{-1}(t,\cdot)$ and ψ^K deduced above we can pass to the limit in (3.76) and get

$$\begin{aligned}
0&=\int_\Omega u(t,x)\eta(x)\,\mathrm{d}x-\int_\Omega u(0,y)\eta((\psi_{t,0})^{-1}(y))\det(D(\psi_{t,0})^{-1})\,\mathrm{d}y\\
&\quad-\int_0^t\int_\Omega z(s,y)\eta((\psi_{t,s})^{-1}(y))\det(D(\psi_{t,s})^{-1})\,\mathrm{d}y\,\mathrm{d}s\\
&=\int_\Omega u(t,x)\eta(x)\,\mathrm{d}x-\int_\Omega u(0,\psi_{t,0}(x))\eta(x)\,\mathrm{d}x-\int_0^t\int_\Omega z(s,\psi_{t,s}(x))\eta(x)\,\mathrm{d}x\,\mathrm{d}s\,.
\end{aligned}$$

Since η was chosen arbitrarily, the fundamental lemma in the calculus of variations guarantees that u and z fulfill (3.70) for a.e. $x\in\Omega$ and $t\in[0,1]$. Finally, Theorem 3.1.8 implies (3.6), which was to be proven.

Claim: There exists a subsequence of u^K (again denoted by $\{u^K\}_{K\in\mathbb{N}}$) such that $u^K(t,\cdot)\rightharpoonup u(t,\cdot)$ weakly in $L^2(\Omega)$ for all $t\in[0,1]$.

Let $\eta \in C_c^\infty(\Omega)$ be an arbitrary test function. For $t \in [0,1]$ and $\tau > 0$ sufficiently small we consider the interval $I \subset [0,1]$ with $t \in I$ and $|I| \leq \tau$. Then,

$$\begin{aligned}
&\int_\Omega (u^K(t,x) - u(t,x))\eta(x)\,\mathrm{d}x \\
&= \fint_I \int_\Omega (u^K(t,x) - u^K(s,x))\eta(x)\,\mathrm{d}x\,\mathrm{d}s + \fint_I \int_\Omega (u(s,x) - u(t,x))\eta(x)\,\mathrm{d}x\,\mathrm{d}s \\
&\quad + \fint_I \int_\Omega (u^K(s,x) - u(s,x))\eta(x)\,\mathrm{d}x\,\mathrm{d}s\,. \qquad (3.77)
\end{aligned}$$

The weak convergence of $u^K \rightharpoonup u$ in $L^2((0,1)\times\Omega)$ implies that the last integral on the right-hand side of (3.77) vanishes as $K \to \infty$. Let

$$\tilde{\eta}^K(t,y) = \eta(\psi^K(t,y))\det(D\psi^K(t,y))\,, \qquad \tilde{\eta}(t,y) = \eta(\psi(t,y))\det(D\psi(t,y))\,.$$

The first integral on the right-hand side of (3.77) can be restated as follows:

$$\begin{aligned}
&\fint_I \int_\Omega (u^K(t,x) - u^K(s,x))\eta(x)\,\mathrm{d}x\,\mathrm{d}s \\
&= \fint_I \int_\Omega u^K(t,\psi^K(t,y))\tilde{\eta}^K(t,y) - u^K(s,\psi^K(s,y))\tilde{\eta}^K(s,y)\,\mathrm{d}y\,\mathrm{d}s \\
&= \fint_I \int_\Omega (u^K(t,\psi^K(t,y)) - u^K(s,\psi^K(s,y)))\tilde{\eta}^K(t,y)\,\mathrm{d}y\,\mathrm{d}s \\
&\quad + \fint_I \int_\Omega u^K(s,\psi^K(s,y))\left(\tilde{\eta}^K(t,y) - \tilde{\eta}^K(s,y)\right)\,\mathrm{d}y\,\mathrm{d}s\,. \qquad (3.78)
\end{aligned}$$

By taking into account (3.75) the first integral on the right-hand side of (3.78) can be estimated as follows:

$$\begin{aligned}
&\left|\fint_I \int_\Omega (u^K(t,\psi^K(t,y)) - u^K(s,\psi^K(s,y)))\tilde{\eta}^K(t,y)\,\mathrm{d}y\,\mathrm{d}s\right| \\
&\leq \sup_{s\in I} \|u^K(t,\psi^K(t,\cdot)) - u^K(s,\psi^K(s,\cdot))\|_{L^2(\Omega)} \|\tilde{\eta}^K(t,\cdot)\|_{L^2(\Omega)} \leq C\tau^{\frac{1}{2}} \|\tilde{\eta}^K(t,\cdot)\|_{L^2(\Omega)}\,,
\end{aligned}$$

which vanishes for $\tau \to 0$. The second integral on the right-hand side of (3.78) vanishes due to the boundedness of u^K and the smoothness of $\tilde{\eta}^K$ and ψ^K as $\tau \to 0$. Analogous estimates apply to the remaining expression in (3.77), in this case u^K, $\tilde{\eta}^K$ and ψ^K are replaced by u, $\tilde{\eta}$, and ψ, respectively. This proves the claim.

limsup-estimate. The proof of the $\limsup$-estimate consists of the following steps:

(i.) *Construction of the recovery sequence.* The recovery sequence is constructed based on a local time averaging of the underlying motion field and *not* – as one might expect – on a (time-averaged) interpolation of the given image path $u \in L^2((0,1)\times\Omega)$. Starting from the thus obtained discrete motion fields, we can construct the associated discrete global flow and the discrete deformations, from which the images can be recovered by sampling the representation formula (3.9) at discrete time points $t_k^K = \frac{k}{K}$.

(ii.) *Proof of the* $\limsup$*-inequality.* To prove the $\limsup$-inequality, we exploit the convexity of the elliptic operator L and use a Taylor expansion of the energy density function W. In particular, the special construction of the discrete motion fields allows the application of Jensen's inequality to establish the $\limsup$-inequality for the terms involving the elliptic operator.

(iii.) *Convergence of the discrete image sequence* u^K *to* u *in* $L^2((0,1)\times\Omega)$. The verification of the convergence of the recovery sequence $\{u^K\}_{K\in\mathbb{N}}$ to u in $L^2((0,1)\times\Omega)$ relies on the strong convergence of the discrete global flow and the discrete deformations to the limiting flow and the identity, respectively.

ad (i.): *Construction of the recovery sequence.*

Without any restriction, we consider an image curve $u \in L^2((0,1)\times\Omega)$ with finite energy and denote the associated velocity field and weak material derivative by $v \in L^2((0,1),\mathcal{B})$ and $z \in L^2((0,1)\times\Omega)$, respectively, *i.e.*

$$\mathcal{E}[u] = \int_0^1 \int_\Omega L[v,v] + \frac{1}{\delta} z^2 \,\mathrm{d}x\,\mathrm{d}t < \infty\,.$$

The construction of the recovery sequence $\{u^K\}_{K\in\mathbb{N}}$ for $K \in \mathbb{N}$ essentially relies on a proper approximation of the discrete velocity fields v^K, which are assumed to be piecewise constant on each interval $[t_{k-1}^K, t_k^K)$ for $t_k^K = \frac{k}{K}$. To this end, we define $v^K\big|_{[t_{k-1}^K, t_k^K)}$ as the local average of v in time w.r.t. the interval $[t_{k-1}^K, t_k^K)$, *i.e.*

$$v^K(t,x) = v_k^K(x) := \fint_{t_{k-1}^K}^{t_k^K} v(s,x)\,\mathrm{d}s \tag{3.79}$$

for $k = 1,\dots,K$, all $t \in [t_{k-1}^K, t_k^K)$ and all $x \in \Omega$. By a standard argument (*cf.* for instance [FL07]) one can infer that v^K converges to v in $L^2((0,1),\mathcal{B})$. Next, we set $\phi_k^K = \mathbb{1} + K^{-1} v_k^K$ and $\mathbf{\Phi}^K = (\phi_1^K,\dots,\phi_K^K)$, and we observe that

$$\begin{aligned}
&\max_{k\in\{1,\dots,K\}} \|\phi_k^K - \mathbb{1}\|_{C^1(\overline{\Omega})} = \max_{k\in\{1,\dots,K\}} K^{-1} \left\| \fint_{t_{k-1}^K}^{t_k^K} v(s,\,\cdot\,)\,\mathrm{d}s \right\|_{C^1(\overline{\Omega})} \\
&\leq \max_{k\in\{1,\dots,K\}} CK^{-1} \fint_{t_{k-1}^K}^{t_k^K} \|v(s,\,\cdot\,)\|_{H^m(\Omega)}\,\mathrm{d}s \leq CK^{-\frac{1}{2}} \left(\int_0^1 \|v(s,\,\cdot\,)\|_{H^m(\Omega)}^2\,\mathrm{d}s \right)^{\frac{1}{2}}.
\end{aligned} \tag{3.80}$$

Hence, choosing K sufficiently large implies $\max_{k=1,\dots,K} \|D\phi_k^K - \mathbb{1}\|_{C^0(\overline{\Omega})} < 1$, which ensures $\phi_k^K \in \mathcal{A}$ and guarantees the existence of the spatial inverse x_k^K of time discrete transport map y_k^K defined as

$$y_k^K(t,x) = x + (t - t_{k-1}^K) K (\phi_k^K(x) - x) \tag{3.81}$$

for $k = 1,\dots,K$ and $t \in [t_{k-1}^K, t_k^K)$ (*cf.* (3.53)). In particular, we can define $\tilde{v}^K$ in the same manner as in the proof of the $\liminf$-estimate (*cf.* (3.59)). The global flow ψ^K, which is associated with $\tilde{v}^K$, is then given as

$$\dot{\psi}^K(t,x) = \tilde{v}^K(t,\psi^K(t,x))$$

with $\psi^K(0,x) = x$ for $x \in \Omega$ and $t \in [0,1]$. Moreover, the induced relative deformation from time t to time s is $\psi_{t,s}^K = \psi^K(s,(\psi^K)^{-1}(t,\,\cdot\,))$, which allows the alternative characterization $\phi_k^K = \psi_{t_{k-1}^K, t_k^K}^K$ of the deformations. We can verify by using Theorem 3.1.7, Theorem 3.1.10 and (3.74) that ψ^K is uniformly bounded in $C^{0,\frac{1}{2}}([0,1], C^{1,\alpha}(\overline{\Omega}))$ for $0 < \alpha < m - 1 - \frac{n}{2}$.

Having defined the discrete flow, we can employ the representation formula (3.9) to recover the approximate discrete image path $\mathbf{u}^K = (u_0^K,\dots,u_K^K) \in (L^2(\Omega))^{K+1}$, *i.e.*

$$u_k^K(x) = u(0, \psi_{t_k^K,0}^K(x)) + \int_0^{t_k^K} z(s, \psi_{t_k^K,s}^K(x))\,\mathrm{d}s \tag{3.82}$$

for $k = 0,\dots,K$. Finally, the time interpolated image path (*cf.* (3.54)) can be retrieved via

$$u^K = \mathcal{U}_K[\mathbf{u}^K, \overline{\mathbf{\Phi}^K}] \quad \text{with} \quad \overline{\mathbf{\Phi}^K} = (\overline{\phi_1^K},\dots,\overline{\phi_K^K}) \in \operatorname*{argmin}_{\widetilde{\mathbf{\Phi}}\in\mathcal{A}^K} \mathbf{E}_K^D[\mathbf{u}, \widetilde{\mathbf{\Phi}}] \tag{3.83}$$

for $K \in \mathbb{N}$.

ad (ii.): *Proof of the* $\limsup$*-inequality.*

In what follows, we will verify the $\limsup$-estimate, *i.e.*

$$\limsup_{K\to\infty} \mathcal{E}_K[u^K] \leq \mathcal{E}[u]\,. \tag{3.84}$$

Taking into account (3.55) and (3.83) we can deduce

$$\mathcal{E}_K[u^K] = \mathbf{E}_K^D[\mathbf{u}^K, \overline{\mathbf{\Phi}^K}] \leq \mathbf{E}_K^D[\mathbf{u}^K, \mathbf{\Phi}^K] = K \sum_{k=1}^{K} \int_\Omega \mathrm{W}(D\phi_k^K) + \gamma |D^m \phi_k^K|^2 + \frac{1}{\delta}(u_k^K \circ \phi_k^K - u_{k-1}^K)^2 \,\mathrm{d}x\,.$$

The relations $(\psi_{t,s}^K)^{-1} = \psi_{s,t}^K$ and $\psi_{t_{k-1}^K, t_{k-1}^K}^K = \mathbb{1}$, the estimate (3.80) for K sufficiently large as well as the uniform boundedness of ψ^K in $C^{0,\frac{1}{2}}([0,1], C^{1,\alpha}(\overline{\Omega}))$ imply via a Taylor expansion

$$\begin{aligned} &\max_{k\in\{1,\dots,K\}} \sup_{s\in[t_{k-1}^K, t_k^K)} \left\| 1 - \det(D(\psi_{t_{k-1}^K, s}^K)^{-1}) \right\|_{C^0(\overline{\Omega})} \\ \leq &\max_{k\in\{1,\dots,K\}} \sup_{s\in[t_{k-1}^K, t_k^K)} \left\| \frac{\det(D\psi_{t_{k-1}^K, t_{k-1}^K}^K) - \det(D\psi_{t_{k-1}^K, s}^K)}{\det(D\psi_{t_{k-1}^K, s}^K)} \right\|_{C^0(\overline{\Omega})} \leq CK^{-\frac{1}{2}}\,. \end{aligned} \tag{3.85}$$

Hence, for any $k \in \{1, \dots, K\}$ we can deduce

$$\int_\Omega (u_k^K \circ \phi_k^K - u_{k-1}^K)^2 \,\mathrm{d}x = \int_\Omega \left(\int_{t_{k-1}^K}^{t_k^K} z(s, \psi_{t_{k-1}^K, s}^K(x)) \,\mathrm{d}s \right)^2 \mathrm{d}x \tag{3.86}$$

$$\leq \frac{1}{K} \int_{t_{k-1}^K}^{t_k^K} \int_\Omega z^2(s,x) \det(D(\psi_{t_{k-1}^K, s}^K)^{-1})(x) \,\mathrm{d}x \,\mathrm{d}s \tag{3.87}$$

$$\leq \frac{1}{K} \left(1 + CK^{-\frac{1}{2}}\right) \int_{t_{k-1}^K}^{t_k^K} \int_\Omega z^2(s,x) \,\mathrm{d}x \,\mathrm{d}s\,. \tag{3.88}$$

Here, the equality in (3.86) is due to the relation (3.82) incorporating the identity $\psi_{t_k^K, s}^K \circ \phi_k = \psi_{t_{k-1}^K, s}^K$, (3.87) follows from Jensen's inequality and the transformation formula, and the inequality in (3.88) can be inferred from (3.85). Furthermore, a Taylor expansion of the energy density around $\mathbb{1}$, (W1) as well as the consistency assumption (W3) result in

$$\begin{aligned} &\int_\Omega \mathrm{W}(D\phi_k^K) + \gamma |D^m \phi_k^K|^2 \,\mathrm{d}x \\ \leq &\int_\Omega \frac{1}{2K^2} D^2\mathrm{W}(\mathbb{1})(Dv_k^K, Dv_k^K) + \frac{\gamma}{K^2} |D^m v_k^K|^2 \,\mathrm{d}x + C \int_\Omega \frac{1}{K^3} |Dv_k^K|^3 \,\mathrm{d}x \\ = &\frac{1}{K^2} \int_\Omega L[v_k^K, v_k^K] \,\mathrm{d}x + \frac{C}{K^3} \int_\Omega |Dv_k^K|^3 \,\mathrm{d}x\,. \end{aligned} \tag{3.89}$$

By combining (3.79) with Jensen's inequality one obtains

$$\begin{aligned} &\int_\Omega L[v_k^K, v_k^K] \,\mathrm{d}x \\ = &\int_\Omega \frac{\lambda}{2} \left(\mathrm{tr} \left(\varepsilon \left[\fint_{t_{k-1}^K}^{t_k^K} v(s,x) \,\mathrm{d}s \right] \right) \right)^2 + \mu \mathrm{tr} \left(\varepsilon \left[\fint_{t_{k-1}^K}^{t_k^K} v(s,x) \,\mathrm{d}s \right]^2 \right) + \gamma \left| D^m \fint_{t_{k-1}^K}^{t_k^K} v(s,x) \,\mathrm{d}s \right|^2 \mathrm{d}x \\ \leq &K \int_\Omega \int_{t_{k-1}^K}^{t_k^K} L[v,v] \,\mathrm{d}t \,\mathrm{d}x\,. \end{aligned} \tag{3.90}$$

To derive an upper bound for the remainder of the Taylor expansion in (3.89) we estimate as follows:

$$\|v_k^K\|_{C^1(\overline{\Omega})}^2 \leq C \sum_{l=1}^{K} \|v_l^K\|_{H^m(\Omega)}^2 \leq C \sum_{l=1}^{K} \fint_{t_{l-1}^K}^{t_l^K} \|v(t,\,\cdot\,)\|_{H^m(\Omega)}^2 \,\mathrm{d}t \leq CK \int_0^1 \|v(t,\,\cdot\,)\|_{H^m(\Omega)}^2 \,\mathrm{d}t \leq CK\,.$$

Here, we used Theorem 1.1.4, Jensen's inequality and $v \in L^2((0,1),\mathcal{B})$. Hence,

$$\max_{k=1,\dots,K} \|v_k^K\|_{C^1(\overline{\Omega})} \leq CK^{\frac{1}{2}},$$

which yields – again in combination with Jensen's inequality – the estimate

$$\begin{aligned}\sum_{k=1}^K \int_\Omega |Dv_k^K|^3 \,\mathrm{d}x &\leq \max_{k=1,\dots,K} \|v_k^K\|_{C^1(\overline{\Omega})} \sum_{l=1}^K \int_\Omega \left| \fint_{t_{l-1}^K}^{t_l^K} Dv(t,x)\,\mathrm{d}t \right|^2 \mathrm{d}x \\ &\leq CK^{\frac{1}{2}} K \sum_{l=1}^K \int_\Omega \int_{t_{l-1}^K}^{t_l^K} |Dv(t,x)|^2 \,\mathrm{d}t\,\mathrm{d}x \leq CK^{\frac{3}{2}}. \end{aligned} \tag{3.91}$$

Altogether, by taking into account the estimates (3.88), (3.89), (3.90) and (3.91) we conclude

$$\begin{aligned}\mathcal{E}_K[u^K] \leq \mathbf{E}_K^D[\mathbf{u}^K, \mathbf{\Phi}^K] &= K \sum_{k=1}^K \int_\Omega \mathrm{W}(D\phi_k^K) + \gamma |D^m \phi_k^K|^2 + \frac{1}{\delta}(u_k^K \circ \phi_k^K - u_{k-1}^K)^2 \,\mathrm{d}x \\ &\leq \sum_{k=1}^K \left(\int_{t_{k-1}^K}^{t_k^K} \int_\Omega L[v_k^K, v_k^K] + \frac{C}{K} |Dv_k^K|^3 + \frac{1}{\delta}\left(1 + CK^{-\frac{1}{2}}\right) z^2(t,x)\,\mathrm{d}x\,\mathrm{d}t \right) \\ &\leq \int_0^1 \int_\Omega L[v,v] + \frac{1}{\delta} z^2(t,x)\,\mathrm{d}x\,\mathrm{d}t + CK^{-\frac{1}{2}} + \frac{C}{\delta} K^{-\frac{1}{2}} = \mathcal{E}[u] + \mathcal{O}(K^{-\frac{1}{2}}), \end{aligned}$$

which readily implies (3.84).

ad (iii.): *Convergence of the discrete image sequence u^K to u in $L^2((0,1)\times\Omega)$.*

It solely remains to verify that $u^K \to u$ in $L^2((0,1)\times\Omega)$ (*cf*. (3.82) for the definition of u^K).

Since $\{\psi^K\}_{K\in\mathbb{N}}$ is uniformly bounded in $C^{0,\frac{1}{2}}([0,1], C^{1,\alpha}(\overline{\Omega}))$, we can extract a subsequence (not relabeled) such that ψ^K converges to ψ in $C^{0,\beta}([0,1], C^{1,\alpha}(\overline{\Omega}))$ for $\beta < \frac{1}{2}$ and $\alpha \in (0, m-1-\frac{n}{2})$. We will tacitly restrict all further considerations to this subsequence. Taking into account Theorem 3.1.10 one can infer

$$\|\psi_{t,\cdot}^K - \psi_{t,\cdot}\|_{C^0([0,1],C^1(\overline{\Omega}))} \to 0, \qquad \|(\psi_{t,\cdot}^K)^{-1} - (\psi_{t,\cdot})^{-1}\|_{C^0([0,1],C^1(\overline{\Omega}))} \to 0 \tag{3.92}$$

for $t \in [0,1]$ as $K \to \infty$.

Claim: For every $t \in [0,1]$

$$\|z(\,\cdot\,, \psi_{t,\cdot}^K(\,\cdot\,)) - z(\,\cdot\,, \psi_{t,\cdot}(\,\cdot\,))\|_{L^2((0,1)\times\Omega)} \to 0, \tag{3.93}$$

$$\|u(0, \psi_{t,0}^K(\,\cdot\,)) - u(0, \psi_{t,0}(\,\cdot\,))\|_{L^2(\Omega)} \to 0 \tag{3.94}$$

as $K \to \infty$. Moreover,

$$\mathcal{U}_K[\mathbf{u}^K, \mathbf{\Phi}^K] \to u \quad \text{in } L^2((0,1)\times\Omega) \text{ as } K \to \infty. \tag{3.95}$$

We will only prove the weak convergence in $L^2((0,1)\times\Omega)$ as well as the convergence of the $L^2((0,1)\times\Omega)$-norms of $z(\,\cdot\,, \psi_{t,\cdot}^K(\,\cdot\,))$ to $z(\,\cdot\,, \psi_{t,\cdot}(\,\cdot\,))$, which is equivalent to (3.93). To this end, choose $\eta \in C_c^\infty((0,1)\times\Omega)$. Then, using the transformation formula we can deduce

$$\begin{aligned}&\int_0^1 \int_\Omega z(s, \psi_{t,s}^K(x))\eta(s,x) - z(s,\psi_{t,s}(x))\eta(s,x)\,\mathrm{d}x\,\mathrm{d}s \\ &= \int_0^1 \int_\Omega z(s,y) \left(\eta(s, (\psi_{t,s}^K)^{-1}(y)) \det(D(\psi_{t,s}^K)^{-1}(y)) - \eta(s, (\psi_{t,s})^{-1}(y)) \det(D(\psi_{t,s})^{-1}(y)) \right) \mathrm{d}y\,\mathrm{d}s, \end{aligned}$$

which vanishes due to (3.92) as $K \to \infty$. By an analogous reasoning one gets

$$\begin{aligned}&\left|\int_0^1 \int_\Omega z^2(s, \psi_{t,s}^K(x)) - z^2(s, \psi_{t,s}(x))\,\mathrm{d}x\,\mathrm{d}s\right| \\ &\leq \int_0^1 \int_\Omega z^2(s,y)\left|\det(D(\psi_{t,s}^K)^{-1}(y)) - \det(D(\psi_{t,s})^{-1}(y))\right|\,\mathrm{d}y\,\mathrm{d}s \to 0\end{aligned}$$

as $K \to \infty$, which straightforwardly implies (3.93). By following the same line of arguments as above the assertion (3.94) can be proven. Finally, the addendum (3.95) can be deduced from (3.82) and Theorem 3.1.8 using the convergence results (3.93) and (3.94).

Claim: The interpolated image curves associated with $\mathbf{\Phi}^K$ and $\overline{\mathbf{\Phi}^K}$ (see (3.83)) asymptotically coincide, *i.e.*

$$\mathcal{U}_K[\mathbf{u}^K, \mathbf{\Phi}^K] - u^K \to 0 \quad \text{in } L^2((0,1)\times\Omega)$$

as $K \to \infty$. Recall that $u^K = \mathcal{U}_K[\mathbf{u}^K, \overline{\mathbf{\Phi}^K}]$ with $\overline{\mathbf{\Phi}^K} = (\overline{\phi_1^K}, \ldots, \overline{\phi_K^K})$ (*cf.* (3.83)).

Using the estimates (3.58) and (3.80) one can infer

$$\max_{k\in\{1,\ldots,K\}} \max\left\{\|\phi_k^K - \mathbb{1}\|_{C^1(\overline{\Omega})}, \|\overline{\phi_k^K} - \mathbb{1}\|_{C^1(\overline{\Omega})}\right\} \leq CK^{-\frac{1}{2}}\,. \tag{3.96}$$

Let $\overline{y_k^K}$ be the discrete transport path associated with $\overline{\mathbf{\Phi}^K}$ (*cf.* (3.81)) and let us denote by $\overline{x_k^K}$ its spatial inverse. Thus,

$$\begin{aligned}&\int_0^1 \int_\Omega \left(\mathcal{U}_K[\mathbf{u}^K, \mathbf{\Phi}^K] - \mathcal{U}_K[\mathbf{u}^K, \overline{\mathbf{\Phi}^K}]\right)^2 \mathrm{d}x\,\mathrm{d}t \\ &\leq C\sum_{k=1}^K \int_{t_{k-1}^K}^{t_k^K} \int_\Omega \left(u_{k-1}^K(x_k^K(t,x)) - u_{k-1}^K(\overline{x_k^K}(t,x))\right)^2 \\ &\qquad + \left(u_k^K \circ \phi_k^K(x_k^K(t,x)) - u_k^K \circ \overline{\phi_k^K}(\overline{x_k^K}(t,x))\right)^2 \mathrm{d}x\,\mathrm{d}t\,,\end{aligned} \tag{3.97}$$

where we exploited the estimate $K(t - t_{k-1}^K) \leq 1$ for all $t \in [t_{k-1}^K, t_k^K]$. In what follows, we will solely prove the convergence of the first integral on the right-hand side of (3.97) to 0 since the corresponding proof for the second integral is analogous (with minor modifications). To this end, we proceed in a similar way as in the approximation argument (3.32) *i.e.* we choose approximating sequences $\{\tilde{u}^j\}_{j\in\mathbb{N}} \subset C^\infty(\Omega)$ and $\{\tilde{z}^j\}_{j\in\mathbb{N}} \subset C^\infty([0,1]\times\Omega)$ such that

$$\|\tilde{u}^j - u(0,\,\cdot\,)\|_{L^2(\Omega)} \to 0\,, \quad \|D\tilde{u}^j\|_{C^0(\overline{\Omega})} \leq Cj\,, \quad \|\tilde{z}^j - z\|_{L^2((0,1)\times\Omega)} \to 0\,, \quad \|D\tilde{z}^j\|_{C^0([0,1]\times\overline{\Omega})} \leq Cj\,.$$

Let us define smooth approximations $\tilde{u}_k^{K,j}$ of u_k^K as follows

$$\tilde{u}_k^{K,j}(x) = \tilde{u}^j(\psi_{t_k^K,0}^K(x)) + \int_0^{t_k^K} \tilde{z}^j(s, \psi_{t_k^K,s}^K(x))\,\mathrm{d}s\,.$$

Thus, by taking into account the uniform convergence of ψ^K to ψ in $C^{0,\beta}([0,1], C^{1,\alpha}(\overline{\Omega}))$, (3.82) as well as Theorem 3.1.10 one can deduce that $\sup_{K\in\mathbb{N}} \max_{k=1,\ldots,K} \|\tilde{u}_k^{K,j} - u_k^K\|_{L^2(\Omega)} \to 0$ as $j \to \infty$ and

$$\begin{aligned}\|D\tilde{u}_k^{K,j}\|_{C^0(\overline{\Omega})} &\leq \left(\|D\tilde{u}^j\|_{C^0(\overline{\Omega})} + \|D\tilde{z}^j\|_{C^0([0,1]\times\overline{\Omega})}\right)\|D\psi^K\|_{C^0([0,1]\times\overline{\Omega})}\|D(\psi^K)^{-1}\|_{C^0([0,1]\times\overline{\Omega})} \\ &\leq C\left(\|D\tilde{u}^j\|_{C^0(\overline{\Omega})} + \|D\tilde{z}^j\|_{C^0([0,1]\times\overline{\Omega})}\right) \leq Cj\,.\end{aligned} \tag{3.98}$$

Next, we employ the particular choice $j = j(K) = \min\{l \in \mathbb{N} : l \geq K^{\frac{1}{4}}\}$ and achieve

$$\begin{aligned}
&\sum_{k=1}^{K} \int_{t_{k-1}^K}^{t_k^K} \int_\Omega \Big(u_{k-1}^K(x_k^K(t,x)) - u_{k-1}^K(\overline{x_k^K}(t,x)) \Big)^2 \,\mathrm{d}x\,\mathrm{d}t \\
&\leq C \sum_{k=1}^{K} \int_{t_{k-1}^K}^{t_k^K} \int_\Omega \Big(u_{k-1}^K(x_k^K(t,x)) - \tilde{u}_{k-1}^{K,j(K)}(x_k^K(t,x)) \Big)^2 + \Big(\tilde{u}_{k-1}^{K,j(K)}(x_k^K(t,x)) - \tilde{u}_{k-1}^{K,j(K)}(\overline{x_k^K}(t,x)) \Big)^2 \\
&\qquad + \Big(\tilde{u}_{k-1}^{K,j(K)}(\overline{x_k^K}(t,x)) - u_{k-1}^K(\overline{x_k^K}(t,x)) \Big)^2 \,\mathrm{d}x\,\mathrm{d}t\,. \qquad (3.99)
\end{aligned}$$

Thus, the first integral on the right-hand side of (3.99) can be bounded by using the transformation formula and (3.96) in the following way:

$$\begin{aligned}
&\sum_{k=1}^{K} \int_{t_{k-1}^K}^{t_k^K} \int_\Omega \Big(u_{k-1}^K(x_k^K(t,x)) - \tilde{u}_{k-1}^{K,j(K)}(x_k^K(t,x)) \Big)^2 \,\mathrm{d}x\,\mathrm{d}t \\
&= \sum_{k=1}^{K} \int_{t_{k-1}^K}^{t_k^K} \int_\Omega \Big(u_{k-1}^K(x) - \tilde{u}_{k-1}^{K,j(K)}(x) \Big)^2 \det(Dy_k^K(t,x)) \,\mathrm{d}x\,\mathrm{d}t \\
&\leq C \max_{k=1,\dots,K} \|u_{k-1}^K - \tilde{u}_{k-1}^{K,j(K)}\|_{L^2(\Omega)}^2 (1 + K^{-\frac{1}{2}})\,,
\end{aligned}$$

which vanishes as $K \to \infty$. Likewise, a similar bound holds true for the last integral in (3.99). Finally, to estimate the middle integral appearing on the right-hand side of (3.99) we proceed as follows:

$$\begin{aligned}
&\sum_{k=1}^{K} \int_{t_{k-1}^K}^{t_k^K} \int_\Omega \Big(\tilde{u}_{k-1}^{K,j(K)}(x_k^K(t,x)) - \tilde{u}_{k-1}^{K,j(K)}(\overline{x_k^K}(t,x)) \Big)^2 \,\mathrm{d}x\,\mathrm{d}t \\
&\leq C \max_{k=1,\dots,K} \|D\tilde{u}_k^{K,j(K)}\|_{C^0(\overline{\Omega})}^2 \max_{l=1,\dots,K} \|x_l^K - \overline{x_l^K}\|_{C^0([t_{l-1}^K, t_l^K]\times\overline{\Omega})}^2 \leq CK^{-\frac{1}{2}}\,,
\end{aligned}$$

where we incorporated (3.96) and (3.98). Here, the estimate

$$\max_{l=1,\dots,K} \|x_l^K - \overline{x_l^K}\|_{C^0([t_{l-1}^K, t_l^K]\times\overline{\Omega})}^2 \leq CK^{-1}$$

can be derived from a Taylor approximation using (3.96) as well as the uniform boundedness of the deformations and their inverse functions in $C^1(\overline{\Omega})$. This proves the claim.

Altogether, u^K converges (strongly) to u in $L^2((0,1)\times\Omega)$, which concludes the proof of the $\limsup$-estimate.

This finishes the proof of the Mosco-convergence of $\mathcal{E}_K$ to $\mathcal{E}$. □

Proof of Theorem 3.5.7. The proof is standard in Γ-convergence theory and is closely linked to Theorem 3.5.4. As a first step, by using (3.49) we can assume that the discrete energy $\mathcal{E}_K[u^K]$ is a priori bounded by $\frac{1}{\delta}\|u_B - u_A\|_{L^2(\Omega)}^2$. Thus, following the same line of arguments as in the proof of the $\liminf$-inequality of Theorem 3.5.6 we can immediately infer that z^K is uniformly bounded in $L^2((0,1)\times\Omega)$ (see (3.60) for the definition of z^K), and a subsequence of the flow ψ^K associated with $\tilde{v}^K$ (*cf.* (3.68)) converges strongly in $C^{1,\alpha}(\overline{\Omega})$. Hence, incorporating (3.69) and the Cauchy–Schwarz inequality one can conclude that

$$\|u_k^K\|_{L^2(\Omega)}^2 \leq C(\|u_A\|_{L^2(\Omega)}^2 + \tfrac{k}{K}\|z^K\|_{L^2((0,1)\times\Omega)}^2)$$

is valid for the minimizer $u^K = \mathcal{U}_K[(u_1^K, \dots, u_K^K), \mathbf{\Phi}^K]$ of $\mathcal{E}_K$, where $\mathbf{\Phi}^K \in \mathcal{A}^K$ are the optimal deformations. Thus, $\{u^K\}_{K\in\mathbb{N}}$ is uniformly bounded in $L^\infty((0,1), L^2(\Omega))$ and a subsequence (not relabeled) converges weakly to $u \in L^2((0,1)\times\Omega)$ in $L^2((0,1)\times\Omega)$.

Let us assume that there is an image path $\tilde{u} \in L^2((0,1)\times\Omega)$ such that

$$\mathcal{E}[\tilde{u}] < \mathcal{E}[u]\,. \qquad (3.100)$$

Then, using the $\limsup$-estimate of Theorem 3.5.6 there exists a sequence $\{\tilde{u}^K\}_{K\in\mathbb{N}} \subset L^2((0,1)\times\Omega)$ satisfying $\limsup_{K\to\infty} \mathcal{E}_K[\tilde{u}^K] \leq \mathcal{E}[\tilde{u}]$. Summing up, we obtain the inequalities

$$\mathcal{E}[u] \leq \liminf_{K\to\infty} \mathcal{E}_K[u^K] \leq \limsup_{K\to\infty} \mathcal{E}_K[\tilde{u}^K] \leq \mathcal{E}[\tilde{u}]\,,$$

which contradicts (3.100). Hence, u minimizes the continuous path energy over all admissible image paths. Finally, the discrete path energies converge to the limiting path energy along the subsequence, *i.e.* $\lim_{K\to\infty} \mathcal{E}_K[u^K] = \mathcal{E}[u]$, which again follows from Theorem 3.5.6. □

3.6 Spatial Discretization

In this section, we will present two different spatial discretization schemes for the time discrete metamorphosis model, which mainly differ in the discrete function spaces for the deformations. In detail, we propose a nonconforming finite element based discretization to model the deformations and images (see Subsection 3.6.1), and a conforming discretization, where the discrete function spaces for the deformations and the images are the space of cubic B-splines and the space of multilinear finite elements, respectively (see Subsection 3.6.2). For convenience, we restrict the following presentation to the case $n = 2$ and $\Omega = [0,1]^2$, the generalization to more general settings is straightforward.

3.6.1 Nonconforming Finite Element Based Spatial Discretization

On the computational domain $\Omega = [0,1]^2$, we consider the regular mesh $\mathcal{T}_h$ with mesh size $h = 2^{-M}$ for a constant $M \in \mathbb{N}$. The mesh $\mathcal{T}_h$ is composed of quadratic cells $\mathcal{C}_l$, $l \in I^{\mathcal{C}}_{\mathcal{V}_h}$, where $I^{\mathcal{C}}_{\mathcal{V}_h}$ represents the index set of all cells. Furthermore, we denote by $\mathcal{V}_h$ the finite element space of piecewise bilinear and globally continuous functions on $\mathcal{T}_h$ (*cf.* [BS08]), and by $\{\Theta^i\}_{i\in I^N_{\mathcal{V}_h}}$ the associated set of basis functions, where $I^N_{\mathcal{V}_h}$ is the index set of all grid nodes $\mathbf{x}_i$ such that $\Theta^i(\mathbf{x}_j) = \delta_{i,j}$ for all $i,j \in I^N_{\mathcal{V}_h}$. For $l \in I^{\mathcal{C}}_{\mathcal{V}_h}$ we denote by Θ^l_α the basis function in the cell $\mathcal{C}_l$ with local index $\alpha \in \{0,1,2,3\}$, and by $I(l,\alpha)$ the global index corresponding to the local index α in the cell $\mathcal{C}_l$, *i.e.* $\Theta^{I(l,\alpha)} = \Theta^l_\alpha$. Finally, $\mathcal{I}_h$ refers to the nodal interpolation operator on the finite element space $\mathcal{V}_h$.

In both spatial discretization schemes to be derived, we choose the aforementioned space $\mathcal{V}_h$ as the discrete function space for the images, *i.e.* $U_k \in \mathcal{V}_h$ with $U_k : \Omega \to \mathbb{R}$ for $k = 0,\dots,K$. The input images are recovered by a nodal interpolation, *i.e.* $U_0 = U_A = \mathcal{I}_h u_A$ and $U_K = U_B = \mathcal{I}_h u_B$, and – without any restriction – are assumed to be in the range $[0,1]$.

In this discretization scheme, the deformations $\Phi_k : \Omega \to \Omega$, $k = 1,\dots,K$, are modeled on the discrete function space $\mathcal{D}_h = \{\Phi \in \mathcal{V}_h^2 \,:\, \Phi = \mathbb{1} \text{ on } \partial\Omega\}$ on the grid $\mathcal{T}_h$. In the applications, it is frequently appropriate to ensure that deformations are not restricted too much by this Dirichlet boundary condition. Thus, instead of imposing the Dirichlet boundary condition directly, we enlarge the computational domain and extend the image intensities with a constant (black) value.

Notation 3.6.1. For a finite element function V in $\mathcal{V}_h$ or $\mathcal{D}_h$, we denote by $\bar{V} = (V(\mathbf{x}_i))_{i\in I^N_{\mathcal{V}_h}}$ the corresponding vector of nodal values with i representing the index in the underlying set of nodes. We note that there exists a one-to-one correspondence between any finite element function V and the associated vector of nodal values $\bar{V}$.

Furthermore, we define the fully discrete counterpart $\mathbf{E}_{K,h}$ of the time discrete path energy $\mathbf{E}_K$ as follows

$$\mathbf{E}_{K,h}[(U_0,\dots,U_K)] = \min_{\substack{\Phi_k\in\mathcal{D}_h,\\ k=1,\dots,K}} \mathbf{E}^D_{K,h}[(U_0,\dots,U_K),(\Phi_1,\dots,\Phi_K)]\,.$$

The energy $\mathbf{E}^D_{K,h}[(U_0,\dots,U_K),(\Phi_1,\dots,\Phi_K)]$ is the discrete counterpart of $\mathbf{E}^D_K$ (*cf.* (3.17)) and is computed by approximating the integrals appearing in the definition of $\mathbf{E}^D_K$ by the Simpson quadrature rule on each cell. In detail, the standard 3-point Simpson quadrature rule for $n = 1$ is extended to the two-dimensional finite element space with 9 points by exploiting the tensor product structure. For $l \in I^{\mathcal{C}}_{\mathcal{V}_h}$ and $q \in \{0,\dots,8\}$, we denote by $\mathbf{x}^l_q$ and ω^l_q the q^{th} quadrature point and the corresponding quadrature weight in the cell $\mathcal{C}_l$, respectively. Let us emphasize that due to the evaluation of image intensities at deformed positions an exact integration with standard quadrature rules is in general not possible. Nevertheless, we observed in our numerical experiments that the

Simpson quadrature rule is capable of reliably computing integrals and – compared to lower order quadrature rules – avoids blurring effects in the neighborhood of interfaces of the images.

Since the regularity requirement for the deformations imposes $m > 1 + \frac{n}{2} = 2$, the higher order measure for friction $|\phi|^2_{H^m(\Omega)}$ appearing in the path energy has to be replaced by a suitable approximation in the solely $H^1(\Omega)$-conforming bilinear finite element space $\mathcal{V}_h$. Therefore, we restrict to even m in this discretization scheme and replace the integrand $|D^m v|^2$ by $|\Delta^{\frac{m}{2}} v|^2$ in the quadratic form (3.1) and correspondingly $|\phi_k|^2_{H^m(\Omega)}$ by $\|\Delta^{\frac{m}{2}} \phi_k\|^2_{L^2(\Omega)}$ in the energy (3.17). Inspired by the weak formulation of Poisson's equation, we set $\Delta^{\frac{m}{2}} V = (\mathbf{M}_h^{-1}\mathbf{S}_h)^{\frac{m}{2}} \bar{V}$ for any $V \in \mathcal{V}_h$, where $\mathbf{M}_h$ and $\mathbf{S}_h$ are the *mass matrix* and the *stiffness matrix*, respectively, *i.e.*

$$(\mathbf{M}_h)_{i,j} = \sum_{l \in I^{\mathcal{C}}_{\mathcal{V}_h}} \sum_{q=0}^{8} \omega_q^l \Theta^i(\mathbf{x}_q^l)\Theta^j(\mathbf{x}_q^l)\,, \qquad (\mathbf{S}_h)_{i,j} = \sum_{l \in I^{\mathcal{C}}_{\mathcal{V}_h}} \sum_{q=0}^{8} \omega_q^l \nabla\Theta^i(\mathbf{x}_q^l) \cdot \nabla\Theta^j(\mathbf{x}_q^l)$$

for $i, j \in I^N_{\mathcal{V}_h}$. To sum up, the fully discrete path energy reads as

$$\begin{aligned}
&\mathbf{E}^D_{K,h}[(U_0, \dots, U_K), (\Phi_1, \dots, \Phi_K)] \\
&= K \sum_{k=1}^{K} \Big(\sum_{l \in I^{\mathcal{C}}_{\mathcal{V}_h}} \sum_{q=0}^{8} \omega_q^l \mathrm{W}(D\Phi_k(\mathbf{x}_q^l)) + \gamma \sum_{c \in \{1,2\}} \mathbf{M}_h(\mathbf{M}_h^{-1}\mathbf{S}_h)^{\frac{m}{2}} \bar{\Phi}_k^c \cdot (\mathbf{M}_h^{-1}\mathbf{S}_h)^{\frac{m}{2}} \bar{\Phi}_k^c \\
&\qquad + \frac{1}{\delta} \sum_{l \in I^{\mathcal{C}}_{\mathcal{V}_h}} \sum_{q=0}^{8} \omega_q^l \left(U_k \circ \Phi_k(\mathbf{x}_q^l) - U_{k-1}(\mathbf{x}_q^l) \right)^2 \Big)\,,
\end{aligned} \tag{3.101}$$

where $\bar{\Phi}_k^c$ refers to the c^{th} component of $\bar{\Phi}_k$.

In what follows, we will develop a minimization algorithm for the computation of a discrete geodesic curve joining two given images U_0 and U_K for fixed $K \geq 2$, which incorporates an alternating update of the images and the deformations (see Algorithm 1). The update scheme for the discrete images requires the solution of a linear system in each step, the optimal deformations are computed via a gradient descent.

Computation of the minimizing images $(U_0, \dots, U_K)$ of $\mathbf{E}^D_{K,h}$ for a fixed vector of deformations. In this paragraph, we will study the numerical minimization of the fully discrete path energy $\mathbf{E}^D_{K,h}$ w.r.t. the image vector for fixed deformations, *i.e.* we are concerned with the minimization problem

$$\min \left\{ \mathbf{E}^D_{K,h}[(U_0, \mathbf{U}, U_K), (\Phi_1, \dots, \Phi_K)] \,:\, \mathbf{U} = (U_1, \dots, U_{K-1}) \in \mathcal{V}_h^{K-1} \right\}$$

for fixed $\mathbf{\Phi} = (\Phi_1, \dots, \Phi_K) \in \mathcal{D}_h^K$ and fixed $U_0, U_K \in \mathcal{V}_h$. It will become apparent that for a fixed vector of spatially discrete deformations $\bar{\mathbf{\Phi}} = (\bar{\Phi}_1, \dots, \bar{\Phi}_K)$ the optimal nodal vector of images $\bar{\mathbf{U}} = (\bar{U}_1, \dots, \bar{U}_{K-1})$ can be recovered from a linear system of equations.

For deformations $\Phi, \Psi \in \mathcal{D}_h$ the entries of the *weighted mass matrix* $\mathbf{M}_h[\Phi, \Psi] = (\mathbf{M}_h[\Phi, \Psi]_{i,j})_{i,j \in I^N_{\mathcal{V}_h}}$ are given by

$$\mathbf{M}_h[\Phi, \Psi]_{i,j} = \sum_{l \in I^{\mathcal{C}}_{\mathcal{V}_h}} \sum_{q=0}^{8} \omega_q^l (\Theta^i \circ \Phi)(\mathbf{x}_q^l)(\Theta^j \circ \Psi)(\mathbf{x}_q^l)\,,$$

where the basis functions of $\mathcal{V}_h$ are evaluated at the deformed quadrature point $\mathbf{x}_q^l$ determined by Φ and Ψ, respectively, and the aforementioned Simpson quadrature rule is employed. The entries of $\mathbf{M}_h[\Phi, \Psi]$ are computed via a cell-wise assembly. In detail, $\mathbf{M}_h[\Phi, \Psi]$ is initialized as the zero matrix. Afterwards, for all $l \in I^{\mathcal{C}}_{\mathcal{V}_h}$ and all $q \in \{0, \dots, 8\}$ one identifies the cells $\mathcal{C}_i, \mathcal{C}_j$ with $\Phi(\mathbf{x}_q^l) \in \mathcal{C}_i$ and $\Psi(\mathbf{x}_q^l) \in \mathcal{C}_j$, respectively, and for all pairs of local indices (β, β') with $\beta, \beta' \in \{0, 1, 2, 3\}$ the expression

$$\omega_q^l (\Theta^i_\beta \circ \Phi)(\mathbf{x}_q^l)(\Theta^j_{\beta'} \circ \Psi)(\mathbf{x}_q^l)$$

is added to $\mathbf{M}_h[\Phi,\Psi]_{I(i,\beta),I(j,\beta')}$. Then, the mismatch term appearing in the discrete path energy $\mathbf{E}^D_{K,h}$ can be reformulated as follows:

$$\begin{aligned}&\frac{K}{\delta}\sum_{k=1}^{K}\sum_{l\in I^c_{\mathcal{V}_h}}\sum_{q=0}^{8}\omega^l_q(U_k\circ\Phi_k(\mathbf{x}^l_q)-U_{k-1}(\mathbf{x}^l_q))^2\\ =\;&\frac{K}{\delta}\sum_{k=1}^{K}\left(\mathbf{M}_h[\Phi_k,\Phi_k]\bar{U}_k\cdot\bar{U}_k-2\mathbf{M}_h[\Phi_k,\mathbb{1}]\bar{U}_{k-1}\cdot\bar{U}_k+\mathbf{M}_h[\mathbb{1},\mathbb{1}]\bar{U}_{k-1}\cdot\bar{U}_{k-1}\right).\end{aligned}$$

The first order condition of $\mathbf{E}^D_{K,h}$ w.r.t. each nodal image vector $\bar{U}_k$ then yields

$$\partial_{\bar{U}_k}\mathbf{E}^D_{K,h}=\frac{2K}{\delta}\left(\left(\mathbf{M}_h[\Phi_k,\Phi_k]+\mathbf{M}_h[\mathbb{1},\mathbb{1}]\right)\bar{U}_k-\mathbf{M}_h[\Phi_k,\mathbb{1}]\bar{U}_{k-1}-\mathbf{M}_h[\Phi_{k+1},\mathbb{1}]^T\bar{U}_{k+1}\right)=0 \tag{3.102}$$

for $k\in\{1,\dots,K-1\}$. Thus, by collecting all equations we can deduce that a necessary condition for $\bar{\mathbf{U}}$ to be a minimizer of $\mathbf{E}^D_{K,h}$ is that $\bar{\mathbf{U}}$ solves the block tridiagonal system of linear equations

$$\mathbf{A}[\mathbf{\Phi}]\bar{\mathbf{U}}=\mathbf{R}[\mathbf{\Phi}]\,, \tag{3.103}$$

where $\mathbf{A}[\mathbf{\Phi}]$ is composed of $(K-1)\times(K-1)$ matrix blocks $\mathbf{A}[\mathbf{\Phi}]_{k,k'}\in\mathbb{R}^{I^N_{\mathcal{V}_h}\times I^N_{\mathcal{V}_h}}$ for $k,k'\in\{1,\dots,K-1\}$ and $\mathbf{R}[\mathbf{\Phi}]$ consists of $K-1$ vector blocks $\mathbf{R}[\mathbf{\Phi}]_k\in\mathbb{R}^{I^N_{\mathcal{V}_h}}$. In this case, the matrix $\mathbf{A}[\mathbf{\Phi}]$ is given by

$$\mathbf{A}[\mathbf{\Phi}]_{k,k-1}=-\mathbf{M}_h[\Phi_k,\mathbb{1}]\,,\quad \mathbf{A}[\mathbf{\Phi}]_{k,k}=\mathbf{M}_h[\Phi_k,\Phi_k]+\mathbf{M}_h[\mathbb{1},\mathbb{1}]\,,\quad \mathbf{A}[\mathbf{\Phi}]_{k,k+1}=-\mathbf{M}_h[\Phi_{k+1},\mathbb{1}]^T\,,$$

and the right-hand side has the form

$$\mathbf{R}[\mathbf{\Phi}]_1=\mathbf{M}_h[\Phi_1,\mathbb{1}]\bar{U}_A\,,\quad \mathbf{R}[\mathbf{\Phi}]_2=\mathbf{R}[\mathbf{\Phi}]_3=\ldots=\mathbf{R}[\mathbf{\Phi}]_{K-2}=0\,,\quad \mathbf{R}[\mathbf{\Phi}]_{K-1}=\mathbf{M}_h[\Phi_K,\mathbb{1}]^T\bar{U}_B\,.$$

Since $\sum_{l\in I^c_{\mathcal{V}_h}}\sum_{q=0}^{8}\omega^l_q(U_k\circ\Phi_k(\mathbf{x}^l_q)-U_{k-1}(\mathbf{x}^l_q))^2$ is convex in U_k as a quadratic function of convex combinations of components of U_k and strictly convex in U_{k-1}, the energy $\mathcal{V}_h^{K-1}\ni\widetilde{\mathbf{U}}\mapsto\mathbf{E}^D_{K,h}[(U_0,\widetilde{\mathbf{U}},U_K),\mathbf{\Phi}]$ turns out to be strictly convex. Thus, there is a unique minimizer $\mathbf{U}=\mathbf{U}[\mathbf{\Phi}]$ for a fixed vector of deformations $\mathbf{\Phi}$, which implies that the matrix $\mathbf{A}[\mathbf{\Phi}]$ is invertible and the unique minimizer is determined by (3.103). Numerically, this system of linear equations is solved with a conjugate gradient method with a diagonal preconditioning (*cf*. line 11 of Algorithm 1).

We remark that in the semi-Lagrangian approach for the flow of diffeomorphisms model, a similar computation as performed in (3.102) appears in the context of the single matching penalty w.r.t. a given end image (*cf*. [BMTY05]).

Computation of the minimizing deformations $(\Phi_1,\dots,\Phi_K)$ of $\mathbf{E}^D_{K,h}$ for a fixed vector of images. In this paragraph, we will derive an optimization scheme to compute the minimizing deformations $\mathbf{\Phi}=(\Phi_1,\dots,\Phi_K)\in\mathcal{D}_h$ of the energy

$$\mathcal{D}_h^K\ni\widetilde{\mathbf{\Phi}}\mapsto\mathbf{E}^D_{K,h}[\mathbf{U},\widetilde{\mathbf{\Phi}}] \tag{3.104}$$

for a fixed vector of images $\mathbf{U}\in\mathcal{V}_h^{K+1}$. We highlight that the elastic registrations performed in this step are appropriate for parallel computing since the deformations are independent of each other and every deformation can thus be updated separately.

Now, to minimize (3.104) w.r.t. Φ_k we employ a Fletcher–Reeves nonlinear conjugate gradient descent scheme with an Armijo step size control incorporating a regularized $H^1(\Omega)$-metric (*cf*. [SYM07]). The variation of the energy $\mathbf{E}^D_{K,h}$ w.r.t. Φ_k in the direction $\Psi\in\{\Phi\in\mathcal{V}_h^2\,:\,\Phi=0\text{ on }\partial\Omega\}$ is given by

$$\begin{aligned}&\partial_{\Phi_k}\mathbf{E}^D_{K,h}[(U_0,\dots,U_K),(\Phi_1,\dots,\Phi_K)](\Psi)\\ =\;&K\sum_{k=1}^{K}\Big(\sum_{l\in I^c_{\mathcal{V}_h}}\sum_{q=0}^{8}\omega^l_q D\mathrm{W}(D\Phi_k(\mathbf{x}^l_q)):D\Psi(\mathbf{x}^l_q)+2\gamma\sum_{c\in\{1,2\}}\mathbf{M}_h(\mathbf{M}_h^{-1}\mathbf{S}_h)^{\frac{m}{2}}\bar{\Phi}^c_k\cdot(\mathbf{M}_h^{-1}\mathbf{S}_h)^{\frac{m}{2}}\bar{\Psi}^c\\ &\qquad+\frac{2}{\delta}\sum_{l\in I^c_{\mathcal{V}_h}}\sum_{q=0}^{8}\omega^l_q(U_k\circ\Phi_k(\mathbf{x}^l_q)-U_{k-1}(\mathbf{x}^l_q))((\nabla U_k\circ\Phi_k(\mathbf{x}^l_q))\cdot\Psi(\mathbf{x}^l_q))\Big)\,.\end{aligned} \tag{3.105}$$

In the numerical applications to real image data, this gradient descent approach often gets stuck in local minima which significantly differ from the global minimum. To circumvent this problem, the following multilevel approach is employed: the input image are restricted to a uniform and regular coarse mesh with mesh size $h = 2^{-M_{\text{init}}}$ with $M_{\text{init}} < M$ (in our case $M_{\text{init}} = 3$) and the optimal deformations on this coarse mesh are computed using the aforementioned gradient descent scheme. Afterwards, both the images and the optimal deformations are prolongated to a finer mesh with mesh size $h = 2^{-M_{\text{init}}-1}$ via a bilinear interpolation and the gradient descent is performed using the prolongated optimal deformations from the coarser mesh as initial values. This scheme is iterated until the level of the mesh coincides with M.

Algorithm 1: Alternating gradient descent scheme to compute the time discrete geodesic path.

Data: input images U_A and U_B, $J \in \mathbb{N}$ such that $K = 2^J$, mesh size h, variance σ^2 for smoothing
Result: approximate minimizer $(U_A = U_0^J, U_1^J, \dots, U_K^J = U_B)$ of $\mathbf{E}_K$
1 smooth $U_0^0 = U_A$ and $U_1^0 = U_B$ with Gaussian filter with variance σ^2;
2 **for** $j = 1$ **to** J **do**
3 $K = 2^j$;
4 $U_{2k}^j = U_k^{j-1}$ for $k = 0, 1, \dots, \frac{K}{2}$;
5 **for** $k = 0$ **to** $\frac{K}{2} - 1$ **do**
6 calculate $\tilde{\Phi} \in \operatorname{argmin}_{\tilde{\Phi} \in \mathcal{D}_h} \mathbf{E}_{1,h}^D[(U_{2k}^j, U_{2k+2}^j), \tilde{\Phi}]$ via multilevel approach;
7 $U_{2k+1}^j = U_{2k+2}^j \circ (\mathbb{1} + 0.5(\tilde{\Phi} - \mathbb{1}))$;
8 **repeat**
9 $\mathbf{U}^{j,old} = (U_1^j, \dots, U_{K-1}^j)$;
10 compute $\mathbf{\Phi}^j = (\Phi_1^j, \dots, \Phi_K^j) \in \operatorname{argmin}_{\mathbf{\Phi} \in \mathcal{D}_h^K} \mathbf{E}_{K,h}^D[(U_A, \mathbf{U}^{j,old}, U_B), \mathbf{\Phi}]$ via multilevel approach;
11 update $\mathbf{U}^j = (U_1^j, \dots, U_{K-1}^j)$ via $\bar{\mathbf{U}}^j = \mathbf{A}[\mathbf{\Phi}^j]^{-1}\mathbf{R}[\mathbf{\Phi}^j]$;
12 **until** $\|\mathbf{U}^{j,old} - \mathbf{U}^j\|_{L^2(\Omega)} \leq \text{THRESHOLD}$;

The alternating update algorithm. In the proposed minimization algorithm, the aforementioned steps are essentially alternated. However, if the input images significantly differ, the elastic registration can get stuck in local minima or does not terminate within a reasonable time despite the multilevel ansatz. Thus, to further improve the robustness of the alternating algorithm, we alter the algorithm in two ways:

1. We employ a cascadic approach starting with a coarse time discretization ($K = 2$) and then successively add further time steps t_k^K by increasing K. To be precise, in each step of this approach we minimize the discrete path energy $\mathbf{E}_{K_{\text{old}}}^D$ w.r.t. the images and deformations for a given length K_{old}, where the outmost images of the sequence $(U_0, \dots, U_{K_{\text{old}}})$ coincide with the input images. Afterwards, we perform a prolongation to the next finer level by inserting a new image between each pair of consecutive images leading to $K_{\text{new}} = 2K_{\text{old}}$. These new images are initialized with the middle image of the warp described by the optimal deformation of the adjacent pair of images. This cascadic approach is terminated if $K = K_{\text{new}}$ (*cf.* lines 4 to 7 in Algorithm 1).

2. Furthermore, we apply a Gaussian filter with variance $\sigma^2 = \frac{5}{4}h$ in the case of color images and $\sigma^2 = \frac{5}{8}h$ in the case of gray-scale images to the input images in a pre-processing step to damp noise.

The resulting alternating minimization algorithm is summarized in Algorithm 1, which is stopped if the $L^2(\Omega)$-norm of two consecutive iterates of the image vector is below a certain threshold value.

3.6.2 Conforming Spatial Discretization with Finite Elements and Cubic Splines

In what follows, we will propose a conforming spatial discretization incorporating a finite element based ansatz space for the image intensity functions and a cubic spline discretization for the deformations on a coarser grid. The discretization of the discrete exponential map for the time discrete metamorphosis model is also based on this discretization scheme (see Section 4.3).

The images are again discretized using the aforementioned space $\mathcal{V}_h$ of bilinear finite element functions on the regular and quadratic mesh $\mathcal{T}_h$ with mesh size $h = 2^{-M}$.

Since we are aiming at a conforming discretization (for small m), we model the displacements $\Phi - \mathbb{1}$ on the $C^2(\Omega)$- and $H^3(\Omega)$-conforming space $\mathcal{S}_H$ of cubic B-splines (recall that we require $m > 1 + \frac{n}{2} = 2$) on the regular and quadratic mesh $\widetilde{\mathcal{T}}_H$ with mesh size $H = 2^{-N}$ for $N < M$ (in all computations shown in this chapter we set $M = N + 1$), which accommodates the fact that deformations are expected to have fewer details than the associated images. To construct the basis functions for $\mathcal{S}_H$, we first consider the basis functions for the one-dimensional space of scalar-valued cubic B-splines. There are three different types of basis functions (see Figure 3.3): boundary basis functions (red), basis functions adjacent to the boundary (blue) and interior basis functions (black). The basis functions for $\mathcal{S}_H$ are defined as a tensor product of the one-dimensional basis functions, and to impose the Dirichlet boundary condition $\Phi = \mathbb{1}$ on $\partial\Omega$, we explicitly remove the boundary basis functions. Finally, the deformation space $\mathcal{D}_H$ is given as the shifted vector-valued space $\mathbb{1} + \mathcal{S}_H^2$.

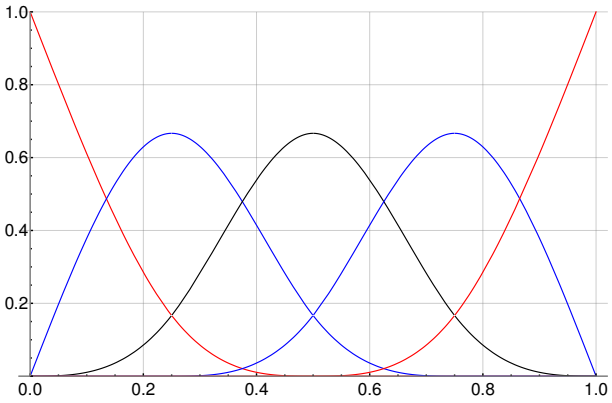

Figure 3.3: Illustration of the basis functions for the space of cubic splines for $n = 1$ and $h = 0.2$.

Instead of the Simpson quadrature rule we employ a Gaussian quadrature of order 5 on both meshes, which proved to be more stable in the numerical applications. Let $I^{\mathcal{C}}_{\mathcal{S}_H}$ be the index set of all cells in the mesh $\widetilde{\mathcal{T}}_H$. For $l \in I^{\mathcal{C}}_{\mathcal{S}_H}$, we denote by $\tilde{\mathbf{x}}^l_q$ and $\tilde{\omega}^l_q$ the q^{th} quadrature point and the corresponding quadrature weight in the cell $\widetilde{\mathcal{C}}_l$ associated with the coarse mesh $\widetilde{\mathcal{T}}_H$ for the deformations, respectively.

To update the images, we proceed in nearly the same way as in the nonconforming discretization scheme, the only difference stems from the replacement of the Simpson by the Gaussian quadrature rule.

The update step for the deformations is again based on the Fletcher–Reeves gradient descent. However, since $\mathcal{V}_h$ and $\mathcal{D}_H$ are modeled on different meshes, we have to adapt (3.101) and (3.105). Despite the requirement $m > 2$ we use $m = 2$ since the deformations are intrinsically $H^3(\Omega)$-regular.

Then, the discrete path energy is given as

$$\begin{aligned}
&\mathbf{E}^D_{K,h}[(U_0, \dots, U_K), (\Phi_1, \dots, \Phi_K)] \\
&= K \sum_{k=1}^{K} \Bigg(\sum_{l \in I^{\mathcal{C}}_{\mathcal{S}_H}} \sum_q \tilde{\omega}^l_q \Big(\mathrm{W}(D\Phi_k(\tilde{\mathbf{x}}^l_q)) + \gamma |D^2 \Phi_k(\tilde{\mathbf{x}}^l_q)|^2 \Big) + \frac{1}{\delta} \sum_{l \in I^{\mathcal{C}}_{\mathcal{V}_h}} \sum_q \omega^l_q \left(U_k \circ \Phi_k(\mathbf{x}^l_q) - U_{k-1}(\mathbf{x}^l_q) \right)^2 \Bigg).
\end{aligned}$$

We highlight the different quadrature schemes for the regularization and the mismatch terms. Moreover, the associated variation in the direction $\Psi \in \{\Phi \in \mathcal{S}_H^2 \,:\, \Phi = 0 \text{ on } \partial\Omega\}$ turns out to be

$$\begin{aligned}
&\partial_{\Phi_k} \mathbf{E}^D_{K,h}[(U_0, \dots, U_K), (\Phi_1, \dots, \Phi_K)](\Psi) \\
&= K \sum_{k=1}^{K} \Bigg(\sum_{l \in I^{\mathcal{C}}_{\mathcal{S}_H}} \sum_q \tilde{\omega}^l_q \Big(D\mathrm{W}(D\Phi_k(\tilde{\mathbf{x}}^l_q)) : (D\Psi(\tilde{\mathbf{x}}^l_q)) + 2\gamma (D^2\Phi_k(\tilde{\mathbf{x}}^l_q)) : (D^2\Psi(\tilde{\mathbf{x}}^l_q)) \Big) \\
&\qquad + \frac{2}{\delta} \sum_{l \in I^{\mathcal{C}}_{\mathcal{V}_h}} \sum_q \omega^l_q (U_k \circ \Phi_k(\mathbf{x}^l_q) - U_{k-1}(\mathbf{x}^l_q)) ((\nabla U_k \circ \Phi_k(\mathbf{x}^l_q)) \cdot \Psi(\mathbf{x}^l_q)) \Bigg).
\end{aligned}$$

Note that the quadrature on the fine mesh is only employed if evaluations of the image intensities are involved. Based on this modified energy, the multilevel Fletcher–Reeves gradient descent is used to perform the elastic registration, where in each multilevel step the difference of the levels of $\mathcal{T}_h$ and $\widetilde{\mathcal{T}}_H$ is exactly 1. To enhance the stability of the resulting alternating algorithm, the same cascadic prolongation approach as well as the same Gaussian filter as in the nonconforming discretization are used (see Algorithm 1, note that $\mathcal{D}_h$ has to be replaced by $\mathcal{D}_H$).

3.7 Numerical Results

In this section, we will present several numerical results for the computation of discrete geodesic curves in the time discrete metamorphosis model. All results are calculated with Algorithm 1 using either the nonconforming finite element scheme or the conforming mixed finite element and cubic B-spline based approach. Most of the results are computed using the simplified energy density (3.20) instead of the theoretically justified Ogden-type density (3.19) since the simplified energy density gives results of comparable visual quality with less computational effort due to the quadratic structure of the regularization term of the deformation energy compared to the complicated nonlinear structure of the Ogden density. The parameter THRESHOLD (see Algorithm 1) is set to 10^{-6} in all results. Many results of this chapter have already been published in [BER15].

Results obtained with the nonconforming discretization. In the nonconforming discretization, we choose $m = 4$, which results in the (approximate) biharmonic higher order regularization term $\gamma\|\Delta^2\Phi\|^2_{L^2(\Omega)}$ in the path energy.

Figure 3.4 depicts a discrete geodesic path obtained with the nonconforming discretization scheme, where the input images are different slices of a 3D magnetic resonance tomography of a human brain with a resolution of 257×257. In the first row, the Ogden energy density (3.19) is employed with parameters $K = 4$, $\delta = 10^{-2}$, $\lambda = 1$, $\mu = \frac{1}{2}$, $q = r = \frac{3}{2}$, $s = \frac{1}{2}$ and $\gamma = 10^{-4}$. Note that this particular choice ignores the theoretical requirement $s > 1$ (*cf*. (W2)), but proves to be more stable. The remaining results are computed using the simplified model (3.20) with parameters $\gamma = 10^{-3}$, $\delta = 10^{-1}$ and $K = 4$ in the second row and $K = 16$ in the third to fifth row. By a visual comparison of the first two rows, it turns out that the diameter of the brain slice in the second rows roughly expands linearly, whereas the Ogden-type material induces a stronger enlargement for small k.

Figure 3.5 shows a geodesic path between two faces from female portrait paintings[1] of size 257×257 computed with the simplified energy density using the nonconforming discretization scheme with parameters $\gamma = 10^{-3}$ and $\delta = 10^{-2}$. The contributions of the regularization and the mismatch term appearing in $\mathbf{E}_2^D[(U_{k-1}, U_k), \Phi_k]$ for $k = 1, \dots, K$ are plotted in Figure 3.6. Note that the method seems to prefer an approximate equidistribution of each contribution as well as the total path energy in time.

The next example (Figure 3.7 to Figure 3.10) demonstrates the applicability of the proposed algorithm to the computation of time discrete geodesic paths in the space of color images. Here, both input images are self-portraits by van Gogh[2] painted in 1889 (see Figure 3.7). Again, we restrict to the simplified energy density with parameters $\gamma = 10^{-3}$ and $\delta = 10^{-2}$ and the nonconforming discretization scheme, and highlight that the algorithm is not limited to this setting. We take into account a straightforward generalization of the model for scalar-/gray-valued images to vector-valued image maps corresponding to the RGB color space, where the only required modification of the method is that $|U_{k+1} \circ \Phi_{k+1} - U_k|^2$ is now the Euclidean norm of the (extended) color vector. One can even enhance the model with further channels, *e.g*. these channels could represent segmented regions of the images which one would like to ensure to be properly matched by transport and not by blending of intensities. A direct computation of the discrete geodesic curve between the original self-portraits U_A^{RGB} and $\tilde{U}_B^{RGB}$ with a resolution of 513×513 failed since the background colors of both self-portraits differ considerably in the RGB color space. Hence, we adjusted the background color of $\tilde{U}_B$ and used the resulting image U_B^{RGB} (see Figure 3.7) for all further computations. Moreover, since the color values of the clothing and the region around the ear are close to the background color w.r.t. the RGB distance, we had to add a fourth (segmentation) channel (*cf*. U_A^S and U_B^S in Figure 3.7) to ensure their proper matching. The time discrete geodesic path for the van Gogh self-portraits

[1] first painting by A. Kauffmann (public domain, see `http://commons.wikimedia.org/wiki/File:Angelika_Kauffmann_-_Self_Portrait_-_1784.jpg`), second painting by R. Peale (GFDL, see `http://en.wikipedia.org/wiki/File:Mary_Denison.jpg`)

[2] both paintings by V. van Gogh (public domain, `http://upload.wikimedia.org/wikipedia/commons/7/71/Vincent_Willem_van_Gogh_102.jpg`, `http://en.wikipedia.org/wiki/File:SelbstPortrait_VG2.jpg`)

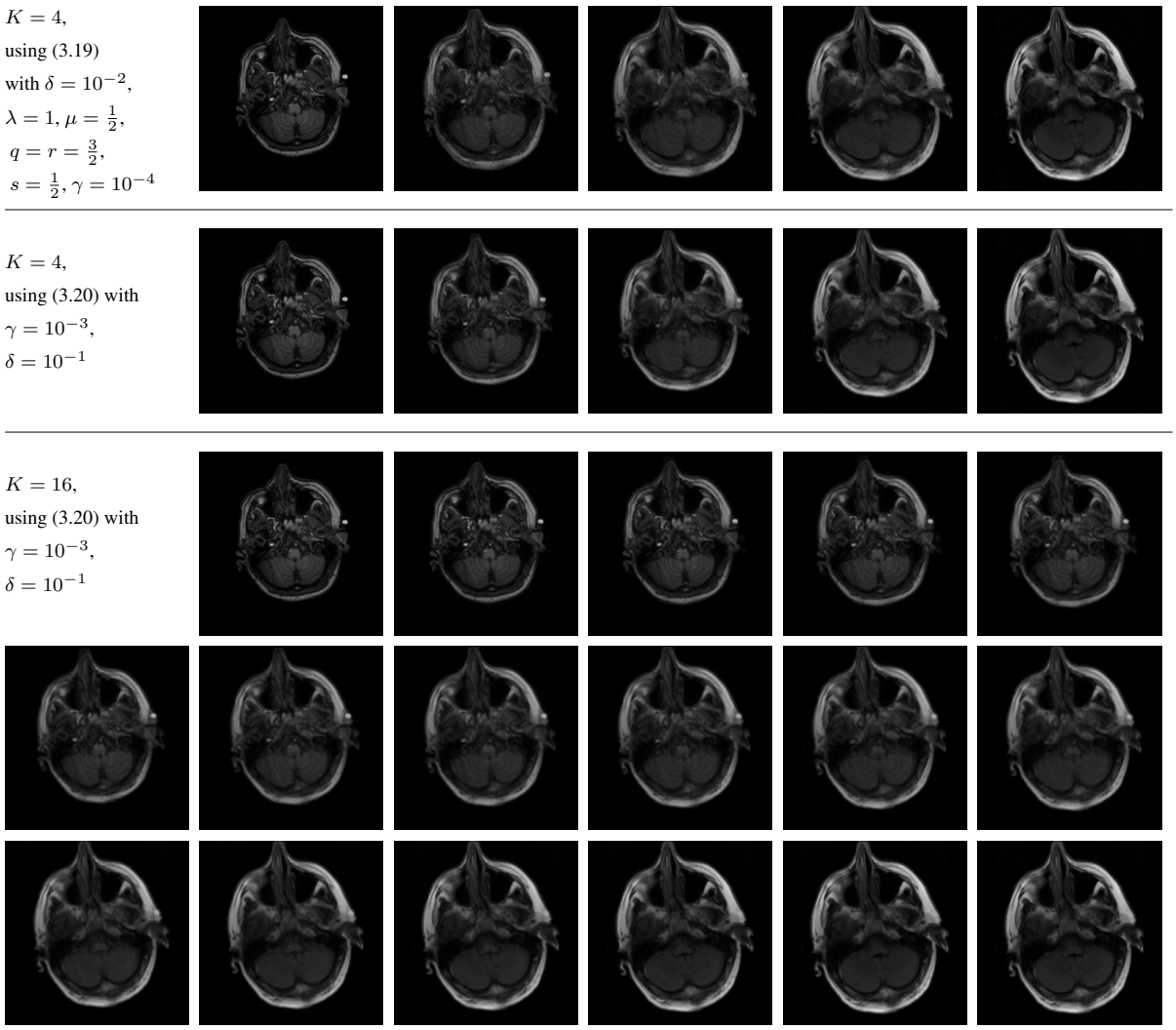

Figure 3.4: Discrete geodesic curve in the metamorphosis model for two slices of an MRI data set of a human brain (data courtesy of H. Urbach, Neuroradiology, University Hospital Bonn) computed with the nonconforming scheme. The Ogden energy density (first row, $K = 4$) is compared to the simplified energy density (with $K = 4$ in the second row, with $K = 16$ in the third to fifth row).

along with the temporal change of the fourth channel is shown in Figure 3.9 for $K = 8$. Figure 3.8 depicts the pullback $U_B^{RGB} \circ \Phi$ along the path $\Phi = \Phi_K \circ \Phi_{K-1} \circ \ldots \circ \Phi_1$ corresponding to the geodesic curve in Figure 3.9. In the last figure of this example (see Figure 3.10), we present the *discrete motion fields* $K(\Phi_k - 1)$ (first row), the *accumulated weak material derivative* $Z_k = K \sum_{l=1}^{k} (U_l \circ \Phi_l - U_{l-1}) \circ X_{l-1}$ using the notation (3.47) for $k = 1, \ldots, 8$ (second row) and the *pullback* sequence $U_8 \circ \Phi_8 \cdots \Phi_l$ for $l = 8, \ldots, 1$ (third row) along the discrete geodesic path. Here, the color wheel on the lower left in the first row indicates both the direction (hue) and the magnitude (color intensity) of the discrete velocities $K(\Phi_k - \mathbb{1})$. We emphasize that the motion field is not constant in time.

The final result obtained with the nonconforming approach and the simplified energy density with parameters $\gamma = 10^{-3}$ and $\delta = 0.05$ is devoted to the MRI tomography scan of a human head of size 129^3. The isosurfaces of the input data U_A and U_B, the side contour plot of U_A and the position of a particular slice are depicted in the first row of Figure 3.11. In the second row, the temporal evolution of this slice along the discrete geodesic path with $K = 3$ is shown. We remark that longer sequences and data sets with higher resolution in 3D are not suitable for the proposed methods due to the long computation time and excessive memory usage.

Figure 3.5: Discrete geodesic curve between two faces from female portrait paintings using the nonconforming discretization.

Results obtained with the conforming discretization. In this paragraph, we will present numerical results computed with the conforming discretization scheme using the simplified energy density (3.20) with parameters $\gamma = 10^{-3}$ and $\delta = 10^{-2}$.

We recomputed the long geodesic curve for the female portrait paintings from Figure 3.5 using the conforming scheme, the results are depicted in Figure 3.12. A direct visual comparison shows that the results of both discretization approaches are (nearly) indistinguishable, the energy contributions emerging from the regularization and the mismatch term also approximately coincide with the corresponding results plotted in Figure 3.6. In further numerical experiments, we could only observe minor visual differences of both discretization approaches for small K and significantly different input images.

As a final example, we present the geodesic curve joining the images of two cars (see Figure 3.13), the initial contours of both cars are retraced to illustrate the motion. It becomes apparent that the proposed scheme is capable of properly rotating and translating objects.

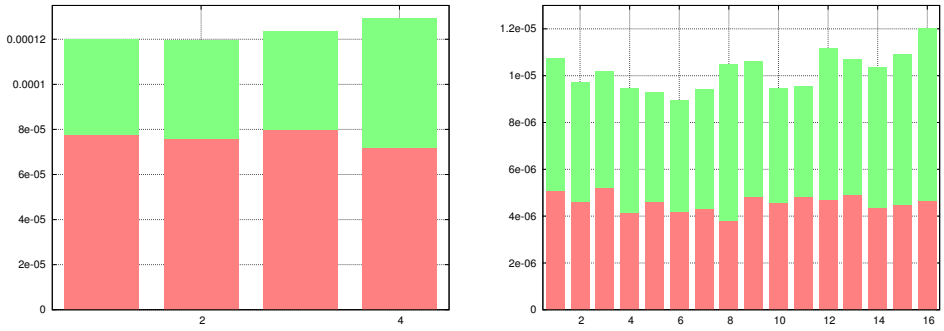

Figure 3.6: Energy contributions of the regularization functional $\int_\Omega \mathrm{W}(D\Phi_k) + \gamma|\Delta^2\Phi_k|^2 \,\mathrm{d}x$ (red) and the matching functional $\frac{1}{\delta}\int_\Omega (U_k \circ \Phi_k - U_{k-1})^2 \,\mathrm{d}x$ (green) for the discrete geodesic path in Figure 3.5 for $K = 4$ (left) and $K = 16$ (right).

Figure 3.7: Original van Gogh self-portraits U_A^{RGB}, $\tilde{U}_B^{RGB}$ and the modulated input image U_B^{RGB} along with the associated fourth channel segmentations U_A^S and U_B^S.

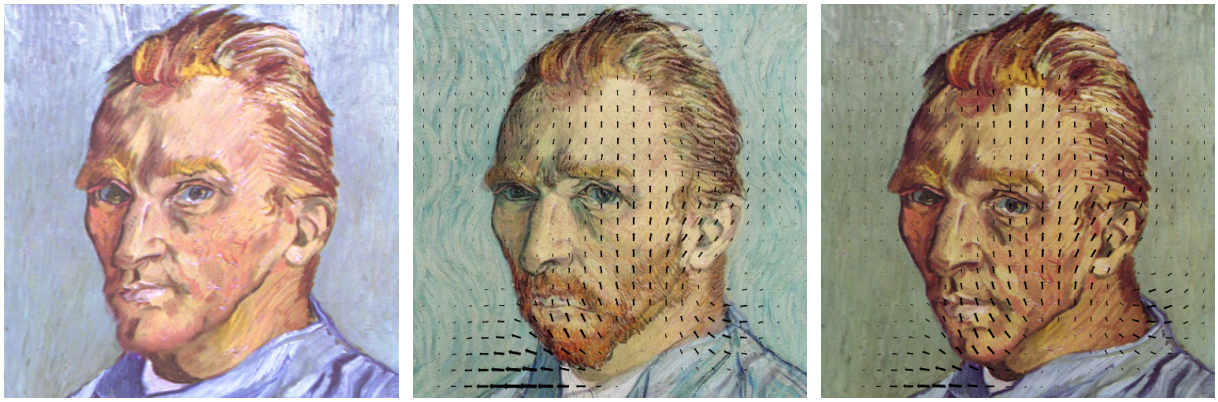

Figure 3.8: Pullback $U_B^{RGB} \circ \Phi_K \circ \cdots \circ \Phi_1$ of U_B^{RGB} along the discrete transport path (left) and visualization of the motion field associated with the outmost images of the sequence (middle and right) for van Gogh self-portraits.

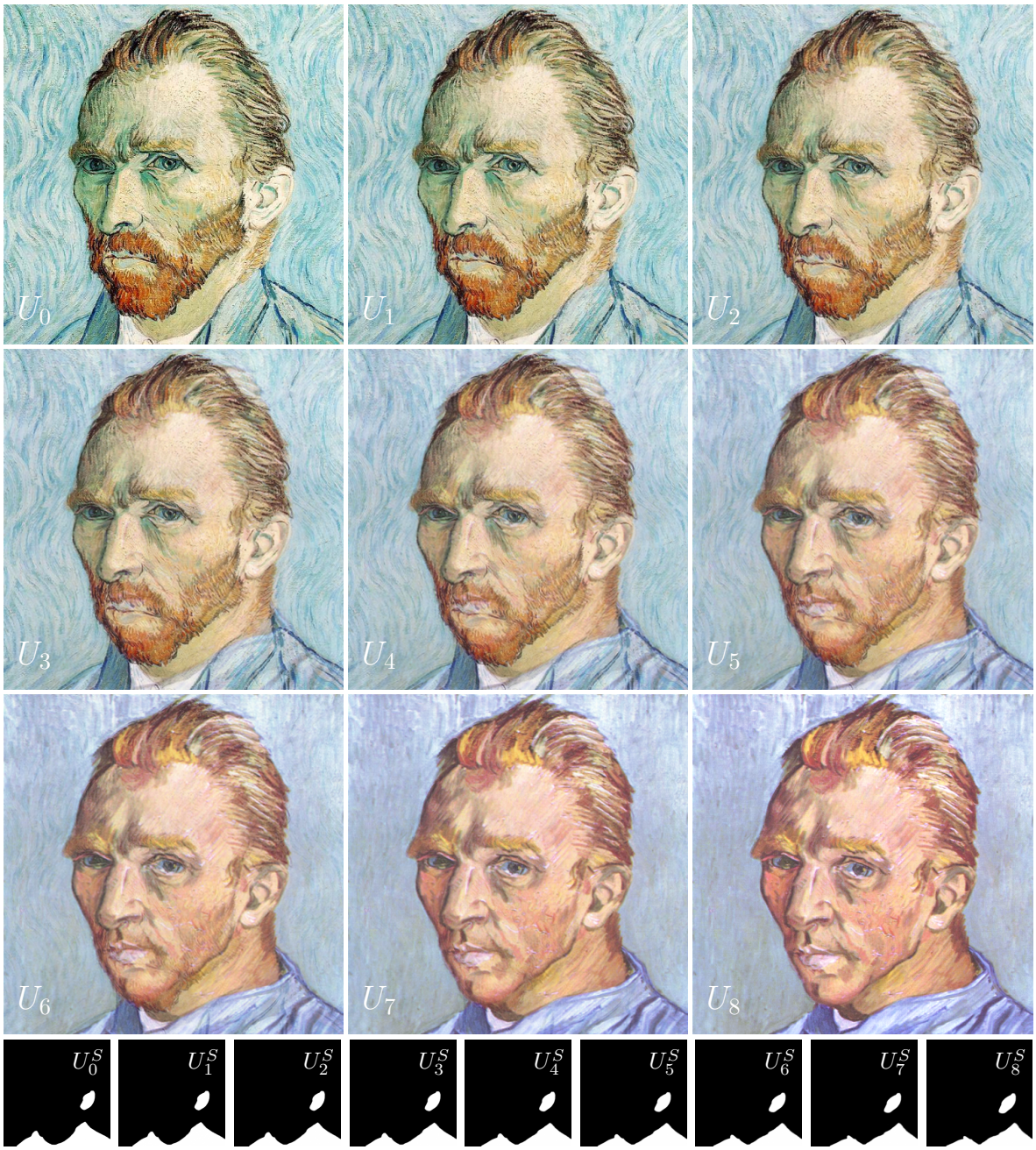

Figure 3.9: Discrete geodesic curve between two van Gogh self-portraits using the energy density (3.20) and the nonconforming discretization scheme for $K = 8$, $\gamma = 10^{-3}$ and $\delta = 10^{-2}$ including the fourth (segmentation) channel (bottom row).

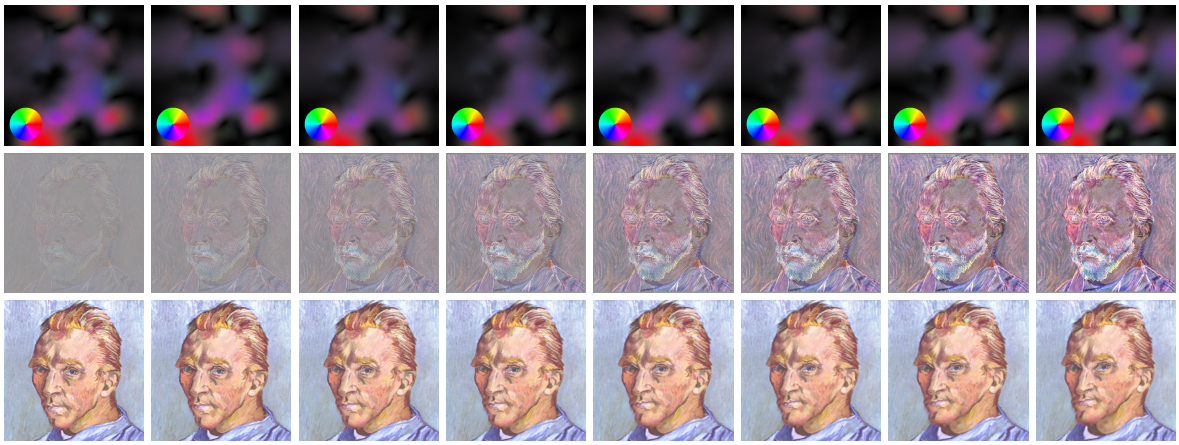

Figure 3.10: Discrete motion fields $K(\Phi_k - 1)$ (first row), accumulated weak material derivative Z_k for $k = 1, \dots, 8$ (second row) and pullback sequence $U_8 \circ \Phi_8 \cdots \Phi_l$ for $l = 8, \dots, 1$ (third row).

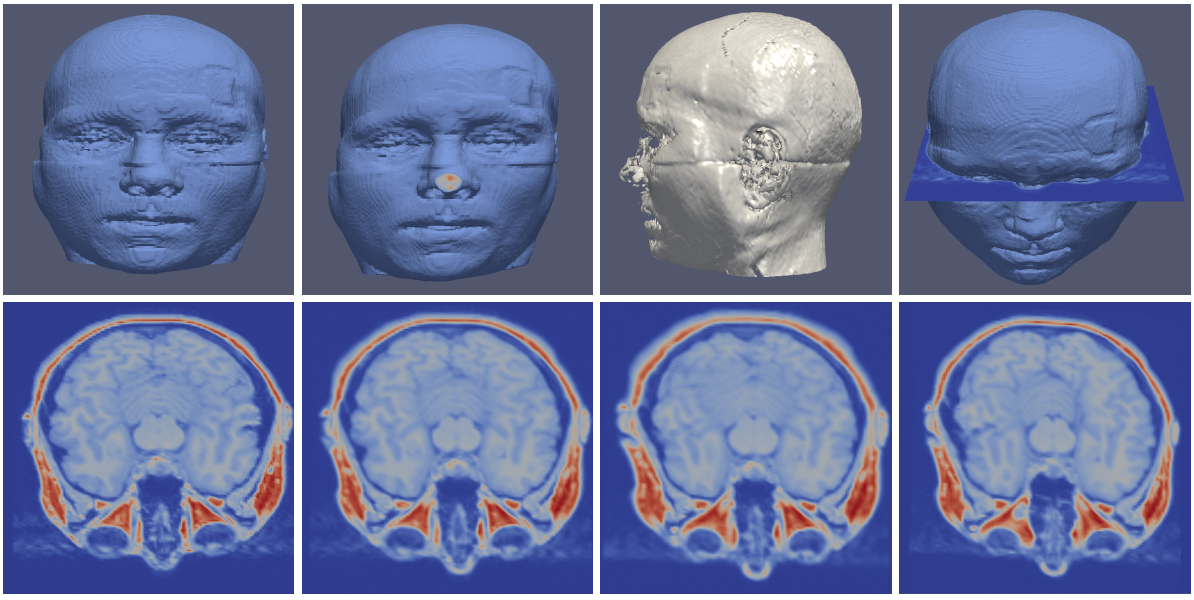

Figure 3.11: First row: isosurfaces of the input data U_A and U_B (first and second image), contour side view of U_A (third image) and the location of a particular slice (fourth image). Second row: temporal evolution of this slice along the time discrete geodesic sequence (nonconforming scheme with $\gamma = 10^{-3}$, $\delta = 0.05$ and $K = 3$).

Figure 3.12: Discrete geodesic curve between two faces from female portrait paintings using the conforming discretization with the simplified energy density.

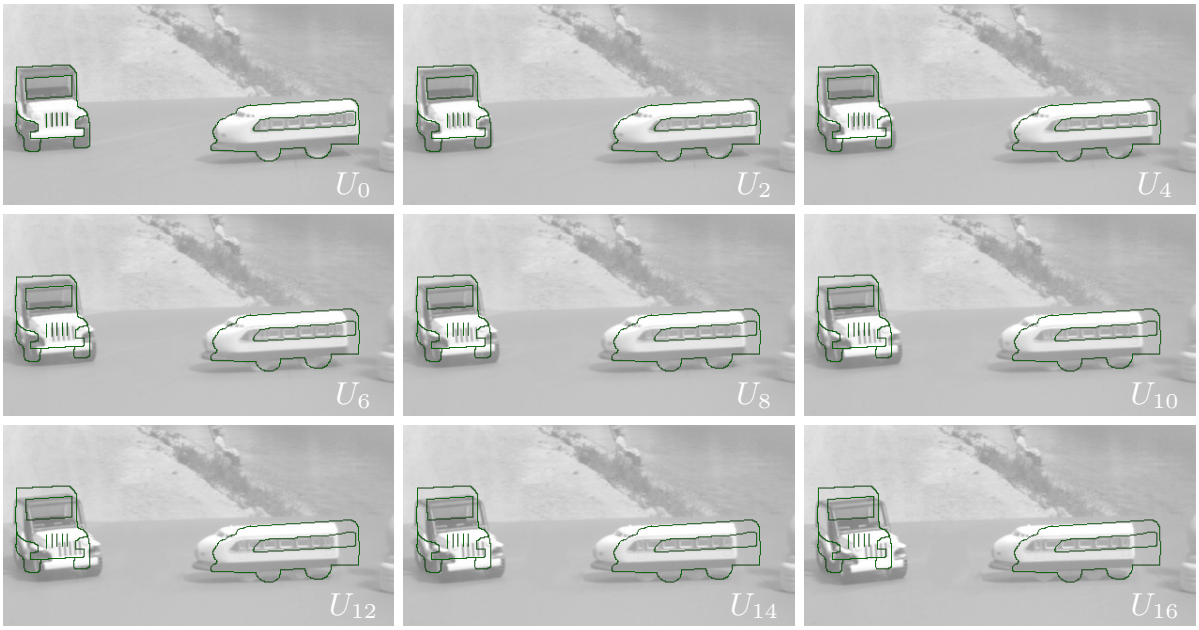

Figure 3.13: Discrete geodesic curve between two cars (conforming discretization with parameters $\gamma = 10^{-3}$ and $\delta = 10^{-2}$ and $K = 16$), the initial contours of the cars are retraced.

3.8 Extensions, Conclusion and Outlook

The variational time discretization of the metamorphosis model is the starting point of several successive publications:

– In [ERS+15] (joint work with Martin Rumpf, Stefan Simon, Kirsten Stahn and Benedikt Wirth), Bézier curves in the space of images are computed using a Riemannian version of de Casteljau's algorithm. The existence and stability of spatially continuous Bézier curves are proven using (3.9), the high regularity of the deformations and the Mosco-convergence. Furthermore, the analogous proof for spatially discrete Bézier curves relies on the preceding existence theorems for the time discrete metamorphosis model. Compared to the geodesic interpolation between several input images (referred to as control points), a spatially discrete Bézier curves between these control points admits a visually higher smoothness in time and the global impact of features of the control images. Figure 3.14 depicts a piecewise geodesic interpolation (second row) of three human faces (first row) as control points as well as the associated quadratic Bézier curve (third row).

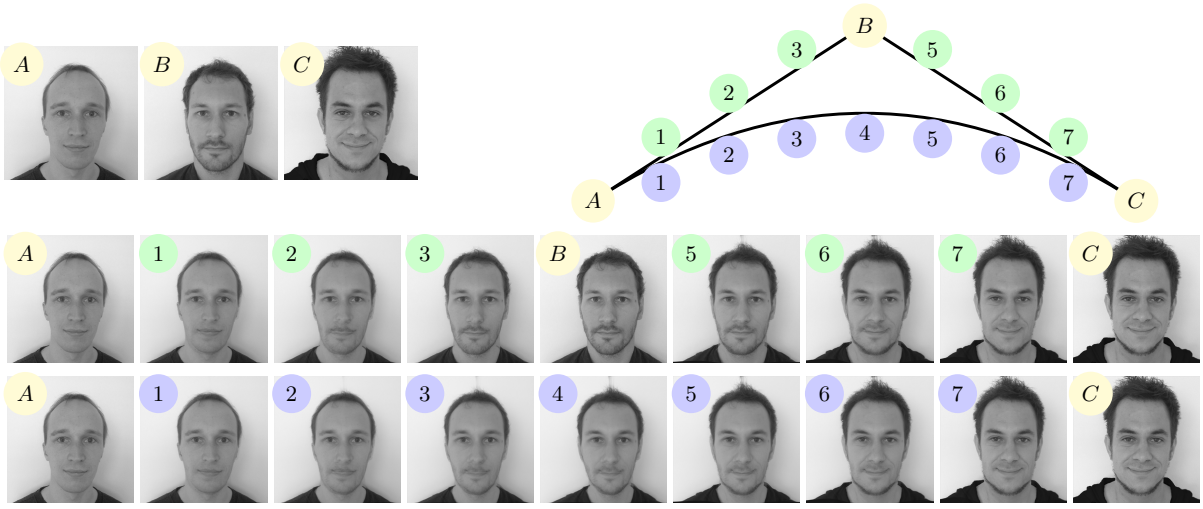

Figure 3.14: Piecewise discrete geodesic (middle) and quadratic Bézier curve (bottom) between human faces ($K = 8$, $\delta = 7.5 \cdot 10^{-3}$, $\gamma = 10^{-3}$).

– In [BBE+17] (joint work with Benjamin Berkels, Michael Buchner, Martin Rumpf and Steffen Schmitz–Valckenberg), the conforming discretization with the simplified energy density is employed to compute a discrete geodesic curve for data acquired with an optical coherence tomography of a human eye suffering from age-related macular degeneration in the years 2012 to 2015. To this end, the piecewise geodesic interpolation of consecutive years is compared to the geodesic curve between the data sets of 2012 and 2015 (see Figure 3.15). Since the time-critical step in the computation of geodesics is the solution to the registration subproblem, the energy and gradient assembly are implemented on the graphics card to speed up the computation time. In detail, elements in the mesh are identified with a thread on the GPU, and for the assembly of the discrete energy a reduction scheme is employed to perform the numerical quadrature.

– The Riemannian exponential map in the time discrete metamorphosis model is rigorously developed and analyzed in Chapter 4 ([ERS17a] and [ERS17b], joint work with Martin Rumpf and Florian Schäfer). Departing from the variational characterization of the one-step extrapolation (*cf*. (2.15)), whose existence and uniqueness follow from a suitable combination of a fixed point iteration and an implicit function type argument, the geodesic curve can be retrieved from the initial image and initial image variation by an iterative application of the one-step extrapolation as shown in Figure 2.1. The numerical optimization scheme relies on a slightly modified fixed point iteration and proves to be efficient.

In this chapter, we have proposed a time discretization of the time continuous metamorphosis model introduced by Trouvé, Younes and coworkers. We were able to prove the existence of time discrete geodesic curves and the

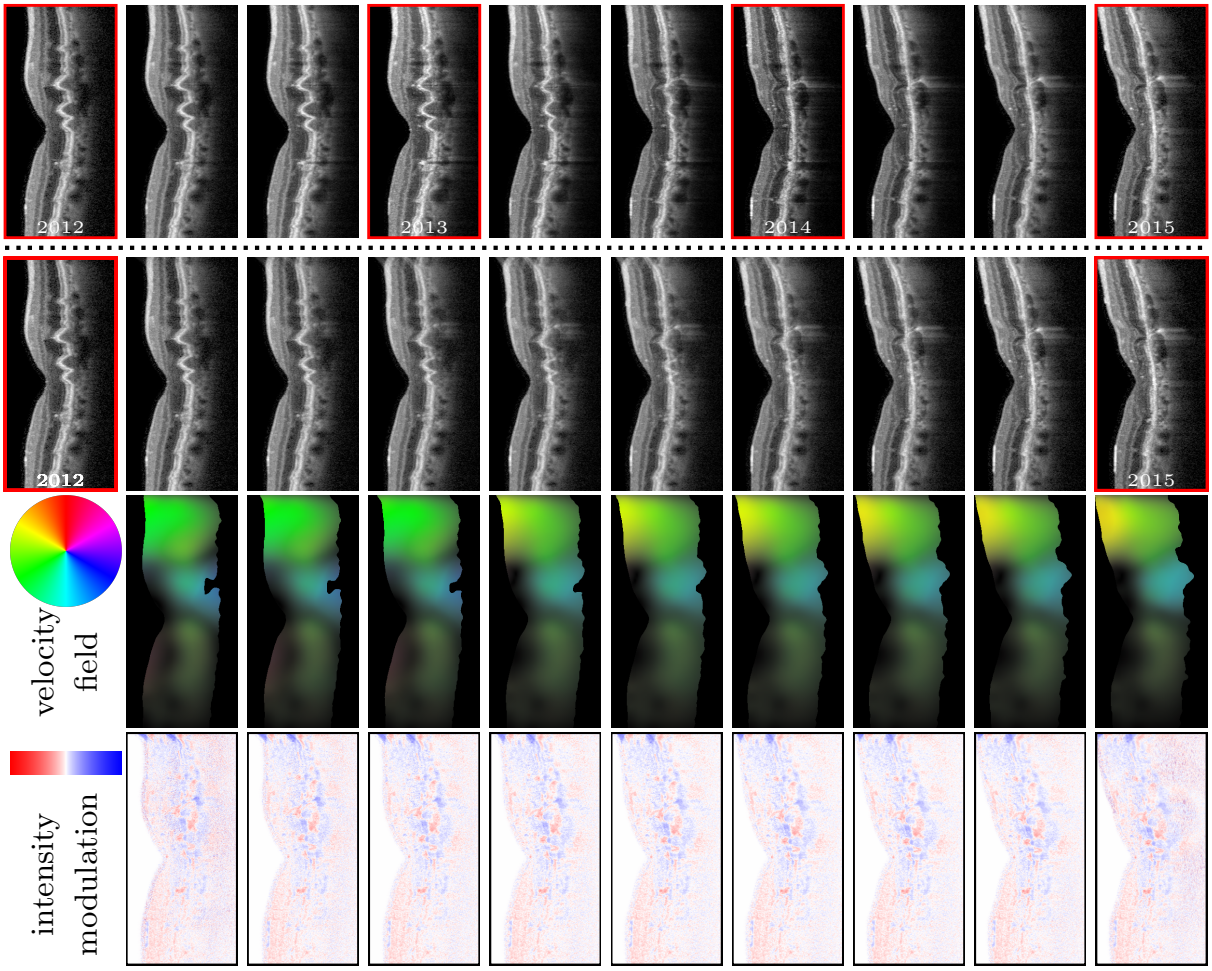

Figure 3.15: First row: piecewise geodesic interpolation for four consecutive years of a human eye for $K = 27$ (input data in red boxes). Second to fourth row: geodesic interpolation between the years 2012 and 2015 ($K = 27$ in each interpolation step), associated discrete velocity fields $K(\Phi_k - \mathbb{1})$ and intensity modulations $K(U_k \circ \Phi_k - U_{k-1})$.

Mosco-convergence of a suitable extension of the time discrete path energy to the time continuous metamorphosis energy functional. Two different discretizations of the fully discrete path energy were employed for an alternating minimization algorithm to compute discrete geodesic curves for numerous gray-scale and color images. However, there are some limitations related to the numerical optimization: the alternating algorithm suffers from a computation time ranging from a few minutes to several hours (in particular in the case of a 3D data set) and a high memory usage, which restricts the number of parallel threads for the registration subproblem. We experimentally exploited a trust region based solver for the registrations, which resulted in a moderate speedup at the expense of an even higher memory usage, but this solver was capable of significantly decreasing the approximation error related to the computation of the deformations. A further possible improvement could rely on duality techniques in PDE constrained optimization to derive a simultaneous optimization scheme for the images and deformations.

Chapter 4

Time Discrete Exponential Map in the Space of Images

In this chapter, we will rigorously define and analyze the discrete exponential map for the time discrete metamorphosis model in order to compute extrapolated image paths of arbitrary length, which in particular allows to (approximately) recover time discrete geodesics if solely the first two images along the sequence are given. To this end, in a first step we establish the (local) existence and (local) uniqueness of the one-step extrapolation. In detail, we derive suitable reformulations of the Euler–Lagrange equations associated with the one-step extrapolation and employ Banach's fixed point theorem to prove the existence of critical points of the Euler–Lagrange equations provided that the input images are weakly differentiable and L^2-close. If the input images are in addition close in H^1, then an implicit function type argument implies the local existence and uniqueness of the extrapolation for a single time step. Then, taking into account the iterative characterization of the general discrete exponential map (*cf*. (2.14)) allows the computation of extrapolated paths of arbitrary length. In all numerical applications, the discretization is based on a spatial Galerkin discretization with cubic B-splines on coarse meshes for the discrete deformations and bilinear and globally continuous finite elements on fine meshes for the image intensities. The minimizing discrete deformation for the registration of the second input image and the unknown extrapolated image in the one-step extrapolation is computed using a fixed point iteration. Afterwards, the optimal extrapolated image can be recovered from a pointwise condition emerging from the Euler–Lagrange equations. Several numerical examples underline the efficiency and stability of the proposed method to real image data.

This chapter is an extended version of the publications [ERS17a] and [ERS17b] (joint work with Martin Rumpf and Florian Schäfer). We refer to Subsection 3.1.3 for an overview of related work.

The structure of this chapter is as follows: In Section 4.1, we propose a slightly modified time discrete metamorphosis model, which essentially differs from the corresponding model presented in the previous chapter in terms of the boundary conditions for the deformations. Afterwards, the Euler–Lagrange equations for a single time step of the discrete exponential map are derived. In Section 4.2, the local existence and local uniqueness of this discrete exponential map are proven based on a suitable combination of Banach's fixed point theorem and the implicit function theorem. An efficient fixed point algorithm to compute the unknown deformation as well as an update formula for the unknown image intensity for the one-step extrapolation are proposed in Section 4.3. Finally, numerical results for different input data are presented in Section 4.4.

4.1 Time Discrete Exponential Map

In this section, we will adapt the iterative definition of the time discrete exponential map (*cf*. (2.14)) to the time discrete metamorphosis model as introduced in Chapter 3. To this end, we will slightly modify the time discretization of the metamorphosis model proposed in Section 3.2 and derive the Euler–Lagrange equations for the exponential map (see Subsection 4.1.1). In Subsection 4.1.2, we will state two reformulations of the Euler–Lagrange equations for the one-step extrapolation, on which the fixed point iterations used in the existence theorem for the discrete exponential map and in the numerical optimization are based.

4.1.1 Variational Time Discretization in the Context of the Discrete Exponential Map

In what follows, we will point out the (minor) differences to the variational time discretization introduced in Chapter 3. As before, we assume that $\Omega \subset \mathbb{R}^n$, $n \in \{2, 3\}$, is a bounded and strongly Lipschitz domain, and for $\gamma, \delta > 0$ we define for arbitrary images $u, \tilde{u} \in L^2(\Omega)$ the *discrete matching energy* (*cf*. (3.13))

$$\mathcal{W}[u, \tilde{u}] = \min_{\phi \in \mathcal{A}} \left\{ \mathcal{W}^D[u, \tilde{u}, \phi] = \int_\Omega \mathrm{W}(D\phi) + \gamma |D^m \phi|^2 + \frac{1}{\delta}(\tilde{u} \circ \phi - u)^2 \,\mathrm{d}x \right\} . \tag{4.1}$$

Contrary to the preceding chapter, m must satisfy $m > 2 + \frac{n}{2}$ and is assumed to be even. The *set of admissible deformations* is defined as

$$\mathcal{A} = \{\, \phi \in H^m(\Omega, \Omega) \,:\, \det(D\phi) > 0 \text{ a.e. in } \Omega, \phi - \mathbb{1} \in H_0^m(\Omega, \Omega) \,\} ,$$

where the weaker boundary condition $\phi = \mathbb{1}$ on $\partial\Omega$ is replaced by $\phi - \mathbb{1} \in H_0^m(\Omega, \Omega)$ (*cf*. (3.14)). With these altered boundary conditions the equality

$$\int_\Omega |\Delta^{\frac{m}{2}} \psi|^2 \,\mathrm{d}x = \int_\Omega |D^m \psi|^2 \,\mathrm{d}x \tag{4.2}$$

for all $\psi \in H_0^m(\Omega, \Omega)$ and even $m \geq 2$ holds true (*cf*. [GGS10, Section 2.2]). For instance, using integration by parts we obtain for $m = 2$

$$\int_\Omega |\Delta\psi|^2 \,\mathrm{d}x = \int_\Omega \sum_{i,j=1}^n \partial_i^2 \psi \cdot \partial_j^2 \psi \,\mathrm{d}x = \int_\Omega \sum_{i,j=1}^n \partial_i \partial_j \psi \cdot \partial_i \partial_j \psi \,\mathrm{d}x = \int_\Omega |D^2 \psi|^2 \,\mathrm{d}x \,.$$

Recall that the polyharmonic operator is inductively defined by $\Delta^l f = \Delta(\Delta^{l-1} f)$ for $f \in H^{2l}(\Omega)$ with $l \geq 2$. This stronger boundary condition is required for both a regularity result (*cf*. Proposition 4.1.2) and a higher order control of the deformations (*cf*. (4.14)). Throughout this chapter, the energy density W is assumed to satisfy (W1) and (W4), which implies that the minimum in (4.1) is actually attained by slightly modifying the proof of Proposition 3.4.2 provided that u and $\tilde{u}$ are sufficiently close in $L^2(\Omega)$.

Next, we define the discrete exponential map in the context of the time discrete metamorphosis model based on the construction in [RW15] and derive the associated Euler–Lagrange equations. The construction of the discrete exponential map is based on the recursive scheme (2.14) visualized in Figure 2.1. For fixed input images u_0 and u_1 we refer to u_0 as the base point and to $\zeta_1 = u_1 - u_0$ as the initial variation of the image u_0, which can be interpreted as the discrete counterpart of the infinitesimal variation in the continuous case.

Let us for the time being assume that $(u_0, u_1, \ldots, u_K)$ for $K \geq 2$ is the unique geodesic curve between u_0 and u_K (for the discussion of uniqueness see below). The *discrete exponential map* is then defined as

$$\mathrm{EXP}_{u_0}^k(\zeta_1) := u_k$$

for $k = 0, \ldots, K$. Since we are assuming uniqueness of the geodesic curve, the definition of $\mathrm{EXP}_{u_0}^k(\zeta_1)$ does not depend on the number of time steps K because $(u_0, u_1, \ldots, u_L)$ for any $L \leq K$ is also a geodesic. Following (2.14), the sequence $(\mathrm{EXP}_{u_0}^k(\zeta_1))_{k \geq 1}$ can be iteratively defined as

$$\mathrm{EXP}_{u_0}^k(\zeta_1) = u_k = \mathrm{EXP}_{u_{k-2}}^2(\zeta_{k-1})$$

for $k \geq 2$, where $\zeta_{k-1} = u_{k-1} - u_{k-2}$ represents the variation in the current step. For the sake of completeness, we define $\mathrm{EXP}_{u_0}^0(\zeta_1) = u_0$ and $\mathrm{EXP}_{u_0}^1(\zeta_1) = u_1 = u_0 + \zeta_1$. Thus, it essentially remains to compute EXP^2 for a given input image u_{k-2} and an image variation $\zeta_{k-1} = u_{k-1} - u_{k-2}$ (see Figure 2.1). There are two major restrictions regarding the input images u_0 and u_1:

1. In the existence and uniqueness result for the discrete exponential map (*cf*. Section 4.2), $H^1(\Omega)$-regularity of the input images is required, which results from the appearance of weak derivatives of the images in the Euler–Lagrange equations for EXP^2 w.r.t. the deformations (see (4.6) and (4.7)). The $H^1(\Omega)$-regularity property is inherited along the discrete extrapolated path, *i.e.* $\mathrm{EXP}_{u_0}^k(u_1 - u_0) \in H^1(\Omega)$ for any $k \geq 1$ provided that $u_0, u_1 \in H^1(\Omega)$ (*cf*. Section 3.4). The weak differentiability of the input data is also a crucial requirement in the initial value problem for the geodesic equation in the continuous metamorphosis model (*cf*. [TY05a, Theorem 7]).

2. The initial variation $\zeta_1 = u_1 - u_0$ is assumed to be sufficiently small in $L^2(\Omega)$ to guarantee the convergence of the fixed point iteration. Recall that this requirement also naturally arose in the context of the time discrete exponential map on Hilbert manifolds (*cf*. Subsection 2.2.3). The smallness of the variations $u_{k-1} - u_{k-2}$ for $k \leq K$ and fixed K is inherited along the geodesic path, *i.e*. the $L^2(\Omega)$-norm of ζ_k can be controlled in terms of the $L^2(\Omega)$-norm of the initial variation ζ_1. In particular, $\mathrm{EXP}^k_{u_0}(\,\cdot\,)$ is well-posed for any sufficiently small initial variation ζ_1 and $k \leq K$.

Henceforth, we assume $u_0, u_1 \in H^1(\Omega)$ with small initial variation $\zeta_1 = u_1 - u_0$ in $L^2(\Omega)$ and define $u_k = \mathrm{EXP}^2_{u_{k-2}}(\zeta_{k-1}) \in H^1(\Omega)$, where we tacitly assume uniqueness (*cf*. Theorem 4.2.2). Moreover, due to the iterative scheme (2.14), we may restrict our presentation to the computation of $u_2 = \mathrm{EXP}^2_{u_0}(\zeta_1)$. To compute u_2, we employ the variational formulation given in (2.15), *i.e*. the equation

$$u_1 = \operatorname*{argmin}_{u \in H^1(\Omega)} \mathcal{W}[u_0, u] + \mathcal{W}[u, u_2] = \operatorname*{argmin}_{u \in H^1(\Omega)} \min_{\phi_1, \phi_2 \in \mathcal{A}} \mathcal{W}^D[u_0, u, \phi_1] + \mathcal{W}^D[u, u_2, \phi_2] \tag{4.3}$$

must hold true.

4.1.2 Euler–Lagrange Equations of the Time Discrete Exponential Map

In this subsection, we will derive the Euler–Lagrange equations for (4.3) and reformulate the Euler–Lagrange equation w.r.t. ϕ_2, on which the fixed point iterations to be considered in later sections will be based.

Given $u_0, u_1 \in H^1(\Omega)$, the first order optimality conditions for (4.3) for $u_2 \in H^1(\Omega)$ and $\phi_1, \phi_2 \in \mathcal{A}$ read as

$$\begin{aligned} \partial_{u_1}(\mathcal{W}^D[u_0, u_1, \phi_1] + \mathcal{W}^D[u_1, u_2, \phi_2])(v) &= 0\,, \\ \partial_{\phi_1}\mathcal{W}^D[u_0, u_1, \phi_1](\psi) &= 0\,, \\ \partial_{\phi_2}\mathcal{W}^D[u_1, u_2, \phi_2](\psi) &= 0 \end{aligned} \tag{4.4}$$

for all $v \in H^1(\Omega)$ and all $\psi \in H^m_0(\Omega)$ for $m > 2 + \frac{n}{2}$. The system (4.4) is equivalent to

$$\int_\Omega (u_1 \circ \phi_1 - u_0) v \circ \phi_1 - (u_2 \circ \phi_2 - u_1) v \,\mathrm{d}x = 0\,, \tag{4.5}$$

$$\int_\Omega D\mathrm{W}(D\phi_1) : D\psi + 2\gamma \Delta^{\frac{m}{2}}\phi_1 \cdot \Delta^{\frac{m}{2}}\psi + \frac{2}{\delta}(u_1 \circ \phi_1 - u_0)(\nabla u_1 \circ \phi_1) \cdot \psi \,\mathrm{d}x = 0\,, \tag{4.6}$$

$$\int_\Omega D\mathrm{W}(D\phi_2) : D\psi + 2\gamma \Delta^{\frac{m}{2}}\phi_2 \cdot \Delta^{\frac{m}{2}}\psi + \frac{2}{\delta}(u_2 \circ \phi_2 - u_1)(\nabla u_2 \circ \phi_2) \cdot \psi \,\mathrm{d}x = 0\,. \tag{4.7}$$

The existence theorem as well as the numerical algorithm are based on fixed point iterations emerging from (4.7) to compute the unknown function ϕ_2. However, the equation in this form is not feasible for a fixed point scheme since it additionally depends on the unknown image u_2. Thus, in Lemma 4.1.1 we will reformulate (4.7) in two ways to circumvent this dependency. Additionally, derivatives of the image intensity functions no longer appear in the second reformulation (4.9). The first reformulation (4.8) will be employed in the existence proof for the time discrete exponential map, whereas the second reformulation (4.9) will be utilized in a modified and spatially discrete fixed point iteration in the numerical optimization.

Lemma 4.1.1 (Reformulation of the Euler–Lagrange equation for ϕ_2)**.** *Let $u_0, u_1, u_2 \in H^1(\Omega)$ such that (*cf. *Proposition 3.4.2)*

$$\|u_1 - u_0\|_{L^2(\Omega)}, \|u_2 - u_1\|_{L^2(\Omega)} \leq C_{\mathcal{W}}\,,$$

$m > 2 + \frac{n}{2}$, m even, and assume that (4.5) *and* (4.6) *hold true.*

(i.) Then (4.7) *is equivalent to*

$$\begin{aligned} \int_\Omega 2\gamma \Delta^{\frac{m}{2}}\phi_2 \cdot \Delta^{\frac{m}{2}}\psi + D\mathrm{W}(D\phi_2) : D\psi + \frac{2}{\delta}(u_1 \circ \phi_1 - u_0)(\nabla u_1 \cdot (D\phi_2)^{-1}\psi) \circ \phi_1 \\ + \frac{1}{\delta}\frac{(u_1 \circ \phi_1 - u_0)^2}{\det(D\phi_1)}\left((D\phi_2)^{-T} : (D^2\phi_2(D\phi_2)^{-1}\psi) - (D\phi_2)^{-T} : D\psi\right) \circ \phi_1 \,\mathrm{d}x = 0 \end{aligned} \tag{4.8}$$

for all $\psi \in H^m_0(\Omega)$.

(ii.) Under the additional assumptions $\partial\Omega \in C^{2m}$ and $u_0, u_1, u_2 \in L^\infty(\Omega) \cap H^1(\Omega)$, the equation (4.7) is equivalent to

$$\begin{aligned}&\int_\Omega 2\gamma\Delta^{\frac{m}{2}}\phi_2 \cdot \Delta^{\frac{m}{2}}\psi + D\mathrm{W}(D\phi_2) : D\psi \,\mathrm{d}x \\ &= \int_\Omega 2\gamma\Delta^{\frac{m}{2}}\phi_1 \cdot \Delta^{\frac{m}{2}}(((D\phi_2)^{-1}\psi)\circ\phi_1) + D\mathrm{W}(D\phi_1) : D(((D\phi_2)^{-1}\psi)\circ\phi_1) \\ &\quad - \frac{1}{\delta}\frac{(u_1\circ\phi_1 - u_0)^2}{\det(D\phi_1)}\left((D\phi_2)^{-T} : (D^2\phi_2(D\phi_2)^{-1}\psi) - (D\phi_2)^{-T} : D\psi\right)\circ\phi_1 \,\mathrm{d}x\,.\end{aligned} \tag{4.9}$$

Here, the notation $(D^2\phi_2(D\phi_2)^{-1}\psi)_{jk} = \sum_{i,l=1}^n \partial_j\partial_k\phi_2^i(D\phi_2)_{il}^{-1}\psi_l$ is used.

Proof. We recall that $\phi_1, \phi_2 \in \mathcal{A}$ are diffeomorphisms due to Proposition 3.4.2.

ad (i.): The transformation formula applied to the energy $\mathcal{W}^D$ yields

$$\mathcal{W}^D[u_1, u_2, \phi_2] = \int_\Omega \mathrm{W}(D\phi_2) + \gamma|\Delta^{\frac{m}{2}}\phi_2|^2 + \frac{1}{\delta}\frac{(u_2 - u_1\circ\phi_2^{-1})^2}{\det(D\phi_2)\circ\phi_2^{-1}}\,\mathrm{d}x\,.$$

Hence, the variation $\partial_{\phi_2}\mathcal{W}^D[u_1, u_2, \phi_2](\psi)$ reads as

$$\begin{aligned}&\int_\Omega D\mathrm{W}(D\phi_2) : D\psi + 2\gamma\Delta^{\frac{m}{2}}\phi_2 \cdot \Delta^{\frac{m}{2}}\psi + \frac{2}{\delta}(u_2 - u_1\circ\phi_2^{-1})\frac{(\nabla u_1 \cdot (D\phi_2)^{-1}\psi)\circ\phi_2^{-1}}{\det(D\phi_2)\circ\phi_2^{-1}} \\ &\quad + \frac{1}{\delta}\frac{(u_2 - u_1\circ\phi_2^{-1})^2}{(\det(D\phi_2))^2\circ\phi_2^{-1}}\left(\mathrm{cof}(D\phi_2) : (D^2\phi_2(D\phi_2)^{-1}\psi) - \mathrm{cof}(D\phi_2) : D\psi\right)\circ\phi_2^{-1}\,\mathrm{d}x = 0\end{aligned}$$

for any $\psi \in H_0^m(\Omega)$. Here, we used the identities $\partial_{\phi_2}\phi_2^{-1}(\psi) = -((D\phi_2)^{-1}\psi)\circ\phi_2^{-1}$, which immediately follows by differentiating $\varepsilon \mapsto (\phi_2 + \varepsilon\psi)\circ(\phi_2 + \varepsilon\psi)^{-1} = \mathbb{1}$ at $\varepsilon = 0$, and $\partial_A \det(A)(B) = \mathrm{cof}(A) : B$ for $A \in \mathrm{GL}(n)$ and $B \in \mathbb{R}^{n,n}$ with $\mathrm{cof}(A) = \det(A)A^{-T}$. By applying the transformation formula w.r.t. ϕ_2 once again one obtains

$$\begin{aligned}&\int_\Omega D\mathrm{W}(D\phi_2) : D\psi + 2\gamma\Delta^{\frac{m}{2}}\phi_2 \cdot \Delta^{\frac{m}{2}}\psi + \frac{2}{\delta}(u_2\circ\phi_2 - u_1)\nabla u_1 \cdot (D\phi_2)^{-1}\psi \\ &\quad + \frac{1}{\delta}\frac{(u_2\circ\phi_2 - u_1)^2}{\det(D\phi_2)}\left(\mathrm{cof}(D\phi_2) : (D^2\phi_2(D\phi_2)^{-1}\psi) - \mathrm{cof}(D\phi_2) : D\psi\right)\,\mathrm{d}x = 0\,.\end{aligned} \tag{4.10}$$

The optimality condition (4.5) implies the pointwise condition

$$u_2\circ\phi_2(x) - u_1(x) = \frac{u_1(x) - u_0\circ\phi_1^{-1}(x)}{\det(D\phi_1)\circ\phi_1^{-1}(x)} \tag{4.11}$$

for a.e. $x \in \Omega$, which is used along with the transformation formula w.r.t. ϕ_1 to remove the dependency of the function u_2 in (4.10) as follows:

$$\begin{aligned}&\int_\Omega D\mathrm{W}(D\phi_2) : D\psi + 2\gamma\Delta^{\frac{m}{2}}\phi_2 \cdot \Delta^{\frac{m}{2}}\psi + \frac{2}{\delta}(u_1\circ\phi_1 - u_0)(\nabla u_1 \cdot (D\phi_2)^{-1}\psi)\circ\phi_1 \\ &\quad + \frac{1}{\delta}\frac{(u_1\circ\phi_1 - u_0)^2}{\det(D\phi_1)}\left(\frac{\mathrm{cof}(D\phi_2) : (D^2\phi_2(D\phi_2)^{-1}\psi) - \mathrm{cof}(D\phi_2) : D\psi}{\det(D\phi_2)}\right)\circ\phi_1\,\mathrm{d}x = 0\,.\end{aligned}$$

The identity $\mathrm{cof}(A) = \det(A)A^{-T}$ for $A \in \mathrm{GL}(n)$ implies (i.).

ad (ii.): The proof of (ii.) follows by inserting the test function $\zeta := ((D\phi_2)^{-1}\psi)\circ\phi_1$ into (4.6). To justify this, we employ Proposition 1.1.4, Proposition 4.1.2 and the classical differential calculus for Sobolev functions [AF03] to deduce $\phi_1, \phi_2 \in H^{2m}(\Omega)$, which implies $\phi_1, \phi_2 \in C^{m+1}(\Omega)$ and thus $\zeta \in H_0^m(\Omega)$. By inserting ζ into (4.6) we get

$$\begin{aligned}&-\int_\Omega \frac{2}{\delta}(u_1\circ\phi_1 - u_0)(\nabla u_1 \cdot (D\phi_2)^{-1}\psi)\circ\phi_1\,\mathrm{d}x \\ &= \int_\Omega 2\gamma\Delta^{\frac{m}{2}}\phi_1 \cdot \Delta^{\frac{m}{2}}(((D\phi_2)^{-1}\psi)\circ\phi_1) + D\mathrm{W}(D\phi_1) : D(((D\phi_2)^{-1}\psi)\circ\phi_1)\,\mathrm{d}x\,.\end{aligned}$$

By adding the above equation to (4.8) we have proven (ii.).

This concludes the proof of the lemma. □

The following regularity result is solely required for the justification of the particular choice of the test function in the proof of Lemma 4.1.1 (ii.).

Proposition 4.1.2. *Let $m - \frac{n}{2} > 2$ and $\partial\Omega \in C^{2m}$. Furthermore, let $u_0, u_1, u_2 \in L^\infty(\Omega) \cap H^1(\Omega)$ and suppose that $\phi_1, \phi_2 \in \mathcal{A}$ satisfy* (4.6) *and* (4.7)*, respectively. Then $\phi_1, \phi_2 \in \mathcal{A} \cap H^{2m}(\Omega)$.*

Proof. We only prove the proposition for ϕ_2, for ϕ_1 one proceeds analogously. Let $w = \phi_2 - \mathbb{1} \in H_0^m(\Omega)$ be the displacement associated with ϕ_2. Using integration by parts of (4.7) we obtain

$$\begin{aligned}\int_\Omega \Delta^{\frac{m}{2}} w \cdot \Delta^{\frac{m}{2}} \psi \,\mathrm{d}x &= -\int_\Omega \tfrac{1}{\gamma\delta}(u_2 \circ \phi_2 - u_1)((\nabla u_2 \circ \phi_2)\cdot\psi) + \tfrac{1}{2\gamma} D\mathrm{W}(D\phi_2) : D\psi \,\mathrm{d}x \\ = -\int_\Omega \tfrac{1}{\gamma\delta}(u_2 \circ \phi_2 - u_1)((\nabla u_2 \circ \phi_2)\cdot\psi) - \tfrac{1}{2\gamma}\mathrm{div}(D\mathrm{W}(D\phi_2))\cdot\psi \,\mathrm{d}x &= \int_\Omega f\cdot\psi\,\mathrm{d}x\end{aligned}$$

for $f = -\frac{1}{\gamma\delta}(u_2 \circ \phi_2 - u_1)(\nabla u_2 \circ \phi_2) + \frac{1}{2\gamma}\mathrm{div}(D\mathrm{W}(D\phi_2)) \in L^2(\Omega, \mathbb{R}^n)$ and all test functions $\psi \in H_0^m(\Omega)$. The assertion of this proposition follows from the general $L^2(\Omega)$-regularity theory for polyharmonic equations as presented in [GGS10, Chapter 2]. □

4.2 Local Existence and Uniqueness of the Time Discrete Exponential Map

In this section, we will prove local existence and local uniqueness of the one-step extrapolation EXP^2.

In Theorem 4.2.1, we prove the existence of a solution vector (u_2, ϕ_1, ϕ_2) to the system of equations (4.5), (4.6) and (4.7) for given input images u_0 and u_1, which are assumed to be $H^1(\Omega)$-regular and sufficiently close in $L^2(\Omega)$. The existence of the minimizing deformation ϕ_1 is immediate due to Proposition 3.4.2. In the subsequent step, we apply Banach's fixed point theorem to (4.8) to prove the existence of a minimizing diffeomorphism ϕ_2. Finally, the optimal image intensity u_2 is computed by employing (4.11) as follows

$$u_2 = \left(\frac{u_1 - u_0 \circ \phi_1^{-1}}{\det(D\phi_1)\circ\phi_1^{-1}}\right)\circ\phi_2^{-1} + u_1 \circ \phi_2^{-1}\,. \tag{4.12}$$

We will frequently refer to the first summand of (4.12) as the *intensity modulation along the geodesic*, the second summand quantifies the contribution due to the *transport*. We highlight that in general this theorem does not imply the uniqueness of the discrete geodesic path (u_0, u_1, u_2) for given images u_0 and u_1.

The uniqueness property of the discrete exponential map is studied in Theorem 4.2.2 under the stronger assumption that u_0 and u_1 are sufficiently close in $H^1(\Omega)$. The proof is based on an implicit function theorem argument, which also implies the local existence of the discrete exponential map in an alternative way.

Theorem 4.2.1 (Existence of solutions to the Euler–Lagrange equations)**.** *Let $m - \frac{n}{2} > 2$, $u_0 \in H^1(\Omega)$ and assume that (W1) and (W4) hold true. Then there are constants $C_u, c_u > 0$ such that for every*

$$u_1 \in \left\{\, u \in H^1(\Omega) \,:\, |u|_{H^1(\Omega)} \le C_u, \|u - u_0\|_{L^2(\Omega)} \le c_u \,\right\}$$

there exists a solution $(u_2, \phi_1, \phi_2) \in H^1(\Omega)\times\mathcal{A}\times\mathcal{A}$ to (4.5)*,* (4.6) *and* (4.7)*. In particular, u_2 solves the defining system of equations for $\mathrm{EXP}^2_{u_0}(u_1 - u_0)$.*

Proof. The proof is separated into five steps:

(i.) *Uniform control of the initial displacement and the initial mismatch.*

Taking into account Proposition 3.4.2, the minimizing deformation $\phi_1 \in \mathrm{argmin}_{\phi\in\mathcal{A}}\,\mathcal{W}^D[u_0, u_1, \phi]$ exists provided that $c_u < C_{\mathcal{W}}$, which we assume hereafter. As a consequence of the optimality of ϕ_1 and (W1) one can infer

$$\mathcal{W}^D[u_0, u_1, \phi_1] \le \mathcal{W}^D[u_0, u_1, \mathbb{1}] = \frac{1}{\delta}\|u_1 - u_0\|^2_{L^2(\Omega)}\,. \tag{4.13}$$

Hence, the relation $\phi_1 - \mathbb{1} \in H_0^m(\Omega)$ as well as (4.2) and (4.13) imply

$$\int_\Omega \gamma |D^m(\phi_1 - \mathbb{1})|^2 \,\mathrm{d}x = \int_\Omega \gamma |\Delta^{\frac{m}{2}}(\phi_1 - \mathbb{1})|^2 \,\mathrm{d}x = \int_\Omega \gamma |\Delta^{\frac{m}{2}} \phi_1|^2 \,\mathrm{d}x \leq \frac{1}{\delta} \|u_1 - u_0\|_{L^2(\Omega)}^2 \leq \frac{c_u^2}{\delta} \,.$$

Thus, the norm equivalence of $\|\cdot\|_{H^m(\Omega)}$ and $|\cdot|_{H^m(\Omega)}$ for the space $H_0^m(\Omega)$, which follows by an iterative application of the Poincaré inequality (*cf*. [AF03, Corollary 6.31]), yields

$$\|\phi_1 - \mathbb{1}\|_{H^m(\Omega)} \leq C \|u_1 - u_0\|_{L^2(\Omega)} \leq C c_u \,. \tag{4.14}$$

Furthermore, taking into account (4.13) we can infer

$$\|u_1 \circ \phi_1 - u_0\|_{L^2(\Omega)} \leq \sqrt{\delta \, \mathcal{W}^D[u_0, u_1, \phi_1]} \leq \sqrt{\delta \, \mathcal{W}^D[u_0, u_1, \mathbb{1}]} = \|u_1 - u_0\|_{L^2(\Omega)} \leq c_u \,. \tag{4.15}$$

(ii.) *Definition of the fixed point mapping $\mathcal{F}$.*

Before defining the fixed point mapping $\mathcal{F} : \mathcal{A} \to \mathcal{A}$ we consider the operators $\mathcal{T}, \mathcal{R} : \mathcal{A} \to H^{-m}(\Omega)$ given by

$$\begin{aligned} \mathcal{T}[\phi](\psi) = \int_\Omega & - D\mathrm{W}(D\phi) : D\psi + D^2\mathrm{W}(\mathbb{1})(D\phi - \mathbb{1}, D\psi) - \frac{2}{\delta}(u_1 \circ \phi_1 - u_0)(\nabla u_1 \cdot (D\phi)^{-1}\psi) \circ \phi_1 \\ & - \frac{1}{\delta} \frac{(u_1 \circ \phi_1 - u_0)^2}{\det(D\phi_1)} \left((D\phi)^{-T} : (D^2\phi (D\phi)^{-1}\psi) - (D\phi)^{-T} : D\psi \right) \circ \phi_1 \,\mathrm{d}x \,, \end{aligned} \tag{4.16}$$

$$\mathcal{R}[\phi](\psi) = \int_\Omega 2\gamma \Delta^{\frac{m}{2}} \phi \cdot \Delta^{\frac{m}{2}} \psi + D^2\mathrm{W}(\mathbb{1})(D\phi - \mathbb{1}, D\psi) \,\mathrm{d}x \tag{4.17}$$

for all $\phi \in \mathcal{A}$ and all $\psi \in H_0^m(\Omega)$. Thus, the reformulation (4.8) of the Euler–Lagrange equation w.r.t. ϕ_2 turns out to be equivalent to

$$\mathcal{T}[\phi_2](\psi) = \mathcal{R}[\phi_2](\psi) \,.$$

In step (iii.) we will show that the operator norm of the nonlinear operator $\mathcal{T}$ can be made arbitrarily small for small quantities of C_u and c_u, and in combination with the invertibility of the linear operator $\mathcal{R}$ by means of the Lax–Milgram theorem to be proven in (iv.) we can deduce that $\mathcal{F} = \mathcal{R}^{-1} \circ \mathcal{T}$ is actually a contraction mapping for suitable values of C_u and c_u. Thus, the fixed point iteration $\phi^{(i+1)} = \mathcal{F}[\phi^{(i)}]$ converges due to Banach's fixed point theorem to the optimal deformation ϕ_2, which is characterized by $\phi_2 = \mathcal{F}[\phi_2]$.

(iii.) *Lipschitz continuity of the nonlinear operator $\mathcal{T}$.*

For $\varepsilon > 0$ sufficiently small, we restrict the operator $\mathcal{T}$ to the domain

$$B_\varepsilon(\mathbb{1}) := \left\{ \phi \,:\, \phi - \mathbb{1} \in H_0^m(\Omega), \|\phi - \mathbb{1}\|_{H^m(\Omega)} < \varepsilon \right\} \,.$$

In particular, depending on C_u and c_u the parameter ε has to be chosen such that $\mathcal{F}$ is a self-map, the details are deferred to step (v.).

A Taylor expansion applied to the first term of $\mathcal{T}$ gives

$$\begin{aligned} D\mathrm{W}(D\phi) : D\psi = {} & D\mathrm{W}(\mathbb{1}) : D\psi + D^2\mathrm{W}(\mathbb{1})(D\phi - \mathbb{1}, D\psi) \\ & + \int_0^1 (1 - \vartheta) D^3\mathrm{W}(\mathbb{1} + \vartheta(D\phi - \mathbb{1}))(D\phi - \mathbb{1}, D\phi - \mathbb{1}, D\psi) \,\mathrm{d}\vartheta \,. \end{aligned}$$

Thus, making use of $\mathrm{W} \in C^4(\mathrm{GL}^+(n))$, $H^m(\Omega) \hookrightarrow C^2(\overline{\Omega})$, $\max_{f \in \overline{B_\varepsilon}(\mathbb{1})} D^j\mathrm{W}(Df) \leq C$ for $j \in \{3, 4\}$

and $D\mathrm{W}(\mathbb{1}) = 0$ we obtain the following estimates for the first two terms of $\mathcal{T}$:

$$\begin{aligned}
&\Big| \int_\Omega -D\mathrm{W}(D\phi) : D\psi + D^2\mathrm{W}(\mathbb{1})(D\phi - \mathbb{1}, D\psi) + D\mathrm{W}(D\tilde\phi) : D\psi - D^2\mathrm{W}(\mathbb{1})(D\tilde\phi - \mathbb{1}, D\psi)\,\mathrm{d}x \Big| \\
&\leq \Big| \int_\Omega \int_0^1 (1-\vartheta)\Big(D^3\mathrm{W}(\mathbb{1} + \vartheta(D\phi - \mathbb{1}))(D\phi - \mathbb{1}, D\phi - \mathbb{1}, D\psi) \\
&\qquad\qquad - D^3\mathrm{W}(\mathbb{1} + \vartheta(D\tilde\phi - \mathbb{1}))(D\tilde\phi - \mathbb{1}, D\tilde\phi - \mathbb{1}, D\psi)\Big)\,\mathrm{d}\vartheta\,\mathrm{d}x \Big| \\
&\leq C\left(\|\phi - \mathbb{1}\|_{H^m(\Omega)}^2 + \|\phi - \mathbb{1}\|_{H^m(\Omega)} + \|\tilde\phi - \mathbb{1}\|_{H^m(\Omega)} \right) \|\phi - \tilde\phi\|_{C^1(\overline\Omega)} \|\psi\|_{H^m(\Omega)} \\
&\leq C(\varepsilon^2 + 2\varepsilon)\|\phi - \tilde\phi\|_{H^m(\Omega)}\|\psi\|_{H^m(\Omega)} \leq C\varepsilon\|\phi - \tilde\phi\|_{H^m(\Omega)}\|\psi\|_{H^m(\Omega)}
\end{aligned}$$

for $\phi, \tilde\phi \in B_\varepsilon(\mathbb{1})$. By decreasing c_u and ε if necessary and using the embedding $H^m(\Omega) \hookrightarrow C^2(\overline\Omega)$ we may assume

$$\|D\phi - \mathbb{1}\|_{C^0(\overline\Omega)} < \tfrac{1}{2}\,, \qquad \|\det(D\phi) - 1\|_{C^0(\overline\Omega)} < \tfrac{1}{2} \tag{4.18}$$

for all deformations ϕ to be considered in this proof, which are additionally $C^1(\Omega)$-diffeomorphisms in view of Theorem 3.4.1 (i.). Using (4.18) we can straightforwardly verify

$$\|\det(D\phi^{-1})\|_{C^0(\overline\Omega)} \leq \Big(1 - \|\det(D\phi) - 1\|_{C^0(\overline\Omega)}\Big)^{-1} < 2\,,\ \|\mathrm{cof}(D\phi)\|_{C^0(\overline\Omega)} \leq C\,,\ \|(D\phi)^{-1}\|_{C^0(\overline\Omega)} \leq C\,.$$

Moreover, due to $(D\phi)^{-1} = (\det(D\phi))^{-1}\mathrm{cof}(D\phi)^T$ the following control of the derivatives of the inverse deformations holds true:

$$\begin{aligned}
&\|(D\phi)^{-1} - (D\tilde\phi)^{-1}\|_{C^0(\overline\Omega)} = \|(\det(D\phi))^{-1}\mathrm{cof}(D\phi)^T - (\det(D\tilde\phi))^{-1}\mathrm{cof}(D\tilde\phi)^T\|_{C^0(\overline\Omega)} \\
&\leq \Big\| \tfrac{(\mathrm{cof}(D\phi))^T}{\det(D\phi)\det(D\tilde\phi)} \Big\|_{C^0(\overline\Omega)} \|\det(D\phi) - \det(D\tilde\phi)\|_{C^0(\overline\Omega)} \\
&\quad + \|(\det(D\tilde\phi))^{-1}\|_{C^0(\overline\Omega)} \|\mathrm{cof}(D\phi)^T - \mathrm{cof}(D\tilde\phi)^T\|_{C^0(\overline\Omega)} \\
&\leq C\|\phi - \tilde\phi\|_{H^m(\Omega)}\,.
\end{aligned} \tag{4.19}$$

By combining the estimates (4.15), (4.18) and (4.19) as well as the Cauchy–Schwarz inequality and the transformation formula we can finally infer the following estimate for the third term of $\mathcal{T}$:

$$\begin{aligned}
&\Big| \int_\Omega (u_1 \circ \phi_1 - u_0)(\nabla u_1 \circ \phi_1) \cdot ((D\phi)^{-1}\psi) \circ \phi_1 - (u_1 \circ \phi_1 - u_0)(\nabla u_1 \circ \phi_1) \cdot ((D\tilde\phi)^{-1}\psi) \circ \phi_1\,\mathrm{d}x \Big| \\
&\leq C\|u_1 \circ \phi_1 - u_0\|_{L^2(\Omega)} |u_1|_{H^1(\Omega)} \|\det(D(\phi_1^{-1}))\|_{C^0(\overline\Omega)}^{\frac{1}{2}} \|(D\phi)^{-1} - (D\tilde\phi)^{-1}\|_{C^0(\overline\Omega)} \|\psi\|_{C^0(\overline\Omega)} \\
&\leq CC_u c_u \|\phi - \tilde\phi\|_{H^m(\Omega)} \|\psi\|_{H^m(\Omega)}\,.
\end{aligned}$$

Likewise, for the fourth term of $\mathcal{T}$ we obtain by the transformation formula and by the usual embedding $H^m(\Omega) \hookrightarrow C^2(\overline\Omega)$

$$\begin{aligned}
&\Big| \int_\Omega \frac{(u_1 \circ \phi_1 - u_0)^2}{\det(D\phi_1)} \Big((D\phi)^{-T} : (D^2\phi(D\phi)^{-1}\psi) - (D\tilde\phi)^{-T} : (D^2\tilde\phi(D\tilde\phi)^{-1}\psi) \\
&\qquad\qquad - (D\phi)^{-T} : D\psi + (D\tilde\phi)^{-T} : D\psi \Big) \circ \phi_1\,\mathrm{d}x \Big| \\
&\leq Cc_u^2 \|(\det(D\phi_1))^{-1}\|_{C^0(\overline\Omega)} \big(\|(D\phi)^{-T} : (D^2\phi(D\phi)^{-1}\psi) - (D\tilde\phi)^{-T} : (D^2\tilde\phi(D\tilde\phi)^{-1}\psi)\|_{C^0(\overline\Omega)} \\
&\qquad\qquad + \|(D\phi)^{-T} : D\psi - (D\tilde\phi)^{-T} : D\psi\|_{C^0(\overline\Omega)} \big) \\
&\leq Cc_u^2 \|\phi - \tilde\phi\|_{H^m(\Omega)} \|\psi\|_{H^m(\Omega)}\,.
\end{aligned}$$

To conclude, for $\|u_1 - u_0\|_{L^2(\Omega)} \leq c_u$ and $|u_1|_{H^1(\Omega)} \leq C_u$ the mapping $\mathcal{T}$ is indeed Lipschitz continuous on the subset $B_\varepsilon(\mathbb{1}) \subset \mathcal{A}$ and the Lipschitz constant is bounded by $C(C_u c_u + c_u^2 + \varepsilon)$.

(iv.) *Invertibility of the linear operator $\mathcal{R}$.*

To prove the invertibility of $\mathcal{R}$, let us first examine the bilinear form

$$\widetilde{\mathcal{R}} : H_0^m(\Omega) \times H_0^m(\Omega) \to \mathbb{R}\,, \quad \widetilde{\mathcal{R}}[\zeta](\psi) \mapsto \int_\Omega 2\gamma \Delta^{\frac{m}{2}} \zeta \cdot \Delta^{\frac{m}{2}} \psi + D^2\mathrm{W}(\mathbb{1})(D\zeta, D\psi)\,\mathrm{d}x\,,$$

which is clearly bounded in $H_0^m(\Omega)$. Furthermore, $\widetilde{\mathcal{R}}$ is coercive since for any $\psi \in H_0^m(\Omega)$ we obtain

$$\|\psi\|^2_{H^m(\Omega)} \leq C|\psi|^2_{H^m(\Omega)} = C \int_\Omega \Delta^{\frac{m}{2}} \psi \cdot \Delta^{\frac{m}{2}} \psi \,\mathrm{d}x \tag{4.20}$$

due to (4.2) and the iterative application of the Poincaré inequality (*cf*. [AF03, Corollary 6.31]). Hence, by the Lax–Milgram Theorem (*cf*. [GT92]) there exists for every $z \in H^{-m}(\Omega)$ a unique $\zeta \in H_0^m(\Omega)$ such that $\widetilde{\mathcal{R}}[\zeta](\psi) = z(\psi)$ and $\widetilde{\mathcal{R}}[\,\cdot\,]^{-1} : H^{-m}(\Omega) \to H_0^m(\Omega)$ is a bounded operator. Finally, taking into account the shift $\mathcal{R}[\phi] = \widetilde{\mathcal{R}}[\phi - \mathbb{1}]$ we can infer that $\mathcal{R}[\,\cdot\,]$ is a bounded and invertible operator with inverse $\mathcal{R}^{-1}[z] = \mathbb{1} + \widetilde{\mathcal{R}}^{-1}[z]$.

(v.) *Contraction property of the fixed point mapping $\mathcal{F}$.*

In this step, we will verify that $\mathcal{F} = \mathcal{R}^{-1} \circ \mathcal{T}$ is indeed a contraction mapping, *i.e*. $\mathcal{F}$ is a self-map and its operator norm is strictly less than 1. Taking into account the boundedness of $\mathcal{R}^{-1}$ and the Lipschitz-continuity of $\mathcal{T}$ shown in the preceding steps we conclude

$$\|\mathcal{F}[\phi] - \mathcal{F}[\tilde{\phi}]\|_{H^m(\Omega)} \leq C\|\mathcal{T}[\phi] - \mathcal{T}[\tilde{\phi}]\|_{H^{-m}(\Omega)} \leq C(C_u c_u + c_u^2 + \varepsilon)\|\phi - \tilde{\phi}\|_{H^m(\Omega)} \tag{4.21}$$

for $\phi, \tilde{\phi} \in B_\varepsilon(\mathbb{1})$, which implies that $\mathcal{F}$ is contractive for sufficiently small C_u, c_u and ε. It remains to demonstrate that $\mathcal{F}$ is a self-map for a proper choice of C_u, c_u and ε, *i.e*. $\mathcal{F} : B_\varepsilon(\mathbb{1}) \to B_\varepsilon(\mathbb{1})$. To this end, let

$$\mathcal{S}[\phi](\psi) = \int_\Omega -D\mathrm{W}(D\phi) : D\psi + D^2\mathrm{W}(\mathbb{1})(D\phi - \mathbb{1}, D\psi)\,\mathrm{d}x$$

for all $\psi \in H_0^m(\Omega)$ denote the first two summands of $\mathcal{T}$. Using (W1) one can verify that $\mathcal{R}^{-1} \circ \mathcal{S}[\mathbb{1}] = \mathbb{1}$ and thus

$$\|\mathcal{F}[\mathbb{1}] - \mathbb{1}\|_{H^m(\Omega)} = \|\mathcal{R}^{-1} \circ \mathcal{T}[\mathbb{1}] - \mathcal{R}^{-1} \circ \mathcal{S}[\mathbb{1}]\|_{H^m(\Omega)} \leq C\|(\mathcal{T} - \mathcal{S})[\mathbb{1}]\|_{H^{-m}(\Omega)} \leq C(C_u c_u + c_u^2)\,.$$

Hence, for any $\phi \in B_\varepsilon(\mathbb{1})$ one gets

$$\begin{aligned} &\|\mathcal{F}[\phi] - \mathbb{1}\|_{H^m(\Omega)} \leq \|\mathcal{F}[\phi] - \mathcal{F}[\mathbb{1}]\|_{H^m(\Omega)} + \|\mathcal{F}[\mathbb{1}] - \mathbb{1}\|_{H^m(\Omega)} \\ &\leq C(C_u c_u + c_u^2 + \varepsilon)\|\phi - \mathbb{1}\|_{H^m(\Omega)} + C(C_u c_u + c_u^2) \leq C(C_u c_u + c_u^2 + \varepsilon)\varepsilon + C(C_u c_u + c_u^2)\,. \end{aligned} \tag{4.22}$$

To sum up, one has to choose $C_u > 0$, $c_u \in (0, C_{\mathcal{W}})$ and $\varepsilon > 0$ such that

- the conditions in (4.18) are satisfied for all $\phi \in B_\varepsilon(\mathbb{1})$ and for the initial deformation ϕ_1,
- $\mathcal{F}$ is contractive, *i.e*. $C(C_u c_u + c_u^2 + \varepsilon) < 1$ (*cf*. (4.21)), and
- $\mathcal{F} : B_\varepsilon(\mathbb{1}) \to B_\varepsilon(\mathbb{1})$ is a self-map, *i.e*. $C(C_u c_u + c_u^2 + \varepsilon)\varepsilon + C(C_u c_u + c_u^2) < \varepsilon$ (see (4.22)),

are satisfied simultaneously, which allows the application of Banach's fixed point theorem to prove the existence of a unique deformation $\phi_2 \in B_\varepsilon(\mathbb{1}) \subset \mathcal{A}$ solving (4.8). Finally, the optimal image intensity u_2 associated with the deformation ϕ_2 is uniquely characterized by (4.12). Thus, there exists a solution $(u_2, \phi_1, \phi_2) \in H^1(\Omega) \times \mathcal{A} \times \mathcal{A}$ to (4.5), (4.6) and (4.7), and u_2 as well as ϕ_2 are unique for a given deformation ϕ_1.

This finishes the proof of the theorem. □

In the subsequent theorem, the local uniqueness and local existence of the discrete exponential map are proven for $H^1(\Omega)$-close input images.

Theorem 4.2.2 (Local uniqueness and well-posedness of the discrete exponential map)**.** *Let $m-\frac{n}{2}>2$ and assume that (W1) and (W4) are valid. Then for every fixed input image $u_0\in H^1(\Omega)$ there exist neighborhoods $\mathbf{U}\subset H^1(\Omega)$ of u_0 and $\mathbf{D}\subset\mathcal{A}$ of $\mathbb{1}$ such that for every $u_2\in\mathbf{U}$ there exists a unique solution $(u_1,\phi_1,\phi_2)\in\mathbf{U}\times\mathbf{D}\times\mathbf{D}$ to the equations* (4.5)-(4.7)*. In particular, the discrete exponential map is locally well-posed and*

$$u_2=\mathrm{EXP}^2_{u_0}(u_1-u_0)\,.$$

Proof. The proof is based on the implicit function theorem applied to the functional

$$\mathcal{J}:H^1(\Omega)\times\mathcal{A}\times\mathcal{A}\to\mathbb{R}\,,\quad (u_2,\phi_1,\phi_2)\mapsto\mathcal{W}^D[u_0,u_1[u_2,\phi_1,\phi_2],\phi_1]+\mathcal{W}^D[u_1[u_2,\phi_1,\phi_2],u_2,\phi_2]\,,$$

where $u_1[u_2,\phi_1,\phi_2]$ denotes the optimal central image along the geodesic curve (u_0,u_1,u_2) depending on u_2, ϕ_1 and ϕ_2 (we omit the dependence on the image u_0). Here, we tacitly assume that $\mathbf{U}$ and $\mathbf{D}$ are sufficiently small such that Proposition 3.4.8 (ii.) actually ensures the existence of a unique image $u_1[u_2,\phi_1,\phi_2]$. To derive an explicit expression for $u_1[u_2,\phi_1,\phi_2]$, we note that the sum of the two matching terms in $\mathcal{J}$ can be rewritten as follows

$$\begin{aligned}&\int_\Omega (u_1[u_2,\phi_1,\phi_2]\circ\phi_1-u_0)^2+(u_2\circ\phi_2-u_1[u_2,\phi_1,\phi_2])^2\,\mathrm{d}x\\&=\int_\Omega (u_1[u_2,\phi_1,\phi_2]\circ\phi_1-u_0)^2+(u_2\circ\phi_2\circ\phi_1-u_1[u_2,\phi_1,\phi_2]\circ\phi_1)^2\det(D\phi_1)\,\mathrm{d}x\,.\end{aligned}$$

Thus, the optimal image intensity map $u_1[u_2,\phi_1,\phi_2]$ is characterized pointwise a.e. in Ω by (*cf*. (4.11))

$$u_1[u_2,\phi_1,\phi_2]\circ\phi_1=\frac{u_0+(u_2\circ\phi_2\circ\phi_1)\det(D\phi_1)}{1+\det(D\phi_1)}\,,$$

which implies that $\mathcal{J}$ admits the explicit form

$$\mathcal{J}[u_2,\phi_1,\phi_2]=\int_\Omega \mathrm{W}(D\phi_1)+\gamma|\Delta^{\frac{m}{2}}\phi_1|^2+\mathrm{W}(D\phi_2)+\gamma|\Delta^{\frac{m}{2}}\phi_2|^2+\frac{h(D\phi_1)}{\delta}(u_2\circ\phi_2\circ\phi_1-u_0)^2\,\mathrm{d}x$$

for $h(A)=\frac{\det(A)}{1+\det(A)}$. Moreover, let us introduce the functional

$$\mathcal{K}:H^1(\Omega)\times\mathcal{A}\times\mathcal{A}\to(H^m_0(\Omega)\times H^m_0(\Omega))'\,,\quad (u_2,\phi_1,\phi_2)\mapsto\partial_{(\phi_1,\phi_2)}\mathcal{J}[u_2,\phi_1,\phi_2]\,.$$

With these definitions at hand, the Euler–Lagrange equations (4.5)-(4.7) turn into the implicit equation

$$\mathcal{K}[u_2,\phi_1,\phi_2]=0\,. \tag{4.23}$$

In what follows, we will employ the implicit function theorem for Banach spaces (*cf*. [Zei95, Chapter 4]) to prove that for every u_2 in a $H^1(\Omega)$-neighborhood of the input image u_0 there exists unique deformations $(\phi_1,\phi_2)[u_2]\in\mathcal{A}\times\mathcal{A}$ in a $H^m(\Omega)$-neighborhood of $(\mathbb{1},\mathbb{1})$ such that (4.23) is valid, which readily implies the claim. Thus, it solely remains to verify that $\partial_{(\phi_1,\phi_2)}\mathcal{K}[u_0,\mathbb{1},\mathbb{1}]=\partial^2_{(\phi_1,\phi_2)}\mathcal{J}[u_0,\mathbb{1},\mathbb{1}]$ is invertible with bounded inverse in order to apply the implicit function theorem. To this end, to compute $\partial^2_{(\phi_1,\phi_2)}\mathcal{J}[u_2,\phi_1,\phi_2]$, we focus on the variation of

$$\widetilde{\mathcal{J}}[u_2,\phi_1,\phi_2]=\int_\Omega h(D\phi_1)(u_2\circ\phi_2\circ\phi_1-u_0)^2\,\mathrm{d}x\,,$$

since the derivation of the other components of $\partial^2_{(\phi_1,\phi_2)}\mathcal{J}[u_2,\phi_1,\phi_2]$ is straightforward. The first derivatives of $\widetilde{\mathcal{J}}$ w.r.t. the deformations in the direction $\psi\in H^m_0(\Omega)$ read as

$$\begin{aligned}\partial_{\phi_1}\widetilde{\mathcal{J}}[u_2,\phi_1,\phi_2](\psi)&=\int_\Omega (u_2\circ\phi_2\circ\phi_1-u_0)^2Dh(D\phi_1):D\psi\\&\quad+2h(D\phi_1)(u_2\circ\phi_2\circ\phi_1-u_0)\nabla(u_2\circ\phi_2\circ\phi_1)\cdot(D\phi_1)^{-1}\psi\,\mathrm{d}x\\&=\int_\Omega (u_2\circ\phi_2\circ\phi_1-u_0)^2Dh(D\phi_1):D\psi-(u_2\circ\phi_2\circ\phi_1)^2\mathrm{div}\left(h(D\phi_1)(D\phi_1)^{-1}\psi\right)\\&\quad+2(u_2\circ\phi_2\circ\phi_1)\mathrm{div}\left(u_0h(D\phi_1)(D\phi_1)^{-1}\psi\right)\,\mathrm{d}x\,,\\\partial_{\phi_2}\widetilde{\mathcal{J}}[u_2,\phi_1,\phi_2](\psi)&=\int_\Omega 2h(D\phi_1)(u_2\circ\phi_2\circ\phi_1-u_0)\nabla(u_2\circ\phi_2\circ\phi_1)\cdot(D(\phi_2\circ\phi_1))^{-1}(\psi\circ\phi_1)\,\mathrm{d}x\\&=\int_\Omega 2(u_2\circ\phi_2\circ\phi_1)\mathrm{div}\left(u_0h(D\phi_1)(D(\phi_2\circ\phi_1))^{-1}(\psi\circ\phi_1)\right)\\&\quad-(u_2\circ\phi_2\circ\phi_1)^2\mathrm{div}\left(h(D\phi_1)(D(\phi_2\circ\phi_1))^{-1}(\psi\circ\phi_1)\right)\,\mathrm{d}x\,.\end{aligned}$$

Here, we used integration by parts alongside the following different versions of the chain rule:

$$\begin{aligned}(\nabla(u_2\circ\phi_2\circ\phi_1))^T &= (\nabla(u_2\circ\phi_2)\circ\phi_1)^T D\phi_1\,,\\ \nabla(u_2\circ\phi_2\circ\phi_1)^2 &= 2(u_2\circ\phi_2\circ\phi_1)\nabla(u_2\circ\phi_2\circ\phi_1)\,,\\ (\nabla(u_2\circ\phi_2\circ\phi_1))^T &= (\nabla u_2\circ(\phi_2\circ\phi_1))^T D(\phi_2\circ\phi_1)\,.\end{aligned}$$

Based on these reformulations the second order variational derivatives of $\widetilde{\mathcal{J}}$ are given by

$$\begin{aligned}\partial^2_{\phi_1}\widetilde{\mathcal{J}}[u_2,\phi_1,\phi_2](\psi,\zeta) = \int_\Omega\ & 2(u_2\circ\phi_2\circ\phi_1-u_0)\nabla(u_2\circ\phi_2)\circ\phi_1\cdot\zeta(Dh(D\phi_1):D\psi)\\ &+(u_2\circ\phi_2\circ\phi_1-u_0)^2D^2h(D\phi_1)(D\psi,D\zeta)\\ &-2(u_2\circ\phi_2\circ\phi_1)\nabla(u_2\circ\phi_2)\circ\phi_1\cdot\zeta\mathrm{div}\left(h(D\phi_1)(D\phi_1)^{-1}\psi\right)\\ &-(u_2\circ\phi_2\circ\phi_1)^2\mathrm{div}\left(\partial_{\phi_1}(h(D\phi_1)(D\phi_1)^{-1})(\zeta)\psi\right)\\ &+2\nabla(u_2\circ\phi_2)\circ\phi_1\cdot\zeta\mathrm{div}\left(u_0h(D\phi_1)(D\phi_1)^{-1}\psi\right)\\ &+2(u_2\circ\phi_2\circ\phi_1)\mathrm{div}\left(u_0\partial_{\phi_1}(h(D\phi_1)(D\phi_1)^{-1})(\zeta)\psi\right)\,\mathrm{d}x\,,\\ \partial^2_{\phi_2}\widetilde{\mathcal{J}}[u_2,\phi_1,\phi_2](\psi,\zeta) = \int_\Omega\ & 2\nabla u_2\circ(\phi_2\circ\phi_1)\cdot(\zeta\circ\phi_1)\mathrm{div}\left(u_0h(D\phi_1)(D(\phi_2\circ\phi_1))^{-1}(\psi\circ\phi_1)\right)\\ &+2(u_2\circ\phi_2\circ\phi_1)\mathrm{div}\left(u_0h(D\phi_1)\partial_{\phi_2}((D(\phi_2\circ\phi_1))^{-1})(\zeta)(\psi\circ\phi_1)\right)\\ &-2(u_2\circ\phi_2\circ\phi_1)\nabla u_2\circ(\phi_2\circ\phi_1)\cdot(\zeta\circ\phi_1)\cdot\\ &\qquad\mathrm{div}\left(h(D\phi_1)(D(\phi_2\circ\phi_1))^{-1}(\psi\circ\phi_1)\right)\\ &-(u_2\circ\phi_2\circ\phi_1)^2\mathrm{div}\left(h(D\phi_1)\partial_{\phi_2}((D(\phi_2\circ\phi_1))^{-1})(\zeta)(\psi\circ\phi_1)\right)\,\mathrm{d}x\,,\\ \partial_{\phi_1}\partial_{\phi_2}\widetilde{\mathcal{J}}[u_2,\phi_1,\phi_2](\psi,\zeta) = \int_\Omega\ & 2\nabla(u_2\circ\phi_2)\circ\phi_1\cdot\psi\mathrm{div}\left(u_0h(D\phi_1)(D(\phi_2\circ\phi_1))^{-1}(\zeta\circ\phi_1)\right)\\ &+2(u_2\circ\phi_2\circ\phi_1)\mathrm{div}\left(u_0\partial_{\phi_1}(h(D\phi_1)(D(\phi_2\circ\phi_1))^{-1}(\zeta\circ\phi_1))(\psi)\right)\\ &-2(u_2\circ\phi_2\circ\phi_1)\nabla(u_2\circ\phi_2)\circ\phi_1\cdot\psi\mathrm{div}\left(h(D\phi_1)(D(\phi_2\circ\phi_1))^{-1}(\zeta\circ\phi_1)\right)\\ &-(u_2\circ\phi_2\circ\phi_1)^2\mathrm{div}\left(\partial_{\phi_1}(h(D\phi_1)(D(\phi_2\circ\phi_1))^{-1}(\zeta\circ\phi_1))(\psi)\right)\,\mathrm{d}x\end{aligned}$$

for $\psi,\zeta\in H^m_0(\Omega)$. Evaluating the second order variational derivatives at the point $(u_0,\mathbb{1},\mathbb{1})$ and taking into account the identity $h(\mathbb{1})=\frac{1}{2}$ yields

$$\begin{aligned}\partial^2_{\phi_1}\widetilde{\mathcal{J}}[u_0,\mathbb{1},\mathbb{1}](\psi,\zeta) &= \int_\Omega -u_0\nabla u_0\cdot\zeta\mathrm{div}(\psi)-u_0^2\mathrm{div}(\partial_{\phi_1}(h(D\phi_1)(D\phi_1)^{-1})|_{\phi_1=\mathbb{1}}(\zeta)\psi)\\ &\quad+\nabla u_0\cdot\zeta\mathrm{div}(u_0\psi)+2u_0\mathrm{div}(u_0\partial_{\phi_1}(h(D\phi_1)(D\phi_1)^{-1})|_{\phi_1=\mathbb{1}}(\zeta)\psi)\,\mathrm{d}x\\ &= \int_\Omega \zeta^T\nabla u_0\nabla u_0^T\psi\,\mathrm{d}x\,,\\ \partial^2_{\phi_2}\widetilde{\mathcal{J}}[u_0,\mathbb{1},\mathbb{1}](\psi,\zeta) &= \int_\Omega \nabla u_0\cdot\zeta\mathrm{div}(u_0\psi)+u_0\mathrm{div}(u_0\partial_{\phi_2}((D(\phi_2\circ\phi_1))^{-1})|_{\phi_2=\mathbb{1}}(\zeta)(\psi\circ\phi_1))\\ &\quad-u_0\nabla u_0\cdot\zeta\mathrm{div}(\psi)-\tfrac{1}{2}u_0^2\mathrm{div}(\partial_{\phi_2}((D(\phi_2\circ\phi_1))^{-1})|_{\phi_2=\mathbb{1}}(\zeta)(\psi\circ\phi_1))\,\mathrm{d}x\\ &= \int_\Omega \zeta^T\nabla u_0\nabla u_0^T\psi\,\mathrm{d}x\,,\\ \partial_{\phi_1}\partial_{\phi_2}\widetilde{\mathcal{J}}[u_0,\mathbb{1},\mathbb{1}](\psi,\zeta) &= \int_\Omega \nabla u_0\cdot\psi\mathrm{div}(u_0\zeta)+2u_0\mathrm{div}(u_0\partial_{\phi_1}(h(D\phi_1)(D(\phi_2\circ\phi_1))^{-1}(\zeta\circ\phi_1))|_{\phi_1=\mathbb{1}}(\psi))\\ &\quad-u_0\nabla u_0\cdot\psi\mathrm{div}(\zeta)-u_0^2\mathrm{div}(\partial_{\phi_1}(h(D\phi_1)(D(\phi_2\circ\phi_1))^{-1}(\zeta\circ\phi_1))|_{\phi_1=\mathbb{1}}(\psi))\,\mathrm{d}x\\ &= \int_\Omega \zeta^T\nabla u_0\nabla u_0^T\psi\,\mathrm{d}x\,.\end{aligned}$$

In the computations above, we employed the identity

$$\begin{aligned}&\int_\Omega u_0^2\mathrm{div}v-2u_0\mathrm{div}(u_0v)\,\mathrm{d}x=\int_\Omega-\nabla u_0^2\cdot v-2u_0\mathrm{div}(u_0v)\,\mathrm{d}x\\ =&\int_\Omega-2\nabla u_0\cdot(u_0v)-2u_0\mathrm{div}(u_0v)\,\mathrm{d}x=\int_\Omega 2u_0\mathrm{div}(u_0v)-2u_0\mathrm{div}(u_0v)\,\mathrm{d}x=0\end{aligned}$$

for any vector field $v \in H_0^1(\Omega, \mathbb{R}^n)$ several times, which is solely based on integration by parts.

To sum up, the second order variation of the functional $\mathcal{J}$ at the point $(u_0, \mathbb{1}, \mathbb{1})$ has the form

$$\partial^2_{(\phi_1,\phi_2)}\mathcal{J}[u_0,\mathbb{1},\mathbb{1}]((\psi_1,\psi_2),(\zeta_1,\zeta_2)) = \int_\Omega 2\gamma\Delta^{\frac{m}{2}}\psi_1\cdot\Delta^{\frac{m}{2}}\zeta_1 + D^2\mathrm{W}(\mathbb{1})(D\psi_1,D\zeta_1) + 2\gamma\Delta^{\frac{m}{2}}\psi_2\cdot\Delta^{\frac{m}{2}}\zeta_2 + D^2\mathrm{W}(\mathbb{1})(D\psi_2,D\zeta_2) + \frac{1}{\delta}(\psi_1+\psi_2)^T\nabla u_0\nabla u_0^T(\zeta_1+\zeta_2)\,\mathrm{d}x\,.$$

By incorporating the estimate

$$\left|\int_\Omega (\psi_1+\psi_2)^T\nabla u_0\nabla u_0^T(\zeta_1+\zeta_2)\,\mathrm{d}x\right| \leq C\|u_0\|^2_{H^1(\Omega)}\|(\psi_1,\psi_2)\|_{H^m(\Omega)}\|(\zeta_1,\zeta_2)\|_{H^m(\Omega)}\,,$$

which follows from the embedding $H^m(\Omega) \hookrightarrow C^2(\overline{\Omega})$, we can immediately deduce that $\partial^2_{(\phi_1,\phi_2)}\mathcal{J}[u_0,\mathbb{1},\mathbb{1}]$ is a continuous bilinear form on $H_0^m(\Omega)\times H_0^m(\Omega)$. Moreover, the coercivity of $\partial^2_{(\phi_1,\phi_2)}\mathcal{J}$ readily follows from the estimate (4.20) employed in the proof of the coercivity of $\mathcal{R}$ (*cf*. Theorem 4.2.1). Finally, the Lax–Milgram Theorem (*cf*. [GT92]) guarantees the invertibility of $\partial^2_{(\phi_1,\phi_2)}\mathcal{J}$, which concludes the proof of this theorem. □

4.3 Spatial Discretization and Fixed Point Algorithm

In this section, we will propose a spatial discretization scheme, which shares many similarities with the conforming discretization presented in Subsection 3.6.2, and a fixed point algorithm based on Lemma 4.1.1 (ii.) to compute the extrapolated path $\{u_k = \mathrm{EXP}^k_{u_0}(u_1-u_0)\}_{k\geq 0}$ for given images $u_0, u_1 \in H^1(\Omega)$. Incorporating the scheme (2.14), we may restrict our presentation to the calculation of $u_2 = \mathrm{EXP}^2_{u_0}(u_1-u_0)$. To this end, we first have to compute the deformations $\phi_1, \phi_2 \in \mathcal{A}$ in a preceding step and exploit the pointwise condition (4.12) to retrieve the unknown image u_2.

To ease the presentation, we restrict ourselves to two-dimensional images on the computational domain $\Omega = [0,1]^2$ and the particular energy density $\mathrm{W}(A) = |A-\mathbb{1}|^2$ (*cf*. (3.20)), and emphasize that the generalization to other settings is straightforward. Moreover, to simplify the numerical implementation we choose $m = 2$ despite the theoretical requirement $m > 2 + \frac{n}{2} = 3$, and highlight that this choice suffices to reliably solve the Euler–Lagrange equations numerically since the regularity of the discrete function space for the deformations is intrinsically determined. Altogether, the discrete energy used in all further numerical experiments in this chapter is defined as

$$\mathcal{W}^D[u,\tilde{u},\phi] = \int_\Omega |D\phi-\mathbb{1}|^2 + \gamma|\Delta\phi|^2 + \frac{1}{\delta}(\tilde{u}\circ\phi - u)^2\,\mathrm{d}x \tag{4.24}$$

for $u, \tilde{u} \in H^1(\Omega)$ and $\phi \in \mathcal{A}$.

The algorithm for the computation of $u_2 = \mathrm{EXP}^2_{u_0}(u_1-u_0)$ includes three steps:

1. The initial deformation $\phi_1 \in \mathcal{A}$ is computed using the Fletcher–Reeves multilevel gradient descent already discussed in detail in Section 3.6.

2. To obtain the optimal deformation $\phi_2 \in \mathcal{A}$, a spatially discrete fixed point iteration is used, which emerges from the reformulation appearing in Lemma 4.1.1 (ii.). We recall that this reformulation requires bounded and weakly differentiable input images, which are additionally close in $L^2(\Omega)$, as well as a sufficiently smooth domain boundary. However, since the computational domain is only Lipschitz we neglect this smoothness requirement w.r.t. the boundary.

3. Finally, as in the existence proof for the discrete exponential map (*cf*. Theorem 4.2.1), the optimal image u_2 is given by the spatially discrete analog of (4.12) resulting from the Euler–Lagrange equation (4.5).

Derivation of the fixed point operator. In what follows, we will discuss the fixed point iteration of step 2 in detail. To this end, we define the nonlinear operator $\widetilde{\mathcal{T}} : \mathcal{A} \to H^{-m}(\Omega)$ as the counterpart of $\mathcal{T}$ (*cf*. (4.16)) for

the second reformulation of Lemma 4.1.1, *i.e.* $\widetilde{\mathcal{T}}[\phi_2; u_0, u_1, \phi_1](\psi) = \mathcal{R}[\phi_2](\psi)$ for all test functions $\psi \in H_0^m(\Omega)$ with $\mathcal{R}$ denoting the linear operator for the fixed point iteration used in Theorem 4.2.1, as follows

$$\begin{aligned}\widetilde{\mathcal{T}}[\phi; u_0, u_1, \phi_1](\psi) &= \int_\Omega 2\gamma\Delta\phi_1 \cdot \Delta(((D\phi)^{-1}\psi)\circ\phi_1) + 2(D\phi_1 - \mathbb{1}) : D(((D\phi)^{-1}\psi)\circ\phi_1) \\ &\qquad - \frac{1}{\delta}\frac{(u_1\circ\phi_1 - u_0)^2}{\det D\phi_1}\left((D\phi)^{-T} : (D^2\phi(D\phi)^{-1}\psi) - (D\phi)^{-T} : D\psi\right)\circ\phi_1 \,\mathrm{d}x \\ &= \int_\Omega -2\gamma D\Delta\phi_1 : (D(((D\phi)^{-1}\psi)\circ\phi_1) - 2\Delta\phi_1 \cdot ((D\phi)^{-1}\psi)\circ\phi_1 \\ &\qquad - \frac{1}{\delta}\frac{(u_1\circ\phi_1 - u_0)^2}{\det D\phi_1}\left((D\phi)^{-T} : (D^2\phi(D\phi)^{-1}\psi) - (D\phi)^{-T} : D\psi\right)\circ\phi_1 \,\mathrm{d}x\,. \end{aligned} \tag{4.25}$$

To derive (4.25) we employed the identities $\partial_A \mathrm{W}(A)(B) = 2(A - \mathbb{1}) : B$ and $\partial_A^2 \mathrm{W}(A)(B, C) = 2B : C$ for $A, B, C \in \mathbb{R}^{n,n}$, and used integration by parts to get the second equality. This ansatz is numerically beneficial because it avoids the evaluation of gradients of image intensities – in contrast to the operator $\mathcal{T}$. In detail, we observed in the numerical experiments that the numerical quadrature scheme to approximate

$$\int_\Omega (u_1\circ\phi_1 - u_0)(\nabla u_1 \cdot (D\phi)^{-1}\psi)\circ\phi_1 \,\mathrm{d}x$$

appearing in the definition of $\mathcal{T}$ is highly inaccurate in a neighborhood of the interfaces of u_1. However, despite these improvements the numerical quadrature scheme for the first integrand in (4.25) is still inaccurate, that is why we additionally rewrite this expression by making use of $A : B = \mathrm{tr}(A^T B)$ as follows

$$\begin{aligned}&\int_\Omega D\Delta\phi_1 : D((D\phi)^{-1}\psi)\circ\phi_1)\,\mathrm{d}x \\ &= \int_\Omega D\Delta\phi_1 : ((D\phi)^{-1}\circ\phi_1)D(\psi\circ\phi_1) + D\Delta\phi_1 : (D((D\phi)^{-1}\circ\phi_1))(\psi\circ\phi_1)\,\mathrm{d}x \\ &= \int_\Omega ((D\phi)^{-T}\circ\phi_1)D\Delta\phi_1 : D(\psi\circ\phi_1) + D\Delta\phi_1 : (D((D\phi)^{-1}\circ\phi_1))(\psi\circ\phi_1)\,\mathrm{d}x\,.\end{aligned}$$

To sum up, the operator $\widetilde{\mathcal{T}}$ admits the representation

$$\begin{aligned}&\widetilde{\mathcal{T}}[\phi; u_0, u_1, \phi_1](\psi) \\ &= \int_\Omega -2\gamma((D\phi)^{-T}\circ\phi_1)D\Delta\phi_1 : D(\psi\circ\phi_1) - 2\gamma D\Delta\phi_1 : (D((D\phi)^{-1}\circ\phi_1))(\psi\circ\phi_1) \\ &\qquad - 2\Delta\phi_1 \cdot ((D\phi)^{-1}\psi)\circ\phi_1 - \frac{1}{\delta}\frac{(u_1\circ\phi_1 - u_0)^2}{\det D\phi_1}\left((D\phi)^{-T} : (D^2\phi(D\phi)^{-1}\psi) - (D\phi)^{-T} : D\psi\right)\circ\phi_1 \,\mathrm{d}x\end{aligned} \tag{4.26}$$

and the resulting fixed point iteration to compute $\phi_2 \in \mathcal{A}$ corresponding to (4.9) is given by

$$\phi^{(j+1)} = \mathcal{R}^{-1} \circ \widetilde{\mathcal{T}}[\phi^{(j)}; u_0, u_1, \phi_1]\,.$$

Spatial discretization scheme and fully discrete operators. As in the conforming discretization of the metamorphosis model (*cf*. Subsection 3.6.2), we use the space of bilinear and globally continuous scalar-valued finite elements $\mathcal{V}_h$ on $\mathcal{T}_h$ and the conforming space of vector-valued cubic B-splines $\mathcal{D}_H = \mathbb{1} + \mathcal{S}_H^2 \subset C^2(\Omega, \mathbb{R}^2)$ on $\widetilde{\mathcal{T}}_H$ to model the images and deformations, respectively. As before, $\mathcal{T}_h$ and $\widetilde{\mathcal{T}}_H$ denote regular meshes on Ω composed of quadratic cells with mesh sizes $h = 2^{-M}$ and $H = 2^{-N}$ for $M = N + 1$. Furthermore, we only impose the Dirichlet boundary condition $\Phi = \mathbb{1}$ on $\partial\Omega$ instead of the stronger boundary condition $\Phi - \mathbb{1} \in H_0^2(\Omega)$ for the discrete deformations $\Phi \in \mathcal{D}_H$ since this choice proved to be sufficient to reliably compute proper deformations. The initial discrete images are retrieved via a nodal interpolation in $\mathcal{V}_h$, *i.e.* $U_i = \mathcal{I}_h u_i$ for $i \in \{0, 1\}$, and assumed to be in the range $[0, 1]$. For further details we refer to Subsection 3.6.2.

Throughout this discretization scheme, we apply a Gaussian quadrature of order 5 on both meshes. To fix the notation, let us define $I^{\mathcal{C}}_{\mathcal{V}_h}$ and $I^{\mathcal{C}}_{\mathcal{S}_H}$ as the index sets of all cells in $\mathcal{T}_h$ and $\widetilde{\mathcal{T}}_H$, respectively. On each cell $\mathcal{C}_l$ in $\mathcal{T}_h$, $l \in I^{\mathcal{C}}_{\mathcal{V}_h}$, and each cell $\widetilde{\mathcal{C}}_{\tilde{l}}$ in $\widetilde{\mathcal{T}}_H$, $\tilde{l} \in I^{\mathcal{C}}_{\mathcal{S}_H}$, we denote by $(\omega^l_q, \mathbf{x}^l_q)$ and $(\tilde{\omega}^{\tilde{l}}_q, \tilde{\mathbf{x}}^{\tilde{l}}_q)$ the pair of the q^{th} quadrature weight and corresponding quadrature point, respectively. Moreover, $I^N_{\mathcal{V}_h}$ and $I^N_{\mathcal{S}_H}$ refer to the index sets of all grid nodes $\mathbf{x}_l$ and $\tilde{\mathbf{x}}_l$ in $\mathcal{T}_h$ and $\widetilde{\mathcal{T}}_H$, respectively.

In a preparatory step, the initial deformation $\Phi_1 \in \operatorname{argmin}_{\Phi\in\mathcal{D}_H} \mathbf{W}^D[U_0, U_1, \Phi]$ is calculated using a Fletcher–Reeves nonlinear conjugate gradient descent multilevel scheme with an Armijo step size control as described in Subsection 3.6.2. When computing $\mathrm{EXP}^k_{U_0}(U_1 - U_0)$ for any $k > 2$ following the iterative scheme, this step is omitted and the optimal deformation computed in the preceding fixed point iteration is used instead.

In what follows, we will define the spatially discrete counterparts of the energy $\mathcal{W}^D$ as well as the operators $\widetilde{\mathcal{T}}$ and $\mathcal{R}$ involved in the fixed point iteration in order to compute the deformation $\Phi_2 \in \mathcal{D}_H$. Whenever the evaluation of image intensities is required, the Gaussian quadrature on the fine mesh $\mathcal{T}_h$ is incorporated for this integrand, otherwise the Gaussian quadrature scheme on the coarse mesh $\widetilde{\mathcal{T}}_H$ is used. The *fully discrete energy* $\mathbf{W}^D$ for $U, \tilde{U} \in \mathcal{V}_h$ and $\Phi \in \mathcal{D}_H$ is defined as (*cf*. (4.24))

$$\begin{aligned}\mathbf{W}^D[U, \tilde{U}, \Phi] = &\sum_{l\in I^{\mathcal{C}}_{\mathcal{S}_H}} \sum_q \tilde{\omega}^l_q \left(|(D\Phi - \mathbb{1})(\tilde{\mathbf{x}}^l_q)|^2 + \gamma|\Delta\Phi(\tilde{\mathbf{x}}^l_q)|^2\right)\\ &+ \frac{1}{\delta}\sum_{l\in I^{\mathcal{C}}_{\mathcal{V}_h}} \sum_q \omega^l_q \left(\tilde{U}(\Phi(\mathbf{x}^l_q)) - U(\mathbf{x}^l_q)\right)^2.\end{aligned}$$

Likewise, the fully discrete counterparts of the operators $\widetilde{\mathcal{T}}$ (*cf*. (4.26)) and $\mathcal{R}$ (*cf*. (4.17)) are accordingly defined as

$$\begin{aligned}\widetilde{\mathbf{T}}[\Phi; U_0, U_1, \Phi_1](\Psi) = \sum_{l\in I^{\mathcal{C}}_{\mathcal{S}_H}} \sum_q \tilde{\omega}^l_q \Big(&- 2\gamma((D\Phi)^{-T} \circ \Phi_1(\tilde{\mathbf{x}}^l_q))D\Delta\Phi_1(\tilde{\mathbf{x}}^l_q) : D(\Psi \circ \Phi_1(\tilde{\mathbf{x}}^l_q))\\ &- 2\gamma D\Delta\Phi_1(\tilde{\mathbf{x}}^l_q) : D((D\Phi)^{-1} \circ \Phi_1(\tilde{\mathbf{x}}^l_q))(\Psi \circ \Phi_1(\tilde{\mathbf{x}}^l_q))\\ &- 2\Delta\Phi_1(\tilde{\mathbf{x}}^l_q) \cdot ((D\Phi)^{-1}\Psi) \circ \Phi_1(\tilde{\mathbf{x}}^l_q)\Big)\\ - \sum_{l\in I^{\mathcal{C}}_{\mathcal{V}_h}} \sum_q \frac{\omega^l_q}{\delta} &\frac{(U_1 \circ \Phi_1(\mathbf{x}^l_q) - U_0(\mathbf{x}^l_q))^2}{\det D\Phi_1(\mathbf{x}^l_q)}\\ &\cdot \left((D\Phi)^{-T} : (D^2\Phi(D\Phi)^{-1}\Psi) - (D\Phi)^{-T} : D\Psi\right) \circ \Phi_1(\mathbf{x}^l_q),\end{aligned}$$

$$\mathbf{R}[\Phi](\Psi) = \sum_{l\in I^{\mathcal{C}}_{\mathcal{S}_H}} \sum_q \tilde{\omega}^l_q \left(2\gamma\Delta\Phi(\tilde{\mathbf{x}}^l_q) \cdot \Delta\Psi(\tilde{\mathbf{x}}^l_q) + 2D\Phi(\tilde{\mathbf{x}}^l_q) : D\Psi(\tilde{\mathbf{x}}^l_q)\right)$$

for $\Psi \in \{\Phi \in \mathcal{S}^2_H \,:\, \Phi = 0 \text{ on } \partial\Omega\}$. Hence, the spatially discrete fixed point iteration to compute $\Phi_2 \in \mathcal{D}_H$ is

$$\Phi^{(j+1)} = \mathbf{R}^{-1} \circ \widetilde{\mathbf{T}}[\Phi^{(j)}; U_0, U_1, \Phi_1] \tag{4.27}$$

for all $j \geq 0$ and initial data $\Phi^{(0)} = \mathbb{1}$. The application of $\mathbf{R}^{-1}$ requires the solution of the associated linear system of equations, which is implemented using a preconditioned conjugate gradient descent with a diagonal preconditioner. Now, the deformation Φ_2 is computed using the fixed point iteration (4.27), which is stopped if the L^∞-difference of the deformations in two consecutive iterations is below the threshold value $\mathrm{THRESHOLD} = 10^{-12}$.

In the final step, the unknown image intensity U_2 is calculated by evaluating the spatially discrete analog of the update formula (4.12) at each node of $\mathcal{T}_h$, *i.e.* (*cf*. Notation 3.6.1)

$$\bar{U}_2 = \left\{U_2(\mathbf{x}_l) = \left(\frac{U_1 - U_0 \circ \Phi_1^{-1}}{\det(D\Phi_1) \circ \Phi_1^{-1}}\right) \circ \Phi_2^{-1}(\mathbf{x}_l) + U_1 \circ \Phi_2^{-1}(\mathbf{x}_l)\right\}_{l\in I^N_{\mathcal{V}_h}}.$$

To compute the approximate inverse deformations $\Phi_i^{-1} \in \mathcal{D}_H$, $i \in \{1, 2\}$, all cells of the grid $\widetilde{\mathcal{T}}_H$ associated with $\mathcal{S}_H$ are traversed and the deformed positions $\Phi_i(\tilde{\mathbf{y}}_j)$ for all vertices $\tilde{\mathbf{y}}_j$, $j \in \{1, \ldots, 4\}$, of the current element

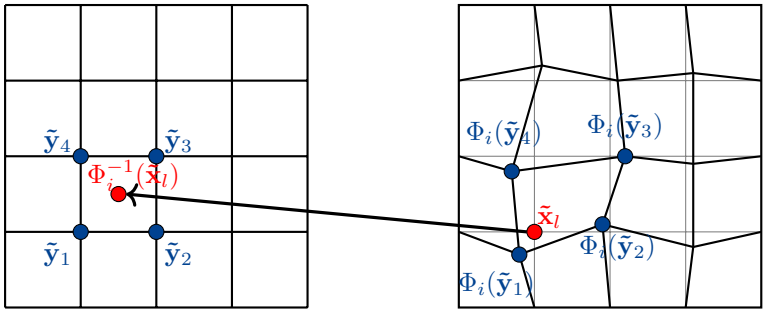

Figure 4.1: Illustration of the computation of the approximate inverse deformation $\Phi_i^{-1}(\mathbf{x}_l)$, $i = 1, 2$.

are computed. If a grid node $\tilde{\mathbf{x}}_l$, $l \in I_{S_H}^N$, lies within the quadrilateral generated by $\{\Phi_i(\tilde{\mathbf{y}}_j)\}_{j\in\{1,\dots,4\}}$, then $\Phi_i^{-1}(\tilde{\mathbf{x}}_l)$ is defined as the bilinear interpolation of the vertices $\{\tilde{\mathbf{y}}_j\}_{j\in\{1,\dots,4\}}$. Furthermore, we explicitly ensure the boundary condition $\Phi_i^{-1}(\tilde{\mathbf{x}}_l) = \tilde{\mathbf{x}}_l$ for $\tilde{\mathbf{x}}_l \in \partial\Omega$ and $l \in I_{S_H}^N$ (*cf*. Figure 4.1).

Anisotropic diffusion filtering. In our numerical experiments, we observed slight local oscillations, which mainly result from the inexact evaluation of the expression $U_1 - U_0 \circ \Phi_1^{-1}$ in the quadrature of the intensity modulation. Since $\mathrm{EXP}_{U_0}^k(U_1 - U_0)$ for $k > 2$ is computed using the aforementioned iterative scheme, these oscillations significantly amplify and propagate along the extrapolated path. Thus, to damp these oscillations and at the same time preserve interfaces and small structures of the image, we apply in a post-processing step the established *anisotropic diffusion filtering* proposed by Perona and Malik (see [PM90]) characterized by

$$\partial_t I - \operatorname{div}\left(\tfrac{1}{1+\lambda^{-2}\|\nabla I\|^2}\nabla I\right) = 0$$

to the intensity modulation $I = U_1 - U_0 \circ \Phi_1^{-1}$ for a weight parameter $\lambda > 0$. Note that in general no global and smooth solutions to this partial differential equation exist (see [Wei98] for further details).[1] In detail, this filter is defined via one semi-implicit time step of the discrete anisotropic diffusion equation on $\mathcal{V}_h$, *i.e.* we apply the operator $(\mathbf{M}_h + \tau\mathbf{S}_h[I,\lambda])^{-1}\mathbf{M}_h$ to $\bar{I}$, where $\mathbf{M}_h$ and $\mathbf{S}_h[I,\lambda]$ are the *mass matrix* and the *anisotropic stiffness matrix* associated with the space $\mathcal{V}_h$ on $\mathcal{T}_h$, *i.e.*

$$(\mathbf{M}_h)_{i,j} = \sum_{l\in I_{\mathcal{V}_h}^C}\sum_q \omega_q^l \Theta^i(\mathbf{x}_q^l)\Theta^j(\mathbf{x}_q^l)\,, \qquad (\mathbf{S}_h[I,\lambda])_{i,j} = \sum_{l\in I_{\mathcal{V}_h}^C}\sum_q \frac{\omega_q^l}{1+\lambda^{-2}\|\nabla I(\mathbf{x}_q^l)\|^2}\nabla\Theta^i(\mathbf{x}_q^l)\cdot\nabla\Theta^j(\mathbf{x}_q^l)\,.$$

Here, $\{\Theta^i\}_{i\in I_{\mathcal{V}_h}^N}$ are the *basis functions* associated with $\mathcal{V}_h$, the indices $i, j \in I_{\mathcal{V}_h}^N$ refer of the nodes in $\mathcal{T}_h$, $\tau > 0$ is the *time step size* and λ is the *gradient magnitude threshold parameter* of the *conductance functional* $f \mapsto \frac{1}{1+\lambda^{-2}\|\nabla f\|^2}$.

All aforementioned steps are summarized in Algorithm 2.

4.4 Numerical Results

In this section, we present several numerical results of the discrete exponential map for artificial as well as real image data in the fully discrete setting, where we employ the algorithm developed in Section 4.3 with parameters $\gamma = 10^{-4}$ and $\delta = 10^{-2}$. Moreover, we choose $\lambda = 0.5$ and $\tau_k = 0.8^{k-2}\cdot 10^{-3}$ whenever the anisotropic diffusion filtering is applied to the image U_k, where k refers to the index of the extrapolated sequence. This exponentially decaying time step size prevents a loss of image features for larger k while at the same time reducing the amplification of noise for the first images along the sequence. All results have been published in [ERS17a] and [ERS17b].

[1] In the terminology of Weickert [Wei98], this filter is isotropic.

Algorithm 2: The fixed point iteration to compute the extrapolated path.

Data: input images $U_0, U_1 \in \mathcal{V}_h$, $K \geq 2$, mesh size h, weight parameters $\tau, \lambda > 0$ for smoothing
Result: discrete extrapolated curve $\{U_k = \mathrm{EXP}^k_{U_0}(U_1 - U_0)\}_{0 \leq k \leq K}$

calculate $\Phi_1 \in \operatorname{argmin}_{\tilde{\Phi} \in \mathcal{D}_H} \mathbf{W}^D[U_0, U_1, \tilde{\Phi}]$;
for $k = 2$ **to** K **do**
  $\Phi^{(0)} = \mathbb{1}$, $j = 0$;
  repeat
    $j = j + 1$;
    $\Phi^{(j)} = \mathbf{R}^{-1} \circ \widetilde{\mathbf{T}}[\Phi^{(j-1)}; U_{k-2}, U_{k-1}, \Phi_{k-1}]$;
  until $\|\Phi^{(j)} - \Phi^{(j-1)}\| \leq \mathrm{THRESHOLD}$;
  $\Phi_k = \Phi^{(j)}$;
  $I = U_{k-1} - U_{k-2} \circ \Phi_{k-1}^{-1}$;
  $\bar{I} = (\mathbf{M}_h + \tau \mathbf{S}_h[I, \lambda])^{-1} \mathbf{M}_h \bar{I}$;
  $\bar{U}_k = \left\{ \left(\frac{\bar{I}}{\det(D\Phi_{k-1}) \circ \Phi_{k-1}^{-1}} + U_{k-1} \right) \circ \Phi_k^{-1}(\mathbf{x}_l) \right\}_{l \in I^N_{\mathcal{V}_h}}$;

Let us first analyze the capability of the time discrete exponential map to translate, shade and rotate image features. To this end, we consider an input image U_0 consisting of three ellipses with different intensities and a resolution of 257×257 (see Figure 4.2). Compared to U_0, the upper left ellipse in U_1 is slightly translated to the bottom and simultaneously expanded, the upper right ellipse is rotated and the third one is also slightly translated with some modulation of the shading. All input images are framed in red and we do not apply the anisotropic diffusion filtering at all. The first row of Figure 4.2 depicts the extrapolated image sequence $\mathrm{EXP}^k_{U_0}(U_1 - U_0)$ for the time steps $k \in \{0, 1, 2, 3, 6, 9\}$. The associated intensity modulations $I_k = U_k \circ \Phi_k - U_{k-1}$ as well as velocity fields $V_k = K(\Phi_k - \mathbb{1})$ are shown in the second and third row, respectively. Here, the leftmost color bar in the second row shows the extremal values of the intensity modulations along the path, and the hue and color intensities as indicated by the leftmost color wheel in the last row refer to the directions and local norms of the velocity fields, respectively. One observes that the initial variation is properly transported along the image path, *i.e.* the rotation, shading and translation of the ellipses are accurately detected and propagated while at the same time the shape of the ellipses is approximately preserved. We highlight that the resulting underlying discrete velocity fields significantly vary in time.

In all further numerical applications, the aforementioned anisotropic diffusion filtering is employed to damp local oscillations and prevent their amplification.

In the application shown in Figure 4.3, we analyze to which extent the time discrete exponential map is capable of recovering a time discrete geodesic curve from the first two images along the sequence. To this end, we again consider the discrete geodesic sequence $(\tilde{U}_0, \ldots, \tilde{U}_{16})$ of the female portraits (*cf*. Figure 3.12) obtained with the conforming discretization approach proposed in Subsection 3.6.2 with $M = 8$ and $N = 7$, and framed input images $\tilde{U}_0$ and $\tilde{U}_{16}$ (first row in Figure 4.3). The associated discrete exponential shooting $(U_0, \ldots, U_{16})$ is visualized in the second and third row for even time steps for $K = 16$, where the initial image $U_0 = \tilde{U}_0$ as well as the initial variation $U_1 - U_0 = \tilde{U}_1 - \tilde{U}_0$ are taken from the geodesic sequence. The corresponding temporally varying discrete velocity fields and intensity modulations for distinct time steps are depicted in the last two rows. As a result, the discrete exponential map is capable of retrieving the geodesic curve quite well for small k, whereas for large k the images U_k and $\tilde{U}_k$ visibly differ. In general, theoretical considerations (*cf*. Theorem 2.2.15) as well as numerical experiments indicate that smaller initial variations for the time discrete exponential map result in a more accurate recovery of the associated time discrete geodesic curve.

Figure 4.4 depicts distinct images of a time discrete parallel transport $(P_0, \ldots, P_{16})$ along the discrete geodesic path $(U_0, \ldots, U_{16})$ shown in Figure 3.12, where in the initial image P_0 the eyes of the woman are darkened and her hair on the left side of the image is extended. The computation of the time discrete parallel transport is based on Schild's ladder as presented in Definition 2.2.16. Here, to perform the interpolation and extrapolation required in the second and third step of (2.16), we employ the geodesic interpolation and extrapolation for the time discrete metamorphosis model presented in the previous and current chapter, respectively. Note that the modifications of the initial image P_0 representing the initial displacement vector are properly propagated along the sequence for

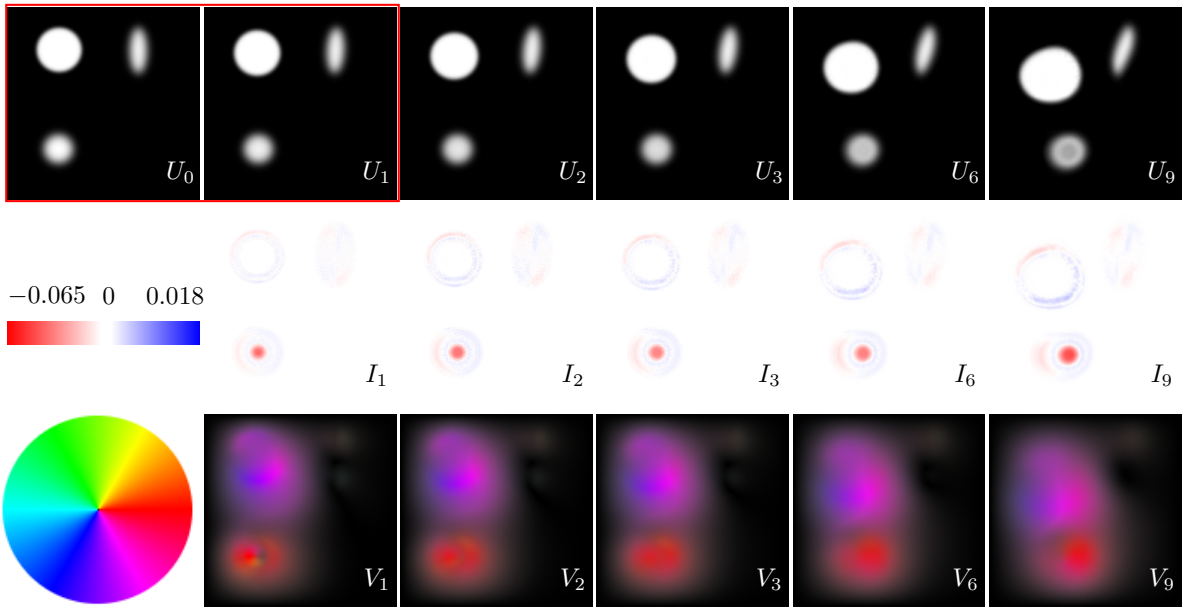

Figure 4.2: First row: The discrete exponential map $\mathrm{EXP}^k_{U_0}(U_1 - U_0)$ for $k = 0, 1, 2, 3, 6, 9$ for images showing three ellipses (input images are framed in red). Second/third row: the associated intensity modulations I_k with a scale encoding the extremal values and the discrete velocity fields V_k (the hue refers to the direction, the intensity is proportional to the local norm of the velocity fields).

small time steps k, but the images P_k and U_k are almost indistinguishable for larger k.

Figure 4.5 (first and third row) depicts a picture detail of the discrete exponential map for the time steps $k \in \{0, 1, 2, 4, 8, 16\}$ applied to two pairs of photos of human faces with a resolution of 1025×1025 of the full images, where the input pictures are consecutive photos of a series at 5 and 7 fps taken with a digital camera, respectively. We observe that small initial variations result in a nonlinear deformation of the lips (first row) and of the lips, the cheeks and the eyes (third row), respectively. Furthermore, the textures are reliably transported along the sequence. The second and fourth row depict the color coded time varying velocity fields.

Figure 4.6 depicts the discrete exponential map for $k \in \{0, \dots, 7\}$ for a pair of images of a dog with a resolution of 1025×1025, where the input pictures are consecutive photos of a series with 7 fps taken with a digital camera. The initial variation contains a slight rotation of the dog's head and a small opening of its eyes, which is accurately propagated along the sequence. Note that an exponential shooting for $k > 7$ collapses since the resulting deformation Φ_8 is no longer bijective and thus an interpenetration of matters occurs.

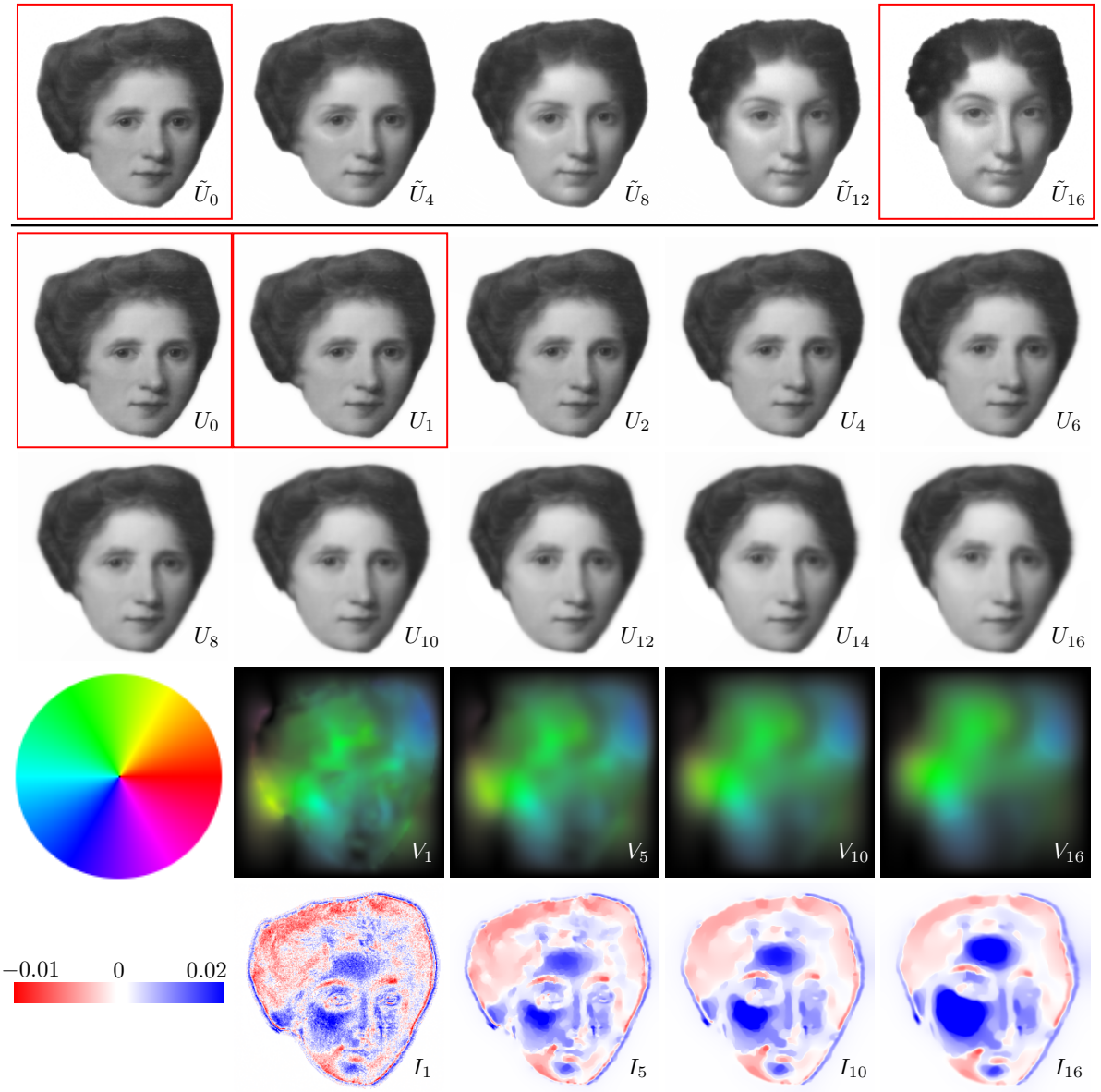

Figure 4.3: The first row depicts distinct images of the same discrete geodesic sequence already shown in Figure 3.12. The discrete exponential map for some time steps is shown in the second and third row, where the input images U_0 and U_1 coincide with $\tilde{U}_0$ and $\tilde{U}_1$ from the geodesic sequence, respectively. In the last two rows, the discrete velocity fields and intensity modulations are visualized for distinct time steps.

Figure 4.4: Discrete parallel transport along the discrete path shown in Figure 3.12. Compared to the original input image U_0, a hair extension on the left side of the image P_0 was performed and the eyes were darkened.

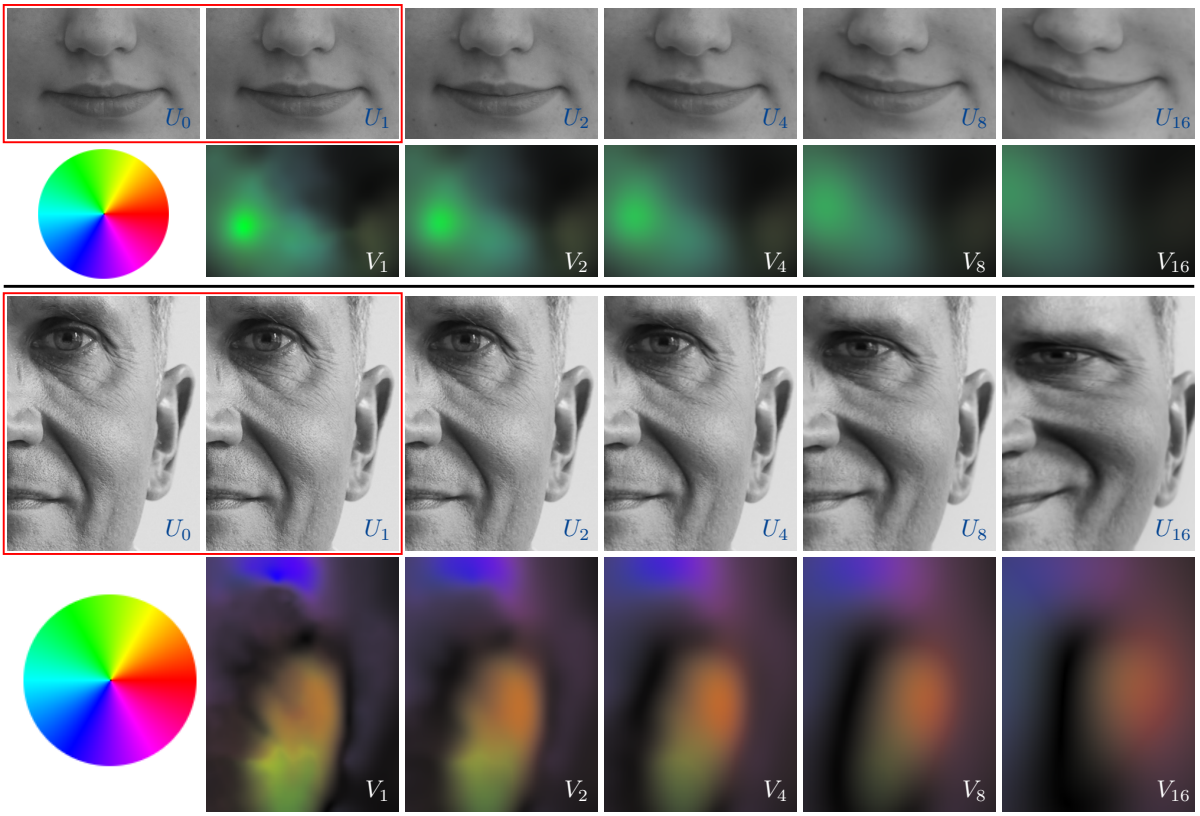

Figure 4.5: First/third row: picture details of $\mathrm{EXP}^k_{U_0}(U_1 - U_0)$ applied to two pairs of photos of human faces for distinct time steps. Second/fourth row: the associated discrete velocity fields V_k.

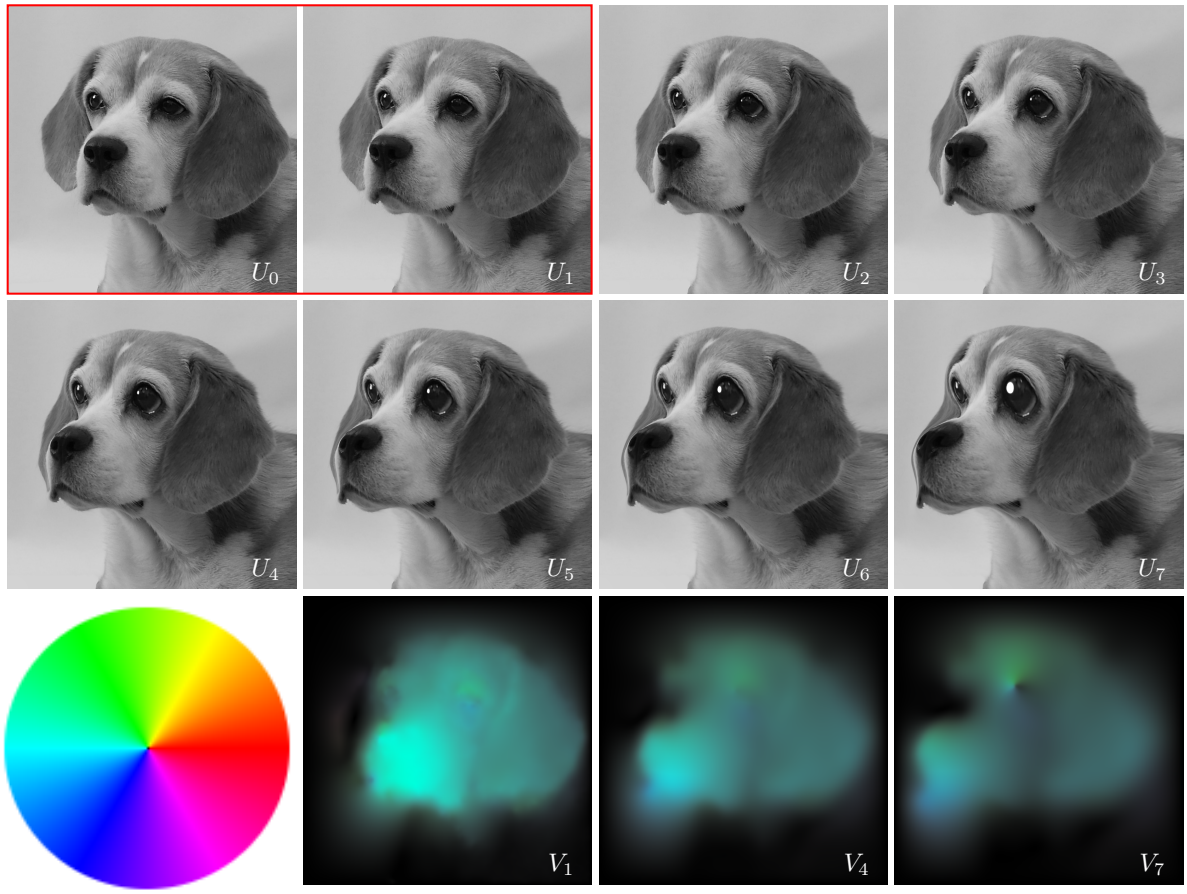

Figure 4.6: First/second row: The discrete exponential map for time steps $k \in \{0, \dots, 7\}$ with two photos of a dog as initial data. Third row: the associated discrete velocity fields for distinct time steps.

Chapter 5

A Posteriori Error Control for the Binary Mumford–Shah Model

In this chapter, we will develop an a posteriori error estimator for the binary Mumford–Shah model. Starting from a *uniformly* convex relaxation of this model originally introduced by Chambolle [Cha05] and Berkels [Ber09], which does not require any constraint in the minimization, we derive a consistent functional a posteriori error estimator to control the L^2-difference of any approximate and the relaxed solution picking up the work by Repin [Rep00, Rep12], where we incorporate a predual formulation of the relaxed model (*cf*. [HK04, Bar15]). Afterwards, by using a cut-out argument a reliable a posteriori error estimator for the binary Mumford–Shah model is derived, which is composed of a weighted sum of the functional estimator and the area of the preimage of an expanded interface region. We present two primal-dual finite element schemes and a classical finite difference discretization. To compute the solution to the relaxed model, a primal-dual algorithm with guaranteed first order convergence (*cf*. [CP11]) as well as a dual gradient descent (*cf*. [Cha04]) are employed. The finite element discretization schemes are computed on an adaptive triangle mesh with hanging nodes, in which each element has a canonical correspondence to a quadtree. The applicability of the proposed method is analyzed in several numerical experiments to real image data.

Many results in this chapter have been published in [BER17] (joint work with Benjamin Berkels and Martin Rumpf).

This chapter is organized as follows: In Section 5.1, we briefly recall the well-known image segmentation functional by Mumford and Shah and provide a short survey of existence and regularity results as well as numerical optimization methods. At the beginning of this section, the foundations of the space of functions of bounded variation and some fundamental theorems in convex analysis are presented. In Section 5.2, we focus on the binary Mumford–Shah model and its basic properties, and prove that by suitably thresholding the minimizer of a uniformly convex relaxed functional the minimizer of the binary Mumford–Shah functional can be exactly retrieved. By combining the predual formulation of the relaxed functional with Repin's primal-dual approach we derive a functional a posteriori error estimator for the relaxed solution based on upper bounds of the duality gap (see Section 5.3). Then, taking into account these functional estimates we use a cut-out argument to infer an a posteriori estimator for the minimizer of the binary Mumford–Shah model. In addition, in a sensitivity analysis we examine the mutual influence of the binary minimizers and the intensity values (see Section 5.4). Two adaptive finite element schemes and a finite difference scheme to discretize the relaxed functional are proposed in Section 5.5. In Section 5.6, a primal-dual algorithm and a purely dual gradient descent to compute the relaxed minimizers are discussed and the cell-wise a posteriori error estimator is defined. Finally, the efficiency and robustness of the proposed error estimator are demonstrated for several images in Section 5.7.

5.1 Review of the Mumford–Shah Model and Related Work

As a general model for (image) segmentation, Mumford and Shah [MS85, MS89] proposed to minimize the energy functional

$$E_{\mathrm{MS}}[u,K] = \int_\Omega \alpha(u-u_0)^2 \,\mathrm{d}x + \int_{\Omega\setminus K} |\nabla u|^2 \,\mathrm{d}x + \beta\mathcal{H}^{n-1}(K) \tag{5.1}$$

among all pairs $(u,K) \in \mathcal{K} = \{K \subset \Omega \text{ is closed and } u \in H^1(\Omega\setminus K)\}$. Here, $\alpha,\beta > 0$ and $u_0 \in L^\infty(\Omega,[0,1])$ is the scalar-valued input image intensity on the bounded image domain $\Omega \subset \mathbb{R}^n$ with Lipschitz boundary. The first summand in (5.1) is the squared $L^2(\Omega)$-norm representing a fidelity term, the squared $H^1(\Omega)$-seminorm of u forces the minimizer to be sufficiently smooth inside the connected components of $\Omega\setminus K$, and the last term penalizes the size of the interface set K. Thus, the resulting minimizer $(\hat{u},\hat{K})$ corresponds to an image segmentation with a discontinuity set $\hat{K}$ separating the image domain into regions, and $\hat{u}$ can be regarded as a piecewise smooth version of u_0.

There is a great variety of theoretical results related to this functional. In what follows, we will present a non-exhaustive overview of various results regarding the existence of minimizers and the regularity of the set $\hat{K}$ (see Subsection 5.1.3) as well as approximating functionals, numerical minimization methods associated with the Mumford–Shah functional and further models for two-phase as well as multi-phase image segmentation (see Subsection 5.1.4). Prior to this, a short survey of the space of bounded functions and distinct results from convex analysis are presented to an extent required for later sections (see Subsection 5.1.1 and Subsection 5.1.2).

5.1.1 Functions of Bounded Variation

In what follows, we will recall the main properties of the spaces $\mathrm{BV}(\Omega)$ and $\mathrm{SBV}(\Omega)$. The latter turns out to be the natural function space for the Mumford–Shah functional. Throughout this chapter, we assume that $\Omega \subset \mathbb{R}^n$ is a bounded domain with Lipschitz boundary. The main references for this section are [EG92, AFP00, Zie89, Amb89].

Definition 5.1.1. A function $f \in L^1(\Omega)$ has *bounded variation in* Ω (notation: $f \in \mathrm{BV}(\Omega)$) if the *total variation* $|\mathrm{D}f|(\Omega)$ is finite, *i.e.*

$$|\mathrm{D}f|(\Omega) := \sup\left\{ \int_\Omega f \mathrm{div}\phi \,\mathrm{d}x \,:\, \phi \in C_c^1(\Omega,\mathbb{R}^n), \|\phi\|_{L^\infty(\Omega)} \le 1 \right\} < \infty\,.$$

Moreover, the norm in $\mathrm{BV}(\Omega)$ is given as $\|f\|_{\mathrm{BV}(\Omega)} = \|f\|_{L^1(\Omega)} + |\mathrm{D}f|(\Omega)$. An $\mathcal{L}^n(\Omega)$-measurable set $\Sigma \subset \Omega$ has *finite perimeter* if $|\mathrm{D}\chi[\Sigma]|(\Omega) < \infty$.

Theorem 5.1.2. *For every function $f \in \mathrm{BV}(\Omega)$ there exists a finite $\mathbb{R}^n$-valued Radon measure $\mathrm{D}f$ such that*

$$\int_\Omega f \mathrm{div}\phi \,\mathrm{d}x = -\int_\Omega \phi \cdot \,\mathrm{d}\mathrm{D}f \quad \forall \phi \in C_c^1(\Omega,\mathbb{R}^n)\,.$$

Proof. See [EG92, Chapter 5.1] and [AFP00, Chapter 3.1]. □

Definition 5.1.3. A sequence $\{f_k\}_{k\in\mathbb{N}} \subset \mathrm{BV}(\Omega)$ *converges weakly-$*$ in* $\mathrm{BV}(\Omega)$ (notation: $f_k \overset{*}{\rightharpoonup} f$) if there exists a function $f \in \mathrm{BV}(\Omega)$ such that $f_k \to f$ in $L^1(\Omega)$ and

$$\int_\Omega \phi \cdot \,\mathrm{d}\mathrm{D}f_k \to \int_\Omega \phi \cdot \,\mathrm{d}\mathrm{D}f \quad \forall \phi \in C_c^0(\Omega,\mathbb{R}^n)\,.$$

Theorem 5.1.4 (Properties of BV functions)**.** *We list several fundamental properties of the space $\mathrm{BV}(\Omega)$:*

(i.) $W^{1,1}(\Omega) \subsetneq \mathrm{BV}(\Omega)$.

(ii.) $\mathrm{BV}(\Omega)$ *is not reflexive.*

(iii.) The total variation is a seminorm and convex on the space $L^1(\Omega)$.

(iv.) *Suppose that* $\{f_k\}_{k\in\mathbb{N}} \subset \mathrm{BV}(\Omega)$ *and* $f_k \to f$ *in* $L^1_{\mathrm{loc}}(\Omega)$ *as* $k \to \infty$. *Then the total variation is lower semicontinuous w.r.t. this sequence,* i.e. $|\mathrm{D}f|(\Omega) \leq \liminf_{k\to\infty} |\mathrm{D}f_k|(\Omega)$.

(v.) *Let* $f \in \mathrm{BV}(\Omega)$. *Then there exists a sequence* $\{f_k\}_{k\in\mathbb{N}} \subset \mathrm{BV}(\Omega) \cap C^\infty(\Omega)$ *such that* $f_k \to f$ *in* $L^1(\Omega)$ *and* $|\mathrm{D}f_k|(\Omega) \to |\mathrm{D}f|(\Omega)$ *as* $k \to \infty$. *This property is called* strict convergence in $\mathrm{BV}(\Omega)$.

(vi.) *Let* $\{f_k\}_{k\in\mathbb{N}} \subset \mathrm{BV}(\Omega)$ *be a sequence which is uniformly bounded in* $\mathrm{BV}(\Omega)$. *Then there exist a subsequence* $\{f_{k_j}\}_{j\in\mathbb{N}}$ *and* $f \in \mathrm{BV}(\Omega)$ *such that* $f_{k_j} \overset{*}{\rightharpoonup} f$ *in* $\mathrm{BV}(\Omega)$ *as* $j \to \infty$.

Proof. See [AFP00, Chapter 3.1] and [EG92, Chapter 5.1/5.2]. □

When minimizing the Mumford–Shah functional w.r.t. the set $\mathrm{BV}(\Omega)$ the infimum is always 0 due to the presence of the Cantor part in $\mathrm{D}f$, that is why we have to restrict to the space $\mathrm{SBV}(\Omega)$ of special functions with bounded variation defined as the set of $\mathrm{BV}(\Omega)$-functions with vanishing Cantor part. The rigorous definition of $\mathrm{SBV}(\Omega)$ requires the following results as a preparatory step:

Definition and Lemma 5.1.5. *Let* $f \in \mathrm{BV}(\mathbb{R}^n)$. *The* (upper and lower) approximate limits of f *for* $x \in \mathbb{R}^n$ *are defined as follows:*

$$f^+(x) = \inf\left\{ t \in \mathbb{R} \,:\, \lim_{r\searrow 0} \frac{|B_r(x) \cap [f > t]|}{r^n} = 0 \right\},\ f^-(x) = \sup\left\{ t \in \mathbb{R} \,:\, \lim_{r\searrow 0} \frac{|B_r(x) \cap [f < t]|}{r^n} = 0 \right\}.$$

(i.) *The functions* f^- *and* f^+ *are Borel measurable and* $-\infty < f^-(x) \leq f^+(x) < \infty$ *for* $\mathcal{H}^{n-1}$*-a.e.* $x \in \mathbb{R}^n$. *If* $f^+(x) = f^-(x)$, *then we call this limit the* approximate limit *(denoted by* $\operatorname{aplim}_{y\to x} f(y)$*).*

(ii.) *The* jump set S_f of f *is the set where the approximate limits do not coincide,* i.e.

$$S_f = \left\{ x \in \mathbb{R}^n \,:\, f^-(x) < f^+(x) \right\}.$$

(iii.) *Let* $a \in \mathbb{S}^{n-1}$. *For* $x \in \mathbb{R}^n$ *we define the half-spaces*

$$H_a^+(x) = \left\{ y \in \mathbb{R}^n \,:\, a \cdot (y - x) \geq 0 \right\}, \qquad H_a^-(x) = \left\{ y \in \mathbb{R}^n \,:\, a \cdot (y - x) \leq 0 \right\}.$$

Then for $\mathcal{H}^{n-1}$*-a.e.* $x \in S_f$ *there exists* $\mathrm{n}_f = \mathrm{n}_f(x) \in \mathbb{S}^{n-1}$ *such that*

$$\lim_{r\searrow 0} \fint_{B_r(x)\cap H^-_{\mathrm{n}_f}(x)} |f - f^+(x)|^{\frac{n}{n-1}}\,\mathrm{d}y = 0\,, \qquad \lim_{r\searrow 0} \fint_{B_r(x)\cap H^+_{\mathrm{n}_f}(x)} |f - f^-(x)|^{\frac{n}{n-1}}\,\mathrm{d}y = 0\,.$$

Proof. See [AFP00, Chapter 3.6] and [EG92, Chapter 5.9]. □

Then, any Radon measure $\mathrm{D}f$ associated with $f \in \mathrm{BV}(\Omega)$ can be decomposed as follows:

Theorem 5.1.6. *Let* $f \in \mathrm{BV}(\Omega)$. *Then* $\mathrm{D}f$ *admits the decomposition* $\mathrm{D}f = [\mathrm{D}f]_{ac} + [\mathrm{D}f]_J + [\mathrm{D}f]_C$ *into Radon measures, where* $[\mathrm{D}f]_{ac}$ *represents the* absolutely continuous *and* $[\mathrm{D}f]_J + [\mathrm{D}f]_C$ *the* singular part of $\mathrm{D}f$ *w.r.t. the* n*-dimensional Lebesgue measure* $\mathcal{L}^n$. *The* approximate differential ∇f *is the density of* $[\mathrm{D}f]_{ac}$ *w.r.t.* $\mathcal{L}^n$. *Moreover,* $[\mathrm{D}f]_J$ (the jump part) *and* $[\mathrm{D}f]_C$ (the Cantor part) *are the restrictions of the singular part to* S_f *and* $\Omega\backslash S_f$, *respectively. Finally,*

$$[\mathrm{D}f]_J\big|_{S_f} = (f^+ - f^-)\mathrm{n}_f\,\mathrm{d}\mathcal{H}^{n-1}\big|_{S_f}\,.$$

Proof. See [AFP00, Chapter 3.6/3.7/3.9]. □

Definition 5.1.7. The space of *special functions of bounded variation in* Ω, which we denote by $\mathrm{SBV}(\Omega)$, is given by $\mathrm{SBV}(\Omega) = \{f \in \mathrm{BV}(\Omega) \,:\, [\mathrm{D}f]_C = 0\}$. Moreover, we set

$$\mathrm{SBV}_{\mathrm{loc}}(\Omega) = \left\{ f \in L^1(\Omega) \,:\, f\big|_{\Omega'} \in \mathrm{SBV}(\Omega') \text{ for all } \Omega' \Subset \Omega \text{ open} \right\}.$$

Finally, a function $f : \Omega \to \mathbb{R}^m$ is a *generalized special function of bounded variation* (notation: $f \in \mathrm{GSBV}(\Omega)$) if $\phi \circ f \in \mathrm{SBV}_{\mathrm{loc}}(\Omega)$ for every $\phi \in C^1(\mathbb{R}^m)$ such that $\nabla\phi$ has compact support.

The space $\mathrm{SBV}(\Omega)$ can be regarded as the space of piecewise bounded $W^{1,1}(\Omega)$-functions in view of the following proposition:

Proposition 5.1.8. *Let $K \subset \Omega \subset \mathbb{R}^n$ be a closed set such that $\mathcal{H}^{n-1}(K) < \infty$ and let $f \in W^{1,1}(\Omega \backslash K) \cap L^\infty(\Omega)$. Then $f \in \mathrm{SBV}(\Omega)$ and $S_f \subset K \cup N$ for a $\mathcal{H}^{n-1}$-null set $N \subset \Omega$.*

Proof. See [AFP00, Chapter 4.1]. □

The existence of minimizers of the Mumford–Shah functional essentially relies on the following compactness theorem in $\mathrm{SBV}(\Omega)$:

Theorem 5.1.9. *Let $\phi : \mathbb{R}_0^+ \to \mathbb{R}_0^+$ be an increasing function such that $\lim_{t\to\infty} \frac{\phi(t)}{t} = \infty$ and assume that $\{f_k\}_{k\in\mathbb{N}} \subset \mathrm{SBV}(\Omega) \cap L^\infty(\Omega)$ fulfills*

$$\limsup_{k\to\infty} \left\{ \|f_k\|_{L^\infty(\Omega)} + \int_\Omega \phi(|\nabla f_k|)\,\mathrm{d}x + \mathcal{H}^{n-1}(S_{f_k}) \right\} < \infty\,.$$

Then there exist a subsequence of $\{f_k\}_{k\in\mathbb{N}}$ (not relabeled) and a function $f \in \mathrm{SBV}(\Omega)$ such that $f_k \to f$ in $L^1_{\mathrm{loc}}(\Omega)$, $\nabla f_k \rightharpoonup \nabla f$ in $L^1(\Omega)$ and $[\mathrm{D}f_k]_J \to [\mathrm{D}f]_J$ weakly as Radon measures.

Proof. See [Amb89]. □

As announced in the introduction, we will propose a uniformly convex relaxation of the binary Mumford–Shah functional, where each minimizer of the binary functional can be exactly recovered from the corresponding minimizer of the relaxed functional via thresholding. The key ingredient of this proof is the *coarea formula in the space* $\mathrm{BV}(\Omega)$:

Theorem 5.1.10 (Coarea formula in $\mathrm{BV}(\Omega)$)**.** *Let $f \in \mathrm{BV}(\Omega)$. Then*

$$|\mathrm{D}f|(\Omega) = \int_{\mathbb{R}} |\mathrm{D}\chi[f > t]|\,\mathrm{d}t\,.$$

Proof. See [AFP00, Chapter 3.3]. □

5.1.2 Foundations of Convex Analysis

In what follows, we will recall some fundamental definitions and theorems from convex analysis to such an extent required for the rest of this chapter. If not otherwise specified, we restrict all definitions and results to the real Banach spaces $\mathbf{V}$ and $\mathbf{W}$ for convenience. We remark that many results shown below remain valid in the case of locally convex real vector spaces. The relevant references for this subsection are [ET99, AF03, Roc97].

Definition 5.1.11. The subsequent list contains several fundamental definitions from convex analysis.

(i.) We denote by $\Gamma(\mathbf{V})$ the set of all convex and lower semicontinuous functionals $J : \mathbf{V} \to \mathbb{R} \cup \{\pm\infty\}$ with the additional property that $J[v] = -\infty$ at any point $v \in \mathbf{V}$ already implies $J \equiv -\infty$. Furthermore, $\Gamma_0(\mathbf{V}) \subset \Gamma(\mathbf{V})$ refers to the subset of all functionals with bounded range.

(ii.) The *dual space* $\mathbf{V}'$ *of* $\mathbf{V}$ is defined as $\mathbf{V}' = \mathcal{L}(\mathbf{V}, \mathbb{R})$, the associated *duality pairing* $\langle \cdot\,, \cdot \rangle_{\mathbf{V}',\mathbf{V}}$ *of* $\mathbf{V}$ *and* $\mathbf{V}'$ is given by $\langle v', v\rangle_{\mathbf{V}',\mathbf{V}} = v'(v)$ for $v \in \mathbf{V}$ and $v' \in \mathbf{V}'$.

(iii.) The *Fenchel conjugate of a functional* $J : \mathbf{V} \to \overline{\mathbb{R}}$ is defined as

$$J^* : \mathbf{V}' \to \overline{\mathbb{R}}\,, \quad v' \mapsto \sup_{v\in\mathbf{V}} \Big(\langle v', v\rangle_{\mathbf{V}',\mathbf{V}} - J[v] \Big)\,.$$

(iv.) A functional $J : \mathbf{V} \to \overline{\mathbb{R}}$ is *subdifferentiable at the point* $v \in \mathbf{V}$ if there exists a continuous affine functional $f : \mathbf{V} \to \overline{\mathbb{R}}$ fulfilling $f \leq J$ and $f[v] = J[v]$. The slope $v' \in \mathbf{V}'$ of f is commonly referred to as a *subgradient of J at the point v*. We denote the set of all subgradients at $v \in \mathbf{V}$ by $\partial J[v]$.

(v.) The *adjoint operator* $\Lambda^* \in \mathcal{L}(\mathbf{W}', \mathbf{V}')$ *of* $\Lambda \in \mathcal{L}(\mathbf{V}, \mathbf{W})$ is defined as

$$\langle w', \Lambda v \rangle_{\mathbf{W}',\mathbf{W}} = \langle \Lambda^* w', v \rangle_{\mathbf{V}',\mathbf{V}} \quad \forall v \in \mathbf{V}\,, \forall w' \in \mathbf{W}'\,.$$

For later reference we list several basic properties of the aforementioned fundamental concepts.

Proposition 5.1.12. *Let* $\mathbf{V}$ *and* $\mathbf{W}$ *be arbitrary Banach spaces.*

(i.) A functional $J : \mathbf{V} \to \overline{\mathbb{R}}$ *is subdifferentiable at* $v \in \mathbf{V}$ *with subgradient* $v' \in \mathbf{V}'$ *if and only if*

$$J[v] + J^*[v'] = \langle v', v \rangle_{\mathbf{V}',\mathbf{V}}\,.$$

(ii.) If $J : \mathbf{V} \to \overline{\mathbb{R}}$ *is Gâteaux differentiable at* $v \in \mathbf{V}$ *with Gâteaux derivative* $J'[v]$*, then* J *is subdifferentiable at* v *and* $\partial J[v] = \{J'[v]\}$.

(iii.) Let $J \in \Gamma(\mathbf{V})$*,* $v \in \mathbf{V}$ *and* $v' \in \mathbf{V}'$*. Then* $v' \in \partial J[v]$ *if and only if* $v \in \partial J^*[v']$.

(iv.) If $J \in \mathcal{L}(\mathbf{V}, \mathbb{R})$ *is convex, then* $\partial J[v] \neq \emptyset$ *for all* $v \in \mathbf{V}$.

(v.) The operator $* : \mathcal{L}(\mathbf{V}, \mathbf{W}) \to \mathcal{L}(\mathbf{W}', \mathbf{V}')$*,* $\Lambda \mapsto \Lambda^*$*, is an isometry,* i.e. $|||\Lambda||| = |||\Lambda^*|||$.

Proof. See [ET99, Chapter 1] and [Roc97]. □

The functional a posteriori error estimator for the binary Mumford–Shah functional is essentially based on the following theorem:

Theorem 5.1.13 (Duality Theorem)**.** *Let* $\mathbf{V}$ *and* $\mathbf{W}$ *be* reflexive *Banach spaces and* $\Lambda \in \mathcal{L}(\mathbf{V}, \mathbf{W})$*. Assume that* $F \in \Gamma_0(\mathbf{V})$*,* $G \in \Gamma_0(\mathbf{W})$*,* $E[v, \Lambda v] = F[v] + G[\Lambda v]$ *for* $v \in \mathbf{V}$*, and*

(i.) there exists $v \in \mathbf{V}$ *such that* $E[v, \Lambda v] < \infty$ *and* $\mathbf{W} \ni w \to E[v, w]$ *is continuous at* Λv*,*

(ii.) E *is coercive on* $\mathbf{V}$*,* i.e. $\lim_{v \in \mathbf{V}, \|v\|_{\mathbf{V}} \to \infty} E[v, \Lambda v] = +\infty$.

Furthermore, we define the Primal Problem $(\mathcal{P})$ *and the associated Dual Problem* $(\mathcal{P}^*)$ *as follows:*

$$\inf_{v \in \mathbf{V}} \Big\{ E[v, \Lambda v] = F[v] + G[\Lambda v] \Big\}\,, \tag{$\mathcal{P}$}$$

$$\sup_{w' \in \mathbf{W}'} \Big\{ -E^*[\Lambda^* w', -w'] = -F^*[-\Lambda^* w'] - G^*[w'] \Big\}\,. \tag{$\mathcal{P}^*$}$$

Then $(\mathcal{P})$ *and* $(\mathcal{P}^*)$ *have at least one solution* $\bar{v} \in \mathbf{V}$ *and* $\bar{w}' \in \mathbf{W}'$*, respectively, and*

$$E[\bar{v}, \Lambda \bar{v}] = \inf \mathcal{P} = \sup \mathcal{P}^* = -E^*[-\Lambda^* \bar{w}', \bar{w}']\,.$$

Finally, the solution admits the characterization $(-\Lambda^* \bar{w}', \bar{w}') \in \partial E[\bar{v}, \Lambda \bar{v}]$*, which is equivalent to*

$$-\Lambda^* \bar{w}' \in \partial F[\bar{v}], \qquad \bar{w}' \in \partial G[\Lambda \bar{v}]\,.$$

Proof. See [ET99, Chapter 3]. □

The proximal mappings of functionals on Hilbert spaces play an important role when applying the primal-dual algorithm in Section 5.6.

Definition 5.1.14. Let $\mathbf{V}$ be a Hilbert space with norm $\|\cdot\|_{\mathbf{V}}$. The *proximal mapping* $\operatorname{prox}_{\tau J}$ *of* $J \in \Gamma(\mathbf{V})$ for $v \in \mathbf{V}$ and a weight parameter $\tau > 0$ reads as

$$\operatorname{prox}_{\tau J}[v] = \operatorname*{argmin}_{\tilde{v} \in \mathbf{V}} J[\tilde{v}] + \tfrac{1}{2\tau} \|v - \tilde{v}\|_{\mathbf{V}}^2\,.$$

Remark 5.1.15. Under suitable assumptions, the proximal mapping $\operatorname{prox}_{\tau J}$ of $J \in \Gamma(\mathbf{V})$ coincides with the resolvent of the maximal monotone operator $\tau \partial J$ and compromises between minimizing J and the squared distance of v and the minimizer $\tilde{v}$. For further details of this mapping we refer to the review article [CP16].

5.1.3 Existence of Minimizers and Regularity Properties of the Discontinuity Set

The proof of the existence of minimizers $(\hat{u}, \hat{K}) \in \mathcal{K}$ of (5.1) dates back to De Giorgi *et al.* [DGCL89] and Ambrosio [Amb89]. The crucial step is to minimize the functional

$$\widetilde{E}_{\mathrm{MS}}[u] = \int_{\Omega} \alpha(u - u_0)^2 + |\nabla u|^2 \,\mathrm{d}x + \beta \mathcal{H}^{n-1}(S_u) \tag{5.2}$$

among all $u \in \mathrm{SBV}(\Omega)$. A straight application of the direct method in the calculus of variations to prove the existence of minimizers for (5.1) fails since $K \mapsto \mathcal{H}^{n-1}(K)$ is in general not lower semicontinuous w.r.t. the Hausdorff metric. We remark that we have to restrict to the space $\mathrm{SBV}(\Omega)$ since $\inf_{u \in \mathrm{BV}(\Omega)} \widetilde{E}_{\mathrm{MS}}[u] = 0$. Combining the lower semicontinuity of the Mumford–Shah functional in $\mathrm{SBV}(\Omega)$ w.r.t. the $L^1_{\mathrm{loc}}(\Omega)$-topology (for details see [Amb89, Section 4]) with the $\mathrm{SBV}(\Omega)$-Compactness Theorem 5.1.9 implies the existence of a minimizer of $\widetilde{E}_{\mathrm{MS}}$. Then, taking into account Proposition 5.1.8 we can infer that $(u, K) \in \mathcal{K}$ implies $u \in \mathrm{SBV}(\Omega)$ and therefore

$$\inf_{(u,K) \in \mathcal{K}} \left\{ E_{\mathrm{MS}}[u, K] = \widetilde{E}_{\mathrm{MS}}[u] \right\} \geq \inf_{u \in \mathrm{SBV}(\Omega)} \widetilde{E}_{\mathrm{MS}}[u] \,.$$

The reverse inequality is essentially a consequence of the approximate closedness of the singular set $S_{\hat{u}}$ with $\hat{u} \in \mathrm{SBV}(\Omega)$ representing a minimizer of $\widetilde{E}_{\mathrm{MS}}$. In detail, for $x \in \Omega \backslash S_{\hat{u}}$ we set $\bar{u}(x) = \operatorname{aplim}_{y \to x} \hat{u}(y)$. Then [DGCL89, Lemma 5.2] states that $\bar{u} \in C^1(\Omega \backslash \overline{S_{\hat{u}}})$ and $\mathcal{H}^{n-1}((\overline{S_{\hat{u}}} \cap \Omega) \backslash S_{\hat{u}}) = 0$. Hence, $(\bar{u}, \overline{S_{\hat{u}}} \cap \Omega) \in \mathcal{K}$ and we obtain

$$\inf_{(u,K) \in \mathcal{K}} E_{\mathrm{MS}}[u, K] \leq E_{\mathrm{MS}}[\bar{u}, \overline{S_{\hat{u}}} \cap \Omega] = \widetilde{E}_{\mathrm{MS}}[\hat{u}] \,,$$

which proves the existence of minimizers for (5.1).

In their seminal publication Mumford and Shah [MS89] conjectured:

Conjecture 5.1.16. *Let $n = 2$ and $(\hat{u}, \hat{K}) \in \mathcal{K}$ be a minimizer of* (5.1)*. Then there exists a set $L \subset \Omega$ such that L is composed of a finite number of $C^{1,\alpha}$-arcs and $\mathcal{H}^1(\hat{K} \Delta L) = 0$.*

To the best of our knowledge, there are only partial answers to this conjecture, see for instance the publications by Larsen [Lar96], David [Dav96] and Ambrosio and Pallara [AP97]. We highlight the partial result due to Bonnet [Bon96], which essentially guarantees the regularity of the discontinuity set up to crack-tips.

Theorem 5.1.17. *Let $(\hat{u}, \hat{K}) \in \mathcal{K}$ be a minimizer of* (5.1)*. Any isolated and connected component of $\hat{K}$ is a finite union of C^1-arcs, which additionally exhibit a $C^{1,1}$-regularity away from crack-tips and can only merge through triple junctions. In this case, a triple junction is a point where three arcs of $\hat{K}$ intersect at an angle of* $120°$.

Bonnet also proved that a higher regularity of the input image implies a higher regularity of the discontinuity set in the following sense:

Theorem 5.1.18. *Under the assumptions of Theorem 5.1.17, if the input image has the property $u_0 \in C^{k,\alpha}(\Omega)$ and the discontinuity set is a C^1-arc in a neighborhood of any point in $\hat{K}$, then this arc is actually $C^{k+2,\alpha}$-regular in this neighborhood.*

For further details concerning the regularity of the discontinuity set such as Ahlfors-regularity and regularity properties of the discontinuity set for almost-minimizers we refer to [Dav05] and the references therein.

5.1.4 Approximation Schemes, Numerical Minimization Methods and Extensions

Since the introduction of the Mumford–Shah functional more than 25 years ago, a great variety of different approaches has been investigated to (numerically) minimize the Mumford–Shah energy functional. One of the main challenges related to this numerical optimization emerges from the right treatment of the free boundary K. Below, we will concentrate on different approximation schemes for the Mumford–Shah energy functional as well as level set methods as prototypes of optimization strategies. Furthermore, the piecewise constant Mumford–Shah model along with its basic properties are briefly discussed. Finally, we conclude this subsection with an overview of other segmentation functionals and extensions that are related to the methods studied below.

Approximation methods employing Γ-convergence and related optimization algorithms. The approximation of the energy functional (5.1) circumvents the challenging approximation of the Hausdorff measure of K by using computationally more feasible functionals.

The probably most common Γ-convergence approximation scheme is due to Ambrosio and Tortorelli (see [AT90, AT92]). In their approach, the set S_u is implicitly characterized by an auxiliary scalar-valued function z, also called phase field, which can be regarded as an approximate indicator function for the set $\Omega \backslash S_u$. The precise statement reads as follows (see [AT92]):

Theorem 5.1.19 (Ambrosio–Tortorelli approximation of the Mumford–Shah functional)**.** *Let $\Omega \subset \mathbb{R}^n$ be a bounded domain and $\mathcal{E}_\varepsilon, \mathcal{E} : (L^2(\Omega))^2 \to \overline{\mathbb{R}}$ be defined as*

$$\mathcal{E}_\varepsilon[u,z] = \begin{cases} \int_\Omega \alpha(u-u_0)^2 + z^2|\nabla u|^2 + \beta\left(\varepsilon|\nabla z|^2 + \frac{(z-1)^2}{4\varepsilon}\right) \mathrm{d}x\,, & \text{if } (u,z) \in (H^1(\Omega))^2 \text{ s.t. } 0 \le z \le 1\,, \\ +\infty\,, & \text{else}\,, \end{cases}$$

$$\mathcal{E}[u,z] = \begin{cases} \widetilde{E}_{\mathrm{MS}}[u]\,, & \text{if } u \in \mathrm{SBV}(\Omega)\,,\ z = 1\,, \\ +\infty\,, & \text{else}\,. \end{cases}$$

Then $\mathcal{E}_\varepsilon$ Γ-converges to $\mathcal{E}$ w.r.t. the $(L^2(\Omega))^2$-topology. Moreover, there exist minimizers $(u_\varepsilon, z_\varepsilon)$ of $\mathcal{E}_\varepsilon$ such that a subsequence of u_ε converges to some minimizer $u \in \mathrm{SBV}(\Omega)$ of $\mathcal{E}$ in $L^2(\Omega)$ as $\varepsilon \to 0$.

The last integrand in the definition of $\mathcal{E}_\varepsilon$ is an approximation of the Hausdorff measure of S_u and is composed of a weighted sum of a gradient penalization term of the phase field and a single-well potential.

A simple optimization approach for $\mathcal{E}_\varepsilon$ involves an alternating minimization w.r.t. u and z, where ε is usually chosen to be of the order of the grid size. Since each subproblem is convex, efficient primal-dual methods can be employed to compute the approximate solution (*cf*. for instance [CP11, BS15b]). The starting point of a second common minimization strategy is the derivation of Euler–Lagrange equations for $\mathcal{E}_\varepsilon$ in u and z, *i.e*.

$$2\alpha(u-u_0) - 2\mathrm{div}(z^2\nabla u) = 0\,, \qquad 2z|\nabla u|^2 - 2\beta\varepsilon\Delta z + \frac{\beta}{2\varepsilon}(z-1) = 0$$

in a weak sense, which are discretized using, for instance, finite differences. Afterwards, a time-dependent scheme in u and a stationary semi-implicit fixed-point scheme in z are incorporated to compute minimizers (we refer to [Sch11, Chapter 25] for details). Contrary to these alternating minimization schemes, Kee and Kim [KK14] analyzed different convex relaxations to replace the non-convex summand $(u,z) \mapsto \int_\Omega z^2|\nabla u|^2 \,\mathrm{d}x$ in the Ambrosio–Tortorelli functional, which allow for joint global optimization for the resulting convex problem. In [BKS03], Brook *et al*. extended an Ambrosio–Tortorelli-type segmentation functional to color images. One major disadvantage when using the aforementioned Ambrosio–Tortorelli approximation for numerical optimization is the dependency of the phase field parameter ε on α, β and the grid size h (see [Sch11, SC14] and the references therein). To circumvent this problem, Bellettini and Coscia [BC94] introduced a functional $\mathcal{E}_{\varepsilon,h}$, which is a modification of $\mathcal{E}_\varepsilon$ for affine finite element spaces $\mathcal{V}_h$ depending on ε and in addition on the mesh size h. By choosing $h = \mathrm{o}(\varepsilon)$ and under some mild additional assumptions they established the Γ-convergence of $\mathcal{E}_{\varepsilon,h}$ to $\mathcal{E}$ provided that $(u_{\varepsilon,h}, z_{\varepsilon,h}) \in \mathcal{V}_h^2$. A further finite element based approximation of $\mathcal{E}_\varepsilon$ is due to Bourdin [Bou99].

For $n = 2$, Chambolle and Dal Maso [CDM99] proposed an approximation which does not require any auxiliary function, and established its Γ-convergence to a variant of $\mathcal{E}$. To this end, they restricted the function space for the images to the affine finite element space $\mathcal{V}_h$ on a triangulation with additional constraints regarding the angles of the elements. The approximating functional $\widetilde{\mathcal{E}}_h$ associated with $\mathcal{E}$ is of the form ($\beta = 1$ for simplicity)

$$\widetilde{\mathcal{E}}_h[u] = \begin{cases} \int_\Omega \alpha(u-u_0)^2 + \frac{1}{h} f(h|\nabla u|^2)\,\mathrm{d}x\,, & \text{if } u \in \mathcal{V}_h\,, \\ +\infty\,, & \text{if } u \in L^2(\Omega)\backslash\mathcal{V}_h\,, \end{cases} \tag{5.3}$$

for a non-decreasing function $f : \mathbb{R}_0^+ \to \mathbb{R}_0^+$ satisfying certain growth conditions. Bourdin and Chambolle [BC00] extended this approach by adding a triangulation dependent local averaging to the approximating functional, which results in a numerically more stable computation of the approximate solutions compared to (5.3).

Braides and Dal Maso [BDM97] proposed an approximation involving non-local integral functionals, and proved the Γ-convergence w.r.t. the $L^p(\Omega)$-topology of ($\beta = 1$ for simplicity, $1 \leq p < \infty$)

$$\widehat{\mathcal{E}}_\varepsilon[u] = \begin{cases} \int_\Omega \alpha(u-u_0)^2 + \frac{1}{\varepsilon} f\left(\varepsilon \fint_{B_\varepsilon(x)\cap\Omega} |\nabla u(y)|^2 \,\mathrm{d}y\right) \mathrm{d}x\,, & \text{if } u \in L^p(\Omega) \cap H^1(\Omega)\,, \\ +\infty\,, & \text{if } u \in L^p(\Omega)\backslash H^1(\Omega)\,, \end{cases}$$

to the Mumford–Shah energy functional with f satisfying growth conditions similar to the ansatz by Chambolle and Dal Maso.

The Γ-convergence approximation due to Grasmair *et al.* [GMS13] relies on the covering of the (expected) discontinuity set by balls of radius ε. Here, the Hausdorff measure of this set is approximated by 2ε multiplied by the number of balls. The main difficulty in this approach arises from the identification of the discontinuity set. The crucial observation is that each component of the minimizer $(\hat{u}, \hat{K})$ of (5.1) is uniquely determined by the other one. Then, a topological asymptotic expansion is employed to approximate $\hat{K}$, which is based on the successive enlargement of an initial approximate discontinuity set by those regions which result in the maximal decay of the energy.

In [She05], Shen introduced a Γ-converging approximation for the piecewise constant Mumford–Shah segmentation (see below), where the length term in the Mumford–Shah model is approximated via a phase field approach, which shares some similarities with the classical work by Modica and Mortola [MM77].

Burger *et al.* [BEZ15] derived a second order approximation of the Mumford–Shah functional which is related to a Cahn–Hilliard-type phase transition model originating from the work by Fonseca and Mantegazza [FM00]. The approximating functional is given by $\check{\mathcal{E}}_\varepsilon : (L^1(\Omega))^2 \to \mathbb{R}$,

$$\check{\mathcal{E}}_\varepsilon[u,z] = \begin{cases} \int_\Omega \alpha(u-u_0)^2 + z^2|\nabla u|^2 + \frac{\beta}{2\sqrt{2}}\left(\frac{(z-1)^2}{\varepsilon} + \varepsilon^3 |D^2 z|^2\right) \mathrm{d}x\,, & \text{if } (u,z) \in H^1(\Omega) \times H^2(\Omega)\,, \\ +\infty\,, & \text{else}\,, \end{cases}$$

and Γ-converges w.r.t. the strong $(L^1(\Omega))^2$-topology to

$$\check{\mathcal{E}}[u,z] = \begin{cases} \widetilde{E}_{\mathrm{MS}}[u]\,, & \text{if } u \in \mathrm{GSBV}(\Omega) \text{ s.t. } \nabla u \in L^2(\Omega)\,, \mathcal{H}^{n-1}(S_u) < \infty\,,\ z = 1\,, \\ +\infty\,, & \text{else}\,. \end{cases}$$

The optimization algorithm for this approximation then exploits the quadratic structure of the subproblems when using an alternating minimization scheme for a slightly altered version of $\check{\mathcal{E}}_\varepsilon$. In numerical experiments, they showed that the contours of the segmented regions look smoother and are less prone to noise compared to the results computed with the aid of the classical Ambrosio–Tortorelli model.

Convex approximations of the Mumford–Shah functional and level set methods. The second major category of minimization algorithms is based on convex approximations of (5.1). In their pioneering work, Alberti *et al.* [ABDM03] proposed a functional lifting of the non-convex Mumford–Shah functional (5.2) defined on an n-dimensional domain to a variational problem over characteristic functions of subgraphs in $\mathbb{R}^{n+1}$, the crucial observation is

$$\widetilde{E}_{\mathrm{MS}}[u] = \sup_{\phi=(\phi^x,\phi^t)\in\mathcal{C}} \int_{\Omega\times\mathbb{R}} \phi \cdot \mathrm{D}\chi[u(x) > t] \tag{5.4}$$

for the convex set of vector fields (in this context these vector fields are known as *calibrations*)

$$\mathcal{C} = \left\{ (\phi^x, \phi^t) \in C^0(\Omega\times\mathbb{R}) \,:\, \phi^t(x,t) \geq \tfrac{|\phi^x(x,t)|^2}{4} - \alpha(t-u_0)^2, \right. \\ \left. \left| \int_{\underline{t}}^{\overline{t}} \phi^x(x,s)\,\mathrm{d}x \right| \leq \beta\,, \forall x \in \Omega\,, \forall t, \underline{t}, \overline{t} \in \mathbb{R} \right\}.$$

Following Pock *et al.* [PCBC09, PCBC10], (5.4) can be converted into a convex optimization problem if we replace $\mathrm{D}\chi[u(x) > t]$ by $\mathrm{D}\tilde{\chi}$ with a function $\tilde{\chi} \in \mathrm{BV}(\Omega\times\mathbb{R})$ satisfying $\lim_{t\to-\infty} \tilde{\chi}(x,t) = 1$ and $\lim_{t\to\infty} \tilde{\chi}(x,t) = 0$,

the resulting functional reads as follows:

$$\widehat{E}_{\mathrm{MS}}[\tilde{\chi}] = \sup_{\phi=(\phi^x,\phi^t)\in\mathcal{C}} \int_{\Omega\times\mathbb{R}} \phi \cdot \mathrm{D}\tilde{\chi}\,. \tag{5.5}$$

Since a coarea formula for the Mumford–Shah functional of the form $\widetilde{E}_{\mathrm{MS}}[u] = \int_0^1 \widetilde{E}_{\mathrm{MS}}[\chi[u > s]]\,\mathrm{d}s$ does in general *not* hold true, a minimizer $\tilde{\chi}^*$ of $\widehat{E}_{\mathrm{MS}}$ is simultaneously a minimizer of $\widetilde{E}_{\mathrm{MS}}$ if and only if $\tilde{\chi}^*$ is binary, which is also in general *not* true. However, since (5.5) allows a saddle-point formulation, efficient primal-dual algorithms can be employed to compute approximate minimizers of (5.4).

A famous level set model for image segmentation was proposed by Chan and Vese [CV01a], which can be regarded as a version of the by now classical active contours model of Caselles *et al.* [CKS97] and extends the general level set approach proposed by Osher and Sethian [OS88]. In particular, this method is feasible to model cusps and allows for changes of the topology. Starting from the two-phase segmentation functional

$$E_{\mathrm{CV}}[K, c_1, c_2] = \int_{\mathrm{inside}(K)} \lambda_1(u_0-c_1)^2\,\mathrm{d}x + \int_{\mathrm{outside}(K)} \lambda_2(u_0-c_2)^2\,\mathrm{d}x + \lambda_3\mathcal{H}^{n-1}(K) + \lambda_4|\mathrm{inside}(K)|\,, \tag{5.6}$$

the associated level set formulation is given by

$$E_{\mathrm{CV}}[\phi, c_1, c_2] = \int_\Omega \lambda_1(u_0-c_1)^2\mathrm{H}(\phi) + \lambda_2(u_0-c_2)^2(1-\mathrm{H}(\phi))\,\mathrm{d}x + \int_\Omega \lambda_3|\nabla\phi|\,\mathrm{d}\delta[\phi=0] + \int_\Omega \lambda_4\mathrm{H}(\phi)\,\mathrm{d}x \tag{5.7}$$

on a bounded domain $\Omega \subset \mathbb{R}^2$ with input image $u_0 \in L^\infty(\Omega, [0,1])$, weight parameters $\lambda_i > 0$, intensity values $c_1, c_2 \in [0,1]$, Dirac measure δ and Heaviside function H. The functional (5.6) represents a classical two-phase segmentation model, which is composed of an $L^2(\Omega)$-fidelity term quantifying the mismatch in both regions as well as a length and an area penalization term of the interface set K. The regions are exactly separated by the discontinuity set K and each region consists of a finite number of connected components. Note that (5.6) is an instance of the binary Mumford–Shah model (5.19) when setting $\lambda_1 = \lambda_2 = \frac{1}{\nu} > 0$, $\lambda_3 = 1$ and $\lambda_4 = 0$. In the level set model (5.7), the segmentation regions are encoded as follows: $x \in \mathrm{inside}(K)$ if $\mathrm{H}(\phi(x)) = 1$ and $x \in \mathrm{outside}(K)$ else. Then, one aims at minimizing (5.7) among all continuous functions $\phi : \Omega \to \mathbb{R}$. If $\lambda_1 = \lambda_2$, the optimal intensity values are characterized as the average of the input image in the associated regions, *i.e.*

$$c_1[\phi] = \frac{\int_\Omega u_0\mathrm{H}(\phi)\,\mathrm{d}x}{\int_\Omega \mathrm{H}(\phi)\,\mathrm{d}x}\,, \qquad c_2[\phi] = \frac{\int_\Omega u_0(1-\mathrm{H}(\phi))\,\mathrm{d}x}{\int_\Omega 1-\mathrm{H}(\phi)\,\mathrm{d}x} \tag{5.8}$$

if the denominators do not vanish. To better handle (5.7) numerically, Chan and Vese regularized H and δ as follows:

$$\mathrm{H}_\varepsilon(x) = \tfrac{1}{2}\left(1 + \tfrac{2}{\pi}\arctan\left(\tfrac{x}{\varepsilon}\right)\right)\,, \qquad \delta_\varepsilon(x) = \mathrm{H}'_\varepsilon(x)$$

for $\varepsilon > 0$. The numerical optimization relies on a finite difference discretization of the regularized energy functional and an alternating update of the intensity values according to (5.8) and of ϕ. The latter update formula is derived from a linearization of the associated Euler–Lagrange equation. In a subsequent publication, Chan and Vese [CV01b] added a second level set function to tackle the problem of a four-phase segmentation, which can be further extended for a segmentation into up to 2^n regions by using n level set functions (see [VC02]). Tsai *et al.* [TYW01] proposed a similar level set approach as Chan and Vese, the main difference is due to the hierarchical method to capture multiple regions. We highlight two drawbacks of various level set based methods: crack-tips can never form since level sets are closed regions and algorithms frequently get stuck in local minima.

Taking into account the level set formulation discussed above, Chan, Esedoḡlu and Nikolova [CEN06] derived a thresholding result which is capable to find global minimizers of the binary Mumford–Shah model. In detail, the starting point is the gradient descent of the regularized version of (5.7) w.r.t. ϕ (with $\lambda_1 = \lambda_2 = \frac{1}{\nu} > 0$, $\lambda_3 = 1$ and $\lambda_4 = 0$), which heuristically yields

$$\partial_t\phi = \mathrm{H}'_\varepsilon(\phi)\left(\mathrm{div}\left(\tfrac{\nabla\phi}{|\nabla\phi|}\right) - \tfrac{1}{\nu}\left((u_0-c_1)^2 - (u_0-c_2)^2\right)\right)\,. \tag{5.9}$$

When omitting the factor $\mathrm{H}'_\varepsilon(\phi)$, one can prove that (5.9) is actually the gradient flow associated with the energy

$$E_{\mathrm{CEN}}[\phi, c_1, c_2] = \int_\Omega |\nabla\phi| + \tfrac{1}{\nu}\left((u_0-c_1)^2 - (u_0-c_2)^2\right)\phi\,\mathrm{d}x\,. \tag{5.10}$$

Let ϕ be a global minimizer of $\mathrm{BV}(\Omega,[0,1]) \ni \tilde{\phi} \mapsto E_{\mathrm{CEN}}[\,\cdot\,,c_1,c_2]$. Then, a fundamental result states that for fixed intensity values $c_1,c_2>0$ and for a.e. $\mu\in[0,1)$ the function $\chi[\phi>\mu]\in\mathrm{BV}(\Omega,\{0,1\})$ is a minimizer of the binary Mumford–Shah model

$$\mathrm{BV}(\Omega,\{0,1\}) \ni \chi \mapsto \int_\Omega \tfrac{(u_0-c_1)^2}{\nu}\chi + \tfrac{(u_0-c_2)^2}{\nu}(1-\chi)\,\mathrm{d}x + |\mathrm{D}\chi|(\Omega)\,.$$

We note that the proofs of this thresholding theorem and the thresholding argument shown in Proposition 5.2.3 both rely on the coarea formula (see Theorem 5.1.10). However, unlike the relaxed functional (5.22) used in Proposition 5.2.3 the functional (5.10) is not uniformly convex in ϕ and the minimization is constrained to the set $\mathrm{BV}(\Omega,[0,1])$, which impedes the derivation of functional a posteriori error estimates for (5.10) using Repin's approach and increases the complexity in the numerical minimization (for further details see next sections).

Bresson *et al*. [BEV$^+$07] proved that a variant of the thresholding result discussed above remains valid after replacing the total variation in the constrained functional (5.10) by the weighted seminorm $\int_\Omega w|\nabla\phi|\,\mathrm{d}x$ for $w\in L^\infty(\Omega,[0,1])$. The resulting functional has the same set of minimizers as the convex unconstrained functional

$$\mathrm{BV}(\Omega)\ni\phi\mapsto\int_\Omega w|\nabla\phi| + \left(\tfrac{(u_0-c_1)^2}{\nu} - \tfrac{(u_0-c_2)^2}{\nu}\right)\phi + \kappa\max\left\{0,2\left|\phi-\tfrac{1}{2}\right|-1\right\}\,\mathrm{d}x \tag{5.11}$$

provided that $\kappa > \frac{1}{2\nu}\|(u_0-c_1)^2-(u_0-c_2)^2\|_{L^\infty(\Omega)}$. By employing a Moreau–Yosida regularization of the first as well as the last two summands separately, global minimizers of (5.11) can be efficiently calculated using an alternating dual descent. Numerical experiments indicate that this model can significantly improve the quality of the segmentation compared to classical level set approaches even if the contrast between meaningful objects is low.

In most of the aforementioned models, the intensity values are assumed to be fixed and known a priori. To overcome this restriction, Brown *et al*. [BCB11] developed a completely convex formulation of the Chan–Vese functional (5.7) (with $\lambda_1=\lambda_2=\lambda>0$, $\lambda_3=1$ and $\lambda_4=0$) incorporating techniques due to [BCB10, GBO12], in which both the segmentation region and the intensity values are unknown. The central idea of this approach is to represent the intensity values c_1 and c_2 as functions $v_i\in\mathrm{BV}(\Omega,\mathbb{R})$ with $\nabla v_i=0$, $i=1,2$. To (numerically) enforce these constraints, an augmented Lagrangian-type penalization algorithm is employed with penalization functions $p_j(v_1,v_2)=r_j\int_\Omega|\nabla v_1|+|\nabla v_2|\,\mathrm{d}x$ for a strictly increasing sequence of positive values r_j with $r_j\to\infty$ as $j\to\infty$. Although the resulting energy functional is non-convex, it can be rewritten as a convex problem by a functional lifting into a higher-dimensional space and – in combination with a thresholding – exact solutions to the original problem can be retrieved in the limit. If the absolute difference of the energy functional evaluated at the corresponding minima for consecutive values of r_j is below a certain threshold value, then a subsequence of this sequence of minimizers converges in $L^1(\Omega)$ to an almost-minimizer of the original functional with optimal intensity values.

The piecewise constant Mumford–Shah model. In what follows, we will list some crucial properties of the piecewise constant Mumford–Shah model as presented in [MS89, MS95, Dav05], which can be seen as the generalization of the binary model that we will focus on throughout this chapter.

The piecewise constant Mumford–Shah model aims at segmenting the image $u_0\in L^\infty(\Omega,[0,1])$ on the bounded image domain $\Omega\subset\mathbb{R}^2$ into a finite number of connected components (called *regions*) by minimizing the functional

$$\widetilde{E}[u,K] = \int_{\Omega\setminus K}\tfrac{1}{\nu}(u-u_0)^2\,\mathrm{d}x + \mathcal{H}^1(K)$$

for $\nu>0$. Here, the regions are determined by the interface set K and u is assumed to be piecewise constant on the connected components of $\Omega\setminus K$. Moreover, for a fixed set K the associated optimal function u coincides with the average of u_0 w.r.t. each region, *i.e.* $u|_{\Omega'} = \fint_{\Omega'}u_0\,\mathrm{d}x$ for each connected component $\Omega'\subset\Omega\setminus K$. Therefore, we simply write $\widetilde{E}[K]$ instead of $\widetilde{E}[u,K]$. Before introducing fundamental properties of the piecewise constant Mumford–Shah model, we give some basic definitions.

Definition 5.1.20. A *segmentation* is a union of a finite number of rectifiable curves. If a segmentation is composed of a finite number of Jordan curves, where two curves only meet at their end points or on $\partial\Omega$, and if each Jordan curve separates two different regions, then this segmentation is 1-*normal*. A segmentation is 2-*normal* if the energy $\widetilde{E}$ strictly increases if two connected components are merged by removing the corresponding curve.

The most important properties of a 1-normal segmentation are phrased in the next theorem:

Theorem 5.1.21. *Every* 1*-normal segmentation* K *can be decomposed into a finite union of Jordan curves meeting only at a finite number of points. If* a *denotes the number of regions,* b *the number of edges and* c *the number of* crossing-points *(*i.e. *those points where at least three Jordan curves have a common end point or where a Jordan curve meets* $\partial\Omega$*), then* $c \leq 2(a-1)$ *and* $b \leq 3(a-1)-2$*.*

Proof. See [MS95, Section 5.2]. □

However, the proper set for the minimization of $\widetilde{E}$ is actually the set of 2-normal segmentations, which has the following additional regularity properties:

Theorem 5.1.22. *A minimizer of the variational problem*

$$\inf\left\{ \widetilde{E}[\tilde{K}] \,:\, \tilde{K} \text{ is a 2-normal segmentation} \right\}$$

is attained and the Jordan curves composing this minimizer are C^2 *with curvature bounded by* $8\frac{\operatorname{osc}(u_0)}{\nu}$*. Moreover, either the Jordan curves meet at triple points under an angle of* $120°$ *or on the boundary* $\partial\Omega$ *under an angle of* $90°$ *provided that the boundary is sufficiently smooth.*

Proof. See [MS95, Section 5.3]. □

For further characteristics of the piecewise constant Mumford–Shah model, we refer to the literature at the beginning of this paragraph and the references therein.

Further variational image segmentation models and extensions. Besides the Mumford–Shah segmentation functional, there are plenty of other segmentation models available in computer graphics, *e.g.* histogram-based thresholding, clustering techniques like K-means clustering, Markov random field based segmentation methods, graph cut based algorithms or watershed segmentation. In what follows, we will briefly comment on some recent variational segmentation models that are closely related to the methods presented above.

Given non-negative potentials $g = (g_1, \dots, g_k) \in (L^2(\Omega))^k$, a common multilabel segmentation problem (also known as the continuous Potts model) reads as

$$\inf\left\{ \sum_{i=1}^{k} \left(\tfrac{1}{2}|\mathrm{D}\chi[E_i]|(\Omega) + \int_{E_i} g_i \,\mathrm{d}x \right) \,:\, \bigcup_{i=1}^{k} E_i = \Omega, E_i \cap E_j = \emptyset \text{ for } i \neq j \right\}, \tag{5.12}$$

which aims at finding a minimal partition of a domain $\Omega \subset \mathbb{R}^n$ separated into Caccioppoli sets E_i such that the sum of the perimeters of E_i and the integral of the related potentials w.r.t. E_i is minimal. The coefficient $\frac{1}{2}$ takes into account that each interface is counted twice in the sum. Note that (5.12) is a specific instance of the piecewise constant Mumford–Shah model when setting $g_i = \frac{1}{\nu}(u_0 - c_i)^2$ for fixed intensity values c_i. An application of standard $\mathrm{BV}(\Omega)$-compactness arguments shows that (5.12) actually attains a minimum, but the numerical computation of this minimizer poses a challenging task. To overcome this problem, Chambolle *et al.* [CCP12] proposed the following reformulation of (5.12):

$$\inf\left\{ \mathcal{J}[v] + \int_\Omega v \cdot g \,\mathrm{d}x \,:\, v = (v_1, \dots, v_k) \in L^2(\Omega, \mathbb{R}^k) \right\} \text{ with } \mathcal{J}[v] = \begin{cases} \frac{1}{2}\sum_{i=1}^{k} |\mathrm{D}v_i|(\Omega)\,, & \text{if } v \in \mathcal{B}\,, \\ +\infty\,, & \text{else}\,, \end{cases} \tag{5.13}$$

where $\mathcal{B} = \{v \in \mathrm{BV}(\Omega, \{0,1\}^k) \,:\, \sum_{i=1}^{k} v_i = 1 \text{ a.e. in } \Omega\}$. Since $\mathcal{B}$ and thus (5.13) are non-convex, one could replace $\mathcal{J}$ by the convex and lower semicontinuous envelope $\mathcal{J}^{**}$ in (5.13) and minimize the resulting convex functional instead. However, since in general no explicit formula for $\mathcal{J}^{**}$ can be derived, one can replace $\mathcal{J}^{**}[v]$ by $\overline{\mathcal{J}}[v] = \int_\Omega \tilde{J}(x, \mathrm{D}v)\,\mathrm{d}x$ such that $\tilde{J}$ is non-negative, continuous and convex in the second argument, and $\overline{\mathcal{J}}$ satisfies $\overline{\mathcal{J}}[v] \leq \mathcal{J}[v]$ for $v \in L^2(\Omega, \mathbb{R}^k)$ as well as $\overline{\mathcal{J}}[v] = \mathcal{J}[v]$ for $v \in \mathcal{B}$. Hence, the convex relaxed minimal partition problem has the form

$$\inf\left\{ \overline{\mathcal{J}}[v] + \int_\Omega v \cdot g \,\mathrm{d}x \,:\, v \in \overline{\mathcal{B}} \right\} \tag{5.14}$$

for the constraint set $\overline{\mathcal{B}} = \{v \in \mathrm{BV}(\Omega, [0,1]^k) \,:\, \sum_{i=1}^k v_i = 1 \text{ a.e. in } \Omega\}$ representing a simplex. In many applications of interest, the minimizers of this variational problem are (nearly) optimal in the sense that the energies of (5.12) and (5.14) (roughly) coincide. Furthermore, minimizers of (5.14) can be computed using efficient primal-dual algorithms. In [ZGFN08], Zach *et al.* examined the variant of (5.13) in which $\mathcal{B}$ is replaced by $\overline{\mathcal{B}}$, and employed a dual descent for the numerical optimization. A primal-dual characterization of the multilabel problem is due to Bae *et al.* [BYT11], where

$$\inf \left\{ \sum_{i=1}^k \left(\tfrac{1}{2}|\mathrm{D}v_i|(\Omega) + \int_\Omega g_i v_i \,\mathrm{d}x \right) \,:\, v \in \overline{\mathcal{B}} \right\}, \tag{5.15}$$

$$\sup \left\{ \int_\Omega \min_{i=1,\dots,k} \left(g_i + \tfrac{1}{2}\mathrm{div} q_i \right) \mathrm{d}x \,:\, q_i \in H_0^1(\Omega, \mathbb{R}^n), \|q_i\|_{L^\infty(\Omega)} \leq \tfrac{1}{2} \text{ for } i = 1, \dots, k \right\} \tag{5.16}$$

are the primal and dual problems, respectively. A crucial theorem then asserts that if for a.e. $x \in \Omega$ an index $i \in \{1, \dots, k\}$ exists such that $g_i(x) + \mathrm{div} p_i^*(x) < g_j(x) + \mathrm{div} p_j^*(x)$ for all $j \neq i$ with (u^*, p^*) being an optimal primal-dual pair associated with (5.15) and (5.16), then u^* is binary and thus a global minimum of (5.12). A similar convex multilabel model was developed by Lellmann *et al.* [LKY+09].

Let us denote by ∇^{FD} the discrete forward finite difference gradient and by $u_0^{(x,y)}$ the locally averaged input image with $(x, y) \in \Omega_N = \{\frac{0}{N}, \dots, \frac{N}{N}\}^2$ for $N \geq 1$. Strekalovskiy and Cremers [SC14] analyzed the convex functional

$$\sum_{(x,y)\in\Omega_N} (u^{(x,y)} - u_0^{(x,y)})^2 + \min \left\{ \nu |\nabla^{FD} u^{(x,y)}|^2, \lambda \right\} \tag{5.17}$$

with a threshold parameter $\lambda > 0$ to compute a piecewise smooth segmentation. In particular, this model is capable of computing real-time video cartooning in combination with a GPU acceleration. Chambolle [Cha95] proved that a slightly altered version of (5.17) Γ-converges to a Mumford–Shah type functional, in which the Hausdorff measure of K is replaced by a l^1-penalization of the discontinuity set.

There is a great variety of further approaches to approximate the total variation numerically. Bartels [Bar16] used the embedding $\mathrm{BV}(\Omega) \cap L^\infty(\Omega)$ into a certain Besov space that nearly coincides with $H^{\frac{1}{2}}(\Omega)$ to improve the step-size restriction for $\mathrm{BV}(\Omega)$-functionals. Following Dobson and Vogel [DV97], the total variation regularization can be smoothly approximated via $\sqrt{|\nabla u|^2 + \varepsilon}$. In [FP03], the convergence of the L^2-gradient flow of this smooth approximation to the total variation flow in L^2 is shown under strong regularity assumptions w.r.t. the solution.

One frequent issue occurring in variational problems involving total variation regularization results from the formation of staircasing. Bredies *et al.* [BKP10] proposed to replace the standard total variation by the *total generalized variation* $\mathrm{TGV}(\Omega)$ defined as

$$\mathrm{TGV}_\xi^k(\Omega)[u] = \sup \left\{ \int_\Omega u \mathrm{div}^k v \,\mathrm{d}x \,:\, v \in C_c^k(\Omega, \mathrm{Sym}^k(\mathbb{R}^n)), \|\mathrm{div}^l v\|_{L^\infty}(\Omega) \leq \xi_l \text{ for } l \in \{0, \dots, k-1\} \right\} \tag{5.18}$$

with $k \geq 1$, $\xi = (\xi_0, \dots, \xi_{k-1}) \in (\mathbb{R}^+)^k$ and $\mathrm{Sym}^k(\mathbb{R}^n)$ denoting the space of symmetric tensors of order k with values in $\mathbb{R}^n$. Note that (5.18) coincides with the usual $\mathrm{BV}(\Omega)$-seminorm provided that $k = 1$ and $\xi_0 = 1$. For suitable choices of k and ξ, one can observe that replacing the total variation by the total generalized variation in various variational problems results in minimizers with sharp discontinuities while at the same time suppressing staircasing effects.

5.2 Binary Mumford–Shah Model and Uniformly Convex Relaxation

In this section, we will examine the *binary Mumford–Shah functional*, which emerges from the general model (5.1) by restricting to the non-convex function space

$$\{\, u = c_1\chi + c_2(1-\chi) \,:\, c_1, c_2 \in [0,1], c_1 \neq c_2, \chi \in \mathrm{BV}(\Omega, \{0,1\}) \,\},$$

where $\Omega \subset \mathbb{R}^n$ is a bounded Lipschitz domain. The associated energy $E : \mathrm{BV}(\Omega, \{0,1\}) \to \mathbb{R}$ can be rewritten as follows:

$$E[\chi] = \int_\Omega \theta_1 \chi + \theta_2(1-\chi) \,\mathrm{d}x + |\mathrm{D}\chi|(\Omega) \tag{5.19}$$

with $\theta_i = \frac{1}{\nu}(c_i - u_0)^2$ for $i = 1, 2$ and a weight parameter $\nu > 0$. With one exception, we assume the intensity values c_1 and c_2 to be fixed. By optimizing E w.r.t. c_1 and c_2 one immediately obtains the optimal intensity values

$$c_1[\chi] = \left(\int_\Omega \chi \, \mathrm{d}x \right)^{-1} \int_\Omega \chi u_0 \, \mathrm{d}x \,, \qquad c_2[\chi] = \left(\int_\Omega 1 - \chi \, \mathrm{d}x \right)^{-1} \int_\Omega (1 - \chi) u_0 \, \mathrm{d}x \tag{5.20}$$

provided that the denominators do not vanish.

Remark 5.2.1. We can assume $\theta_1, \theta_2 \geq c > 0$ without restriction since (5.19) can be restated as

$$E[\chi] = \int_\Omega (\theta_1 - \theta_2)\chi \, \mathrm{d}x + |\mathrm{D}\chi|(\Omega) + \int_\Omega \theta_2 \, \mathrm{d}x \,, \tag{5.21}$$

which means that a constant can be added to θ_1 and θ_2 without affecting the set of minimizers of E.

We remark that E is commonly minimized w.r.t. the set $\mathrm{BV}(\Omega) \times [0, 1]^2$ of characteristic functions and intensity values such that the minimizer (χ^*, c_1^*, c_2^*) satisfies $c_i^* = c_i[\chi^*]$ for $i = 1, 2$. In Section 5.4, we will analyze a bootstrap scheme that yields an a posteriori error theory for this full model with varying intensity values by iteratively applying the a posteriori error estimator for fixed intensity values and an update of the intensity values according to 5.20. However, as we will point out, this scheme fails in the numerical applications.

Uniformly convex relaxation of the binary Mumford–Shah model. In this paragraph, we will introduce a uniformly convex relaxation of (5.19) and prove a thresholding theorem that can be employed to exactly retrieve minimizers of the binary model from minimizers of the relaxed functional.

As outlined above, following [Ber09, Ber10] we consider the following convex relaxed functional of (5.19):

$$E^{\mathrm{rel}}[u] = \int_\Omega u^2\theta_1 + (1 - u)^2\theta_2 \, \mathrm{d}x + |\mathrm{D}u|(\Omega) \,, \tag{5.22}$$

which is minimized over all $u \in \mathrm{BV}(\Omega, \mathbb{R})$. Due to the quadratic growth in u every minimizer exhibits a tendency towards 0 and 1. Note that we can assume $\theta_1, \theta_2 \geq c > 0$ without restriction in view of Remark 5.2.1, which implies the *uniform convexity* of (5.22). Furthermore, E^{rel} coincides with E on the set $\mathrm{BV}(\Omega, \{0, 1\})$. We stress that a significant advantage of this model compared to the functional (5.10) is that (5.22) has not to be constrained to functions with range $[0, 1]$, which poses a major drawback in the numerical optimization of the model due to Chan, Esedoḡlu and Nikolova (see Subsection 5.1.4).

For the sake of completeness, we briefly present the existence proof of a minimizer of E^{rel} (for a more detailed exposition we refer to [AFP00]), which relies on the direct method in the calculus of variations:

Theorem 5.2.2 (Existence of a minimizer of E^{rel})**.** *Under the assumptions above, E^{rel} has a unique minimizer u such that $u \in [0, 1]$.*

Proof. Let $\{u_k\}_{k\in\mathbb{N}} \subset \mathrm{BV}(\Omega)$ be a minimizing sequence for E^{rel}, *i.e.* $E^{\mathrm{rel}}[u_k] \to \inf_{\tilde{u}\in\mathrm{BV}(\Omega)} E^{\mathrm{rel}}[\tilde{u}]$ as $k \to \infty$ and $E^{\mathrm{rel}}[u_k] \leq \overline{E^{\mathrm{rel}}} < \infty$ for a fixed constant $\overline{E^{\mathrm{rel}}}$. Since

$$E^{\mathrm{rel}}[\min\{\max\{0, v\}, 1\}] \leq E^{\mathrm{rel}}[v]$$

for all $v \in \mathrm{BV}(\Omega)$, we can assume that $\{u_k\}_{k\in\mathbb{N}}$ is uniformly bounded in $L^\infty(\Omega, [0, 1])$. Moreover, by taking into account the estimate $\sup_{k\in\mathbb{N}} |\mathrm{D}u_k|(\Omega) \leq \overline{E^{\mathrm{rel}}}$ Theorem 5.1.4 (vi.) implies the existence of a subsequence (not relabeled) that converges weakly-$*$ in $\mathrm{BV}(\Omega)$ to $u \in \mathrm{BV}(\Omega, [0, 1])$. Now, the existence of minimizers can be inferred from the lower semicontinuity of the functional along the sequence. In detail, the total variation is lower semicontinuous due to Theorem 5.1.4 (iv.), the analogous property for the data term can be shown by using the $L^1(\Omega)$-convergence as well as the $L^\infty(\Omega)$-boundedness along the sequence. Finally, the uniqueness of the minimizer is implied by the strict convexity of E^{rel}. □

Next, we present the thresholding theorem for E^{rel}, which allows to exactly retrieve a minimizer of the binary Mumford–Shah functional and on which both the numerical optimization as well as the a posteriori error theory rely. We highlight the analogy of Proposition 5.2.3 with the thresholding assertion for the model by Chan, Esedoḡlu and Nikolova.

Proposition 5.2.3 (Convex relaxation and thresholding (*cf*. [Ber09, Ber10]))**.** *Under the assumptions above, the minimizer* $u \in \mathrm{BV}(\Omega)$ *of* E^{rel} *satisfies*

$$\chi[u > 0.5] \in \operatorname*{argmin}_{\tilde{\chi} \in \mathrm{BV}(\Omega,\{0,1\})} E[\tilde{\chi}]\,. \tag{5.23}$$

Remark 5.2.4. Proposition 5.2.3 is a version of a more general result (*cf*. [Cha05, CD09, Jal14]): Let $\Psi : \Omega \times \mathbb{R} \to \mathbb{R}$ be measurable, $\Psi(\,\cdot\,, t) \in L^1(\Omega)$ for a.e. $t \in \mathbb{R}$, $\Psi(x, \,\cdot\,) \in C^1(\mathbb{R})$ be strictly convex for a.e. $x \in \Omega$, $\Psi(x,t) \geq c|t| - C$ and

$$E_\Psi[u] = \int_\Omega \Psi(x,u)\,\mathrm{d}x + |\mathrm{D}u|(\Omega)\,.$$

Then, there exists a minimizer $u \in \operatorname{argmin}_{\tilde{u}\in\mathrm{BV}(\Omega)} E_\Psi[\tilde{u}]$ and for all $s \in \mathbb{R}$

$$\chi^s := \chi[u > s] \in \operatorname*{argmin}_{\chi\in\mathrm{BV}(\Omega,\{0,1\})} \int_\Omega \partial_t\Psi(x,s)\chi\,\mathrm{d}x + |\mathrm{D}\chi|(\Omega)\,.$$

By setting

$$\Psi(x,t) = t^2\theta_1(x) + (1-t)^2\theta_2(x) \tag{5.24}$$

and $s = \frac{1}{2}$, the assertion (5.23) follows due to $\partial_t\Psi(x, \frac{1}{2}) = \theta_1(x) - \theta_2(x)$ and (5.21).

Proof. For the sake of completeness, we sketch the proof for the relaxed model (5.22) with Ψ given by (5.24), the general case readily follows. Due to Fubini's Theorem one obtains

$$\int_\Omega \Psi(x,u)\,\mathrm{d}x = C_\Psi + \int_0^1 \int_\Omega \partial_t\Psi(x,t)\chi[u > t]\,\mathrm{d}x\,\mathrm{d}t \tag{5.25}$$

for $C_\Psi = \int_\Omega \Psi(x,0)\,\mathrm{d}x$ and all $u \in \mathrm{BV}(\Omega,[0,1])$. For $s \in \mathbb{R}$ we consider

$$\chi^s \in \operatorname*{argmin}_{\chi\in\mathrm{BV}(\Omega,\{0,1\})} \left\{ E_s^{\mathrm{rel}}[\chi] = \int_\Omega \partial_t\Psi(x,s)\chi\,\mathrm{d}x + |\mathrm{D}\chi|(\Omega) \right\}.$$

Using the coarea formula (see Theorem 5.1.10), (5.25) and the definition of χ^s one can conclude

$$E^{\mathrm{rel}}[u] = \int_\Omega \Psi(x,u)\,\mathrm{d}x + |\mathrm{D}u|(\Omega) \geq C_\Psi + \int_0^1 E_s^{\mathrm{rel}}[\chi^s]\,\mathrm{d}s\,.$$

The following monotonicity result is due to [ACC05]:
Claim: Let $h_1, h_2 \in L^1(\Omega)$ be such that $h_1 < h_2$ a.e. in Ω and assume that

$$\chi_i \in \operatorname*{argmin}_{\chi\in\mathrm{BV}(\Omega,\{0,1\})} \int_\Omega h_i\chi\,\mathrm{d}x + |\mathrm{D}\chi|(\Omega)$$

for $i \in \{1,2\}$. Then $\chi_1 \geq \chi_2$ a.e. in Ω.

Set $\Sigma_i = [\chi_i = 1]$. The optimality of χ_i implies

$$\begin{aligned}
\int_\Omega h_1\chi[\Sigma_1]\,\mathrm{d}x + |\mathrm{D}\chi[\Sigma_1]|(\Omega) &\leq \int_\Omega h_1\chi[\Sigma_1\cup\Sigma_2]\,\mathrm{d}x + |\mathrm{D}\chi[\Sigma_1\cup\Sigma_2]|(\Omega)\,,\\
\int_\Omega h_2\chi[\Sigma_2]\,\mathrm{d}x + |\mathrm{D}\chi[\Sigma_2]|(\Omega) &\leq \int_\Omega h_2\chi[\Sigma_1\cap\Sigma_2]\,\mathrm{d}x + |\mathrm{D}\chi[\Sigma_1\cap\Sigma_2]|(\Omega)\,.
\end{aligned}$$

Since $|\mathrm{D}\chi[\Sigma_1\cup\Sigma_2]| + |\mathrm{D}\chi[\Sigma_1\cap\Sigma_2]| \leq |\mathrm{D}\chi[\Sigma_1]| + |\mathrm{D}\chi[\Sigma_2]|$ (*cf*. [AFP00, Proposition 3.38]), by adding both inequalities above we obtain

$$\int_\Omega h_1(\chi[\Sigma_1\cup\Sigma_2] - \chi[\Sigma_1])\,\mathrm{d}x \geq \int_\Omega h_2(\chi[\Sigma_2] - \chi[\Sigma_1\cap\Sigma_2])\,\mathrm{d}x\,,$$

which implies $\int_\Omega (h_1 - h_2)\chi[\Sigma_2 \backslash \Sigma_1]\,\mathrm{d}x \geq 0$. Now, taking into account $h_1 < h_2$ we deduce $|\Sigma_2 \backslash \Sigma_1| = 0$, which proves the claim.

Since both θ_1 and θ_2 are strictly positive (see Remark 5.2.1), we obtain that $s \mapsto \partial_t \Psi(x,s)$ is strictly increasing in s for a.e. $x \in \Omega$. Let $h_i = \partial_t \Psi(x, s_i)$ for $s_1 < s_2$. Now, the claim above implies that $\chi^{s_1} \geq \chi^{s_2}$ a.e. in Ω. Furthermore, the function $u^*(x) = \sup\{s \in \mathbb{R} \,:\, \chi^s(x) = 1\}$ is well-defined, Lebesgue measurable and $\chi[u^* > s] = \chi^s$. Then, using the coarea formula we get $u^* \in \mathrm{BV}(\Omega)$ and $C_\Psi + \int_0^1 E_s^{\mathrm{rel}}[\chi[u^* > s]]\,\mathrm{d}s = E^{\mathrm{rel}}[u^*]$. Thus,

$$E^{\mathrm{rel}}[u] \geq C_\Psi + \int_0^1 E_s^{\mathrm{rel}}[\chi[u^* > s]]\,\mathrm{d}s = E^{\mathrm{rel}}[u^*] \geq E^{\mathrm{rel}}[u]\,,$$

which shows that all inequalities are actually equalities and the characteristic function $\chi[u > s]$ is a minimizer of E_s^{rel} for a.e. $s \in [0,1]$. It remains to prove that this property holds true for the particular value $s = \frac{1}{2}$. To this end, we consider a monotonously decreasing sequence $\{s_n\}_{n\in\mathbb{N}} \subset [\frac{1}{2}, 1]$ such that $\chi[u > s_n]$ is a minimizer of $E_{s_n}^{\mathrm{rel}}$ and $s_n \to \frac{1}{2}$. For any $\tilde{\chi} \in \mathrm{BV}(\Omega, \{0,1\})$ we can infer taking into account the dominated convergence theorem, the weak-$*$ convergence of $\chi[u > s_n]$ to $\chi[u > \frac{1}{2}]$ in $\mathrm{BV}(\Omega)$ and the lower semicontinuity of the total variation along this sequence (*cf*. Theorem 5.1.4 (iv.))

$$E_{\frac{1}{2}}^{\mathrm{rel}}[\tilde{\chi}] = \liminf_{n\to\infty} E_{s_n}^{\mathrm{rel}}[\tilde{\chi}] \geq \liminf_{n\to\infty} E_{s_n}^{\mathrm{rel}}[\chi[u > s_n]] \geq E_{\frac{1}{2}}^{\mathrm{rel}}[\chi[u > \tfrac{1}{2}]]\,.$$

We omit further details. This finishes the sketch of the proof. □

A priori error estimate for a relaxed binary Mumford–Shah functional. We conclude this section with an a priori error estimate for a minimizer of an ROF-type model (see [ROF92]), from which a minimizer of the binary Mumford–Shah model can be exactly recovered via a suitable thresholding. In detail, we set $\Psi(x,s) = \frac{1}{2}(s - (\theta_2(x) - \theta_1(x)))^2$. Following Remark 5.2.4, the superlevel set for the threshold value $s = 0$ of the minimizer of the ROF model

$$\widetilde{E}_{\mathrm{ROF}}[v] = \int_\Omega \tfrac{1}{2}(v - (\theta_2 - \theta_1))^2\,\mathrm{d}x + |\mathrm{D}v|(\Omega) \tag{5.26}$$

for $v \in \mathrm{BV}(\Omega)$ is a minimizer of $\int_\Omega (\theta_1 - \theta_2)\chi\,\mathrm{d}x + |\mathrm{D}\chi|(\Omega)$ and therefore of E taking into account (5.21) (*cf*. [Ber09]). In what follows, we will derive $L^2(\Omega)$-a priori error bounds for a finite difference minimizer of $\widetilde{E}_{\mathrm{ROF}}$ for $n = 2$ by using techniques developed in [WL11]. To this end, let us first define generalized Lipschitz spaces:

Definition 5.2.5. For any $p \geq 1$, the *$L^p(\Omega)$-modulus of smoothness for $f \in L^p(\Omega)$* is defined as

$$\omega(f,t)_{L^p(\Omega)} = \sup_{s\in\mathbb{R}^2, |s|<t} \left(\int_{[x,x+s]\subset\Omega} |f(x+s) - f(x)|^p\,\mathrm{d}x \right)^{\frac{1}{p}}.$$

Here, $[x, x+s] = \{\lambda x + (1-\lambda)(x+s) \,:\, \lambda \in [0,1]\}$. Then, for $\alpha > 0$ the *Lipschitz space* $\mathrm{Lip}(\alpha, L^p(\Omega))$ is characterized by $\mathrm{Lip}(\alpha, L^p(\Omega)) = \{f \in L^p(\Omega) \,:\, |f|_{\mathrm{Lip}(\alpha,L^p(\Omega))} < \infty\}$ with seminorm and norm given by

$$|f|_{\mathrm{Lip}(\alpha,L^p(\Omega))} = \sup_{t>0} t^{-\alpha}\omega(f,t)_{L^p(\Omega)}\,, \qquad \|f\|_{\mathrm{Lip}(\alpha,L^p(\Omega))} = \|f\|_{L^p(\Omega)} + |f|_{\mathrm{Lip}(\alpha,L^p(\Omega))}\,, \tag{5.27}$$

respectively.

For the verification that (5.27) actually defines a (semi-)norm as well as for further details we refer to [WL11]. Next, we restrict our presentation to the computational domain $\Omega = [0,1]^2$ and define $\Omega_h = \{(i,j) \in \mathbb{Z}^2 \,:\, 0 \leq i,j < N\}$ as the corresponding discrete domain with mesh size $h = N^{-1}$ for $N \in \mathbb{N}$. Furthermore, we cover the computational domain by the sets $\Omega_{h,\xi} = \{x \in \Omega \,:\, h\xi^i \leq x^i < h(\xi^i + 1) \text{ for } i = 1,2\}$ for $\xi \in \{0, \dots N-1\}^2$. The *piecewise constant injector* I_h assigns to a discrete function $v_h : \Omega_h \to \mathbb{R}$ the function $I_h[v_h] \in L^1(\Omega)$ defined as $I_h[v_h](x) = v_h(\xi)$ if $x \in \Omega_{h,\xi}$. Vice versa, the *piecewise constant projector* P_h projects any $v \in L^1(\Omega)$ onto the space of discrete functions via $P_h[v](\xi) = \fint_{\Omega_{h,\xi}} v\,\mathrm{d}x$ for $\xi \in \{0, \dots N-1\}^2$. We define $\mathrm{TV}_h[v_h] = \frac{1}{4}\sum_{\boxminus,\boxplus\in\{-,+\}} \mathrm{TV}_h^{(\boxminus,\boxplus)}[v_h]$ as the *(isotropic) discrete total variation*, where $\mathrm{TV}_h^{(\boxminus,\boxplus)}[v_h]$ for $\boxminus, \boxplus \in \{-,+\}$ and a discrete function v_h is given by

$$h \sum_{(i,j)\in\Omega_h} \sqrt{\Big(\mathrm{Ext}_h[v_h]((i,j) \boxminus (1,0)) - \mathrm{Ext}_h[v_h](i,j)\Big)^2 + \Big(\mathrm{Ext}_h[v_h]((i,j) \boxplus (0,1)) - \mathrm{Ext}_h[v_h](i,j)\Big)^2}\,.$$

Here, $\mathrm{Ext}_h : \{\Omega_h \to \mathbb{R}\} \to \{\mathbb{Z}^2 \to \mathbb{R}\}$ denotes the *extension operator* that reflects a discrete function on each boundary side. For instance, $\mathrm{Ext}_h[v_h](i,j) = v_h(2N-i-1,j)$ if $N \le i < 2N$, $0 \le j < N$. Finally, the discrete analogon of $\widetilde{E}_{\mathrm{ROF}}$ is given by

$$\widetilde{E}_{\mathrm{ROF},h}[v_h] = \tfrac{1}{2}\|I_h[v_h - P_h[\theta_2 - \theta_1]]\|^2_{L^2(\Omega)} + \mathrm{TV}_h[v_h]$$

for any discrete function v_h. With these preparations at hand, we can now state the central a priori theorem for (5.26):

Theorem 5.2.6 (A priori error estimate for a relaxed binary Mumford–Shah model)**.** *Let $\Omega = [0,1]^2$, $\alpha > 0$, $h = N^{-1}$ for $N \in \mathbb{N}$ and assume that the input image satisfies $u_0 \in \mathrm{Lip}(\alpha, L^2(\Omega)) \cap L^\infty(\Omega,[0,1])$. For minimizers $\bar{u}$ and $\bar{u}_h$ of $\widetilde{E}_{\mathrm{ROF}}$ and $\widetilde{E}_{\mathrm{ROF},h}$, respectively, the a priori bound*

$$\|I_h[\bar{u}_h] - \bar{u}\|^2_{L^2(\Omega)} \le C\frac{(c_2-c_1)^2}{\nu^2}\left(C + |u_0|_{\mathrm{Lip}(\alpha,L^2(\Omega))}\right)^2 h^{\frac{\alpha}{1+\alpha}}$$

with a constant $C > 0$ holds true. In particular, $I_h[\bar{u}_h] \to \bar{u}$ in $L^2(\Omega)$ for $h \searrow 0$.

Proof. The following assertion is proven in [WL11, Theorem 4.2]: for $g \in \mathrm{Lip}(\alpha, L^2(\Omega))$ the minimizers $\bar{v} \in \mathrm{BV}(\Omega)$ and $\bar{v}_h : \Omega_h \to \mathbb{R}$ of

$$v \mapsto \tfrac{1}{2}\|v-g\|^2_{L^2(\Omega)} + |\mathrm{D}v|(\Omega)\,, \qquad v_h \mapsto \tfrac{1}{2}\|I_h[v_h - P_h[g]]\|^2_{L^2(\Omega)} + \mathrm{TV}_h[v_h]\,,$$

respectively, are related by

$$\|I_h[\bar{v}_h] - \bar{v}\|^2_{L^2(\Omega)} \le C\|g\|^2_{\mathrm{Lip}(\alpha,L^2(\Omega))} h^{\frac{\alpha}{1+\alpha}}\,.$$

Next, we will prove

$$\|\theta_2 - \theta_1\|_{\mathrm{Lip}(\alpha,L^2(\Omega))} \le \tfrac{|c_2-c_1|}{\nu}\left(4 + 2|u_0|_{\mathrm{Lip}(\alpha,L^2(\Omega))}\right)\,, \tag{5.28}$$

which readily implies the theorem by setting $g = \theta_2 - \theta_1$. Since $|\Omega| = 1$, $0 \le c_1, c_2 \le 1$ and $u_0 \in L^\infty(\Omega,[0,1])$ one can infer

$$\|\theta_2 - \theta_1\|_{L^2(\Omega)} \le \tfrac{1}{\nu}\big(2\,|c_2-c_1|\,\|u_0\|_{L^2(\Omega)} + |c_1+c_2|\,|c_2-c_1|\big) \le \tfrac{4}{\nu}|c_2-c_1|\,.$$

Furthermore, a straightforward computation shows

$$\omega(\theta_2-\theta_1,t)_{L^2(\Omega)} = \sup_{s\in\mathbb{R}^2,|s|<t}\left(\int_{[x,x+s]\subset\Omega}\left|\tfrac{2}{\nu}(c_2-c_1)(u_0(x+s)-u_0(x))\right|^2\,\mathrm{d}x\right)^{\frac{1}{2}}\,,$$

which implies $|\theta_2-\theta_1|_{\mathrm{Lip}(\alpha,L^2(\Omega))} \le \frac{2}{\nu}|c_2-c_1|\,|u_0|_{\mathrm{Lip}(\alpha,L^2(\Omega))}$ and (5.28). □

Remark 5.2.7. In principle, one could have developed the a posteriori theory for the binary Mumford–Shah functional starting from the functional $\widetilde{E}_{\mathrm{ROF}}$ instead of E^{rel}, since the functional (5.26) complies with the same vital prerequisites required for the a posteriori theory for (5.19) as the functional (5.22), *e.g.* the thresholding theorem or the duality-based functional a posteriori error estimator (see below). However, unlike the minimizer of the relaxed Mumford–Shah model (5.22), the $L^\infty(\Omega)$-bound for the minimizer $\bar{u}$ of $\widetilde{E}_{\mathrm{ROF}}$ depends on the $L^\infty(\Omega)$-bound of the input image, the intensity values and ν, and thus requires a more involved cutoff argument to deduce the counterpart of Theorem 5.4.1 for $\widetilde{E}_{\mathrm{ROF}}$. Explicitly, this upper bound reads as

$$\|\bar{u}\|_{L^\infty(\Omega)} \le \tfrac{2}{\nu}(1 + \|u_0\|_{L^\infty(\Omega)})|c_2-c_1|$$

and is implied by a straightforward truncation argument.

5.3 Functional A Posteriori Error Estimates

In this section, we will derive a functional a posteriori estimate for the relaxed functional (5.22). To this end, we employ a primal-dual error estimate originally proposed by Repin [Rep00, Rep12] and exploit the uniform convexity of the relaxed binary Mumford–Shah functional. However, unlike many other approaches (see [Han05] for an overview) the starting point is the *predual functional* D^{rel} of E^{rel} defined as $(D^{\mathrm{rel}})^* = E^{\mathrm{rel}}$.

There are several drawbacks when choosing E^{rel} as the primal functional. Since, to the best of our knowledge, no full characterization of the space $\mathrm{BV}'(\Omega)$ as the dual space of $\mathrm{BV}(\Omega)$ exists (see [DP98, Tor16] for partial results), a derivation of an a posteriori error estimator for E^{rel} would be challenging. In particular, the functional error estimators incorporating Repin's approach exclusively work for reflexive Banach spaces, and the computation of the proximal mappings in $\mathrm{BV}'(\Omega)$ in a closed form required for the duality-based algorithms does not appear to be feasible. Moreover, the right choice of the discrete function space to properly model $\mathrm{BV}'(\Omega)$ is numerically demanding.

The predual formulation of variational problems in $\mathrm{BV}(\Omega)$ already examined in the context of a generalized ROF model by Hintermüller and Kunisch [HK04] overcomes all these problems. Bartels [Bar15] picked up this predual formulation and inferred an explicitly computable a posteriori error estimate for the standard ROF model using Repin's abstract framework. We will roughly follow Bartels' ansatz to derive a functional error estimator associated with (5.22).

The predual formulation of the relaxed binary Mumford–Shah model. As pointed out above, the starting point for the derivation of the functional a posteriori error estimate for the relaxed binary Mumford–Shah functional is the following predual functional

$$D^{\mathrm{rel}}[q] = F[q] + G[\Lambda q] \tag{5.29}$$

for all $q \in \mathcal{Q}$. Here, $F : \mathcal{Q} \to \overline{\mathbb{R}}$ and $G : \mathcal{V} \to \overline{\mathbb{R}}$ are the predual functionals corresponding to the total variation and the data term, respectively, which are supposed to be proper, convex and lower semicontinuous. In addition, $\mathcal{V}$ and $\mathcal{Q}$ are assumed to be reflexive Banach spaces and $\Lambda \in \mathcal{L}(\mathcal{Q}, \mathcal{V})$. Throughout this chapter, we set $\mathcal{Q} = H_N(\mathrm{div}, \Omega)$ (see Section 1.1 for the definition), $\mathcal{V} = L^2(\Omega) \cong (L^2(\Omega))'$ and $\Lambda = \mathrm{div}$, where $\Lambda^* = -\nabla$ holds in the sense

$$(\Lambda^* v, q)_{L^2(\Omega)} = (v, \mathrm{div} q)_{L^2(\Omega)} \tag{5.30}$$

for all $v \in \mathcal{V}$ and all $q \in \mathcal{Q}$. Then, we define F and G as follows (recall that the intensity values c_1 and c_2 are fixed):

$$F[q] = \mathbb{I}[\overline{B_1}(0)][q] = \begin{cases} 0\,, & \text{if } |q| \leq 1 \text{ a.e. }, \\ +\infty\,, & \text{else}\,, \end{cases} \qquad G[v] = \int_\Omega \frac{\frac{1}{4}v^2 + v\theta_2 - \theta_1\theta_2}{\theta_1 + \theta_2}\,\mathrm{d}x\,.$$

Proposition 5.3.1. *Under the assumptions above, the relation* $(D^{rel})^* = E^{rel}$ *is valid,* i.e.

$$(D^{rel})^*[v] = G^*[v] + F^*[-\Lambda^* v] = \int_\Omega v^2\theta_1 + (1-v)^2\theta_2\,\mathrm{d}x + |\mathrm{D}v|(\Omega) = E^{rel}[v]\,. \tag{5.31}$$

Proof. Theorem 5.1.13 implies that $(D^{\mathrm{rel}})^*$ admits the decomposition $(D^{\mathrm{rel}})^*[v] = G^*[v] + F^*[-\Lambda^* v]$ and the Fenchel conjugates of F and G can be separately computed. Thus, incorporating the denseness of $C_c^1(\Omega)$ in $H_N(\mathrm{div}, \Omega)$ w.r.t. $\|\cdot\|_{H(\mathrm{div},\Omega)}$ as well as (5.30) one gets that for any $v \in \mathrm{BV}(\Omega)$

$$|\mathrm{D}v|(\Omega) = \sup_{q\in\mathcal{Q}, \|q\|_\infty \leq 1} \int_\Omega v\mathrm{div} q\,\mathrm{d}x = \sup_{q\in\mathcal{Q}} \left(-\int_\Omega v\mathrm{div} q\,\mathrm{d}x - \mathbb{I}[\overline{B_1}(0)][q] \right) = F^*[-\Lambda^* v]\,.$$

To compute G^*, we first note that

$$G^*[v] = \sup_{w\in L^2(\Omega)} \big((v, w)_{L^2(\Omega)} - G[w] \big) \tag{5.32}$$

holds true for any $v \in L^2(\Omega)$, where we employed the identification $(L^2(\Omega, \mathbb{R}))' \cong L^2(\Omega, \mathbb{R})$. By computing the first variation w.r.t. w of the right-hand side of (5.32) in the direction $\tilde{w} \in L^2(\Omega)$ we get

$$\int_\Omega v\tilde{w} - \frac{\frac{1}{2}w\tilde{w} + \tilde{w}\theta_2}{\theta_1 + \theta_2}\,\mathrm{d}x = 0\,,$$

which implies that the supremum in (5.32) is attained for $w = 2v(\theta_1 + \theta_2) - 2\theta_2$. By inserting this maximizer into (5.32) one can infer that G is actually the predual functional of the data term G^*. This finishes the proof of this proposition. □

Functional a posteriori error estimate for the relaxed binary Mumford–Shah functional. In what follows, we will derive a functional a posteriori error estimate for (5.22) by employing the fundamental relation given in Proposition 5.3.1 as well as Repin's abstract framework. We highlight that a crucial prerequisite to apply this framework is the uniform convexity of G^*. To this end, let us briefly introduce two measures quantifying the uniform convexity and the strict monotonicity of a functional $J \in \Gamma_0(X)$ on a generic Banach space X (*cf.* [Rep00, Rep12, Bar15]).

Definition 5.3.2. Let X be a Banach space and $J \in \Gamma_0(X)$.

(i.) J is *uniformly convex* if there exists a functional $\Phi_J : X \to \mathbb{R}_0^+$ such that

$$J\left[\tfrac{x_1+x_2}{2}\right] + \Phi_J(x_2 - x_1) \leq \tfrac{1}{2}(J[x_1] + J[x_2])$$

for all $x_1, x_2 \in X$, and $\Phi_J(x) = 0$ if and only if $x = 0$.

(ii.) We denote by $\Psi_J : X \to \mathbb{R}_0^+$ a functional that satisfies

$$\langle x', x_2 - x_1\rangle_{X',X} + \Psi_J(x_2 - x_1) \leq J[x_2] - J[x_1] \tag{5.33}$$

for all $x_1, x_2 \in X$ and all $x' \in \partial J[x_1]$.

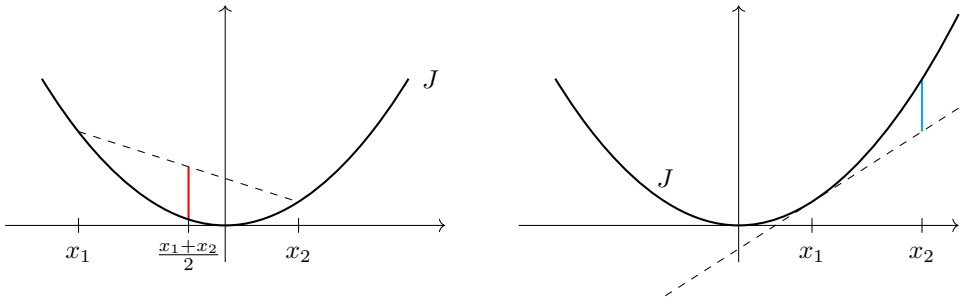

Figure 5.1: Schematic drawing of Φ_J (red line, left) and Ψ_J (blue line, right).

Remark 5.3.3. (i.) One can show via a Taylor expansion that the optimal functionals Φ_J and Ψ_J associated with $J \in \Gamma_0(X) \cap C^2(X)$ admit the representation

$$\Phi_J(x) = \tfrac{1}{8}\lambda_{\min}(D^2J(x))|x|^2\,, \qquad \Psi_J(x) = \tfrac{1}{2}\lambda_{\min}(D^2J(x))|x|^2\,,$$

where $\lambda_{\min}(D^2J(x))$ denotes the smallest eigenvalue of the Hessian of J at x.

(ii.) We observe that any Ψ_J which satisfies (5.33) is bounded by the *Bregman distance* Ψ_J^* (*cf.* [Bre67]), *i.e.*

$$\Psi_J(x_2 - x_1) \leq \Psi_J^*(x_1, x_2) = \sup_{x' \in \partial J[x_1]} J[x_2] - J[x_1] - \langle x', x_2 - x_1\rangle_{X',X}$$

for all $x_1, x_2 \in X$.

The central a posteriori error estimate to be presented in Theorem 5.3.4 relies on the subsequent relations that directly emerge from the Duality Theorem 5.1.13:

$$E^{\mathrm{rel}}[u] = (D^{\mathrm{rel}})^*[u] = -D^{\mathrm{rel}}[p]\,, \tag{5.34}$$

$$E^{\mathrm{rel}}[v] = (D^{\mathrm{rel}})^*[v] \geq -D^{\mathrm{rel}}[q] \tag{5.35}$$

for all $q \in \mathcal{Q}$ and all $v \in \mathcal{V}$. Here, $p \in \mathcal{Q}$ and $u \in \mathcal{V}$ are minimizers of D^{rel} and $E^{\text{rel}} = (D^{\text{rel}})^*$, respectively. Note that (5.34) holds true if and only if $-\Lambda^* u \in \partial F[p]$ and $u \in \partial G[\Lambda p]$. The relation (5.35) is known as the *weak complementarity principle*.

Theorem 5.3.4. *Let $u \in \mathcal{V}$ be the minimizer of E^{rel} for fixed intensity values $c_1 \neq c_2$. Then, for any $v \in \mathcal{V}$ and $q \in \mathcal{Q}$ a functional a posteriori error estimator for* (5.22) *is given by*

$$\|u - v\|^2_{L^2(\Omega)} \leq \operatorname{err}^2_u[v, q, c_1, c_2] := \frac{2\nu}{(c_1 - c_2)^2}(E^{rel}[v] + D^{rel}[q])\,. \tag{5.36}$$

Proof. We first prove the following inequality (*cf*. [Bar15]):

$$\Phi_{F^*}(-\Lambda^*(v-u)) + \Phi_{G^*}(v-u) + \Psi_{E^{\text{rel}}}\left(\frac{v-u}{2}\right) \leq \tfrac{1}{2}(E^{\text{rel}}[v] + D^{\text{rel}}[q]) \tag{5.37}$$

for all $q \in \mathcal{Q}$ and all $v \in \mathcal{V}$. In fact, thanks to the definition of the uniform convexity one gets

$$\begin{aligned}&\Phi_{F^*}(-\Lambda^*(v-u)) + \Phi_{G^*}(v-u)\\ &\leq \tfrac{1}{2}\left(F^*[-\Lambda^* v] + G^*[v] + F^*[-\Lambda^* u] + G^*[u]\right) - \left(F^*\left[-\Lambda^*\frac{u+v}{2}\right] + G^*\left[\frac{u+v}{2}\right]\right).\end{aligned} \tag{5.38}$$

Furthermore, by exploiting the monotonicity of E^{rel} as well as $0 \in \partial E^{\text{rel}}[u]$ due to the minimizing property of u we can deduce

$$\Psi_{E^{\text{rel}}}\left(\frac{v-u}{2}\right) \leq F^*\left[-\Lambda^*\frac{u+v}{2}\right] + G^*\left[\frac{u+v}{2}\right] - \left(F^*[-\Lambda^* u] + G^*[u]\right)\,. \tag{5.39}$$

By adding (5.38) and (5.39) it follows that

$$\begin{aligned}\Phi_{F^*}(-\Lambda^*(v-u)) + \Phi_{G^*}(v-u) + \Psi_{E^{\text{rel}}}\left(\frac{v-u}{2}\right) &\leq \tfrac{1}{2}\left(F^*[-\Lambda^* v] + G^*[v]\right) - \tfrac{1}{2}\left(F^*[-\Lambda^* u] + G^*[u]\right)\\ &= \tfrac{1}{2}(E^{\text{rel}}[v] - E^{\text{rel}}[u]) \leq \tfrac{1}{2}(E^{\text{rel}}[v] + D^{\text{rel}}[q])\,.\end{aligned}$$

The last inequality is an immediate consequence of the weak complementarity principle (5.35).

In the case of the binary Mumford–Shah model, a straightforward computation shows

$$\Phi_{F^*} \equiv 0\,, \qquad \Phi_{G^*}(v) = \frac{1}{4}\int_\Omega v^2(\theta_1 + \theta_2)\,\mathrm{d}x\,, \qquad \Psi_{E^{\text{rel}}}(v) = \int_\Omega v^2(\theta_1 + \theta_2)\,\mathrm{d}x\,.$$

Hence, by applying (5.37) to this particular choice we obtain for all $v \in \mathcal{V}$ and all $q \in \mathcal{Q}$

$$\int_\Omega (u-v)^2(\theta_1 + \theta_2)\,\mathrm{d}x \leq E^{\text{rel}}[v] + D^{\text{rel}}[q]\,.$$

Finally, Young's inequality $\frac{1}{2}(a-b)^2 \leq a^2 + b^2$ with $a = c_1 - u_0$ and $b = c_2 - u_0$ yields $\frac{1}{2\nu}(c_1 - c_2)^2 \leq \theta_1 + \theta_2$, which implies the estimate (5.36). □

We highlight that $\operatorname{err}^2_u[v, q, c_1, c_2]$ is both *reliable*, *i.e.* $\operatorname{err}^2_u[v, q, c_1, c_2]$ is always an upper bound for the real error, and *consistent*, *i.e.* $\operatorname{err}^2_u[v, q, c_1, c_2] \to 0$ if $v \to u$ and $q \to p$ w.r.t. the corresponding Banach space topology. A local error estimator, which is based on $\operatorname{err}^2_u[v, q, c_1, c_2]$, will be discussed in Section 5.6.

5.4 A Posteriori Error Estimates for the Binary Mumford–Shah Model

In this section, we will derive an a posteriori error theory for the binary Mumford–Shah model with fixed intensity values incorporating the functional a posteriori estimator for E^{rel} (*cf*. Theorem 5.3.4) as well as the thresholding result shown in Proposition 5.2.3. Afterwards, we will expand this estimator to the general binary Mumford–Shah model with varying intensity values and we will discuss the limitations of this ansatz.

A posteriori error estimator for E with fixed intensity values. In many numerical applications, one observes that the minimizer u of the relaxed binary Mumford–Shah model (5.22) is approximately piecewise constant with steep profiles at the interfaces. Moreover, the Lebesgue measure of the set $[\frac{1}{2} - \eta < u < \frac{1}{2} + \eta]$ for small $\eta > 0$ is negligible compared to the size of the domain due to the preference of u for the values 0 respectively 1 induced by the particular structure of E^{rel}. We will exploit these facts to derive an error estimator for the binary Mumford–Shah functional E. In detail, one observes that for any approximate solution $v \in \mathrm{BV}(\Omega)$ of E^{rel} the following set inclusion for the symmetric difference of $[u > \frac{1}{2}]$ and $[v > \frac{1}{2}]$ holds true:

$$\left[u > \tfrac{1}{2}\right] \Delta \left[v > \tfrac{1}{2}\right] \subseteq [|u - v| > \eta] \cup [\tfrac{1}{2} - \eta \leq v \leq \tfrac{1}{2} + \eta]\,. \tag{5.40}$$

The Lebesgue measure of the first set on the right-hand side of (5.40) can be controlled by $\eta^{-2}\mathrm{err}_u^2[v, q, c_1, c_2]$. Likewise, the Lebesgue measure of

$$\mathcal{S}_{v,\eta} := [\tfrac{1}{2} - \eta \leq v \leq \tfrac{1}{2} + \eta]$$

as the *set of non-properly identified regions* is explicitly computable and expected to be small taking into account the aforementioned experimental results. In this case, η is a weight parameter that needs to be optimized. The a posteriori estimator for (5.19) then follows in combination with the thresholding (*cf*. Proposition 5.2.3), the precise statement is as follows:

Theorem 5.4.1 (A posteriori error estimator for E)**.** *Let $u \in \mathrm{BV}(\Omega, [0,1])$ be the minimizer of E^{rel} for fixed intensity values $c_1, c_2 \in [0,1]$, $c_1 \neq c_2$. Then, the following a posteriori error bound for the minimizer $\chi = \chi[u > \frac{1}{2}] \in \mathrm{BV}(\Omega, \{0,1\})$ of the binary Mumford–Shah functional holds true:*

$$\left\|\chi - \chi[v > \tfrac{1}{2}]\right\|_{L^1(\Omega)} \leq \mathrm{err}_\chi[v, q] := \inf_{\eta \in (0, \frac{1}{2})} \left(\mathcal{L}^n(\mathcal{S}_{v,\eta}) + \frac{1}{\eta^2}\mathrm{err}_u^2[v, q, c_1, c_2] \right) \tag{5.41}$$

for all $v \in \mathcal{V}$ and all $q \in \mathcal{Q}$.

Proof. Choose $\eta \in (0, \frac{1}{2})$. Then, by an inclusion argument one can infer

$$\left[u > \tfrac{1}{2}\right] \Delta \left[v > \tfrac{1}{2}\right] \subseteq [|u - v| > \eta] \cup \left[\tfrac{1}{2} - \eta \leq v \leq \tfrac{1}{2} + \eta\right] = [|u - v| > \eta] \cup \mathcal{S}_{v,\eta}\,.$$

Hence,

$$\left\|\chi - \chi[v > \tfrac{1}{2}]\right\|_{L^1(\Omega)} = \mathcal{L}^n\left(\left[u > \tfrac{1}{2}\right] \Delta \left[v > \tfrac{1}{2}\right]\right) \leq \mathcal{L}^n([|u - v| > \eta]) + \mathcal{L}^n(\mathcal{S}_{v,\eta})\,. \tag{5.42}$$

To derive (5.42), we used Proposition 5.2.3 and the simple fact that $\|\chi[A] - \chi[B]\|_{L^1(\Omega)} = \mathcal{L}^n(A \Delta B)$ for measurable sets $A, B \subset \Omega$. Taking into account Theorem 5.3.4 we can further estimate

$$\mathcal{L}^n([|u - v| > \eta]) \leq \int_{[|u-v|>\eta]} \frac{(u - v)^2}{\eta^2}\,\mathrm{d}x \leq \frac{1}{\eta^2}\mathrm{err}_u^2[v, q, c_1, c_2]\,.$$

By taking the infimum w.r.t. $\eta \in (0, \frac{1}{2})$ we have proven (5.41). □

Remark 5.4.2. (i.) Note that the reliable a posteriori error estimator err_χ merely requires a conforming space and is not tailored to a specific finite element space. The estimator err_χ is consistent if there exists $\eta_0 \in (0, \frac{1}{2})$ such that $\mathcal{L}^n(\mathcal{S}_{v,\eta}) \to 0$ if $v \to u$ in $L^2(\Omega)$ for all $\eta \in (0, \eta_0)$, which is implied by the consistency of the functional a posteriori error estimator err_u^2.

(ii.) We stress that the evaluation of (5.41) is not computationally expensive compared to the calculation of the primal and the dual solution. In fact, to compute err_χ a single computation of err_u^2 has to be performed, followed by an optimization of η w.r.t. a discrete subset of $(0, \frac{1}{2})$. Note that the computational complexity to evaluate $\mathcal{L}^n(\mathcal{S}_{v,\eta})$ is in general negligible.

A posteriori error estimator for E with varying intensity values. In what follows, we will propose a numerical scheme to reliably compute an a posteriori error estimator in case of an alternating update of the approximate solutions and the intensity values. To this end, in a first step we will examine the effect of an ε-perturbation of the intensity values on the error estimator. In the second step, a sensitivity analysis is performed to estimate the error emerging from the update of the intensity values. Finally, by combining both steps one could derive an a posteriori error estimator incorporating the updated intensity values. Unfortunately, it will become apparent in the numerical applications that this scheme is computationally *not* feasible since the decrease of the absolute value of the perturbed error estimator is not sufficiently large. In this paragraph, we will tacitly assume that the optimal binary minimizers are not constant to exclude trivial cases.

As a preparatory step, we will derive an a posteriori error estimate for the minimizer of the binary model with intensity values $\tilde{c}_i \in [0,1]$ for $i = 1,2$, which are assumed to be in the intervals $[c_i - \varepsilon, c_i + \varepsilon] \cap [0,1]$ around the given intensity values $c_i \in [0,1]$ for a fixed bandwidth parameter $\varepsilon > 0$. Here, the bandwidth parameter is chosen such that both intervals do not overlap, *i.e.* $|c_1 - c_2| > 2\varepsilon$. We consider the functionals

$$E^{\mathrm{rel}}[v, \tilde{c}_1, \tilde{c}_2] = \int_\Omega \tfrac{(\tilde{c}_1 - u_0)^2}{\nu} v^2 + \tfrac{(\tilde{c}_2 - u_0)^2}{\nu} (1-v)^2 \,\mathrm{d}x + |\mathrm{D}v|(\Omega)\,, \tag{5.43}$$

$$E[\chi, \tilde{c}_1, \tilde{c}_2] = \int_\Omega \tfrac{(\tilde{c}_1 - u_0)^2}{\nu} \chi + \tfrac{(\tilde{c}_2 - u_0)^2}{\nu} (1-\chi) \,\mathrm{d}x + |\mathrm{D}\chi|(\Omega) \tag{5.44}$$

for all $v \in \mathrm{BV}(\Omega, [0,1])$ and all $\chi \in \mathrm{BV}(\Omega, \{0,1\})$. Furthermore, let $u_{(\tilde{c}_1,\tilde{c}_2)} \in \mathrm{BV}(\Omega,[0,1])$ and $\chi_{(\tilde{c}_1,\tilde{c}_2)} = \chi[u_{(\tilde{c}_1,\tilde{c}_2)} > \frac{1}{2}] \in \mathrm{BV}(\Omega,\{0,1\})$ be minimizers of (5.43) and (5.44), respectively. Then, Theorem 5.3.4 and a monotonicity argument imply

$$\|u_{(\tilde{c}_1,\tilde{c}_2)} - v\|^2_{L^2(\Omega)} \leq \sup\left\{ \mathrm{err}_u^2[v,q,\hat{c}_1,\hat{c}_2] \,:\, \hat{c}_i \in \overline{B_\varepsilon}(c_i), i \in \{1,2\} \right\} \leq \mathrm{err}_u^{2,\varepsilon}[v,q,c_1,c_2]$$

for all $v \in \mathcal{V}$ and all $q \in \mathcal{Q}$, where $\mathrm{err}_u^{2,\varepsilon}$ is the ε-perturbed a posteriori error estimator

$$\mathrm{err}_u^{2,\varepsilon}[v,q,c_1,c_2] := \frac{2\nu}{(|c_1-c_2|-2\varepsilon)^2}\Bigg(\int_\Omega v^2 \theta_1^{\max} + (1-v)^2 \theta_2^{\max} \,\mathrm{d}x + |\mathrm{D}v|(\Omega) \\ + \int_\Omega \tfrac{\frac{1}{4}(\mathrm{div} q)^2}{\theta_1^{\min}+\theta_2^{\min}} + \max\left\{ \tfrac{(\mathrm{div} q)\theta_2^{\max}}{\theta_1^{\min}+\theta_2^{\min}}, \tfrac{(\mathrm{div} q)\theta_2^{\min}}{\theta_1^{\max}+\theta_2^{\max}} \right\} - \tfrac{\theta_1^{\min}\theta_2^{\min}}{\theta_1^{\max}+\theta_2^{\max}} \Bigg) \,\mathrm{d}x\,.$$

Here, $\theta_i^{\min}(x)$ and $\theta_i^{\max}(x)$ are the minimal respectively maximal values of $\theta_i(x)$ for $\tilde{c}_i$ in $\overline{B_\varepsilon}(c_i) \cap [0,1]$, *i.e.*

$$\theta_i^{\min}(x) = \tfrac{1}{\nu} \min_{c \in \overline{B_\varepsilon}(c_i)\cap[0,1]} (c - u_0(x))^2\,, \qquad \theta_i^{\max}(x) = \tfrac{1}{\nu} \max_{c \in \overline{B_\varepsilon}(c_i)\cap[0,1]} (c - u_0(x))^2$$

for $i = 1,2$. Furthermore, by incorporating Theorem 5.4.1 the corresponding a posteriori error estimator for (5.44) reads as

$$\|\chi_{(\tilde{c}_1,\tilde{c}_2)} - \chi[v > \tfrac{1}{2}]\|_{L^1(\Omega)} \leq \mathrm{err}_\chi^\varepsilon[v,q,c_1,c_2] := \inf_{\eta \in (0,\frac{1}{2})} \left(\mathcal{L}^n(\mathcal{S}_{v,\eta}) + \tfrac{1}{\eta^2} \mathrm{err}_u^{2,\varepsilon}[v,q,c_1,c_2] \right).$$

In other words, $\mathrm{err}_\chi^\varepsilon[v,q,c_1,c_2]$ represents an a posteriori error bound for all binary minimizers of (5.44) associated with the intensity values $\tilde{c}_i \in \overline{B_\varepsilon}(c_i)$.

Next, we perform a sensitivity analysis to estimate the distance of the optimal intensity values $c_i = c_i[\chi_{(\tilde{c}_1,\tilde{c}_2)}]$ and $c_i[\chi]$ (*cf.* (5.20)) associated with $\chi_{(\tilde{c}_1,\tilde{c}_2)}$ and $\chi = \chi[v > \frac{1}{2}]$ for any $v \in \mathcal{V}$ and $i = 1,2$, respectively. If we further assume

$$\min\{\|\chi\|_{L^1(\Omega)}, \|1-\chi\|_{L^1(\Omega)}\} > 0\,, \qquad |c_1 - c_2| > 2\varepsilon\,, \qquad c_i[\chi] \in \overline{B_\varepsilon}(c_i)\,,$$

then we obtain the following error estimates for the intensity parameters:

$$|c_1[\chi] - c_1| \leq \frac{\|(\chi - \chi_{(\tilde{c}_1,\tilde{c}_2)})u_0\|_{L^1(\Omega)}}{\|\chi\|_{L^1(\Omega)}} + \left| \frac{1}{\|\chi_{(\tilde{c}_1,\tilde{c}_2)}\|_{L^1(\Omega)}} - \frac{1}{\|\chi\|_{L^1(\Omega)}} \right| \|\chi_{(\tilde{c}_1,\tilde{c}_2)}u_0\|_{L^1(\Omega)}$$

$$\leq \frac{2\|\chi_{(\tilde{c}_1,\tilde{c}_2)} - \chi\|_{L^1(\Omega)}}{\|\chi\|_{L^1(\Omega)}} \leq \frac{2\,\mathrm{err}_\chi^\varepsilon[v,q,c_1,c_2]}{\|\chi\|_{L^1(\Omega)}}\,, \tag{5.45}$$

$$|c_2[\chi] - c_2| \leq \frac{2\|\chi_{(\tilde{c}_1,\tilde{c}_2)} - \chi\|_{L^1(\Omega)}}{\|1-\chi\|_{L^1(\Omega)}} \leq \frac{2\,\mathrm{err}_\chi^\varepsilon[v,q,c_1,c_2]}{\|1-\chi\|_{L^1(\Omega)}} \tag{5.46}$$

for $q \in \mathcal{Q}$.

By combining the ε-perturbed error estimators for the primal and the dual solution with the sensitivity analysis for the intensity values in an alternating update scheme one could derive reliable a posteriori error estimators for (5.43) and (5.44) in the case of varying intensity values. Unfortunately, in the numerical experiments it becomes apparent that the decrease of the ε-perturbed a posteriori error estimates $\mathrm{err}_u^{2,\varepsilon}$ and $\mathrm{err}_\chi^\varepsilon$ is not sufficient to initiate a bootstrap iteration to successively update the intensity values and simultaneously decrease the error quantities on the right-hand sides of (5.45) and (5.46). In detail, in the best case for $\|\chi\|_{L^1(\Omega)} \approx \|1-\chi\|_{L^1(\Omega)} \approx 0.5$ the amplification factor $2\max\{(\|\chi\|_{L^1(\Omega)})^{-1}, (\|1-\chi\|_{L^1(\Omega)})^{-1}\}$ appearing in (5.45) and (5.46) is roughly 4, but in general this factor is unbounded. Hence, an essential prerequisite for the applicability of this scheme is a substantial decline in the quantity of the ε-perturbed functional a posteriori error estimates in each iteration step compared to this amplification factor, which could not be observed in the numerical applications. We refer to Section 5.7 for an explicit evaluation of the sensitivity of a relaxed solution.

5.5 Finite Element and Finite Difference Discretization

In this section, we will propose three different discretization schemes to compute the primal and the dual solution associated with E^{rel}. To this end, we first introduce an adaptive triangle mesh with hanging nodes, which allows a canonical correspondence to a quadtree ($n = 2$) or octree ($n = 3$). Afterwards, two finite element discretization schemes on this adaptive grid are presented, in which the primal functions are modeled as piecewise affine and globally continuous finite element functions. Both schemes only differ in the discretization of the discrete gradient operator Λ_h and accordingly in the choice of the discrete dual function spaces. Additionally, we adapt a widespread finite difference scheme – originally proposed for the ROF model – to the relaxed binary Mumford–Shah model in order to compare the quantities of the a posteriori error estimator of this established finite difference discretization with the finite element schemes. Henceforth, to simplify the presentation we always assume $\Omega = [0,1]^2$, the generalization to domains with polygonal boundary in arbitrary dimensions readily follows.

Adaptive triangle grid with hanging nodes. In what follows, we will construct an adaptive triangle grid admitting hanging nodes, which will be used in both finite element discretization schemes below.

As a first step, we describe the construction of an adaptive regular quadratic grid $\mathcal{M}_h$ on the image domain Ω. For this reason, let us recall that a quadtree T (for $n = 3$ an octree) is a tree structure where each node has either four children (for $n = 3$, eight children) or is a leaf node. Then, each cell of $\mathcal{M}_h$ has a one-to-one correspondence to a leaf of the quadtree T and is quadratic, which means that in each refinement of a cell of $\mathcal{M}_h$ this cell is divided into four quadratic cells via an edge bisection. Furthermore, we ensure that the level of cells with a common edge differs at most by one, which implies that on each edge not more than one hanging node can exist (in all further considerations, we omit hanging nodes on the boundary). The advantage of this particular adaptive mesh construction is the effective organization of the adaptivity due to the quadtree structure. Figure 5.2 depicts an admissible (left) as well as an inadmissible (right) refinement. Finally, the associated adaptive triangle mesh $\mathcal{S}_h$ is then obtained via a splitting of each quadratic cell into 2 triangles $\mathscr{T}$ (for $n = 3$ into 6 simplices) employing a cross subdivision (see second drawing in Figure 5.2).

The function h assigns to each quadratic grid cell $\mathscr{C} \in \mathcal{M}_h$ its mesh size, *i.e.*

$$h(\mathscr{C}) = 2^{-l(\mathscr{C})} \quad \text{with } l(\mathscr{C}) \in \{L_{\mathrm{init}}, \dots, L_{\mathrm{full}}\}\,.$$

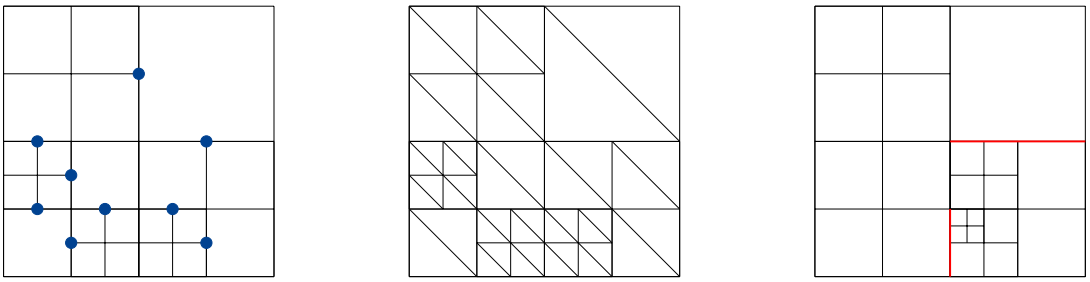

Figure 5.2: Left: admissible refinement with level one transitions, hanging nodes are marked by blue points. Middle: cross subdivision of the leftmost quadratic domain. Right: non-admissible refinement with level two transitions, the corresponding edges are traced in red.

Here, L_{init} refers to the initial mesh size and L_{full} to the maximum resolution. Throughout this chapter we suppose, if not otherwise specified, that the input image u_0 is an element of $\mathcal{V}_0$ as the space of piecewise affine and globally continuous finite elements on the uniform and regular grid $\mathcal{M}_{h,0}$ with mesh size $2^{-L_{\text{full}}}$. Furthermore, we denote by N_v the number of degrees of freedom in $\mathcal{M}_h$, which coincides with the difference of the number of all grid nodes and the number of hanging nodes.

(FE) Conforming finite element discretization on $\mathcal{S}_h$. The finite element discretization scheme to be presented below, which we denote by (FE), is an adaptation of a discretization for variational problems in $\mathrm{BV}(\Omega)$ originally proposed by Bartels [Bar15, Bar12]. On the aforementioned adaptive triangle grid $\mathcal{S}_h$ we introduce the conforming discrete function spaces (*cf*. [BS08])

$$\begin{aligned}\mathcal{V}_h &= \left\{ v_h \in C^0(\overline{\Omega}) \,:\, v_h\big|_{\mathscr{T}} \text{ is affine } \forall \mathscr{T} \in \mathcal{S}_h \right\}, \\ \mathcal{Q}_h &= \left\{ q_h \in \mathcal{V}_h^2 \,:\, q_h \cdot \mathrm{n} = 0 \text{ on } \partial\Omega \right\}\end{aligned}$$

as discrete counterparts of $\mathcal{V} = L^2(\Omega)$ and $\mathcal{Q} = H_N(\mathrm{div}, \Omega)$, respectively. The value of a discrete function $v_h \in \mathcal{V}_h$ or $q_h \in \mathcal{Q}_h$ at a hanging node coincides with the average of the function values at both adjacent degrees of freedom. To accommodate the boundary condition in the space $\mathcal{Q}_h$, the values at boundary nodes are altered after each update in a postprocessing step if required. Furthermore, we set $N_v = \dim \mathcal{V}_h$ and $N_q = \dim \mathcal{Q}_h = 2N_v$.

Next, we define the discrete predual data term $G_h : \mathcal{V}_h \to \mathbb{R}$ and the discrete predual total variation $F_h : \mathcal{Q}_h \to \mathbb{R}$ as follows:

$$F_h[q_h] = \mathbb{I}[\overline{B_1}(0)][q_h], \qquad G_h[v_h] = \int_\Omega \frac{\frac{1}{4}v_h^2 + v_h\theta_{2,h} - \theta_{1,h}\theta_{2,h}}{\theta_{1,h} + \theta_{2,h}} \,\mathrm{d}x\,. \tag{5.47}$$

Here, $\theta_{i,h} = \mathcal{I}_h(\theta_i) = \mathcal{I}_h(\frac{1}{\nu}(c_i - u_0)^2)$ for $i = 1, 2$ for an input image $u_0 \in \mathcal{V}_0$, where $\mathcal{I}_h$ denotes the Lagrange interpolation in the space $\mathcal{V}_h$. We endow $\mathcal{V}_h$ with the usual $L^2(\Omega)$-product $(\,\cdot\,,\,\cdot\,)_2$ and $\mathcal{Q}_h$ with the lumped mass product

$$(\,\cdot\,,\,\cdot\,)_h : \mathcal{Q}_h \times \mathcal{Q}_h \to \mathbb{R}, \qquad (q_h, p_h)_h \mapsto \int_\Omega \mathcal{I}_h(q_h \cdot p_h)\,\mathrm{d}x \quad \forall q_h, p_h \in \mathcal{Q}_h\,. \tag{5.48}$$

The dual spaces of $\mathcal{V}_h$ and $\mathcal{Q}_h$ are identified in terms of these inner products via the Riesz representation theorem, which yields

$$F_h^*[q_h] = \int_\Omega \mathcal{I}_h(|q_h|)\,\mathrm{d}x\,, \qquad G_h^*[v_h] = \int_\Omega v_h^2\theta_{1,h} + (1 - v_h)^2\theta_{2,h}\,\mathrm{d}x\,. \tag{5.49}$$

The proof that G_h^* is the Fenchel conjugate of G_h is nearly identical to the proof of Proposition 5.3.1, the corresponding assertion for F_h^* is a consequence of

$$F_h^*[q_h] = \sup_{p_h \in \mathcal{Q}_h} \int_\Omega \mathcal{I}_h(q_h \cdot p_h)\,\mathrm{d}x - \mathbb{I}[\overline{B_1}(0)][p_h] = \int_\Omega \mathcal{I}_h\left(q_h \cdot \bar{p}_h\right)\,\mathrm{d}x - \mathbb{I}[\overline{B_1}(0)][\bar{p}_h] = \int_\Omega \mathcal{I}_h(|q_h|)\,\mathrm{d}x \tag{5.50}$$

for $q_h \in \mathcal{Q}_h$, where the supremum is attained at $\bar{p}_h \in \mathcal{Q}_h$, which is given by $\bar{p}_h(x) = \frac{q_h(x)}{|q_h(x)|}$ if $q_h(x) \neq 0$ and $\bar{p}_h(x) = 0$ else for any node x of the grid.

Let us denote by $\mathcal{P}_h$ the orthogonal L^2-projection $\mathcal{P}_h : L^2(\Omega) \to \mathcal{V}_h$. The *discrete divergence Λ_h in the case (FE)* is defined as

$$\Lambda_h : \mathcal{Q}_h \to \mathcal{V}_h\,, \qquad q_h \mapsto \mathcal{P}_h \mathrm{div} q_h\,,$$

and the adjoint operator $\Lambda_h^* : \mathcal{V}_h \to \mathcal{Q}_h$ is implicitly characterized by the duality

$$(\Lambda_h^* v_h, q_h)_h = (v_h, \mathcal{P}_h \mathrm{div} q_h)_2 \tag{5.51}$$

for all $v_h \in \mathcal{V}_h$ and all $q_h \in \mathcal{Q}_h$. Bearing in mind the divergence theorem, we refer to the negative adjoint operator $-\Lambda_h^* : \mathcal{V}_h \to \mathcal{Q}_h$ as the *discrete gradient operator for the discretization (FE)*.

(FE') Nonconforming finite element discretization with natural gradient operator on $\mathcal{S}_h$. The subsequent finite element approach (denoted by (FE')) is motivated by the simple observation that the gradient of a globally continuous and cell-wise affine finite element function on $\mathcal{S}_h$ is constant in the interior of the cells. Thus, the discrete function spaces for the discretization (FE') on the aforementioned adaptive triangle grid $\mathcal{S}_h$ are

$$\begin{aligned}
\mathcal{V}_h &= \left\{ v_h \in C^0(\overline{\Omega}) \,:\, v_h\big|_{\mathscr{T}} \text{ is affine } \forall \mathscr{T} \in \mathcal{S}_h \right\}\,, \\
\widetilde{\mathcal{Q}_h} &= \left\{ q_h \in L^\infty(\Omega, \mathbb{R}^2) \,:\, q_h\big|_{\mathscr{T}} \equiv \text{const.} \; \forall \mathscr{T} \in \mathcal{S}_h \right\}\,.
\end{aligned}$$

Both spaces are endowed with the standard $L^2(\Omega)$-product adapted to the corresponding dimension and we set $N_v = \dim \mathcal{V}_h$ and $N_q = \dim \widetilde{\mathcal{Q}_h}$. Obviously, N_q is twice the number of simplices in $\mathcal{S}_h$. The functionals F_h, G_h and G_h^* are defined as in the discretization (FE) (see (5.47) and (5.49)). Due to the modification of $\widetilde{\mathcal{Q}_h}$ compared to (FE) we get for the approach (FE')

$$F_h^*[q_h] = \int_\Omega |q_h| \,\mathrm{d}x\,, \tag{5.52}$$

the proof is similar to (5.50) with minor modifications.

Starting from the *discrete gradient operator* $-\Lambda_h^* : \mathcal{V}_h \to \widetilde{\mathcal{Q}_h}$, $-\Lambda_h^* v_h = \nabla v_h$ for the discretization (FE'), we can infer that the *discrete divergence* $\Lambda_h : \widetilde{\mathcal{Q}_h} \to \mathcal{V}_h$ is implicitly characterized by

$$\int_\Omega \Lambda_h q_h v_h \,\mathrm{d}x = \int_\Omega q_h \cdot \Lambda_h^* v_h \,\mathrm{d}x = -\int_\Omega q_h \cdot \nabla v_h \,\mathrm{d}x$$

for all $v_h \in \mathcal{V}_h$ and all $q_h \in \widetilde{\mathcal{Q}_h}$. Again, to satisfy the boundary conditions for any $q_h \in \widetilde{\mathcal{Q}_h}$, we set the corresponding boundary values of q_h to 0 if required. In the special case of the computational domain $\Omega = [0,1]^2$ on the adaptive triangle grid $\mathcal{S}_h$, we have to ensure that the first component of q_h vanishes on the left and right boundary side and the second component on the top and bottom boundary side. Since $\widetilde{\mathcal{Q}_h}$ is not contained in $H_N(\mathrm{div}, \Omega)$, this discretization scheme is nonconforming. Hence, to compute the local error estimator a projection onto a conforming finite element subspace of $H_N(\mathrm{div}, \Omega)$ has to be performed (for details see Section 5.6).

(FD) Finite difference scheme on a regular mesh. As a last discretization scheme, we present a finite difference discretization (FD) following Chambolle [Cha04] to compare the quantities of the a posteriori error estimator of the finite element approaches above with a more standard scheme in image processing like (FD).

Let $N > 1$ be the width and height of the input image measured in number of pixels. Then, we consider the *lattice* $\Gamma_N = \{1, \dots, N\} \times \{1, \dots, N\}$ with *mesh size* $h = (N-1)^{-1}$ and $N_v = N^2$ nodes, which coincide in this case with the degrees of freedom. Furthermore, we set $N_q = 2N_v$. Every discrete primal function $\mathbf{V}_h : \Gamma_N \to \mathbb{R}$ and discrete dual function $\mathbf{Q}_h : \Gamma_N \to \mathbb{R}^2$ then has a one-to-one correspondence (below we identify the corresponding objects for simplicity) to a vector $\mathbf{V}_h \in \mathbb{R}^{N_v}$ and $\mathbf{Q}_h \in (\mathbb{R}^2)^{N_v} \cong \mathbb{R}^{N_q}$, respectively. If we replace integration by summation, the discrete analogs of F and G are given by

$$\mathbf{F}_h[\mathbf{Q}_h] = \max_{i=1,\dots,N_v} \mathbb{I}[\overline{B_1}(0)][\mathbf{Q}_h^i]\,, \qquad \mathbf{G}_h[\mathbf{V}_h] = \sum_{i=1}^{N_v} \left(\frac{\frac{1}{4}(\mathbf{V}_h^i)^2 + \mathbf{V}_h^i \boldsymbol{\Theta}_{2,h}^i - \boldsymbol{\Theta}_{1,h}^i \boldsymbol{\Theta}_{2,h}^i}{\boldsymbol{\Theta}_{1,h}^i + \boldsymbol{\Theta}_{2,h}^i} \right)\,.$$

Here, the discrete functions $\mathbf{\Theta}_{j,h}$ associated with the input image $U_0 \in \mathbb{R}^{N_v}$ are given by $\mathbf{\Theta}^i_{j,h} = \frac{1}{\nu}(c_j - U^i_0)^2$ for $1 \leq i \leq N_v$ and $j \in \{1,2\}$. If we endow the spaces $\mathbb{R}^{N_v}$ and $(\mathbb{R}^2)^{N_v}$ with the standard Euclidean product, a similar proof as presented in the previous discretization schemes yields

$$\mathbf{F}^*_h[\mathbf{Q}_h] = \sum_{i=1}^{N_v} |\mathbf{Q}^i_h|\,, \qquad \mathbf{G}^*_h[\mathbf{V}_h] = \sum_{i=1}^{N_v} (\mathbf{V}^i_h)^2 \mathbf{\Theta}^i_{1,h} + (1 - \mathbf{V}^i_h)^2 \mathbf{\Theta}^i_{2,h}\,.$$

Finally, we employ the forward difference operator with periodic boundary conditions as the *discrete gradient operator* $-\mathbf{\Lambda}^*_h : \{\Gamma_N \to \mathbb{R}\} \to \{\Gamma_N \to \mathbb{R}^2\}$, *i.e.*

$$(-\mathbf{\Lambda}^*_h \mathbf{V}_h)(i,j) = \frac{1}{h} \begin{pmatrix} \mathbf{V}_h((i \bmod N) + 1, j) - \mathbf{V}_h(i,j) \\ \mathbf{V}_h(i, (j \bmod N) + 1) - \mathbf{V}_h(i,j) \end{pmatrix},$$

for all $1 \leq i,j \leq N$, the modulo operators guarantee the periodicity at each boundary side. Moreover, the operator $-\mathbf{\Lambda}^*_h$ is the negative adjoint of the operator $\mathbf{\Lambda}_h : \{\Gamma_N \to \mathbb{R}^2\} \to \{\Gamma_N \to \mathbb{R}\}$ representing the *discrete divergence in the case (FD)*. The latter operator coincides with the common backward difference quotient.

5.6 Duality-Based Algorithms and Adaptive Mesh Refinement

A standard and widespread strategy to adaptively approximate the numerical solution to a variational problem is based on the loop depicted in Figure 5.3 (*cf*. [BNQ$^+$09]), which consists of the four steps SOLVE, ESTIMATE, MARK and REFINE.

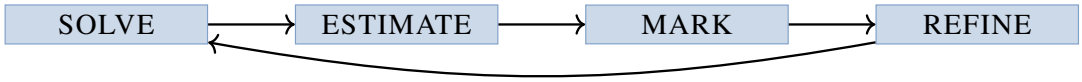

Figure 5.3: Adaptive refinement scheme composed of a loop of four steps.

In this section, we will follow this scheme to compute minimizers of the binary Mumford–Shah model and elaborate on each of the four steps. Concerning the first step (SOLVE), we apply a primal-dual algorithm with first order convergence due to Chambolle and Pock [CP11] to each of the discretization schemes presented in Section 5.5. As an alternative, a dual gradient descent for the scheme (FE) is derived in order to compare the performance of both algorithms. In the subsequent paragraph, other common related duality-based algorithms are briefly discussed. Afterwards, based on Theorem 5.3.4 we propose a local a posteriori error estimator, which is applicable to all discretization schemes (ESTIMATE) and on which the marking rule of the cells in the adaptive grid for the finite element schemes relies (MARK). In the final step, the refinement of a cell is performed via a cross subdivision as already discussed in Section 5.5 (REFINE). Again, we restrict our presentation to the computational domain $\Omega = [0,1]^2$ for convenience.

Primal-dual algorithm with first order convergence. In this paragraph, we will elaborate on the computation of discrete minimizers for the binary Mumford–Shah functional obtained with a primal-dual minimization algorithm by Chambolle and Pock [CP11] for all discretization schemes presented in Section 5.5. The main benefits of this particular algorithm are its versatility in the applications in the field of convex optimization and its fast guaranteed convergence.

As a first step, we derive a reformulation of F_h and G_h as well as their Fenchel conjugates for the schemes (FE) and (FE') (see (5.47), (5.49) and (5.52)), which are defined on vectors rather than on finite element functions. To this end, we identify each $v_h \in \mathcal{V}_h$, $q_h \in \mathcal{Q}_h$ and $\widetilde{q_h} \in \widetilde{\mathcal{Q}_h}$ with the vectors $\mathbf{V}_h \in \mathbb{R}^{N_v}$, $\mathbf{Q}_h \in (\mathbb{R}^2)^{N_v}$ and $\widetilde{\mathbf{Q}_h} \in (\mathbb{R}^2)^{\#\mathcal{S}_h}$, respectively, in terms of

$$\mathbf{V}^i_h = v_h(X^i)\,, \qquad \begin{cases} \mathbf{Q}^i_h = q_h(X^i)\,, & \text{for (FE)}\,, \\ \widetilde{\mathbf{Q}^j_h} = \widetilde{q_h}(\mathscr{T}_j)\,, & \text{for (FE')}\,, \end{cases} \tag{5.53}$$

for all $1 \leq i \leq N_v$ and all $1 \leq j \leq \#\mathcal{S}_h$ with $\#\mathcal{S}_h$ denoting the number of simplices in $\mathcal{S}_h$. Here, X^i represents the i^{th} degree of freedom in the current adaptive mesh $\mathcal{S}_h$, and $\widetilde{q_h}(\mathscr{T}_j)$ denotes the value of the piecewise constant finite element function $\widetilde{q_h}$ evaluated at the simplex $\mathscr{T}_j \in \mathcal{S}_h$. The functionals $\mathbf{F}_h$, $\mathbf{G}_h$, $\mathbf{F}_h^*$ and $\mathbf{G}_h^*$ operating on these vectors are then defined by evaluating the corresponding functionals at the discrete spaces. For example, $\mathbf{G}_h[\mathbf{V}_h] := G_h[v_h]$ for any $v_h \in \mathcal{V}_h$ and $\mathbf{V}_h \in \mathbb{R}^{N_v}$ related by (5.53).

Notation 5.6.1. To facilitate the presentation, we use the variable N_q to denote the dimension of the predual spaces for all discretizations, although its value differs depending on the discretization considered.

The matrix representations $\mathbf{M}_h \in \mathbb{R}^{N_v,N_v}$ and $\widetilde{\mathbf{M}_h} \in \mathbb{R}^{N_q,N_q}$ of the inner products in all discretization schemes associated with the primal and dual discrete spaces, respectively, are given as follows:

$$\text{(FE):} \qquad \mathbf{M}_h\mathbf{V}_h \cdot \mathbf{U}_h = \int_\Omega u_h v_h \,\mathrm{d}x\,, \qquad \widetilde{\mathbf{M}_h}\mathbf{P}_h \cdot \mathbf{Q}_h = \int_\Omega \mathcal{I}_h(p_h \cdot q_h)\,\mathrm{d}x\,, \tag{5.54a}$$

$$\text{(FE'):} \qquad \mathbf{M}_h\mathbf{V}_h \cdot \mathbf{U}_h = \int_\Omega u_h v_h \,\mathrm{d}x\,, \qquad \widetilde{\mathbf{M}_h}\widetilde{\mathbf{P}_h} \cdot \widetilde{\mathbf{Q}_h} = \int_\Omega \widetilde{p_h} \cdot \widetilde{q_h}\,\mathrm{d}x\,, \tag{5.54b}$$

$$\text{(FD):} \qquad \mathbf{M}_h = \mathbb{1}\,, \qquad \widetilde{\mathbf{M}_h} = \mathbb{1}\,, \tag{5.54c}$$

for all $u_h, v_h \in \mathcal{V}_h$, all $p_h, q_h \in \mathcal{Q}_h$ and all $\widetilde{p_h}, \widetilde{q_h} \in \widetilde{\mathcal{Q}_h}$. Thus, $\mathbf{M}_h$ is the mass matrix for both of the approaches (FE) and (FE'), and $\widetilde{\mathbf{M}_h}$ is the lumped mass matrix in the case (FE) and the diagonal mass matrix with entries representing the volume of the associated element in the case (FE'). In the finite difference discretization, both $\mathbf{M}_h$ and $\widetilde{\mathbf{M}_h}$ coincide with the identity matrix of the corresponding size since the inner product is simply the Euclidean product.

Let $\mathbf{\Lambda}_h \in \mathbb{R}^{N_v,N_q}$ and $-\mathbf{\Lambda}_h^* \in \mathbb{R}^{N_q,N_v}$ be the matrix representations of the discrete divergence and the discrete gradient, respectively. The definition of the adjoint operator implies

$$\mathbf{M}_h\mathbf{\Lambda}_h\mathbf{Q}_h \cdot \mathbf{V}_h = (\Lambda_h q_h, v_h) = ((q_h, \Lambda_h^* v_h)) = \widetilde{\mathbf{M}_h}\mathbf{Q}_h \cdot \mathbf{\Lambda}_h^*\mathbf{V}_h$$

for all $\mathbf{V}_h \in \mathbb{R}^{N_v}$ and all $\mathbf{Q}_h \in \mathbb{R}^{N_q}$, where $(\,\cdot\,,\,\cdot\,)$ and $((\,\cdot\,,\,\cdot\,))$ denote the inner products on the discrete spaces $\mathcal{V}_h$ and $\mathcal{Q}_h$ (respectively $\widetilde{\mathcal{Q}_h}$). Since both $\mathbf{M}_h$ and $\widetilde{\mathbf{M}_h}$ are positive definite and symmetric matrices and thus invertible, we get

$$\mathbf{\Lambda}_h^* = \widetilde{\mathbf{M}_h}^{-1}\mathbf{\Lambda}_h^T\mathbf{M}_h\,.$$

Note that $\mathbf{\Lambda}_h^* = \mathbf{\Lambda}_h^T$ for the discretization (FD).

Summing up, by taking into account (5.29), (5.31) and (5.53) the *discrete predual energy* $\mathbf{D}_h^{rel} : \mathbb{R}^{N_q} \to \mathbb{R}$ and the *discrete energy* $\mathbf{E}_h^{rel} : \mathbb{R}^{N_v} \to \mathbb{R}$ are given by

$$\mathbf{D}_h^{rel}[\mathbf{Q}_h] = \mathbf{F}_h[\mathbf{Q}_h] + \mathbf{G}_h[\mathbf{\Lambda}_h\mathbf{Q}_h]\,, \qquad \mathbf{E}_h^{rel}[\mathbf{V}_h] = \mathbf{F}_h^*[-\mathbf{\Lambda}_h^*\mathbf{V}_h] + \mathbf{G}_h^*[\mathbf{V}_h]\,.$$

To apply the primal-dual algorithm, we have to compute the proximal mapping operators $\operatorname{prox}_{\sigma\mathbf{F}_h}[\mathbf{Q}_h]$ and $\operatorname{prox}_{\tau\mathbf{G}_h^*}[\mathbf{V}_h]$, where the corresponding inner products are given by (5.54a)-(5.54c). The results are collected in the following proposition:

Proposition 5.6.2. *Let $\sigma, \tau > 0$.*

(i.) The proximal mapping of the total variation is given by

$$(\operatorname{prox}_{\sigma\mathbf{F}_h}[\mathbf{Q}_h])^i = \frac{\mathbf{Q}_h^i}{\max\{|\mathbf{Q}_h^i|, 1\}}\,, \tag{5.55}$$

*where either $1 \leq i \leq N_v$ (for (FE) and (FD)) or $1 \leq i \leq \#\mathcal{S}_h$ (for (FE')). Recall that – depending on the finite element discretization – $\mathbf{Q}_h^i \in \mathbb{R}^2$ either refers to a nodal or a cell-wise evaluation of the dual solution (*cf. (5.53)*).*

(ii.) In the finite element discretization schemes, we define the weighted mass matrix for a weight $w_h \in \mathcal{V}_h$ *by*

$$\mathbf{M}_h[\mathbf{W}_h]\mathbf{U}_h \cdot \mathbf{V}_h = \int_\Omega w_h u_h v_h \,\mathrm{d}x$$

for all $u_h, v_h \in \mathcal{V}_h$. Furthermore, $\mathbf{\Theta}_{i,h}$ is related to $\theta_{i,h} = \mathcal{I}_h(\theta_i)$ via (5.53) *for $i \in \{1,2\}$. Then, the proximal mapping of the data term reads as*

$$\operatorname{prox}_{\tau \mathbf{G}_h^*}[\mathbf{V}_h] = \left(\mathbf{M}_h[1 + 2\tau(\mathbf{\Theta}_{1,h} + \mathbf{\Theta}_{2,h})]\right)^{-1} \mathbf{M}_h \left(\mathbf{V}_h + 2\tau \mathbf{\Theta}_{2,h}\right) . \tag{5.56}$$

(iii.) In the case of the finite difference discretization, the proximal mapping of the data term is as follows:

$$\left(\operatorname{prox}_{\tau \mathbf{G}_h^*}[\mathbf{V}_h]\right)^i = \frac{\mathbf{V}_h^i + 2\tau \mathbf{\Theta}_{2,h}^i}{1 + 2\tau(\mathbf{\Theta}_{1,h}^i + \mathbf{\Theta}_{2,h}^i)} \qquad \text{for } 1 \le i \le N_v . \tag{5.57}$$

Proof. We only prove (5.55) for (FD) and (5.56), the other cases follow with minor modifications. One obtains for the discretization scheme (FD)

$$\begin{aligned} \operatorname{prox}_{\sigma \mathbf{F}_h}[\mathbf{Q}_h] &= \operatorname*{argmin}_{\mathbf{P}_h \in \mathbb{R}^{N_v}} \left\{ |\mathbf{Q}_h - \mathbf{P}_h|^2 + 2\sigma \max_{i=1,\dots,N_v} \mathbb{I}[\overline{B_1}(0)][\mathbf{P}_h^i] \right\} \\ &= \operatorname*{argmin}_{\mathbf{P}_h \in \mathbb{R}^{N_v}} \left\{ \, |\mathbf{Q}_h - \mathbf{P}_h|^2 \, : \, |\mathbf{P}_h^i| \le 1 \; \forall i \in \{1, \dots, N_v\} \, \right\} , \end{aligned}$$

which readily implies (5.55).

Moreover, for any $\mathbf{V}_h \in \mathbb{R}^{N_v}$ we get for (FE) and (FE')

$$\operatorname{prox}_{\tau \mathbf{G}_h^*}[\mathbf{V}_h] = \operatorname*{argmin}_{u_h \in \mathcal{V}_h} \|u_h - v_h\|_{L^2(\Omega)}^2 + 2\tau G_h^*[u_h] .$$

By taking the variation of the right-hand side w.r.t. u_h in the direction $\tilde{u}_h \in \mathcal{V}_h$ we immediately obtain

$$\int_\Omega \tilde{u}_h (u_h - v_h + 2\tau u_h \theta_{1,h} + 2\tau(u_h - 1)\theta_{2,h}) \, \mathrm{d}x = 0 .$$

Then, by rearranging all terms one gets (5.56). The proof of (5.57) is quite similar, we omit further details. □

After these preparations, we can now apply the primal-dual Algorithm 3 (see [CP11, Algorithm 1]) to compute approximations of the discrete primal solution $\mathbf{U}_h \in \mathbb{R}^{N_v}$ and the discrete dual solution $\mathbf{P}_h \in \mathbb{R}^{N_q}$ on a given (adaptive) triangle mesh with fixed intensity values c_1 and c_2. Although this algorithm has guaranteed convergence for all initial data $(\mathbf{U}_h^0, \mathbf{P}_h^0) \in \mathbb{R}^{N_v} \times \mathbb{R}^{N_q}$, it turns out that by using the nodal interpolation of the primal and dual solution of the preceding refinement step as an initialization a significant speed-up can be observed. In the first refinement step, all vectors are initialized with the zero vector in the corresponding dimension. Moreover, using diagonal preconditioning one could improve the convergence speed of Algorithm 3 without any further step size control (see [Poc11]).

Algorithm 3: Primal-dual algorithm used to minimize $\mathbf{E}_h^{rel}$.

Data: proximal mappings $\operatorname{prox}_{\sigma \mathbf{F}_h}$ and $\operatorname{prox}_{\tau \mathbf{G}_h^*}$, differential operator $\mathbf{\Lambda}_h$, initial data $(\mathbf{U}_h^0, \mathbf{P}_h^0)$, step sizes $\tau, \sigma > 0$

Result: approximate primal/dual solution $(\mathbf{U}_h, \mathbf{P}_h)$

$k = 0$;
$\bar{\mathbf{U}}_h^0 = \mathbf{U}_h^0$;
repeat
  $k = k + 1$;
  $\mathbf{P}_h^k = \operatorname{prox}_{\sigma \mathbf{F}_h}[\mathbf{P}_h^{k-1} - \sigma \mathbf{\Lambda}_h^* \bar{\mathbf{U}}_h^{k-1}]$;
  $\mathbf{U}_h^k = \operatorname{prox}_{\tau \mathbf{G}_h^*}[\mathbf{U}_h^{k-1} + \tau \mathbf{\Lambda}_h \mathbf{P}_h^k]$;
  $\bar{\mathbf{U}}_h^k = 2\mathbf{U}_h^k - \mathbf{U}_h^{k-1}$;
until $\|\mathbf{U}_h^k - \mathbf{U}_h^{k-1}\|_\infty \le \mathrm{THRESHOLD}$;
$\mathbf{U}_h = \mathbf{U}_h^k$, $\mathbf{P}_h = \mathbf{P}_h^k$;

Following [CP11, Theorem 1], the convergence of Algorithm 3 is guaranteed if

$$\tau\sigma \left|||\mathbf{\Lambda}_h|||\right|^2 < 1 \tag{5.58}$$

for fixed parameters $\sigma > 0$ and $\tau > 0$. The subsequent lemma provides estimates for the quantity $|||\mathbf{\Lambda}_h|||$ for all discretization schemes depending solely on the (minimal) mesh size.

Lemma 5.6.3. *Let $n = 2$ and $h_{\min} = \min_{\mathscr{C}\in\mathcal{S}_h} h(\mathscr{C})$. Then the operator norms can be estimated as follows:*

$$\text{(FE):}\quad \left|||\mathbf{\Lambda}_h|||\right|^2 \leq 96(3+2\sqrt{2})h_{\min}^{-2}\,, \tag{5.59a}$$

$$\text{(FE')}:\quad \left|||\mathbf{\Lambda}_h|||\right|^2 \leq 48(3+2\sqrt{2})h_{\min}^{-2}\,, \tag{5.59b}$$

$$\text{(FD):}\quad \left|||\mathbf{\Lambda}_h|||\right|^2 \leq 8h^{-2}\,. \tag{5.59c}$$

Proof. The proof of (5.59b) relies on the inverse estimate for piecewise affine finite elements of the form

$$\|\nabla v_h\|_{L^2(\mathscr{C})} \leq \frac{\sqrt{6}\mathcal{H}^1(\partial\mathscr{C})}{|\mathscr{C}|}\|v_h\|_{L^2(\mathscr{C})}$$

for all $\mathscr{C}\in\mathcal{S}_h$ and all $v_h\in\mathcal{V}_h$ (see [ÖRW10]). Hence,

$$\begin{aligned}\|\nabla v_h\|_{L^2(\Omega)} &= \sum_{\mathscr{C}\in\mathcal{S}_h}\|\nabla v_h\|_{L^2(\mathscr{C})} \leq \sum_{\mathscr{C}\in\mathcal{S}_h}\left(\frac{\sqrt{6}\mathcal{H}^1(\partial\mathscr{C})}{|\mathscr{C}|}\|v_h\|_{L^2(\mathscr{C})}\right) \leq \sup_{\widetilde{\mathscr{C}}\in\mathcal{S}_h}\left(\frac{\sqrt{6}\mathcal{H}^1(\partial\widetilde{\mathscr{C}})}{|\widetilde{\mathscr{C}}|}\right)\sum_{\mathscr{C}\in\mathcal{S}_h}\|v_h\|_{L^2(\mathscr{C})}\\ &\leq \sup_{\widetilde{\mathscr{C}}\in\mathcal{S}_h}\left(\frac{\sqrt{6}(2+\sqrt{2})h(\widetilde{\mathscr{C}})}{\frac{h(\widetilde{\mathscr{C}})^2}{2}}\right)\sum_{\mathscr{C}\in\mathcal{S}_h}\|v_h\|_{L^2(\mathscr{C})} \leq 2\sqrt{6}(2+\sqrt{2})h_{\min}^{-1}\|v_h\|_{L^2(\Omega)}\,,\end{aligned} \tag{5.60}$$

and due to Proposition 5.1.12 (v.) we obtain

$$\left|||\mathbf{\Lambda}_h|||\right|^2 = \left|||\mathbf{\Lambda}_h^*|||\right|^2 \leq (2\sqrt{6}(2+\sqrt{2})h_{\min}^{-1})^2 = 48(3+2\sqrt{2})h_{\min}^{-2} \approx 279.8h_{\min}^{-2}\,.$$

To prove (5.59a), we use the duality relation (5.51) as follows (for the definition of $\|\cdot\|_h$ see (5.48)):

$$\begin{aligned}\left|||\mathbf{\Lambda}_h|||\right|^2 = \left|||\mathbf{\Lambda}_h^*|||\right|^2 &= \left(\max_{v_h\in\mathcal{V}_h,\|v_h\|_{L^2(\Omega)}=1}\ \max_{q_h\in\mathcal{Q}_h,\|q_h\|_h=1}\int_\Omega \mathcal{I}_h(\Lambda_h^* v_h\cdot q_h)\,\mathrm{d}x\right)^2\\ &= \left(\max_{v_h\in\mathcal{V}_h,\|v_h\|_{L^2(\Omega)}=1}\ \max_{q_h\in\mathcal{Q}_h,\|q_h\|_h=1}\int_\Omega v_h\mathcal{P}_h\mathrm{div}q_h\,\mathrm{d}x\right)^2\\ &\leq \max_{v_h\in\mathcal{V}_h,\|v_h\|_{L^2(\Omega)}=1}\|v_h\|_{L^2(\Omega)}^2\ \max_{q_h\in\mathcal{Q}_h,\|q_h\|_h=1}\|\mathcal{P}_h\mathrm{div}q_h\|_{L^2(\Omega)}^2\\ &= \max_{\substack{q_h\in\mathcal{Q}_h,\\ \|q_h\|_h=1}}\|\mathcal{P}_h\mathrm{div}q_h\|_{L^2(\Omega)}^2 \leq \max_{\substack{q_h\in\mathcal{Q}_h,\\ \|q_h\|_h=1}}\|\mathrm{div}q_h\|_{L^2(\Omega)}^2\,.\end{aligned}$$

Recall that $\mathcal{Q}_h = \mathcal{V}_h^2$ (up to boundary conditions) in the discretization (FE). Thus, the inverse estimate (5.60) implies

$$\max_{\substack{q_h\in\mathcal{Q}_h,\\ \|q_h\|_h=1}}\|\mathrm{div}q_h\|_{L^2(\Omega)}^2 \leq 2\max_{\substack{v_h\in\mathcal{V}_h,\\ \|v_h\|_h=1}}\|\nabla v_h\|_{L^2(\Omega)}^2 \leq 2\cdot 48(3+2\sqrt{2})h_{\min}^{-2}\max_{\substack{v_h\in\mathcal{V}_h,\\ \|v_h\|_h=1}}\|v_h\|_{L^2(\Omega)}^2\,.$$

A convexity argument shows that $\|v_h\|_{L^2(\Omega)} \leq \|v_h\|_h$ for $v_h\in\mathcal{V}_h$ with equality for constant v_h, which implies

$$\max_{\substack{v_h\in\mathcal{V}_h,\\ \|v_h\|_h=1}}\|v_h\|_{L^2(\Omega)}^2 = 1$$

and thus the estimate (5.59a). The proof of (5.59c) can be found in [Cha04]. □

Since h and $h_{\min}$ are known prior to the execution of the algorithm, the parameters σ and τ can be chosen according to Lemma 5.6.3 to satisfy the relation (5.58). The algorithm is executed until the maximum norm of $\mathbf{U}_h^k - \mathbf{U}_h^{k-1}$ is below the threshold value $\mathrm{THRESHOLD} = 10^{-8}$. Alternatively, one could have chosen a stopping criterion that relies on the primal-dual gap $\mathbf{E}_h^{rel}[\mathbf{U}_h^k] + \mathbf{D}_h^{rel}[\mathbf{P}_h^k]$, but this requires several additional evaluations of both energies, which is computationally more costly.

Remark 5.6.4. (i.) Since $\mathbf{G}_h^*$ is uniformly convex, one could have chosen the accelerated algorithm [CP11, Algorithm 2], which is superior to Algorithm 3 in terms of the convergence rate ($\mathcal{O}(k^{-2})$ compared to $\mathcal{O}(k^{-1})$). However, since the step sizes σ and τ change in each iteration step of the accelerated algorithm, the computation of $\mathrm{prox}_{\tau\mathbf{G}_h^*}$ requires the inversion of a matrix depending on τ (*cf.* (5.56)) in all iteration steps and thus results in a considerably longer computation time. In contrast, Algorithm 3 uses fixed step sizes and thus the inverse of the sparse, symmetric and positive-definite matrix $\mathbf{M}_h[1 + 2\tau(\mathbf{\Theta}_{1,h} + \mathbf{\Theta}_{2,h})]$ must be computed only once using a fast Cholesky decomposition (see [CDHR08]).

(ii.) We also implemented an alternating descent method for the Lagrangian following Bartels (see [Bar15, Algorithm A']) to compute minimizers of the relaxed binary Mumford–Shah model for the discretization (FE), which was about 20% to 40% slower in terms of CPU time than Algorithm 3 to achieve the same stopping condition.

Projected dual gradient descent. In this paragraph, we will derive a projected dual gradient descent for the minimization of E^{rel} using the discretization (FE) in order to compare the quality of the approximate solutions and the required CPU time with the primal-dual algorithm. To this end, we modify a semi-implicit gradient descent w.r.t. the dual variable originally proposed by Chambolle [Cha04] for the ROF model employing a finite difference scheme. Henceforth, we refer to this algorithm as (FE_D), and we note that this algorithm can also be derived for the discretizations (FE') and (FD) with minor modifications.

Let $\mathrm{TV}[u] = |\mathrm{D}u|(\Omega)$ for $u \in \mathrm{BV}(\Omega)$. The first order condition for E^{rel} implies

$$\kappa := -(2u\theta_1 + 2(u-1)\theta_2) \in \partial \mathrm{TV}[u]\,.$$

Due to Proposition 5.1.12 (iii.) we can infer

$$u \in \partial \mathrm{TV}^*[\kappa]\,, \tag{5.61}$$

and by incorporating $u = \frac{2\theta_2 - \kappa}{2(\theta_1+\theta_2)}$ one can deduce that (5.61) is the first order condition of the functional

$$\int_\Omega \frac{1}{4(\theta_1+\theta_2)} \left(\kappa - 2\theta_2\right)^2 \,\mathrm{d}x + \mathrm{TV}^*[\kappa]\,. \tag{5.62}$$

In what follows, we are aiming at minimizing (5.62). To this end, we recall that $\mathrm{TV}^*[\kappa] = \mathbb{I}[S][\kappa]$ for the set

$$S = \overline{\left\{\, \mathrm{div} f \,:\, f \in H_N(\mathrm{div}, \Omega), \|f\|_{L^\infty(\Omega)} \le 1 \,\right\}}\,.$$

Due to the assumptions regarding θ_i we infer that $w := (4(\theta_1+\theta_2))^{-1} \in L^\infty(\Omega, \mathbb{R}^{>0})$ is almost everywhere strictly positive, which allows us to define the weighted L^2-space $L^2(\Omega, w)$ endowed with the norm $\|f\|^2_{L^2(\Omega,w)} = \int_\Omega w|f|^2\,\mathrm{d}x$. Thus, we observe that the unique minimizer of (5.62) is given by $\kappa = \mathcal{P}_S[2\theta_2]$, where $\mathcal{P}_S$ denotes the orthogonal projection onto the set S w.r.t. $L^2(\Omega, w)$, *i.e.*

$$\mathcal{P}_S[f] = \operatorname*{argmin}_{g\in S} \|g - f\|^2_{L^2(\Omega,w)}\,. \tag{5.63}$$

To compute $\kappa = \mathcal{P}_S[2\theta_2]$, we alternatingly perform an unconstrained gradient descent for (5.63) and a projection onto S. The update formula for the unconstrained dual descent is given by

$$p^{k+1} = p^k - \tau\nabla(w(\mathrm{div} p^k - 2\theta_2)) \tag{5.64}$$

for the fixed mesh dependent step size $\tau = \gamma h_{\min} > 0$ with $\gamma = 0.05$ and $h_{\min} = \min_{\mathscr{C}\in\mathcal{M}_h} h(\mathscr{C})$. Next, we want to replace the differential operators in (5.64) by their counterparts in the scheme (FE). To this end, we multiply

each term in (5.64) by a test function $q \in \mathcal{Q}_h$, apply $\int_\Omega \mathcal{I}_h(\,\cdot\,)\,\mathrm{d}x$ on both sides, and replace ∇ and div by $-\Lambda_h^*$ and Λ_h as introduced in the discretization (FE), respectively. Hence, in combination with (5.51) we get

$$\begin{aligned}\int_\Omega \mathcal{I}_h(p^{k+1}\cdot q)\,\mathrm{d}x &= \int_\Omega \mathcal{I}_h(p^k\cdot q)\,\mathrm{d}x + \tau\int_\Omega \mathcal{I}_h(\Lambda_h^*(w(\Lambda_h p^k - 2\theta_2))\cdot q)\,\mathrm{d}x\\ &= \int_\Omega \mathcal{I}_h(p^k\cdot q)\,\mathrm{d}x + \tau\int_\Omega (w(\Lambda_h p^k - 2\theta_2))\mathcal{P}_h\mathrm{div} q\,\mathrm{d}x\,. \end{aligned} \tag{5.65}$$

Next, we rewrite (5.65) in matrix-vector notation, which is more appropriate for numerical applications. To this end, we define the matrices $\mathbf{M}_h$ (lumped mass matrix) and $\mathbf{L}_j$ as follows:

$$\mathbf{M}_h\mathbf{V}_h\cdot\widetilde{\mathbf{V}_h} = \int_\Omega \mathcal{I}_h(v_h\cdot\widetilde{v_h})\,\mathrm{d}x\,, \qquad \mathbf{L}_j\mathbf{V}_h\cdot\widetilde{\mathbf{V}_h} = \int_\Omega v_h\cdot\partial_j\widetilde{v_h}\,\mathrm{d}x$$

for $j=1,2$ and all $v_h, \widetilde{v_h}\in\mathcal{V}_h$. Furthermore, we set $\mathbf{W}_h^i = w(X^i)$, where we recall that X^i represents the i^{th} degree of freedom in the current adaptive mesh $\mathcal{S}_h$. Then, (5.65) implies

$$[\mathbf{P}_h^{k+1}]_j = [\mathbf{P}_h^k]_j + \tau\mathbf{M}_h^{-1}\mathbf{L}_j(\mathbf{W}_h(\mathbf{\Lambda}_h\mathbf{P}_h^k - 2\mathbf{\Theta}_{2,h})) \quad \text{for } j=1,2\,, \tag{5.66}$$

where $[\mathbf{P}_h^k]_j$ refers to the j^{th} component of $\mathbf{P}_h^k$. Note that all matrices and vectors apart from $\mathbf{P}_h^k$ on the right-hand side of (5.66) are fixed. We remark that the computation of $\mathbf{M}_h^{-1}$ is fast due to its diagonal structure.

In the second step of the alternating update, the dual variable is projected onto the set S by clamping the dual solution if necessary in the same manner as in (5.55).

The alternating update algorithm is stopped if the $L^\infty(\Omega)$-distance of two successive iterates of the dual solution is below the threshold value $\mathrm{THRESHOLD} = 10^{-8}$. The primal solution can then be retrieved via the formula

$$u = \frac{\theta_2 - \mathcal{P}_S[\theta_2]}{\theta_1+\theta_2}\,,$$

which easily follows from the definition of κ. We refer to [CM87] for a converge analysis of the resulting Algorithm 4.

Algorithm 4: Projected dual descent for the discretization (FE).

Data: initial value $\mathbf{P}_h^0$, differential operator $\mathbf{\Lambda}_h$, matrices $\mathbf{M}_h, \mathbf{L}_j, \mathbf{W}_h$, vectors $\mathbf{\Theta}_{1,h}, \mathbf{\Theta}_{2,h}$, step size $\tau = \gamma h_{\min}$
Result: approximate primal/dual solution $(\mathbf{U}_h, \mathbf{P}_h)$

```
k = 0;
repeat
    k = k + 1;
    [P_h^k]_j = [P_h^{k-1}]_j + τ M_h^{-1} L_j (W_h (Λ_h P_h^{k-1} − 2Θ_{2,h})) for j = 1, 2;
    P_h^k = ( (P_h^k)^i / max{|(P_h^k)^i|, 1} )_{i=1,...,N_v};
until ‖P_h^k − P_h^{k-1}‖_∞ ≤ THRESHOLD;
P_h = P_h^k;
U_h = ( (Θ_{2,h}^i − (Λ_h P_h)^i) / (Θ_{1,h}^i + Θ_{2,h}^i) )_{i=1,...,N_v};
```

Related duality-based algorithms in convex optimization. In the past decades, many algorithms to tackle the prototype convex minimization problem

$$\inf_{u\in\mathrm{BV}(\Omega)}\int_\Omega G[u]\,\mathrm{d}x + |\mathrm{D}u|(\Omega) \tag{5.67}$$

with G being convex, proper and lower semicontinuous were proposed. In what follows, we will list some recent algorithms which are suitable for the minimization of (5.67) and of more general optimization problems as alternatives to the algorithms used in this thesis. Due to the great variety of different algorithms, this list is by far not

exhaustive and we refer to the excellent review articles [BSS15, BP13, CCC$^+$10, CP16] and the references therein for further details.

As pointed out in [CP11, Section 4], Algorithm 3 possesses structural similarities with the established Douglas–Rachford splitting algorithm as well as its most prominent variant, the alternating direction method of multipliers (ADMM, *cf*. [BPC$^+$10] and the references therein). Bredies and Sun [BS15a, BS15b] proposed a preconditioned Douglas–Rachford algorithm that slightly outperforms Algorithm 3 in some numerical experiments. A further common minimization algorithm for functionals of the form (5.67) with possibly non-smooth terms is the fast iterative shrinkage-thresholding algorithm (FISTA), which has the convergence rate $\mathcal{O}(k^{-2})$ (see [BT09]). Goldstein and Osher [GO09] developed a split Bregman method, where the functional G is replaced by its Bregman distance and the optimization relies on a standard Bregman iteration. Finally, the inertial proximal algorithm for nonconvex optimization (iPiano, *cf*. [OCBP14]) turns out to be an efficient instance of a forward-backward splitting algorithm for functionals composed of a differentiable and a convex function.

A posteriori error estimator and refinement methods. So far, we mainly focused on the SOLVE step of the adaptive refinement paradigm (*cf*. Figure 5.3), *i.e*. the computation of the primal solution $\mathbf{U}_h$ and the dual solution $\mathbf{P}_h$. Before proceeding to the ESTIMATE step, we have to postprocess the solution vector $(u_h, p_h) \in \mathcal{V}_h \times \mathcal{Q}_h$ if required to remove local oscillations, which are likely to deteriorate the quality of the a posteriori estimator (*cf*. the numerical results in [Bar15]). Moreover, a projection of the solution vectors onto conforming spaces has to be performed if required in order to evaluate the a posteriori error estimator. The methods to calculate the postprocessed solution vector $(\bar{u}_h, \bar{p}_h)$ significantly differ in all discretization schemes:

(FE)/(FE$_D$): Since this discretization scheme is conforming, no projection of the solution vector is required. However, we observe (slight) local oscillations in both the primal and the dual solution, that is why we apply a smoothing filter based on an implicit time step of the discrete heat equation. In detail, let $\mathbf{M}_h$ and $\mathbf{S}_h$ be the mass and the stiffness matrix in the space of affine and globally continuous finite elements on the underlying adaptive triangle mesh $\mathcal{S}_h$. The postprocessed solution vector $(\bar{u}_h, \bar{p}_h)$ is obtained by applying the discrete operator $(\mathbf{M}_h + \iota \mathbf{S}_h)^{-1}\mathbf{M}_h$ to u_h and to each component of p_h separately. Here, we choose $\iota = c \cdot h_{\min}^2$, where $h_{\min}$ denotes the minimal mesh size of the current adaptive grid, with $c = 3$ and $c = 6$ for the primal and the dual solution, respectively, since we observed stronger oscillations in the dual solution.

(FE'): In this discretization, the dual space $\widetilde{\mathcal{Q}_h}$ is not $H_N(\mathrm{div}, \Omega)$-conforming. Therefore, we employ an $L^2(\Omega)$-projection of the dual solution p_h onto the space $\mathcal{V}_h^2$ of piecewise affine and globally continuous finite elements after the execution of the algorithm. The advantage of this discretization is the absence of oscillations in the primal solution. However, the dual solution slightly oscillates, that is why we apply the aforementioned smoothing filter based on the discrete heat equation. We experimentally observed that the best parameter choice for this filter is $\iota = 0.75 \cdot h_a^{0.9}$, where h_a denotes the average cell size on the current adaptive mesh.

(FD): To evaluate the a posteriori error estimator in the finite difference context, we employ a bilinear nodal interpolation of $\mathbf{U}_h$ and $\mathbf{P}_h$ to obtain the postprocessed solution vector $(\bar{u}_h, \bar{p}_h) \in \widehat{\mathcal{V}_h} \times \widehat{\mathcal{Q}_h}$, where

$$\widehat{\mathcal{V}_h} = \left\{ \widehat{v_h} \in C^0(\overline{\Omega}) \,:\, \widehat{v_h}\big|_{\mathcal{C}} \text{ is bilinear } \forall \mathcal{C} \in \mathcal{M}_{h,0} \right\}, \qquad \widehat{\mathcal{Q}_h} = \left\{ \widehat{q_h} \in \widehat{\mathcal{V}_h^2} \,:\, \widehat{q_h} \cdot \mathrm{n} = 0 \text{ on } \partial\Omega \right\},$$

and $\mathcal{M}_{h,0}$ denotes the regular mesh composed of quadratic elements with mesh size $2^{-L_{\mathrm{full}}}$ (see page 131). Furthermore, by using the bilinear interpolation once again we can assume $u_0 \in \widehat{\mathcal{V}_h}$. In this discretization, no smoothing filter is applied.

In all aforementioned schemes, the boundary values of the dual solution are altered in a further postprocessing step if required to satisfy the boundary condition. In our experiments, we observed that the choice of smoothing methods and parameters above outperforms other tested choices for the corresponding discretizations. Ultimately, the discrete solution to the original problem (5.19) is given by $\bar{\chi}_h = \chi[\bar{u}_h > \frac{1}{2}]$.

In what follows, we will comment on the remaining steps of the adaptive refinement paradigm:

Regarding the calculation of the (local) a posteriori error estimator in the ESTIMATE step, we define the local error estimator for each pair of postprocessed primal-dual solution $(\bar{u}_h, \bar{p}_h)$ and each cell $\mathscr{C}_0$ of the full resolution

image grid $\mathcal{M}_{h,0}$ as follows (see Theorem 5.3.4):

$$\operatorname{err}^2_{u,\mathscr{C}_0}[\bar{u}_h,\bar{p}_h] = \frac{2\nu}{(c_1-c_2)^2}\Bigg(\int_{\mathscr{C}_0} \bar{u}_h^2\theta_{1,h} + (1-\bar{u}_h)^2\theta_{2,h} + |\nabla\bar{u}_h| + \frac{\frac{1}{4}(\operatorname{div}\bar{p}_h)^2 + (\operatorname{div}\bar{p}_h)\theta_{2,h} - \theta_{1,h}\theta_{2,h}}{\theta_{1,h}+\theta_{2,h}}\,\mathrm{d}x\Bigg).$$

Here, $\theta_{i,h}$ is set to $\mathcal{I}_h(\theta_i)$ with $\mathcal{I}_h$ denoting the Lagrange interpolation on the corresponding discrete function space associated with the primal solution. We compute $\operatorname{err}^2_{u,\mathscr{C}_0}$ by using a Gaussian quadrature of order 4 on the simplices $\mathscr{T}_0$ composing the cell $\mathscr{C}_0 \in \mathcal{M}_{h,0}$ for (FE), (FE$_D$) and (FE'), and a Gaussian quadrature of order 5 directly on the cell $\mathscr{C}_0$ for (FD). The resulting local error estimator for a cell $\mathscr{C} \in \mathcal{M}_h$ as well as the global estimator are given by

$$\operatorname{err}^2_{u,\mathscr{C}}[\bar{u}_h,\bar{p}_h] = \sum_{\mathscr{C}_0\subset\mathscr{C}} \operatorname{err}^2_{u,\mathscr{C}_0}[\bar{u}_h,\bar{p}_h]\,, \qquad \operatorname{err}^2_{u}[\bar{u}_h,\bar{p}_h] = \sum_{\mathscr{C}\in\mathcal{M}_h} \operatorname{err}^2_{u,\mathscr{C}}[\bar{u}_h,\bar{p}_h]\,,$$

respectively. Note that $\operatorname{err}^2_{u,\mathscr{C}}[\bar{u}_h,\bar{p}_h]$ is in general not an upper bound for the local error $\|u-\bar{u}_h\|^2_{L^2(\mathscr{C})}$ of the approximate solution $\bar{u}_h$ on the (adaptive) grid and the minimizer u of E^{rel}. To obtain the associated error estimator err_χ for the binary model, we have to compute the optimal balance parameter η_{optimal} (*cf*. Theorem 5.4.1). To this end, we minimize

$$\eta \mapsto |\mathcal{S}_{\bar{u}_h,\eta}| + \frac{1}{\eta^2}\operatorname{err}^2_u[\bar{u}_h,\bar{p}_h]$$

w.r.t. the discrete set $\{0.005i : i \in 1,\dots,99\} \subset (0,0.5)$.

In the finite element discretizations, we MARK those cells $\mathscr{C} \in \mathcal{S}_h$ for refinement whose local error estimators exceed a certain percentage of the largest local error estimator, *i.e*.

$$\operatorname{err}^2_{u,\mathscr{C}}[\bar{u}_h,\bar{p}_h] \geq \alpha \max_{\mathscr{C}'\in\mathcal{S}_h} \operatorname{err}^2_{u,\mathscr{C}'}[\bar{u}_h,\bar{p}_h]\,,$$

where α is a fixed threshold in $(0,1)$. In all computations, we choose $\alpha = 0.2$. It turns out that this method is prone to outliers, that is why we additionally sort all local estimators $\operatorname{err}^2_{u,\mathscr{C}}$ according to their size (starting with the smallest) and mark the cells in the upper decile for refinement as well. Apart from the example involving the Gaussian kernels (see below), we only refine those cells $\mathscr{C}$ fulfilling $h(\mathscr{C}) > 2^{-L_{\mathrm{full}}}$ to prevent cell sizes which are below the cell size of the input images.

In the final step of the adaptive refinement paradigm (REFINE) for the schemes (FE), (FE$_D$) and (FE'), all cells that were previously marked are refined using the cell subdivision procedure described in Section 5.5.

5.7 Numerical Results

In this section, we will present numerical results for the a posteriori error estimator of the Mumford–Shah functional. In particular, we will investigate the behavior of the error estimator for four different input images[1] shown in Figure 5.4 along with the model parameters. Furthermore, we will experimentally verify the theoretical result that small perturbations of the input image can lead to topology changes of the thresholded segmented image using a checkerboard example (see Figure 5.10). In the final example (*cf*. Figure 5.11), the descent rate of the a posteriori error estimator will be presented for 15 cycles of the adaptive refinement for an analytic function representing the input image. All results in this section have been published in [BER17].

Since we assumed the intensity values to be constant, suitable approximations of the optimal values of c_1 and c_2 are computed using a 2-*means clustering algorithm* (*Lloyd's Algorithm*) with initial values 1 and 0 (Algorithm 5, *cf*. [Llo82]). In detail, in each iteration of Algorithm 5 the Voronoi sets $\mathcal{C}_1^k$ and $\mathcal{C}_2^k$ (*cf*. line 4) are computed, which contain the indices of the pixelwise input data vector U_0 that are closest to the current intensity values c_1^k and c_2^k, respectively. In the next iteration step (*cf*. line 5), the intensity values are updated by averaging U_0 w.r.t. the corresponding Voronoi set. The resulting fixed intensity values are given in Figure 5.4.

[1] Flower image: "Leucanthemum vulgare" by Derek Ramsey/Chanticleer Garden (desaturated from original), used under CC BY-SA 3.0, `https://commons.wikimedia.org/wiki/File:Leucanthemum_vulgare_%27Filigran%27_Flower_2200px.jpg`. Cameraman image: copyright by Massachusetts Institute of Technology, used with explicit permission.

image	(a)	(b)	(c)	(d)
resolution	2049×2049	2049×2049	2049×2049	513×513
c_1	0.999772	0.893734	0.664404	0.602566
c_2	$1.99 \cdot 10^{-4}$	0.030416	0.167763	0.092273
ν	$5 \cdot 10^{-3}$	$5 \cdot 10^{-3}$	10^{-3}	$5 \cdot 10^{-3}$

Figure 5.4: Input images along with the corresponding image resolution (in pixels) and model parameters c_1, c_2 and ν.

Algorithm 5: 2-means clustering algorithm (Lloyd's Algorithm).

Data: input image U_0, initial intensity values $c_1^0 = 1$ and $c_2^0 = 0$
Result: approximate optimal intensity values c_1 and c_2

$k = 0$;
repeat
  $k = k + 1$;
  $\mathcal{C}_i^k = \left\{ j \in \{1, \dots, N_v\} \,:\, |U_0^j - c_i^{k-1}| \leq |U_0^j - c_l^{k-1}| \text{ for } l = 1, 2 \right\}$ for $i = 1, 2$;
  $c_i^k = \frac{1}{\#\mathcal{C}_i^k} \sum_{j \in \mathcal{C}_i^k} U_0^j$ for $i = 1, 2$;
until $\max\{|c_1^k - c_1^{k-1}|, |c_2^k - c_2^{k-1}|\} \leq 10^{-4}$;
$c_1 = c_1^k$, $c_2 = c_2^k$;

The input image $u_0 \in \mathcal{V}_0$ is obtained by a nodal interpolation of the pixelwise input data vector U_0. For the discretizations (FE), (FE$_D$) and (FE'), $\mathcal{V}_0$ denotes the space of affine and globally continuous finite element functions on a uniform triangle mesh with mesh size $h = 2^{-L_{\text{full}}}$ ($L_{\text{full}} = 9$ for (d), $L_{\text{full}} = 11$ else). For the finite difference discretization (FD), we choose $\mathcal{V}_0$ as the space of bilinear finite element functions on a regular and uniform mesh composed of quadratic cells with grid size $h = 2^{-L_{\text{full}}}$. The mesh prior to the first execution of the algorithm is a uniform and regular mesh with mesh size $h = 2^{-L_{\text{init}}}$ on the computational domain $\Omega = [0, 1]^2$ ($L_{\text{init}} = 3$ for (d), $L_{\text{init}} = 5$ else).

In all computations, we use $\tau = 10^{-5}$ and $\sigma = 5 \cdot 10^{-5}$ (Algorithm 3) and $\gamma = 0.05$ for the dual gradient descent (Algorithm 4). For all computations involving the input images (a)-(d), we perform 10 cycles of the adaptive refinement loop (*cf*. Figure 5.3) as presented in the preceding sections. Since we stop the refinement of a cell if its cell size coincides with the mesh size of the input image, we do in general not expect the error estimators err_u^2 and err_χ to converge to 0.

Table 5.1 lists the quantities of the (rescaled) primal and dual energies, the functional error estimator err_u^2, η_{optimal} (the value of η corresponding to the optimal a posteriori error bound for given err_u^2) as well as the estimator err_χ for the input images (a)-(d) after the 10^{th} refinement step of the adaptive algorithm. In addition, the corresponding values for the discretization (FD) on the full resolution grid of the input image are presented. In Figure 5.5, the values of the a posteriori error estimators err_u^2 and err_χ after each adaptive refinement loop for the input images (a)-(d) and all proposed finite element discretization schemes are related to the number of degrees of freedom in the current adaptive mesh in a log-log plot. We highlight the following observations:

– The scheme (FE) performs comparably to the discretization (FE$_D$), but slightly better than the scheme (FE').

– In all finite element schemes, both err_u^2 and err_χ decay monotonously and with roughly a constant slope. However, err_χ is approximately one order of magnitude larger than err_u^2.

– After 7 iteration steps, there is hardly any decrease in the values of err_u^2 and err_χ for image (a) because all

		(a)	(b)	(c)	(d)
$\frac{2\nu}{(c_1-c_2)^2}E[\bar{u}_h]$	(FE)	0.022422	0.078461	0.124137	0.203797
	(FE$_D$)	0.022421	0.078632	0.124659	0.204353
	(FE')	0.022249	0.077981	0.122572	0.202494
	(FD)	0.022493	0.078814	0.122777	0.205645
$\frac{2\nu}{(c_1-c_2)^2}D[\bar{p}_h]$	(FE)	-0.021736	-0.075971	-0.117785	-0.183819
	(FE$_D$)	-0.021757	-0.075870	-0.117973	-0.181720
	(FE')	-0.020973	-0.071333	-0.111234	-0.166114
	(FD)	-0.021520	-0.075455	-0.119865	-0.188600
err_u^2	(FE)	6.86e-04	0.002490	0.006352	0.019978
	(FE$_D$)	6.63e-04	0.002761	0.006686	0.022633
	(FE')	0.001276	0.006647	0.011338	0.036380
	(FD)	9.73e-04	0.003359	0.002912	0.017045
η_{optimal}	(FE)	0.39	0.3225	0.2825	0.3075
	(FE$_D$)	0.385	0.325	0.2725	0.315
	(FE')	0.45	0.3675	0.31	0.3275
	(FD)	0.4375	0.345	0.24	0.3025
err_χ	(FE)	0.008847	0.038502	0.160912	0.373173
	(FE$_D$)	0.008704	0.041019	0.167892	0.394317
	(FE')	0.009816	0.068514	0.227060	0.545201
	(FD)	0.008223	0.0425225	0.109039	0.339256

Table 5.1: The table lists the rescaled energies evaluated at the discrete solution $(\bar{u}_h, \bar{p}_h)$, the error estimator err_u^2 for the relaxed solution, the optimal threshold value η_{optimal} and the resulting a posteriori estimator err_χ for the $L^1(\Omega)$-error associated with the characteristic function $\bar{\chi}_h = \chi[\bar{u}_h > \frac{1}{2}]$ (after 10 cycles of the adaptive algorithm for all finite element discretization schemes).

cells near the boundary of the circle are at the level of the input image grid and thus no further refinement is allowed. In this artificial example, the best value of err_χ among all examples with real image data is achieved and the deviation $\|\bar{\chi}_h - \chi\|_{L^1(\Omega)}$ of $\bar{\chi}_h = \chi[\bar{u}_h > \frac{1}{2}]$ from the unknown minimizer χ after the last iteration is at most 1%.

– The highest values of both error estimators can be observed for image (d). This results from the general observation that input images with a higher resolution lead to smaller quantities of the a posteriori error estimators since image features can be better captured on finer grids.

In the first row of Figure 5.6, the primal solutions for the flower image in the first to the fifth cycle of the mesh refinement computed with the adaptive algorithm for the discretization (FE') are depicted. The second row visualizes the associated color coded adaptive grids with a color scale ranging from blue (coarsest cells) to green (finest cells). One observes that the proposed method leads to significantly refined grid cells in the neighborhood of the interfaces of the flower. Moreover, when looking at the deciles of the primal solution it turns out that $\bar{u}_h(x) \in [0, 0.1] \cup [0.9, 1]$ for $x \in \Omega' \subset \Omega$ with $\frac{|\Omega'|}{|\Omega|} \approx 0.9$, *i.e.* the primal solutions are approximately binary up to a negligible set. Recall that this observation was the starting point for the proof of Theorem 5.4.1.

In the first and third row of Figure 5.7, the primal solutions, both components of the dual solutions as well as the thresholded solutions $\bar{\chi}_h = \chi[\bar{u}_h > \frac{1}{2}]$ for the images (b) and (c) computed with the discretization (FE') are displayed. Furthermore, the first images in the second and fourth row depict the associated adaptive triangle meshes after the 6^{th} refinement step with black regions representing not refined cells. Again, finer cells are concentrated near the interfaces of the moon and the flower, respectively. The adjacent images show color coded deciles of $\bar{u}_h$ and thus explicitly encode the sets $\mathcal{S}_{\bar{u}_h,\eta}$ for $\eta \in \{0.1, 0.2, 0.3, 0.4\}$. Finally, the last images in the second and fourth row contain the function plots of $\eta \mapsto \mathcal{L}^2(\mathcal{S}_{\bar{u}_h,\eta})$ and $\eta \mapsto \mathrm{err}_\chi$ for $\eta \in (0, 0.5)$. Here, $\eta \mapsto \mathrm{err}_\chi$ refers to a variation of the optimal balance parameter η in (5.41) and it turns out that this function possesses several local extrema.

Figure 5.8 depicts the relaxed primal solutions $\bar{u}_h$ and the associated components of the dual solutions $\bar{p}_h$ for

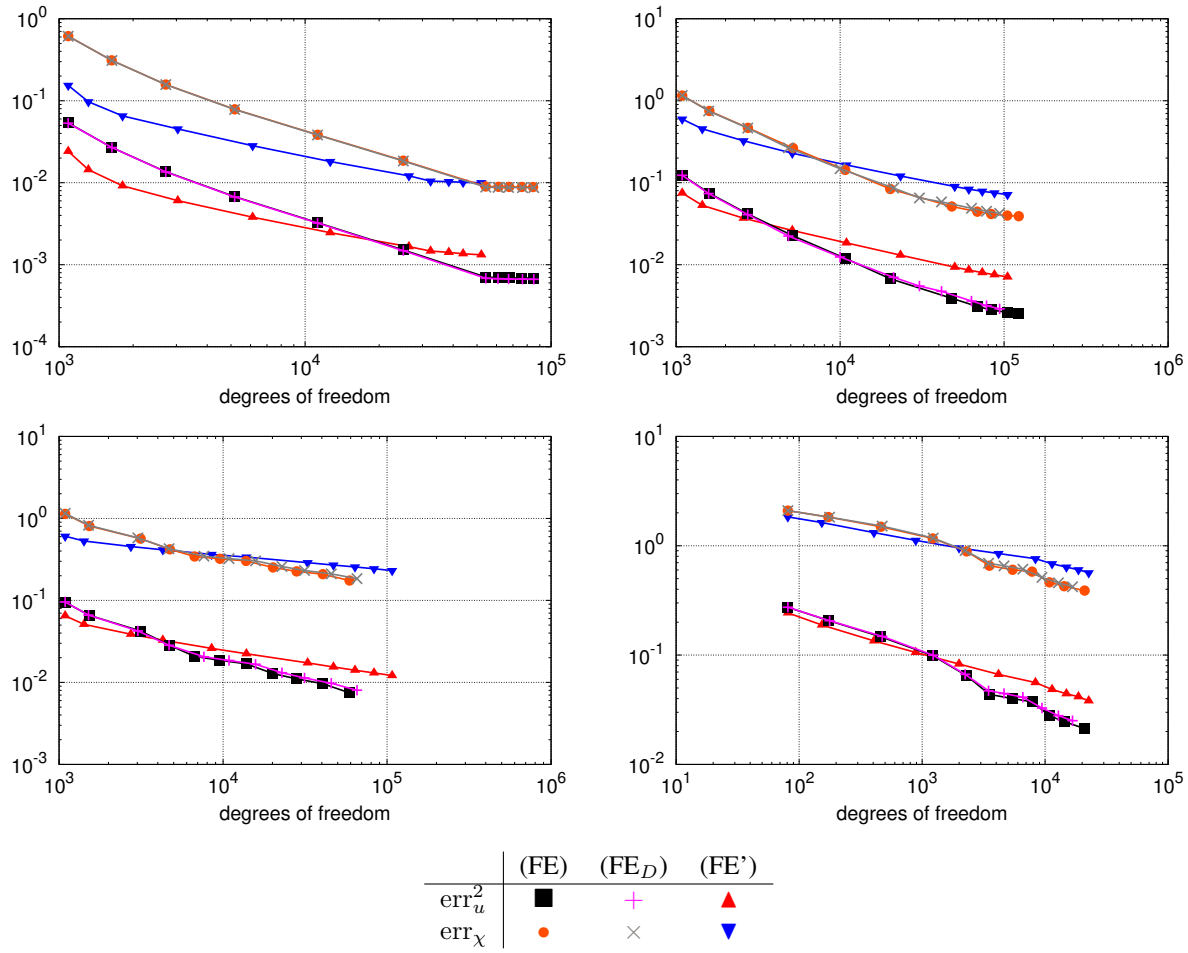

Figure 5.5: The values of err_u^2 and err_χ are displayed in relation to the number of degrees of freedom in a log-log plot for the images (a) (upper left), (b) (upper right), (c) (lower left) and (d) (lower right).

the input images (b) and (c) using the discretization schemes (FE) and (FD). We do not show the results for (FE$_D$) for any image since they are (almost) indistinguishable from the results for (FE).

Moreover, the mesh in the 5^{th} and 10^{th} iteration, the relaxed solutions $\bar{u}_h$, $[\bar{p}_h]_1$ and $[\bar{p}_h]_2$ as well as the thresholded solution $\bar{\chi}_h$ after 10 cycles of the algorithm for the input image (d) using the discretization (FE') are depicted in Figure 5.9.

Finally, the proposed discretization schemes were compared in terms of the relative CPU time for the images (b) and (d) in the last iteration. To enforce comparable conditions, the stopping criterion was set to $\|\mathbf{P}_h^k - \mathbf{P}_h^{k-1}\|_\infty < 10^{-6}$ and the primal and dual solution were initialized with constant values. In comparison with the discretization scheme (FE), the scheme (FE') required comparable CPU time (image (b): -6.7%, image (d): $+6.5\%$), whereas (FE$_D$) performed slower for larger images (image (b): $+30.4\%$, image (d): -0.1%).

The minimizers of the full as well as the binary Mumford–Shah model are in general not unique. A standard example for the non-uniqueness of both models is as follows (*cf.* [DS95]): let $\Omega = [0,1]^2$, $\lambda > 0$ and $u_0(x,y) = \lambda\chi[y > \frac{1}{2}]$. Then there exists a parameter $\lambda_{\text{full}} > 0$ such that for $\lambda = \lambda_{\text{full}}$ the full Mumford–Shah model (5.1) with $\alpha = \beta = 1$ admits the minimizers $u = u_0$ with the singular set $S_u = (0,1) \times \{\frac{1}{2}\}$ and $u(x,y) = \tilde{u}(y)$ with $\tilde{u} \in C^1(0,1)$. In the case of the binary model, the minimizers have the structure $\chi = \chi[y > \frac{1}{2}]$ or $\chi = \text{const.}$ provided that $\lambda = \lambda_{\text{binary}}$ for a suitable choice of $\lambda_{\text{binary}} > 0$. A further prominent counterexample for the non-uniqueness emerges from input images with a checkerboard pattern or, in its simplest form, input images with alternating intensities 0 and 1 on all quadrants (*cf.* upper left image in Figure 5.10). David [Dav05, Section A.5] examined the latter case for the full Mumford–Shah model and argued that even very small perturbations located

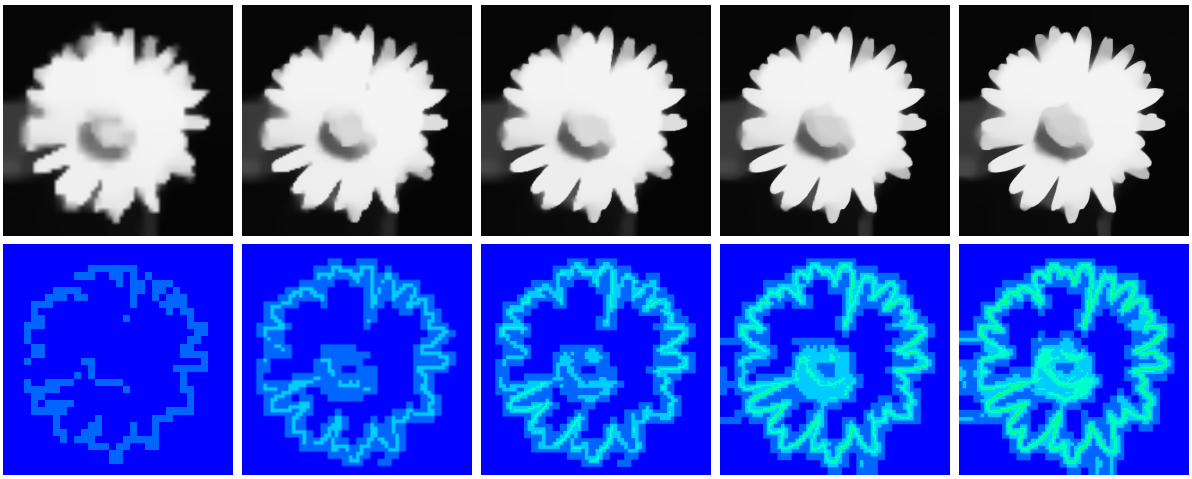

Figure 5.6: The sequence of solutions $\bar{u}_h$ (first row) and a color coding of the corresponding fineness of the adaptive meshes (second row) at the 1^{st}, 2^{nd}, 3^{rd}, 4^{th} and 5^{th} iteration of the adaptive algorithm applied to the input image (c) and computed using the (FE') discretization.

at the center of the image could lead to a topology change in the segmented solution ("butterfly effect"). In Figure 5.10, the sensitivity of the adaptive scheme w.r.t. the topology of the segmentation is investigated. To this end, we compute – using the scheme (FE) and 10 cycles of the adaptive scheme – the relaxed minimizers for two versions of the simple checkerboard pattern with a resolution of 2049×2049, fixed intensity values $c_1 = 1$, $c_2 = 0$ and a regularization parameter $\nu = 0.01$. In the first version, the four pixels in the center are set to black, in the second version these pixels are set to white. Although the relaxed solutions $\bar{u}_h$ associated with both versions are nearly indistinguishable (see second column of Figure 5.10) since each $\bar{u}_h$ is approximately $\frac{1}{2}$ in a neighborhood of the center (*cf*. third column), a change of the topology can be observed in the thresholded solutions (see fourth column). This experimentally proves that the proposed algorithm is capable of properly detecting topology changes. As a consequence of the non-uniqueness of the solutions and the sensitivity to small perturbations of the input image, a neighborhood of the center is contained in the set of non-properly identified phases $\mathcal{S}_{\bar{u}_h,\eta}$ even for small η. In particular, this results in a high local contribution of this neighborhood to the a posteriori error estimate err_χ.

Since subpixel refinement is prohibited, *i.e.* $h(\mathscr{C}) \geq 2^{-L_{\text{full}}}$ for every cell $\mathscr{C} \in \mathcal{M}_h$, the error estimators err_u^2 and err_χ have in general a strictly positive lower bound depending on the input image and the resolution, although we expect both estimators to converge to 0 as $h \to 0$. To further examine this asymptotic behavior, we apply the aforementioned methods to an analytic function consisting of the superposition of two Gaussian kernels. To this end, starting from an initial grid with a uniform mesh size $h = 2^{-4}$, we project the analytic function after each refinement step onto the uniform grid with mesh width $h_{\min}$ and evaluate the error estimators on the current adaptive grid, which allows an unlimited refinement of each cell. The results are shown in Figure 5.11 with parameters $c_1 = 0.495349$, $c_2 = 0.056845$ and $\nu = 5 \cdot 10^{-3}$ using the discretizations (FE) and (FE'). One observes that the quantities of the error estimators decay monotonically as expected. However, since the absolute values of the slopes of the functions $\{\#\text{degrees of freedom} \mapsto \operatorname{err}_u^2\}$ and $\{\#\text{degrees of freedom} \mapsto \operatorname{err}_\chi\}$ decline for larger numbers of degrees of freedom, a further significant decrease of the error estimators requires a much larger number of degrees of freedom at the expense of very long computation times.

In the final example, we analyze the applicability of the error estimator for varying intensity values (*cf*. p. 129). Figure 5.12 depicts the function plot $\varepsilon \mapsto \operatorname{err}_u^{2,\varepsilon}[\bar{u}_h, \bar{p}_h, c_1, c_2]$ with fixed primal $\bar{u}_h$ and dual solution $\bar{p}_h$ obtained with the discretization (FE) after the 10^{th} iteration for the images (b) and (c). One observes that the ε-perturbed error estimator for image (b) is less sensitive to small fluctuations in the intensity values compared to image (c) due to a stronger variation of image intensities along the interfaces in image (b). However, in both examples it turns out that the decrease of the functional a posteriori error estimator is not sufficient to compensate the amplification factor appearing in the definition of the updated bandwidth parameter (see (5.45) and (5.46)), which demonstrates that the a posteriori error estimator incorporating varying intensity values is not feasible for practical applications.

5.8 Conclusion and Outlook

In this chapter, we have developed a novel a posteriori error estimator for the binary Mumford–Shah model employing duality techniques and a suitable cut-out argument. In various numerical examples the applicability of this approach to real image data was demonstrated. The proposed method is capable of properly detecting interfacial structures of the input images and allows to compute a visually convincing binary segmentation of the images along with a substantial decrease in the number of degrees of freedom compared to the input image.

However, we essentially identified the following drawbacks of this approach: Although from a theoretical point of view one would expect functional error estimates with an arbitrarily small value, we have never observed error quantities – even in the case of analytic input data – substantially below 10^{-4} for the functional a posteriori error estimator err_u^2. Furthermore, the quantity of the a posteriori estimator err_χ strongly depends on the measure of the preimage set of a η-neighborhood of the threshold value $\frac{1}{2}$ and thus on the interfacial structure of the input image, which results in relatively large values of err_χ for input images that, for instance, exhibit strong local oscillations or noise. Moreover, although a theoretical scheme to derive error estimators for the binary model with varying intensity values is available, this scheme fails in the numerical applications. Finally, let us remark that the proposed method is restricted to the binary Mumford–Shah model and not suited for general multilabel segmentation problems unless a convex approximation of these problems is available.

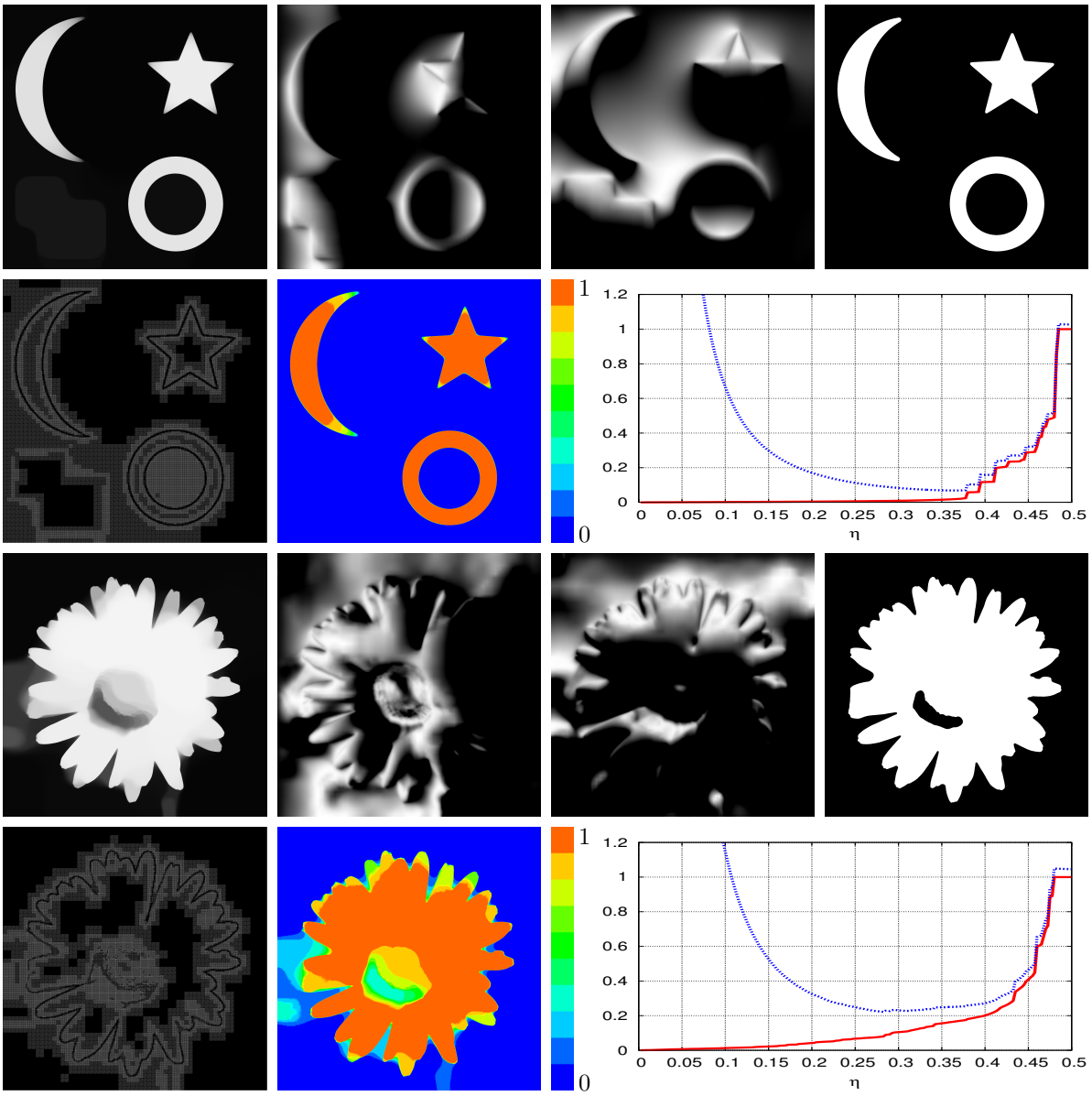

Figure 5.7: The relaxed solutions $\bar{u}_h$, $[\bar{p}_h]_1$, $[\bar{p}_h]_2$ and the resulting solutions $\bar{\chi}_h$ computed with the discretization scheme (FE') are shown after the 10^{th} iteration of the adaptive scheme for the images (b) (first row) and (c) (third row). In the second and fourth row, the adaptive grid (after the 6^{th} refinement step), deciles of the discrete solutions $\bar{u}_h$ encoded with different colors, and the functions $\eta \mapsto \mathcal{L}^2(\mathcal{S}_{\bar{u}_h,\eta})$ (red solid line) and $\eta \mapsto \operatorname{err}_\chi$ (blue dashed line) after the 10^{th} refinement step are visualized.

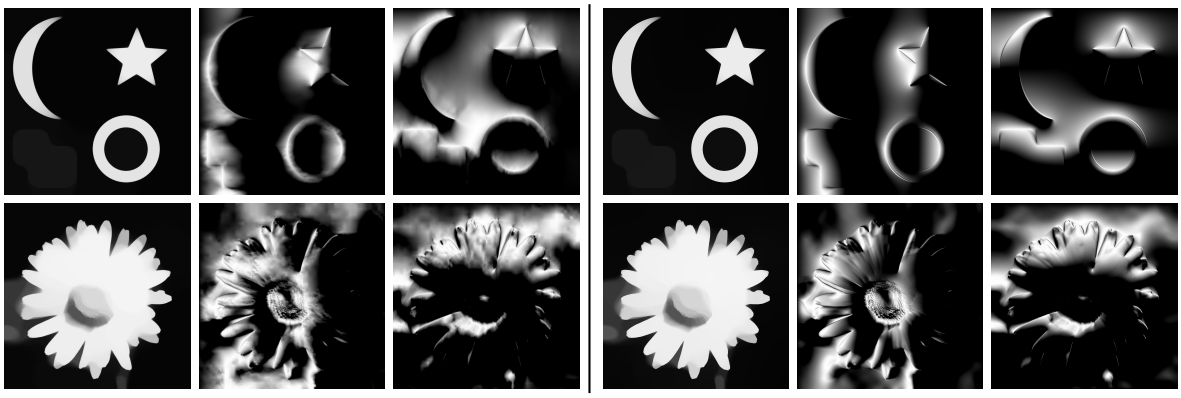

Figure 5.8: Relaxed solutions $\bar{u}_h$, $[\bar{p}_h]_1$, $[\bar{p}_h]_2$ for the input images (b) (top row) and (c) (bottom row) using the discretization schemes (FE) (left, after 10 cycles of the adaptive algorithm) and (FD) (right).

Figure 5.9: The mesh in the 5^{th} and 10^{th} iteration, the relaxed solutions $\bar{u}_h$, $[\bar{p}_h]_1$, $[\bar{p}_h]_2$ and the thresholded solution $\bar{\chi}_h$ for the input image (d) using the discretization (FE') after 10 cycles of the algorithm.

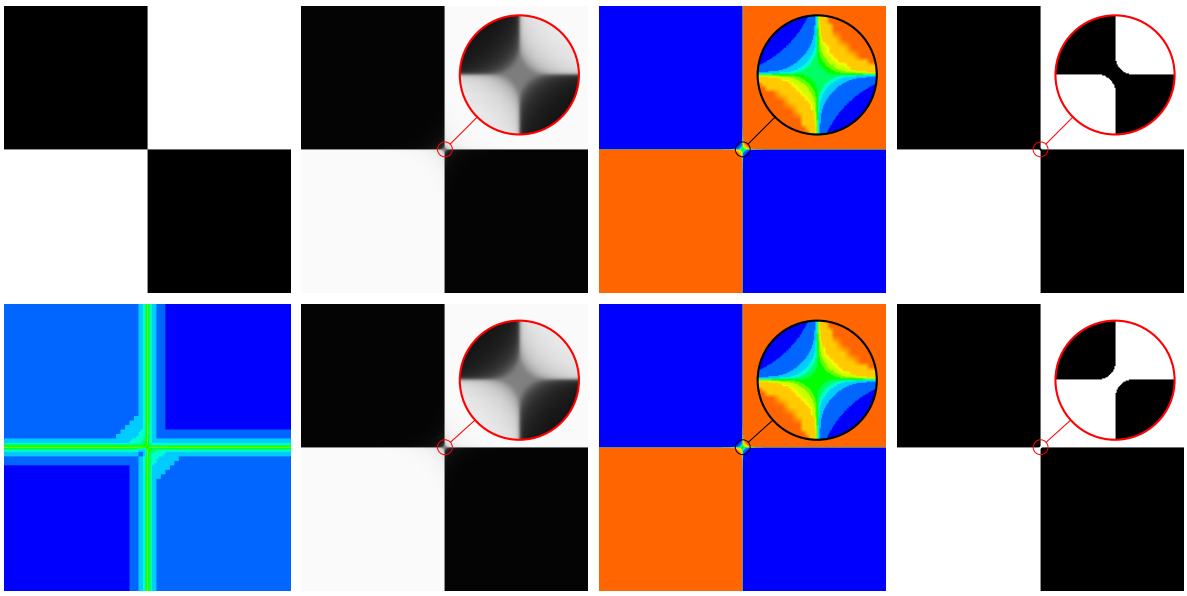

Figure 5.10: The original input image with a resolution of 2049×2049 and the adaptive mesh after the 6^{th} iteration with white pixels in the center of the input image (first column). Second to fourth column: the relaxed solutions $\bar{u}_h$ (with parameters $c_1 = 1$, $c_2 = 0$ and $\nu = 0.01$), the decile plots and the thresholded solutions $\bar{\chi}_h$ for black pixels (first row) and white pixels in the center (second row) along with the corresponding zoom of the centers (with zoom factor 8) after the 10^{th} iteration using the discretization (FE).

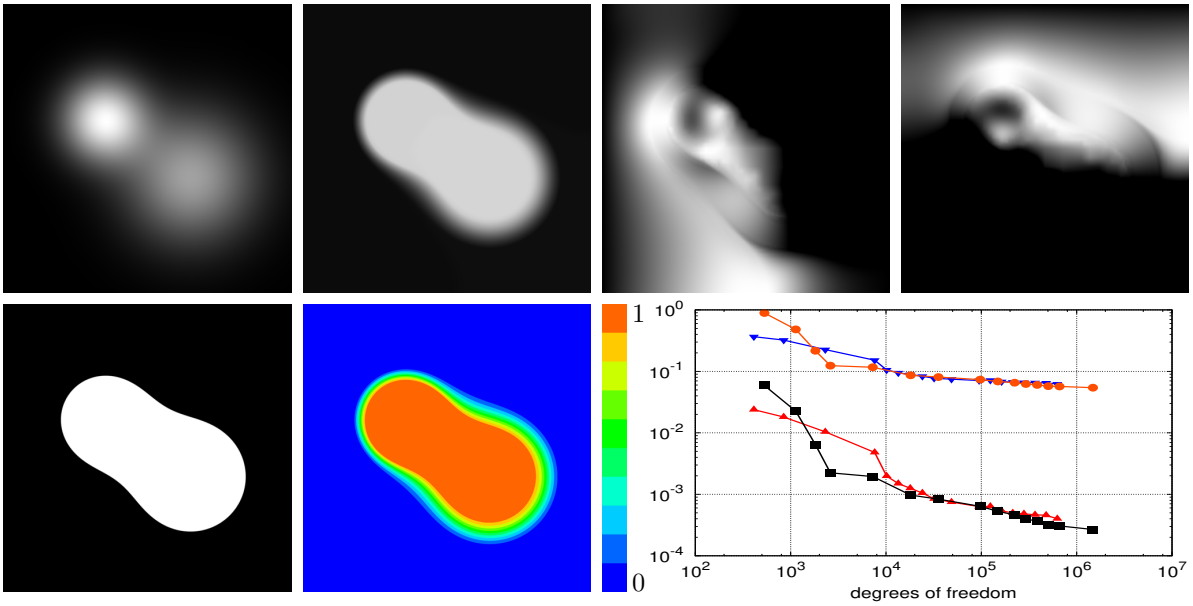

Figure 5.11: First row: Input image u_0 composed of the superposition of two Gaussian kernels, numerical solutions $\bar{u}_h$, $[\bar{p}_h]_1$ and $[\bar{p}_h]_2$ computed with the adaptive algorithm using the discretization scheme (FE') after the 15^{th} cycle. Second row: thresholded solution $\bar{\chi}_h$, deciles and the error estimators in a log-log plot (err_u^2 (▲), err_χ (▼) for the discretization (FE') and err_u^2 (■), err_χ (●) for the discretization (FE)) after the last iteration.

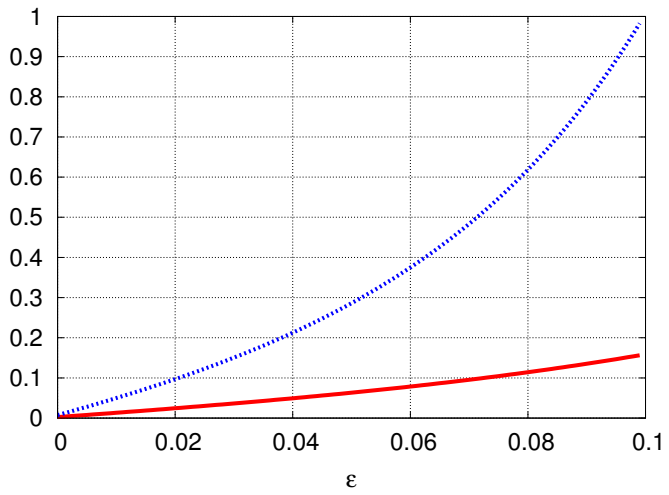

Figure 5.12: The function plot $\varepsilon \mapsto \mathrm{err}_u^{2,\varepsilon}$ for the images (b) (red solid line) and (c) (blue dashed line) using the discretization (FE) after the 10^{th} iteration.

Appendix A

Bibliography

[ABDM03] G. Alberti, G. Bouchitté, and G. Dal Maso. The calibration method for the Mumford-Shah functional and free-discontinuity problems. *Calc. Var. Partial Differential Equations*, 16 (3):299–333, 2003.

[ACC05] F. Alter, V. Caselles, and A. Chambolle. A characterization of convex calibrable sets in $\mathbb{R}^N$. *Math. Ann.*, 332(2):329–366, 2005.

[AF03] R. A. Adams and J. J. F. Fournier. *Sobolev spaces*, volume 140 of *Pure and Applied Mathematics (Amsterdam)*. Elsevier/Academic Press, Amsterdam, second edition, 2003.

[AFP00] L. Ambrosio, N. Fusco, and D. Pallara. *Functions of bounded variation and free discontinuity problems*. Oxford Mathematical Monographs. Oxford University Press, New York, 2000.

[AK98] V. Arnold and B. Khesin. *Topological methods in hydrodynamics*. Springer, 1998.

[Alt06] H. W. Alt. *Lineare Funktionalanalysis*. Springer Verlag, fifth edition, 2006.

[Amb89] L. Ambrosio. Variational problems in SBV and image segmentation. *Acta Appl. Math.*, 17:1–40, 1989.

[AP97] L. Ambrosio and D. Pallara. Partial regularity of free discontinuity sets I. *Annali della Scuola Normale Superiore di Pisa*, 24:1–38, 1997.

[Arn66] V. Arnold. Sur la géométrie différentielle des groupes de Lie de dimension infinie et ses applications à l'hydrodynamique des fluides parfaits. *Ann. Inst. Fourier (Grenoble)*, 16(1):319–361, 1966.

[AS53] W. Ambrose and I. M. Singer. A theorem on holonomy. *Trans. Amer. Math. Soc.*, 75:428–443, 1953.

[AT90] L. Ambrosio and V. M. Tortorelli. Approximation of functionals depending on jumps by elliptic functionals via Γ-convergence. *Comm. Pure Appl. Math.*, 43:999–1036, 1990.

[AT92] L. Ambrosio and V. M. Tortorelli. On the approximation of free discontinuity problems. *Bollettino dell'Unione Matematica Italiana, Sezione B*, 6(7):105–123, 1992.

[Att84] H. Attouch. *Variational convergence for functions and operators*. Applicable Mathematics Series. Pitman (Advanced Publishing Program), Boston, MA, 1984.

[Bal81] J. M. Ball. Global invertibility of Sobolev functions and the interpenetration of matter. *Proc. Roy. Soc. Edinburgh*, 88A:315–328, 1981.

[Bar12] S. Bartels. Total variation minimization with finite elements: convergence and iterative solution. *SIAM J. Numer. Anal.*, 50(3):1162–1180, 2012.

[Bar15] S. Bartels. Error control and adaptivity for a variational model problem defined on functions of bounded variation. *Math. Comp.*, 84(293):1217–1240, 2015.

[Bar16] S. Bartels. Broken Sobolev space iteration for total variation regularized minimization problems. *IMA J. Numer. Anal.*, 36(2):493–502, 2016.

[Bat99] G. K. Batchelor. *An introduction to fluid dynamics*. Cambridge Mathematical Library. Cambridge University Press, Cambridge, 1999.

[BB00] J.-D. Benamou and Y. Brenier. A computational fluid mechanics solution to the Monge-Kantorovich mass transfer problem. *Numer. Math.*, 84(3):375–393, 2000.

[BBE+17] B. Berkels, M. Buchner, A. Effland, M. Rumpf, and S. Schmitz-Valckenberg. GPU based image geodesics for optical coherence tomography. In *Bildverarbeitung für die Medizin*, Informatik aktuell, pages 68–73. Springer, 2017.

[BC94] G. Belletini and A. Coscia. Discrete approximation of a free discontinuity problem. *Num. Funct. Anal. Optim.*, 15:201–224, 1994.

[BC00] B. Bourdin and A. Chambolle. Implementation of an adaptive Finite-Element approximation of the Mumford-Shah functional. *Numer. Math.*, 85(4):609–646, 2000.

[BCB10] E. S. Brown, T. F. Chan, and X. Bresson. A convex relaxation method for a class of vector-valued minimization problems with applications to Mumford-Shah segmentation. Technical report, UCLA CAM Report 10-43, 2010.

[BCB11] E. S. Brown, T. F. Chan, and X. Bresson. Completely convex formulation of the Chan-Vese image segmentation model. *International Journal of Computer Vision*, 98:103–121, 2011.

[BDM97] A. Braides and G. Dal Maso. Non-local approximation of the Mumford-Shah functional. *Calc. Var.*, 5:293–322, 1997.

[Ber09] B. Berkels. An unconstrained multiphase thresholding approach for image segmentation. In *Proceedings of the Second International Conference on Scale Space Methods and Variational Methods in Computer Vision (SSVM 2009)*, volume 5567 of *Lecture Notes in Computer Science*, pages 26–37. Springer, 2009.

[Ber10] B. Berkels. *Joint methods in imaging based on diffuse image representations*. Dissertation, University of Bonn, 2010.

[BER15] B. Berkels, A. Effland, and M. Rumpf. Time discrete geodesic paths in the space of images. *SIAM J. Imaging Sci.*, 8(3):1457–1488, 2015.

[BER17] B. Berkels, A. Effland, and M. Rumpf. A posteriori error control for the binary Mumford-Shah model. *Math. Comp.*, 86(306):1769–1791, 2017.

[BEV+07] X. Bresson, S. Esedoḡlu, P. Vandergheynst, J.-P. Thiran, and S. Osher. Fast global minimization of the active contour/snake model. *J. Math. Imaging Vision*, 28(2):151–167, 2007.

[BEZ15] M. Burger, T. Esposito, and C. Zeppieri. Second-order edge-penalization in the Ambrosio-Tortorelli functional. *Multiscale Model. Simul.*, 13(4):1354–1389, 2015.

[BK89] R. Bajcsy and Kovačič. Multiresolution elastic matching. *Comput. Vision Graphics Image Process.*, 46(1):1–21, 1989.

[BKP10] K. Bredies, K. Kunisch, and T. Pock. Total generalized variation. *SIAM J. Imaging Sci.*, 3(3):492–526, 2010.

[BKS03] A. Brook, R. Kimmel, and N. A. Sochen. Variational restoration and edge detection for color images. *J. Math. Imag. and Vis.*, 18:247–268, 2003.

[BMS17] M. Bačák, M. Montag, and G. Steidl. Convergence of functions and their Moreau-Yosida envelopes on Hadamard spaces. Preprint, 2017.

[BMTY02] M. F. Beg, M. Miller, A. Trouvé, and L. Younes. Computational anatomy: Computing metrics on anatomical shapes. In *Proceedings of 2002 IEEE ISBI*, pages 341–344, 2002.

[BMTY05] M. F. Beg, M. I. Miller, A. Trouvé, and L. Younes. Computing large deformation metric mappings via geodesic flows of diffeomorphisms. *Inter. J. Comput. Vision*, 61(2):139–157, 2005.

[BNQ+09] S. Bertoluzza, R. H. Nochetto, A. Quarteroni, K. G. Siebert, and A. Veeser. Multiscale and adaptivity: Modeling, numerics and applications, 2009. C.I.M.E. Summer School (Lecture Notes).

[Bog07] V. I. Bogachev. *Measure theory. Vol. I*. Springer-Verlag, Berlin, 2007.

[Bon96] A. Bonnet. On the regularity of the edge set of Mumford-Shah minimizers. *Prog. in Nonlinear Differential Equations and Their Applications*, 25:93–103, 1996.

[Bou99] B. Bourdin. Image segmentation with a finite element method. *RAIRO - Modélisation mathématique et analyse numérique*, 33(2):229–244, 1999.

[BP13] S. Boyd and N. Parikh. Proximal algorithms. *Foundations and Trends in Optimization*, 1(3):123–231, 2013.

[BPC+10] S. Boyd, N. Parikh, E. Chu, B. Peleato, and J. Eckstein. Distributed optimization and statistical learning via the alternating direction method of multipliers. *Foundations and Trends in Machine Learning*, 3:1–122, 2010.

[Bra06] A. Braides. *A Handbook of Γ-Convergence*, volume III of *Handbook of differential equations: stationary partial differential equations*. Elsevier/North-Holland, Amsterdam, 2006.

[Bre67] L. M. Bregman. The relaxation method of finding the common point of convex sets and its application to the solution of problems in convex programming. *USSR Computational Mathematics and Mathematical Physics*, 7:200–217, 1967.

[BS08] S. C. Brenner and L. R. Scott. *The mathematical theory of finite element methods*, volume 15 of *Texts in Applied Mathematics*. Springer, New York, third edition, 2008.

[BS15a] K. Bredies and H. P. Sun. Preconditioned Douglas-Rachford algorithms for TV- and TGV-regularized variational imaging problems. *J. Math. Imaging Vision*, 52(3):317–344, 2015.

[BS15b] K. Bredies and H. P. Sun. Preconditioned Douglas-Rachford splitting methods for convex-concave saddle-point problems. *SIAM J. Numer. Anal.*, 53(1):421–444, 2015.

[BSS15] M. Burger, A. Sawatzky, and G. Steidl. First order algorithms in variational image processing, 2015. preprint.

[BT09] A. Beck and M. Teboulle. A fast iterative shrinkage-thresholding algorithm for linear inverse problems. *SIAM J. Imaging Sci.*, 2(1):183–202, 2009.

[BYT11] E. Bae, J. Yuan, and X.-C. Tai. Global minimization for continuous multiphase partitioning problems using a dual approach. *Int. J. Comput. Vis.*, 92(1):112–129, 2011.

[CCC+10] A. Chambolle, V. Caselles, D. Cremers, M. Novaga, and T. Pock. An introduction to total variation for image analysis. In *Theoretical foundations and numerical methods for sparse recovery*, volume 9 of *Radon Ser. Comput. Appl. Math.*, pages 263–340. Walter de Gruyter, Berlin, 2010.

[CCP12] A. Chambolle, D. Cremers, and T. Pock. A convex approach to minimal partitions. *SIAM J. Imaging Sci.*, 5(4):1113–1158, 2012.

[CCT16] N. Charon, B. Charlier, and A. Trouvé. Metamorphoses of functional shapes in Sobolev spaces. arXiv:1608.01832, 2016.

[CD09] A. Chambolle and J. Darbon. On total variation minimization and surface evolution using parametric maximum flows. *International Journal of Computer Vision*, 84(3):288–307, 2009.

[CDHR08] Y. Chen, T. A. Davis, W. W. Hager, and S. Rajamanickam. Algorithm 887: CHOLMOD, supernodal sparse Cholesky factorization and update/downdate. *ACM Trans. Math. Software*, 35(3):Art. 22, 14, 2008.

[CDM99] A. Chambolle and G. Dal Maso. Discrete approximation of the Mumford-Shah functional in dimension two. *M2AN Math. Model. Numer. Anal.*, 33(4):651–672, 1999.

[CEN06] T. F. Chan, S. Esedoḡlu, and M. Nikolova. Algorithms for finding global minimizers of image segmentation and denoising models. *SIAM J. Appl. Math.*, 66(5):1632–1648, 2006.

[CGT00] A. R. Conn, N. I. M. Gould, and P. L. Toint. *Trust-region methods*. MPS/SIAM Series on Optimization. Society for Industrial and Applied Mathematics (SIAM), Philadelphia, PA; Mathematical Programming Society (MPS), Philadelphia, PA, 2000.

[Cha95] A. Chambolle. Image segmentation by variatonal methods: Mumford-Shah functional and the discrete approximations. *SIAM J. Appl. Math.*, 55(3):827–863, 1995.

[Cha04] A. Chambolle. An algorithm for total variation minimization and applications. *J. Math. Imaging Vision*, 20(1-2):89–97, 2004.

[Cha05] A. Chambolle. Total variation minimization and a class of binary MRF models. In A. Rangarajan et al., editors, *Energy Minimization Methods in Computer Vision and Pattern Recognition*, volume 3757 of *LNCS*, pages 136–152. Springer, 2005.

[Cia88] P. G. Ciarlet. *Mathematical elasticity. Vol. I*, volume 20 of *Studies in Mathematics and its Applications*. North-Holland Publishing Co., Amsterdam, 1988. Three-dimensional elasticity.

[CKS97] V. Caselles, R. Kimmel, and G. Sapiro. Geodesic active contours. *International Journal of Computer Vision*, 22(1):61–79, 1997.

[CM87] P. H. Calamai and J. J. Moré. Projected gradient methods for linearly constrained problems. *Mathematical Programming*, 39:93–116, 1987.

[CM90] A. J. Chorin and J. E. Marsden. *A mathematical introduction to fluid mechanics*, volume 4 of *Texts in Applied Mathematics*. Springer-Verlag, New York, second edition, 1990.

[CP11] A. Chambolle and T. Pock. A first-order primal-dual algorithm for convex problems with applications to imaging. *J. Math. Imaging Vision*, 40(1):120–145, 2011.

[CP16] A. Chambolle and T. Pock. An introduction to continuous optimization for imaging. *Acta Numer.*, 25:161–319, 2016.

[CRM96] G. Christensen, R. D. Rabbitt, and M. I. Miller. Deformable templates using large deformation kinematics. *IEEE Transactions on Image Processing*, 5(10):1435–1447, 1996.

[CSM03] D. Cohen-Steiner and J.-M. Morvan. Restricted Delaunay triangulations and normal cycle. In *Proc. of Symposium on Computational Geometry*, pages 312–321, 2003.

[CV01a] T. F. Chan and L. A. Vese. Active contours without edges. *IEEE Transactions on Image Processing*, 10(2):266–277, 2001.

[CV01b] T. F. Chan and L. A. Vese. A level set algorithm for minimizing the Mumford-Shah functional in image processing. In *IEEE/Computer Society Proceedings of the 1st IEEE Workshop on Variational and Level Set Methods in Computer Vision*, pages 161–168, 2001.

[Dac08] B. Dacorogna. *Direct methods in the calculus of variations*, volume 78 of *Applied Mathematical Sciences*. Springer, New York, second edition, 2008.

[Dav96] G. David. C^1-arcs for minimizers of the Mumford-Shah functional. *SIAM J. Appl. Math.*, 56(3):783–888, 1996.

[Dav05] G. David. *Singular sets of minimizers for the Mumford-Shah functional*, volume 233 of *Progress in Mathematics*. Birkhäuser Verlag, Basel, 2005.

[DGCL89] E. De Giorgi, M. Carriero, and A. Leaci. Existence theorem for a minimum problem with free discontinuity set. *Arch. Rat. Mech. and Anal.*, 108:195–218, 1989.

[DGM98] P. Dupuis, U. Grenander, and M. I. Miller. Variational problems on flows of diffeomorphisms for image matching. *Quart. Appl. Math.*, 56:587–600, 1998.

[DM93] G. Dal Maso. *An introduction to* Γ*-convergence*. Progress in Nonlinear Differential Equations and their Applications, 8. Birkhäuser Boston, Inc., Boston, MA, Boston, 1993.

[DP98] T. De Pauw. On SBV dual. *Indiana Univ. Math. J.*, 47(1):99–121, 1998.

[DS95] G. David and S. Semmes. On a variational problem from image processing. In *Proceedings of the Conference in Honor of Jean-Pierre Kahane (Orsay, 1993)*, 1995.

[DV97] D. C. Dobson and C. R. Vogel. Convergence of an iterative method for total variation denoising. *SIAM J. Numer. Anal.*, 34(5):1779–1791, October 1997.

[DZ11] M. C. Delfour and J.-P. Zolésio. *Shapes and geometries*, volume 22 of *Advances in Design and Control*. Society for Industrial and Applied Mathematics (SIAM), Philadelphia, PA, second edition, 2011. Metrics, analysis, differential calculus, and optimization.

[EG92] L. Evans and R. Gariepy. *Measure Theory and Fine Properties of Functions*. CRC Press, 1992.

[ERS+15] A. Effland, M. Rumpf, S. Simon, K. Stahn, and B. Wirth. Bézier curves in the space of images. In *Proc. of International Conference on Scale Space and Variational Methods in Computer Vision*, volume 9087 of *Lecture Notes in Computer Science*, pages 372–384. Springer, Cham, 2015.

[ERS17a] A. Effland, M. Rumpf, and F. Schäfer. Image extrapolation for the time discrete metamorphosis model – existence and applications, 2017. submitted.

[ERS17b] A. Effland, M. Rumpf, and F. Schäfer. Time discrete extrapolation in a Riemannian space of images. In *Proc. of International Conference on Scale Space and Variational Methods in Computer Vision*, volume 10302, pages 473–485. Springer, Cham, 2017. Lecture Notes in Computer Science.

[ET99] I. Ekeland and R. Témam. *Convex analysis and variational problems*. Society for Industrial and Applied Mathematics, Philadelphia, PA, USA, 1999.

[FJMM03] G. Friesecke, R. D. James, M. G. Mora, and S. Müller. Derivation of nonlinear bending theory for shells from three-dimensional nonlinear elasticity by Gamma-convergence. *C. R. Math. Acad. Sci. Paris*, 336(8):697–702, 2003.

[FJSY09] M. Fuchs, B. Jüttler, O. Scherzer, and H. Yang. Shape metrics based on elastic deformations. *J. Math. Imaging Vision*, 35(1):86–102, 2009.

[FL07] I. Fonseca and G. Leoni. *Modern methods in the calculus of variations:* L^p *spaces*. Springer Monographs in Mathematics. Springer, New York, 2007.

[FLS16] J. H. Fitschen, F. Laus, and G. Steidl. Transport between RGB images motivated by dynamic optimal transport. *J. Math. Imaging Vision*, 56(3):409–429, 2016.

[FM00] I. Fonseca and C. Mantegazza. Second order singular perturbation models for phase transitions. *SIAM J. Math. Anal.*, 31(5):1121–1143, 2000.

[FM04] B. Fischer and J. Modersitzki. A unified approach to fast image registration and a new curvature based registration technique. *Linear Algebra Appl.*, 380:107–124, 2004.

[FP03] X. Feng and A. Prohl. Analysis of total variation flow and its finite element approximations. *M2AN Math. Model. Numer. Anal.*, 37(3):533–556, 2003.

[Fri13] H. Fritz. Isoparametric finite element approximation of Ricci curvature. *IMA J. Numer. Anal.*, 33(4):1265–1290, 2013.

[GBO12] T. Goldstein, X. Bresson, and S. Osher. Global minimization of Markov random fields with applications to optical flow. *Inverse Probl. Imaging*, 6(4):623–644, 2012.

[GGS10] F. Gazzola, H.-C. Grunau, and G. Sweers. *Polyharmonic boundary value problems*, volume 1991 of *Lecture Notes in Mathematics*. Springer-Verlag, Berlin, 2010. Positivity preserving and nonlinear higher order elliptic equations in bounded domains.

[GMS13] M. Grasmair, M. Muszkieta, and O. Scherzer. An approach to the minimization of the Mumford-Shah functional using Γ-convergence and topological asymptotic expansion. *Interfaces Free Bound.*, 15(2):141–166, 2013.

[GO09] T. Goldstein and S. Osher. The split Bregman method for L^1-regularized problems. *SIAM J. Imaging Sci.*, 2(2):323–343, 2009.

[GR64a] A. E. Green and R. S. Rivlin. Multipolar continuum mechanics. *Arch. Rat. Mech. Anal.*, 17:113–147, 1964.

[GR64b] A. E. Green and R. S. Rivlin. Simple force and stress multipoles. *Arch. Rat. Mech. Anal.*, 16:325–353, 1964.

[GT92] D. Gilbarg and N. S. Trudinger. *Elliptic partial differential equations of second order*. Classics in Mathematics. Springer-Verlag, Berlin, 1992.

[Han05] W. Han. *A Posteriori Error Analysis Via Duality Theory*, volume 8 of *Advances in Mechanics and Mathematics*. Springer, 2005.

[HB67] W. F. Hughes and J. A. Brighton. *Theory and problems of fluid dynamics*. Schaum Publishing, 1967.

[HJ90] R. A. Horn and C. R. Johnson. *Matrix analysis*. Cambridge University Press, Cambridge, 1990. Corrected reprint of the 1985 original.

[HJS+12] Y. Hong, S. Joshi, M. Sanchez, M. Styner, and M. Niethammer. Metamorphic geodesic regression. In *Proc. of International Conference on Medical Image Computing and Computer-Assisted Intervention*, volume 7512 of *Lecture Notes in Computer Science*, pages 197–205, 2012.

[HK04] M. Hintermüller and K. Kunisch. Total bounded variation regularization as a bilaterally constrained optimization problem. *SIAM J. Appl. Math.*, 64(4):1311–1333, 2004.

[HK14] S. Hencl and P. Koskela. *Lectures on mappings of finite distortion*, volume 2096 of *Lecture Notes in Mathematics*. Springer, Cham, 2014.

[HP11] K. Hildebrandt and K. Polthier. Generalized shape operators on polyhedral surfaces. *Comput. Aided Geom. Design*, 28(5):321–343, 2011.

[HPW06] K. Hildebrandt, K. Polthier, and M. Wardetzky. On the convergence of metric and geometric properties of polyhedral surfaces. *Geom. Dedicata*, 123:89–112, 2006.

[HRS+14] B. Heeren, M. Rumpf, P. Schröder, M. Wardetzky, and B. Wirth. Exploring the geometry of the space of shells. *Comput. Graph. Forum*, 33(5):247–256, 2014.

[HRS+16] B. Heeren, M. Rumpf, P. Schröder, M. Wardetzky, and B. Wirth. Splines in the space of shells. *Comput. Graph. Forum*, 35(5):111–120, 2016.

[HRWW12] B. Heeren, M. Rumpf, M. Wardetzky, and B. Wirth. Time-discrete geodesics in the space of shells. *Comput. Graph. Forum*, 31(5):1755–1764, 2012.

[HTY09] D. Holm, A. Trouvé, and L. Younes. The Euler-Poincaré theory of metamorphosis. *Quart. Appl. Math.*, 67:661–685, 2009.

[HZN09] G. L. Hart, C. Zach, and M. Niethammer. An optimal control approach for deformable registration. In *IEEE Computer Society Conference on Computer Vision and Pattern Recognition*, 2009.

[Jal14] K. Jalalzai. Discontinuities of the minimizers of the weighted or anisotropic total variation for image reconstruction. arXiv:1402.0026, 2014.

[JM00] S. C. Joshi and M. I. Miller. Landmark matching via large deformation diffeomorphisms. *IEEE Trans. Image Process.*, 9(8):1357–1370, 2000.

[Ken84] D. G. Kendall. Shape manifolds, Procrustean metrics, and complex projective spaces. *Bull. London Math. Soc.*, 16(2):81–121, 1984.

[KK14] Y. Kee and J. Kim. A convex relaxation of the Ambrosio-Tortorelli elliptic functionals for the Mumford-Shah functional. In *IEEE Conference on Computer Vision and Pattern Recognition*, 2014.

[Kli95] W. P. A. Klingenberg. *Riemannian geometry*, volume 1 of *de Gruyter Studies in Mathematics*. Walter de Gruyter & Co., Berlin, second edition, 1995.

[KMN00] A. Kheyfets, W. A. Miller, and G. A. Newton. Schild's ladder parallel transport procedure for an arbitrary connection. *Internat. J. Theoret. Phys.*, 39(12):2891–2898, 2000.

[KSMJ04] E. Klassen, A. Srivastava, W. Mio, and S. H. Joshi. Analysis of planar shapes using geodesic paths on shape spaces. *IEEE Trans. Pattern Anal. Mach. Intell.*, 26(3):372–383, 2004.

[KSNS07] E. Kalogerakis, P. Simari, D. Nowrouzezahrai, and K. Singh. Robust statistical estimation of curvature on discretized surfaces. In *Proc. of Eurographics Symposium on Geometry Processing*, pages 13–22, 2007.

[Lan95] S. Lang. *Differential and Riemannian Manifolds*, volume 160 of *Graduate Texts in Mathematics*. Springer-Verlag, New York, third edition, 1995.

[Lar96] C. J. Larsen. Proof of the Mumford-Shah conjecture for two shaded image segmentations. Technical report, Carnegie Mellon University, 1996.

[LDR95] H. Le Dret and A. Raoult. The nonlinear membrane model as variational limit of nonlinear three-dimensional elasticity. *J. Math. Pures Appl. (9)*, 74(6):549–578, 1995.

[LKY+09] J. Lellmann, J. Kappes, J. Yuan, F. Becker, and C. Schnörr. Convex multi-class image labeling by simplex-constrained total variation. In *Proceedings of the Second International Conference on Scale Space Methods and Variational Methods in Computer Vision (SSVM 2009)*, volume 5567 of *Lecture Notes in Computer Science*. Springer, 2009.

[Llo82] S. P. Lloyd. Least squares quantization in PCM. *IEEE Trans. Inform. Theory*, 28(2):129–137, 1982.

[LMOW04] A. Lew, M. Marsden, M. Oritz, and M. West. Variational time integrators. *Int. J. Numer. Meth. Engng*, 60:153–212, 2004.

[Mag04] J.-P. Magnot. Structure groups and holonomy in infinite dimensions. *Bull. Sci. Math.*, 128(6):513–529, 2004.

[MDSB02] M. Meyer, M. Desburn, P. Schröder, and A. H. Barr. Discrete differential-geometry operators for triangulated 2-manifolds. *VisMath*, 2002.

[MF03] J. Modersitzki and B. Fischer. Curvature based image registration. *J. Math. Imaging Vision*, 18(1):81–85, 2003.

[MH83] J. E. Marsden and T. J. R. Hughes. *Mathematical foundations of Elasticity*. Prentice–Hall, Englewood Cliffs, 1983.

[MM77] L. Modica and S. Mortola. Un esempio di Γ^--convergenza. *Boll. Un. Mat. Ital. B (5)*, 14(1):285–299, 1977.

[MM06] P. W. Michor and D. Mumford. Riemannian geometries on spaces of plane curves. *J. Eur. Math. Soc.*, 8(1):1–48, 2006.

[MM07] P. W. Michor and D. Mumford. An overview of the Riemannian metrics on spaces of curves using the Hamiltonian approach. *Appl. Comput. Harmon. Anal.*, 23(1):74–113, 2007.

[MO04] S. Müller and M. Ortiz. On the Γ-convergence of discrete dynamics and variational integrators. *J. Nonlinear Sci.*, 14(3):279–296, 2004.

[MOHR13] B. R. Munson, T. H. Okiishi, W. W. Huebsch, and A. P. Rothmayer. *Fundamentals of fluid mechanics*. Wiley, seventh edition, 2013.

[Mos69] U. Mosco. Convergence of convex sets and of solutions of variational inequalities. *Advances in Math.*, 3:510–585, 1969.

[MRSS15] J. Maas, M. Rumpf, C. Schönlieb, and S. Simon. A generalized model for optimal transport of images including dissipation and density modulation. *ESAIM Math. Model. Numer. Anal.*, 49(6):1745–1769, 2015.

[MS85] D. Mumford and J. Shah. Boundary detection by minimizing functionals. In *IEEE Conference on Computer Vision and Pattern Recognition*, 1985.

[MS89] D. Mumford and J. Shah. Optimal approximations by piecewise smooth functions and associated variational problems. *Comm. Pure Appl. Math.*, 42(5):577–685, 1989.

[MS95] J.-M. Morel and S. Solimini. *Variational methods in image segmentation*. Progress in Nonlinear Differential Equations and their Applications, 14. Birkhäuser Boston, Inc., Boston, MA, 1995.

[MTY02] M. I. Miller, A. Trouvé, and L. Younes. On the metrics and Euler-Lagrange equations of computational anatomy. *Annu. Rev. Biomed. Eng.*, 4(1):375–405, 2002.

[MTY06] M. I. Miller, A. Trouvé, and L. Younes. Geodesic shooting for computational anatomy. *J. Math. Imaging Vision*, 24(2):209–228, 2006.

[MTY15] M. I. Miller, A. Trouvé, and L. Younes. Hamiltonian systems and optimal control in computational anatomy: 100 years since D'Arcy Thompson. *Annu. Rev. Biomed. Eng.*, 17:447–509, 2015.

[MWS06] B. Massey and J. Ward-Smith. *Mechanics of Fluids*. Taylor & Francis, 2006.

[MY01] M. I. Miller and L. Younes. Group actions, homeomorphisms, and matching: a general framework. *Int. J. Comput. Vis.*, 41(1–2):61–84, 2001.

[Nir66] L. Nirenberg. An extended interpolation inequality. *Ann. Scuola Norm. Sup. Pisa*, 20:733–737, 1966.

[NŠ91] J. Nečas and M. Šilhavý. Multipolar viscous fluids. *Quart. Appl. Math.*, 49(2):247–265, 1991.

[OBJM11] S. Ober-Blöbaum, O. Junge, and J. E. Marsden. Discrete mechanics and optimal control: an analysis. *ESAIM Control Optim. Calc. Var.*, 17(2):322–352, 2011.

[OCBP14] P. Ochs, Y. Chen, T. Brox, and T. Pock. iPiano: inertial proximal algorithm for nonconvex optimization. *SIAM J. Imaging Sci.*, 7(2):1388–1419, 2014.

[ÖRW10] S. Özışık, B. Riviere, and T. Warburton. On the constants in inverse inequalities in L^2. Technical Report 10-19, Department of Computational & Applied Mathematics, Rice University, 2010.

[OS88] S. Osher and J. A. Sethian. Fronts propagating with curvature-dependent speed: algorithms based on Hamilton-Jacobi formulations. *J. Comput. Phys.*, 79(1):12–49, 1988.

[PCBC09] T. Pock, D. Cremers, H. Bischof, and A. Chambolle. An algorithm for minimizing the Mumford-Shah functional. In *IEEE 12th International Conference on Computer Vision*, 2009.

[PCBC10] T. Pock, D. Cremers, H. Bischof, and A. Chambolle. Global solutions of variational models with convex regularization. *SIAM J. Imaging Sci.*, 3(4):1122–1145, 2010.

[Pey15] G. Peyré. Entropic approximation of Wasserstein gradient flows. *SIAM J. Imaging Sci.*, 8(4):2323–2351, 2015.

[PM90] P. Perona and J. Malik. Scale-space and edge detection using anisotropic diffusion. *IEEE Transactions on Pattern Analysis and Machine Intelligence*, 12(7):629–639, 1990.

[Poc11] T. Pock. Diagonal preconditioning for first order primal-dual algorithms in convex optimization. In *IEEE International Conference on Computer Vision (ICCV)*, pages 1762 – 1769, 2011.

[PPO14] N. Papadakis, G. Peyré, and E. Oudet. Optimal transport with proximal splitting. *SIAM J. Imaging Sci.*, 7(1):212–238, 2014.

[Ray45] J. W. S. Rayleigh. *The Theory of Sound*. Dover Publications, New York, N. Y., second edition, 1945.

[RE55] R. S. Rivlin and J. L. Ericksen. Stress-deformation relations for isotropic materials. *J. Rational Mech. Anal.*, 4:323–425, 1955.

[Rep00] S. I. Repin. A posteriori error estimation for variational problems with uniformly convex functionals. *Math. Comp.*, 69(230):481–500, 2000.

[Rep12] S. I. Repin. On measures of errors for nonlinear variational problems. *Russian J. Numer. Anal. Math. Modelling*, 27(6):577–584, 2012.

[Roc97] R. T. Rockafellar. *Convex analysis*. Princeton Landmarks in Mathematics. Princeton University Press, Princeton, NJ, 1997. Reprint of the 1970 original, Princeton Paperbacks.

[ROF92] L. Rudin, S. Osher, and E. Fatemi. Nonlinear total variation based noise removal algorithms. *Physica D*, 60:259–268, 1992.

[RW09a] M. Rumpf and B. Wirth. An elasticity approach to principal modes of shape variation. In *Proc. of International Conference on Scale Space Methods and Variational Methods in Computer Vision*, volume 5567 of *Lecture Notes in Computer Science*, pages 709–720, 2009.

[RW09b] M. Rumpf and B. Wirth. A nonlinear elastic shape averaging approach. *SIAM J. Imaging Sci.*, 2(3):800–833, 2009.

[RW11] M. Rumpf and B. Wirth. Variational methods in shape analysis. In O. Scherzer, editor, *Handbook of Mathematical Methods in Imaging*, pages 1363–1401. Springer, 2011.

[RW13] M. Rumpf and B. Wirth. Discrete geodesic calculus in shape space and applications in the space of viscous fluidic objects. *SIAM J. Imaging Sci.*, 6(4):2581–2602, 2013.

[RW15] M. Rumpf and B. Wirth. Variational time discretization of geodesic calculus. *IMA J. Numer. Anal.*, 35(3):1011–1046, 2015.

[RY13] C. L. Richardson and L. Younes. Computing metamorphoses between discrete measures. *J. Geom. Mech.*, 5(1):131–150, 2013.

[RY16] C. L. Richardson and L. Younes. Metamorphosis of images in reproducing kernel Hilbert spaces. *Adv. Comput. Math.*, 42(3):573–603, 2016.

[Sak96] T. Sakai. *Riemannian Geometry*. Amer. Math. Soc., 1996.

[San15] F. Santambrogio. *Optimal transport for applied mathematicians*. Progress in Nonlinear Differential Equations and their Applications, 87. Birkhäuser/Springer, Cham, 2015. Calculus of variations, PDEs, and modeling.

[SC14] E. Strekalovskiy and D. Cremers. Real-time minimization of the piecewise smooth Mumford-Shah functional. In *Computer Vision – ECCV*, 2014.

[SCC06] F. R. Schmidt, M. Clausen, and D. Cremers. Shape matching by variational computation of geodesics on a manifold. In *Proc. of Conference on Pattern Recognition*, volume 4174 of *Lecture Notes in Computer Science*, pages 142–151. Springer, 2006.

[Sch11] O. Scherzer, editor. *Handbook of Mathematical Methods in Imaging*. Springer, 2011.

[She05] J. Shen. Γ-convergence approximation to piecewise constant Mumford-Shah segmentation. In *Proceedings of the 7th International Conference on Advanced Concepts for Intelligent Vision Systems (ACIVS 2005)*, volume 3708 of *Lecture Notes in Computer Science*, pages 499–506. Springer, 2005.

[SMSY11] G. Sundaramoorthi, A. Mennucci, S. Soatto, and A. Yezzi. A new geometric metric in the space of curves, and applications to tracking deforming objects by prediction and filtering. *SIAM J. Imaging Sci.*, 4(1):109–145, 2011.

[SYM07] G. Sundaramoorthi, A. Yezzi, and A. Mennucci. Sobolev active contours. *Int. J. Comput. Vis.*, 73(3):345–366, 2007.

[Tau95] G. Taubin. Estimating the tensor of curvature of a surface from a polyhedral approximation. In *Proc. of International Conference on Computer Vision*, pages 902–907, 1995.

[Tor16] M. Torres. On the dual of BV. Contemporary Mathematics, 2016. to appear.

[Tro95] A. Trouvé. An infinite dimensional group approach for physics based models in pattern recognition. In *International Journal of Computer Vision*, 1995.

[Tro98] A. Trouvé. Diffeomorphisms groups and pattern matching in image analysis. *International Journal of Computer Vision*, 28 (3):213–221, 1998.

[TY05a] A. Trouvé and L. Younes. Local geometry of deformable templates. *SIAM J. Math. Anal.*, 37(1):17–59, 2005.

[TY05b] A. Trouvé and L. Younes. Metamorphoses through Lie group action. *Found. Comput. Math.*, 5(2):173–198, 2005.

[TYW01] A. Tsai, A. Yezzi, and A. Willsky. Curve evolution implementation of the Mumford-Shah functional for image segmentation, denoising, interpolation, and magnification. *IEEE Transactions on Image Processing*, 10(8):1169–1186, 2001.

[VC02] L. Vese and T. F. Chan. A multiphase level set framework for image segmentation using the Mumford and Shah model. *International Journal of Computer Vision*, 50(3):271–293, 2002.

[VRRC12] F.-X. Vialard, L. Risser, D. Rueckert, and C. J. Cotter. Diffeomorphic 3D image registration via geodesic shooting using an efficient adjoint calculation. *International Journal of Computer Vision*, 97:229–241, 2012.

[VRRH12] F.-X. Vialard, L. Risser, D. Rueckert, and D. D. Holm. Diffeomorphic atlas estimation using geodesic shooting on volumetric images. *Annals of the BMVA*, 2012:1–12, 2012.

[VS09] F.-X. Vialard and F. Santambrogio. Extension to BV functions of the large deformation diffeomorphisms matching approach. *Comptes Rendus Mathematique*, 347:27–32, 2009.

[Wal35] A. Wald. Begründung einer koordinatenlosen Differentialgeometrie der Flächen. Ergebn. math. Kolloqu. Wien 7, 1935. pages 24–46.

[War83] F. W. Warner. *Foundations of differentiable manifolds and Lie groups*, volume 94 of *Graduate Texts in Mathematics*. Springer-Verlag, New York-Berlin, 1983. Corrected reprint of the 1971 edition.

[WBRS11] B. Wirth, L. Bar, M. Rumpf, and G. Sapiro. A continuum mechanical approach to geodesics in shape space. *Int. J. Comput. Vis.*, 93(3):293–318, 2011.

[Wei98] J. Weickert. *Anisotropic diffusion in image processing*. European Consortium for Mathematics in Industry. B. G. Teubner, Stuttgart, 1998.

[WL11] J. Wang and B. J. Lucier. Error bounds for finite-difference methods for Rudin-Osher-Fatemi image smoothing. *SIAM J. Numer. Anal.*, 49(2):845–868, 2011.

[YMSM08] L. Younes, P. W. Michor, J. Shah, and D. Mumford. A metric on shape space with explicit geodesics. *Atti Accad. Naz. Lincei Cl. Sci. Fis. Mat. Natur. Rend. Lincei (9) Mat. Appl.*, 19(1):25–57, 2008.

[You98] L. Younes. Computable elastic distances between shapes. *SIAM J. Appl. Math*, 58(2):565–586, 1998.

[You07] L. Younes. Jacobi fields in groups of diffeomorphisms and applications. *Q. Appl. Math*, pages 113–134, 2007.

[You10] L. Younes. *Shapes and diffeomorphisms*, volume 171 of *Applied Mathematical Sciences*. Springer-Verlag, Berlin, 2010.

[Zei95] E. Zeidler. *Applied functional analysis*, volume 109 of *Applied Mathematical Sciences*. Springer-Verlag, New York, 1995. Main principles and their applications.

[ZGFN08] C. Zach, D. Gallup, J.-M. Frahm, and M. Niethammer. Fast global labeling for real-time stereo using multiple plane sweeps. VMV, 2008.

[Zie89] W. P. Ziemer. *Weakly differentiable functions*, volume 120 of *Graduate Texts in Mathematics*. Springer-Verlag, New York, 1989.

[ZYHT07] L. Zhu, Y. Yang, S. Haker, and A. Tannenbaum. An image morphing technique based on optimal mass preserving mapping. *IEEE Trans. Image Process.*, 16(6):1481–1495, 2007.

Appendix B

Notation

General sets and related operations

$\mathbb{N}$	set of natural numbers, $\mathbb{N} = \{0, 1, 2, \ldots\}$
$\mathbb{N}^+$	set of positive natural numbers, $\mathbb{N}^+ = \{1, 2, 3, \ldots\}$
$\mathbb{Q}$	set of rational numbers
$\mathbb{R}$	set of real numbers
$\overline{\mathbb{R}}$	$\overline{\mathbb{R}} = \mathbb{R} \cup \{\infty\}$
$\mathbb{R}^+$	set of strictly positive real numbers
$\mathbb{R}_0^+$	set of non-negative real numbers
$\mathbb{C}$	set of complex numbers
$B_r(a)$	open ball of radius r around a w.r.t. underlying topology
$\overline{B_r}(a)$	closed ball of radius r around a w.r.t. underlying topology
$[f > c]$	for a measurable function $f : S \to \mathbb{R}$, $[f > c] = \{\, x \in S \,:\, f(x) > c \,\}$,
	the same applies to $[f \geq c]$, $[f = c]$, $[f \leq c]$ and $[f < c]$
S^c	complement of the set S
$\chi[S]$	characteristic function of the set S, *i.e.* $\chi[S](x) = 1$ if $x \in S$ and $\chi[S](x) = 0$ if $x \notin S$
$\mathbb{I}[S]$	indicator function of the set S, *i.e.* $\mathbb{I}[S](x) = \infty$ if $x \in S$ and $\mathbb{I}[S](x) = 0$ if $x \notin S$
$S' \Subset S$	S' is compactly contained in S
$S \Delta S'$	symmetric difference of S and S'

Measure and integration theory

n	outer normal
$\#(S)$	cardinality of the set S
$\lvert S \rvert = \mathcal{L}^n(S)$	n-dimensional Lebesgue measure of S
$\mathcal{H}^{n-1}$	$(n-1)$-dimensional Hausdorff-measure
$⨍_S$	$⨍_S f \,\mathrm{d}x = \frac{1}{\lvert S \rvert} \int_S f \,\mathrm{d}x$
H	Heaviside function, *i.e.* $\mathrm{H}(x) = 1$ if $x \geq 0$ and $\mathrm{H}(x) = 0$ if $x < 0$
$\delta[S]$	Dirac measure of S

Linear algebra

$\mathbb{1}$	identity mapping or identity matrix (depending on the context)
A^T	transpose of the matrix A
A^{sym}	symmetric part of the matrix A, *i.e.* $A^{\mathrm{sym}} = \frac{1}{2}(A + A^T)$
$\det$	determinant of matrix
tr	trace of a matrix, *i.e.* $\mathrm{tr}(A) = \sum_{i=1}^{n} a_{i,i}$ for $A = (a_{i,j})_{1 \le i,j \le n} \in \mathbb{R}^{n,n}$
cof	cofactor matrix, *i.e.* $\mathrm{cof}(A) = \det(A) A^{-T}$
$\|A\|_F$	Frobenius norm of the matrix A, *i.e.* $\|A\|_F = \sqrt{\mathrm{tr} A^T A}$
$\mathrm{GL}(n)$	group of invertible matrices in $\mathbb{R}^{n,n}$
$\mathrm{GL}^+(n)$	group of invertible matrices in $\mathbb{R}^{n,n}$ with positive determinant
$\mathrm{SL}(n)$	group of invertible matrices in $\mathbb{R}^{n,n}$ with determinant 1
$\mathrm{O}(n)$	group of orthogonal matrices in $\mathbb{R}^{n,n}$
$\mathrm{SO}(n)$	special orthogonal group, *i.e.* orthogonal matrices in $\mathbb{R}^{n,n}$ with determinant 1
$a \cdot b$	inner product of $a, b \in \mathbb{R}^n$
$a \times b$	cross product of $a, b \in \mathbb{R}^3$

Function spaces and differential geometry

$C^k(\Omega)$	space of k times continuously differentiable functions
$C^{k,\alpha}(\Omega)$	space of (k, α)-Hölder continuous functions
$L^p(\Omega)$	p-Lebesgue space on Ω with norm $\|\cdot\|_{L^p(\Omega)}$, $1 \le p \le \infty$
$W^{m,p}(\Omega)$	(m,p)-Sobolev space with norm $\|\cdot\|_{W^{m,p}(\Omega)}$ and seminorm $\|\cdot\|_{W^{m,p}(\Omega)}$, $1 \le p \le \infty$, $m \in \mathbb{N}$
$H^m(\Omega)$	$H^m(\Omega) = W^{m,2}(\Omega)$
$\mathrm{BV}(\Omega)$	space of functions with bounded variation
$\|\mathrm{D}f\|(\Omega)$	seminorm in the space $\mathrm{BV}(\Omega)$
$\mathrm{SBV}(\Omega)$	space of special functions with bounded variation
$\mathrm{GSBV}(\Omega)$	space of generalized special functions with bounded variation
$\rightharpoonup$	weak convergence w.r.t. the underlying topology
$\mathrm{osc}(f)$	oscillation of f, *i.e.* $\mathrm{osc}(f) = \sup_{x \in \Omega} f(x) - \inf_{x \in \Omega} f(x)$
$\mathcal{I}_h$	Lagrange interpolation operator
$\mathfrak{X}(\mathcal{M})$	the set of all smooth vector fields on a manifold $\mathcal{M}$
$\mathcal{F}(\mathcal{M})$	the set of all smooth scalar-valued functions on a manifold $\mathcal{M}$

Convex analysis

$\mathbf{V}'$	dual space of the function space $\mathbf{V}$
$\mathcal{L}(\mathbf{V}, \mathbf{W})$	set of all bounded linear operators from $\mathbf{V}$ to $\mathbf{W}$
$\langle v', v \rangle_{\mathbf{V}', \mathbf{V}}$	duality pairing of $v \in \mathbf{V}$ and $v' \in \mathbf{V}'$
J^*	Fenchel-conjugate of J
∂J	set of all subgradients of J
J'	Gâteaux derivative of J

Index